

The Stability of the Remnant Luminescence Emissions of Alkali Feldspar.

**Sally Anne Alexander
B.Sc. (Hons.), Cardiff**

Thesis presented for the degree of Doctor of Philosophy

University of Glasgow

Department of Geographical & Earth Sciences

November 2007

© Sally Alexander 2007



Abstract.

The stability of the remnant luminescence of an extensive and well characterised suite of alkali and plagioclase feldspars has been investigated using a wide variety of luminescence techniques. The commonly reported loss of stored charge from feldspars during dark storage, a process termed anomalous fading, has been a contentious issue within the field of luminescence dating for over thirty years. Models that have been proposed to account for this phenomenon have included disorder and substitutions within the feldspar crystal lattice, creation of populations of defects by radiation damage during burial and modification of defect populations by weathering. The aims of this research project were to test these and other models that have been proposed to predict the propensity of feldspars to fade.

The feldspars used in this study were extracted from a variety of well characterised igneous rocks (plutonic and minor intrusions and lavas), metamorphic rocks, sedimentary rocks and soils formed on granites. The effect of HF acid etching on signal stability was also investigated. These samples were coarsely crushed and feldspars separated for the manufacture of polished grain mounts that were used for characterisation of the chemical composition, microtexture, mineralogy and optical cathodoluminescence (CL) characteristics of the feldspar population in each sample. Following further crushing to 125-250µm the different feldspar minerals were separated from each other and from quartz using sodium polytungstate (SPT) heavy liquid techniques and the mineralogy of each powder was determined by X-ray mapping in the scanning electron microscope. Remnant luminescence measurements were carried out on these powders using the Risø multistimulation technique (employing in sequence infra-red stimulated luminescence (IRSL), optically stimulated luminescence (OSL) and thermoluminescence (TL)), the SUERC manual TL reader and the SUERC pulsed photostimulated luminescence (PPSL) reader. In addition to these conventional luminescence techniques a number of experimental methods were designed and constructed to explore specific aspects of luminescence behaviour including near-IR emission by TL stimulation and the lifetime of luminescence emission by high repetition PPSL with asynchronous measurements.

Results of the remnant luminescence work measurements showed that the signal in most of the laboratory irradiated feldspars samples was stable after two months of dark storage. This stability is partly a consequence of the preheating regime, which successfully emptied all of the thermally unstable traps. The only consistent levels of instability were in feldspars from metamorphic rocks and a syenite formed by hydrothermal alteration of a granite. Natural weathering and the HF acid etching used to simulate its effects did not enhance fading rates and in fact was very effective in

removing thermally unstable signals. A model developed from these results is that lattice strain can have a significant impact on the stability of stored charge, which was demonstrated by microtextural differences between fading and non-fading samples. This is an important conclusion as many of the models that have been developed to account for anomalous fading have a consequence for strain in the feldspar lattice. Regions of high lattice strain, such as the boundaries between alkali and plagioclase in perthitic intergrowths cause defects to cluster at these sites, which is a prerequisite for the currently accepted proximity models of fading. The long duration and low temperature preheat was used in conjunction with an additive dose procedure developed in this project to date samples as part of a large international archaeological project and the results produced were in agreement with external age controls.

Near-IR TL emissions were measurable from one of the alkali feldspar samples, but using the system developed within the project, luminescence from the sample was difficult to isolate from thermal background. The two PPSL systems, one detecting the blue emission and the other the near-IR were successful but signal intensities were low, due either to insufficient strength of the stimulation source or optical attenuation by over-filtration. Results of this study have provided important new information on the nature of defects associated with fading behaviour and geological/mineralogical controls on their presence within alkali feldspars and have also helped to outline a number of different avenues for technological solutions to the problem of anomalous fading.

Declaration.

The material presented in this thesis summarises the results of three years of independent research carried out at the Department of Geographical and Earth Sciences, University of Glasgow and the Scottish Universities Environmental Research Centre (SUERC), East Kilbride. The research was supervised by Dr. Martin Lee (University of Glasgow) and Dr. David Sanderson (SUERC).

This thesis is the result of my own research and any published or unpublished work of other researchers has been given full acknowledgement in the text.

A handwritten signature in black ink, appearing to read 'S Alexander', written in a cursive style.

Sally A. Alexander

November 2007.

Acknowledgements.

I would like to thank my supervisors Dr. Martin Lee and Dr. David Sanderson for their help and guidance throughout this project.

I would also like to thank the past and present geology post grads for supplying some much needed humour and moral support. In particular I would like to thank Kate and Davie for putting up with me for three and a half years and for sharing the belief that rugby really is that important. Aisling for taking me for beers and cocktails when I looked like I needed them. Dan and Jamie for taking me to the snow and reminding me that life really did exist away from the computer. Duncan for sharing those long weekends and late nights in the department and keeping me sane.

I would like to thank all the staff and students at GES and SUERC, in particular the wine tasters.

Many many thanks to the Physics group at EK (past and present) for being incredible. Thanks in particular to Lorna, Simon, Saffron, Colin, Iona, Rob, Jody, Chris and Alan.

I'd like to thank Kathy and Rona for getting me through the last year with your friendship and support.

I'd like to thank the members of the Johnstone SAC and all its friends for giving me great memories and great friends, in particular Christina, Graeme and Iona.

I'd like to thank Heather and Jenn for helping to keep me sane and for the care packages.

I'd like to give extra special thanks to my family for their unwavering love, support and belief through this projects entirety. Rona for being an unbelievable friend and 'landlady' and Martin for his incredible help, support and advice over the years and especially the last few months.

This research was made possible through an EPSRC grant.

Table of Contents.

Abstract.....i

Declaration.....iii

Acknowledgements.....iv

Table of Contents..... v

List of Figures..... xv

List of Tables.....xxii

Chapter 1: Introduction..... 1

1.1 Luminescence Phenomena. 1

1.2 Luminescence Dating..... 1

1.3 Estimated Dose (De).....2

1.4 Dose Rate.....3

1.4.1 The Importance of Luminescence Dating.3

1.5 Luminescence of Feldspars.4

1.5.1 Potential Importance in Luminescence Dating.....4

1.5.2 Feldspar Mineralogy.4

1.5.3 Mineralogical Controls on Feldspar Luminescence.8

1.6 Anomalous Fading of Feldspar Luminescence. 10

1.6.1 Variations in Anomalous Fading with Feldspar Mineralogy..... 10

1.7 Aims of this Study.....12

Chapter 2: The Theory of Luminescence and Anomalous Fading.....13

2.1 Introduction.....13

2.2 Luminescence.13

2.2.1 Luminescence Mechanisms.13

2.2.1.1 Traps and Recombination Centres.13

2.2.1.2 Trap Lifetimes.....16

2.3 A Brief Outline of the Evolution of the Field of Luminescence.....16

2.3.1 Historical Background.....17

2.3.2 Applications of Luminescence.....	18
2.3.2.1 Radiation Dosimetry.....	18
2.3.2.2 Age Determination.....	18
2.3.2.3 Geological Applications.....	18
2.3.3 The Emergence of PSL Techniques.	19
2.4 The Luminescence of Quartz.....	19
2.5 The Luminescence of Feldspar.....	20
2.5.1 Feldspar Crystal Structure and its Relation to Luminescence.....	21
2.6 Initial Observations of Anomalous Fading.	21
2.6.1 Anomalous Fading in the Dating Literature.....	22
2.6.1.1 Successes in Dating Using Feldspar Luminescence.	22
2.6.1.2 Unsuccessful Dating Studies Using Feldspar Luminescence....	23
2.6.2 Identifying Fading in Feldspars.....	24
2.6.2.1 Summary.	25
2.6.2.2 Variations in Signal Stability with Feldspar Mineralogy.....	26
2.6.2.2.1 Order Versus Disorder.....	26
2.6.2.2.2 Chemistry.....	27
2.6.3 Fading and the Proximity Models Used to Describe it.	28
2.6.3.1 The Localised Transition Model.	28
2.6.3.2 Quantum Mechanical Tunnelling.	29
2.6.3.2.1 Afterglow of Quantum Mechanical Tunnelling.	30
2.6.3.2.2 Thermal Assistance of Tunnelling.	31
2.6.3.3 Tunnelling and Non-radiative Stored Signal Loss.	32
2.6.4 Tunnelling Model at the Expense of Localised Transition.	33
2.6.4.1 Describing Fading Induced Decay of Luminescence Using t^{-1} ...	34
2.7 Solving the Problem of Anomalous Fading in Feldspars.	35
2.7.1 Circumvention Using the Near-IR Emission.....	35
2.7.1.1 Introduction.....	35
2.7.1.2 The Paris Group.....	36
2.7.1.3 Fattahi and Stokes.	38
2.7.1.3.1 IR-IRSL.	38
2.7.1.4 The Viability of the Near-IR Luminescence Emission.	38
2.7.2 Measurement Techniques and Correction Factors.....	39
2.7.2.1 Proposed Mathematical Correction Techniques.....	39
2.7.2.1.1 The Fadia Protocol.	39
2.7.2.1.2 The 'g' Method.	40
2.7.2.1.3 Dose Rate Correction.	41
2.7.2.2 Discussion.	41
2.8 Research Strategy.....	42

Chapter 3: Measurement Techniques and Instrumentation.....	44
3.1 Introduction.....	44
3.2 Selection and Characterisation of the Sample Set.....	44
3.2.1 Sample Selection.....	45
3.2.2 Sample Preparation 1.....	46
3.2.2.1 The GES Separation Technique.....	46
3.2.2.2 The SUERC Separation Technique.....	48
3.2.2.3 Sample Preparation for Characterisation.....	49
3.2.2.3.1 Polished Grain Mounts.	49
3.2.2.3.2 Powders.	49
3.2.3 Sample Characterisation by X-Ray Diffraction (XRD).	49
3.2.3.1 The XRD System Specification.....	49
3.2.3.2 Measurement Regime.....	49
3.2.4 Sample Characterisation Using the ESEM.	50
3.2.4.1 System Specification.....	50
3.2.4.2 Measurement Regime.....	50
3.2.5 Quantitative Chemical Analysis by Electron Microprobe.	50
3.2.5.1 System Specification.....	50
3.2.5.2 Measurement Regime.....	51
3.2.6 Optical CL Imaging.	51
3.2.6.1 System Specification.....	52
3.2.6.2 Measurement Regime.....	52
3.3 Remnant Luminescence.	53
3.3.1 The Stimulation Techniques.....	53
3.3.1.1 Historical Application of IRSL.....	54
3.3.1.2 Historical Application of OSL.	54
3.3.1.3 Historical Application of TL.....	55
3.3.1.4 Rationale for IR-TL Measurements.....	56
3.3.1.5 The Rationale for Pulsed PSL Measurements.	56
3.3.1.6 The Argument for Preheating.....	57
3.3.2 Sample Preparation for Luminescence Measurements.....	58
3.3.3 The Risø Daybreak Automatic Readers.....	59
3.3.3.1 System Specification.....	59
3.3.3.1.1 PMT Response and Optical Filtration.	59
3.3.3.2 Measurement Regime for the Multi-stimulation Risø Work.....	62
3.3.3.3 Data Analysis.....	63
3.3.4 The SUERC Manual Readers.	65
3.3.4.1 The ELSEC Irradiator.....	65
3.3.4.2 The SUERC PPSL System.....	65

3.3.4.2.1 System Specification.	65
3.3.4.2.2 PMT Response and Optical Filtration.	65
3.3.4.2.3 Measurement Regime.	69
3.3.4.3 Data Analysis.....	69
3.3.4.4 The SUERC TL System.	69
3.3.4.4.1 System Specification.	69
3.3.4.4.2 PMT Response and Optical Filtration.	70
3.3.4.4.3 Measurement Regime.	71
3.3.4.4.4 Data Analysis.	71
3.3.5 The Prototype IR-TL System.....	71
3.3.5.1 System Specification.....	71
3.3.5.2 PMT Response and Optical Filtration.	72
3.3.5.3 Measurement Regime.....	74
3.3.5.4 Data Analysis.....	74
3.4 Pulsed Photostimulated Luminescence (PPSL).....	74
3.4.1 The Blue PPSL System.	74
3.4.1.1 System Specification.....	74
3.4.1.2 PMT Response and Optical Filtration.	75
3.4.1.3 Overview of Measurement Regimes.....	77
3.4.2 The IR PPSL System.....	77
3.4.2.1 System Specification.....	77
3.4.2.2 PMT Response and Optical Filtration.	80
3.4.2.3 Overview of Measurement Regimes.....	82
3.5 Luminescence Dating.....	82
3.5.1 Overview of Current Dating Techniques.	82
3.5.1.1 Multiple Aliquot Techniques.	82
3.5.1.2 Single Aliquot Protocols.	84
3.5.1.3 SAAD Protocol.	84
3.6 The Adapted SARA Technique Used in this Study.	85
3.6.1 Sample Preparation for the adapted SARA Feldspar Dating.	85
Chapter 4: Mineralogy of the Sample Set.	88
4.1 Introduction.....	88
4.2 Feldspars from Slowly Cooled Plutonic Igneous Rocks.....	88
4.2.1 The Arran Granite (AG).	90
4.2.1.1 Feldspar Mineralogy, Microtexture and Composition.	90
4.2.2 The Ballater Granite (B).....	91
4.2.2.1 Feldspar Mineralogy, Microtexture and Composition.	92
4.2.2.2 Fresh Ballater Granite (B1).	92

4.2.2.3 Weathered Ballater Granite (B2).....	93
4.2.3 The Cairngorm Granite (CG).	93
4.2.3.1 Feldspar Mineralogy, Microtexture and Composition.	94
4.2.3.1.1 Fresh Cairngorm Granite (CG1).....	95
4.2.3.2 Weathered Cairngorm Granite (CG2).....	96
4.2.4 The Helmsdale Samples.....	96
4.2.4.1 Feldspar Mineralogy, Microtexture and Composition.	97
4.2.4.1.1 Helmsdale Granite (Helms).	97
4.2.4.1.2 Helmsdale Arkose (Ark).....	98
4.2.5 Peterhead Granite (GU3).....	99
4.2.5.1 Feldspar Mineralogy, Microtexture and Composition.	99
4.2.6 The Ross of Mull Granite.	100
4.2.6.1 Feldspar Mineralogy, Microtexture and Composition.	101
4.2.6.1.1 Ross of Mull Granite (H9).	101
4.2.6.1.2 Ross of Mull Granite (H10).	102
4.2.6.1.3 Ross of Mull Hydrothermal Syenite (H11).....	103
4.2.7 The Shap Granite.....	104
4.2.7.1 Feldspar Mineralogy, Microtexture and Composition.	105
4.2.7.1.1 Fresh Shap Granite (Ditlefsen).....	105
4.2.7.1.2 Unweathered Shap Granite (UWSH).	106
4.2.7.1.3 Weathered Shap Granite (WSH).....	107
4.2.7.1.4 HF Acid Etched Shap Granite.	108
4.2.8 Strontian Granodiorite (H8).	110
4.2.8.1.1 Feldspar Mineralogy, Microtexture and Composition. .	111
4.3 Silicic Minor Igneous Intrusions.	112
4.3.1 Feldspar Mineralogy, Microtexture and Composition.....	112
4.3.1.1 Bute Pitchstone Porphyry (H2).	113
4.3.1.2 Bute Pitchstone Porphyry (H3).	114
4.4 Igneous Calcic Plagioclase.	115
4.4.1 Connemara Gabbro Pegmatite (H1).	115
4.4.1.1 Feldspar Mineralogy, Microtexture and Composition.....	116
4.4.2 Troctolite Pegmatite and Anorthosite from Hallival (units 1-5), Rum....	117
4.4.2.1 Feldspar Mineralogy, Microtexture and Composition.	118
4.4.2.1.1 Rum Anorthosite (H5).....	118
4.4.2.1.2 Rum Troctolite Pegmatite (H7).....	119
4.5 Extrusive Igneous Rocks.....	119
4.5.1 Patmos Sanidine.....	120
4.5.1.1 Feldspar Mineralogy, Microtexture and Composition.	120
4.5.2 Etna Basaltic Lava (Etna).	121

4.5.2.1 Feldspar Mineralogy, Microtexture and Composition.....	122
4.6 Metamorphic Rocks.....	123
4.6.1 Glen Tarbert Migmatite (GU2).....	123
4.6.1.1 Feldspar mineralogy, Microtexture and Composition.....	124
4.6.2 Lewisian and Torridon Gneiss.....	125
4.6.2.1 Feldspar Mineralogy, Microtexture and Composition.....	125
4.6.2.1.1 Torridon Hornblende Gneiss (GU1).	126
4.6.2.1.2 Lewisian Gneiss (LG).	127
4.7 F1 Laboratory Standard.	127
4.7.1 Feldspar Mineralogy, Microtexture and Composition.....	128
4.8 The Problems with SPT Heavy Liquid Separation of Feldspars.	129
4.9 Summary.	131
Chapter 5: The Stability of the Remnant Luminescence of Alkali Feldspars.....	140
5.1 Introduction.....	140
5.2 Remnant luminescence results from dark storage.....	144
5.2.1 Plutonic Igneous and Associated Rocks.....	145
5.2.1.1 Discussion of Results.....	149
5.2.2 Silicic Minor Igneous Intrusions.....	150
5.2.2.1 Discussion of Results.....	151
5.2.3 Igneous Calcic Plagioclase.....	152
5.2.3.1 Discussion of Results.....	153
5.2.4 Extrusive Igneous Rocks.....	154
5.2.4.1 Discussion of Results.....	154
5.2.5 Metamorphic Rocks.....	155
5.2.5.1 Discussion of Results.....	156
5.2.6 The Laboratory Standard.....	157
5.2.6.1 Discussion of Results.....	157
5.2.7 Naturally Weathered Igneous.....	157
5.2.7.1 Discussion of the Influence of Weathering.	159
5.2.8 HF Acid Etched Igneous and Associated Rocks.....	161
5.2.8.1 Discussion of the Influence of HF Acid Etching.....	162
5.3 Testing Previous Models of Anomalous Fading in Feldspars.	163
5.3.1 Cooling Rate and Order-Disorder of Alkali Feldspars.....	163
5.3.2 Calcium Concentration of Plagioclase Feldspars.	164
5.3.3 Natural Weathering and Laboratory Etching.....	165
5.3.4 Geological age.....	166
5.4 Controls on Anomalous Fading in the Present Sample Set.....	167
5.4.1 The Impact on Fading Rates of Specific Stimulation Sources.....	167

5.4.2 Discussion of Results.	171
5.5 The Impact on Fading Rates of Specific Geological Variables.	172
5.5.1 Erosion and Deposition.....	172
5.5.2 Hydrothermal Alteration.....	173
5.5.3 Metamorphism.	173
5.6 The Influence of Preheating.....	174
5.6.1 Preheating Induced Anti-fading.	175
5.7 Discussion and Conclusions.	175
Chapter 6: Exploring Other Luminescence Techniques.....	178
6.1 Introduction.....	178
6.2 Near-IR TL.....	179
6.2.1 Introduction.	179
6.2.2 Results of Investigating the near-IR TL of Feldspars.....	180
6.2.2.1 Initial RTL Work on PMT and Filter Combinations.	180
6.2.3 Discussion.....	188
6.3 Pulsed Photostimulated Luminescence.....	189
6.3.1 Introduction.	189
6.3.2 Pulsed 'Blue' IRSL.	189
6.3.2.1 Equipment and Experimental Design.	190
6.3.2.2 Results.....	192
6.3.2.3 Discussion.	196
6.3.3 Pulsed 'Red' IRSL.....	196
6.3.3.1 Equipment and Experimental Design.	197
6.3.3.2 Results.....	201
6.3.3.2.1 Measuring Dose Dependence.....	201
6.3.3.2.2 Increase in Pulse Length to Increase Stimulation.....	203
6.3.3.2.3 The Affects of Preheating.	204
6.3.3.2.4 Stimulation to Bleach Luminescence-Pulse Length.....	206
6.3.3.2.5 Stimulation to Bleach Luminescence-Diode Number. .	208
6.3.3.2.6 Length of Measurement Cycle.....	210
6.3.3.3 Discussion.	211
6.4 Dating using feldspars.....	211
6.4.1 Introduction and Background Information.	211
6.4.2 Results.	212
6.4.2.1 Sample 1579.	212
6.4.2.2 Sample 1580.	214
6.4.2.3 Alpha Efficiency.....	215
6.4.2.4 Water Content, Fading and Dose Rate.....	215

6.4.2.5 Apparent Ages.....	215
6.4.3 Discussion.....	216
6.5 Al Versus SS Discs in Fine Grained Optical Dating.	218
6.5.1 Introduction.	218
6.5.2 Experimental Design.....	219
6.5.3 Results.	220
6.5.4 Discussion.....	220
6.5.5 Discussion.....	222
6.5.6 Conclusions of this Calibration Investigation.....	223
6.6 Conclusions.....	223
Chapter 7: Discussion.....	224
7.1 Introduction.....	224
7.2 The Mechanisms of Anomalous Fading in Alkali Feldspars.....	224
7.2.1 Tunnelling Models.....	224
7.2.2 Geological and Mineralogical Controls on Fading Behaviour.....	225
7.2.2.1 Geological Age.	225
7.2.2.2 Si,Al Order-Disorder.....	226
7.2.2.3 Lattice substitutions.....	228
7.2.2.4 Weathering.	229
7.3 Solutions to Anomalous Fading in Feldspars.	230
7.3.1 Using Conventional Measurement Systems.	230
7.3.2 Further Development of Experimental Measurement Techniques.	230
7.3.2.1 The Far Red Feldspar Emission and Related Techniques.	231
7.3.2.2 Mineralogical Controls and Atomic-scale Processes.	233
7.4 The Future of Feldspar Luminescence Dating.	236
References.....	238
Appendix A.	247
A.1 Introduction.	247
A.2 Plutonic Igneous and Associated Rocks.	248
A.2.1 Arran Granite.	248
A.2.2 Ballater Granite.....	249
A.2.3 Cairngorm Granite.....	250
A.2.4 Helmsdale Granite.....	251
A.2.5 Helmsdale Arkose.	253
A.2.6 Peterhead Granite.	255
A.2.7 Ross of Mull Granite.....	256
A.2.8 Ross of Mull Hydrothermal Syenite.....	259

A.2.9 Shap Granite.	261
A.2.9.1 Fresh Shap Granite.....	261
A.2.9.2 Unweathered Shap Granite.	262
A.2.10 Strontian Granodiorite.	264
A.3 Silicic Minor Igneous Intrusions.	265
A.3.1 Bute Pitchstone Porphyry.....	265
A.3.2 Canisp quartz-syenite.....	267
A.4 Igneous Calcic Plagioclase.....	269
A.4.1 Connemara Gabbro Pegmatite.	269
A.4.2 Rum Anorthosite.....	270
A.4.3 Rum Troctolite Pegmatite.....	271
A.5 Extrusive Igneous Rocks.	272
A.5.1 Patmos Sanidine.	272
A.5.2 Etna Basaltic Lava.....	274
A.6 Metamorphic Rocks.	275
A.6.1 Glen Tarbert Migmatite.....	275
A.6.2 Lewisian Gneiss.	277
A.6.3 Torridonian Hornblende Gneiss.	279
A.7 Naturally Weathered Igneous Rocks.....	280
A.7.1 Naturally Weathered Ballater Granite.	280
A.7.2 Naturally Weathered Cairngorm Granite.	282
A.7.3 Naturally Weathered Shap Granite.	283
A.8 HF Acid Etched Igneous and Associated Rocks.....	284
A.8.1 Shap Granite.	284
A.8.1.1 1 Minute HF Acid Etched.....	284
A.8.1.2 3 Minutes HF Acid Etched.	286
A.8.1.3 15 Minutes HF Acid Etched.	287
A.9 Laboratory Standard.	289
A.9.1 F1.....	289
Appendix B.	290
B.1 Introduction.	290
B.2 Plutonic Igneous and Associated Rocks.	291
B.2.1 Arran Granite.	291
B.2.2 Ballater Granite.....	293
B.2.3 Cairngorm Granite.....	295
B.2.4 Helmsdale Granite.....	297
B.2.5 Helmsdale Arkose.	298
B.2.6 Peterhead Granite.	299

B.2.7 Ross of Mull Granite.....	300
B.2.8 Ross of Mull Hydrothermal Syenite.....	303
B.2.9 Shap Granite.	305
B.2.10 Strontian Granodiorite.	306
B.3 Silicic Minor Igneous Intrusions.....	307
B.3.1 Pitchstone Porphyry.	307
B.3.2 Bute Pitchstone Porphyry (H3).....	308
B.3.3 Canisp Quartz-Syenite.	309
B.4 Igneous Calcic Plagioclase.....	311
B.4.1 Connemara Gabbro Pegmatite.	311
B.4.2 Rum Anorthosite.....	312
B.4.3 Rum Troctolite Pegmatite.....	313
B.5 Extrusive Igneous Rocks.	314
B.5.1 Patmos Sanidine.	314
B.5.2 Etna Basaltic Lava.....	315
B.6 Metamorphic Rocks.	316
B.6.1 Glen Tarbert Migmatite.....	316
B.6.2 Lewisian Gneiss.	317
B.6.3 Torridonian Hornblende Gneiss.	318
B.7 Naturally Weathered Igneous Rocks.....	320
B.7.1 Ballater Granite.....	320
B.7.2 Cairngorm Granite.....	322
B.7.3 Shap Granite.	324
B.8 Artificially Weathered Feldspars.....	325
B.8.1 Artificially Weathered Shap Granite.....	325
B.8.1.1 1 Minute HF Acid Etched.....	325
B.8.1.2 3 Minutes HF Acid Etched.	326
B.8.1.3 15 Minutes HF Acid Etched.	327
B.8.2 Artificially Weathered Helmsdale Arkose.....	328
B.8.2.1 1 Minute HF Acid Etched.....	328
B.8.2.2 3 Minutes HF Acid Etched.	329
B.8.2.3 15 Minutes HF Acid Etched.	330
B.8.3 Artificially Weathered Helmsdale Granite.	331
B.8.3.1 1 Minute HF Acid Etched.....	331
B.8.3.2 3 Minutes HF Acid Etched.	332
B.8.3.3 15 Minutes HF Acid Etched.....	333
B.9 Laboratory Standard.	334
B.9.1 F1.....	334

List of Figures.

Chapter 1:

Figure 1.1 Age range of luminescence dating with other chronological techniques.	2
Figure 1.2 Ternary diagrams for disordered and ordered ternary feldspars.	6
Figure 1.3 Image of Shap Granite. The alkali feldspar phenocrysts are pink.	6
Figure 1.4 Image of Shap Granite in plain polarised transmitted light.....	7
Figure 1.5 Schematic of a Shap Granite alkali feldspar's microtextures and defects.....	7
Figure 1.6 Emission spectra from orthoclase; phosphorescence, OSL and TL.....	9
Figure 1.7 Emission spectra from sanidine; phosphorescence, OSL and TL.	9
Figure 1.8 Stability diagram for the four polymorphs of K-feldspar..	11

Chapter 2:

Figure 2.1 Energy level diagram.....	14
Figure 2.2 Common electronic transitions in (crystalline) semiconductors and insulators.	15
Figure 2.3 Recombination by tunnelling.	29
Figure 2.4 Recombination by thermal tunnelling.....	30
Figure 2.5 Recombination via an excited state – the localised transition model.....	30
Figure 2.6 The one electron/ one hole model.	32
Figure 2.7 TL glow curves for a sanidine feldspar crystal from Eifel, Germany	37

Chapter 3:

Figure 3.1 Density ranges of Alkali feldspar, plagioclase and Quartz and SPT.....	47
Figure 3.2 Spectral response of an Electron Tubes 9235 PMT.....	60
Figure 3.3 Spectral transmittance of UG11 and the 9235B PMT.	60
Figure 3.4 Spectral response of BG39, GG395 and the 9814 PMT.....	66
Figure 3.5 Insert to adapt the SURRC PPSL system for disc measurements.	66
Figure 3.6 Spectral response of KG1, Corning 7-59 and the 9883 PMT.....	70
Figure 3.7 Spectral response of the Electron Tubes P25232-05 PMT.....	72

Figure 3.8 Spectral response of RG665, Corning 7-59 and P25232-05 PMT.....	72
Figure 3.9 Flanges and filter holders for the small red sensitive photodetector (A).....	73
Figure 3.10 Flanges and filter holders for the small red sensitive photodetector (B).....	73
Figure 3.11 Spectral Response of BG39 and 9883QB PMT.	75
Figure 3.12 Schematic of the cooled 'red' system.	78
Figure 3.13 The configuration of the experimental near-IR pulsed system.....	78
Figure 3.14 Efficiency of the cooled housing with cooling water temperature.	79
Figure 3.15 Typical spectral response of the Hamamatsu R2257 PMT.....	80
Figure 3.16 Spectral response of KG1, RG695, OG530, R2557 and IF stack.....	80
Figure 3.17 'Regenerative dose-response curve' (Aitken 1998)..	83
Figure 3.18 'Additive dose-Response curve' (Aitkin 1998).....	83

Chapter 4:

Figure 4.1 Mineralogy, microtexture and composition of AG1.....	91
Figure 4.2 Mineralogy, microtexture and composition of B1.....	92
Figure 4.3 Mineralogy, microtexture and composition of B2.....	93
Figure 4.4 Mineralogy, microtexture and composition of CG1.	95
Figure 4.5 Mineralogy, microtexture and composition of CG2.	96
Figure 4.6 Mineralogy, microtexture and composition of Helms.....	98
Figure 4.7 Mineralogy, microtexture and composition of Ark.....	99
Figure 4.8 Mineralogy, microtexture and composition of GU3.	100
Figure 4.9 Mineralogy, microtexture and composition of H9.	102
Figure 4.10 Mineralogy, microtexture and composition of H10.	103
Figure 4.11 Mineralogy, microtexture and composition of H11.	104
Figure 4.12 Mineralogy, microtexture and composition of fresh Shap.	105
Figure 4.13 Mineralogy, microtexture and composition of unweathered Shap.	106
Figure 4.14 Mineralogy, microtexture and composition of weathered Shap.	107
Figure 4.15 Mineralogy, microtexture and composition of 1 minute etched Shap.	108
Figure 4.16 Mineralogy, microtexture and composition of 3 minute etched Shap.	109
Figure 4.17 Mineralogy, microtexture and composition of 15 minute Shap.	109

Figure 4.18 Mineralogy, microtexture and composition of H8.	111
Figure 4.19 Mineralogy, microtexture and composition of H2.	113
Figure 4.20 Mineralogy, microtexture and composition of H3.	114
Figure 4.21 Mineralogy, microtexture and composition of H4.	115
Figure 4.22 Mineralogy, microtexture and composition of H1.	117
Figure 4.23 Mineralogy, microtexture and composition of H5.	118
Figure 4.24 Mineralogy, microtexture and composition of H7.	119
Figure 4.25 Mineralogy, microtexture and composition of Patmos sanidine.....	121
Figure 4.26 Mineralogy, microtexture and composition of Etna	123
Figure 4.27 Mineralogy, microtexture and composition of GU2.	124
Figure 4.28 Mineralogy, microtexture and composition of GU1.	126
Figure 4.29 Mineralogy, microtexture and composition of Lewisian gneiss.	127
Figure 4.30 Mineralogy, microtexture and composition of the F1 standard.	128
Figure 4.31 Levels of SPT success in obtaining clean feldspar separates.	130
Figure 4.32 Backscattered electron ESEM images of grain separates.	131

Chapter 5:

Figure 5.1 Stability diagram for the samples used in this study..	144
Figure 5.2. Secondary electron ESEM images of Shap Granite alkali feldspars	159

Chapter 6:

Figure 6.1 Spectral response of the PMT and the various filters used in this study	181
Figure 6.2 Emission from F1 with no optical filtration.	183
Figure 6.3 Emission from F1 filtered with UG11 and GG420.	184
Figure 6.4 F1 dose dependence with UG11 and OG590..	185
Figure 6.5 F1 dose dependence with UG11 and the stack of 1mm interference filters ...	186
Figure 6.6 The typical Spectral Response of BG39 (1mm) and 9883QB PMT.....	190
Figure 6.7 Time dependence of signal loss..	193
Figure 6.8 Dose dependence study with 1kgy, 100Gy, and 10Gy F1 discs.....	202
Figure 6.9 Increasing pulse length to increase stimulation power.	204

Figure 6.10 Phosphorescence Vs. luminescence.....	205
Figure 6.11 Pulse length Vs. Bleaching (A).	206
Figure 6.12 Pulse length Vs. Bleaching (B)..	207
Figure 6.13 Pulse length Vs. Bleaching (C)..	208
Figure 6.14 Pulse length Vs. Bleaching (D).	209
Figure 6.15 50Gy F1 disc, 1 μ s pulse and a 200ns dwell time.	210
Figure 6.16 Aluminium (a) and Stainless Steel (b) De values for 1579.....	213
Figure 6.17 Aluminium (a) and Stainless Steel (b) De values for 1580.....	214
Figure 6.18 NERC EFCHED estimated doses.....	217
Figure 6.19 Results of fading tests conducted as part of the NERC EFCHED project....	218

Chapter 7:

Figure 7.1 Map showing geological Vs. fading domains in northern North America.....	225
---	-----

Appendix A:

Figure A.1 Arran granite – probe analysis results.....	248
Figure A.2 Ballater granite – probe analysis results.	249
Figure A.3 Cairngorm granite – probe analysis results.....	250
Figure A.4 Helmsdale granite – probe analysis results.....	251
Figure A.5 Helmsdale granite – probe analysis points.....	252
Figure A.6 Helmsdale arkose – probe analysis results.....	253
Figure A.7 Helmsdale Arkose – probe analysis results.	254
Figure A.8 Peterhead granite – probe analysis results.....	255
Figure A.9 Ross of Mull granite (H9) – probe analysis results.	256
Figure A.10 Ross of Mull granite (H10) – probe analysis points.	257
Figure A.11 Ross of Mull granite (H10) – probe analysis results.	258
Figure A.12 Ross of Mull hydrothermal syenite – probe analysis results.....	259
Figure A.13 Ross of Mull hydrothermal syenite – probe analysis results.....	260
Figure A.14 Fresh Shap granite – probe analysis results.....	261
Figure A.15 Unweathered Shap granite – probe analysis results.	262

Figure A.16 Unweathered Shap granite – probe analysis points.	263
Figure A.17 Strontian granodiorite – probe analysis results.	264
Figure A.18 Bute Pitchstone porphyry (H2) – probe analysis results.	265
Figure A.19 Bute Pitchstone porphyry – probe data results.	266
Figure A.20 Canisp quartz-syenite – probe analysis results.	267
Figure A.21 Canisp quartz-syenite – probe analysis results.	268
Figure A.22 Connemara gabbro pegmatite – probe analysis results.	269
Figure A.23 Rum anorthosite – probe analysis results.	270
Figure A.24 Rum troctolite pegmatite – probe analysis results.	271
Figure A.25 Patmos sanidine - probe analysis points.	272
Figure A.26 Patmos sanidine – probe analysis results.	273
Figure A.27 Etna basaltic lava – probe analysis results.	274
Figure A.28 Glen Tarbert migmatite – probe analysis results.	275
Figure A.29 Glen Tarbert migmatite – probe analysis results.	276
Figure A.30 Lewisian gneiss – probe analysis results.	277
Figure A.31 Lewisian gneiss – probe analysis results.	278
Figure A.32 Torridonian hornblende gneiss – probe analysis results.	279
Figure A.33 Ballater granite – probe analysis results.	280
Figure A.34 Weathered Ballater granite – probe analysis points.	281
Figure A.35 Weathered Cairngorm granite – probe analysis results.	282
Figure A.36 Weathered Shap granite – probe analysis results.	283
Figure A.37 1 minute HF acid etched shap granite – probe analysis results.	284
Figure A.38 1 minute HF acid etched shap granite – probe analysis results.	285
Figure A.39 3 minutes HF acid etched Shap granite - probe analysis results.	286
Figure A.40 15 minute HF acid etched Shap granite – probe analysis results.	287
Figure A.41 15 minute HF acid etched Shap granite – probe analysis results.	288
Figure A.42 F1 – probe analysis results.	289

Appendix B:

Figure B.1 Risø IRSL (a), OSL (b), TL (c), Manual TL (d), PPSL (e) for AG1 (A).....	291
---	-----

Figure B.2 Risø IRSL (a), OSL (b), TL (c), Manual TL (d), PPSL (e) for AG1 (B).....	292
Figure B.3 Risø IRSL (a), OSL (b), TL (c), Manual TL (d), PPSL (e) for B1 (A).	293
Figure B.4 Risø IRSL (a), OSL (b), TL (c), Manual TL (d), PPSL (e) for B2 (B).	294
Figure B.5 Risø IRSL (a), OSL (b), TL (c), Manual TL (d), PPSL (e) for CG1 (A).	295
Figure B.6 Risø IRSL (a), OSL (b), TL (c), Manual TL (d), PPSL (e) for CG1 (B).	296
Figure B.7 Risø IRSL (a), OSL (b) and TL (c) for Helms.....	297
Figure B.8 Risø IRSL (a), OSL (b) and TL (c) for Ark.	298
Figure B.9 Risø IRSL (a), OSL (b), TL (c), Manual TL (d), PPSL (e) for GU3.	299
Figure B.10 Risø IRSL (a), OSL (b), TL (c), Manual TL (d), PPSL (e) for H9 (A)	300
Figure B.11 Risø IRSL (a), OSL (b), TL (c), Manual TL (d), PPSL (e) for H9 (B)	301
Figure B.12 Risø IRSL (a), OSL (b), TL (c), Manual TL (d), PPSL (e) for H10.	302
Figure B.13 Risø IRSL (a), OSL (b), TL (c), Manual TL (d), PPSL (e) for H11 (A).	303
Figure B.14 Risø IRSL (a), OSL (b), TL (c), Manual TL (d), PPSL (e) for H11 (B).	304
Figure B.15 Risø IRSL (a), OSL (b) and TL (c) for Shap.....	305
Figure B.16 Risø IRSL (a), OSL (b), TL (c), Manual TL (d), PPSL (e) for H8.	306
Figure B.17 Risø IRSL (a), OSL (b), TL (c), Manual TL (d), PPSL (e) for H2.	307
Figure B.18 Risø IRSL (a), OSL (b), TL (c), Manual TL (d), PPSL (e) for H3	308
Figure B.19 Risø IRSL (a), OSL (b), TL (c), Manual TL (d), PPSL (e) for H4 (A).	309
Figure B.20 Risø IRSL (a), OSL (b), TL (c), Manual TL (d), PPSL (e) for H4 (B).	310
Figure B.21 Risø IRSL (a), OSL (b), TL (c), Manual TL (d), PPSL (e) for H1.	311
Figure B.22 Risø IRSL (a), OSL (b), TL (c), Manual TL (d), PPSL (e) for H5.	312
Figure B.23 Risø IRSL (a), OSL (b), TL (c), Manual TL (d), PPSL (e) for H7.	313
Figure B.24 Risø IRSL (a), OSL (b) and TL (c) for Patmos sanidine	314
Figure B.25 Risø IRSL (a), OSL (b) and TL (c) for Etna.....	315
Figure B.26 Risø IRSL (a), OSL (b), TL (c), Manual TL (d), PPSL (e) for GU2	316
Figure B.27 Risø IRSL (a), OSL (b) and TL (c) for Lewisian gneiss.....	317
Figure B.28 Risø IRSL (a), OSL (b), TL (c), Manual TL (d), PPSL (e) for GU1 (A).	318
Figure B.29 Risø IRSL (a), OSL (b), TL (c), Manual TL (d), PPSL (e) for GU1 (B)	319
Figure B.30 Risø IRSL (a), OSL (b), TL (c), Manual TL (d), PPSL (e) B2 (A).....	320
Figure B.31 Risø IRSL (a), OSL (b), TL (c), Manual TL (d), PPSL (e) for B2 (B).	321

Figure B.32 Risø IRSL (a), OSL (b), TL (c), Manual TL (d), PPSL (e) for the CG2 (A) ...	322
Figure B.33 Risø IRSL (a), OSL (b), TL (c), Manual TL (d), PPSL (e) for CG2 (B)	323
Figure B.34 Risø IRSL (a), ROSL (b) and TL (c) for weathered Shap.	324
Figure B.35 Risø IRSL (a), OSL (b) and TL (c) for 1 min Shap.	325
Figure B.36 Risø IRSL (a), OSL (b) and TL (c) for 3 min Shap.	326
Figure B.37 Risø IRSL (a), OSL (b) and TL (c) for 15 min Shap.	327
Figure B.28 Risø IRSL (a), OSL (b) and TL (c) for 1 min Ark.	328
Figure B.39 Risø IRSL (a), OSL (b) and TL (c) for 3 min Ark.	329
Figure B.40 Risø IRSL (a), OSL (b) and TL (c) for 15 min Ark.	330
Figure B.41 Risø IRSL (a), OSL (b) and TL (c) for 1 min Helms.	331
Figure B.42 Risø IRSL (a), OSL (b) and TL (c) for 3 min Helms.	332
Figure B.43 Risø IRSL (a), OSL (b) and TL (c) for 15 min Helms.	333
Figure B.44 Risø IRSL (a), OSL (b) and TL (c) for F1.	334

List of Tables.

Chapter 3:

Table 3.1 The sample set, reference numbers and locality	45
Table 3.2 Electron microprobe quantitative analysis detection and calibration standards.	51
Table 3.3 Luminescence emission characterised by stimulation source.....	52
Table 3.4 The systems used and the luminescence measurements made with them.....	53
Table 3.5 Optical attenuation by optical filtration and the Risø Daybreak PMT.....	61
Table 3.6 PSL settings for the Risø sequences.....	63
Table 3.7 Optical attenuation by optical filtration and the SUERC Manual PPSL PMT	67
Table 3.8 Optical attenuation by optical filtration and the SUERC Manual TL PMT	68
Table 3.9 Optical attenuation by optical filtration and the SUERC IR-TL PMT.	74
Table 3.10 Optical attenuation by optical filtration and the SUERC blue-PPSL PMT.....	76
Table 3.11 Optical attenuation by optical filtration and the SUERC IR-PPSL PMT.	81

Chapter 4:

Table 4.1 The sample set used for remnant luminescence work.	89
Table 4.2 Arran granite feldspar chemical compositions (Mol%).	91
Table 4.3 Chemical compositions of Ballater granite feldspars (Mol%).	92
Table 4.4 Chemical compositions of Cairngorm granite feldspars (Mol%).....	94
Table 4.5 Chemical compositions of Helmsdale granite feldspars (Mol%).	97
Table 4.6 Chemical compositions of Peterhead granite feldspars (Mol%).....	99
Table 4.7 Chemical compositions of Ross of Mull granite and syenite (Mol%).....	101
Table 4.8 Chemical compositions of Shap granite feldspars (Mol%).	105
Table 4.9 Strontian granodiorite feldspar chemical compositions (Mol%).....	111
Table 4.10 Chemical composition of pitchstone porphyry feldspars (Mol%).....	112
Table 4.11 Chemical composition of the gabbro pegmatite feldspar (Mol%).....	116
Table 4.12 Chemical composition of the Hallival sample's feldspar (Mol%).	118
Table 4.13 Chemical composition of the Patmos sanidine (Mol%).	120

Table 4.14 Chemical composition of feldspars from the Etna basalt (Mol%).	122
Table 4.15 Chemical composition of the migmatite feldspars (Mol%).	124
Table 4.16 Chemical compositions of feldspars from the gneiss samples (Mol%).	125
Table 4.17 Chemical composition of the F1 feldspar standard (Mol%).	128
Table 4.18 The sample set, reference numbers and locality.	132
Table 4.19 The approximate compositions of the density fractions.	135
Table 4.20 Microtexture, composition and optical-CL of the plutonic igneous samples.	136
Table 4.21 Microtexture, composition and optical-CL of the silicic intrusion samples.	137
Table 4.22 Microtexture, composition and optical-CL of the calcic plagioclase samples.	137
Table 4.23 Microtexture, composition and optical-CL of the extrusive igneous samples	138
Table 4.24 Microtexture, composition and optical-CL of the Metamorphic samples.	138
Table 4.25 Microtexture, composition and optical-CL of weathered igneous samples	139
Table 4.26 Microtexture, composition and optical-CL of the HF acid etched samples.	139
Table 4.27 Microtexture, composition and optical-CL of F1	139

Chapter 5:

Table 5.1 Sample set by geological association.	142
Table 5.2 Remnant luminescence values for the Arran granite (AG1).	145
Table 5.3 Remnant luminescence values for the Ballater granite (BG1).	145
Table 5.4 Remnant luminescence values for the Cairngorm granite (CG1).	146
Table 5.5 Remnant luminescence values for the Helmsdale granite (Helms).	146
Table 5.6 Remnant luminescence values for the Helmsdale arkose (Ark).	146
Table 5.7 Remnant luminescence values for the Peterhead granite (GU3)	147
Table 5.8 Remnant luminescence values for the Ross of Mull granite (H9).	147
Table 5.9 Remnant luminescence values for the Ross of Mull granite (H10).	147
Table 5.10 Remnant luminescence values for the Ross of Mull syenite (H11).	148
Table 5.11 Remnant luminescence values for the fresh and unweathered Shap.	148
Table 5.12 Remnant luminescence values for the Strontian granodiorite (H8).	148
Table 5.13 Remnant luminescence values for plutonic and associated rocks.	149
Table 5.14 Remnant luminescence values for the Bute pitchstone porphyry (H2).	150

Table 5.15 Remnant luminescence values for the Bute pitchstone porphyry (H3)150

Table 5.16 Remnant luminescence values for the Canisp quartz-syenite (H4).150

Table 5.17 Remnant luminescence values for the silicic igneous intrusion samples.....151

Table 5.18 Remnant luminescence values for the gabbro pegmatite (H1).152

Table 5.19 Remnant manual TL in 100°C groups for the gabbro pegmatite (H1).152

Table 5.20 Remnant luminescence values for the Rum anorthosite (H5)152

Table 5.21 Remnant manual TL in 100°C groups for the Rum anorthosite (H5).153

Table 5.22 Remnant luminescence values for the Rum troctolite pegmatite (H7).....153

Table 5.23 Remnant TL in 100°C groups for the Rum troctolite pegmatite (H7)153

Table 5.24 Remnant luminescence values for the igneous calcic plagioclase samples..153

Table 5.25 Remnant luminescence values for the Patmos sanidine.....154

Table 5.26 Remnant luminescence values for the Etna basaltic lava.154

Table 5.27 Remnant luminescence values for the extrusive igneous samples.....154

Table 5.28 Remnant luminescence values for the migmatite (GU2).....155

Table 5.29 Remnant luminescence values for the Lewisian gneiss.....155

Table 5.30 Remnant luminescence values for the Torridon gneiss (GU1)156

Table 5.31 Remnant manual TL in 100°C groups for the Torridon gneiss (GU1).....156

Table 5.32 Remnant luminescence values for the metamorphic samples.....156

Table 5.33 Remnant luminescence values for the laboratory standard (F1).157

Table 5.34 Remnant luminescence values for the Ballater granite (BG2).157

Table 5.35 Remnant luminescence values for the Cairngorm granite (CG2).158

Table 5.36 Remnant luminescence values for the Shap granite (WSH).....158

Table 5.37 Remnant luminescence for the fresh vs. weathered Ballater granite.....160

Table 5.38 Remnant luminescence for the fresh vs. weathered Cairngorm granite.160

Table 5.39 Remnant luminescence for the fresh vs. weathered Shap granite.....161

Table 5.40 Remnant luminescence values for the HF acid etched Shap granite161

Table 5.41 Remnant luminescence values for the HF acid etched arkose.161

Table 5.42 Remnant luminescence values for the acid etched Helmsdale granite.162

Table 5.43 Remnant luminescence values for three alkali feldspar-rich polymorphs.....164

Table 5.44 Remnant luminescence for plagioclase-rich samples ordered by An.165

Table 5.45 Remnant luminescence for plagioclase-rich samples ordered by age.....166

Table 5.46 Alkali feldspar samples that do not fade in IRSL or OSL.167

Table 5.47 Alkali feldspar samples that fade in IRSL or OSL.....169

Table 5.48 Alkali feldspar samples that do not fade in Riso TL.....169

Table 5.49 Alkali feldspar samples that fade in Riso TL.170

Table 5.50 Alkali feldspar samples that do not fade in manual TL.170

Table 5.51 Alkali feldspar samples that fade in manual TL.171

Table 5.52 Remnant luminescence for Helmsdale granite and its associated arkose.....172

Table 5.53 Remnant luminescence for RoM granite and its associated syenite.....173

Table 5.54 Remnant luminescence for granodiorite and associated migmatite.....173

Table 5.55 Remnant luminescence values for unpreheated vs. preheated samples.174

Chapter 6:

Table 6.1 The optical attenuation by optical filters and the p25232-05 module (A).181

Table 6.2 The optical attenuation by optical filters and the p25232-05 module (B).182

Table 6.3. The optical attenuation by optical filters and the p25232-05 module (C).182

Table 6.4. The spectral response of the p25232-05 module.183

Table 6.5 Raw data (with background subtraction) for Figure 6.4 (d).187

Table 6.6 Optical attenuation by optical filtration and the SUERC blue-PPSL PMT.....191

Table 6.7 Time dependence on signal loss, with and without preheating194

Table 6.8 The different filter combinations tested with the R2257 red sensitive PMT.197

Table 6.9 PMT dark count and diode breakthrough with thermoelectric cooling.201

Table 6.10 Estimated mineral percentages of samples 1579 and 1580.211

Table 6.11 Comparison of linear vs. non-linear regression - De values for 1579.213

Table 6.12 Comparison of linear vs. non-linear regression - De values for 1580.215

Table 6.13 Apparent ages (Ka) from 1579 and 1580 compared to the age from 1653. ..216

Table 6.14 Results of gamma to Risø and ELSEC beta sources.....220

Table 6.15 Doubling the SS discs to remove variations in source geometry.221

Table 6.16 Results of comparing the sample coverage of the two discs.222

Chapter 7:

Table 7.1 Comparison of results gained by measuring fading rates of alkali feldspars...227

Table 7.2 A brief outline of the potential of each technique/approach in future work234

1

Introduction.

1.1 Luminescence Phenomena.

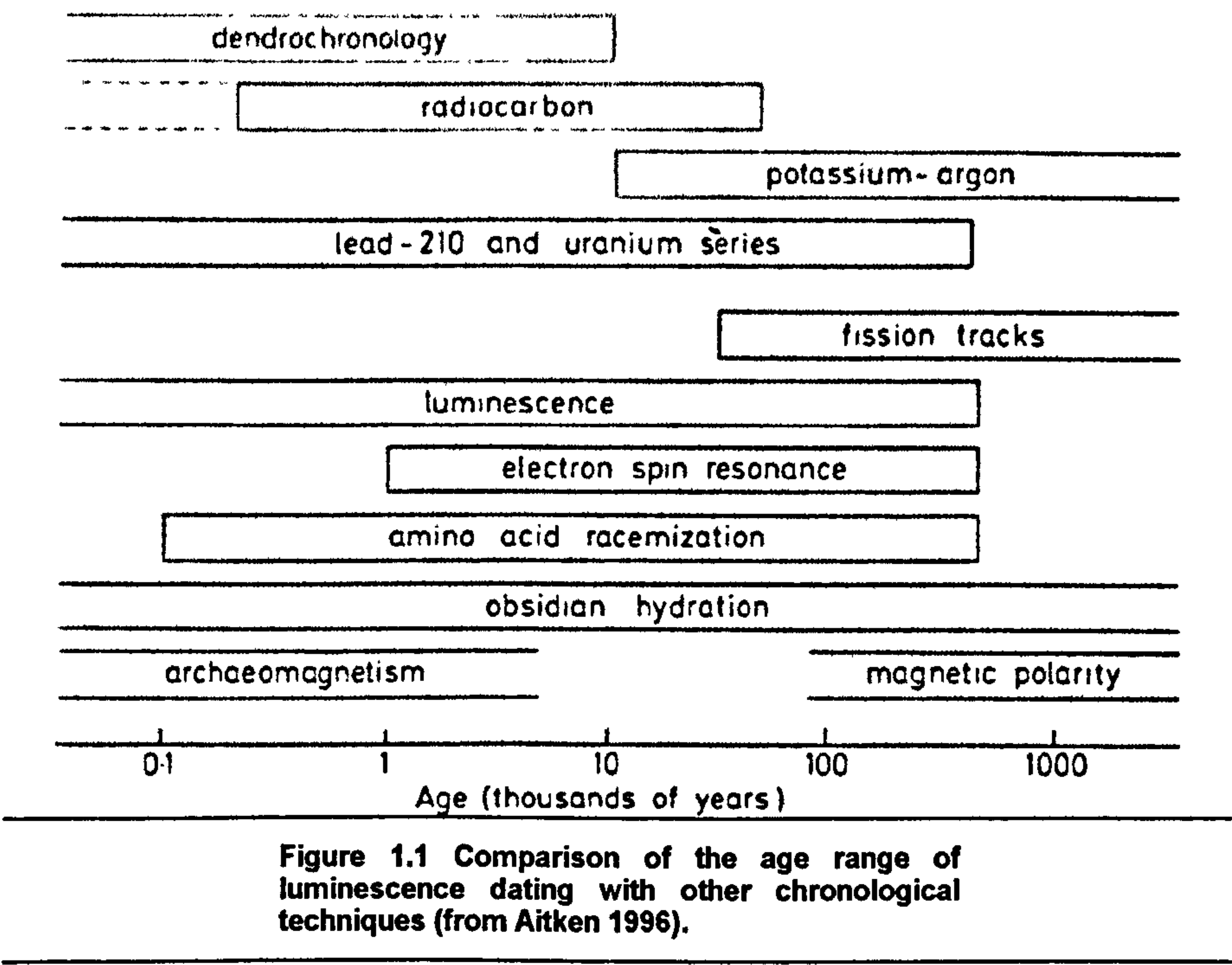
Luminescence techniques have a broad applicability and are used routinely in many disciplines, such as medicine, archaeology, geology, dosimetry, construction (evaluating fire damage), detecting irradiated components in food, geomorphology and authenticity testing of art. Luminescence is the emission of electromagnetic radiation, as photons, from an insulator or semiconductor. Aitken (1998) describes luminescence as “the memory of accumulated exposure to nuclear radiation.” In fact this ‘memory’ describes the process of electrons diffusing from their initial place in their parent atoms to the vicinity of a lattice defect where they become essentially trapped until subsequent exposure to energy releases them. Crucially, the wavelength of the emitted light is dependant on the luminescent material, rather than the energy of the incident radiation (McKeever, 1985).

Photon emission from a material can be stimulated by both radiative and non-ionising energies. Radiation induced luminescence from insulators can either take place during excitation by ionising radiation (i.e., radioluminescence, prompt fluorescence) or after the excitation source has been removed (e.g., phosphorescence) (Smith 1998). Non-radiative energies stimulate luminescence after the material had already undergone excitation and they are in the form of light (photostimulated luminescence or PSL), or heat (thermoluminescence or TL). The term PSL is interchangeable with optically stimulated luminescence (OSL) although in this study OSL is used to describe UV-blue light stimulated luminescence and PSL is a generic term applied to all light based stimulation. Photons are emitted when charge carriers relax from higher energy states and recombine (e.g. for an electron at a hole centre) and the models describing this will be discussed in Chapter 2.

1.2 Luminescence Dating.

Despite the cross-disciplinary nature of luminescence, this study has focused on its chronological applications, particularly in archaeology and geochronology. Luminescence dating is a versatile

technique that has seen application in a number of disciplines. This technique utilises the signals generated by long-term exposure of mineral grains to ionising radiation in order to date events on a 10^2 - 10^6 year timescale. The accuracy of the dates obtained is ± 5 -10% in heated materials and ± 10 -20% for naturally deposited sediments (Smith, 1998). Luminescence dating is one of many chronological techniques currently available to researchers and Figure 1.1 shows how its range compares with that of other methods available to archaeologists and geochronologists.



Dating using luminescence requires measurement of the amount of trapped charge and comparison of this value with the rate at which the material has been dosed by ionising radiation. The age obtained is known as the ‘zeroing event’ and, as its name suggests, it corresponds to the moment when the trapped charge within the insulator was at zero. The trapped charge can be emptied by post-formational heating, either geological or anthropological, by exposure to light (bleaching), or by mechanical grinding (McKeever, 1985). From the moment of zeroing, charge begins to accumulate through exposure to ionising radiation from the surroundings, or even within the material (which is given a value known as the ‘dose’) and at a rate (the ‘dose rate’) that is assumed to be constant through the period being dated. To determine the time that has elapsed since zeroing a simple age equation is employed:

Age = Estimated dose (De)/Dose rate

[1.1]

1.3 Estimated Dose (De).

The first part of equation [1.1], the estimated dose (De), is calculated from the luminescence emitted from the collected samples by stimulation of the stored signal. A number of methods to

obtain this signal are available and so to calculate the D_e once the intensity of luminescence has been measured. The detail of the process of obtaining an accurate age is outside the scope of this project but some of the techniques are discussed in the next chapter.

1.4 Dose Rate.

In Section 1.1 the effect of ionising radiation on the electrons contained within the crystal lattice was noted, yet not the opportunities for exposure. For natural luminescence (not laboratory induced) ionising radiation originates in the environment immediately surrounding the mineral grain (and for some minerals such as K-feldspar and zircon within the mineral itself). This environmental radiation will be specific to a particular location and type of material that contains the mineral grain (i.e., sediment, rock or pottery).

Within the material surrounding a mineral grain (e.g., sediment or rock) may be the radioactive isotopes of a number of elements such as uranium, thorium, rubidium and potassium. As these isotopes decay they release ionising radiation that is absorbed by the other constituents of the sediment or rock, including quartz and feldspar, whose duration of exposure to this radiation dose can be determined using luminescence techniques. It is the radiation damage within these minerals that forms the structurally unstable electron traps within their lattice (Prescott and Robertson, 1997; Wintle and Huntley, 1982). Cosmic radiation can also cause this damage though its effects are sufficiently small to be discounted (Aitken, 1985; 1992; 1994).

When samples for luminescence dating are collected, the intensity of radiation in the surrounding environment must be catalogued and assumed to have been constant throughout the time period of interest (i.e., the last zeroing event). The same assumption is made for water content which is important because moisture, particularly within sediments, can affect the dose rate significantly. The environmental radiation is measured both at the sample site and also on sub-samples in the laboratory as part of the dating process. After all of these variables have been taken into account, the rate at which the mineral grains have been exposed to ionising radiation can be calculated.

1.4.1 The Importance of Luminescence Dating.

Despite the large number of chronological techniques available to researchers (Fig. 1.1), luminescence dating is one of the few that can be used to determine the age of sediment since deposition. This is because it is the last period of exposure to sunlight (i.e., during transport and deposition) that is being dated, rather than initial exposure upon weathering of the sediment grains from the parent rock or sediment. Obtaining an accurate chronology of depositional events is especially important in relation to studies of climate change and environmental reconstruction (Aitken, 1998).

A good example of the importance of luminescence dating, principally optically stimulated luminescence (OSL), is in the dating of loess. This silt-grade aeolian sediment forms thick deposits extending from north-western Europe across northern Asia to China and elsewhere. Transportation and deposition of loess is indicative of dry and windy conditions that are typically associated with periods of glaciation. Quartz OSL has been used with considerable success in dating these deposits and so helping to produce global stratigraphic correlations. Palaeoenvironmental indicators may also be detected within palaeosols, colluvium and fluvial deposits using luminescence techniques (Balescu *et al.*, 2003; Duller, 1992; Duller, 1994b; Fattahi and Stokes, 2003b; Spencer and Owen, 2004; Wintle, 1990; Zhou and Wintle, 1994). Dating of climatic events is not the only chronological application of luminescence; for example it has been applied successfully to characterising sand deposited by tsunamis (Bishop *et al.*, 2005), thus giving an insight into the chronology of past seismic events, and also in dating of past volcanic eruptions by analysis of lavas and ash deposits (Fattahi and Stokes 2003). The above are just a small sample of luminescence applications and more will be discussed in Chapter 2, but the above have an increasing relevance to science and the world at large today.

1.5 Luminescence of Feldspars.

1.5.1 Potential Importance in Luminescence Dating.

At the present day most luminescence dating studies use quartz, but this has not always been the case. Feldspars have played an important role in the evolution of this field owing to their luminescence characteristics, which make them attractive dosimeters. Feldspars have a high TL sensitivity with low doses making them suitable for dating younger samples, but also have a high saturation level that enables them to be used for dating of older samples, up to a million years in age. (Aitken, 1985; McKeever, 1985) Furthermore, these minerals have a linear dose response and are readily bleached by sunlight. Feldspars are found in almost every geological context and geomorphological setting, even those devoid of quartz. The use of feldspars as an accurate dosimeter and chronological medium is therefore highly desirable, and it is the proliferation of anomalous fading that prevents it from regaining its popularity.

1.5.2 Feldspar Mineralogy.

The feldspars are a large group of framework aluminosilicate minerals. The common structural feature of these minerals is the silicon tetrahedron comprising four oxygen and one silicon atom (SiO_4), with the O atoms being shared between adjacent tetrahedra. Replacement of one-in-two or one-in-four of the Si atoms by Al allows the insertion of cations into the lattice, principally K, Na, and Ca, although Ba may also be included. This extensive degree of substitution gives rise to a

range of chemical compositions; KAlSi_3O_8 , $\text{NaAlSi}_3\text{O}_8$, and $\text{CaAl}_2\text{Si}_2\text{O}_8$ are end-members of a solid-solution series that is conventionally represented on a ternary diagram as the orthoclase, albite and anorthite components (Or, Ab and An) respectively (Figure 1.2).

The Na-Ca feldspars, known collectively as the plagioclase group, form a continuous series from albite (Ab) to anorthite (An), with intermediate compositions. Their structural state is largely controlled by thermal history, in particular cooling rate of the parent rock following crystallisation. The differences between these states can involve changes in the lattice geometry and varying degrees of ordering of the Al and Si atoms. Feldspars whose composition range between the albite and orthoclase end-members (alkali feldspar series) may form a complete solid-solution series if they crystallise at high temperatures and cool rapidly (monoclinic sanidine or triclinic anorthoclase) (Deer *et al.*, 1996; Krbetschek *et al.*, 1997; Krbetschek and Rieser, 1995). However, when crystallisation occurs slowly the initially homogeneous crystal has time to exsolve into lamellae of Na-rich (Ab) feldspars (typically low albite) and K-rich (Or) feldspars (monoclinic orthoclase with an intermediate ordering or fully ordered triclinic low microcline) (Fig. 1.2). In those alkali feldspars with dominant orthoclase or microcline the intergrowth texture is described as perthitic (Figs 1.3, 1.4 and 1.5) whereas an antiperthite has dominant plagioclase (Fig. 1.2).

In addition to exsolution microtextures that form by interdiffusion of Na and K ions (Figs 1.4 and 1.5), alkali feldspars almost always interact with water in their parent igneous/metamorphic rock during cooling. These deuteric or hydrothermal reactions cause a further episode of unmixing of K-feldspar and albite into coarser micropore- and defect-rich patch perthites (Figs 1.4 and 1.5) (Lee *et al.* 1995).

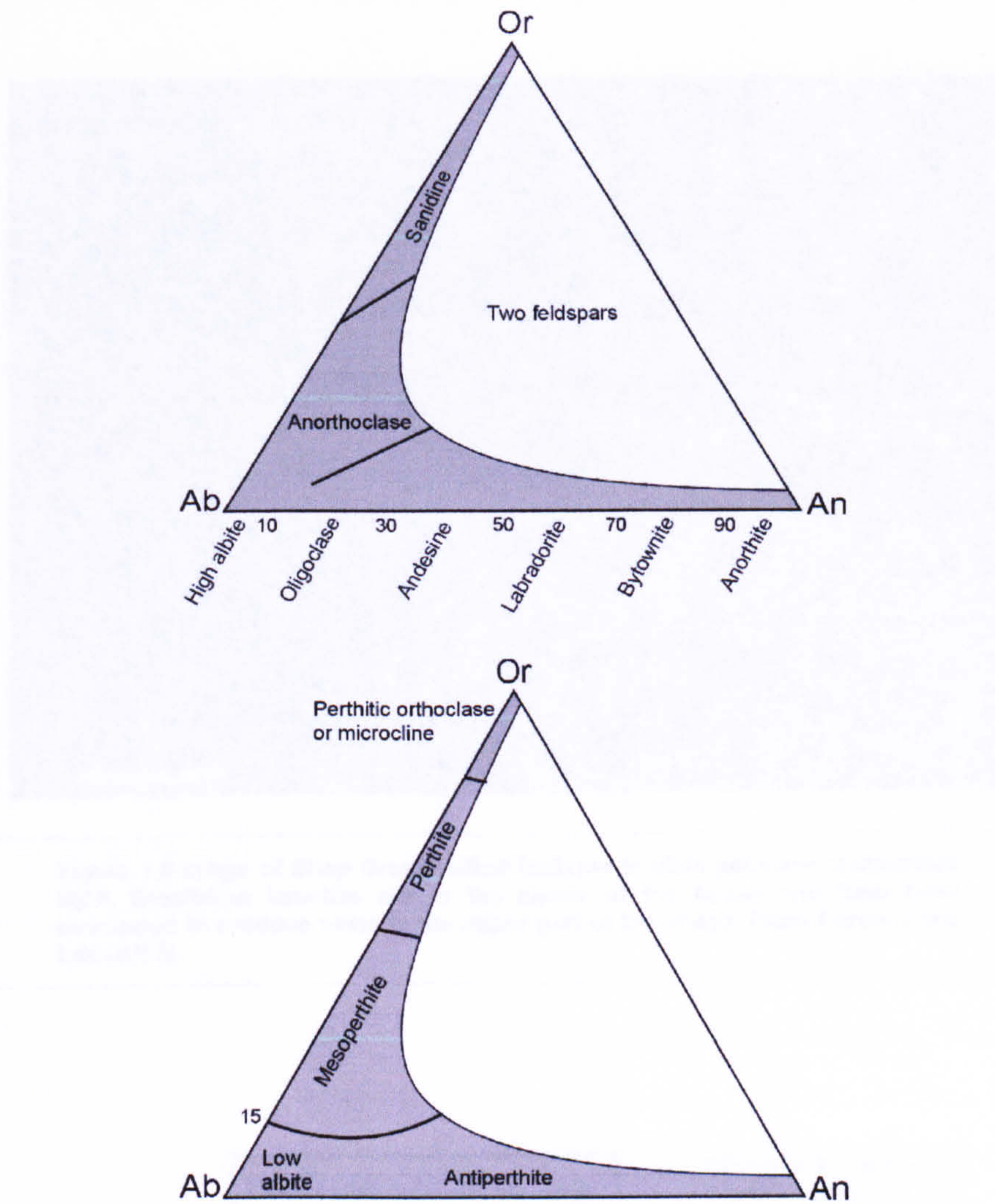


Figure 1.2. ternary diagrams for disordered (upper diagram) and ordered (lower diagram) ternary feldspars (Deer, 1996).

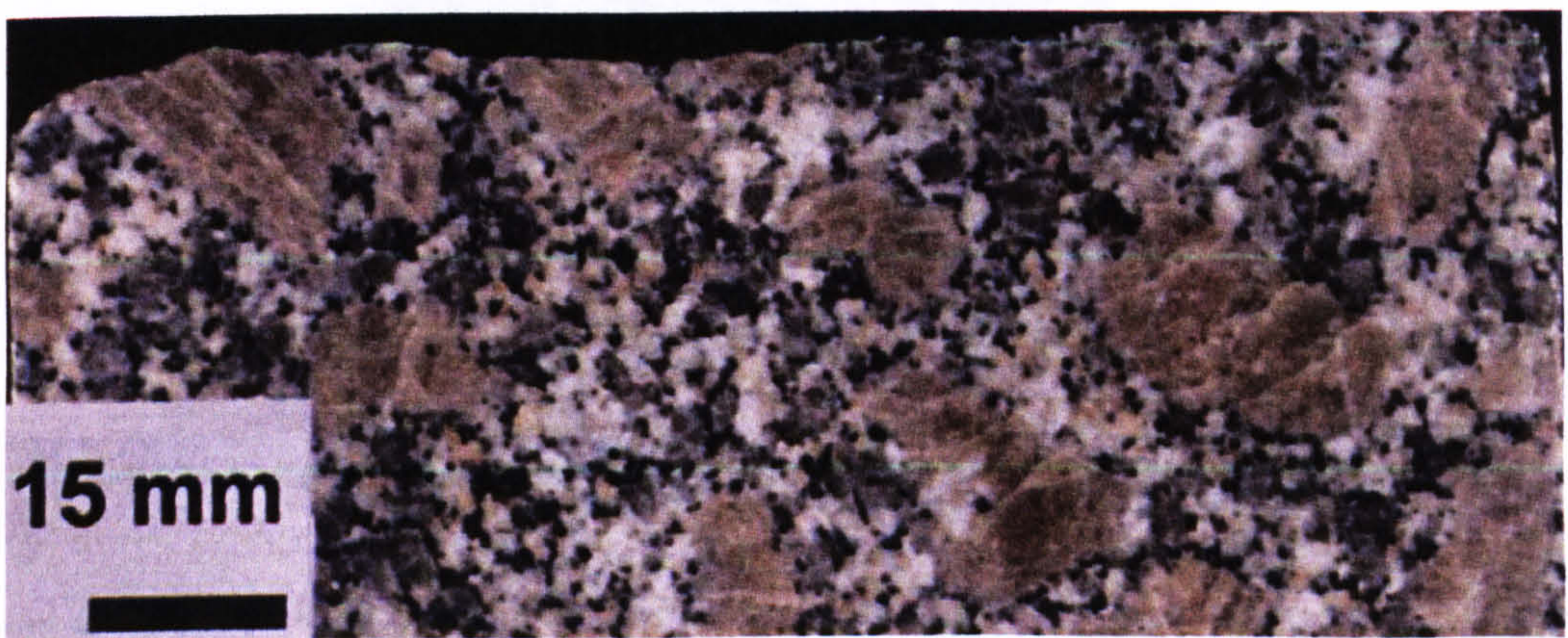


Figure 1.3 Image of Shap Granite. The alkali feldspar phenocrysts are pink. From Parsons and Lee (2005).

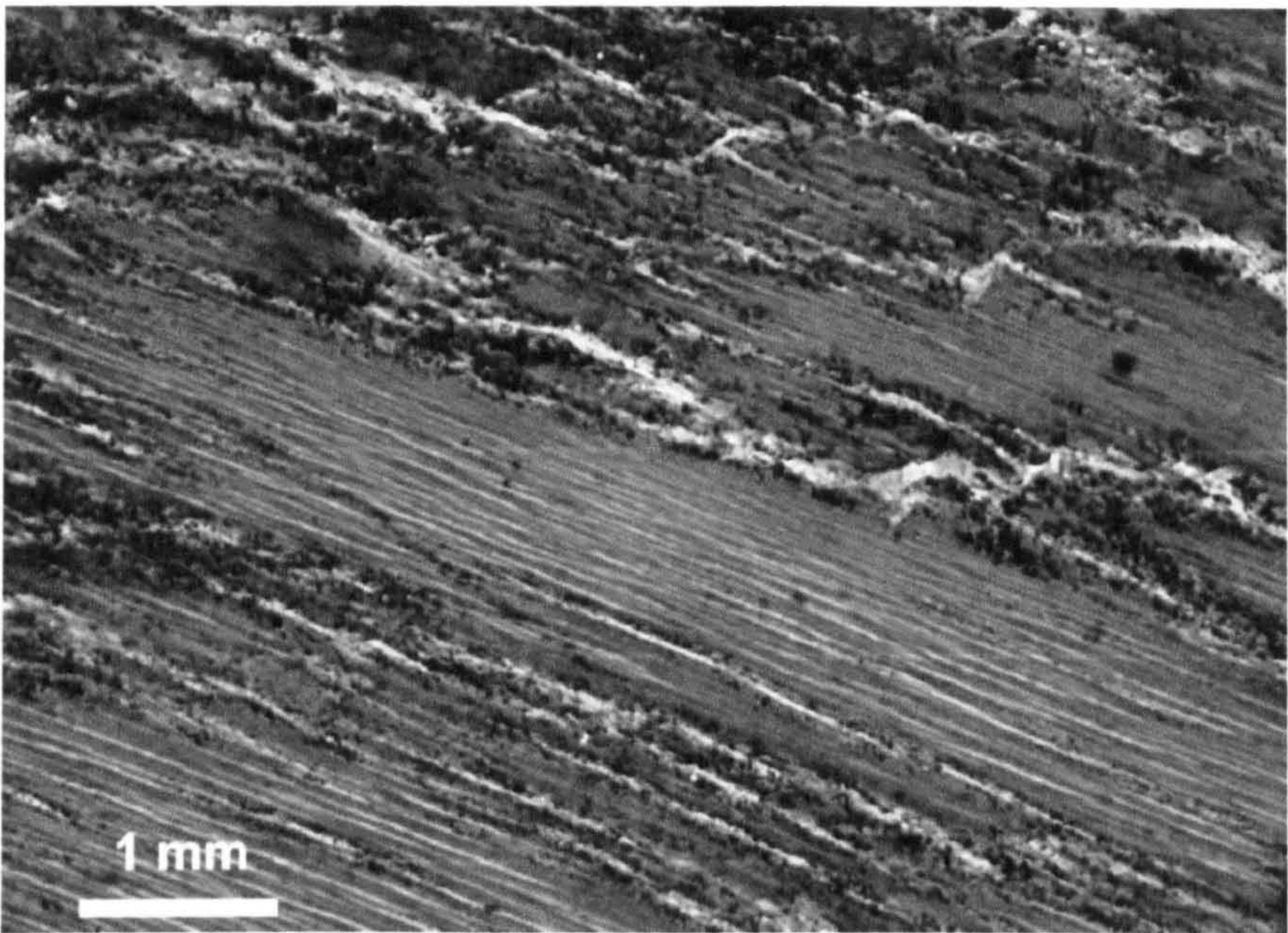


Figure 1.4 Image of Shap Granite alkali feldspar in plain polarised transmitted light. Exsolution lamellae are in the centre of the image and have been coarsened to produce veins in the upper part of the image. From Parsons and Lee (2005).

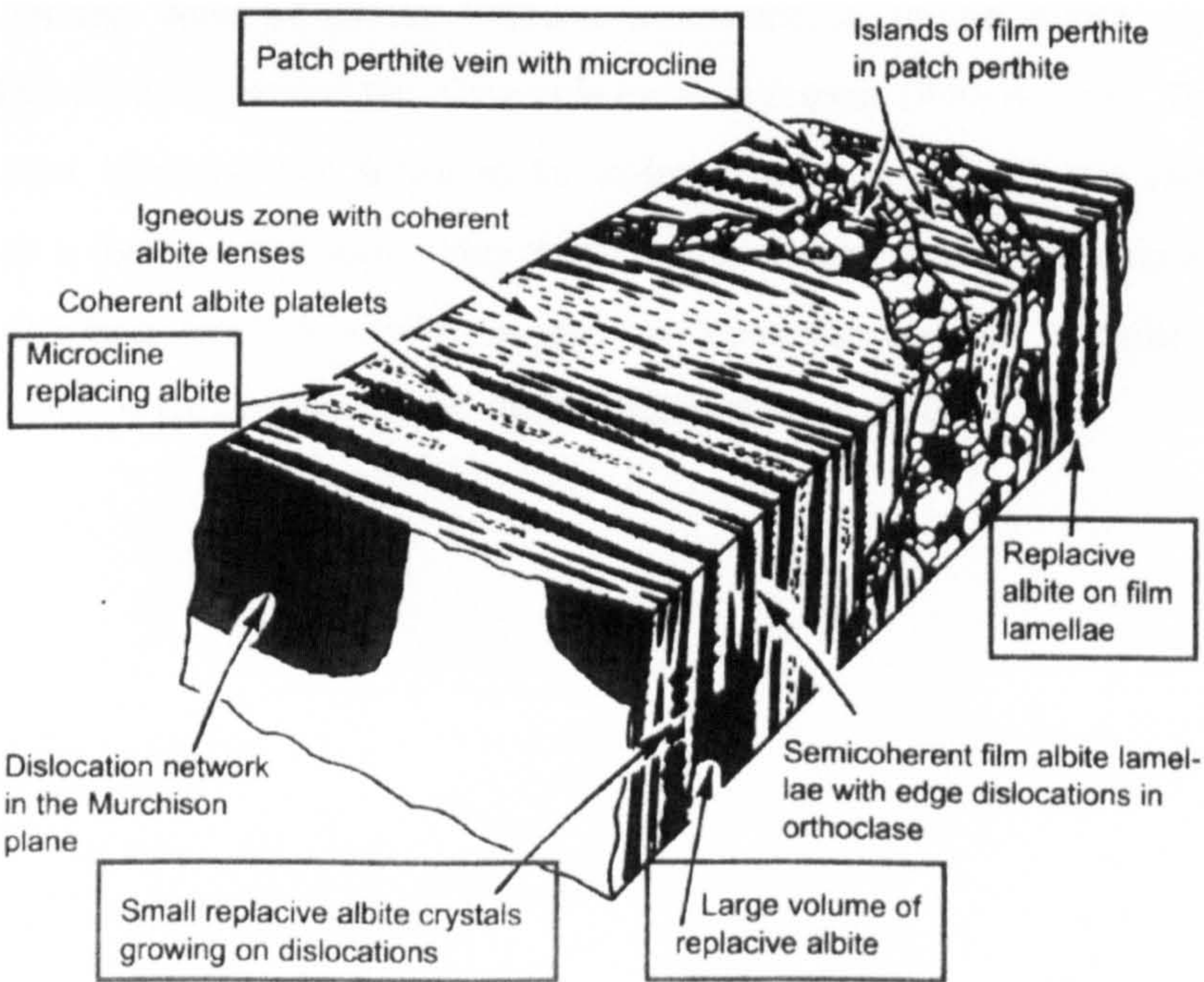


Figure 1.5 Schematic diagram of a Shap Granite alkali feldspar crystal showing the wealth of microtextures and defects within this typical granite feldspar. From Parsons and Lee (2005).

1.5.3 Mineralogical Controls on Feldspar Luminescence.

The luminescence emitted by feldspars as part of the radiative process is linked to their crystal structure, itself with a number of determinants including chemical composition (Figs 1.6 and 1.7). Feldspars vary widely in structural state and chemical composition and furthermore contain different types of inclusions. Thus, as luminescence results can be influenced strongly by the mineralogical purity of the powdered sample being used, single crystals from museum collections are often used in studies designed to investigate the fundamental determinants on feldspar luminescence properties. Useful though studies of such samples may be, they will be a poor proxy for the types of feldspars analysed routinely in dating studies (Krbetschek *et al.*, 1997), and museum descriptions do not always agree with the results of subsequent mineralogical and luminescence investigations (Krbetschek and Rieser, 1995).

Because some members of the feldspar group have high luminescence intensities (e.g., albite and oligoclases) but others have much lower intensities (e.g. alkali feldspars of intermediate chemical compositions and plagioclases), the net luminescence from a powdered feldspar sample may contain a component of, or even be overwhelmed by emission from trace mineral phases or grains with high luminescence intensities (Krbetschek *et al.*, 1997). For example, the alkali feldspars almost always contain more than one mineral in perthitic intergrowth (e.g., albite and microcline/orthoclase). This is also true of polymineral samples where feldspar luminescence emissions can swamp those of quartz. Feldspar luminescence, unlike quartz, can be stimulated using light in the infrared part of the electromagnetic spectrum (800-900nm). This phenomenon allows the feldspar luminescence signal to be isolated within a polymineral sample rather than having to rely on a rigorous and sometimes unsuccessful density separation techniques. This IRSL technique has also been used to screen samples for ‘contamination’ of feldspar-rich samples by quartz (Duller, 2003; Wallinga and Duller, 2000; Wallinga *et al.*, 2000).

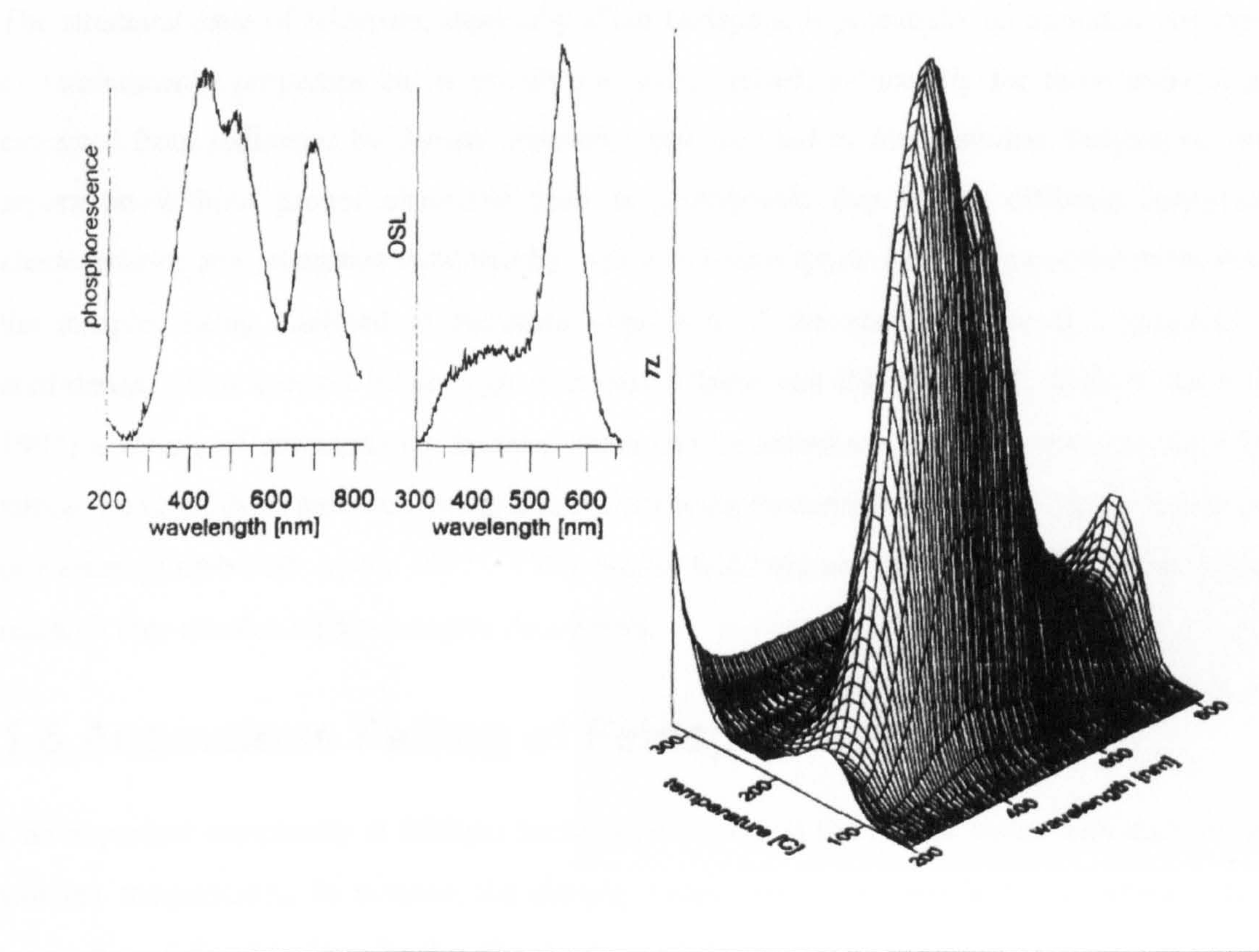


Figure 1.6. Emission spectra from orthoclase; phosphorescence, OSL and TL from left to right. From Krbetschek and Rieser (1995).

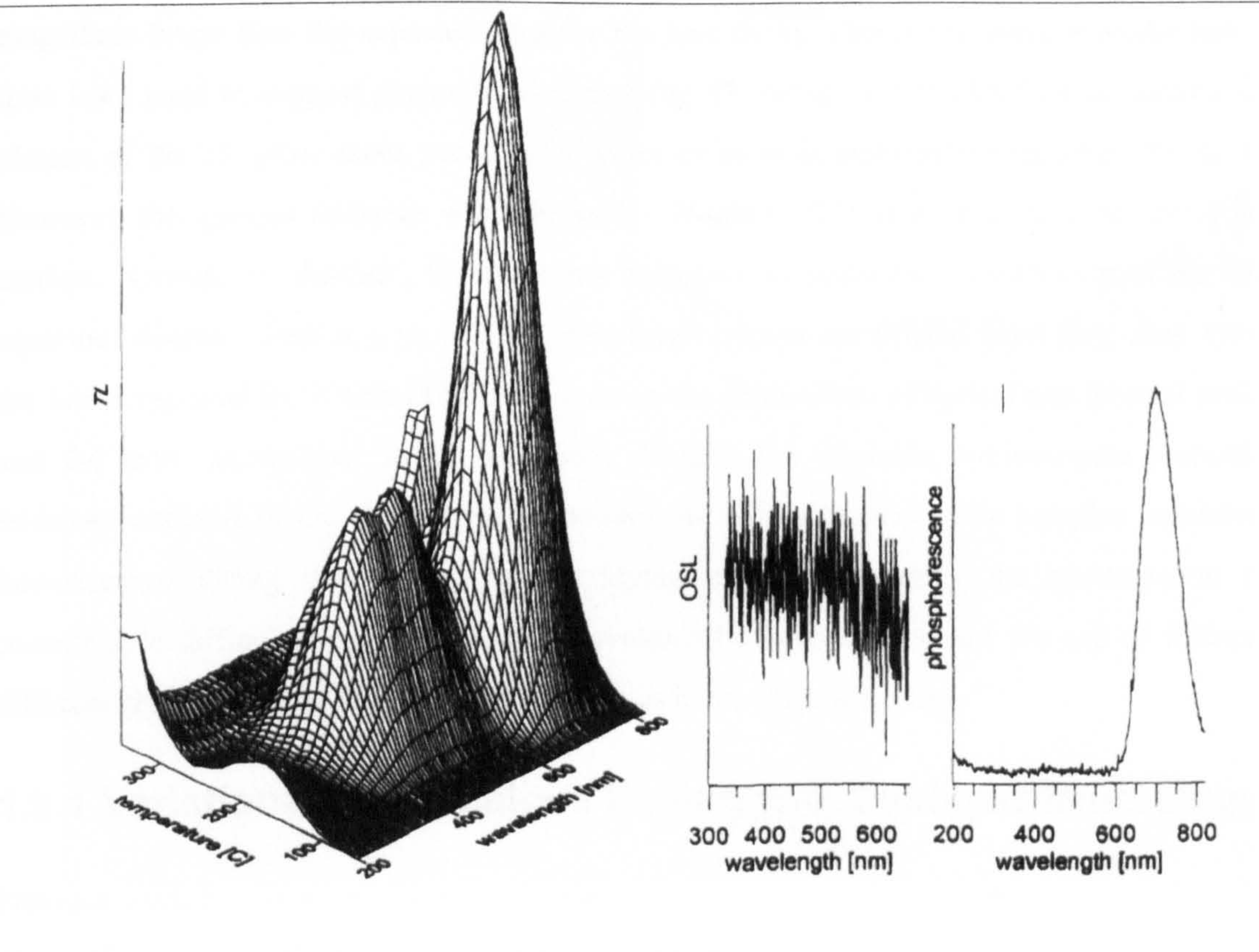


Figure 1.7. Emission spectra from sanidine; phosphorescence, OSL and TL from left to right. From Krbetschek and Rieser (1995).

The structural state of feldspars, especially alkali feldspars, is potentially an important determinant of luminescence properties but is usually not characterised, particularly for those mineral grains extracted from sediments by density separation that are used in dating studies. Relying on density separation without proper characterisation is problematic due to the differing luminescence characteristics and intensities exhibited by various feldspar types. Knowledge of the mineralogy of the samples being analysed is therefore imperative if the results are to be interpreted with confidence. From spectral luminescence studies (Clarke and Rendell, 1997; Rendell and Clarke, 1997) a variety of emissions are known, which can be linked to particular defects in the feldspar lattice. Some of these emission bands also occur during thermally or photostimulated luminescence processes (Krbetschek *et al.*, 1997). Thus, whilst feldspars are highly desirable in luminescence research they are also highly complex dosimeters.

1.6 Anomalous Fading of Feldspar Luminescence.

One important complexity in feldspar luminescence work is the loss of signal with dark storage at ambient temperatures. In essence, the sample ‘fades’ over time. Wintle (1973) coined the term ‘anomalous fading’ to describe this phenomenon while attempting to obtain TL ages from feldspars separated from extrusive igneous rocks. Feldspar dates obtained were found to be up to an order of magnitude lower than the expected ages for the lava flows. Theoretical considerations had at the time been used to support assumptions underlying TL dating that the lifetime of carriers on the plateau of the TL glow curve was of $\sim 10^5$ years or more at ambient temperatures (Smith 1998). However, the igneous feldspars were shown by Wintle (1973) to have undergone severe loss of carriers. Normal, or ‘thermal’, fading occurs according to statistical consideration of the lifetime equation, whereby there is a probability that charge carriers are evicted from their sites. However the losses reported by Wintle (1973) fall outside the explanation of optical and thermal excitation and the term ‘anomalous’ fading was born. Despite the desirable luminescence properties of feldspars outlined in the above section, anomalous fading renders some samples redundant for luminescence dating. Difficulties in quantifying and circumventing the phenomenon reflect considerable difficulties in correlating observations between studies and the use of feldspars of different properties derived from different sources in the various studies.

1.6.1 Variations in Anomalous Fading with Feldspar Mineralogy.

Previous work has found a wide range in the magnitude of signal loss from feldspars, described in terms of anomalous fading, from no reported fading (Sanderson, 1988) to severe and consistent fading (Huntley and Lamothe, 2001; Spooner, 1992). The differences between the types of feldspars that exhibit anomalous fading is considerable and authors have proposed a range of explanations for the phenomenon, for example disorder in the crystal structure to account for

observed contrasts in the behaviour of feldspars from rapidly cooled (volcanic) sources (sanidine) and slowly cooled (plutonic) rocks (orthoclase and microcline) (Huntley and Lamothe, 2001; Zink *et al.*, 1995) (Fig. 1.6). Feldspars that have cooled rapidly are believed to be more prone to anomalous fading than their more slowly cooled counterparts due to contrasts between clustered (slowly cooled) and randomly distributed (rapidly cooled) defects. There is also the possibility of a structural reorganisation during cooling or after a long-term ambient temperature process of a specific high-temperature (disordered) feldspar to a lower temperature (more ordered) structural type. In fact Visocekas (1994) suggested that there is a closer relationship between anomalous fading and crystal disorder than was previously thought and this idea was developed by Visocekas and Zink (1999) who proposed that an ambient temperature phase shift could explain the contradictory observations of feldspar instability in younger formations compared to its stability in older formations. Another theory is that fading rates are controlled by differences in major or minor element chemistry between feldspars, such as calcium concentrations and impurities substituting into the lattice (Huntley and Lian, 2006). These structural correlations support the proximity models that have been put forward to explain fading of the feldspar luminescence signal and this relationship will be explained in greater detail in the next chapter.

Huntley (2006) also stated that the fading rate increases with laboratory dose, especially large doses, which hints at control on fading of age since zeroing although it can be argued that exposing these minerals to large geologically instant doses is too different from processes in the natural environment to be a worthwhile proxy.

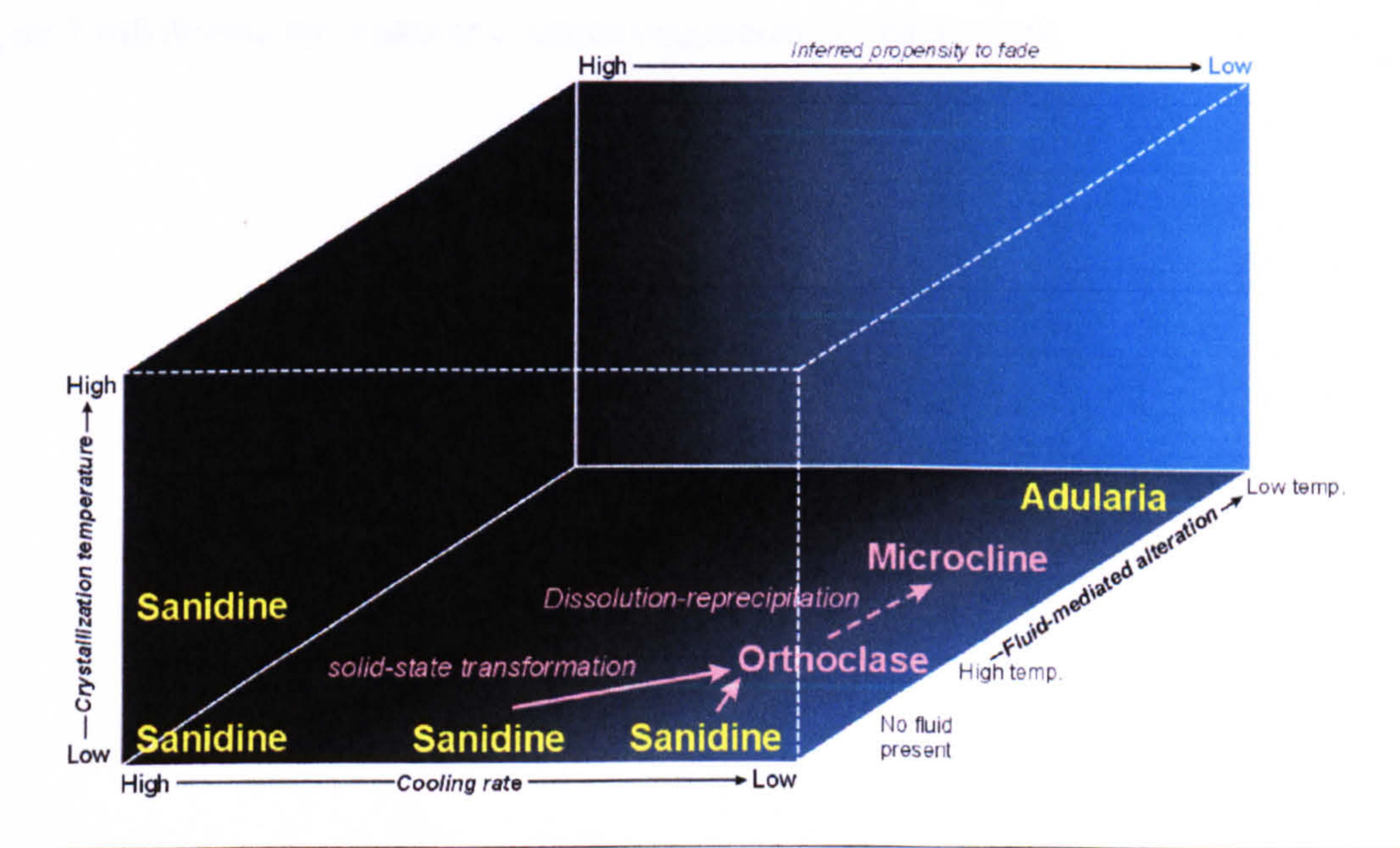


Figure 1.8. Stability diagram for the four polymorphs of K-feldspar. Sanidine crystallizes from high temperature melts and will transform to orthoclase via solid state diffusion if cooling rates are sufficiently slow. The presence of a fluid is required to complete the orthoclase-microcline transformation (Parsons and Lee, 2006). Adularia forms by direct precipitation from low temperature fluids in hydrothermal and diagenetic systems. Also on the diagram is indicated the propensity of the different K-feldspar polymorphs to fade.

Understanding the influence, or lack thereof, of the above factors and variables on the phenomenon adds to the understanding of fading and its highly variable nature. The more is known about the nature of the problem and its underlying mineralogical controls the closer is an all-encompassing circumvention of this signal loss. If solutions cannot be found from better understanding of anomalous fading feldspars will become a non-chronological luminescent mineral.

1.7 Aims of this Study.

The aim of this thesis is to evaluate the possibility of predicting the presence of fading, or even fading rate, by knowledge of a feldspar sample and its geological background. A variety of samples were obtained and categorised by crystal structure, chemical composition, thermal history and microtexture. Their remnant luminescence signals from varied stimulation techniques and detection wavelengths were measured and grouped using different variables to determine if any pattern can be determined.

Chapter 2 presents the problem of anomalous fading in its historical context and its relationship to present-day luminescence research. Emphasis is placed on reported causes of the phenomenon and the past and current ideas for circumventing fading. The success and problems of each will also be discussed. Chapter 3 outlines the equipment that was utilised in this project and reasons for selection of each piece of equipment. In Chapter 4, the mineralogy of the sample set is described. Chapter 5 outlines results of remnant luminescence measurements and Chapter 6 presents results from some newly developed luminescence techniques, and an example of dating using feldspars. Chapter 7 will discuss the results and outline suggestions for future work.

2

The Theory of Luminescence and Anomalous Fading.

2.1 Introduction.

This chapter will outline luminescence theory and the models used to describe it, with emphasis on the historical development of the techniques that utilise the phenomenon. Then modern luminescence research will be examined, focusing on that carried out on the phenomenon of feldspar anomalous fading. The models that have been proposed to explain the process of loss of charge carriers during storage will be presented and critically discussed, as will the methods that have been suggested to circumvent the phenomenon.

2.2 Luminescence.

Knowledge of luminescence models is a prerequisite for understanding the research that has been carried out on the anomalous fading of feldspars, in particular the processes that have been put forward to explain it. The models presented below underpin our current knowledge of luminescence and draw on the pioneering work carried out in the 1940's by Randall and Wilkins (1945) and Garlick and Gibson (1948).

2.2.1 Luminescence Mechanisms.

2.2.1.1 Traps and Recombination Centres.

As mentioned in the previous chapter, the luminescence signal is produced by stimulation of trapped charge that has accumulated within a mineral lattice as a direct result of exposure to ionising radiation. According to quantum theory, orbiting electrons of a single atom can only occupy discrete energies (Spencer, 1996). The atom has a number of associated energy levels and the electrons occupy the lower levels. In a solid, as the atoms become closer together the narrow energy levels become wider bands of allowed energies, each band consisting of closely spaced energy levels. The bands of permissible energy are called the allowed bands. The energy regions

between these are called the forbidden bands or band gaps (Spencer, 1996). A simple model for explaining the relationship between these band gaps is the 'energy level diagram'.

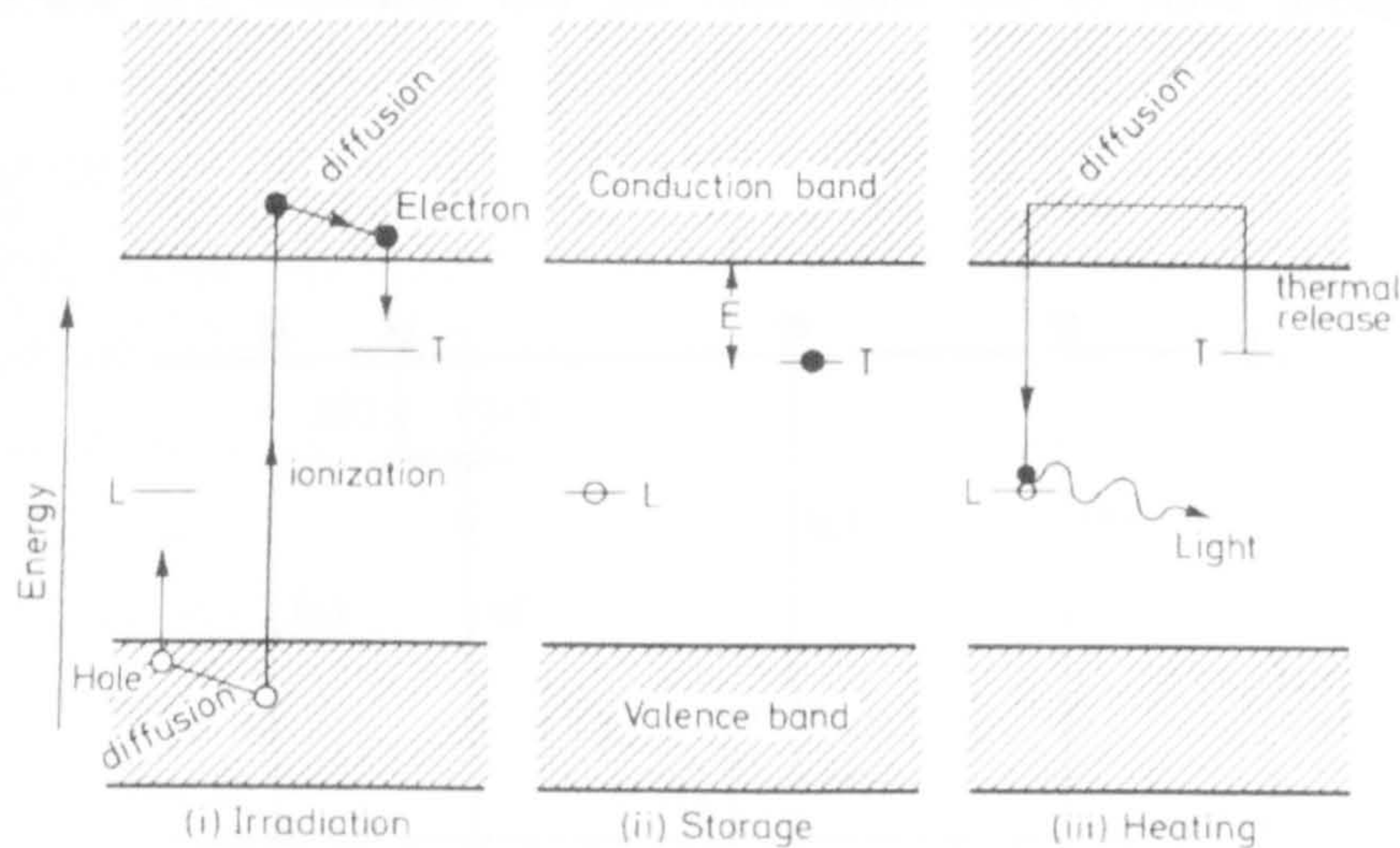


Figure 2.1. Energy level diagram from Aitken (1988)

Figure 2.1 shows the three stages involved in the production of the luminescence signal. Irradiation (i) forms trapped electrons and holes, or donor and receptor sites. When an electron is detached from its nucleus it is said to leave a 'hole' where another electron can be readily accepted. Those holes can diffuse around the valence band, while the free electrons diffuse around the conduction band. During ionisation the holes and electrons, through the supply of radiation, move into an intermediate energy band level where they become trapped for the storage period (ii), which is the time between irradiation and stimulation.

It must be emphasised that Figure 2.1 presents a highly simplified model and in reality a much larger number of traps and electrons are involved. The process by which these electrons become trapped is thought to relate to defects that produce a local deficit of negative charge in the lattice. The number and type of defects present within a particular mineral will depend on its crystal structure, the concentration of impurities and its formation process (Aitken, 1985). In reality luminescence is generated by the movement of electrons and holes around the various energy levels. This change in population is implemented by electronic transitions from one energy level to another.

Transition (a) in Figure 2.2 is the excitation of a valence electron from a host atom into the conduction band, in which state it has sufficient energy to move freely through the lattice. Thus this transition corresponds to the process of ionisation and results from the absorption of energy from an external source (e.g. radiation). For every free electron in the conduction band a free hole is left behind in the valence band. Thus, ionisation creates free electron-hole pairs that may wander

through the crystal until such time as they become trapped at defect centres, transitions (a) and (b). The localised electrons and holes may be released from their traps by thermal or optical excitation, transitions (c) and (f), whereupon they are once again free to move through the crystal (McKeever).

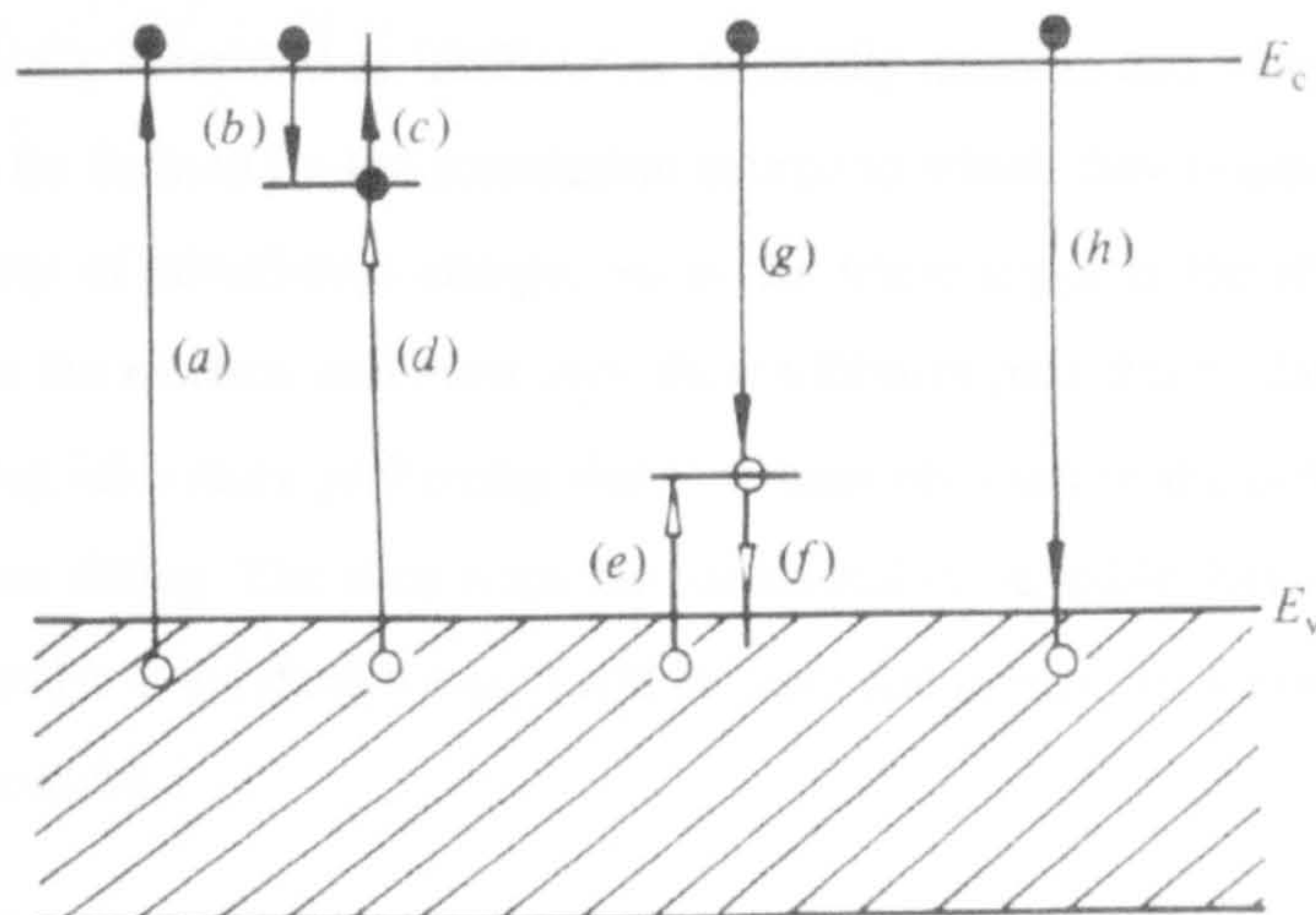


Figure 2.2 Common electronic transitions in (crystalline) semiconductors and insulators: (a) ionisation; (b) and (e) electron and hole trapping respectively; (c) and (f) electron and hole release; (d) and (g) indirect recombination; (h) direct recombination. Electrons, solid circles; electron transitions, solid arrows; holes, open circles; hole transitions, open arrows. (from McKeever 1995).

A second possibility for free electrons and holes is that they may recombine with a charge carrier of opposite sign, either directly, transition (h), or indirectly by recombining with a previously trapped carrier, transitions (d) and (g). If either of these recombination mechanisms is accompanied by the emission of light (i.e. it is radiative) then luminescence is the observed product.

Localised energy levels can act as either traps or recombination centres and it becomes pertinent to determine what distinguishes a recombination centre from a simple trap. The classification that is used to distinguish the types is based upon the relative probabilities of recombination and thermal excitation. For the electron-trapping centre, if transition (c) is more probable than transition (d), then the centre is classed as a trap. Conversely, if transition (d) is more probable than (c), then the energy level corresponds to a recombination centre. The same is true for the hole centre and transitions (g) and (f) (McKeever 1985).

The electrons of importance to luminescence phenomena are generated as a product of the radioactive decay of isotopes within the environment immediately surrounding (or even within) the luminescent material and due to the deficit of negative charge in the crystal, they are attracted to

the traps or holes (Aitken, 1985). A mineral exposed to a radiation source will thus build up a population of trapped electrons that will be proportional to the radiation dose received (until saturation is reached). Once trapped, electrons can be released into the conduction band by vibration of the crystal lattice. As temperature increases, so do the vibrations and the probability of eviction. Different traps are more able to ‘shield’ electrons from such vibration, and are termed ‘deep’ traps as the energy required to evict the electron is greater (Anthony, 2003). On this basis, traps can be simplistically classified as ‘shallow’ or thermally unstable and ‘deep’ or stable (dating) traps. Traps can also be defined by the stimulation source to which they respond, which is related directly to the intensity of stimulation energy. So as the name suggests the shallow traps require little energy to release the electron and have very short lifetimes (minutes to days). It is these traps that are emptied during laboratory preheating that is commonly used in the preparation of mineral grains for luminescence dating. The deep traps are considered to be stable, having a lifetime of tens to millions of years, and it is the charge stored within these that is used for luminescence dating and other dosimetry applications.

2.2.1.2 Trap Lifetimes.

The varying degrees of stability of traps, which was described briefly above, can be explained by thermodynamics. The stability of a trap is dependent on a number of factors: time, temperature and the depth of the trap all play an important role in the ability of each defect to retain trapped electrons. The expected lifetime of a particular trap is expressed by the following equation.

$$\tau = s^{-1} \exp(E/kT) \quad [2.1]$$

Thus, at a storage temperature T , the mean lifetime of a trap, τ is described by its trapping parameters E and s , where s is the escape frequency, E represents the trap depth (Figure 2.3) and k is the Boltzmann’s constant ($8.617 \times 10^{-5} \text{ eVK}^{-1}$).

Equation 2.1 predicts that the lifetime of a trap with a given value of s and E decreases exponentially with storage temperature. Therefore, the higher the value of activation energy, in this case temperature, the more stable the trap. This is an important consideration in luminescence dating as the identification and stimulation of traps that are stable over the geological/archaeological time period is a key factor in being able to determine the correct age of the sample.

2.3 A Brief Outline of the Evolution of the Field of Luminescence.

The evolution of the field of luminescence spans from the medieval period to the present day and will undoubtedly continue to evolve well into the future. Whilst medieval alchemists were aware

that some minerals emitted a faint glow when heated in the dark (Becker, 1974), one of the earliest scientific recordings of what is now termed TL was by Robert Boyle in a paper he presented to the Royal Society on 28th October 1663. A famous and much quoted extract from this presentation follows:

“I also brought it (a diamond) to some kind of glimmering light, by taking it to bed with me, and holding it a good while upon a warm part of my naked body” (Boyle, 1664).

Thus, although most of the vast amount of published literature in this field is concentrated around the mid 20th century to the present, luminescence is in no way an exclusively modern field of research.

2.3.1 Historical Background.

Early luminescence work was not of a quantitative nature because prior to the start of the 20th century the light detection systems available simply did not have the sensitivity to measure the luminescence signals emitted from synthetic and natural materials. The main application during the 19th century was as a geological tool, specifically for mineral identification and despite the observation of luminescence at this time, the process was not properly understood. Boyle (1664) stimulated a TL signal from body heat and more conventionally with a candle, friction and a hot iron and in 1667 Elsholtz observed a similar effect from the mineral fluorspar (fluorite) (from McKeever 1985). Early interpretations of the phenomenon were that heat itself was being directly converted into light and most of the contemporary observations supported this theory. It was the work of Du Fey that challenged this consensus and in 1726 he suggested that luminescence was due to sulphur which burned when heated; subsequent work by him provided the first clear evidence that TL was a form of delayed phosphorescence. In 1738 Du Fey showed using experiments on natural quartz that TL could be reactivated by exposure of the sample to light. Heat was now recognised as the stimulation source and not its cause (from McKeever 1985).

Early luminescence work led to some important discoveries in both chemistry and physics. Edmond Becquerel's attempt to record luminescence from uranium using photographic emulsions led to the discovery of natural radiation in 1896. This work enabled the use of α particles in a scattering experiment in 1911 that produced the Rutherford model of the atom, which in turn led to the Bohr model in 1913, forming the basis of atomic physics (Spencer, 1996).

The first recorded use of artificial TL was by Wiedemann and Schmidt (1895), who irradiated a synthetically produced phosphor using an electron beam. Work of a similar nature was carried out by Trowbridge and Burbank (1898). They exposed fluorite to X-rays after the natural signal had been removed in order to synthesise TL from minerals. Marie Curie continued this work in her

doctorate and in 1904 she discovered that β -rays from radium could restore TL (see McKeever 1985).

Once the ability to artificially generate TL by radiation had been discovered it opened up the possibility of detailed experimental research (Wick, 1924; 1927; 1928) which made the link between the temperature on the TL glow curve and trap depth. This preliminary work allowed Randall and Wilkins (1945) to formulate first order theories and Garlick and Gibson (1948) second order theories of kinetics.

2.3.2 Applications of Luminescence.

2.3.2.1 Radiation Dosimetry.

The intensity of TL is the result of a competition between trap filling by radiation and trap emptying by thermal excitation. For irradiation at a given temperature, many materials display an intensity of TL that is proportional to the amount of radiation absorbed. Farrington Daniels, in the 1950's, was the first to propose using TL as a radiation dosimeter and the first proper application of this idea was the use of LiF to measure radiation following an atomic weapons test. Lithium Fluoride (LiF) was found by Daniels to be a good dosimeter due to its high sensitivity level and small pellets of the material were used to measure internal radiation doses received by cancer patients treated with radioactive isotopes (Daniels *et al.*, 1953). TL of LiF is still used to measure radiation doses today.

2.3.2.2 Age Determination.

The relationship of TL intensity to absorbed dose led to the obvious use of this technique for sediment/rock age determination. This application of TL was first suggested by Daniels *et al.* (1953), who offered the premise that the natural TL from rocks is directly related to the radioactivity of uranium, thorium and potassium in the environment. This is termed the 'geological dose'. However, age determination using TL did not really become established until a signal was recorded from samples of ancient pottery and it immediately found a niche as an archaeological dating tool. The method of TL dating progressed through the 1960's and 1970's via the development of mineral extraction techniques and the introduction of fine grain techniques by quartz inclusion (Flemming, 1966).

2.3.2.3 Geological Applications.

Daniels *et al.* (1953) stated that of over 3000 natural materials he had studied (mostly granites and limestone) approximately 75% were found to exhibit natural TL of such intensity that it was easily measured. The remaining 25% were also thought to emit TL, but of lower intensity (McKeever

1985). The principle assumption of this work was that the TL is a measure of the absorbed radiation dose since the specimen was last heated, which in the case of an igneous rock is its formation and for a metamorphic rock is the most recent episode of burial and/or tectonic deformation.

Age determination is not the only way that TL is utilised in geology. It has found to be a sensitive tool in radioactive source detection, and in some instances can be more sensitive than the scintillator of a Geiger counter. This application has found widespread use in mining and has been applied to detecting nuclear fallout from nuclear testing and disasters (e.g., Chernobyl) (Fisk and Sanderson, 1999).

Other geological applications involve the study of meteorites and lunar material. Studies of meteorites began in the 1950s but more recent work has provided information on their nearness to the sun whilst in space and the time meteorites have spent on Earth. Work on lunar materials has also been used to rule out TL as an explanation of anomalous brightness from regions of the moons surface, but promoted the use of TL as a technique to establish heat flow characteristics beneath the lunar surface, and to measure solar flare activity over the last 10^4 years (McKeever 1985).

2.3.3 The Emergence of PSL Techniques.

Whilst the use of optically stimulated luminescence (OSL) to generate a luminescence signal from a material had been introduced early in the evolution of dosimetry, with the observation of bleaching and phototransfer effects, it was the publication of work by Huntley *et al.* (1985b) on optical dating of sediments that created a new field of luminescence research. Optical dating is now a chronological technique in its own right and fundamental research into the processes governing PSL has been conducted (Clark *et al.*, 1997; Sanderson and Clark, 1994) via analysis of the luminescence as a function of time and this work will be discussed in later chapters.

2.4 The Luminescence of Quartz.

Currently quartz is the favoured dosimeter in archaeological dating, especially using the OSL techniques that have developed rapidly since the mid 1980's. This method has advantages over TL because OSL of quartz is known to bleach much faster during transport and sedimentation under natural light than most of its TL components (Krbetschek *et al.*, 1997). The OSL emission is predominantly in the ultraviolet as is that of the 110 and 325°C TL peaks. The range of dates accessible using quartz is controlled by the level of radioactivity in its surrounding environment and is thought to be ≤ 150 ka. Quartz OSL has been used as a successful and accurate chronological technique since its development over a quarter of a century ago but it has not been without its share of problems. Its age range is limited by its saturation level despite having theoretical trap lifetimes

of millions of years (Aitken, 1998). There are issues with recuperation changes in sensitivity (Guibert *et al.*, 2001; Hutt *et al.*, 2001; Ward *et al.*, 2003) and most importantly in the case of the work here, the intensity of quartz luminescence is much lower than that of feldspar.

2.5 The Luminescence of Feldspar.

Since the work of Mejdahl in the mid 1980s, feldspars have been used widely for palaeodosimetry. They have proved particularly popular because of the technical ease with which an optically stimulated luminescence signal can be obtained and their potential for use in luminescence dating over a wider time range than quartz (Duller, 1997). Although feldspars are more mineralogically and chemically complex than quartz, they have several practical advantages that have encouraged extensive research into their luminescence behaviour. The advantages of feldspars in luminescence applications have been outlined in the Introduction so will be summarised here as three points. Firstly, geological samples have a higher intrinsic intensity of luminescence than quartz, which means they can be used to measure lower absorbed radiation doses. Secondly, alkali feldspars contain a significant proportion of potassium, whose radioactive isotope (^{40}K) can contribute significantly to the total ionising radiation dose of the crystal. This internal component is unaffected by variations in interstitial water or in the thickness of the overburden and hence the overall uncertainty in the dose rate is reduced (Duller, 1997). Thirdly, Hutt *et al.* (1988) discovered that it was possible to obtain an IRSL signal from feldspars using stimulation from ~800-950nm. This is important because quartz does not produce an IRSL signal or that such a signal is several orders of magnitude weaker than that from feldspars (Godfrey-Smith and Cada, 1996). Thus, potential complications from overlapping quartz and feldspar emission spectra in polymineral samples are eliminated.

While existing spectral information on feldspar emissions is limited, it has been summarised by Krbetschek *et al.* (1997). Nine emission bands have been identified: 275-290nm, 320-340nm, 390-440nm, 450-490nm, 500-540nm, 560-570nm, 580-600nm, 700-760nm, and emissions >800nm. The most common signal used in TL dating studies is the UV-blue (390-440nm). The majority of feldspars show a double peak glow curve, with peaks centred on 280°C and 350°C at a heating rate of 5°Cs⁻¹. The mean lifetimes of these traps are in the region of 2.5x10⁴ and 2.8x10⁶ ka respectively (Anthony, 2003). The proximity of the nine emission bands to each other makes effective isolation of a single band using combinations of filters problematic. Within OSL dating of feldspar, the main IR emission peak utilised is at ~855nm, which Clark and Sanderson (1994) have shown to be a broad peak.

2.5.1 Feldspar Crystal Structure and its Relation to Luminescence.

The luminescence of a feldspar is controlled by its chemical composition and crystal structure. For a single mineral group they vary widely in their structural and chemical composition and furthermore feldspar commonly contain different types of inclusions. Understanding the nature of these variables is important when classifying the luminescence behaviour of a dating sample. For example, perthitic alkali feldspars show features of both end members of the alkali feldspar groups, while non-perthitic feldspars are dominated by emissions from one of the end members.

As stated in Chapter 1, the mineralogical purity of a sample is very important in understanding its luminescence behaviour. This is also true of its chemistry because feldspars can be very brightly or weakly luminescent (Krbetschek *et al.*, 1997). Intermediate examples of both alkali and plagioclase feldspars are characterised by low TL intensities, with the latter experiencing a further decrease in intensity with increasing Ca concentrations. K-rich and Na-rich feldspars usually have the highest intensity TL peaks. Also, the brightest luminescence is emitted by feldspars with a disordered lattice (Krbetschek *et al.*, 1997). It is those minerals that have crystallised at high temperatures and have a high structural state that have a disordered lattice. An excellent example of this is monoclinic sanidine, a high temperature polymorph of $K(AlSi_3O_8)$, which is mostly found within extrusive igneous rocks. The next stage is the intermediate temperature structural state and the ordered polymorph monoclinic orthoclase. The low temperature state (triclinic microcline) is less symmetrical, has a lower structural state and has an ordered lattice. These minerals are compositionally comparable, but the differences in crystal structure relate to crystallisation temperature and cooling rate.

2.6 Initial Observations of Anomalous Fading.

Age underestimation from attempts to date sediments or artefacts by feldspar luminescence is not a new phenomenon. The unexplained loss of stored charge from minerals has been known of since the late 1960's when studies of lunar materials reported unexpectedly young ages (McKeever, 1985). In the early 1970's when the possibility of using other minerals in luminescence dating was explored, it was discovered that this unexpected age underestimation is not restricted to feldspars but includes zircon and fluorapatite (Wintle, 1973). As explained above, a material is luminescent when an electron is excited from a donor to an acceptor trap. The signal is said to 'fade' when the above takes place without input of energy or the associated release of light at room temperature.

The term 'anomalous fading' was coined because the initial measurements of this loss of stored signal could not be explained by the physics of kinetics. The term is still widely used today but as this chapter shows there is no rigorous definition of the phenomenon. There are many

contradictions between published studies, with any deviation from the expected age in a feldspar-dominated sample being accounted for by this anomaly. Anomalous fading is in fact very difficult to qualify as its effects reported in the literature are highly variable in terms of signal loss and sample type and the underlying cause may still be poorly understood. When it is used to describe an age underestimation, the reference most commonly cited is the PhD study of Wintle (1973) and related publications. She attempted to date geologically young lava flows in the Massif Central Region of France by feldspar TL. The basalts contained the plagioclase feldspars labradorite, andesine and bytownite, while associated rhyolites contained the alkali feldspar sanidine, and each one produced a significant age underestimation. Wintle stated that this was due to the loss of charge carriers from the traps that emit signal in the 350-400°C section of the TL glow curve. This loss was ascribed to anomalous fading and the term was adopted because the theoretical lifetime of the charge carriers at ambient temperatures should be $10^5 - 10^6$ years. The results of Wintle's study showed that a variety of feldspars fade; out of a group of twenty mineral samples, four were reported as having less than 5% fading and the remaining sixteen up to 40%. It was also concluded that even if feldspar samples showed no measurable fading over a short time period (four weeks) following laboratory irradiation it should not be taken for granted that the sample will not suffer any unexplainable loss of signal during burial over much longer timescales. Thus, while the initial loss occurs within a short period of time after irradiation there may also be long-term and more gradual signal deterioration. However, it is important to note that measurements by Wintle were made without preheating and as a consequence the results may be inaccurate due to an overprinting by the expected and well understood thermal fading.

2.6.1 Anomalous Fading in the Dating Literature.

There have been both successful and unsuccessful feldspar dating studies carried out on both archaeological and geological sample. From the vast amount of literature on the problem of anomalous fading of feldspars it is easily assumed that all attempts to date using feldspar luminescence encounter the phenomenon of this unexplained signal loss. There is in fact evidence of both good and bad examples of feldspar stability present in the literature and some are discussed below to justify the continued use of this mineral group and the need for further investigation of such a mercurial process.

2.6.1.1 Successes in Dating Using Feldspar Luminescence.

Huxtable *et al.* (1972) used TL to date 31 baked clay balls. Out of this large sample suite only one exhibited unexplained signal loss at a rate greater than 10% a month, but even this sample fell within errors of external age controls. Studies by Mejdahl (1983) on feldspar grains from Scandinavian pottery, burnt stones and glacial sediments indicated that fading is not a problem

when using these materials, for samples up to 10^4 years old. However, work by Wintle (1985) on feldspar TL from fine-grain loess samples suggests that fading may be a significant problem in samples that have been exposed to ionising radiation for a more prolonged period (Aitken, 1985).

Hong *et al.* (2003) successfully determined the sedimentation rate of a recently deposited tidal flat. They used IRSL to measure K-feldspar grains extracted from five samples that were collected from a core taken from the flat. The very low luminescence intensity in the surface sample indicated that the material was well bleached at deposition. Recuperation before and after preheating was investigated on natural and laboratory bleached surface samples and were considered in the age calculations. The five IRSL age estimates show a reasonable stratigraphic correlation allowing the authors to conclude that ISRL dating can contribute significantly to their field of research. Duller has undertaken considerable research on dune sands from New Zealand including dating using K-feldspars. In his 1992 paper, Duller compared TL and IRSL for determining the equivalent dose from extracted K-feldspar. With the exception of a modern dune sand, the two methods yielded comparable results in spite of the differences in the nature of the two signals being measured. When attempting to date samples from elsewhere in New Zealand, Duller (1994b) used coarse grained K-rich feldspar extracts from twelve dune sands. Luminescence ages were again calculated using TL and IRSL measurements to determine total bleach and regeneration equivalent doses for each sample. No systematic differences were observed between results obtained using any of these methods. Withstanding the uncertainties of the independent ages of some of the samples, comparisons of the quartz and feldspar luminescence ages can be obtained for samples younger than 130ka. Duller suggests that older samples underestimate the true age due to the long term fading identified in previous studies. However, in his attempt to date older (130-350Ka) sediments an age underestimation was not found (Duller 1994).

2.6.1.2 Unsuccessful Dating Studies Using Feldspar Luminescence.

Whittle (1975a) attempted to date Egyptian pre-dynastic sherds and they reported that nearly all exhibited a debilitating signal loss. Studies carried out on Neolithic and Chalcolithic samples from central Portugal (Whittle and Arnaud, 1975b) also indicated that anomalous fading is prevalent in feldspar dominated samples, with 52 out of 55 sherds suffering an unexplained signal decay during laboratory tests. When Balescu *et al.* (2003) attempted to determine the chronology of Pleistocene loess deposits from Romania, all of their results suffered from a severe age underestimation. They used a modified version of Wallinga's (2000) multi-aliquot protocol and the preheat applied was 260°C for 60 seconds, with the resulting age underestimation more than 40% in some samples. The main constituent of these samples was albite, which given current thinking should be datable. These samples also contained a small component of sanidine, around 3%. If this uncommon and unstable feldspar variety had a much brighter luminescence than the other luminescent constituents

of the sample, then the sanidine could be a major contributor to the net signal, thus explaining the high levels of signal instability. A lack of sample homogeneity and possibly too short a preheat time could also account for at least some, if not all, of the age underestimation in this sample.

Spencer and Owen (2004) carried out a comprehensive comparison of OSL and cosmogenic radionuclide (CRN) ages. This was the first time that CRN ages from moraine boulders have been validated using OSL dating of glaciogenic sediments from the same moraine ridge. Single grain OSL measurements were carried out on quartz and K-feldspars extracted from twelve Quaternary glaciogenic sediments. Rapid signal saturation in preliminary additive dose IRSL K-feldspar luminescence growth data was interpreted as evidence of insufficiently bleached latent luminescence, with these data yielding overestimated ages in the majority of the samples. This is the opposite of problems usually reported from feldspar IRSL ages. Further analysis was then made, concentrating on replicating SAR-dose measurements of quartz, using blue-green stimulation. The SAR sensitivity correction method repeatedly failed in two of the samples and another one exhibited significant thermal transfer. Nevertheless, three of the eight glacial successions were dated using quartz luminescence. There is some discussion about the possibility of inherited components in the CRN data although in terms of palaeoclimatic interpretations both dating techniques give concordant results. So despite the serious accuracy issues suffered by the majority of quartz samples and the question mark over the accuracy of the CRN data, there was significant bias against the feldspar results, this was due to the ingrained distrust of luminescence workers owing to uncertainties about the stability of feldspar luminescence as a whole.

2.6.2 Identifying Fading in Feldspars.

The above provide a small window into documented cases of anomalous fading in dating and show that results are variable, even when the monitoring procedures have been used. It must be pointed out that most tests for fading are carried out on samples that have been heated or bleached to remove the natural signal. These luminescence stability tests are thus second glow measurements and such procedures use various storage times ranging from 18 hours to 2 months. These are far shorter than geological timescales and so there is a potential that long-term fading will not be observed during these tests.

A different method of identifying fading was developed as part of the study of Portuguese sherds by Whittle (1975b). Here, first glow fading studies (an artificial dose being added to the natural) were carried out on five of the fourteen that showed less than 3% fading over a two-month period. Only one of these passed the 46 day first-glow test and it was noted that this fine grain date was still 36% lower than the quartz inclusion date from the sherd. So, from the same sherd there were two separate and completely different dates, even when the fine grain sample had passed the

laboratory fading test. As there was no external age control it is not obvious which of the dates was accurate. Both the feldspars and the quartz will have undergone the same exposure to environmental and external radiation conditions, so the mineralogy of the two must come under scrutiny when such differences in estimated dose (D_e) are observed.

At the moment there is no better way of detecting any anomalous signal loss other than long-term storage tests, preferably using both second and first glow techniques. Another approach that may be more representative of the original fading is to perform the tests on discs which have been given a test dose after the natural TL has been erased by exposure to UV, as it has been used in the dating of marine sediments (Wintle and Huntley, 1978). This method would have the advantage of being a first glow measurement but would not have the disadvantage of its effect being diluted by the presence of natural TL. However, the true problem remains that fading tests themselves may be highly inaccurate due to the nature of the techniques, principally variations in glows used and storage times employed.

Work carried out by Chen and colleagues (Chen and HagYahya, 1997; Chen *et al.*, 2000) suggests that many of the age underestimations reported in the literature may not actually be due to the deleterious effects of anomalous fading but a consequence of incorrect laboratory procedures when measuring feldspar samples. They suggest that a possible explanation of anomalous fading in TL may, in some cases, be what they call 'normal fading' in disguise. The existence of non-radiative centres that are competing with the radiative luminescence centres produce a very narrow TL peak. The apparent kinetic parameters, say E and s in first order kinetics, may appear to be much larger than the real values due to the narrowing of the peak. This in turn results in the expectation of a very long decay time, t , at room temperature for example. The real values of the parameters are however such that the loss of trapped carriers is orders of magnitude faster. The effective expected lifetimes are up to five orders of magnitude greater than those of the observed effect, which can explain, at least in some cases, the age underestimation that results.

2.6.2.1 Summary.

The underlying complexities associated with the apparent variability of fading rates are becoming apparent. Dating studies using feldspars can be successful in producing ages comparable to external age controls (Huxtable 1972), or a complete failure (Whittle 1975a,b), with many examples falling between. Some authors have even gone as far as to claim that fading is inherent to some extent within all feldspars (Huntley and Lamothe, 2001; Spooner, 1992). Different dating studies report contrasting rates of fading for similar samples, similar environments and ages. Loess has been a success story but even then there are reports of age underestimation (Duller, 1992). Feldspar dates are discarded in favour of those from quartz based on what are sometimes potentially inaccurate

external age controls. In Spencer and Owen (2004) the difficulty in obtaining even a few quartz De that compliment the suspect CRN data would benefit greatly from the ability to measure stable feldspar signals. This is just a small indication of the need within the luminescence community for feldspars to be re-established as an accurate dosimeter. However it is difficult to resolve an issue regarding phenomenon that are hard to explain and workers on the problem know only that feldspar as a mineral species can exhibit anomalous fading.

2.6.2.2 Variations in Signal Stability with Feldspar Mineralogy.

The feldspar group has a broad range of chemistry and crystal structure and these variations control their luminescence behaviour. Evidence for comparable influence on anomalous fading is also apparent (e.g., elevated fading with increased calcium in the lattice (Huntley and Lian, 2006) and from volcanic material (Visocekas *et al.*, 1998)).

2.6.2.2.1 Order Versus Disorder.

Visocekas *et al.* (1998) state that the observed differences in the magnitude of fading between feldspar minerals relates to the conditions under which they crystallise. Crystal structure influences fading by controlling the amount of disorder in the lattice. In fact, this has been one of the few general consensuses since the work of Wintle (1973; 1974; 1982). The most seriously affected samples are those containing a high proportion of grains derived from comparatively recent volcanic eruptions and such minerals will have an Al-Si disordered lattice.

Visocekas *et al.* (1998) used the structural differences between high sanidine and low microcline to explain the relative amounts of fading from each. They claimed that the differences between the radiative energy storage and decay processes can be explained solely by the crystal structure. All feldspars are constructed from SiO_4 tetrahedra. A given fraction (25%) of the Si^{4+} ions are substituted by Al^{3+} and there is charge compensation from the introduction of alkali ions at interstitial positions. In feldspar that has crystallised slowly at a low temperature, such as microcline, there is a periodic sequence of Al- and Si-bearing tetrahedra, which is the stable form at room temperature. By contrast, sanidine has what can be called an anti-structure, in that the Al and Si tetrahedra are randomly distributed and unstable at room temperatures. The preservation and apparent stability of this structure is explained by the rapid crystallisation at high temperature that ‘freezes’ the crystal lattice in this disordered structural state; in theory this type of alkali feldspar is stable only at a temperature very close to its melting point. It is possible for the sanidine to revert to microcline at room temperature, but only through a solid-state transformation that requires geological timescale. Parsons and Lee (2005) discuss such issues in greater detail. One of the most interesting characteristics of the early anomalous fading studies of volcanic samples is the focus on rapidly fading sanidine. This feldspar is scarce in crustal rocks and sediments and has many

features that are not shared by more abundant feldspars. Taking into account the unusual crystal structure of sanidine, the question has to be asked about the accuracy and applicability of these studies in trying to quantify and qualify the problem of unexplained signal loss in the feldspar mineral series as a whole.

From a sample perspective even if there is such a clear separation between fading and non-fading feldspars as suggested by Visocekas *et al.* (1998), it does not help in dating applications. The comparable densities of feldspars crystallised at high and lower temperatures precludes easy separation using traditional heavy liquid techniques. The possibility of recrystallisation to a lower structural state also contributes to the scarcity of sanidines in sediments. It is therefore unfortunate that these feldspars have a high luminescence sensitivity compared to their immediate neighbours on the ternary diagram (Figure 1.2) and so if present these minerals will be producing the dominant luminescence signal.

Recently, Huntley and Lian (2006) have described the fading rates of a variety of alkali and plagioclase feldspars separated from sediments. They reported that all the seventy-seven mineral separates fade at rates ranging from 1 to 10%/decade. They also observed that feldspars extracted from plutonic-sourced sediments do not fade any less than those from volcanic regions. The results go against the popular theory of the influence of structural order/disorder on fading rates. They also conclude that age of the samples may be important with the older samples having a greater propensity to fade due to higher levels of radiation damage. In fact it was suggested by Lamothe (*pers. com.*) that this may be due to Uranium content and high levels of alpha radiation that produce greater amounts of damage, particularly in the case of alpha tracks that produce clustering of defects.

2.6.2.2.2 Chemistry.

The correlation between fading and Si, Al disorder is noted by Spooner (1994). He found evidence for mineralogical control on luminescence stability by undertaking measurements of anomalous fading of IRSL on a suite of feldspars stored for periods of up to 15 months at temperatures from around 10°C to 100°C. Examples of feldspars representative of each major compositional regime of the ternary system were found to fade whereas others were stable. Non-fading behaviour was observed only from samples of end-members (or near end-member) species of the ternary system. These ordered feldspars are likely to have been formed by very gradual transition from the disordered structure into which feldspars crystallise on cooling from the molten state (Zink *et al.*, 1995).

Of the individual feldspars reported in Huntley and Lian (2006), the rate of fading in the plagioclase feldspar series increases with calcium (Ca) content (An). In a later study Huntley *et al.*

(2007) used this correlation with Ca content to explain the tunnelling (see section 2.6.3.2) exhibited by plagioclase feldspars. Huntley *et al.* (2007) concluded that with up to 5% Ca content, the tunnelling is a direct consequence of this cation-induced defect. He also conceded that the presence of Mn^{2+} ions, due to the two-phase nature of their samples, must also cause tunnelling. Plagioclase crystals with low Ca (i.e., albite) contents have no detectable fading and as a result have prospects for optical dating of up to one million years or more. This work is supported by several arguments that the centres to which the electrons tunnel to produce the loss of signal are not impurities but structural defects. However, the two labradorite samples that Huntley *et al.* (2007) used have similar Ca contents but very different fading rates and are an indication that the Ca atom itself is probably not the centre to which an electron tunnels, but that the centre is a result of the replacement of the Na by Ca, or Al by Si. It is possible that Fe^{3+} rather than Ca, plays an important role.

2.6.3 Fading and the Proximity Models Used to Describe it.

Ever since its discovery, the causes of fading have been extensively studied and debated. Currently there are two competing theories, described by proximity models, known as the localised transition model and quantum mechanical tunnelling. Neither model has been shown to completely encompass all the known facets of anomalous fading, but at present the latter is the most commonly quoted explanation.

The two models are believed to operate at different temperatures with tunnelling expected to dominate at temperatures ambient and below and localised transition at high temperatures (Templer, 1986). Although the tunnelling model in its simplest form appeared initially to be temperature independent as there is no energy barrier to scale (Figure 2.3), a localised transition relies on some temperature increase to achieve sufficient energy to reach the excited state (Figure 2.5). Visocekas *et al.* (1976) adjusted this model to satisfy observed temperature dependence of fading (Figure 2.4). The thermally assisted tunnelling model allows for the charge carrier to be thermally excited before tunnelling.

2.6.3.1 The Localised Transition Model.

This model is based on the sub-conduction band localised transitions that were suggested by Templer (1986) to account for the fading of zircon when stored at elevated temperatures. Conventional models of luminescence involve the transition between a trap and the conduction or valence bands. However for the case of adjacent defects, a trap and centre may share an excited state that lies between the trap and the conduction band, allowing charge recombination to occur via this state. This model considers that only a limited proportion of the trapped electrons have the necessary mechanism for escape. The weak temperature dependence of this model implies that

fading can be accelerated by increasing temperature. Templer’s work on zircons found that heating the sample for one week at ~100°C emptied all the fading traps that had been filled by the laboratory irradiation. Though successful for zircons, he warned that a different heating regime may be necessary for other minerals.

2.6.3.2 Quantum Mechanical Tunnelling.

This is an athermal model requiring no addition of energy into the crystal lattice and is the most commonly quoted explanation of signal loss; it involves the tunnelling of trapped charge carriers to recombination centres through energy barriers. The luminescence model describes how the electron is excited from its trap through external energy induced lattice vibrations, into the conduction band, then relaxes and is recombined, resulting in an emission of a photon. Through tunnelling this recombination occurs instantaneously but at much lower energy levels than would otherwise be required and any luminescence signal is lost. It is a non-radiative process. This tunnelling effect is described by Visocekas *et al.* (1998) and the importance of its emitted afterglow in characterising fading is outlined below.

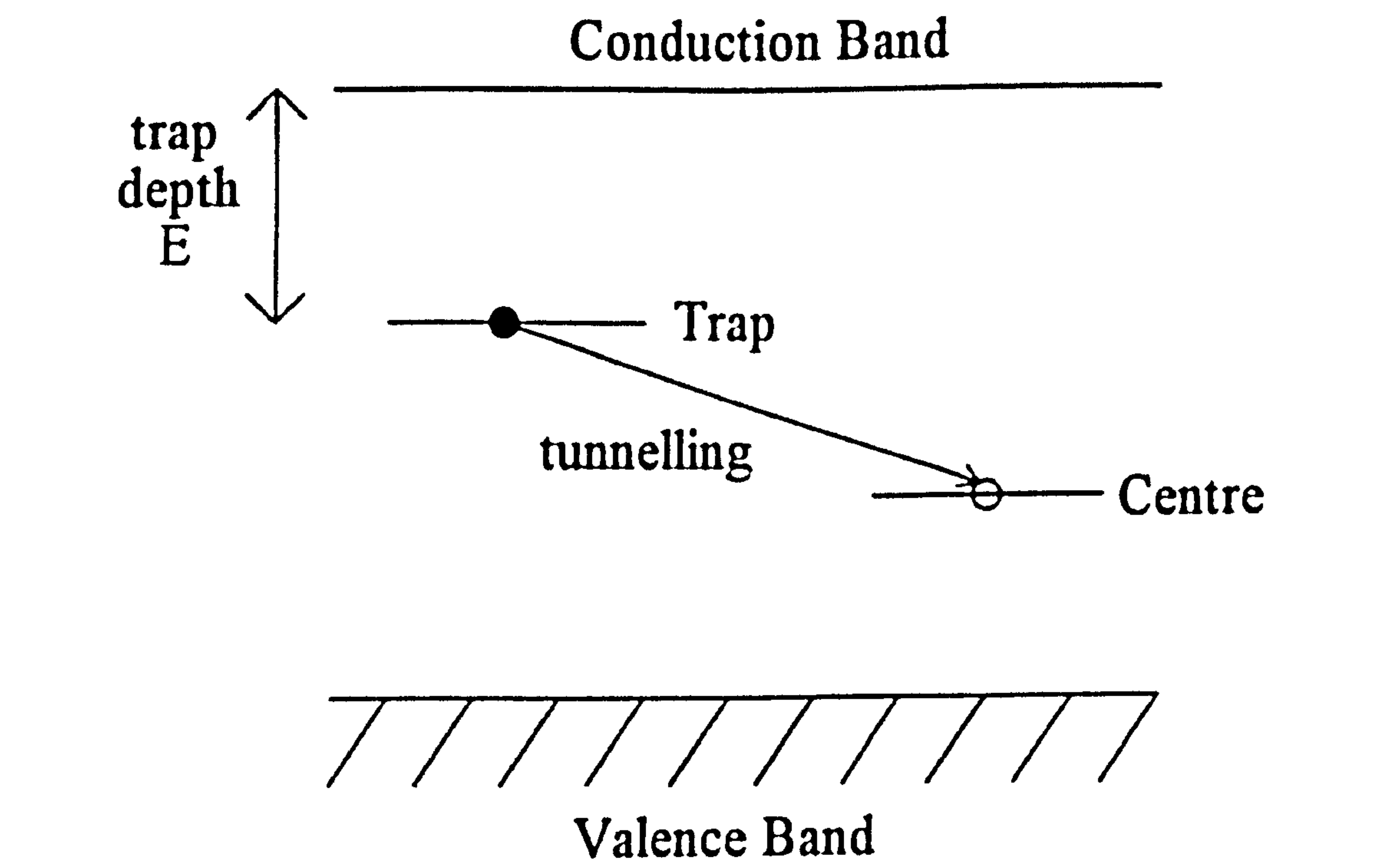


Figure 2.3 Recombination by tunnelling (Smith, 1998).

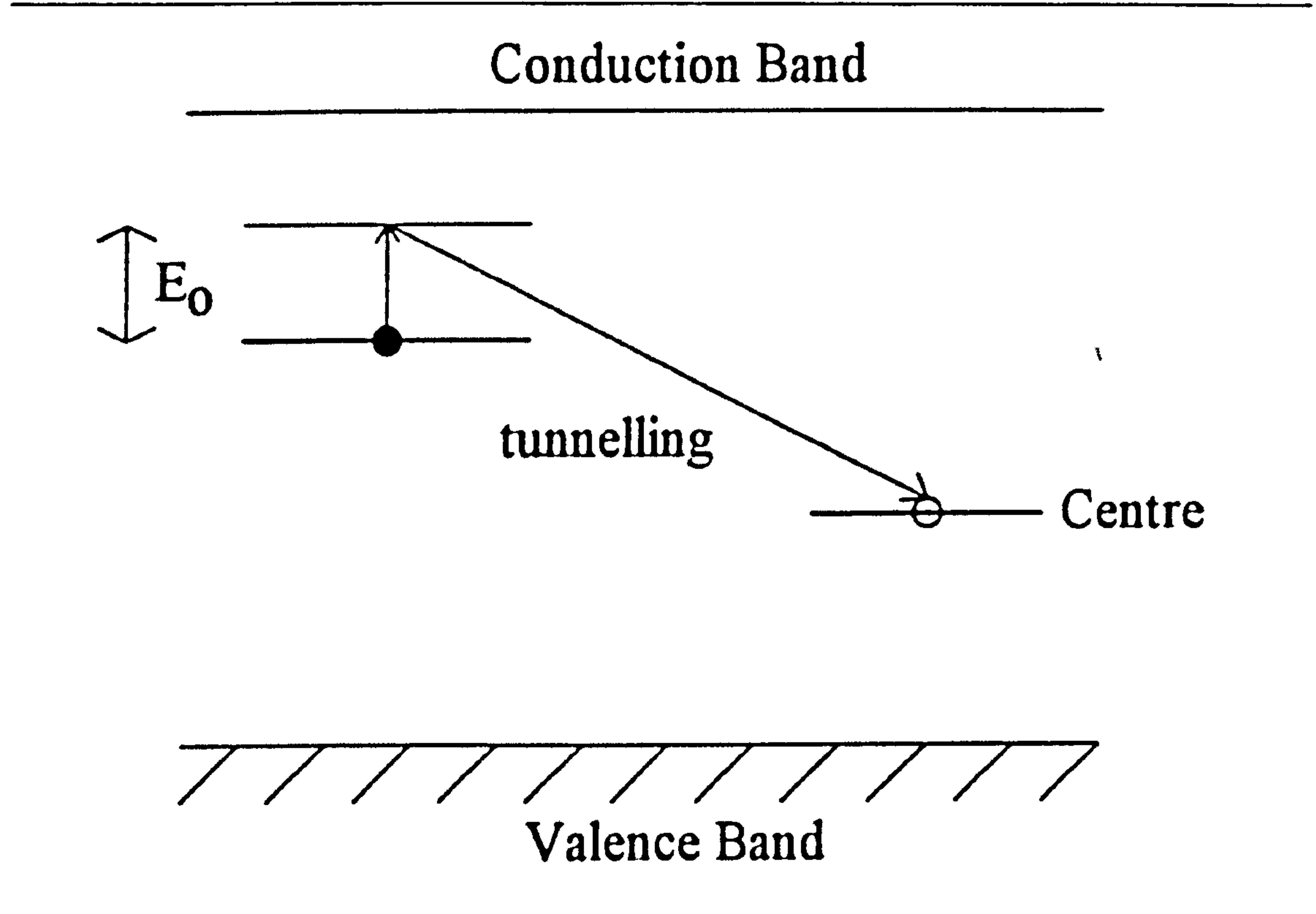


Figure 2.4 Recombination by thermal tunnelling (Smith, 1998).

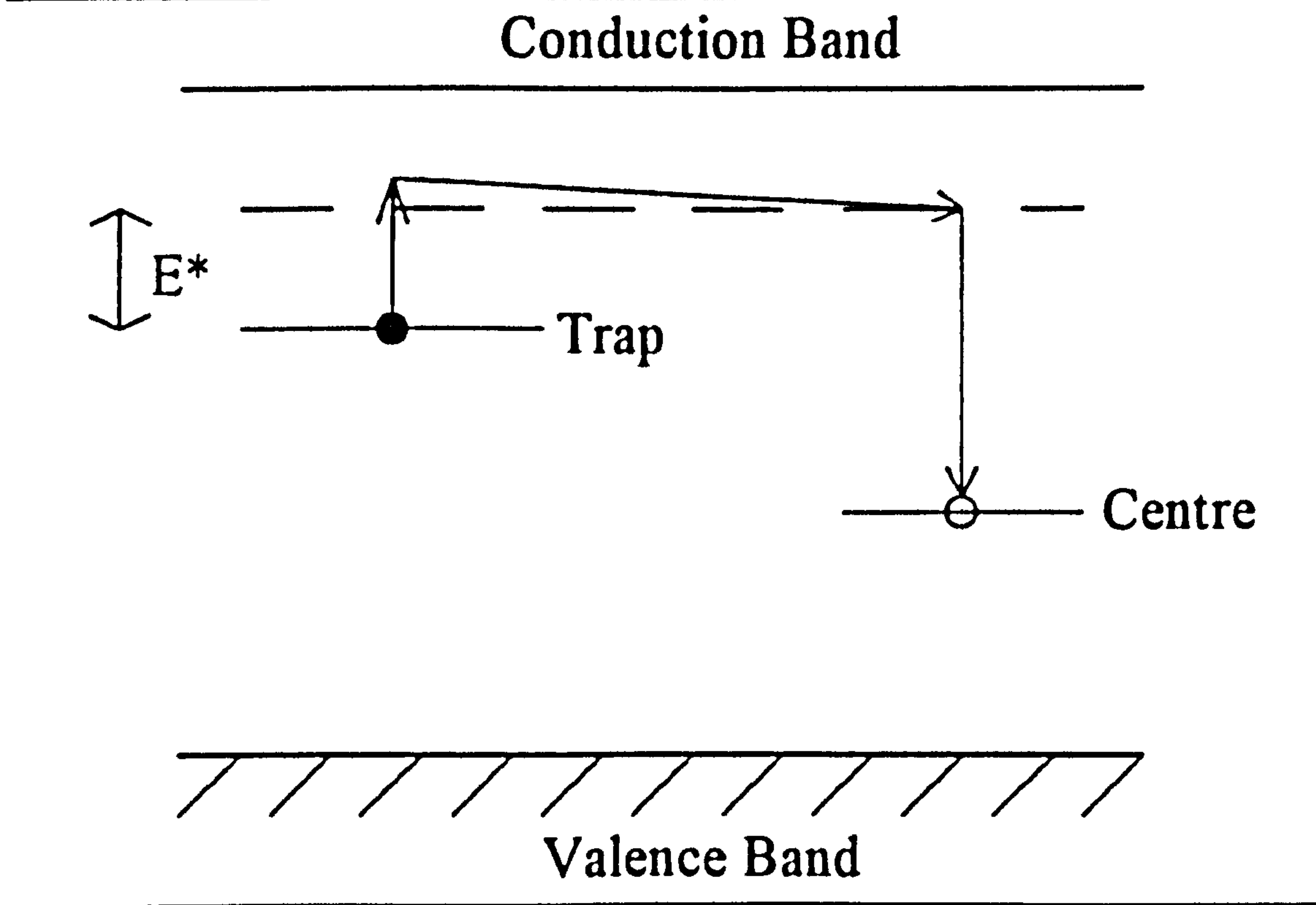


Figure 2.5 Recombination via an excited state – the localised transition model (Smith, 1998).

2.6.3.2.1 Afterglow as an Indicator of Quantum Mechanical Tunnelling.

Hoogenstraaten (1958) observed athermal fading of doped ZnS at liquid nitrogen temperature (LNT). The intensity of the afterglow emitted by the sample is also related to the levels of fading.

The afterglow spectrum indicated that the same centres were being activated as in TL (Visocekas *et al.*, 1976). Hoogenstraaten's proposal that this afterglow was due to tunnelling was applied to explain short-term fading of lunar materials (Garlick and Robinson, 1972) and volcanic feldspars (Wintle, 1973). This study of tunnelling afterglow and its diagnostic possibilities for fading have been taken further by a number of workers, though two groups dominate recent literature: Zink and Visocekas, and Stokes and Fattahi and their contributions will be outlined below.

Visocekas *et al.* (1994) described how a classical thermally stimulated intensity $I(t)$ is expected to substitute down to zero, that is noise level, at around 250 or 230K. With feldspars, $I(t)$ settles down to a lower but non-zero level at around 250K. This is described as the first classical feature of the tunnelling process. With prolonged measurement of afterglow at 80K, the $I(t)$ observed is characteristic of the kinetics of tunnel afterglow:

$$I(t) = (\ln(1+\theta/t)) \quad [2.1]$$

(within an accuracy of a few percent). After some time, $I(t)$ may be approximated by:

$$I(t) = A/t \quad [2.2]$$

(where t is the time since the end of irradiation; C is a constant; θ is the duration of irradiation; $A=C.\theta$)

After some time a final linear heating at around 250K yields the usual TL glow curves that increase until thermal emission dominates the total measured signal.

2.6.3.2.2 Thermal Assistance of Tunnelling.

Initial work predicted that the process of quantum mechanical tunnelling was athermal and work on zircons supported this suggestion (Hoogenstraten, 1958). Yet Visocekas *et al.* (1994) show that this athermal model may not be correct for feldspars. The adapted tunnelling mechanism proposed by Visocekas (1996) describes a process where by an increase in temperature causes electrons to cross into traps at different energy levels by 'hopping' rather than a free release of charge. Taking the one electron, one hole model (Figure 2.6), it can be seen how this thermal process would allow for the age underestimations recorded in the literature. As increasing temperature causes the lattice to vibrate, electrons are shaken free of their traps, but rather than diffusing through the conduction band and entering a luminescence centre, they hop to new acceptors in a completely non-radiative process. This hypothesis requires a stimulation of the lattice source but does not produce luminescence.

2.6.3.3 The Relationship Between Tunnelling and Non-radiative Stored Signal Loss.

If tunnelling is, as many in the luminescence community have now accepted, the cause of the loss of stored charge termed 'anomalous fading', how does it describe observed differences in magnitude of fading between minerals? Visocekas (1979) suggests that one condition favourable for fading could be a relatively low potential barrier for the tunnelling. It is apparent that when the barrier is lowered from 3.5eV to 0.6eV, the lifetime for a given pair (trap and hole) is shortened significantly. Visocekas (1974) explained fading observed in calcite in terms of Gruyere cheese, because the probability of a charge tunnelling to a nearby recombination centre is a direct function of the distance between them. The life expectancy of a pair separated by 2nm is only 10^{-4} sec, whereas if the distance between the two is 4nm then the lifetime increases to about one year and at 5nm the life expectancy should be ~ 1 million years. Thus traps that are very close to a recombination centre lose their electrons almost immediately and as time goes on the distance between remaining traps and centres increases (the holes in the cheese grow larger) until the life expectancy is longer than the time period being measured and the remaining signal is stable.

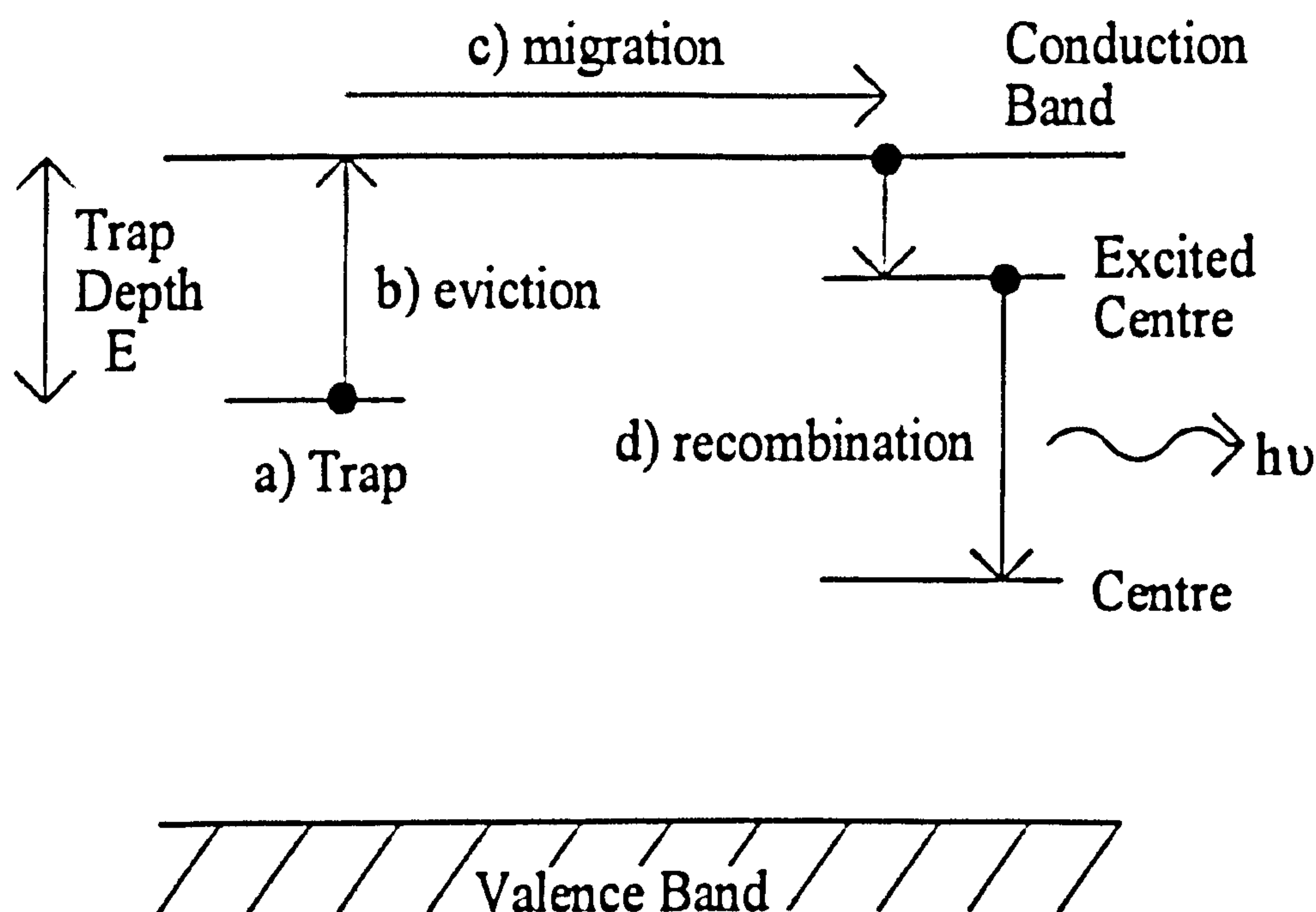


Figure 2.6 The one electron/ one hole model. a) ionising radiation results in trapping of energy carriers; b) eviction from trapped site due to external stimulating energy; c) charge carriers migrate through the conduction band; d) charge carriers relax and recombine (From Smith, 1996).

Further work in this area has resulted in the disappointing conclusion that most feldspar fade as all of those studied exhibit this diagnostic afterglow (Visocekas *et al.*, 1994). Interestingly the feldspars that fade most severely have a higher intensity of tunnel afterglow emission than less severely fading materials, with the afterglow being emitted in the far-red region of the spectrum.

2.6.4 Quantum Mechanical Tunnelling Model at the Expense of Localised Transition.

Neither of these two competing explanations has been able to account completely for all the results and variations of anomalous fading that have been reported in the literature. If thermally assisted signal loss is responsible then the issue of anomalous fading may be overcome (i.e., if the movement of electrons is temperature controlled then using preheating regimes to remove charge from the unstable traps is a potential solution). This approach has been successful in some dating studies (e.g., Sanderson 1988) and storage at elevated temperatures has revealed promising results in studies of removal of 'fading' from zircon (Templer, 1986). Despite the evidence for localised transitions in the literature (Sutton and Zimmerman, 1978), and that this model has adequately explained fading of some feldspars, it is quantum mechanical tunnelling that has become the most widely accepted model. This possibly thermal (historically athermal) process predicts a bleak future for dating using feldspars.

Studies by Visocekas and co-workers (Visocekas *et al.*, 1976; Visocekas *et al.*, 1994) on calcite and feldspars concluded that the presence of a low temperature (down to liquid nitrogen temperature) afterglow is the physical manifestation of quantum mechanical tunnelling. This tunnel afterglow is a time dependant phenomenon, and its intensity is proportional to time (t^{-1}), where t is time since irradiation, with tunnelling becoming increasingly difficult. Therefore, the number of electrons detrapped, and signal lost, is proportional to $\log t$ (Visocekas, 1979). This result gives strong support for models of fading by tunnelling because localised transitions would yield an exponential time dependence. However, because it requires no real addition of energy into the lattice, there is a problem with completely athermal recombination; defects would have to be very close to each other for electrons to be able to cross the energy barrier. There is some question as to whether, even with defect clustering due to disorder in feldspars cooled rapidly from high temperatures, the gaps between defects are too great for such a low energy process to occur.

If temperature-dependant tunnelling is the most feasible mechanism of non-radiative detrapping and retrapping, there may still be a stable signal that can be used for dating. However, it must be emphasised that such a stable signal will only exist if the time period being dated is greater than the time taken for 'unstable traps' to empty by tunnelling. If so, would the correct pre-heating regime allow for the removal of the charge from the traps that are unstable on a laboratory storage timescale? Would such a pre-treatment be applicable to all feldspars, or would different samples require a regime specific to the size of the holes in the 'cheese' (Visocekas *et al.*, 1976) of the minerals that constitute the sample? It is also possible that both tunnelling and localised transitions are linked and can affect the same crystal and even the same traps. Both have temperature-dependent characteristics, with tunnelling acting on traps at lower temperatures and localised

transitions at higher temperatures (Aitken, 1992). It is also possible that different feldspars are affected by each mechanism to a different degree. Could it be that the feldspar samples that respond well to preheat treatments (Sanderson, 1988) (plutonic) fade by the localised transitions, whereas the samples that still exhibit significant fading after pre-treatment (Smith, 1998) are affected by tunnelling?

2.6.4.1 Describing Fading Induced Decay of Luminescence Using t^{-1} .

As outlined above, the decay of afterglow following a t^{-1} law has been used to 'prove' that anomalous fading is a product of tunnelling rather than localised transitions. However, historically this t^{-1} decay has been described for other, not so 'anomalous' phenomena. Isothermal analysis of monomolecular luminescence was first described by Randall and Wilkins (1945). Initial assumptions were that the decay of luminescence intensity with time is controlled by first-order kinetics. If the order of kinetics takes on any value other than one, a non-exponential decay is expected. Randall and Wilkins (1945) discovered that the decay is in fact not-exponential and that of non first-order luminescence, with the rate of decay being dependant on the initial trapped charge population. Early studies showed that the actual decay of luminescence follows a general t^{-x} law. The special case, which appears to be quite common, of $x=1$, is apparent when the possibility of uniformly distributed traps is considered (Randall and Wilkins, 1945). Visocekas *et al.* (1976) found temperature dependant t^{-1} decay from calcite and also interpreted it in terms of uniformly distributed traps. In general, a t^{-x} behaviour can be explained by the presence of trap distributions with the value of x depending on the exact nature of the distribution (McKeever, 1985).

The work of Visocekas *et al.* (1976) demonstrated the relationship between afterglow and anomalous fading. They undertook detailed experiments on calcite in which it was observed that the intensity (I) of the afterglow at LNT immediately following the radiation follows a hyperbolic law.

$$I = \alpha t^{-1}$$

[2.3]

A temperature independent hyperbolic decay of luminescence is symbolic of a mechanism for the reduction of the trapped charge by tunnelling. Having demonstrated the probability of low temperature afterglow originated from tunnelling, Visocekas (Visocekas, 1979; Visocekas *et al.*, 1976) confirmed the relationship between the luminescence emitted as afterglow and the lost TL as anomalous fading. He stated that the light emitted as afterglow is equal to the light lost in TL and used the t^{-1} to prove the tunnelling nature of fading in feldspars.

However, in several articles a temperature independent (or nearly so) t^{-1} decay law has been observed, which is inconsistent with thermal detrapping models (Visocekas *et al.*, 1976). The

model proposed to account for this law is that of quantum mechanical tunnelling from one site to another nearby. Sometimes this tunnelling takes place only after the thermal excitation of the donor electrons from a deep level to a shallower one. This process is termed thermally assisted tunnelling. Visocekas *et al.* (1976) concluded that the observation of a low temperature signal with a decay rate of t^{-1} is diagnostic of anomalous fading by athermal or thermal tunnelling. Early models describing the kinetics of luminescence, particularly phosphorescence (Randall and Wilkins, 1945), predicted this same hyperbolic decay for a signal emitted after irradiation. Quantum mechanical tunnelling and thermally assisted tunnelling follow the same decay laws as afterglow and phosphorescence. It must be disputed that the existence of an emission with this decay is diagnostic of anomalous fading although the links cannot be denied.

The conclusions that feldspars fade following t^{-1} and that this is directly related to tunnelling were disputed by work carried out by Smith (1998). He studied the relationship between fading and tunnelling in volcanic feldspars and his results were in agreement with those of other workers in that, as expected, all his samples exhibited strong fading at ambient temperatures, losing 30-80% of signal in 1-2 weeks. However he reported that the time dependence did not generally follow the expected t^{-1} decay associated with the athermal trapping model with randomly distributed defects. Storage at elevated temperatures increased fading rates, possibly consistent with the thermally assisted tunnelling (but not with random distribution of defects) or the localised transition model. Therefore, using a t^{-1} decay model to describe tunnelling could be misleading as such a decay rate has been ascribed to both non-tunnelling afterglow and phosphorescence. Smith (1998) has also demonstrated that not all fading follows such time dependence.

2.7 Solving the Problem of Anomalous Fading in Feldspars.

2.7.1 Circumvention Using the Near-IR Emission.

2.7.1.1 Introduction.

An offshoot of Visocekas's work was the discovery of apparently stable regions of the feldspar emission spectrum. It is ironic that IR afterglow is described as diagnostic of tunnelling and therefore used to 'prove' fading, whereas red TL (RTL) emission is apparently stable even when the UV-blue emission from the same feldspar grains fades severely. The afterglow emission occurs in the IR range (630-850nm) and is centred on a peak at 710nm, which is linked directly to the substitution of the Fe^{3+} ion into the lattice (Fattahi and Stokes, 2000; Visocekas *et al.*, 1994). Extensive research has been carried out on understanding the processes behind this emission and fading.

2.7.1.2 A Summary of the Far Red Work Carried Out By the Paris Group.

Having found almost ubiquitous fading of the UV-blue TL feldspar emission, Zink, Visocekas and colleagues (Visocekas, 1979; Visocekas, 2000; Visocekas *et al.*, 1976; Visocekas and Guerin, 2006; Visocekas *et al.*, 1994; Visocekas *et al.*, 1996; Visocekas *et al.*, 1998; Visocekas and Zink, 1999; Zink and Visocekas, 1996; Zink and Visocekas, 1997; Zink *et al.*, 1995) have shifted the focus of their research to the little studied near-IR side of the spectrum and their work has shown promising results for measuring a stable feldspar luminescence emission.

One of their studies was on the fading characteristics of sanidine and they concluded that although the afterglow occurred in the IR only, both the blue and IR emission bands exhibited some amount of fading. Zink *et al.* (1995) states, “The blue TL peak decays at all temperatures following a typical ‘anomalous fading’ pattern. The IR peak decays as well, but a fading acting rather on the lower temperatures of the TL peak”. This process was documented as being quite extreme in volcanic sanidine. Still, it has been observed that bleaching of the ‘blue’ emission during OSL measurements results in the IR emission being bleached in parallel and it is difficult to enhance or bleach either signal independently of each other (Zink *et al.*, 1995). This study concluded with a number of points important to the usefulness of feldspars for geological dating. They found that the minor amount of IR signal loss with storage is a result of thermal quenching. Therefore, at higher temperatures most of Fe^{3+} induced signal decays by non-radiative processes and as a result the IR emission that is observed during TL is only a small proportion of the signal that should be present. However, as there is evidence that IR is far more stable than the blue emission it may therefore be more usable for dating. Despite the focus placed on the IR emission, work by Visocekas and colleagues has demonstrated that the less fading IR band can be used as a gauge for loss of signal from the blue (Visocekas, 2000).

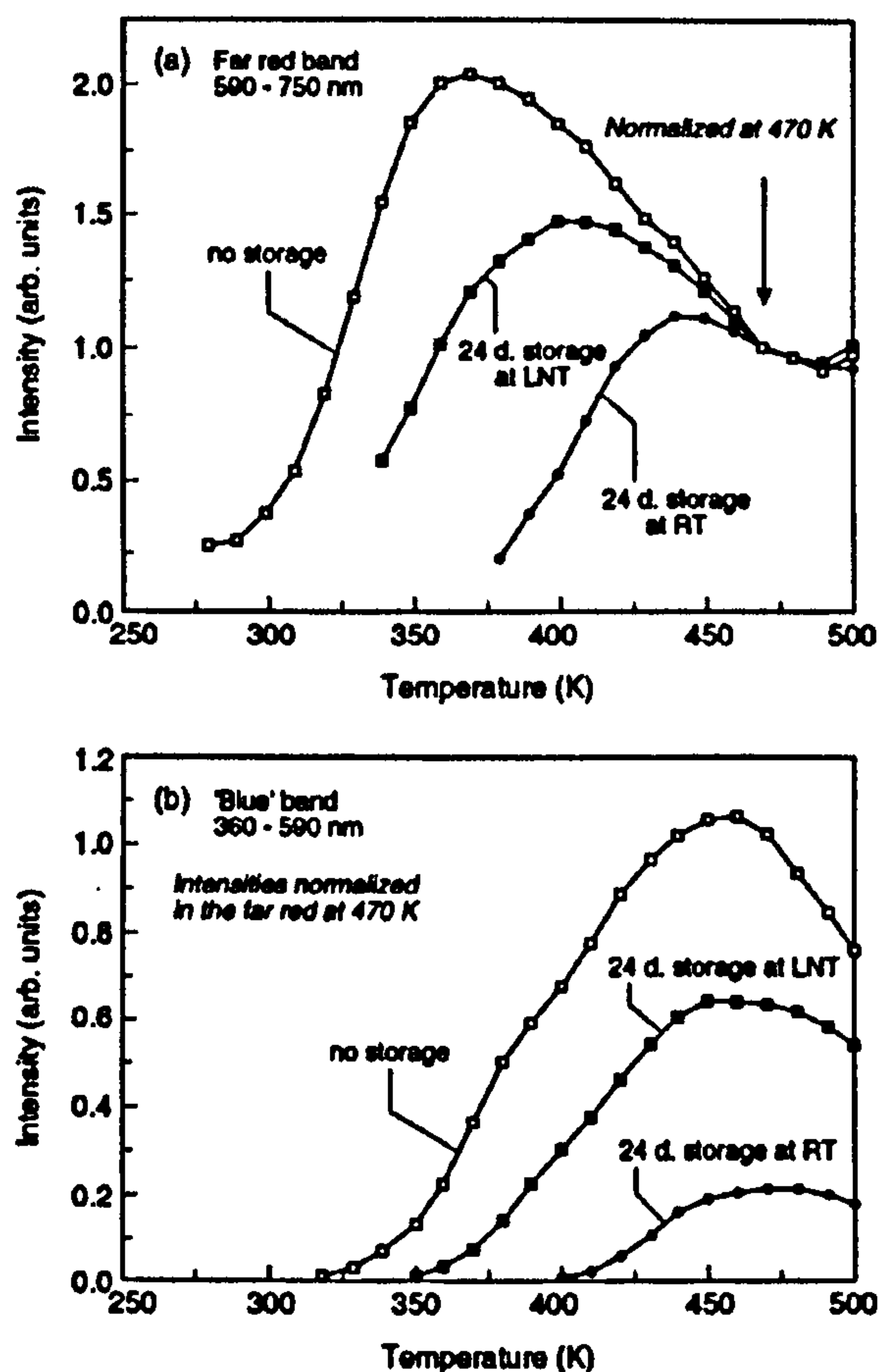


Figure 2.7. TL glow curves for a sanidine feldspar crystal from Eifel, Germany following a 250Gy irradiation and three different storage conditions as shown, 10Kmin^{-1} heating rate, and separation of the 'blue' and 'far red' emissions. (a) TL curves in the far red band (590-750nm). (b) related TL curves in the blue band (360-590nm), showing considerable anomalous fading. (reproduced from Visocekas and Zink (1999).

The observed differences in stability of the two emission bands has become the basis of a method for evaluating the amount of fading in a feldspar sample (Visocekas 2000). The comparison here is not made between the amounts of signal measured at the different storage times, but rather TL is measured in the two spectral ranges simultaneously. At every temperature point the ratio between the two bands (B_{ir}) is computed and to monitor fading these ratios are compared. When fading is present, values of B_{ir} decrease during storage, according to the logarithmic law. A temperature dependence of fading has been firmly established through these results. The IR signal itself is seen to fade at high temperatures, and is thought to be a result of the thermal activation of deep traps. These traps are known to be emptied by OSL and also at low temperatures by thermal far-red tunnelling effects. With thermal stimulation this charge may reach higher traps that are less localised than the deeper traps and can therefore be emptied by tunnelling giving rise to this fading. These results have shown that the presence of fading in the TL of feldspars appears experimentally as rather variable depending on the position of the emission within the spectrum.

2.7.1.3 Fattahi and Stokes.

A major contributor to the work on IR luminescence has been the Oxford Luminescence Research Group, particularly Fattahi and Stokes. In 2003, Fattahi and Stokes reported that the IR-TL from a selection of K-feldspar samples had been successfully measured. High temperature IR-TL (300-450°C) they claim, exhibits greater stability than the usual UV-blue range. They also concluded that the previous work (Zink and Visocekas, 1997) was correct as they were also able to show that IR-TL from feldspars does not fade. It was discovered that the signal is bleachable with IR exposure and that around a third of the total trapped charge responsible for the orange-red IRSL signal gives rise to that of IR-TL, indicating that some traps and centres contribute to both emissions.

2.7.1.3.1 IR-IRSL.

A recent development from IR-TL is the promising area of IR-IRSL dating. This technique has been successfully used for dating in conjunction with the SAR method (Fattahi and Stokes, 2003c; Fattahi *et al.*, 2004a). The potential of the IR (833±5nm) stimulated near-IR emission (λ emission =600-750nm), or IR-IRSL, from K-feldspar as a dosimeter has been extensively studied (Fattahi and Stokes 2003, 2004). The authors have presented evidence that SAR techniques can successfully and accurately recover a known laboratory dose in IR-IRSL from K-feldspar separates. It has additionally been demonstrated that reconstruction of a laboratory dose is achieved easily using the SAR protocol. Equivalent doses for natural samples examined give results that are consistent with the far-red emission being immune from the effects of fading.

2.7.1.4 The Viability of the Near-IR as a Detectable Stable Feldspar Luminescence Emission.

Given the success of using high temperature IR-TL for recovering laboratory doses why has it not become a widespread technique in feldspar dating? There are a number of reasons for this, both instrumental and practical. In the former it is unfortunately true that the detection of luminescence emission is overwhelmingly biased towards the UV-blue portions of the electromagnetic spectrum. This is due to a number of factors including the general performance of this region of luminescence emission as an integrating dosimeter for quartz in the time range Ca 0-150ka (Fattahi and Stokes, 2003b) and the historical development of blue sensitive PMT's. Practically there is also a significant problem in the separation of near-IR luminescence from thermal incandescence and other background contributions. For example, while Visocekas and Zink (1994) define IR-TL as that centred on the stable 700-710nm emission, the work carried out by Fattahi and Stokes is based around the 600-700nm part of the spectrum (i.e., between the stable peak and the blue region that suffers the greatest amount of fading). Fattahi and Stokes' movement to shorter wavelengths has

been made in response to the difficulty in detecting longer wavelength TL in the presence of background noise. The early work by Visocekas *et al.* (1994) has been very successful in low temperature IR-TL, though background interference is highly problematic above 300-350°C. This orange-red emission has proved easier to separate from background noise giving an improved signal-to-noise ratio, but it has shifted away from the peak of interest so championed by the work of Visocekas and Zink. Both groups however have observed promising results in terms of dating volcanic samples using feldspars.

2.7.2 Measurement Techniques and Correction Factors.

Understanding the process behind the phenomenon of anomalous fading is only one part of the large field of research that has developed since Wintle highlighted the problem in 1973. The models outlined above have been utilised by workers experimenting with methods to correct for any resulting age underestimation. These solutions have been many and varied, some can even be described as contradictory. What follows is a brief outline of the main correction techniques that have been presented in the literature and the successes and problems associated with them. One such technique advocated by Wintle (1978), using accurate fading calculations from tests carried out on discs which have been given a test dose after the natural TL has been erased by exposure to UV, has already been discussed above.

2.7.2.1 Proposed Mathematical Correction Techniques

2.7.2.1.1 The Fadia Protocol.

A correction method proposed by Lamothe and Auclair (1999) was called the 'Fadia Protocol' This method was developed to resolve age shortfalls in IRSL results, then extended to work utilizing single feldspar grains rather than the conventional multiple grain samples. This single grain method has since been used widely in the dating of quartz, but there have been problems with applications to feldspars owing to fading. The Fadia protocol has been developed to resolve this issue and can be represented as:

$$R_1(t_1) = R_1(t_2) = R_1^0 \text{ (the larger this number then the greater the fading)}$$

[2.4]

Where R_1 = the laboratory luminescence compared with natural thermoluminescence, t_1 = prompt measurement after irradiation, t_2 = delayed measurement after irradiation and R_1^0 the ratio between the two.

The protocol works on the assumption that measuring the IRSL of single grains as soon as possible after irradiation, $R_1(t_1)$, and after some delay, $R_1(t_2)$, should make it possible to plot the latter

against the former for a series of grains, extrapolate to equation 2.4, and hence to zero fading (Lamothe and Auclair, 1999). However, the comparison of the two times (t_1 and t_2) can create a very steep Fadia line, and as a result causes high errors in the R_1^0 value.

This approach, using the “differential decay of single grains or single aliquots from the same sample” (Lamothe and Auclair, 1999), has many shortfalls that cannot be easily overcome, meaning that it is not universally applicable. Firstly, there is difficulty in detecting bleached grains and grains that have a certain level of natural luminescence intensity with a minimum of 300-500 counts/sec. This makes the technique very difficult to apply to younger sediments, which is problematic as the ability to date younger samples is one of the biggest selling points of the technique. Another problem stems from the actual methodology of the procedure. The Fadia protocol is a type of ‘Single Aliquot Regenerative Dose’ technique (see Chapter 3). In this technique grains are exposed to a number of laboratory doses, which in some cases leads to thermal and optical erosion. When the correction procedure relies on comparing two measurements to produce a ratio, the fact that either or both has the potential to change as a result of the measurement procedure is an important issue. Another problem is that the basic principles of this method state that fading is logarithmic and temperature independent, but evidence to the contrary has been described in previous sections. In spite of these issues, this was the first approach to offer potential corrections for fading of samples of any age up to saturation.

2.7.2.1.2 The ‘g’ Method.

Another single aliquot technique called the ‘g’ method, was outlined by Lamothe *et al.* (2003). It is based on measurement of the percentage fading loss of luminescence per decade of time; a parameter termed (g) by Aitken (1985). This correction is obtained by integrating the loss of luminescence over geological time, the resulting luminescence intensity being I_f . This I_f is compared with the luminescence intensity recorded in the laboratory before fading, termed the prompt signal (I_0). The approach introduces a correction by assuming that:

$$I_f/I_0 = T_f/T$$

[2.5]

(where T is the true age and T_f is the age measured before correction).

The advantage of this method is that fading can be corrected on a single aliquot, but it can only be applied to the linear part of the growth curve and therefore only to young samples.

Huntley (1997) described the opposite to this ‘g’ technique in an earlier paper. This method proposed making an equivalent dose determination using a very large number of discs, which

would enable division of these aliquots into smaller groups based on the amount of fading. From these groups a number of equivalent doses would be attained and plotted on a dose versus fading graph. A line of best fit would then be used to extrapolate to zero fading and as a result the actual equivalent dose could be obtained. Once again there are problems with this correction technique, two being most noticeable. If the difference in the equivalent doses between the groups is small then it will result in clustering of points on the graph with a line of best fit being impossible at worst, and highly inaccurate at best. Also the method does not make allowances for any long-term fading of the sample.

2.7.2.1.3 Dose Rate Correction.

Lamothe *et al.* (2003) proposed another method to counteract the fading problem, which they claim yields a “prediction of long term anomalous fading of feldspar IRSL”. They described an equation called dose rate correction (DRC), which deals with the unwanted loss of luminescence signal as a function of three variables; (i) the measured fading rate, (ii) the laboratory radiation dose rate and (iii) the environmental dose rate. This new method should be applicable to a single aliquot and over the whole range of radiation dose up to saturation. It is based on the understanding that geologically old sediments that are at saturation contain, “a density of electron traps in equilibrium” (Lamothe et al, 2003). This statement signifies that the amount of charge being lost through tunnelling is equal to the amount being claimed by capture and this DRC protocol attempts to recreate the process under laboratory conditions. By giving the sample a much higher dose rate in a geologically brief instant, this could be seen as a perturbation of the equilibrium. As the massive influx of charges stops, detrapping starts, always at the same rate and equilibrium is restored after a certain time. The principle behind this procedure is that by exposing the sample to a laboratory radiation dose of about 10^9 times the environmental rate it is possible to assess the extent of the detrapping and signal decay as a function of the rates involved. If this decay were predictable, then it would be possible to correct for any fading. Unfortunately, there are known issues with recreating the natural irradiation process in the laboratory and problems in recreating natural signal due to the exposure to larger dose rates (Wallinga, *pers. com*).

2.7.2.2 Discussion.

The lack of universal adoption of one of these correction techniques by the luminescence community, even though all have been shown (even if only in the case of one study) to work, indicates the true scale of the problem that exists in dealing with fading-induced age underestimation. As has been described above, an understanding of the mineralogy and of the composition of the samples is imperative for measuring and interpreting the nature and magnitude of signal loss recorded from a given sample set. Without this attention to detail and with reliance on

mathematical corrections, especially from comparative measurements that are prone to measurement regime-induced sensitivity shifts (Zhou and Wintle, 1994), the fading figures that are produced are not guaranteed to be accurate. In other words, it is hard to be certain that any underestimation is the product of fading only. Each technique outlined above is based on the premise that the samples will behave in a specific way and there is good control over the variables that could affect the outcome. The high levels of chemical and crystallographic variability (along with the sensitivity issue) within the feldspar series does not really allow for such sweeping generalisations. It is often the case that these corrections are simply unable to cope with inter-sample variations and after successfully producing corrected ages for one sample fails to do so for another.

2.8 Research Strategy.

Anomalous fading of feldspars is still as debilitating an issue for the luminescence dating community today as it was when it was reported by Wintle (1973). Despite the advances in this chronological technique there is still no model that adequately describes the process and no all-encompassing correction technique. There is, however, a vast library of reported observations and two of the important areas within this area of research are as follows: (i) the mineralogical controls that underpin fading including the models that have evolved from them and (ii) the range of measurement techniques that have been used to identify and circumvent anomalous fading.

One aim of this project was to take the principles outlined in this chapter and use them to predict the level of signal stability within a set of ‘common-garden’ feldspars. The temptation to use museum quality specimens has been resisted for the reasons outlined in the previous chapter (i.e. museum single crystals are unrepresentative of feldspars in sediments) and instead rock samples from common crustal lithologies, particularly their representatives in Scotland, have been collected. The samples were chosen to cover a wide range of geological backgrounds, including plutonic (fresh and weathered samples), recent extrusive igneous (obviously outwith the British Isles), metamorphic rocks, and pegmatitic samples. Their remnant luminescence signals were measured using OSL, IRSL and TL techniques, with commercially available automatic luminescence readers and their manual equivalents in the SUERC luminescence laboratories, each with varying emission detection ranges.

The remnant signals of feldspars extracted from rock samples may not be comparable with those from dating sediments as they have been processed in the laboratory rather than having experienced extended durations of weathering and transportation. Parish (1994) suggested that weathering may enhance anomalous fading by selectively destroying stable traps to leave an unstable populations. Therefore, remnant luminescence measurements were undertaken on suites of alkali feldspars from

a number of granites, each suite comprising grains that have been mechanically separated from fresh granite, naturally weathered soils formed on the granite and grains etched in HF acid for different lengths of time.

The final aim of this study was to construct a red sensitive system with a low signal-to-background ratio that can measure luminescence in the time domain. Having outlined the current interest in this area of research it was important to assess the feasibility of constructing such a system from scratch and to determine the ease with which a convincing luminescence signal could be measured, with comparison of dose response and stimulation levels.

The results of this study were also used to construct an adapted fine-grain SARA technique for feldspars. It was used to date samples in tandem with a current international NERC funded dating study.

3

Measurement Techniques and Instrumentation.

3.1 Introduction.

This chapter outlines the measurement techniques and instrumentation that will be employed to fulfil the aims of the project, with particular attention on the measurement regime and system settings. The initial stage of the study involved fieldwork to collect the samples that were then prepared for various mineralogical characterisation techniques. This preparation is described along with an outline of the sample set. A more detailed description of the feldspars used for this research is presented in the following chapter.

The remnant luminescence measurements and techniques used will be discussed prior to an outline of the experiments and instrumentation, with reference to the importance of the different systems and the quantification of anomalous fading in feldspars. The final operating conditions of the two experimental pulsing systems will also be described as well as the dating work. This chronological study was slightly outside of the original scope of the project, but the importance of quantifying the stability of feldspars in an actual dating context, as opposed to artificial remnant luminescence measurements, cannot be overestimated. There will also be a brief description of the measurement techniques employed in luminescence dating and the evolution of this project's adapted SARA protocol.

3.2 Selection and Characterisation of the Sample Set.

The importance of comprehensive sample characterisation was outlined in the previous chapter and a lack of even a basic knowledge may significantly hinder dating work. There are instances within the literature where the samples are simply referred to as 'feldspars', which anyone familiar with mineralogy will recognise as being a very non-descriptive and uninformative term. As mentioned previously, the feldspar group comprises a complex mineral series, with significant variations between minerals in crystal structure and/or chemistry. When the potential mineralogical controls on luminescence behaviour have been outlined in the literature (Krbetschek *et al.*, 1997;

Krbetschek and Rieser, 1995), the lack of comprehensive characterisation often evident within this previous work is puzzling.

Another important issue arising from previous studies has been that most work is carried out on museum quality samples, and an emphasis is placed on those that are known to suffer significant anomalous fading (Fattahi and Stokes, 2003a; Spooner, 1994; Zink and Visocekas, 1997). This research is important when attempting to determine reasons behind the phenomenon, because it is essential that the sample being used displays the behaviour of interest. The rapidly cooled volcanic feldspars that are quoted widely in the literature to explain anomalous fading are in fact very uncommon in sediments and sanidine itself has very unusual properties (Parsons and Lee, 2005). Therefore the emphasis here is on common, or ‘every-day’ feldspars, examples of which can be found in most geological settings and dating environments.

3.2.1 Sample Selection.

The previous work on anomalous fading that was outlined in Chapter 2 has guided the selection and collection of a sample set that should contain feldspars with a wide range of instabilities. It includes feldspars that should fade significantly, such as sanidines (Smith, 1998; Visocekas *et al.*, 1998; Zink and Visocekas, 1997), to minerals from plutonic igneous and pegmatitic contexts that current models predict should exhibit a higher level of stability. The samples also include naturally and artificially weathered feldspars to test Parish’s theories regarding enhancement of signal instability due to erosion and transport of feldspar grains (Parish, 1994). Within the sample set as a whole there will be more subtle chemical and textural variations that could also prove to be significant for understanding anomalous fading.

Northern Britain is blessed with a wide range of rock types and a broad geochronology. As a result most of the samples used herein are taken from Scottish and Northern English localities. Table 3.1 lists the sample types, internal and external reference numbers, and sampling locality (where known).

Table 3.1 The sample set, reference numbers and locality (listed in order of preparation for luminescence work).

Sample	Host Rock	Internal Reference	External Reference	Location
1	Shap Granite	Shap	N/A	Shap, Northern England
2	Helmsdale Granite	Helms	N/A	Helmsdale, Northeast Scotland.
3	Helmsdale Arkose	Ark	N/A	Helmsdale, Northeast Scotland.
4	Lewisian Gneiss	LG	N/A	Northwest Scotland
5	Patmos Sanidine	PS	N/A	Patmos, Greece

6	F1	F1	N/A	Laboratory Standard
7	Etna Basaltic Lava	Etna	N/A	Mount Etna lava field Currywongaun, Connemara, Eire
8	Gabbro Pegmatite	H1	M106104	
9	Pitchstone Porphyry	H2	TYR2895	Glen Callum, Bute
10	Feldspar Crystals (from above)	H3	106431	Glen Callum, Bute
11	Orthoclase Crystals	H4	M6908	Summit of Canisp, Assynt
12	Anorthosite (or AN85)	H5	111288	Hallival, Rum
13	Crushed Granite	H6	78	Pass of Ballater, Scotland
14	Troctolite Pegmatite	H7	JF87.5.17	Unit 15, Hallival, Rum
15	Strontian Granodiorite	H8	2003.135	Road cut, Strontian, Scotland
16	Ross of Mull Granite	H9	2000.5	Camas Tuath Quarry, Mull Tonmore Quarry, Fionnphort, Mull
17	Ross of Mull Granite	H10	178	
18	Hydrothermal Syenite	H11	JF93.10A	Tonmore, Fionnphort, Mull
19	Hornblende Gneiss	GU1	M8	Torridon, Northwest Scotland
20	Migmatite	GU2	M15	Glen Tarbet, Invernesshire
21	Peterhead Granite	GU3	I3	Peterhead
22	Ballater Granite	B1	N/A	Ballater Pass scree slope NO 36759 97018 EI' 277m
23	Soil sample of weathered Ballater Granite	B2	N/A	Ballater Pass scree slope NO 36759 97018 EI' 277m
24	Cairngorm Granite	C1	N/A	Cairngorm Mt road cutting NH 98780 07165 EI' 561m
25	Weathered Cairngorm Granite	C2	N/A	Cairngorm Mt road cutting NH 98780 07165 EI' 561m

The above samples were collected at different times and initially studied as two distinct sets because of this. The first set samples were largely investigated in 2003/2004 and the latter 2005/2006. The boundary is between at samples 7 and 8.

3.2.2 Sample Preparation 1.

3.2.2.1 The GES Separation Technique.

As the feldspars were mostly collected as constituents of large rock specimens, or individual phenocrysts, the first preparation stage was to crush the samples to produce feldspar grains. Initially the outer 'weathered' surface of the larger samples was removed using a rock breaker. In most cases the weathered rind was discarded, though not in the case of the Helmsdale and Shap granites as these outer surfaces were used to test Parish's theory. The small pieces of rock were broken down further using a jaw crusher, then using a series of metal sieves grains of ~2mm were

extracted. At this stage a few grains of each sample were taken out for mineral characterisation (large grains are important for feldspar mineralogy work owing to the relatively coarse scale of the exsolution microtextures). The bulk of the sample was further crushed to yield a 125-250µm grain size fraction.

The samples that were obtained as single crystals and the large feldspar phenocrysts that could be separated easily from their parent rock were crushed to a powder using a pestle and mortar. A ~2mm sub-sample was extracted for characterisation and the remaining grains were ground until the main grain size was ~125-250µm. The powders were then cleaned in an ultrasonic bath to remove any fine silt sized material that may have adhered to grain surfaces.

The 125-250µm grain size fraction was processed further using mineral separation techniques to extract feldspars only from the polymineral powder. As stated above the sample suite consisted of two distinct groups defined by differences in collection periods and this division is only relevant to the mineral separation techniques used. The heavy liquid mineral separation of group one was carried out at the University of Glasgow and the second group of samples were density separated at SUERC.

For the first group of samples (1-7 in Table 3.1), the first stage was to remove some of the heavy minerals using a magnetic separator before moving onto heavy liquids. In the mineralogy laboratories of the Department of Geographical and Earth Sciences (GES) at the University of Glasgow this density separation is carried out using sodium polytungstate (SPT). By using this liquid at different densities it should be relatively straightforward to extract and separate minerals of specific densities. Prior to separation using heavy liquids, the samples had an acid pre-treatment (10% HCL for 40 minutes) to remove calcium-rich minerals that react with the SPT. The separation used SPT with a density of ~2.65g/cm³ which to lies close to the quartz/feldspar boundary (Figure 3.1).

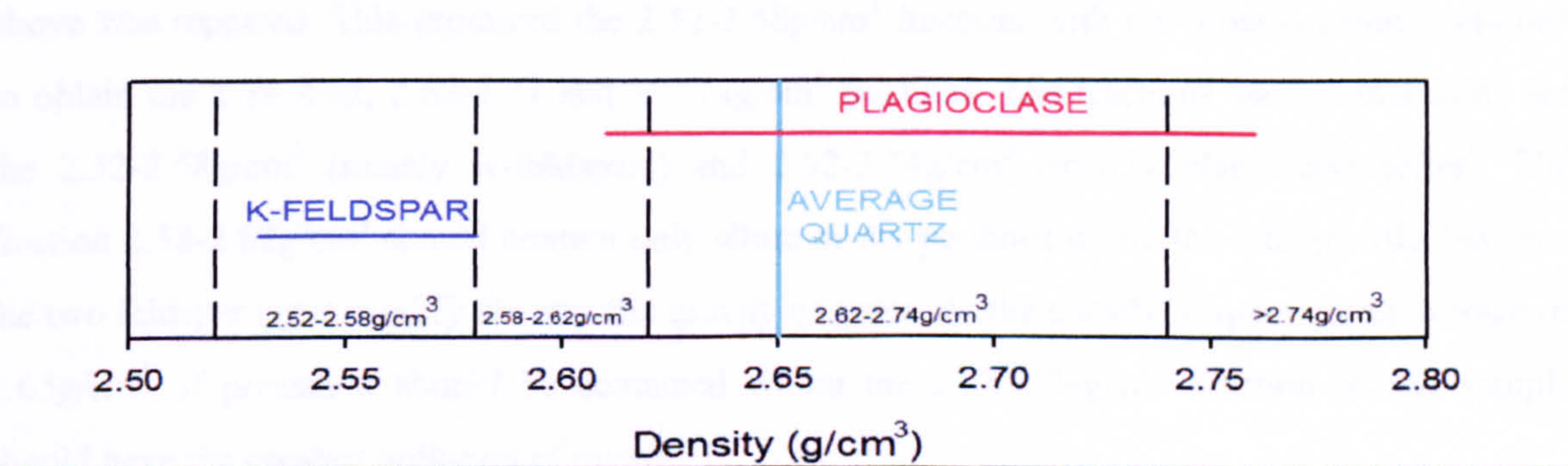


Figure 3.1 Density ranges of the K-feldspars and plagioclase series plotted with the four relevant SPT ranges. Quartz is also plotted as an average value. In reality the two feldspar series overlap and a perthitic albite should lie in the 2.53-2.62g/cm³ range. The density of perthite is important (see Chapter 4) and illustrates the potential downfalls of using SPT to separate differing feldspar chemistries from each other and indeed quartz.

3.2.2.2 The SUERC Separation Technique.

For the second sample set an attempt was made to remove quartz prior to heavy liquid separation. This involved hand picking feldspars for the polymineral powder at the ~2mm grain size stage using an optical microscope and tweezers. The problem of intergrowths of quartz with feldspar still remained but overall the final powders should be purer than sample group 1. Due to the addition of the extra handpicking step, magnetic separation was no longer required.

For this second set of powders a more rigorous SUERC SPT mineral separation technique was employed (Anthony, 2003). This protocol used four different densities of solution (2.52, 2.58, 2.62, and 2.74g/cm³) (Figure 3.1) in order to separate the different feldspar series as well as feldspar from the quartz.

The powders were added to a series of test tubes to a depth of ~1-2cm, depending on its diameter. The 2.52g/cm³ SPT was then added to all the test tubes before they were shaken vigorously in order to mix the powder completely through the column. The test tubes were then centrifuged for a few minutes to facilitate the density separation. Any of the material floating after this process has a specific gravity <2.52g/cm³. This fraction was then poured into a clean test tube along with the SPT, with care so the material that has collected at the bottom of the test tube was not disturbed. Water was added to the removed SPT to reduce its density and the material was left to settle and then the SPT was drawn off. Into this test tube was added deionised water and the process of mixing and centrifugation was carried out five times with fresh water for each cycle to remove SPT adhering to the grains. Once the water had been decanted the tube was filled with acetone and shaken once again. Any remaining SPT will precipitate to form a chalky solution as it reacts with the acetone. The washing was repeated until the acetone remained clear. The samples were then oven dried at 50°C.

The >2.52g/cm³ residue was then mixed with the 2.58g/cm³ density SPT and the process outlined above was repeated. This produced the 2.52-2.58g/cm³ fraction, with the process being continued to obtain the 2.58-2.62, 2.62-2.74 and > 2.74g/cm³ fractions. The fractions used in this study are the 2.52-2.58g/cm³ (mainly K-feldspars) and 2.62-2.74g/cm³ (mainly plagioclase series). The fraction 2.58-2.62g/cm³ should contain only albite or the perthites where the intergrowths between the two feldspar types modify the specific gravity of grain. As the density of quartz is an average of 2.65g/cm³, if present it should be contained within the 2.62-2.74g/cm³ fraction so this sample should have the greatest pollution of quartz.

3.2.2.3 Sample Preparation for Characterisation.

3.2.2.3.1 Polished Grain Mounts.

For good backscattered electron images of the feldspar microtextures the grains from the 2mm and 125-250 μ m size fractions were prepared as polished thin sections and the flat grain surfaces also facilitated spot microanalysis by giving consistency of analyses within and between grains. This is important when comparing the results of the various characterisation techniques as presented in the next chapter. These grain mounts were prepared using powders before SPT separation.

3.2.2.3.2 Powders.

After the GES and SUERC density separation techniques had produced the various mineral fractions, the proportions of alkali and plagioclase feldspar and quartz in each was determined by X-ray elemental mapping in the GES ESEM (see below). Using adhesive stubs the grains could be placed directly into the sample chamber at low vacuum without the need for the production of thin sections and without risk of loose grains damaging the machine. This was an important step in the characterisation process as it used the same powders on which remnant luminescence work was undertaken. The proportions of quartz, alkali and plagioclase feldspars in the X-ray maps were estimated visually by comparison of the Na, K and Ca components.

3.2.3 Sample Characterisation by X-Ray Diffraction (XRD).

3.2.3.1 The XRD System Specification.

The system is a Phillips PW 1050/35 X-ray diffractometer that uses cobalt X-rays and the powder patterns are acquired using a vertical goniometer and computer controlled step scanner. The data was processed using the Traces V4.0 computer graphics programme that searches a comprehensive database to identify the minerals.

3.2.3.2 Measurement Regime.

XRD work used the fine grain separates, post-SPT separation, to test whether the density fractions contained the minerals that were expected and also to identify the structural state of the feldspars (e.g. high, intermediate or low microcline). In practice it was difficult to identify the feldspars unambiguously by XRD as powder patterns of different members of the groups are so similar, which is especially problematic for perthitic alkali feldspars that comprise the majority of the sample set.

3.2.4 Sample Characterisation Using the Environmental Scanning Electron Microscope (ESEM).

The ESEM at GES was used in this project for a number of tasks. High resolution backscattered electron images of grains were obtained so that subsequent work could identify any relationship between microstructure, such as perthitic textures, and luminescence behaviour of the finer grain fraction. The microscope was also used to obtain X-ray maps of the 125-250 μ m powders in order to determine the mineralogy of the powders (see above).

3.2.4.1 System Specification.

The system is a FEI Quanta 200F environmental SEM with a Schottky field-emission electron gun. A low vacuum setting was used for the uncoated powders; whereas a high vacuum setting was used to study the carbon coated polished grain mounts. The microscope is equipped with X-ray and electron detection capabilities enabling comprehensive morphological, microstructural and crystallographic characterisation of materials. The Everhart-Thomley Secondary Electron (SE) detector was utilised to give high-resolution topographic images of the grains sub-sampled from those used in the luminescence measurements.

3.2.4.2 Measurement Regime.

The polished grain mounts were mounted within the sample chamber and backscattered images were taken at x100 and x400 magnification. X-ray mapping used the ESEM operated at a vacuum of 530 torr, an accelerating voltage of 20KV, a column aperture size 4, a working distance of 11 μ m (recommended by the manufacturer) and the two magnification settings of x100 and x200. The elemental mapping used a resolution of 256x200 pixels with a 64 repetition for each map. The EDAX X-ray system was set up to map for aluminium (Al), silicon (Si), potassium (K), calcium (Ca), and sodium (Na). Each element is assigned a different colour and so the maps can be used to give an indication of the level of sample homogeneity and purity. X-ray maps were made of both the polished grain mounts and the 125-250 μ m separated powders.

3.2.5 Quantitative Chemical Analysis by Electron Microprobe.

3.2.5.1 System Specification.

A CAMECA SX50 was used to carry out quantitative chemical analysis on the carbon coated polished grain mounts using a beam current of 20nA, an accelerating voltage of 15Kv and a defocused spot of 10 μ m. The elements chosen for quantitative analysis and the standards used to calibrate the electron probe are listed in Table 3.2.

Table 3.2 Electron microprobe quantitative analysis detection and calibration standards.

Element and X-ray line.	Standard
Na Kα	Jadeite
Mg Kα	Magnesium oxide (periclase)
Fe Kα	Iron sulphide
Al Kα	Corundum
Si Kα	K-Feldspar
K Kα	K-Feldspar
Mn Kα	Manganese metal
Ca Kα	Calcium silicate (wollastonite)

3.2.5.2 Measurement Regime.

The microprobe analysis built on results from the ESEM work. Using the images taken with the ESEM backscattered electron detector, the beam was directed to the different phases within the grains. These analyses gave a detailed indication of mineral chemistry to compare with CL images in order to quantify the control that major, minor and trace element chemical composition has on luminescence properties and emission bands. Prior to the electron probe work the polished grain mounts were coated with carbon and grounded using silver paint. Two glass slides were mounted within the probe at a time and the run was programmed with the required spot coordinates in advance.

3.2.6 Optical CL Imaging.

Cathodoluminescence (CL) does not rely on stored charge for the production of a measurable signal (Table 3.3). In CL the charge is supplied by an electron beam that simultaneously produces an optical emission. The energy (wavelength) of the photon and the probability of it being emitted depends on the material, its purity and its defect state. CL is not a dating technique but is used as a diagnostic tool to study the trace element and/or defect composition of a sample. Each trap type that is associated with a defect or an impurity within the lattice, such as the Fe³⁺ ion in feldspar, emits luminescence in a specific wavelength, in this case around 700-720nm. If optical filtration is relied upon to supply the detection window then it is imperative that it is centred on the correct area of the spectrum.

3.2.6.1 System Specification.

The optical CL work was carried out using a CITL Techosyn 8200 MK 4 mounted on a Zeiss Axioplan petrological microscope. The instrument was operated at ~26Kv and using a 220nA beam current.

3.2.6.2 Measurement Regime.

CL images were obtained from the polished grain mounts, allowing a direct comparison with both the BSE images, X-ray maps and the electron probe data using the microscope digital mounted camera. Images were recorded and were taken using an x4 or x10 objective in order to match the images with those taken on the ESEM and microprobe for cross-referencing and analysis.

Table 3.3 Luminescence emission characterised by stimulation source.

Luminescence Technique.	Stimulation Source.
Thermoluminescence (TL) (0-500°C) (McKeever, 1985) and high temperature TL (>500°C) (Spencer, 1996).	Emission of light from an insulator, or semiconductor that has been exposed to ionising radiation, by application of heat.
Photostimulated luminescence (PSL) (Aitken, 1992; Huntley, 1985a).	Emission of light from an insulator, or semiconductor that has been exposed to ionising radiation, through stimulation using light.
Continuous wave photostimulated luminescence (CW-PSL).	Measurements take place simultaneously with stimulation, with optical filters being used to separate light from the diode from that emitted by the sample.
Green-PSL (Jain and Singhvi, 2001).	PSL stimulated using a green laser.
Blue-PSL.	Within this project this is termed OSL, and describes stimulation using a UV-blue emission.
Infrared (IR) PSL (Spooner, 1992).	This is termed IRSL or IR-OSL although in this study it will be exclusively referred to as the former. This technique uses a stimulation source > 600nm.
Pulsed Photostimulated Luminescence (PPSL) (Clark <i>et al.</i> , 1997; Sanderson and Clark, 1994; Tsukamoto <i>et al.</i> , 2006).	This is a much less common form of PSL and the stimulation is delivered in pulses rather than continuously.
Cathodoluminescence (CL) (Rendell and Clarke, 1997).	Excitation by electron beam. A diagnostic tool rather than a dating technique.

Radioluminescence (RL) (Schilles and Habermann, 2000; Trautmann <i>et al.</i> , 2000).	Excitation by nuclear reactions, i.e. X-rays, γ -rays, β -rays etc (Smith 1998).
Afterglow (Visocekas <i>et al.</i> , 1994; Visocekas and Zink, 1995).	Luminescence immediately after irradiation has ceased.
Phosphorescence (Aitken, 1994).	Temperature dependant luminescence after irradiation has ceased.

3.3 Remnant Luminescence.

In this study, the stability of feldspar luminescence was determined not through the production of De values, but rather by measurement of remnant luminescence signals, the nature of which will be described below. These signals were produced using three stimulation sources, IRSL, OSL and TL, using three separate systems. One system (Risø reader) enables a single multistimulation run for one detection range, while the other two, a manual TL system and a manual PPSL system, use slightly different detection ranges through a variation in optical filtration (Table 3.4). The use of differently configured instruments allowed for comparisons to be made not only between stability of luminescence and variables including mineral chemistry (Huntley and Lian, 2006; Pooilton *et al.*, 2003), thermal history and weathering (Parish, 1994), but also in the emission range being measured. Using a range of stimulation and detection wavelengths was important as different feldspar minerals can luminesce at contrasting wavelengths and the luminescence at some wavelengths is more stable than from others (Visocekas, 2000).

Table 3.4 The systems used and the luminescence measurements made with them.

Luminescence System	Measurements carried out.
Risø Daybreak automatic readers	Multistimulation: consecutive IRSL, OSL and TL.
SUERC manual PPSL reader	Pulsed OSL
SUERC manual TL reader	TL
Adapted red TL reader	Red TL
Blue pulsed system	Pulsed OSL
Cooled near-IR pulsed system	Pulsed Near-IRSL

3.3.1 The Stimulation Techniques.

The name given to emitted luminescence is related to the type of stimulation energy that is applied to the material. Definitions of different stimulation techniques are listed in Table 3.3, although not all of these techniques were used in this study.

The techniques used include the conventional stimulation sources: IRSL, OSL and TL. In addition pulsed PSL techniques, blue OSL and near-IRSL were investigated, as well as red TL. Before the relevant luminescence readers are described and measurement settings outlined, a brief history of these techniques will be presented.

3.3.1.1 Historical Application of IRSL.

A number of studies have demonstrated that emission spectra from different feldspars minerals vary both in output wavelength and luminescence efficiency, and this variance is related to composition (Krbetschek *et al.*, 1997; Krbetschek and Rieser, 1995). For example anorthites and labradorites have extremely weak, usually thermally unstable luminescence; albites and oligoclases luminesce very brightly and have emission spectra that include a high intensity 550nm band, but also emit strongly in the near UV region. These chemically and structurally related emission variations are of significance for luminescence work not only in detection but also with regard to stimulation wavelengths.

For most feldspars, but not quartz, IR light in the region of 800-900nm can stimulate luminescence emission. The optimal stimulation waveband for dating applications using feldspars is 850-900nm (Spooner, 1992) and the most convenient source of illumination is 880nm light emitting diodes (LEDs). IRSL has a number of advantages over OSL stimulation. Firstly, IR stimulation leaves a broad range of wavelengths available for detection, thus providing a stronger signal and a possibility of isolating emissions from particular minerals using different combinations of optical filters. Secondly, IRSL is more effectively bleached at deposition than those bands stimulated by other PSL wavelengths (Spooner, 1992). Lastly, adequate stimulation power can be provided by an array of a dozen or so LED's, which are cheap and convenient.

Godfrey-Smith (1996) undertook a study comparing the IR stimulation spectroscopy of microclines, plagioclases, quartz extracts and feldspar dominated extracts from sediments. All of these samples were given a short sharp preheat (195°C/10secs) to ensure that only carriers evicted from thermally stable traps were measured. A single stimulation peak was found in all samples, at 845nm in the microclines, most of the plagioclases and all the feldspar dominated sediments. The peak occurs at 840nm in two nearly end-member Na-plagioclases as well as all quartz extracts. Godfrey-Smith (1996) suggested that the light stimulates an Al^{3+} (alkali) complex, which is a major (~25%) component of all feldspars and a common impurity substituting for Si^{4+} in natural quartz.

3.3.1.2 Historical Application of OSL.

A significant development in luminescence dating came when Huntley *et al* (1985b) carried out a trial of the applicability of optical dating. This development was a consequence of unsatisfactory

results from TL dating of sediments, but has also been subsequently applied to dating pottery and radiation dosimetry as well as the detection of irradiated food. Early work on the UV stimulation of calcite concluded that laser-induced luminescence could be used in archaeological dating (Huntley *et al.*, 1985b). However, calcite is not easily bleached by sunlight and it therefore cannot itself be used in this application. This thinking was carried forward and the first real demonstration that optical dating of sediments was possible was made at the Simon Fraser University in 1985 (Huntley *et al.*, 1985b). From this and subsequent studies, optical dating is now widespread in the luminescence community and has developed at the expense of TL (Aitken, 1994; Aitken, 1998; Clark, 1992).

In OSL dating there is a dependence of luminescence emission not only on the intensity of the stimulation source but also on the temperature at which the sample is held during measurement. In the case of the stimulation source, doubling the power doubles the rate at which the photons arrive at the sample, which can double the amount of electrons released from a particular trap type (i.e., the luminescence per unit time). The eviction rate of trapped electrons from both quartz and feldspars is highly dependent on sample temperature and increases by 1% per degree centigrade above room temperature. Hence, a substantial increase in OSL intensity can be obtained by holding the sample at around 50°C during stimulation and measurement. This is highly important when analysing young and particularly dim samples, as the elevated signal improves signal-to-background ratio (Aitken, 1992). However, there is the problem of the competing effect of thermal quenching (Poolton *et al.*, 1995; Roque *et al.*, 2004) whereby the efficiency of the luminescence centres (i.e. photon emission per electron arriving) decreases as the temperature is increased. This effect is strong in quartz and as a result the total number of photons emitted (the light sum) decreases with temperature even though there may be an initial increase in the rate of emission (Ward *et al.*, 2003). In most types of feldspars the quenching is weaker and the light sum actually increases with temperature due to an emitted electron having an increased likelihood of reaching a luminescence centre, again adding to the attraction of feldspar as a replacement for quartz in dating.

3.3.1.3 Historical Application of TL.

Thermoluminescence (TL) describes the heating of a material to a predetermined temperature, using a defined heating rate and measuring the weak emission of light that is produced (McKeever, 1985). In this study a temperature range of 0-500°C was used at a heating rate of 5°C/sec, with the sample being heated twice, as during measurement at elevated temperatures the equipment produces thermal radiation, also termed 'black-body' or 'background'. Most TL software can automatically subtract the signal measured in this second heating from the first, leaving only the sample's luminescence signal.

A typical TL glow curve appears as a smooth continuum of emission (see Figure 2.7) but in fact comprises a series of overlapping peaks (Aitken, 1985). Each type of electron trap has a glow peak $\sim 50^\circ\text{C}$ in width, with the position of each peak on the glow curve relating to the depth of the traps and therefore the magnitude of energy required to empty them. The temperature region below 200°C is not used in dating, as these shallow traps are unstable on geological timescales.

3.3.1.4 Rationale for IR-TL Measurements.

Since Visocekas *et al* (1994) first published results on the far-red emission of feldspars, there has been hope within the luminescence community that possible an answer to the parasitical loss of trapped charge had been found. Work by Visocekas and co-workers (Visocekas, 1979; Visocekas, 2000; Visocekas and Guerin, 2006; Visocekas *et al.*, 1994; Visocekas *et al.*, 1996; Visocekas *et al.*, 1998; Visocekas and Zink, 1999; Zink and Visocekas, 1996; Zink and Visocekas, 1997; Zink *et al.*, 1995) has focused on the 600-900nm TL emission, which as stated above is not covered by conventional TL systems for a number of practical reasons. One reason is that the PMT sensitivity declines significantly in this range; another is the competition with thermal emission, which hinders TL measurements as temperatures are raised. The main work in near-IR-TL in the present study was carried out using a GaAs photocathode, which has to be cooled to -30°C as such modules are prone to high dark counts, but its spectral sensitivity is reasonably flat from 200-900nm (Visocekas *et al.*, 1994).

Another feature of RTL is that it is optically bleachable (Bos *et al.*, 1994; Zink and Visocekas, 1997), with oligoclases bleaching from wavelengths between 703-800nm, although Bos *et al* (1994) did not study the effects of wavelengths exceeding this range which include those currently used in IRSL. Zink and Visocekas (1997) studied the effect of sunlight exposure on the blue and red TL emission bands of feldspar, using a museum quality sanidine phenocryst. For the RTL emissions (590-750nm), the intensity was reduced by around 70% after just two hours exposure to sunlight. In another experiment using the same sample, the sunlight was filtered through a series of long wave pass optical filters (300-780nm). Zink (1997) observed that the shorter sunlight wavelengths (around 350-400nm), showed higher bleaching efficiency with similar bleaching results in both blue and red emission bands.

3.3.1.5 The Rationale for Pulsed PSL Measurements.

There are two main reasons for using pulsed stimulation of optical luminescence (PPSL) instead of continuous wave (CW) PSL. One is to improve signal-to-background ratios, which as has been discussed above is crucial in continuing the development of the red IRSL and TL work, the other reason is to investigate the time-dependence of luminescence emission relative to stimulation (Bailiff and Mikhailik, 2003; Chithambo and Galloway, 2000). An improvement to the signal-to-

background ratio is achieved because the measurement technique is to pulse the stimulation source and to record the resulting luminescence signal when in the off part of the stimulation cycle. This eliminates the competition from the stimulation source (e.g., diode breakthrough). However, timing of recording of the emitted luminescence must be very accurate. It is also important to select a stimulating pulse width that experimentally offers the best signal-to-background ratio (i.e., sufficiently long to stimulate but not too long to cause short-lived, or almost instantaneous, luminescence to be contained within the pulse) (Clark, 1992). The latter requires a very fast pulsing module and multi channel scalar (MCS). In addition, by separating stimulation and detection by time, the method enables detection of luminescence in emission bands that are close to, or even part of, the wavelength range used in stimulation. Apart from an improved signal-to-background ratio, time-resolved luminescence spectra may also aid in the understanding of the physical processes responsible for luminescence and could eventually lead to an improvement in dating performance. This is a topic discussed in detail by Sanderson and Clarke (1994). They state that while most luminescence is continuous wave (CW) and therefore stimulation and signal are recorded synchronously, the resulting 'shine down' curves convey little information on the underlying mechanism. This is because the stimulation of individual trapping centres occurs randomly throughout the measurement period and is coupled to an ill-defined delay associated with recombination or competing processes.

Despite the advantages of PPSL, can it be used for dating? Tsukamoto *et al* (2006) suggest that it can. They studied the relative contribution of long life components (quoted here as being above 20 μ s, which is significantly different to that quoted in the work by Sanderson and Clarke (1994)) of K-feldspars. Conclusions from Tsukamoto *et al* (2006) suggest that for any one feldspar sample, red and blue IRSL signals have a greater contribution of long-lifetime components than UV IRSL. Tsukamoto *et al* (2006) found this long-life component was significantly more stable than shorter lifetime components, by comparing natural/regenerated and prompt/delayed time resolved IRSL. A comparison of PPSL and CWPSL derived equivalent dose values was made using four feldspar samples. For pulsed IRSL, the signal was collected between 10 and 100 μ s after the diodes were switched off, to avoid all contributions from short lifetime components (Tsukamoto *et al.*, 2006). In all cases the pulsed values were larger than the CW values, regardless of the feldspar type and detection window. The pulsed values were also consistent with those calculated from quartz. The results were interpreted as evidence that the long lifetime component does not suffer from fading and can be used for dating.

3.3.1.6 The Argument for Preheating.

In a TL glow curve the luminescence associated with traps of increasing depth is displayed as a plot of signal intensity against temperature; effectively this is an expression of increasing electron-

retention lifetime. PSL lacks a simple diagnostic feature, such as the 200°C boundary in TL, to distinguish luminescence from stable and unstable traps (McKeever, 1985). A preheating regime has therefore been introduced to guard against the contamination of the thermally stable dating signal by luminescence from shallow traps. Prior to measurement of both the natural and artificially induced luminescence, the grains are heated sufficiently to empty unstable traps. An indication that the degree of preheating is adequate can be obtained by checking whether it removes all the TL peaks except those that are in plateau (Aitken, 1985). A more definite procedure is to determine the paleodose after successive preheats of increased severity; when the heating has been sufficient to empty all shallow traps the paleodose levels off to a preheat plateau. An abbreviated, though less satisfactory, version of this procedure is to accept a plateau in the natural versus artificial PSL as an indication that the correct regime has been established. Stringency of preheating can be increased both by holding the temperature constant and increasing the duration or vice versa; in general terms a preheat is either long duration (using a moderate temperature) or short duration (using a higher temperature).

It had been demonstrated by Tso (1996) that an unstable IRSL signal still exists even after preheating at 220°C for ten minutes, which has removed 36% and 68% of the natural IRSL from K-feldspars and plagioclase, respectively. These results have raised questions about removing unstable signals using preheat procedures. If a polymineral sample such as loess contains a large proportion of this unstable signal a small percentage of it will likely remain in the measurement cycle and so may be quantitatively important in comparison to a stable signal. Unfortunately, when preheating at a higher temperature is employed, the signal remaining might be at a comparable level to the noise level of the PMT. Avoidance of a contaminating signal from light sensitive shallow traps, was initially seen as the reason for preheating. However, there is also the need to avoid indirect contamination resulting from charge transfer; and also in the case of quartz there is the possibility of preheat-induced changes in the luminescence sensitivity (Ward *et al.*, 2003).

3.3.2 Sample Preparation for Luminescence Measurements.

For luminescence measurements in this study the 125-250µm powders were dispensed onto 8mm diameter stainless steel discs. Each measured sample set and their individual SPT density fractions (where appropriate) comprised twenty aliquots (i.e., individual discs) allowing for the monitoring and correction of inter-disc heterogeneity and machine drift. Ideally the powder should occupy the centre of the disc ~2mm from its edge. The sample was then carefully scattered across the central area covered with silicon grease so that there was a complete coverage. Once this had been done, using a set of tweezers the discs were lifted up, and turned upside down, and given a vigorous shake to leave a single layer of grains on the grease. The discs were weighed to four decimal places both before and after powder dispensing to account for potential problems from loss of grains

during luminescence measurements (see Section 6.5 for more detail on the influence of sample coverage on luminescence results).

3.3.3 The Risø Daybreak Automatic Readers.

The SUERC Physics group has two of these systems, purchased a few years apart. These have been designated within the laboratory as Risø 1 and 2 owing to their age gap, they difference in configuration and this will be outlined in a subsequent section. These systems were designed and built at the Risø National Laboratory in Denmark and are the most popular reader within luminescence laboratories due to their multi-stimulation automated design (Botter-Jensen *et al.*, 2003).

3.3.3.1 System Specification.

One of the main advantages of the Risø readers is that their measurement cycle is completely automated. They irradiate the sample using a Sr/Y-90 beta source; have preheating capabilities and IRSL, OSL and TL measurement regimes. Risø 1 delivers a dose of 6.525 ± 0.04 Gys/min and Risø 2 6.065 ± 0.5 Gys/min. Both systems used blue diodes (470nm) for OSL measurements, but for IRSL the earlier reader (Risø 1) uses a red LED (875nm) array and Risø 2 a red laser (830nm). Once the samples have been loaded into the chamber, using a 48-sample carousel, they remain inside until the pre-programmed measurement sequence is complete. Such automation is highly advantageous because handling the discs between irradiation, heating and measurement opens up the possibility of loss of grains and a change in signal intensity between successive readings that is unrelated to the intrinsic luminescence properties of the mineral grains of interest. Also, when working with mineralogically heterogeneous samples even having the disc orientated differently on the heater plate between glows (measurement cycles) can have a significant impact on reproducibility of the data.

3.3.3.1.1 PMT Response and Optical Filtration.

Both Risø readers are fitted with an Electron Tubes 9235B Photo Multiplier Tube (PMT). This has a 52mm diameter end window lens with a blue-green sensitive bialkali photocathode and a large active diameter (48mm). It has 13 high gain, high stability, SbCs dinodes of linear focused designs. This means that the photocathode is optimised to detect low light levels. Its borosilicate window limits its detection window to 290-630nm and light is filtered through 7mm of the Hoya U340 filter. This is a blue-green band pass filter similar to Schott UG11 and is transparent to light from UV to blue wavelengths. The optical attenuation of this filter and PMT are calculated in Table 3.5, and is illustrated visually in Figures 3.2 and 3.3.

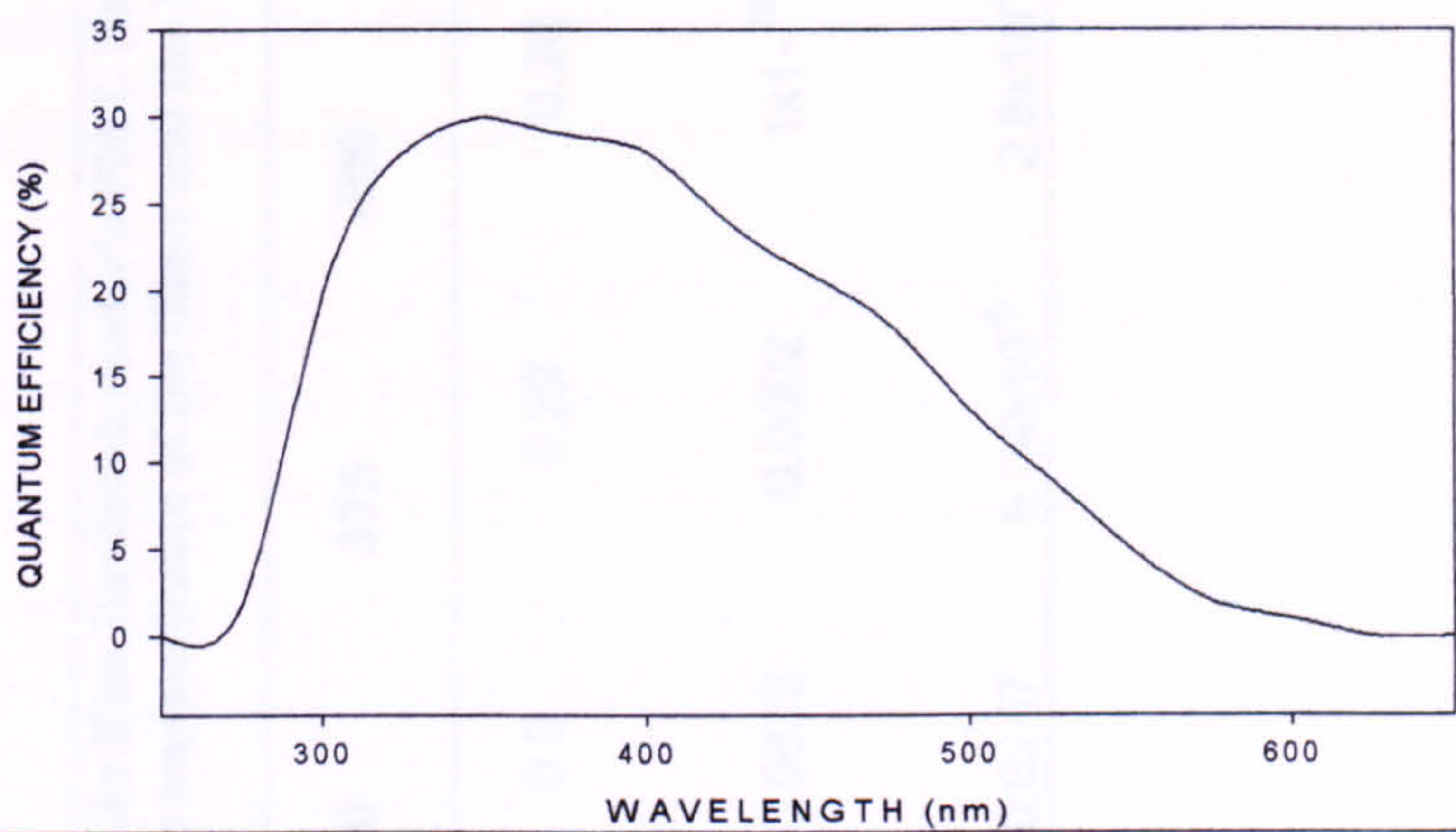


Figure 3.2 Typical spectral response of an Electron Tubes 9235 PMT with a borosilicate window (reproduced from the Electron Tubes catalogue)

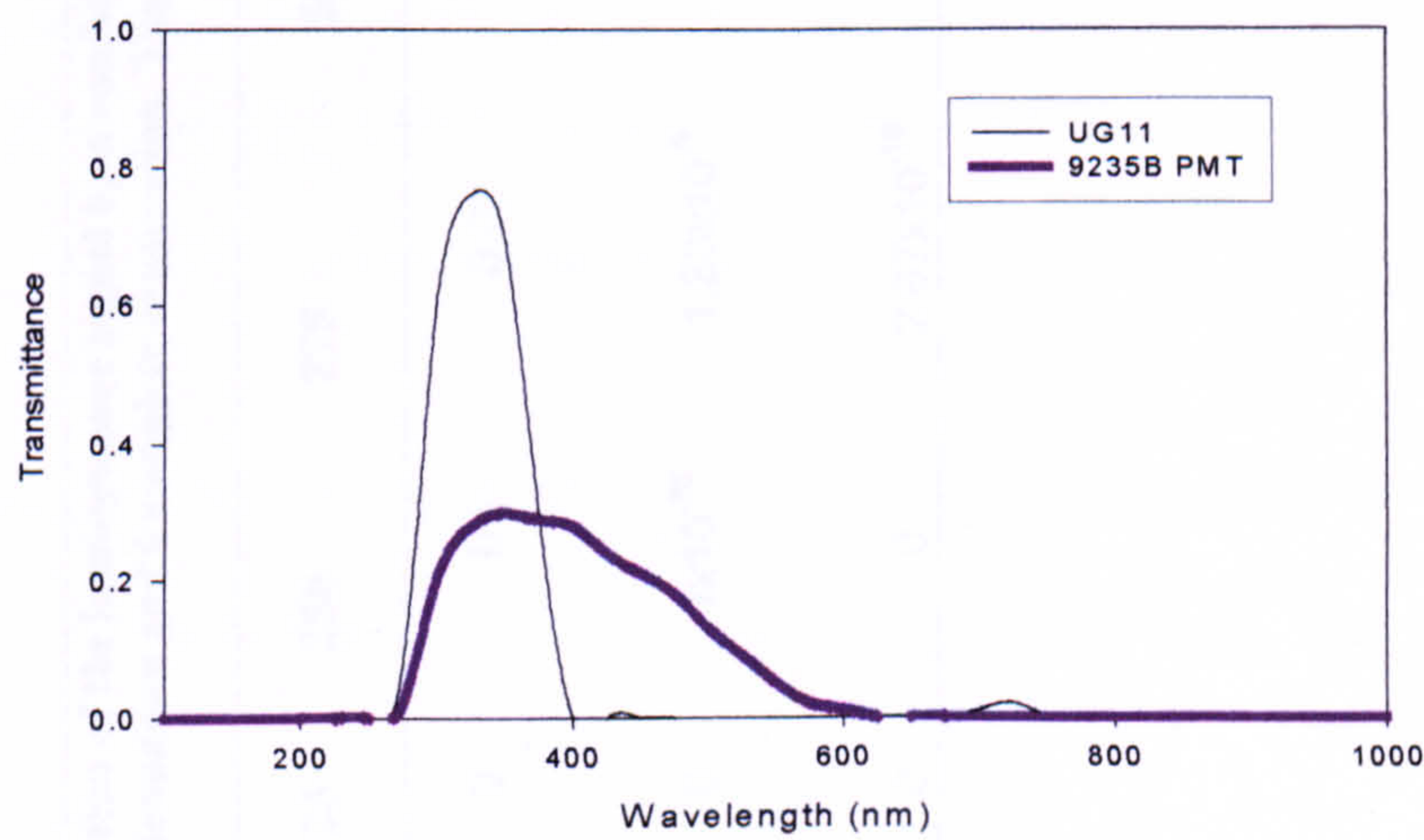


Figure 3.3 The typical spectral transmittance of UG11 (1mm) and the 9235B PMT. The Hoya U340 is similar in characteristics to the UG11 (plotted from manufacture guidelines).

Table 3.5 Optical attenuation of the luminescence signal by a combination of optical filtration and the Risø Daybreak reader's PMT. Numbers range from 1 being no attenuation and 0 complete attenuation. The figure is a multiplication of the transmittance of the filters and the PMTs.										
Wavelength (nm)	225	250	275	300	325	350	375	400	425	
9235B PMT	0	0	0.02	0.2	0.28	0.3	0.29	0.28	0.24	
UG11 (7mm)	0	1×10^{-35}	1.33×10^{-8}	0.0279	0.1464	0.0823	0.0002	1×10^{-28}	0	
Optical Attenuation.	0	0	2.67×10^{-10}	0.0056	0.0410	0.0247	6.34×10^{-5}	2.8×10^{-29}	0	

3.3.3.2 Measurement Regime for the Multi-stimulation Risø Work.

The first stage in preparation of the powders for luminescence measurements was to remove any residual stored signal. As the rock samples were processed to a powder in natural light, and were also exposed to the light of the optical microscope during hand picking, they should have been sufficiently bleached. Nevertheless, each disc was put through an initial TL run before measurement as a convenient bleaching process.

After the natural signals had been removed the powders were given an artificial radiation dose in the laboratory. For these remnant luminescence measurements the dose was 10Gys administered by the Risø system's internal beta source. Each sample underwent three measurements, called glows. Glow 1 and 3 were prompt, occurring immediately after post-irradiation preheating, whilst glow 2 was a delayed measurement made after a period of storage. For measurements made in this study the delay was an average of two months.

The preheat regime chosen as most suitable for remnant luminescence measurement was 135°C for 16 hours. This long and low temperature regime had been used successfully in previous studies at the SUERC luminescence laboratories (Anthony, 2003; Smith, 1998). Each set of twenty prepared discs were split into two aliquots of ten, a prompt normalisation set and a delayed set and the remnant luminescence was measured in the following steps:

1. Glow 1. All twenty discs were given a 10Gy beta dose, preheated (outside the reader in an oven) and measured using the multi-stimulation technique on the Risø reader.
2. The delayed set were re-irradiated (again 10Gys) and stored in the dark at ambient temperature.
3. After two months storage the ten 'prompt' aliquots were given the same 10Gy dose.
4. Glow 2. All twenty discs were preheated and measured using the multistimulation technique.
5. Glow 3. All twenty discs were re-dosed with 10Gys, preheated and read again.

The settings for the stimulation sources are outlined in Table 3.6 below:

Table 3.6 PSL settings for the Risø sequences.		
Setting	Infrared	Blue-OSL
Light Source	IR Diodes (laser in Riso 2)	Blue Diodes
Optical power (%)	60	60
Duration of stimulation (secs)	40	40
Time per data point (secs)	0.16	0.16
Total number of data points	250	250
Number of data points acquired during stimulation	230	230
Data points before/after stimulation	10/10	10/10
Read temperature (°C)	50	125
Heating rate (°C/sec)	5	5

The TL settings comprised a ramp and reheat cycle. The sample was heated to 500°C at a rate of 5°C/second. It was then allowed to cool before being heated again under the same conditions, to allow for the background signal to be measured and subtracted from the results.

3.3.3.3 Data Analysis.

The Risø systems come with a software package including a number of data analysis programmes. The data from each measurement run are generated as basic binary (*.bin) files, which can be then processed using the ‘Luminescence Analysis’ programme, which enables the user to view the individual glow files for each disc, the section of the run its from and the source of the stimulation.

The luminescence programme enables an easy and quick assessment of the glow curves of the individual discs and diagnosis of any problems. It also allows the data to be broken down into smaller stimulation and glow-specific bin files. These files were then processed further using the ‘TL/OSL Viewer’ programme allowing the binary data to be converted into a format compatible with Microsoft Excel. The data can be exported in two forms; an *.ASCII file which contains the

data as a whole block, or as an integer file that allows the data to be separated into user defined integrals, that is particular regions of interest from the glow curves.

For this study the PSL and TL data, recorded as 250 separate binary channels, or segments, were divided into the following integrals, or regions of interest. The complimentary Risø software allows for the designation of ten integrals and the size of each is optional. In this instance nine were used and they were divided as follows: channels 71-90, 91-110, 111-130, 131-150, 151-170, 171-190, 191-210, 211-230, 231-250. In TL each individual binary channel contains 2°C (500°C in 250 data channels) so these integrated data sets equate to 141-180°C, 181-220°C, 221-260°C, 261-300°C, 301-340°C, 341-380°C, 381-420°C, 421-460°C, 461-500°C. In the case of the PSL (IRSL and blue OSL) the chosen integrals were: 1-10, 11-20, 21-30, 31-60, 61-90, 91-120, 121-180, 181-240, 241-250 and these relate to the length of time the shine down curve is measured.

This integration of the glow and shine down curves is, in the terms of curve shape analysis, arbitrary in nature. No two discs curves were identical and it is common for the curves to change in shape to some degree between measurement cycles. In the case of the TL the fact that the integrals do not start at 1°C but rather at 141°C is significant. It prevents the unstable signal from the shallow traps interfering with the dating signal. In PSL the integrals started out at their narrowest width as these initial few seconds are the area of shine down curve that contain the majority of the signal. As the channels moved towards the tail of the curve they increased in width due to the sharp decrease in measured signal.

Data from all sets of integrals are then processed further in Excel. All the data from the three glows is inserted into a single spreadsheet for easy comparison. One of the initial analyses that must be carried out is a comparison between glows one and three. All of these measurements were multi-aliquot and the sensitivity change between glows in each was averaged across all the discs. Each of these numbers has a standard deviation [equation 3.1] and an error as a percentage of the average signal.

$$\text{STDEV} = (\text{average sensitivity change} / \text{SQRT} [\text{number of aliquots}])$$

[3.1]

The remnant luminescence is then calculated by a direct comparison of glows two and three. The average of the delayed set is then taken using the same techniques as those employed for calculating the sensitivity changes. These numbers, mean, standard deviation and percentage error were then divided (prompt/storage) to give the remnant luminescence as a ratio.

$$\text{Mean luminescence} \times \text{SQRT} (\% \text{ error} / \text{mean stored})^2 + (\% \text{ error} / \text{mean prompt})^2$$

[3.2]

In a further step the standard error of the remnant luminescence, called here standardised fading is calculated as follows and the results are presented in Appendix B.

Standardised Fading = (1-mean remnant luminescence of an integral/ % error)

[3.3]

Results from remnant luminescence, standard deviation, percentage errors and standardised fading are all mean totals and they are described as such in later chapters.

3.3.4 The SUERC Manual Readers.

3.3.4.1 The ELSEC Irradiator.

Unlike their Risø counterparts the SUERC manual readers do not have their own irradiation sources and two external beta ELSEC 9022 automatic irradiator systems are used, each with different strength sources. ELSEC 1 delivers a dose of 2.2104 ± 0.04 Gys/min, and ELSEC 2 28.26 ± 0.5 Gys/min.

3.3.4.2 The SUERC PPSL System.

3.3.4.2.1 System Specification.

The PPSL system, as its name suggests, uses pulsed stimulation. The photon counting is synchronised to the stimulation pulses, such that when the LED's are on, the counter accumulates signal from the sample as well as from any background signals. During the period when the LED's are off, the system background count is subtracted from the accumulated counts. This 'Up-down' count system minimises the effect of background, thereby increasing the system's sensitivity to samples that may have a weak PSL signal.

3.3.4.2.2 PMT Response and Optical Filtration.

The stimulation source is an array of infrared (~850nm) LED's that are pulsed symmetrically on and off for equal periods. The photons produced by the sample are detected using an Electron Tubes 9814 PMT operated in the photon counting mode. As with all other systems utilised in this study, optical filtration was used to define both the stimulation and detection wavelengths. The filters in front of the attached PMT were 4mm of BG39, 3mm of GG395 and an Environ 450 short pass filter, together giving a narrow detection window (Figure 3.4. and Table 3.7).

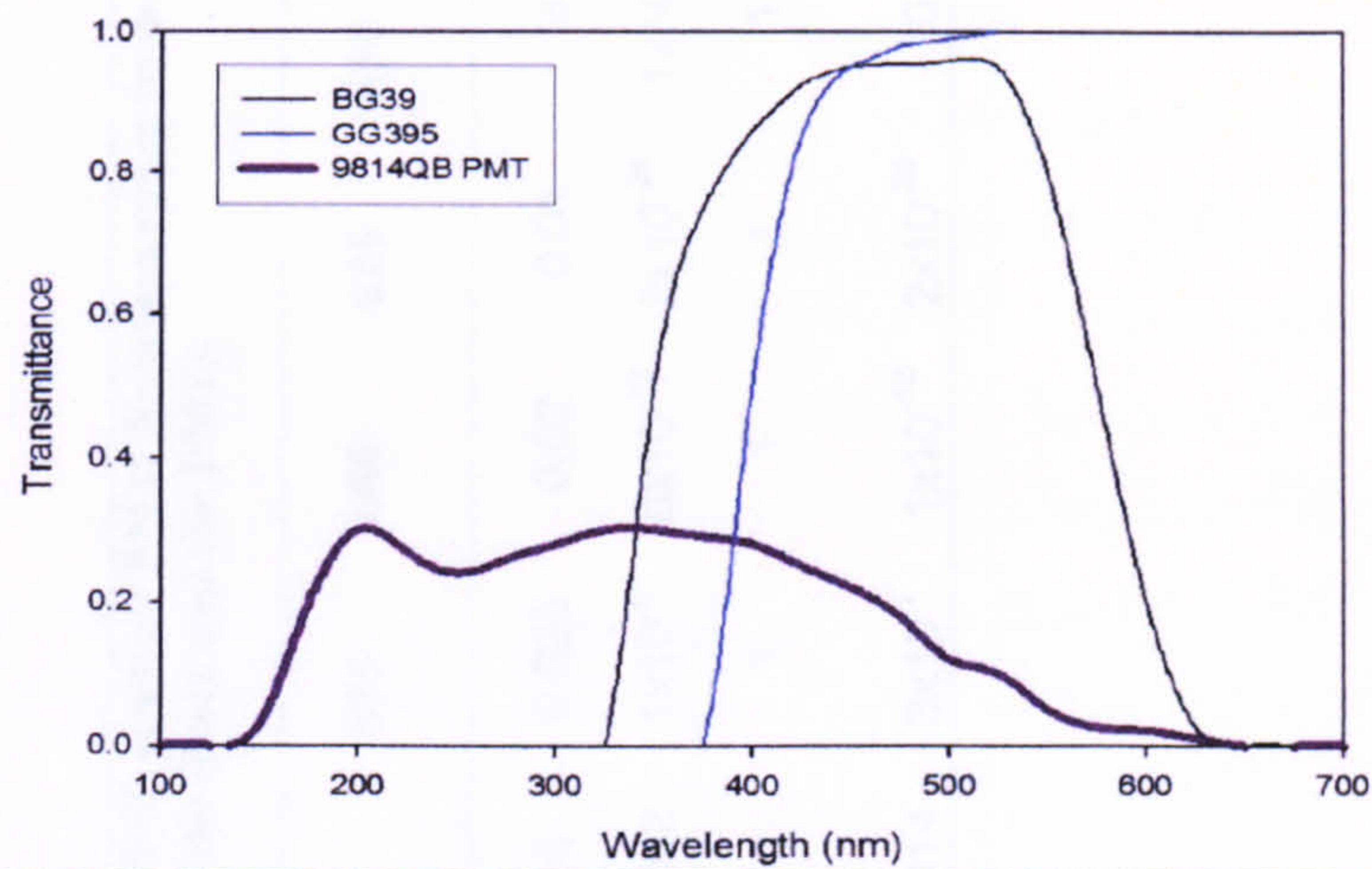


Figure 3.4 The typical spectral response of BG39, GG395 (1mm) and the 9814 PMT. The SUERC PPSL system also has an Envin 450 short pass filter that cuts out the signal below this (450nm) wavelength.

The PPSL system is designed to hold petri dishes in the sample draw so an adapter to position the discs consistently in the centre of the diode array and PMT was constructed (Figure 3.5).



Figure 3.5 Insert to adapt the SUERC PPSL system for measurement of luminescence of powders on discs.

Table 3.7 Optical attenuation of the luminescence signal by a combination of optical filtration and the SUERC Manual PPSL reader's PMT. Numbers range from 1 being no attenuation and 0 complete attenuation. The figure is a multiplication of the transmittance of the filters and the PMTs.

Wavelength (nm)	325	350	375	400	425	450	475	500	525	550	575	600	625	650
9814QB PMT	0.3	0.3	0.29	0.28	0.25	0.22	0.18	0.12	0.1	0.05	0.025	0.02	0.01	0
BG39 (4mm)	1×10^{-80}	1×10^{-5}	0.0100	0.0895	0.2873	0.4401	0.4787	0.5204	0.4401	0.0282	1×10^{-5}	6×10^{-12}	2×10^{-26}	1×10^{-48}
GG395 (3mm)	0	0	1×10^{-12}	0.125	0.6141	0.8574	0.9412	0.9703	1	1	1	1	1	1
Optical Attenuation	0	0	2×10^{-15}	0.0031	0.0441	0.0830	0.0811	0.0606	0.0440	0.0014	3×10^{-7}	1×10^{-13}	2×10^{-28}	0

Table 3.8 Optical attenuation of the luminescence signal by a combination of optical filtration and the SUERC Manual TL reader's PMT. Numbers range from 1 being no attenuation and 0 complete attenuation. The figure is a multiplication of the transmittance of the filters and the PMTs.															
Wavelength (nm)	300	325	350	375	400	425	450	475	500	525	550	575	600	625	650
9883QB	0.18	0.22	0.24	0.23	0.2	0.19	0.16	0.12	0.1	0.07	0.05	0.02	0.01	0	0
KG1 (3mm)	1x10 ⁻⁵	0.216	0.5927	0.7915	0.7536	0.681	0.705	0.753	0.8044	0.729	0.729	0.729	0.6361	0.5615	0.405
7-59 (3mm)	0.0001	0.2746	0.512	0.6141	0.512	0.157	0.024	0.001	1x10 ⁻⁷	0	0	0	0	0	0
Optical Attenuation.	4x10 ⁻¹⁰	0.0131	0.0728	0.1118	0.0772	0.0204	0.003	7x10 ⁻⁵	1x10 ⁻⁸	0	0	0	0	0	0

3.3.4.2.3 Measurement Regime.

The measurement regime utilised by the PPSL reader was the same as outlined in section 3.3.3.2, although here each disc was loaded and measured in turn. Also with the manual readers the size of the aliquots has been reduced to 10 discs divided into two sets of 5. Each aliquot was measured for 60sec with the final 10 seconds being subtracted as late light. This is a form of background subtraction because between 50 and 60 seconds in the shine down curve the sample is producing negligible (or no) luminescence. The late light was subtracted from the total count and it was this new total that was processed. This procedure was carried out for all of the 10 discs, in common with the automatic readers to produce three glows for the prompt and delayed set.

3.3.4.3 Data Analysis.

The SURRC PPSL reader records the luminescence signal in two formats, as a *.PSL file, which contained the signal from individual discs and a *.SUM file, which contained the total luminescence counts for all the discs in a run, or in the case of this study the sample glow. It was the *.SUM file that was used for further analysis and was exported directly into an Excel spreadsheet, where the remnant signals were extracted using the same procedure as outlined in section 3.3.3.3.

3.3.4.4 The SUERC TL System.

This manual TL system allowed a comparison of remnant luminescence measurements with results from the automatic TL reader. The SUERC TL system has a different detection range and a more accurate heating system than the Risø reader as it has less thermal lag.

3.3.4.4.1 System Specification.

The SUERC TL reader was one of the three systems used in this study designed for manual luminescence measurements. The thermostimulation interfaces with a computer running relevant software and an analogue to digital converter (ADC) card allows the software to control the reader's temperature. The PC also has a Multi-Channel Scaler (MCS) card that is used to record the TL signal.

The heater plate, on which the sample disc sits during stimulation, lies in a machined aluminium chamber and its temperature is controlled by a welded Chrome-Alumel (Type K) thermocouple during linear heating of the disc. The thin thermocouple wires used in this design allow for accurate temperature measurements because they conduct little heat from the plate (Spencer, 1996).

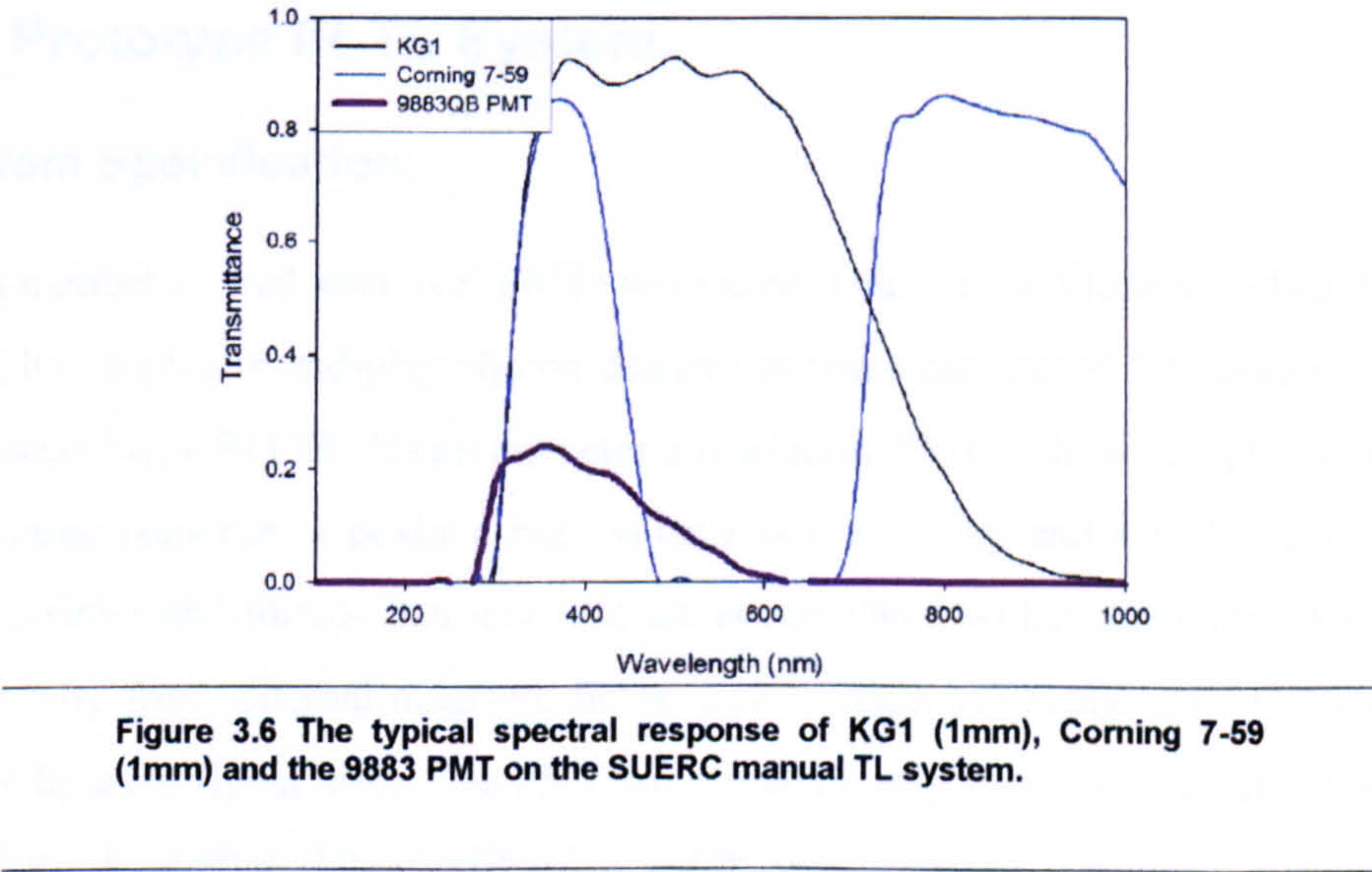
In this system each disc was placed on the heater plate (the Risø heater plate by contrast is on a mechanism that lifts the disc from its slot on the carousel) using tweezers, before being heated to

500°C with the luminescence emission being measured every degree using the MCS. The sample was then reheated to 500°C while the MCS recorded the background. The system was programmed to automatically subtract this set of readings from luminescence measurements during the first heating. This ‘background’ is electrical noise within the system and thermal incandescence from the heater plate.

As with all of the measurement systems used in this study, being able to account for drift in both the stimulation and measuring conditions is essential. A normalisation cycle was used to diagnose any changes between glows but unless there was a significant change in the equipment most of any variation recorded was accounted for by sensitivity changes in the minerals, especially feldspars, during repetitive cycles of irradiation, heating and measurement. However, day-to-day variations can also occur within the PMT. This was true of both its ability to detect photons and also the tube’s ‘dark count’. The latter is unique to each individual PMT and can range from tens to hundreds of counts/sec. The dark count was highly responsive to changes in laboratory temperature and works best at an ambient temperature of around 20°C. If the ambient temperature rose then so did the dark count such that a 5°C temperature increase could possibly double the PMT’s internal dark count. Another potential variable, which must be measured on a daily basis, at the very least, is the photon counting ability of the PMT, known as the ‘light count’. This is carried out using a reference light source and the value is again unique to each tube and varies on a day-to-day basis.

3.3.4.4.2 PMT Response and Optical Filtration.

The manual TL reader has an Electron Tubes 9883QB PMT with a detection window defined by the following optical filters: 3mm of KG1 and 3mm of Corning 7-59 (Figure 3.6 and Table 3.8).



3.3.4.4.3 Measurement Regime.

Discs were loaded into the manual TL system for determination of the remnant TL immediately after being measured on the manual PPSL reader. Within the manual TL reader, in common to the Risø TL measurements, the discs were heated to a temperature of 500°C at a heating rate of 5°C/sec. A second heating cycle was used for background subtraction.

3.3.4.4.4 Data Analysis.

As the manual TL readers were designed 'in house' they lack purposely written software. The TL programme that runs the manual reader reproduces glow curves, already minus the thermal background, as a column of 10°C integrals (running from 0-500°C). They are created as *.PSL files and before the next stage of data analysis can take place these must be renamed as *.TL files with a corresponding glow number, e.g. *.tl1, *.tl2, *.tl3. These can then be added to a TLAN (TL analysis) programme, which turns each of the three glows into matrix files; *.mat1, *.mat2 and *.mat3. Matrix four is a comparison of glows one and three, the normalisation control to check for and record any change in sample sensitivity created by repeated irradiation and stimulation, and also any change in the machine's operating conditions between glows.

The storage period between the first and second glows was two months and ideally there would be little reason for changes in instrument sensitivity during this time but the equipment was used for other measurements and any deviations of the conditions from glow to glow must be taken into account to produce accurate results. The fifth matrix is the one that measures any change in signal that occurs with storage. This matrix will also include any changes in the instrumentation operating conditions, which is why normalisation is important.

3.3.5 The Prototype IR-TL System.

3.3.5.1 System Specification.

In this study a number of 'red sensitive' PMTs were used. One was an Electron Tubes P25232-05 photodetector. It is a plug-in-and-play photon detector package configured for photon counting. It comprises a selected type 9113B, 25mm diameter end window PMT with an S20 photocathode that has a high infrared response, a positive high voltage power supply and a high-speed amplifier-discriminator, counter and micro-controller. All are encapsulated within a cylindrical metal case, providing immunity from external magnetic fields. Low voltage and signal output connections to the package are by axial flying leads. The PMT has a spectral response range of 280-850nm with a peak of ~400nm. A similar 'blue-sensitive' portable system constructed from this design has already been field tested (Bishop *et al.*, 2005).

The luminescence signal is recorded by the Electron Tubes EM6 counter timer software. The detector package plugs into a port in the PC and works on a similar basis to the PPSL software whereby the photons are counted into channels with a width of 1sec. The stimulating energy was supplied by the heater plate of the SUERC Manual TL reader and the photodetector package was mounted onto this using a set of specially designed flanges (Figure 3.9 and 3.10).

3.3.5.2 PMT Response and Optical Filtration.

This red sensitive photodetector package was filtered up using 3mm of RG665 and 3mm of Corning 7-59 in an attempt to improve the signal-to-background ratio by cutting out the wavelength of the blackbody irradiation emissions (Figures 3.7, 3.8 and Table 3.9).

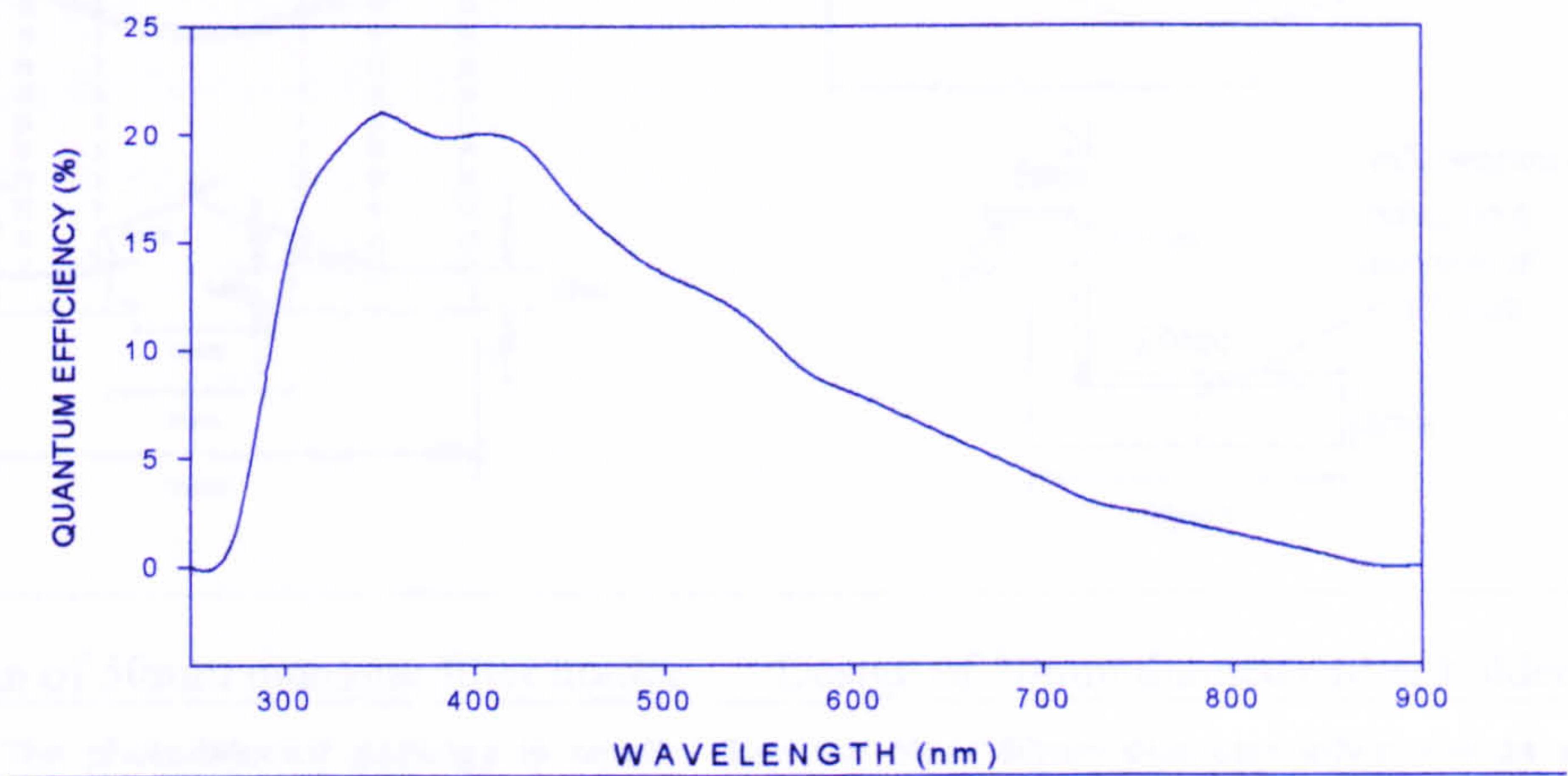


Figure 3.7 Typical spectral response of the Electron Tubes P25232-05 photodetector package.

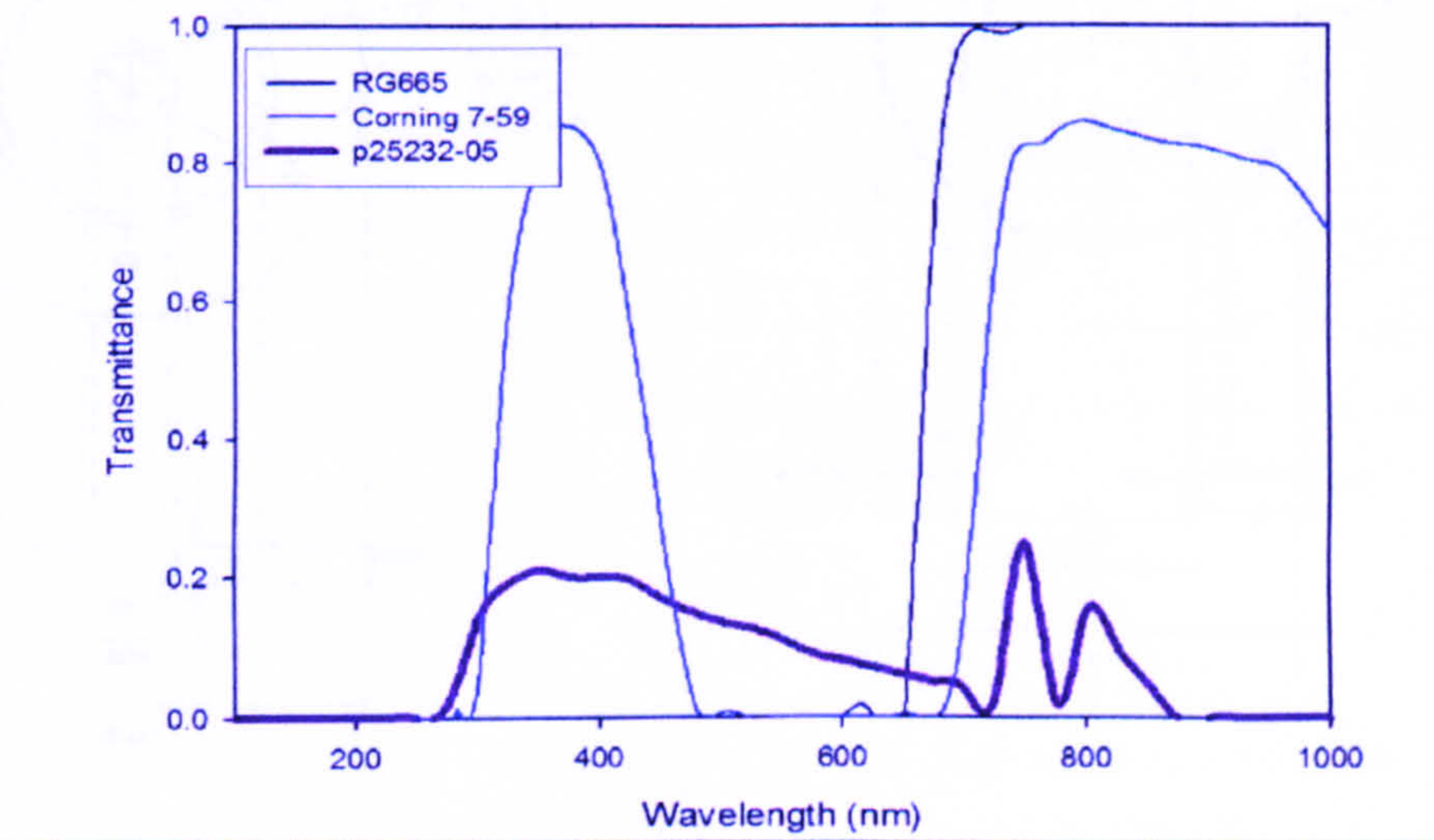
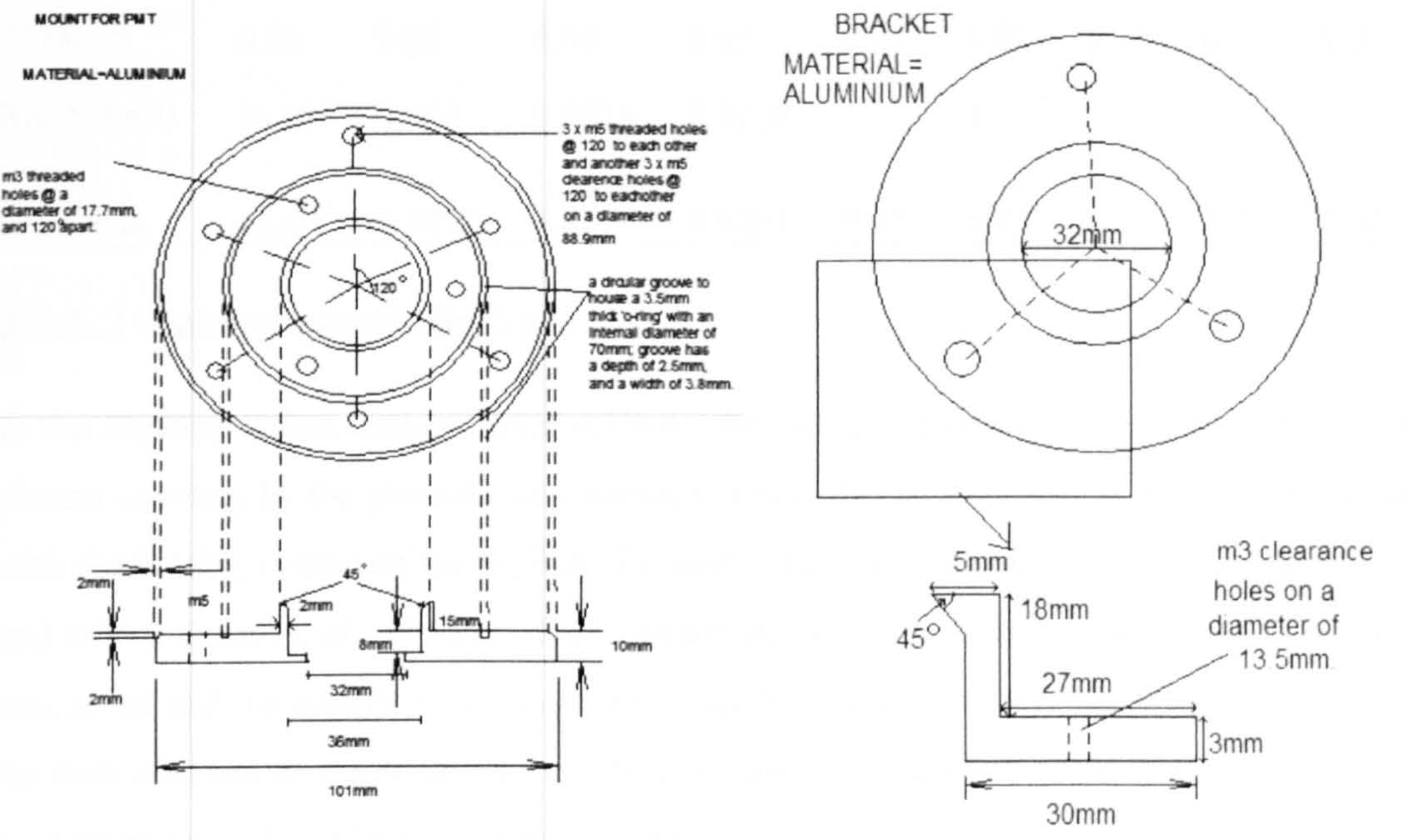


Figure 3.8. Typical spectral response of RG665, Corning 7-59 (1mm) and the P25232-05 photon counting module.

Design of flange for small diameter red tube

Bracket that holds PMT into flange and creating a light tight seal



Design of 50mm diameter filter holder Design of 10mm diameter filter holder

Figure 3.9 The photodetector package is smaller than the other 50mm diameter tubes and as a result new filter flanges had to be designed. This was done with the Autodesk CAD programme.

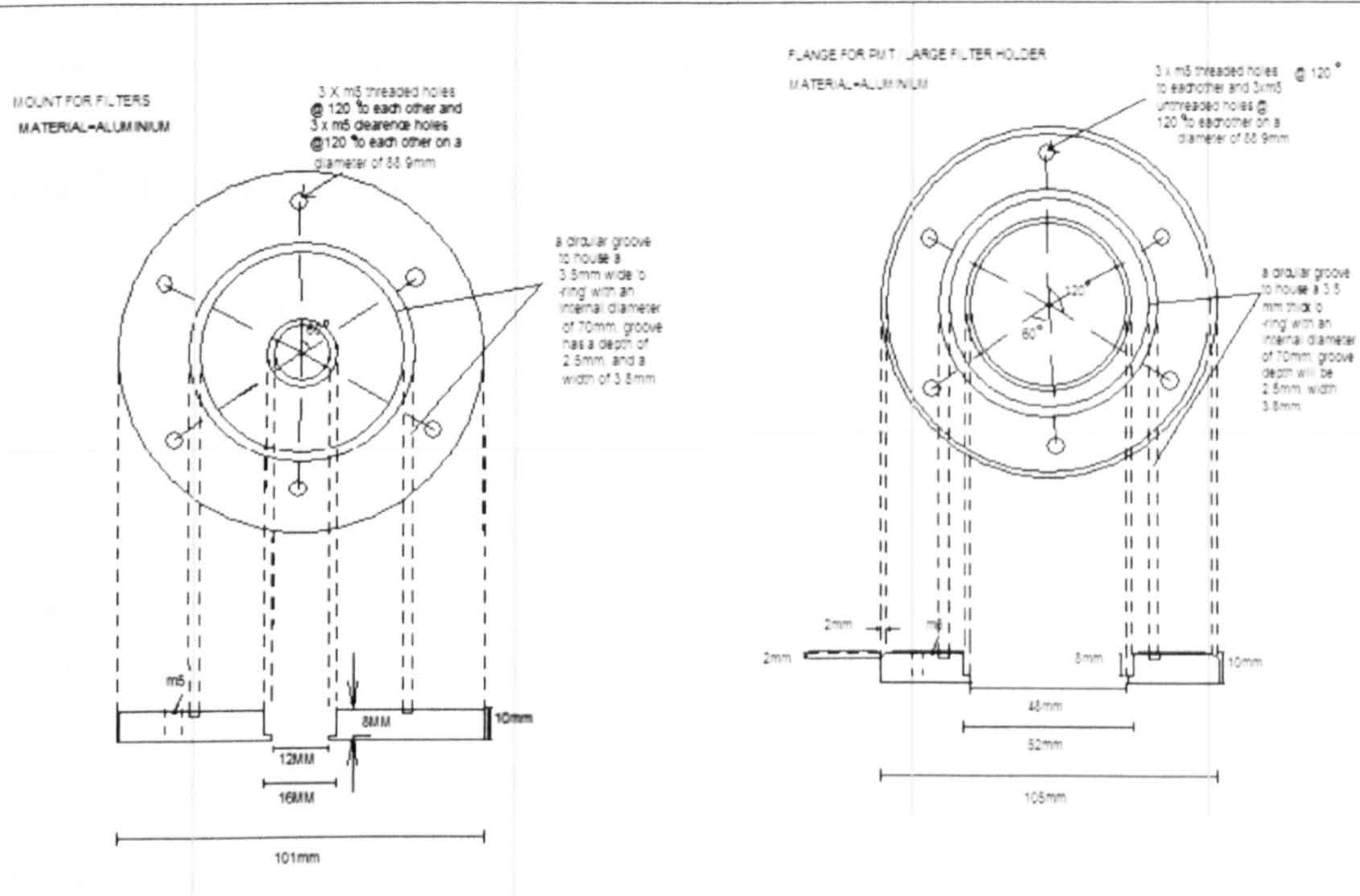


Figure 3.10. Flanges and filter holders for the small red sensitive photodetector package.

Table 3.9 Optical attenuation of the luminescence signal by a combination of optical filtration and the SUERC IR-TL system's PMT. Numbers range from 1 being no attenuation and 0 complete attenuation. The figure is a multiplication of the transmittance of the filters and the PMTs.

Wavelength (nm)	650	675	700	725	750	775	800	825	850	875
P25232-05	0.06	0.05	0.04	0.03	0.25	0.02	0.15	0.1	0.05	0
RG665 (3mm)	1×10^{-9}	0.343	0.9413	0.9703	1	1	1	1	1	1
Optical Attenuation.	6×10^{-11}	0.0172	0.0377	0.0291	0.25	0.02	0.15	0.1	0.05	0

3.3.5.3 Measurement Regime.

In the Electron Tubes counter timer software the user sets a measurement time, during which the photon counting by the photodetector package is recorded as a column of data. To synchronise this with the heating system of the SUERC TL reader these measurements were set to one channel/sec and with a duration of 100secs, which corresponded with a 5°C/sec heating rate. The initial data was saved and the system reset during the ramp delay period so that the reheat was also measured for each disc and then subtracted later. This system does not allow for an instant subtraction of the background signal, unlike the manual TL and Risø software.

3.3.5.4 Data Analysis.

The columns of data were plotted into glow curves using a combination of Excel and Sigma Plot and regions of interest were separated to determine whether an IR-TL signal was measurable.

3.4 Pulsed Photostimulated Luminescence (PPSL).

3.4.1 The Blue PPSL System.

For this study a pulsed PSL unit was constructed that allowed better control of the pulsed stimulation source than the manual PSL reader whilst providing the ability to heat the sample that was being stimulated, either before as a preheat, or during measurement. Instead of the drawer arrangement of the SUERC PPSL system, a sample chamber and heater plate design was used, which was the same as that in the SUERC manual TL reader.

3.4.1.1 System Specification.

The 'blue' pulsed PSL system has an array of 18 high power 880nm LEDs configured in six three LED bundles focused on the sample holder, in this case the heater plate. The driver for these LEDs was capable of generating pulse widths between 1µs and 5s, with a delay time between events of

between 10μs and 0.5s. The diodes were powered using a constant potential source with resistive current limitation to control the pulsing.

A MCS similar to that in the manual TL readers was used for recording data and measurement was in pass mode with an external trigger (the diodes). Each pass was summed so that the signal from each was added to the previous signal. Owing to very low signal intensities in comparison with CW-PSL, this was the only way to obtain useable data. Each pass of the MCS was controlled by the rising edge of the pulse and therefore recorded the signal emitted during stimulation and after the diodes had been turned off. Due to the factors outlined above, such as PMT drift and possible sample contamination within the chamber, it was good practice to measure the dark and light count every day before and after a sample run. The nature of the stimulation regimes also made it important to monitor any breakthrough from the diodes. The heater plate and nitrogen supply (TL should not be recorded in the presence of oxygen) allowed analysis of the effect of preheat temperature on the samples without removing and handling the discs.

3.4.1.2 PMT Response and Optical Filtration.

The blue PPSL system had an Electron Tubes 9883QB PMT and its detection range was defined by positioning of 8.5mm of 49mm diameter BG-39 optical filter between the LED array and the quartz window to stop any breakthrough from the LED’s (Figures 3.11 and Table 3.10).

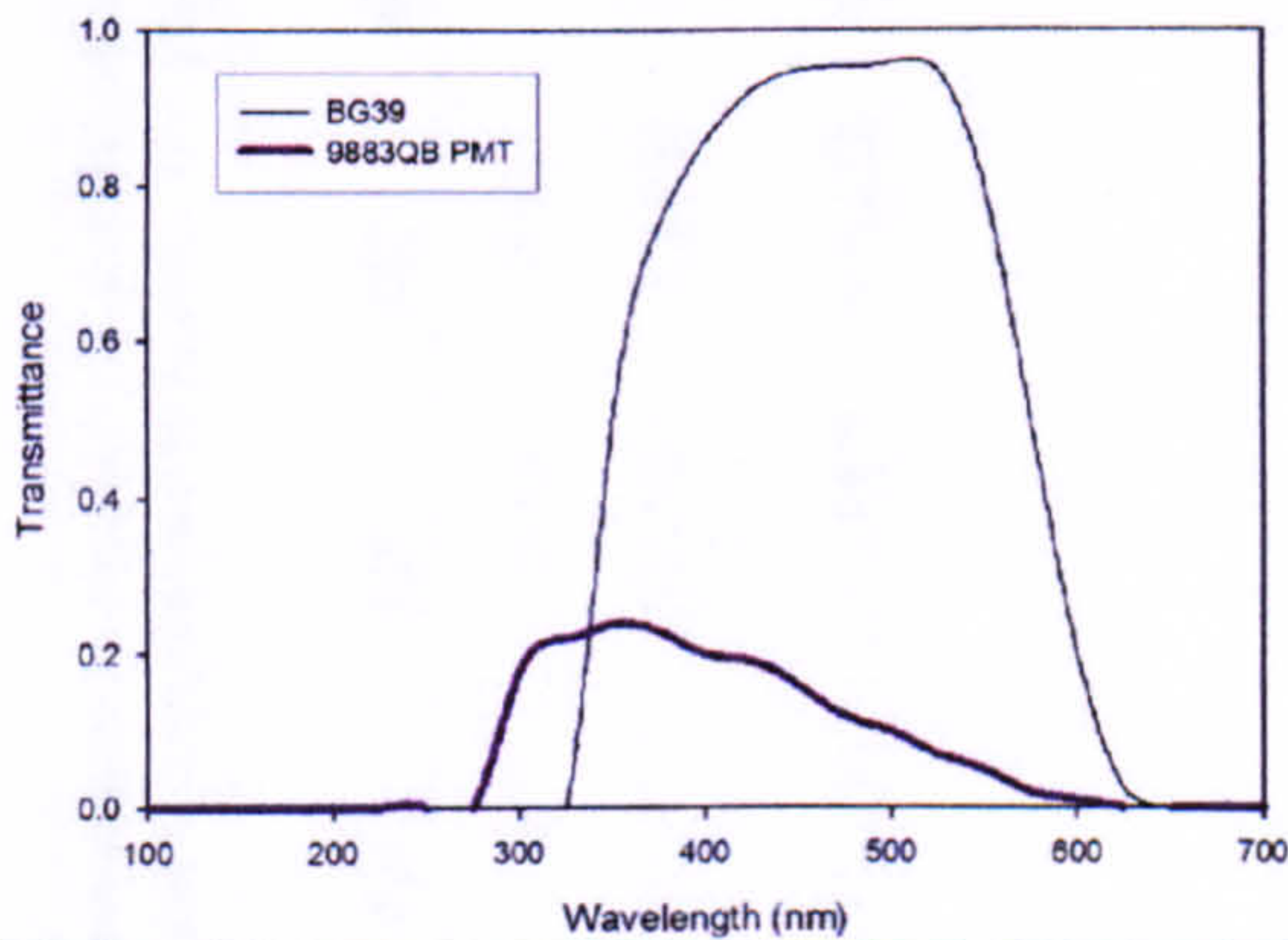


Figure 3.11 The typical Spectral Response of BG39 (1mm) and 9883QB PMT.

Table 3.10 Optical attenuation of the luminescence signal by a combination of optical filtration and the SUERC blue-PPSL system’s PMT. Numbers range from 1 being no attenuation and 0 complete attenuation. The figure is a multiplication of the transmittance of the filters and the PMTs.

Wavelength (nm)	350	375	400	425	450	475	500	525	550	575	600	625	650
9883QB PMT	0.24	0.23	0.2	0.19	0.16	0.12	0.1	0.07	0.05	0.02	0.01	0	0
BG39 (8.5nm)	0.0028	0.0867	0.2775	0.5155	0.6466	0.6761	0.7068	0.6466	0.1501	0.0028	1.1×10^{-6}	2×10^{-14}	3×10^{-26}
Optical Attenuation.	0.0007	0.0199	0.0555	0.0979	0.1035	0.0811	0.0707	0.0453	0.0075	5.5×10^{-5}	1.1×10^{-8}	0	0

3.4.1.3 Overview of Measurement Regimes.

For measurements carried out using this reader the pulsing module was set to deliver a pulse width of 20 μ s and was triggered externally by the MCS software. The frequency of the pulses were 1460 μ s (14ms). On the MCS the dwell time of each channel was 10 μ s, the first two channels recording the within-pulse luminescence as well as the stimulation source.

A number of measurements were made using this system to test two hypotheses: (i) can microsecond pulses stimulate a luminescence signal without significantly bleaching the mineral? (ii) Could microsecond pulses be used to carry out a single aliquot single glow fading test? These measurements will be outlined in greater detail in a subsequent chapter.

3.4.2 The IR PPSL System.

The promising results from the blue pulsed system and the extensive literature on the success of using the near-IR emission from feldspars encouraged the following work on constructing a red-sensitive time domain system with a low signal-to-background ratio.

3.4.2.1 System Specification.

This system utilised the same sample chamber and pulse driver module as the above 'blue' system but that is where the similarities end. The diode array was much smaller; comprising just two LEDs, due to problems of breakthrough to the PMT. Breakthrough was a much larger problem in this system than with blue PPSL because the detection window (~710nm) was closer to the stimulation wavelength (940nm).

The PMT used was the Hamamatsu R2257 red sensitive module, whose specifications are described below. A major issue in any red sensitive detection system is background signal and these 'red' tubes have very high dark counts; this module at plateau has an ambient temperature dark count of ~14 000cts/sec, compared to the 30cts/sec for the PMT used in the blue system. This figure was not an anomaly and a significantly higher dark count was in fact expected. To reduce this background signal the PMT was coupled with a cooled housing (Hamamatsu C4877 Series Thermoelectric Cooler). It is a high performance water cooled unit designed to accommodate most commercially available PMT's with a head diameter of 51mm (2") or 38mm (1½").

The cooled housing is bulkier and much heavier than the usual PMT that sits on top of the sample chamber, so a stand and lift system had to be designed for use in the system (can be seen in operation in Figure 3.13). Due to the additional weight and having water running through the

system (through a set of rubber tubes), the sample chamber was moved up and down for sample loading. Figure 3.12 is a schematic of the design of the complete system.

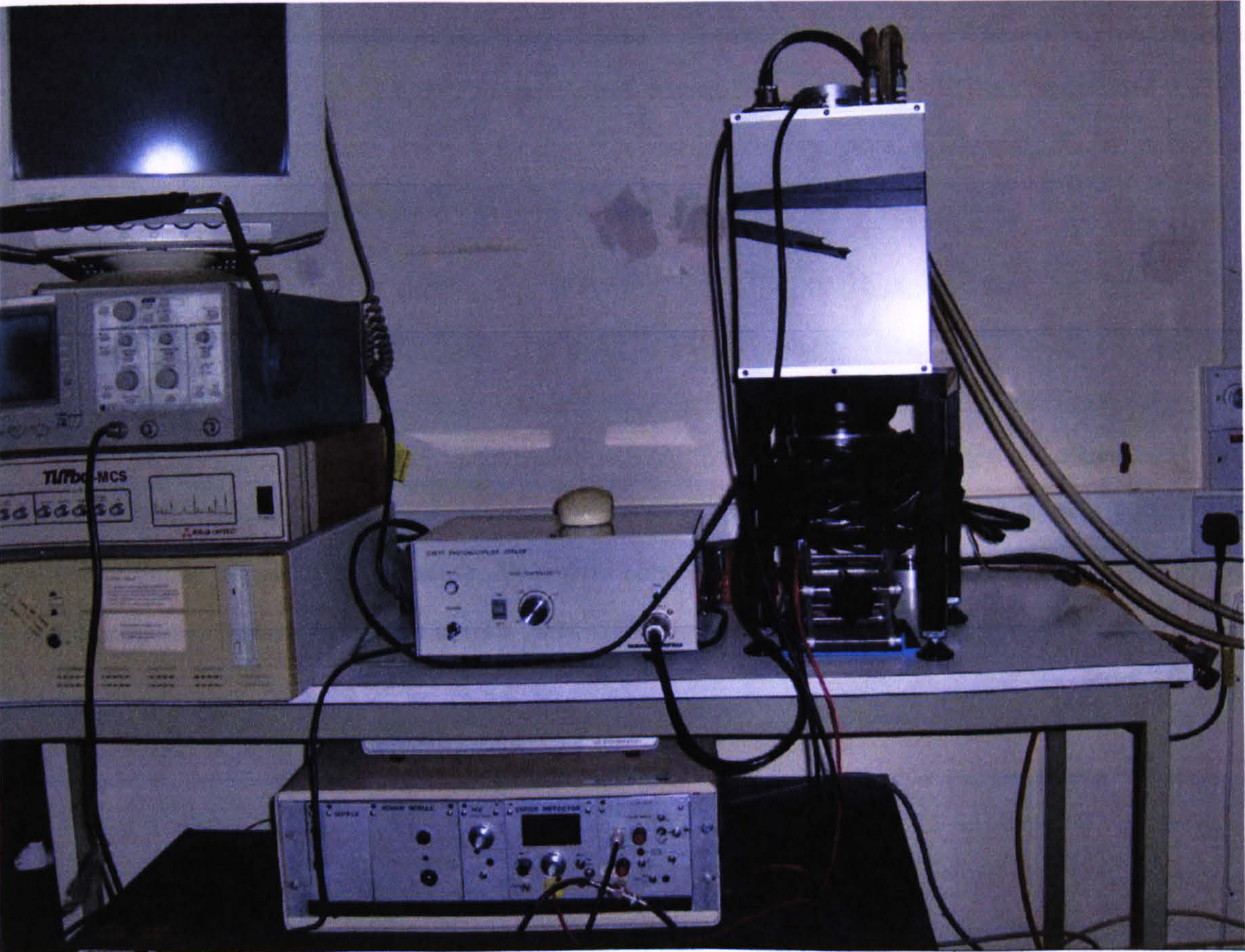
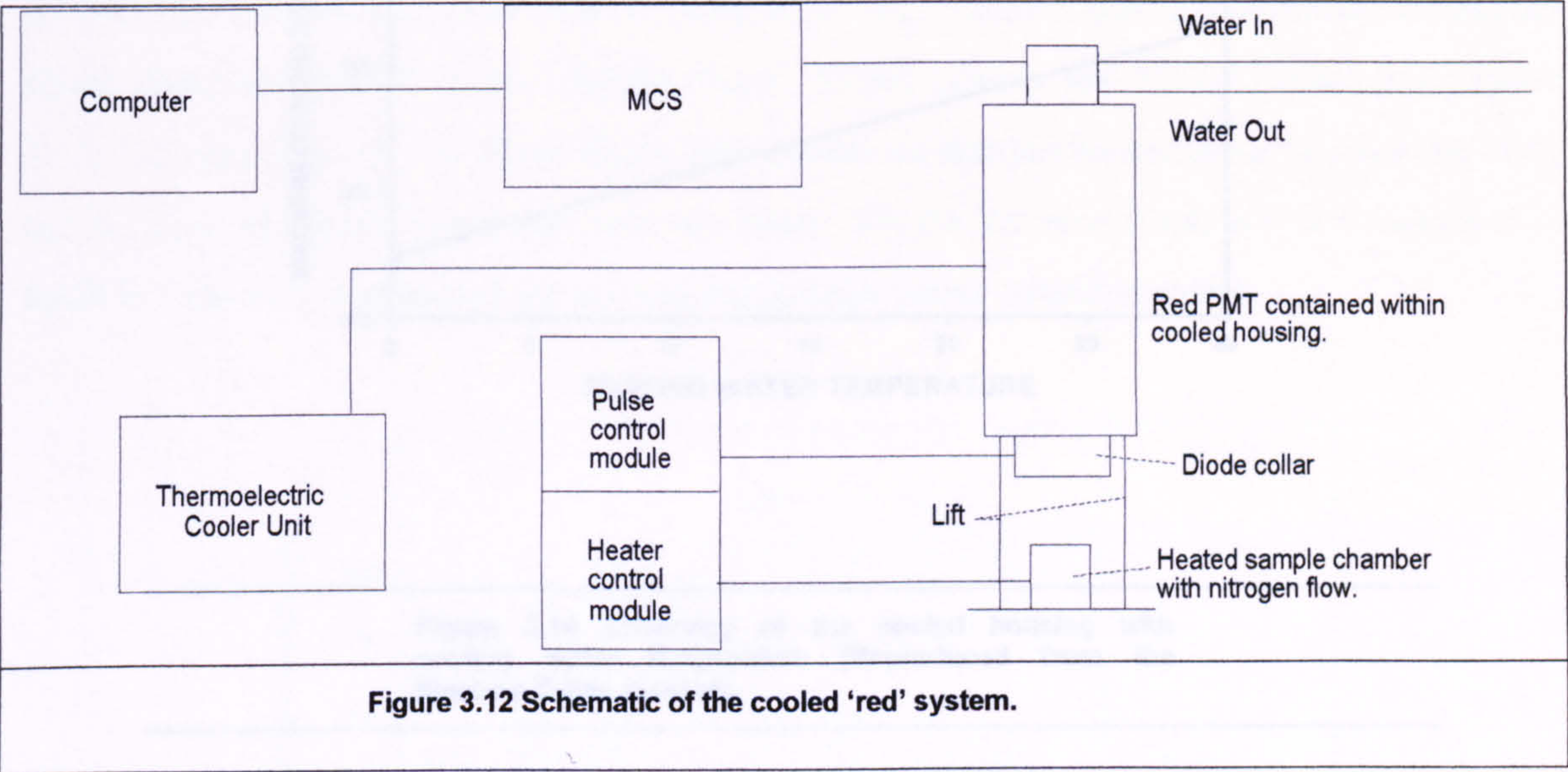


Figure 3.13 The configuration of the experimental near-IR pulsed system. (see schematic in Figure 3.12)

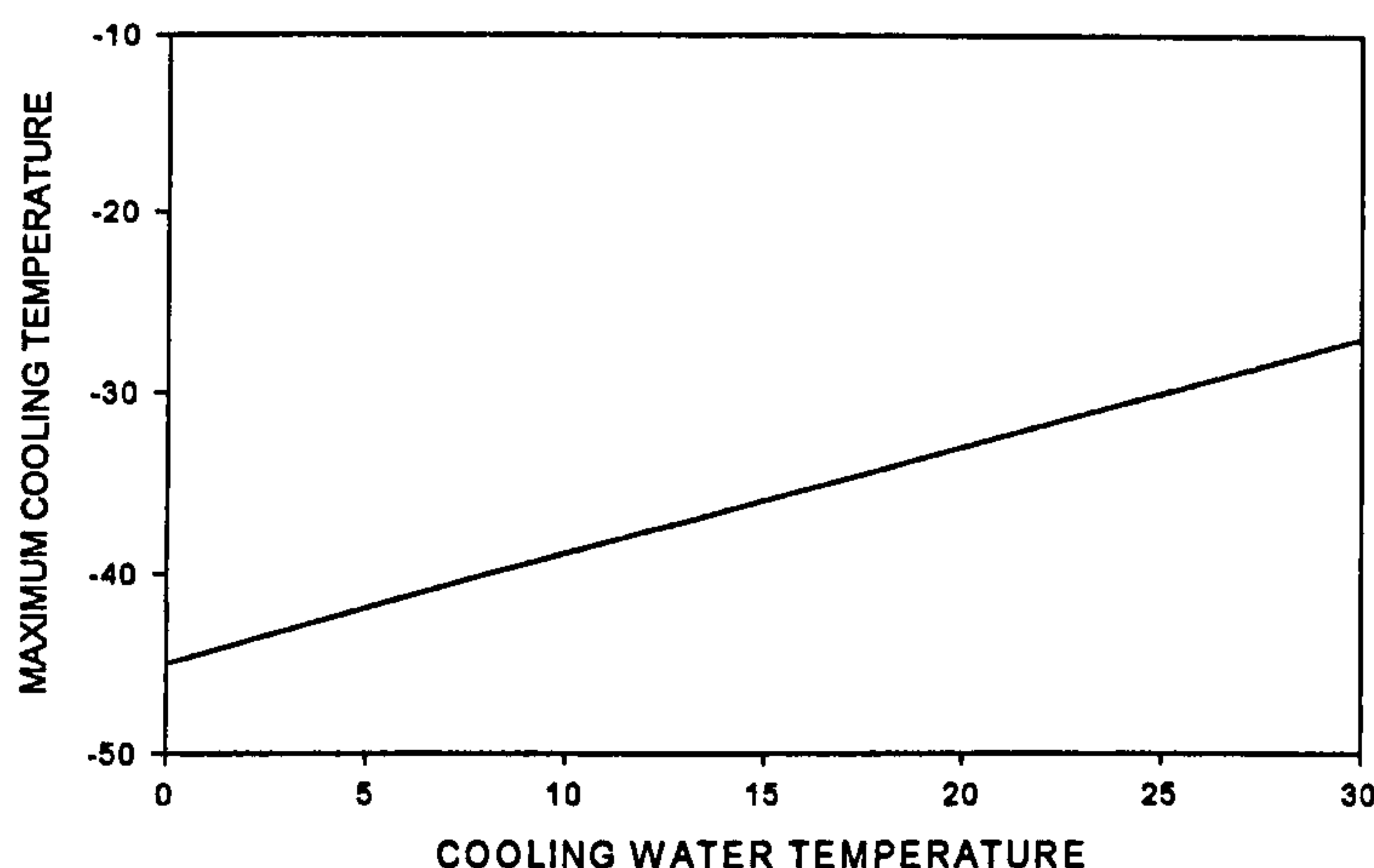


Figure 3.14 Efficiency of the cooled housing with cooling water temperature (Reproduced from the Electron Tubes manual).

The housing will take water at ambient temperature and cool the enclosed PMT to around -30°C . It is recommended that the system is always set to cool to below 0°C as condensation is a concern. As the graph in Figure 3.14 shows, it is straightforward to cool the tube to -30 to -40°C . The mains water temperature was $\sim 20^{\circ}\text{C}$ (high summer) and setting the cooler to -10°C could achieve a dark count of 200-220 counts/sec. Even with this low cooler setting there was a significant decrease from the 14000 counts/sec seen at room temperature (28°C).

With a cooled system and a dark count reduction of ~ 13800 counts/sec the next problem to overcome during instrument development was LED breakthrough. There are a number of reasons why this happens including incorrect or insufficient optical filtration. Dirty filters (fingerprints are known to phosphoresce), rim leaks and backscattering from reflective surfaces are also a potential problem. Ill-fitting optical filters cause the rim leaks and even the smallest gap between filter and collar can cause a large breakthrough. Two sets of filters were used in this system. One set sat in front of the stimulation source, a single 940nm LED, the other between the PMT quartz window and the sample chamber. As the LED's peak emission was at a wavelength greater than the planned detection window, long pass filters were placed in front of the diode.

The near-IR PPSL system had an EG&G ORTEC Turbo-MCS with its A67-BI companion software. The usual MCS programme that has been used in the 'blue' pulsed system has a lower limit of 1 microsecond dwell time and a pass count of 30 000. The turbo MCS gives the capability for a 5ns to 65535sec dwell time and a pass count of 20ns. Thus there is the opportunity to measure much smaller and then more detailed channel widths and acquire a higher signal count measuring more passes.

3.4.2.2 PMT Response and Optical Filtration.

The optical filtration comprised two separate filter stacks. The first consisted of six, 3mm thick RG 850s in front of the diodes. The second stack sat in front of the PMT detection window and consisted of 3mm GG420, 3mm of KG1, 3mm of RG695, 12mm of specially produced interference filters, designated SP057 (4mm), SP060 (2mm), SP062 (2mm), and SP058 (4mm) (see Figures 3.15, 3.16 and Table 3.11). These filters were chosen so that luminescence could reach the PMT but the level of system ‘cross-talk’ was minimised. All the filtration work, which is described in detail in Chapter 6, was carried out at room temperature unless otherwise stated.

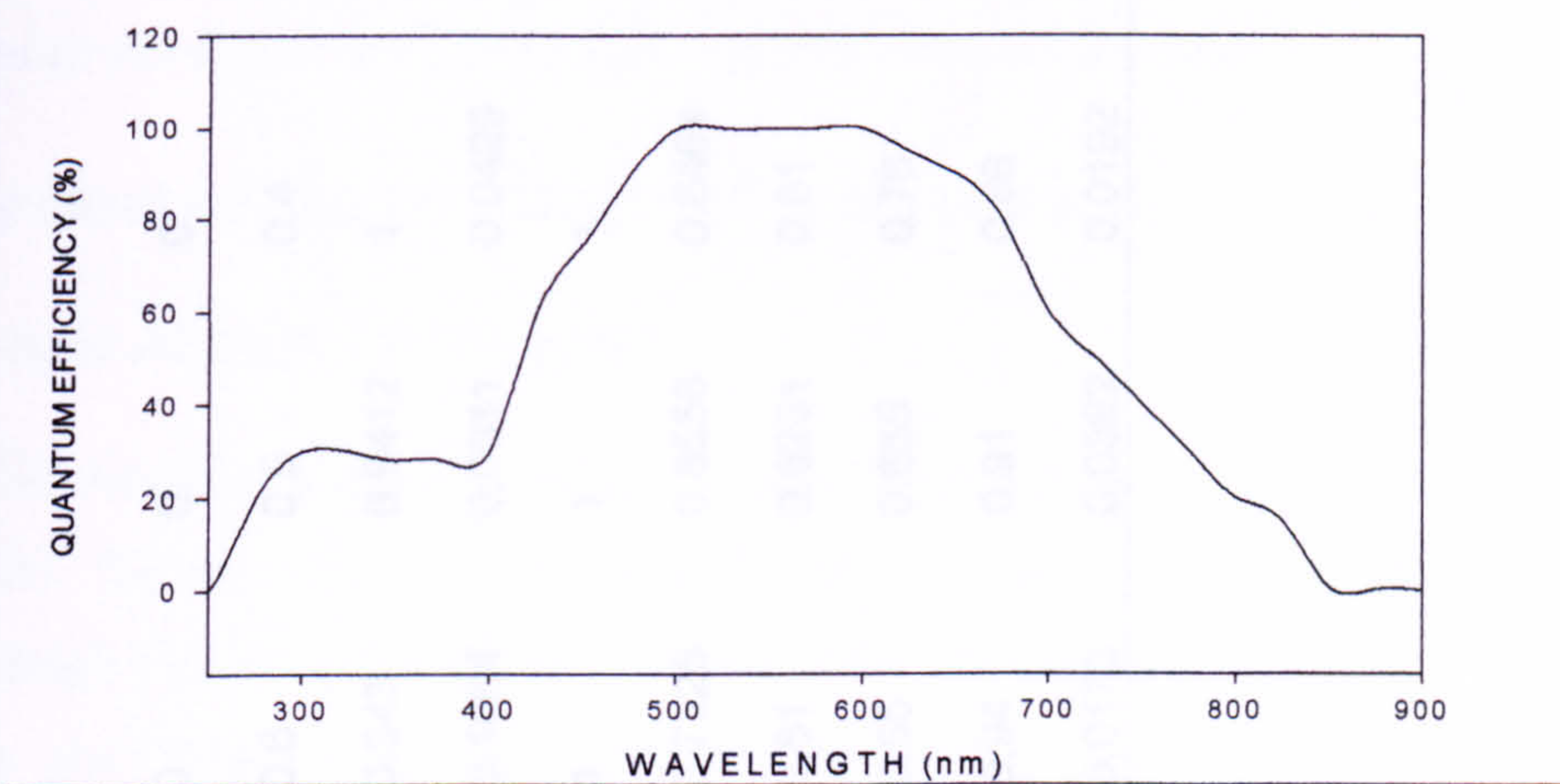


Figure 3.15 Typical spectral response of the Hamamatsu R2257 PMT

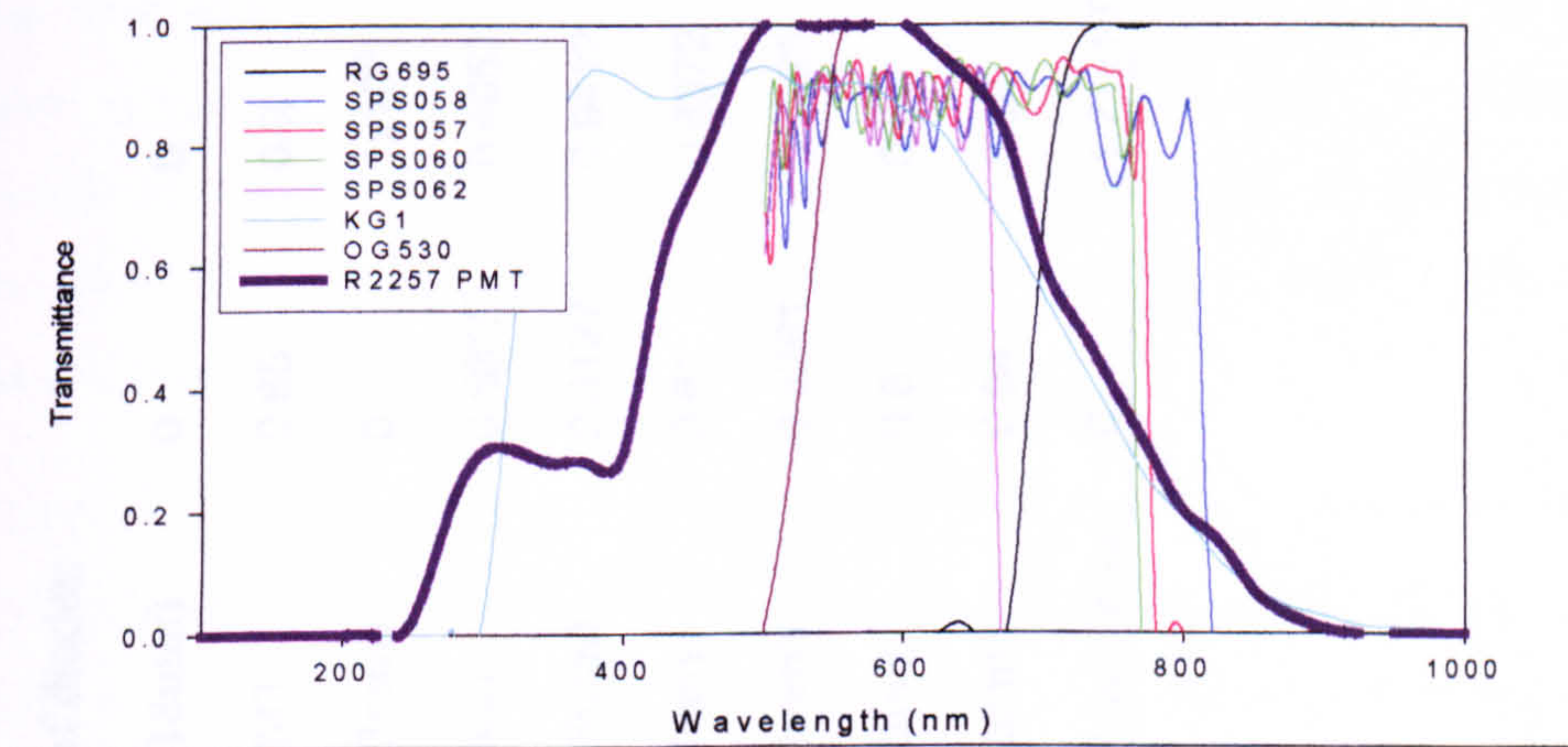


Figure 3.16 The typical spectral response of KG1, RG695, OG530, SPS57, SPS58, SPS60, SPS62 and R2557.

Table 3.11 Optical attenuation of the luminescence signal by a combination of optical filtration and the SUERC IR-PPSL system's PMT. Numbers range from 1 being no attenuation and 0 complete attenuation. The figure is a multiplication of the transmittance of the filters and the PMTs.

Wavelength (nm)	625	650	675	700	725	750	775	800
In front of diodes:								
RG850 (18mm)	0	0	0	0	0	0	1×10^{-90}	1×10^{-54}
R2257 PMT	0.95	0.9	0.8	0.6	0.5	0.4	0.3	0.2
RG695 (3mm)	0	1×10^{-9}	1×10^{-6}	0.343	0.9412	1	1	1
KG1(3 mm)	0.5615	0.4052	0.2746	0.1664	0.0911	0.0429	0.0156	0.0069
GG420 (3mm)	0.9127	0.9412	1	1	1	1	1	1
SP057 (4mm)	0.81	0.8372	0.8336	0.7225	0.8556	0.8464	0.1560	0
SP058 (4mm)	0.8281	0.7225	0.81	0.81	0.8281	0.81	0.5329	0.64
SP062 (2mm)	0.8	0.84	0.87	0.55	0.655	0.76	0.02	0
SP060 (2mm)	0.84	0.88	0.9	0.94	0.91	0.86	0.01	0
Optical Attenuation.	0	1.71×10^{-10}	1.45×10^{-7}	0.0173	0.0362	0.0192	2.6×10^{-7}	0

3.4.2.3 Overview of Measurement Regimes.

The measurements undertaken with this system are outlined in a subsequent chapter, however they were all based around testing the ability of this system to detect IR stimulated IR-PPSL with a low signal-to-background ratio.

3.5 The Equipment and Measurement Techniques Used for Luminescence Dating in this Study.

In part of this study a current SARA method was adapted in an attempt to date samples from an important Russian site as part of a NERC-funded international dating project.

3.5.1 Overview of Current Dating Techniques.

3.5.1.1 Multiple Aliquot Techniques.

Multiple aliquot techniques are carried out using both additive and regeneration methods (described in Aitken 1992). The regenerative method is a laboratory procedure where the equivalent dose is determined through measuring a range of increasing doses that encompass the natural to produce a dose response plot (Figure 3.17). The additive method measures luminescence in feldspars by giving additional doses to the sample followed by a long period of storage at ambient temperatures and then a shorter period at elevated temperatures.

The aliquots of mineral powders are prepared and divided into groups, typically half a dozen or so, with one group kept specifically for measurement of the natural luminescence. In the additive method the other groups are given various doses using a laboratory radiation source. Before the measurement cycle all the groups, including the 'natural' group for dating, are preheated. These discs then have their luminescence measured and from each group the signal is averaged and plotted to make a 'dose-response plot' (Figure 3.18).

The plot in Figure 3.18 shows the growth of OSL signal with dose. Here it is linear but when working with older samples and therefore larger doses, there is an issue with sublinearity (i.e., whereby the growth of signal reduces as applied dose is increased). In young samples with low doses the problem is supralinearity, the opposite effect, which is common in TL but unusual in OSL. Using this dose response curve, paleodose is read off as the intercept of the growth curve with the dose axis (P). This example is an ideal curve and procedures and solutions have been developed for processing less than ideal results.

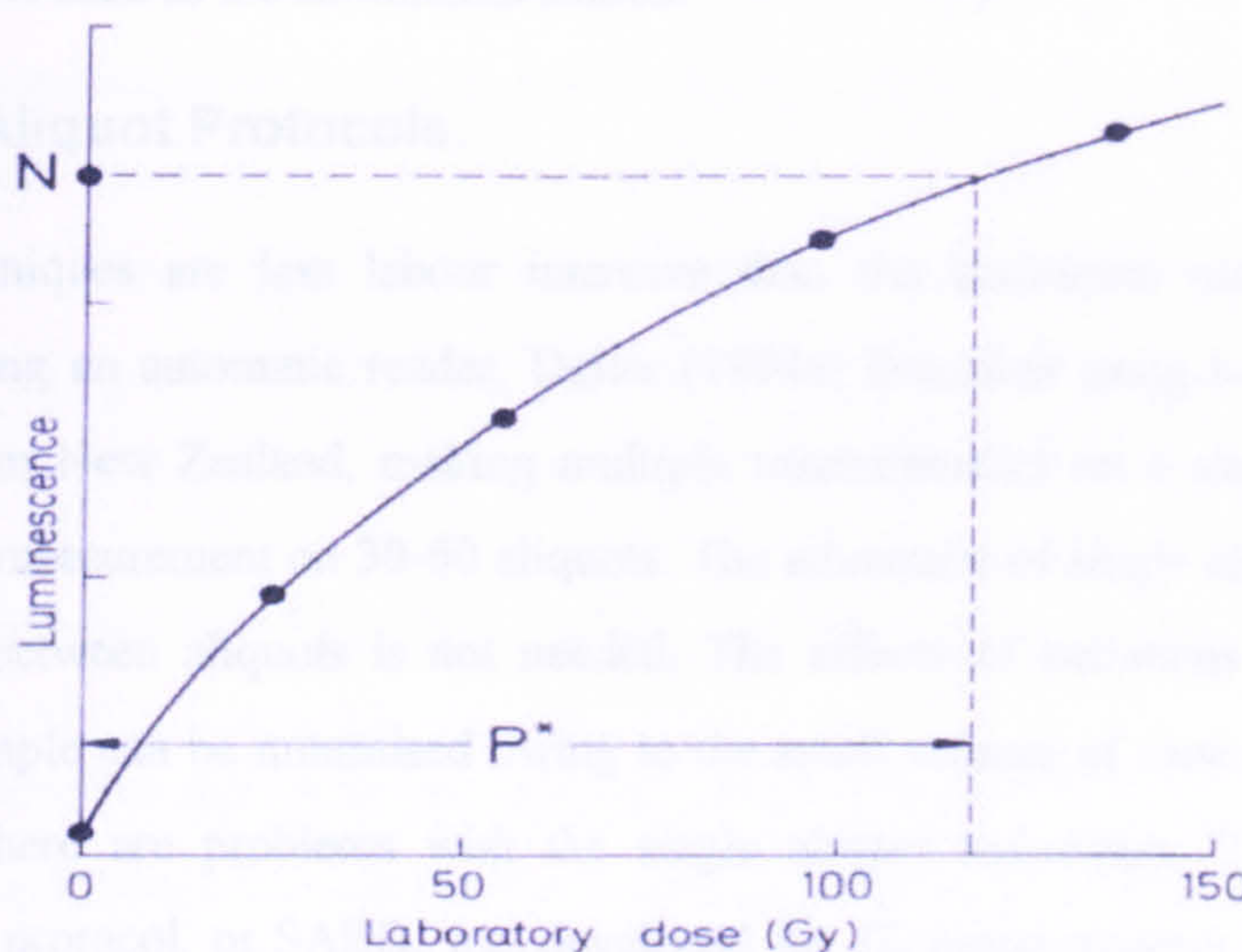


Figure 3.17 'Regenerative dose-response curve' (Aitken 1998). N is the natural luminescence signal and P the palaeodose by regeneration.

In the multi-aliquot regeneration method a number of aliquots, each comprising half a dozen or so discs, are used though all but the natural set are zeroed before being given the laboratory doses. The paleodose is then obtained by direct comparison of the natural signal with that on the resulting growth curve.

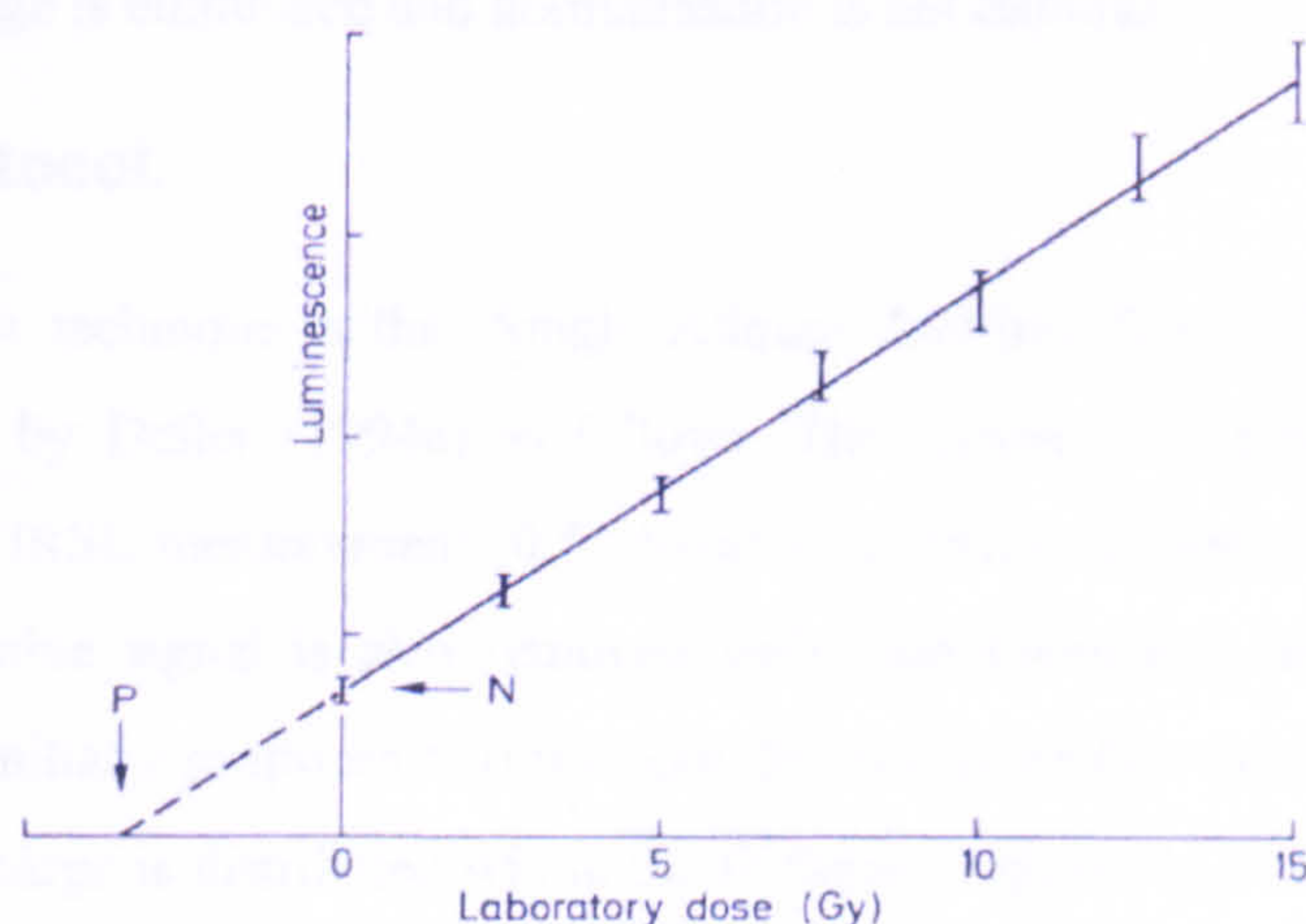


Figure 3.18 'Additive dose-Response curve' (Aitkin 1998). N is the 0Gy laboratory dose and P is the palaeodose.

The advantage of the regenerative method is that no extrapolation is needed and the palaeodose is calculated by interpolation, so uncertainties produced by the non-linearities mentioned above are reduced, if not eliminated completely. The critical disadvantage of this regenerative method is that if there is a change in sensitivity (luminescence emission per unit dose), caused by the zeroing and irradiation of the laboratory sets, the accuracy with which their luminescence signal can be correlated with the natural is an issue. This means that the interpolated paleodose will be in error with a sensitivity correction. Auclair *et al.* (2003) state that no matter what technique is used for

dating of feldspars, the results will suffer an age underestimation and wide equivalent paleodose distribution if IRSL is used as the stimulation source.

3.5.1.2 Single Aliquot Protocols.

Single aliquot techniques are less labour intensive than the traditional multi-aliquot methods especially when using an automatic reader. Duller (1994a) describes using both methods to date dune sediments from New Zealand, making multiple measurements on a single 5-10mg aliquot rather than a single measurement on 30-60 aliquots. The advantage of single aliquot techniques are that normalisation between aliquots is not needed. The effects of variations in mineralogy and bleaching of the sample can be minimised owing to the small volume of sample required. Despite these advantages, there are problems with the single aliquot techniques. The 'Single Aliquot Regenerative Dose' protocol, or SARD, was developed for TL measurements. Murray and Wintle (2003) first introduced it as a possible answer to precision and accuracy problems that made measuring smaller amounts of fading in feldspars very difficult. However, continued re-heating of the same aliquot causes sensitivity changes in the sample. The same is true of IRSL measurement and bleaching cycles. The latter may be due to the fact that the IR part of the spectrum cannot bleach out the whole signal. However, Wallinga *et al.* (2000) concluded that the SARD protocol has a number of advantages over previously used procedures: it is very precise, the problem of grain loss during storage is eliminated and normalisation is not required.

3.5.1.3 SAAD Protocol.

Another single aliquot technique is the 'Single Aliquot Additive Dose' (SAAD) protocol. This method was outlined by Duller (1994a) as follows. The sample is preheated at 200°C for ten minutes prior to each IRSL measurement (0.5 second exposure to IR while holding the sample at 50°C). Part of the stable signal is also removed with each preheating and this loss has to be corrected for. Duller initially proposed two methods for this correction that are based on differing ideas about how the charge is distributed within the feldspar or quartz crystal during irradiation and preheating. The two methods differ depending on whether it is assumed that this distribution is dependent on previous exposure to preheating and irradiation or "that the trapped charge induced by each dose given to the sample behaves independently of the others" (Duller 1994). The latter assumption was found to be valid through the experiments and procedures outlined by Duller, though both have one major flaw, in that they postulate that the growth of the signal as a function of dose is linear, which is not true when analysing older samples. Therefore the corrections are invalid and an age underestimation occurs. This realisation has led to the development of a third corrective method. This alternative approach treats the loss of trapped charge from the stable traps as a 'negative dose', causing a reduction in the 'effective dose' to the sample in each cycle. This

alternative method comes with its own flaw as the dose is compared rather than to luminescence emission, so for the corrections to be calculated the equivalent dose must be known. To overcome this Duller suggests a procedure where at first the equivalent dose is estimated to be zero, with successive equivalent doses being estimated as above. Yet, despite all these methods and alternative approaches there are still inconsistencies in the results produced. Therefore, it can be concluded from Duller's work that while the SAAD approach does solve the problem of sensitivity changes, it itself is shown to produce inaccurate dating results for older samples.

3.6 The Adapted SARA Technique Used in this Study.

For dating applications in this study an adapted single aliquot additive regenerative (SARA) technique was used as follows. The sample was processed and deposited onto discs under dark light conditions allowing the natural signal to be measured. This signal was collected using a simple 2 second P-PSL measurement that allowed for later IR normalisation without any bleaching. All the measurements were carried out using the manual PSL system described above and a preheat of 135°C for 16 hours. The original SARA method involves several groups of samples irradiated additively with known doses prior to optical measurement. Each group of samples was calibrated using a regenerative read out procedure that could in theory suffer systematic errors due to uncorrected sensitivity changes. By conducting a regression between the apparent doses of each group and the known added dose such sensitivity changes can be corrected. In this SARA technique a long fading stabilising heating procedure was introduced between the additive cycle and the readout cycle. The two samples had subsets of both aluminium and stainless steel disc types that had doses of 40, 80, 120, 160, 200 and 240 Grays. Each of these measurements was carried out over 300 seconds and had a late light count of 10 seconds.

3.6.1 Sample Preparation for the adapted SARA Feldspar Dating.

The sample preparation techniques used in this study of feldspar dating were slightly different from the dating sample preparation techniques employed at the SUERC luminescence laboratories. The technique used here was the same as that utilised to date fine grained samples from sediments from Clyde, Washington State (USA) carried out in 2000 at the SUERC laboratories (Richardson, 2005).

All the measurements described in this chapter so far have been made on coarse-grained (125-250µm) material, but for dating the fine grain method, using a grain size fraction of 4 -11µm was chosen. This grain size range has two advantages over the coarse method. Firstly, the modal grain sizes of such material (30-50µm) was in the dust range, so using a sample from this fraction rather than the coarse sand would give a better geomorphic history of the sediment. Secondly the 30-50µm fraction is sufficiently fine that the whole of each grain will be susceptible to alpha

irradiation, which negates the need for calculations dealing with attenuation, or etching. This fine-grained material was however hard to separate into specific mineral fractions unlike the previous geological samples in this project. The choice of IRSL as the stimulation source will give some degree of insight into the source of the signal despite being a polymineral sample (Richardson, 2005).

To remove the required fraction from the cores that were collected during fieldwork in Russia and the Ukraine during 2004, sample preparation was carried out under red light conditions. The material separated for luminescence measurements was first treated with dilute (10%) hydrochloric acid to remove any carbonates and then with hydrogen peroxide to remove any organic matter. The remaining sediment was washed using deionised water. To obtain the required fraction this sediment was separated using sodium oxalate rather than SPT. The sample was suspended in 20cm column of 0.01N sodium oxalate for twenty minutes. To create the correct strength of solution 0.33grams were added to 500 millilitres of de-ionised water. The oxalate does not easily dissolve in the water so it required vigorous shaking of the bottle until the crystals had been observed to vanish. The solution was then added to a 1000 millilitre settling tube, complete with stopper, to the required depth. The previously prepared sediment was then dispensed into the solution and the stopper placed back into the top of the tube. The solution was then shaken so that the sediment grains did not stick together in any way. Ideally all the sediment would start from the top of the 20cm column, but when the solution was added as slurry it coagulated and dropped to the bottom of the column. The action of shaking meant that the grains were spread throughout the whole column and some started at different heights than the rest, meaning that some fine grains started near the bottom and settled out quickly. The effects of this can be seen later on in the experiment.

The density of this solution meant that after the 20 minutes the $>11\mu\text{m}$ grains had separated out. The oxalate and the remaining sediment were then poured off and left for another four hours allowing the $>4\mu\text{m}$ grains to settle out. The suspended material was then poured off and discarded. The sediment that had settled out after the four hours consisted of the $4 - 11\mu\text{s}$ fraction. To be sure the separation was complete this fraction was put through the 20cm column twice more until the column is relatively clear after the four hours.

Once the required fraction had been separated out, cleaned and dried, the next stage was to dispense it onto discs for measurement. Ideally at this point, for the dispensing method, the sample mass should have been greater than 2 grams. This amount of sample was then placed in a 200ml acetone solution (be aware that the amount of acetone will vary with the amount of sample obtained); the aim was to have $\sim 2\text{mg}$ per disc. There was sufficient solution to allow for a 2ml acetone/sediment solution to be dispensed onto 100 steel discs. The discs used measured 0.8mm and were constructed from stainless steel. Each one was pre-weighed before being placed into a

small test tube. The test tubes themselves measured 1mm in diameter and were chosen due to their almost exact match with the diameter of the disks. The 0.1mm clearance around the disc allowed for easier placement and extraction of the discs.

Using a specialist pipette, which can be set to decant the required amount of liquid at a time, enabled a quick and accurate dispensing method. Through a small experiment the amount of liquid dispensed with each push of the button was accurately measured and it was discovered that the first few dispensations were well below the required volume. Another issue was keeping the amount of actual sediment being drawn up into the pipette in solution. For this to remain constant the medium had to be kept in motion, keeping the grains in a state of agitation and equally distributed throughout the acetone. It was this last consideration that may account for the inconsistency in weight distribution found across the 100 discs, resulting in the occurrence of outliers in the dataset and a large standard deviation. Out of these 100, 64 were chosen to be used in the SARA fine grained dating procedure. They were chosen for equal coverage of the disc surface and also by sample weight. Discs with between 1-1.2 milligrams of sample were ideal, and those with significantly higher weights were not used for dating. These 'extra' discs were used for optical and scanning electron microscopy. These characterisations were employed to ensure that the dispensing technique developed had allowed for the settlement of grains in a single layer and also to quantify and classify the nature and types of minerals present. Work by Lang and Mauz (2004) claimed that aluminium discs work better than stainless steel when fine grained discs are dispensed in this manner. They claim that the grains adhere better to the aluminium. This hypothesis was tested and the results are presented in Chapter 6. For this dating run both disc types were prepared.

4

Mineralogy of the Sample Set.

4.1 Introduction.

Now that the theory of luminescence and anomalous fading has been discussed and the techniques and equipment described, this chapter outlines the mineralogy of the sample set. The samples were chosen to include feldspars whose geological background suggests that they are likely to fade but also feldspars from common crustal rocks that supply most of the feldspars that occur in archaeological material and sediments of interest in luminescence dating.

The following descriptions are divided by the geological background of the feldspar's source rock and each section contains a brief overview of the geological history of the sampling location before outlining the results of the mineralogical characterisation work that was undertaken. Note that the samples are not necessarily discussed in order of their geological context listed in Table 4.1 for brevity; for example, the fresh, naturally weathered and HF acid etched Shap feldspar samples are discussed together in the same section. The naturally weathered samples are extracted from surface soils and the HF treatment is carried out on sub-samples of the fresh material. HF etching has already been shown to attack the same regions of the mineral surfaces (Lee *et al.*, 1995) and the possibility of it being a good substitution for weathering processes will be investigated.

4.2 Feldspars from Slowly Cooled Plutonic Igneous Rocks.

The majority of this subgroup comprised feldspars extracted from granitic rocks. This is a very common rock type and those samples chosen have been previously well characterised. If previous work on fading is to be believed these rocks, which crystallized slowly and from relatively low temperatures should contain feldspars that have a low susceptibility to fading. This is because their crystal lattice is more ordered than in feldspars that crystallize rapidly from molten rock (i.e., volcanic) thus preventing the low energy movement of electrons, or at least decreasing the probability that signal loss by this means will occur. If this principle is broadly applicable then whole geographical areas could be opened up for reliable feldspar luminescence dating. Through

studying a wide variety of granites and associated slow cooling rock types we have tested this hypothesis and the results are presented in the subsequent chapters.

Table 4.1 The sample set used for remnant luminescence work. Geological ages are taken from the literature that will be discussed in the remainder of this Chapter.

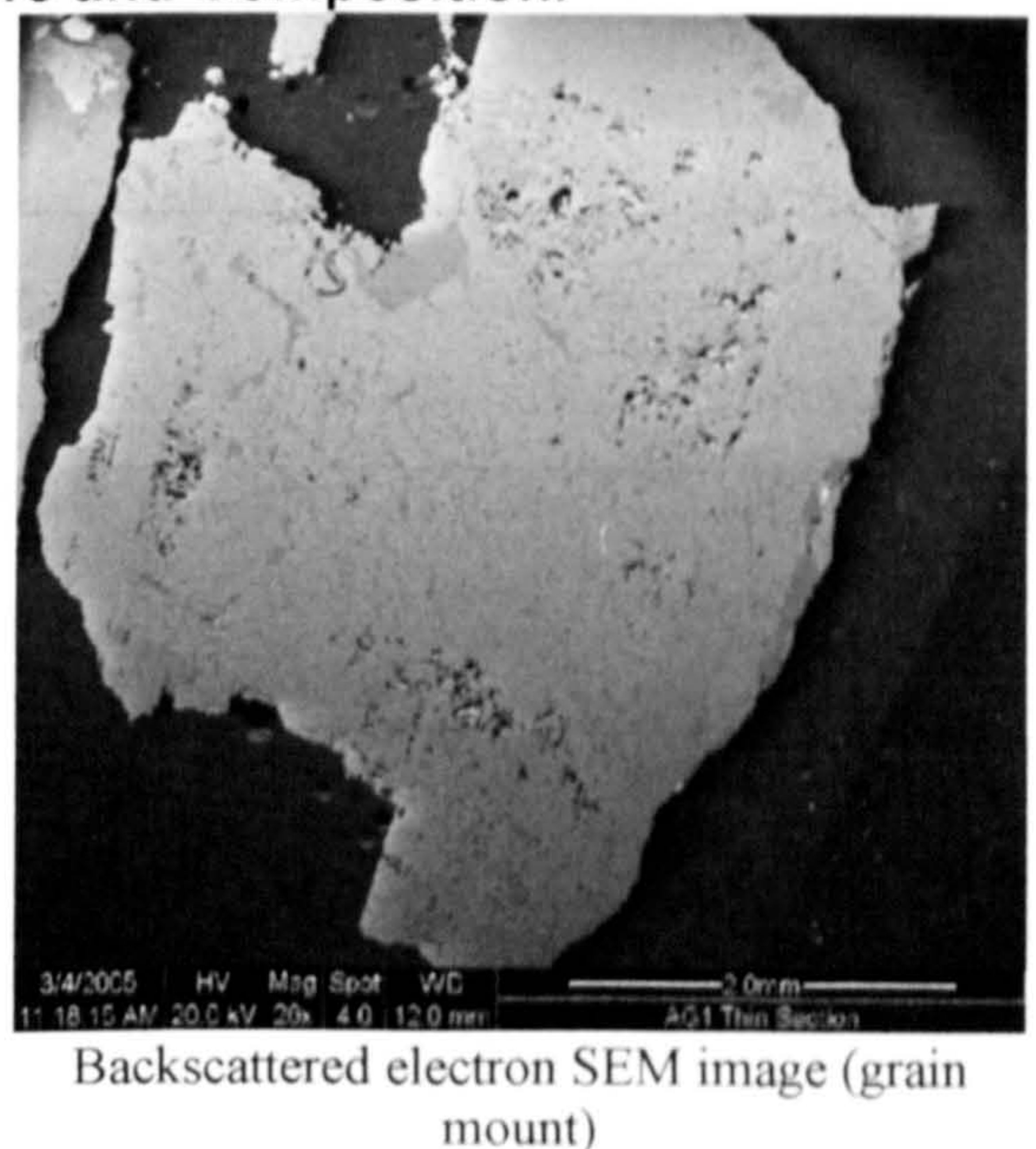
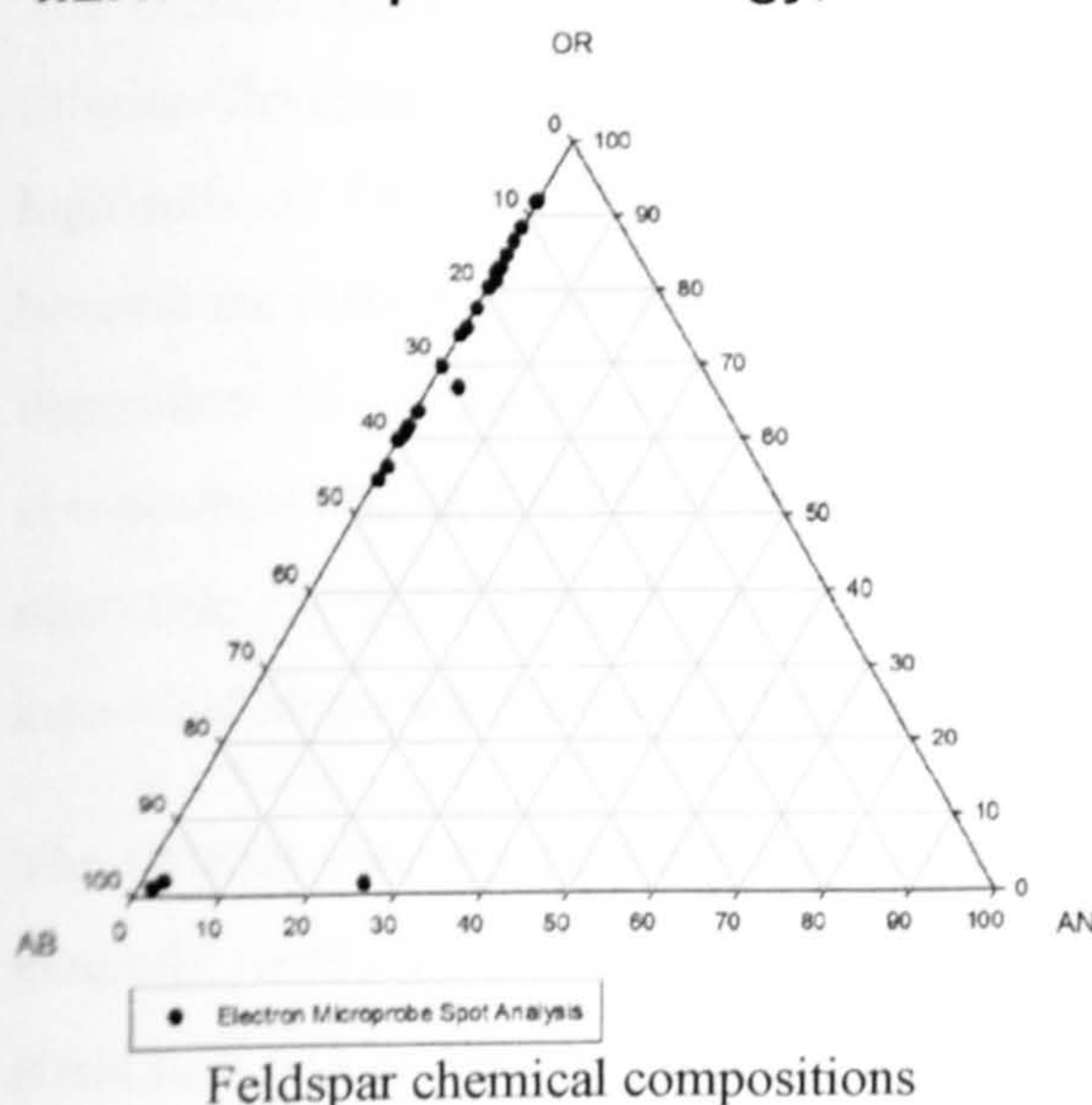
Rock and sample name		Geological age
Plutonic igneous & associated rocks		
	Arran Granite	58.5 Ma
	Ballater Granite	425-400 Ma
	Cairngorm Granite	Silurian Devonian Boundary
	Helmsdale Granite	420-400 Ma
	Helmsdale arkose	Lower Devonian
	Peterhead Granite	432 ± 7 Ma
	Ross of Mull Granite	414 Ma
	Ross of Mull Granite	414 Ma
	Ross of Mull Syenite	414 Ma
	Shap Granite	394 Ma
	Strontian Granodiorite	435 ± 10
Silicic minor igneous intrusions		
	Bute pitchstone porphyry (H2)	Palaeogene
	Bute pitchstone porphyry (H3)	Palaeogene
	Canisp quartz-syenite (H4)	437 ± 4.8 Ma
Igneous calcic plagioclase		
	Connemara gabbro pegmatite	475 Ma
	Rum anorthosite	~60 Ma
	Rum troctolite pegmatite	~60 Ma
Extrusive igneous rocks		
	Patmos sanidine	6.5-4 Ma
	Etna basalt	Recent
Metamorphic rocks		
	Glen Tarbert migmatite	435 ± 10 Ma
	Lewisian gneiss	2850-2700
	Torridon hornblende gneiss	2850-2700
Naturally weathered igneous		
	Ballater Granite	n/a
	Cairngorm Granite	n/a
	Shap Granite	n/a
HIF acid etched igneous & associated rocks		
	Shap (1 min, 3 mins, 15 mins)	n/a
	Helmsdale arkose (1 min, 3 mins, 15 mins)	n/a
	Helmsdale Granite (1 min, 3 mins, 15 mins)	n/a
Laboratory standard		
	F1	Unknown

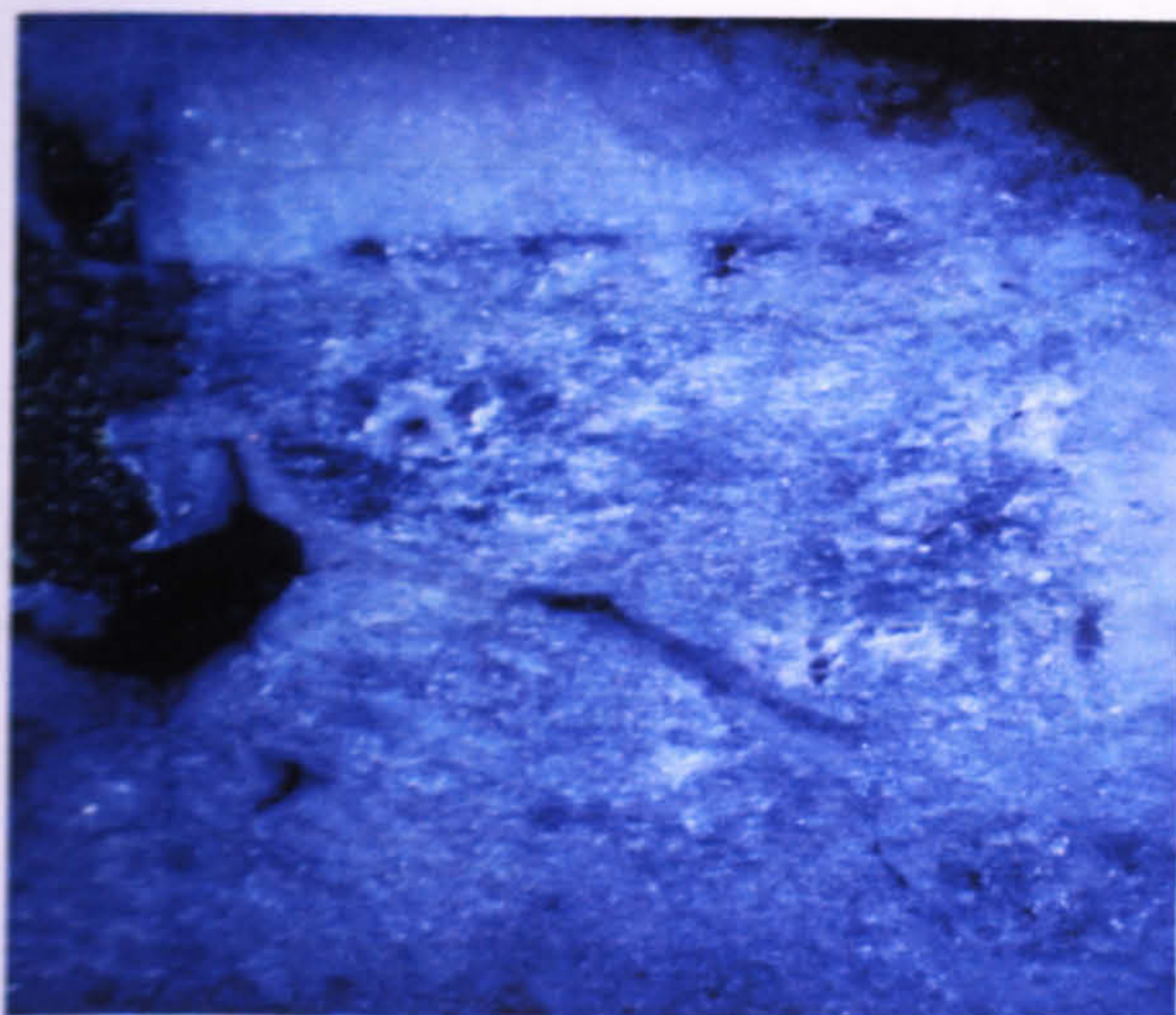
4.2.1 The Arran Granite (AG).

Using ^{40}Ar - ^{39}Ar , the northern Arran granite complex, from which this sample was taken, has been dated at $\sim 58.5\text{Ma}$ (Trewin, 2002). The Island of Arran contains the most southerly major intrusive complexes of the Scottish sector of the Tertiary Igneous Province. They were emplaced into Dalradian Supergroup phyllites overlain by various Palaeozoic and Mesozoic sedimentary rocks (Trewin, 2002). There are two main discrete centres of activity; the northern granite centre and the central ring complex. The northern centre has an outcrop diameter of 10-12km and comprises a coarse grained outer granite and a fine grained inner granite. Both intrusions are non-porphyritic and biotite bearing. It was the outer granite that was emplaced into the phyllites of the Dalradian Supergroup, except along the NE and eastern margins where it is in contact with Ordovician and lower Old Red Sandstone strata. The thermal aureole of the granite stretches several hundred metres. Xenolithic marginal facies occurs locally as does veining of the country rocks by apophyses of the granite. Emplacement of the outer granite involved the diapiric intrusion of magma into the downward dipping limb of a major synform in the Dalradian country rocks, refolding and upwardly displacing it to produce a marginal synform. The younger, finer grained inner granite outcrops on the western part of the Northern Granite Centre. It has sharp well defined and generally steeply dipping contacts with the outer granite. Suites of basaltic dykes trending either NW-SE or N-S, and numerous thin aplite sheets and veins cut both granites. A late stage 'crush-zone' affects both intrusions, trending approximately north.

The sample of granite used was collected by Martin Lee from the western edge of the outer granite where it is exposed in Glen Catacol (Grid Ref: NR924 483). It is important to note that the granite exposed at this locality had been weathered.

4.2.1.1 Feldspar Mineralogy, Microtexture and Composition.





Optical CL image (grain mount)

SPT fraction (g/cm ³)	Mineralogy
<2.62	---
2.52-2.58	A ₁₀₀ P ₀ Q ₀
2.58-2.62	---
2.62-2.74	A ₂₅ P ₂₅ Q ₅₀
>2.74	---
Not SPT separated	---

Mineralogy of the density fractions

Figure 4.1. Mineralogy, microtexture and composition of the Arran granite feldspars (AG1).

Table 4.2. Arran granite feldspar chemical compositions (Mol%).

Sample	Alkali feldspar			Free plagioclase feldspar		
	Ab	An	Or	Ab	An	Or
Arran Granite (AG1)	17	0	83	96	2	2

The alkali feldspars are blue luminescent microcline microperthites with fine veins of albite. The occasional inclusions of free plagioclase are albite with no distinctive CL emission. The SPT separation has been effective and the 2.52-2.58g/cm³ fraction is pure alkali feldspar.

4.2.2 The Ballater Granite (B).

The Ballater granite is one of the Scottish 'Newer Granites' whose ages (425-400Ma) straddle the Silurian-Devonian boundary and were intruded extensively into both the Northern and Grampian highlands of Scotland (Trewin *et al.*, 1987). These granites formed above a subduction zone beneath the margin of Laurentia. Rapid uplift and erosion followed and they were unroofed prior to deposition of the Devonian Lower Old Red Sandstone. The Ballater granite is adamellitic in composition and is inferred to have been volatile-rich as it contains numerous quartz veins andmiarolitic cavities. Some of these cavities contain beryl and fluorite is also common, both as an interstitial phase and along joint planes (Trewin *et al.*, 1987).

The Granite outcrops on both sides of the River Dee in Aberdeenshire. Unweathered (B1) and naturally weathered (B2) samples of the granite were collected at the Pass at Ballater on the B972 (Grid Ref: NO 36759 97018 elevation 277m), which is a steep sided valley that runs to the north of

the town of Ballater. Various facies of the granite are exposed in the scree and debris at the base of the crags on the northern side of the Pass.

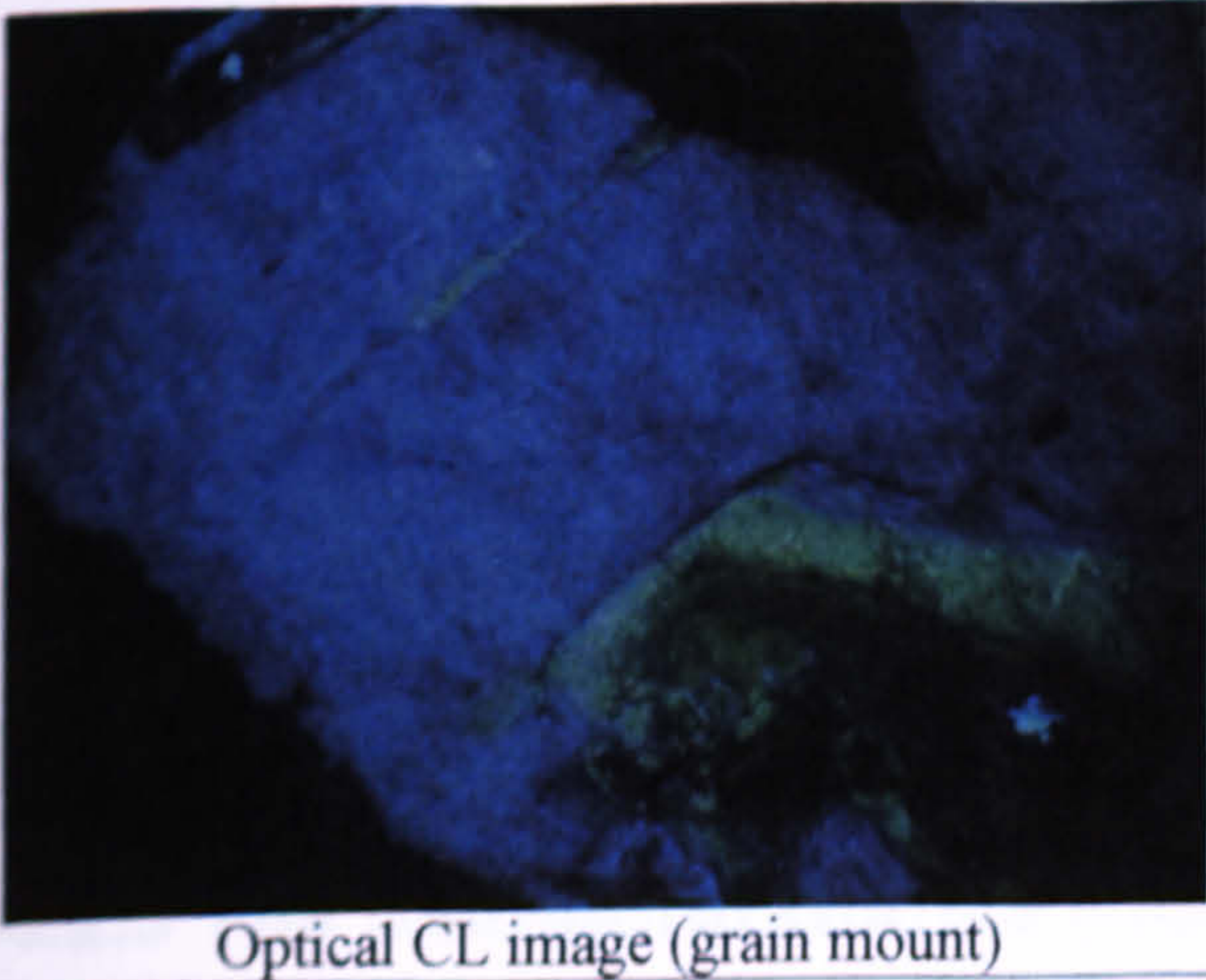
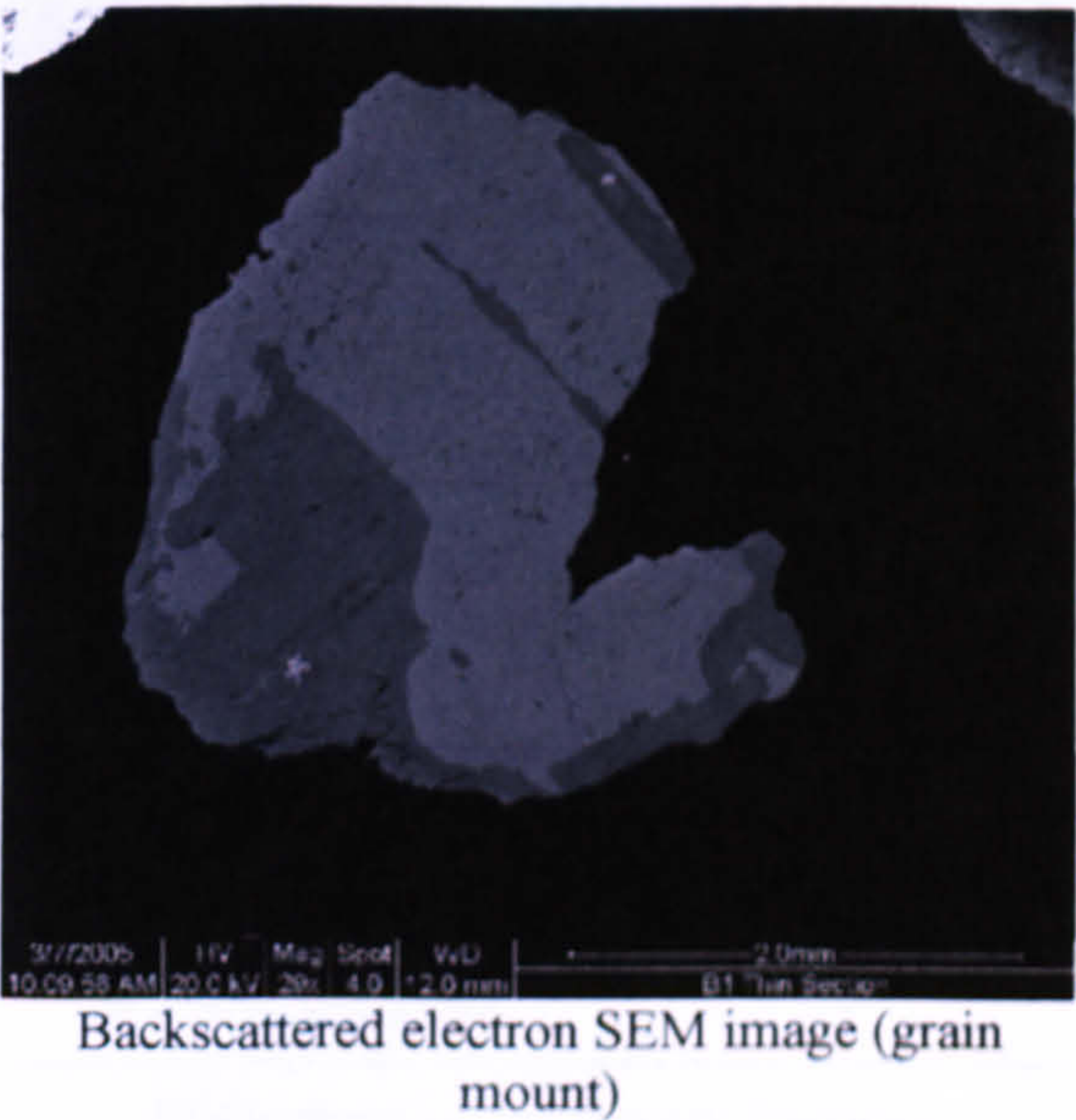
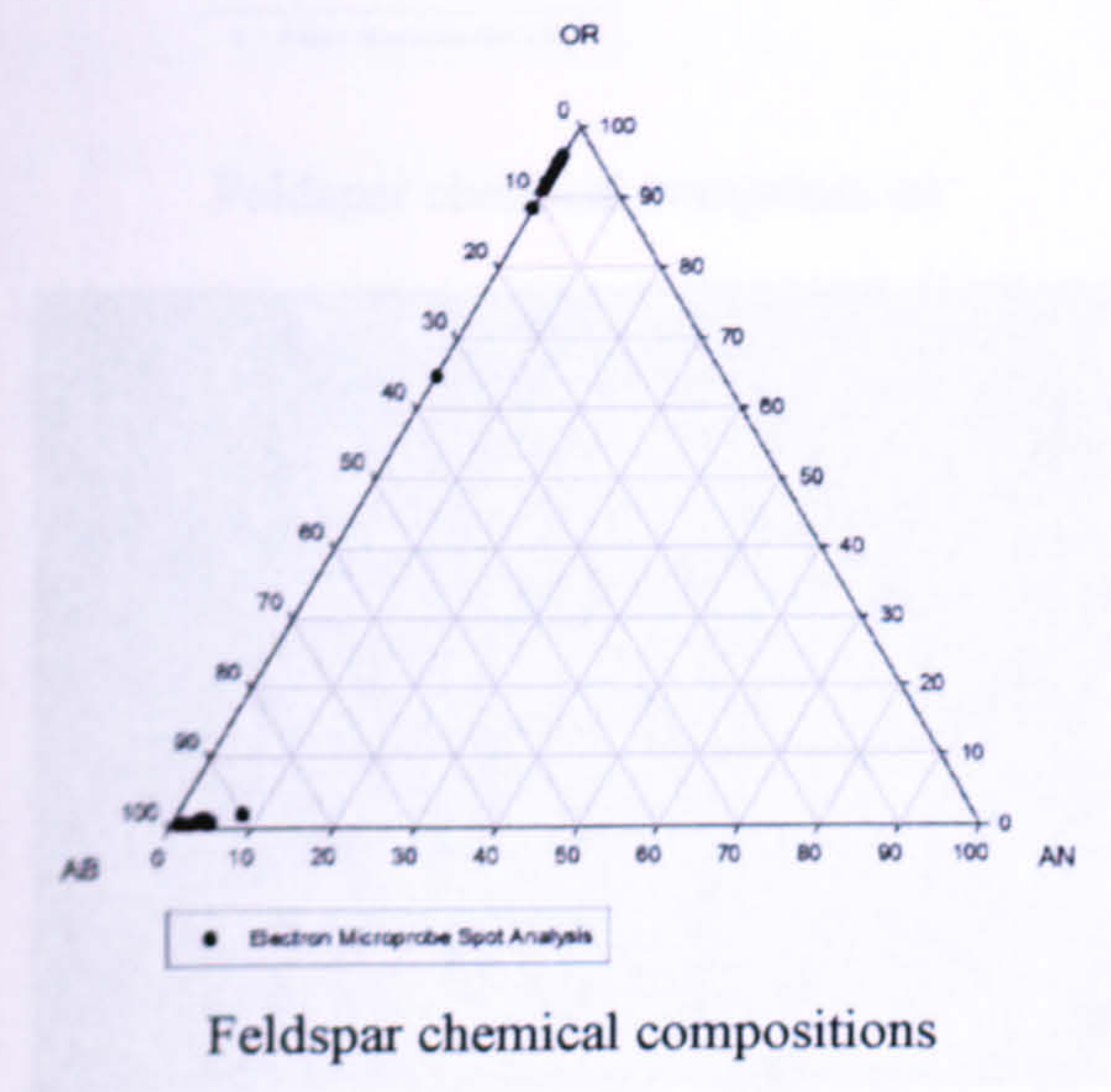
4.2.2.1 Feldspar Mineralogy, Microtexture and Composition.

4.2.2.2 Weathered Ballater Granite (B2)

Table 4.3. Chemical compositions of Ballater granite feldspars (Mol%).

Sample	Alkali Feldspar			Free plagioclase feldspar		
	Ab	An	Or	Ab	An	Or
Fresh Ballater Granite (B1)	6	0	94	96	3	1
Weathered Ballater Granite (B2)	7	0	93	96	3	1

4.2.2.2 Fresh Ballater Granite (B1).



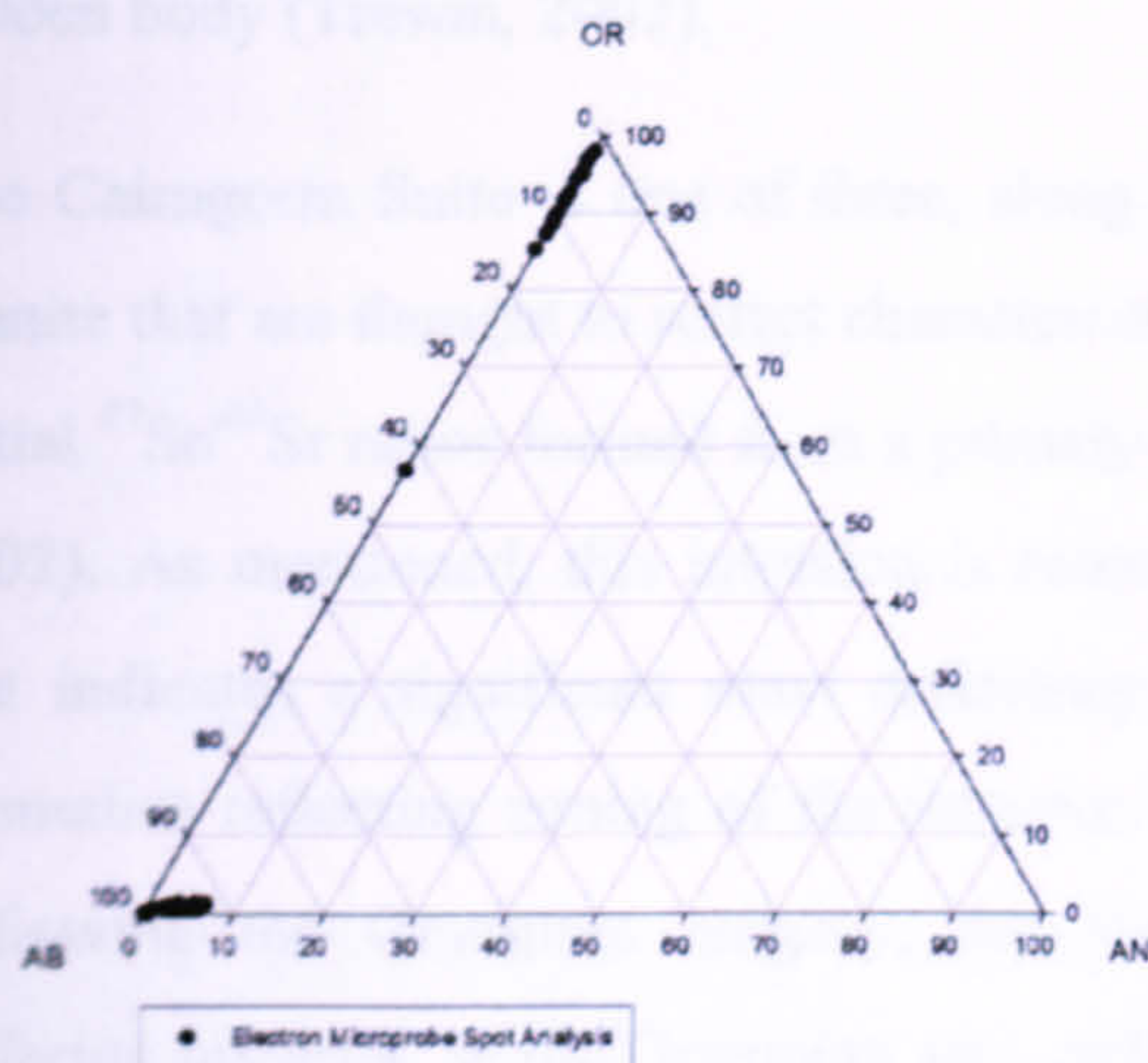
SPT fraction (g/cm ³)	Mineralogy
<2.62	---
2.52-2.58	A ₂₀ P ₆₀ Q ₂₀
2.58-2.62	---
2.62-2.74	A ₁₀ P ₈₀ Q ₁₀
>2.74	---
Not SPT separated	---

Mineralogy of the density fractions

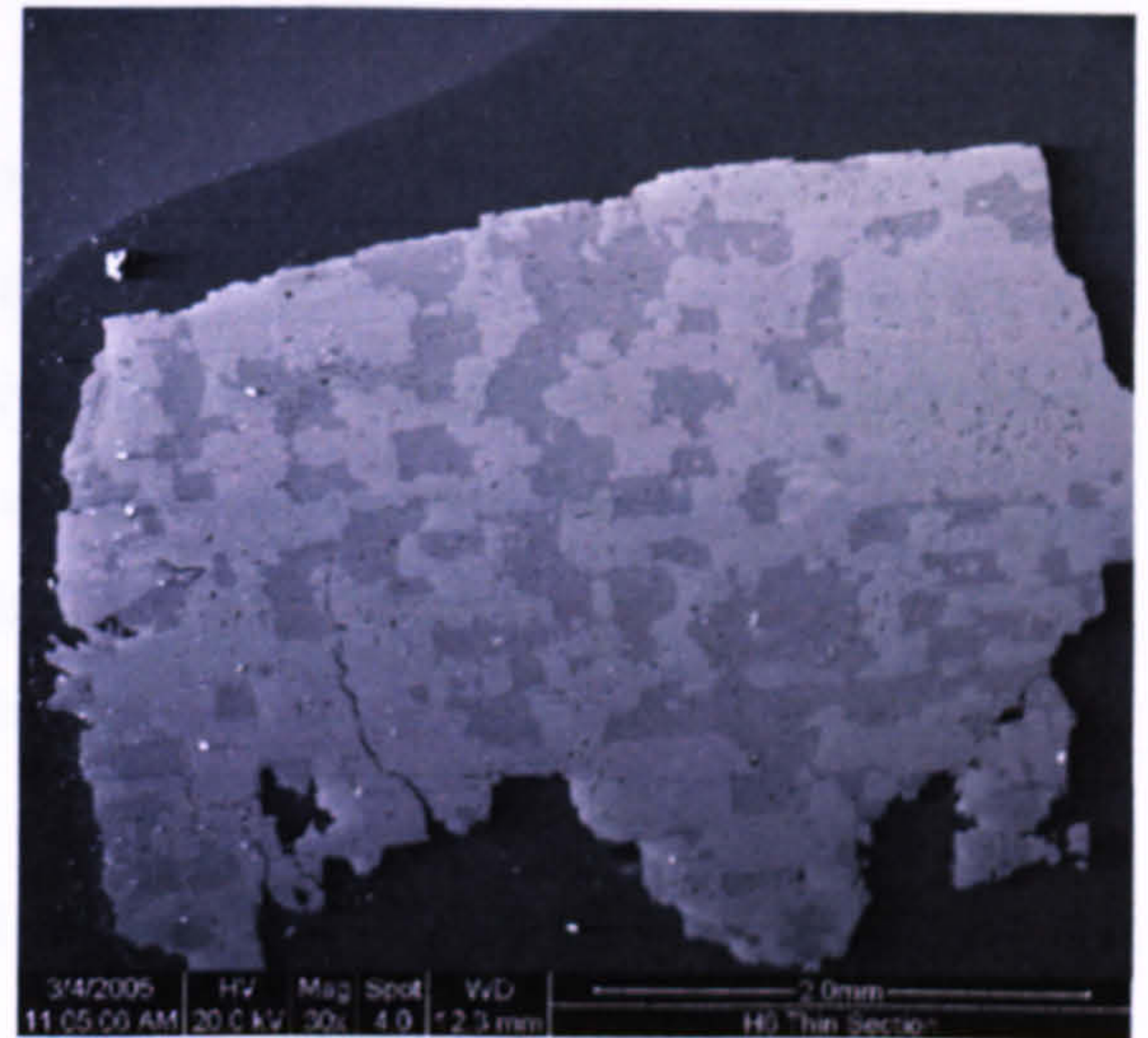
Figure 4.2. Mineralogy, microtexture and composition of fresh Ballater granite feldspars (B1).

The alkali feldspar is a blue luminescent very fine orthoclase microperthite and is intergrown with large inclusions of free plagioclase (albite) with green CL. Importantly, the density separation has not worked as expected and plagioclase (albite) is the most abundant feldspar mineral in both SPT fractions.

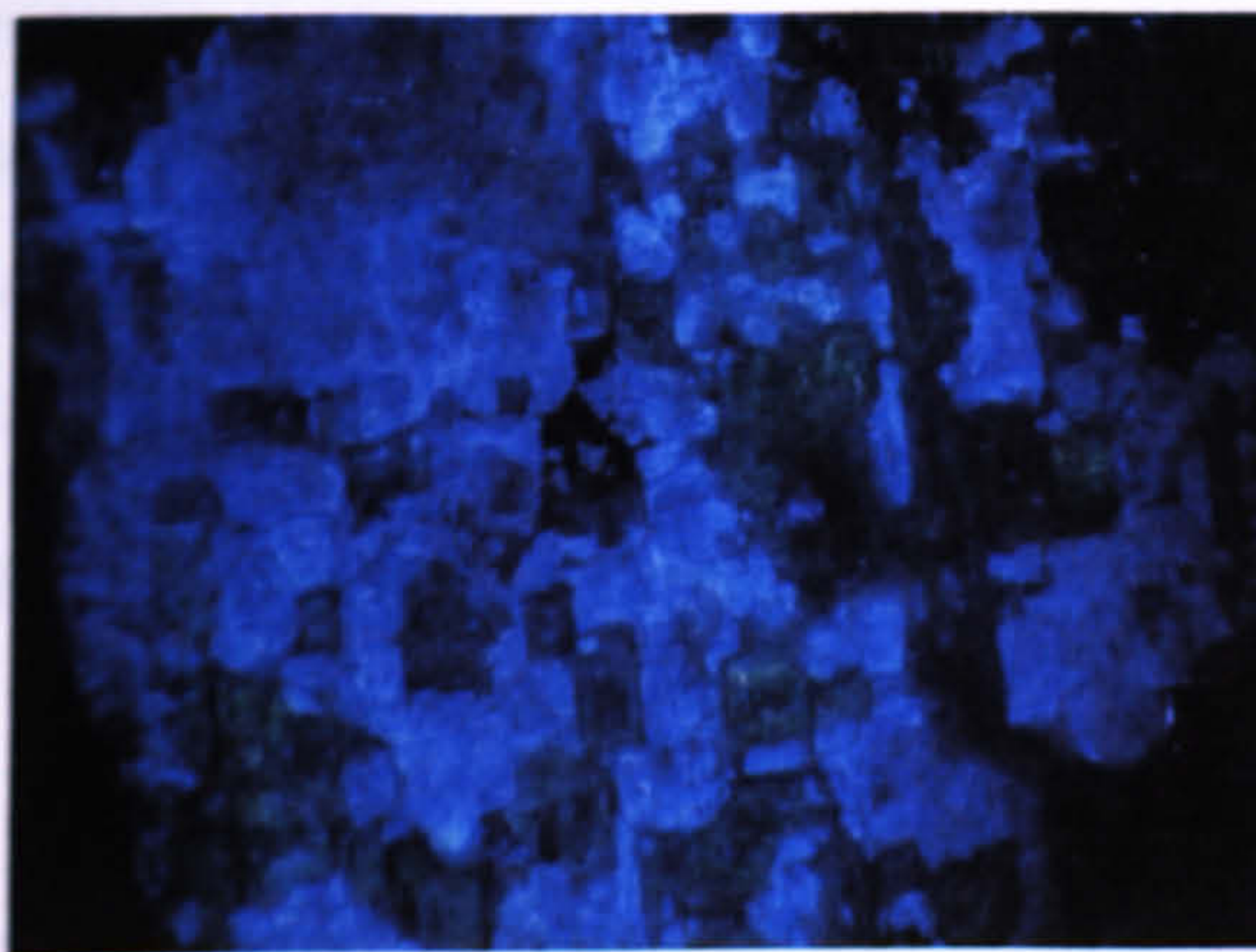
4.2.2.3 Weathered Ballater Granite (B2).



Feldspar chemical compositions



Backscattered electron SEM image (grain mount)



Optical CL image (grain mount)

SPT fraction (g/cm ³)	Mineralogy
<2.62	---
2.52-2.58	A ₉₀ P ₁₀ Q ₀
2.58-2.62	---
2.62-2.74	A ₁₀ P ₈₀ Q ₁₀
>2.74	---
Not SPT separated	---

Mineralogy of the density fractions

Figure 4.3. Mineralogy, microtexture and composition of weathered Ballater granite feldspars (B2).

The weathered Ballater Granite feldspars are mineralogically and chemically comparable to those from the fresh granite. The optical CL image illustrates the difference in CL colour between the intergrown alkali feldspar (blue) and free plagioclase (green). Importantly, this density separation was much more effective than for the fresh granite sample and the 2.52-2.58g/cm³ fraction is relatively pure alkali feldspar.

4.2.3 The Cairngorm Granite (CG).

This granite is part of the Cairngorm suite of Newer Granites which consist of granite plutons that occur mainly in the northern Grampian Highlands (Trewin, 2002). Most of these plutons are comprised of coarse-grained biotite-monzogranite, although there are also microgranites and

megacrystic K-Feldspar bearing types that occur as textural variations on a local level. The Cairngorm Granite is one of many in this suite and is associated with significant magnetic anomalies. The suite has a gross E-W alignment that reflects a deep crustal control. There is also an E-W trending gravity low between two other granitic bodies which suggests the presence of a deep, large batholith, with the granites outcropping at the surface are being cupolas originating from this hidden body (Trewin, 2002).

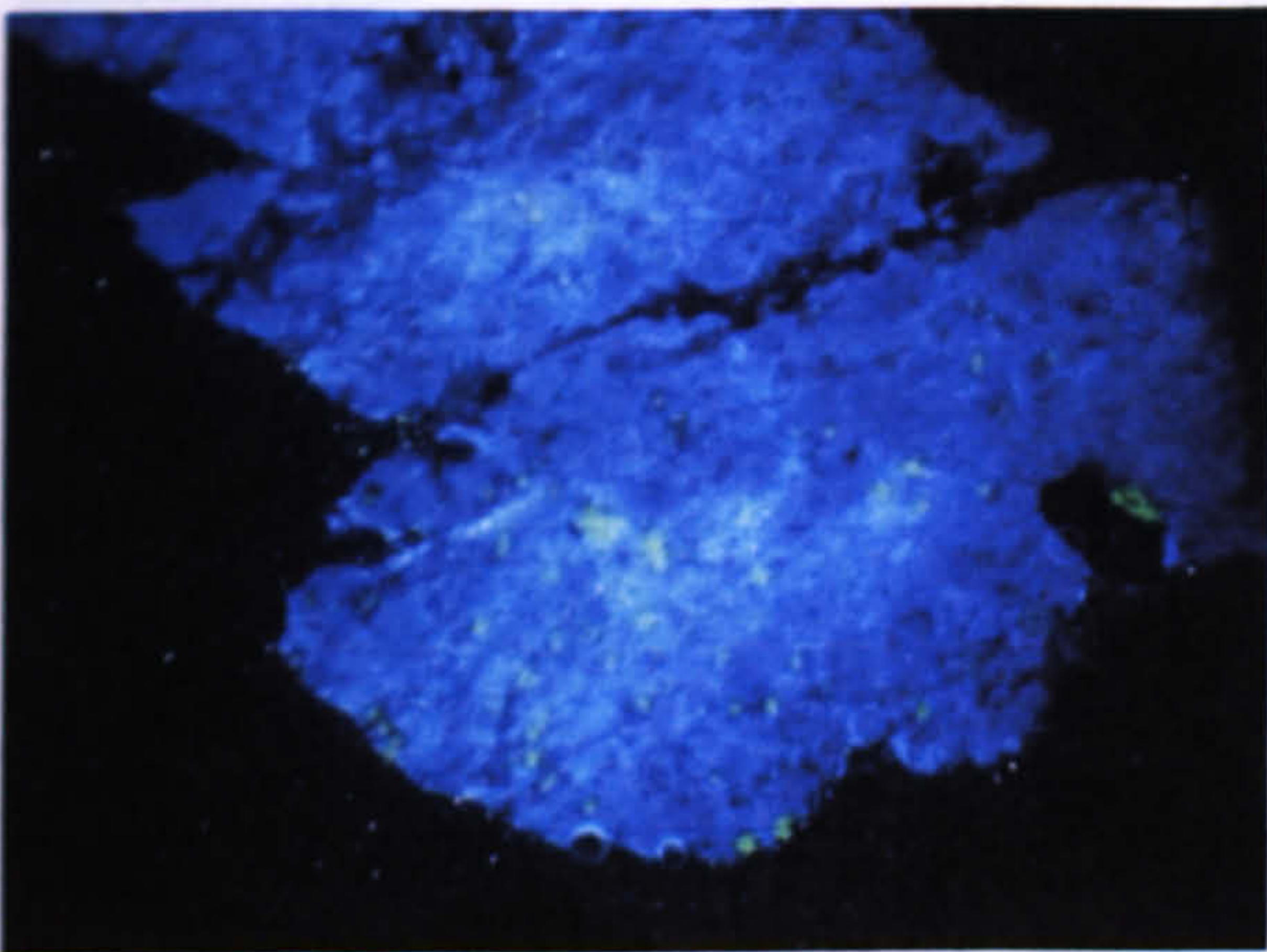
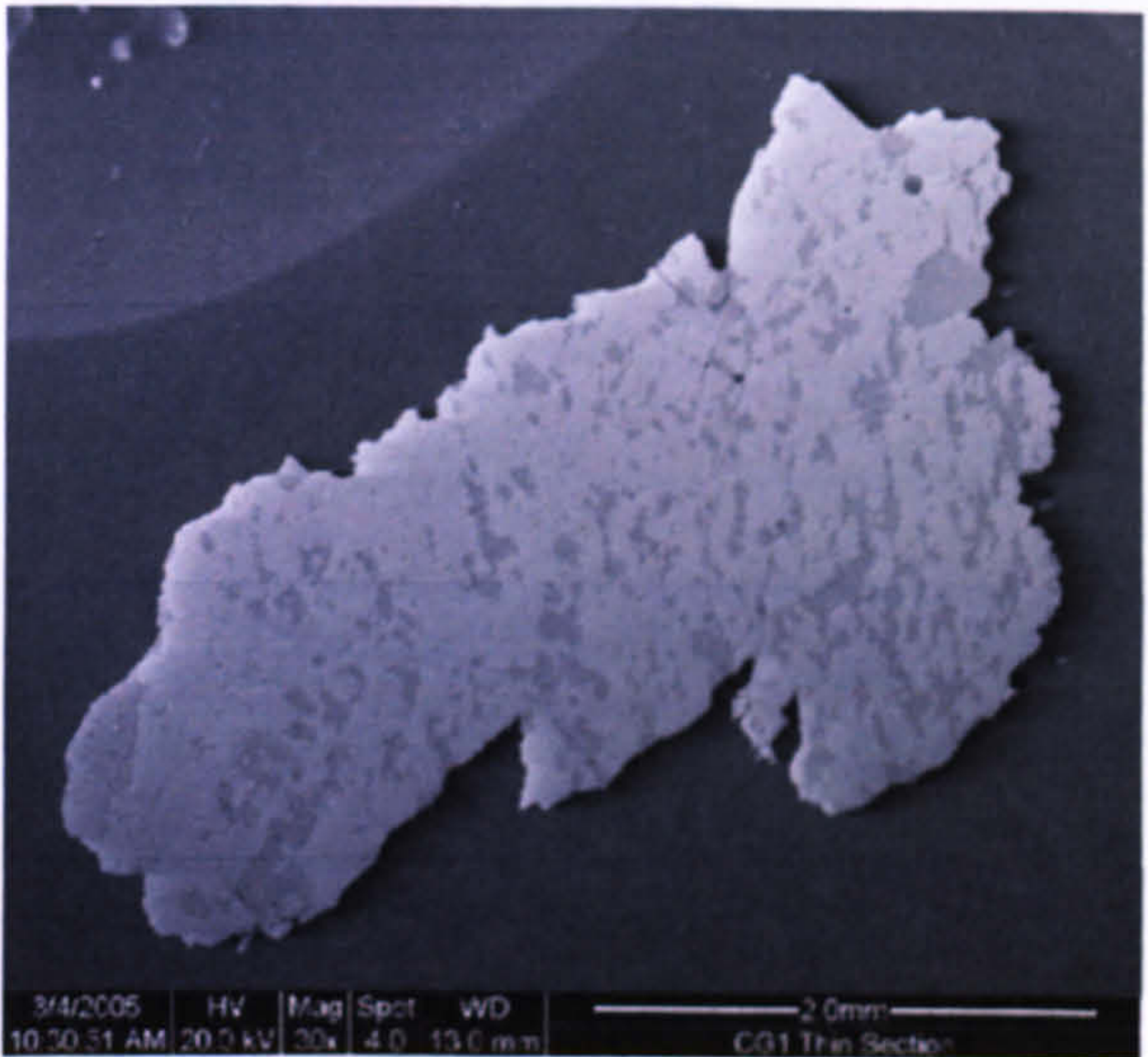
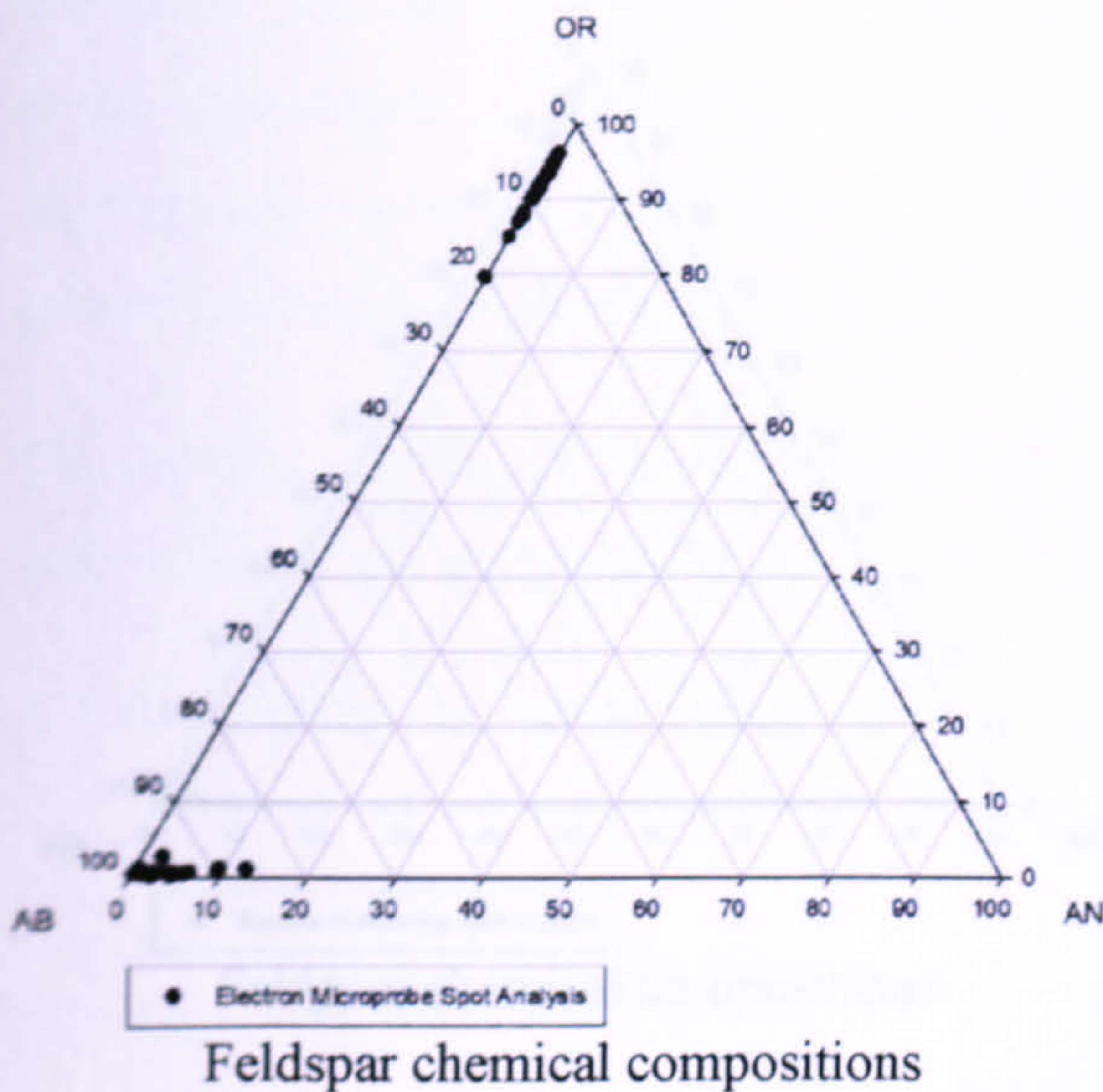
The Cairngorm Suite is one of three, along with the Argyll and South Scotland, distinct types of granite that are thought to reflect characteristics of the deeper crust. It is an I-Type granite with low initial $^{87}\text{Sr}/^{86}\text{Sr}$ ratios formed from a primary mantle derived melt with crustal contribution (Trewin, 2002). As mentioned, this intrusion is associated with a strong negative Bouger gravity anomaly that indicates a significant mass deficiency within the upper 10km of crust. Annular magnetic anomalies reflecting zoning of the intrusion into distinct phases has been implied for this pluton. Following the Grampian orogeny, the Northern highlands and the Grampian terraines have differing histories. In the Grampian area, uplift and cooling followed the orogeny and the intrusion of the ‘older granites’.

The samples used in this study were collected from an outcrop of the granite on Cairngorm (Grid Ref: NH 98780 07165 elevation 561m). There are two samples, a fresh granite (CG1) and naturally weathered granite (CG2), which consisted of soil with sand to pebble sized pieces of granite and individual feldspar crystals.

4.2.3.1 Feldspar Mineralogy, Microtexture and Composition.

Table 4.4. Chemical compositions of Cairngorm granite feldspars (Mol%).						
Sample	Alkali Feldspar			Free plagioclase feldspar		
	Ab	An	Or	Ab	An	Or
Fresh Cairngorm Granite (CG1)	7	0	93	95	4	1
Weathered Cairngorm Granite (CG2)	7	0	93	97	2	1

4.2.3.1.1 Fresh Cairngorm Granite (CG1).



SPT fraction (g/cm ³)	Mineralogy
<2.62	---
2.52-2.58	A ₉₀ P ₁₀ Q ₀
2.58-2.62	---
2.62-2.74	A ₆₀ P ₃₈ Q ₂
>2.74	---
Not SPT separated	---

Mineralogy of the density fractions

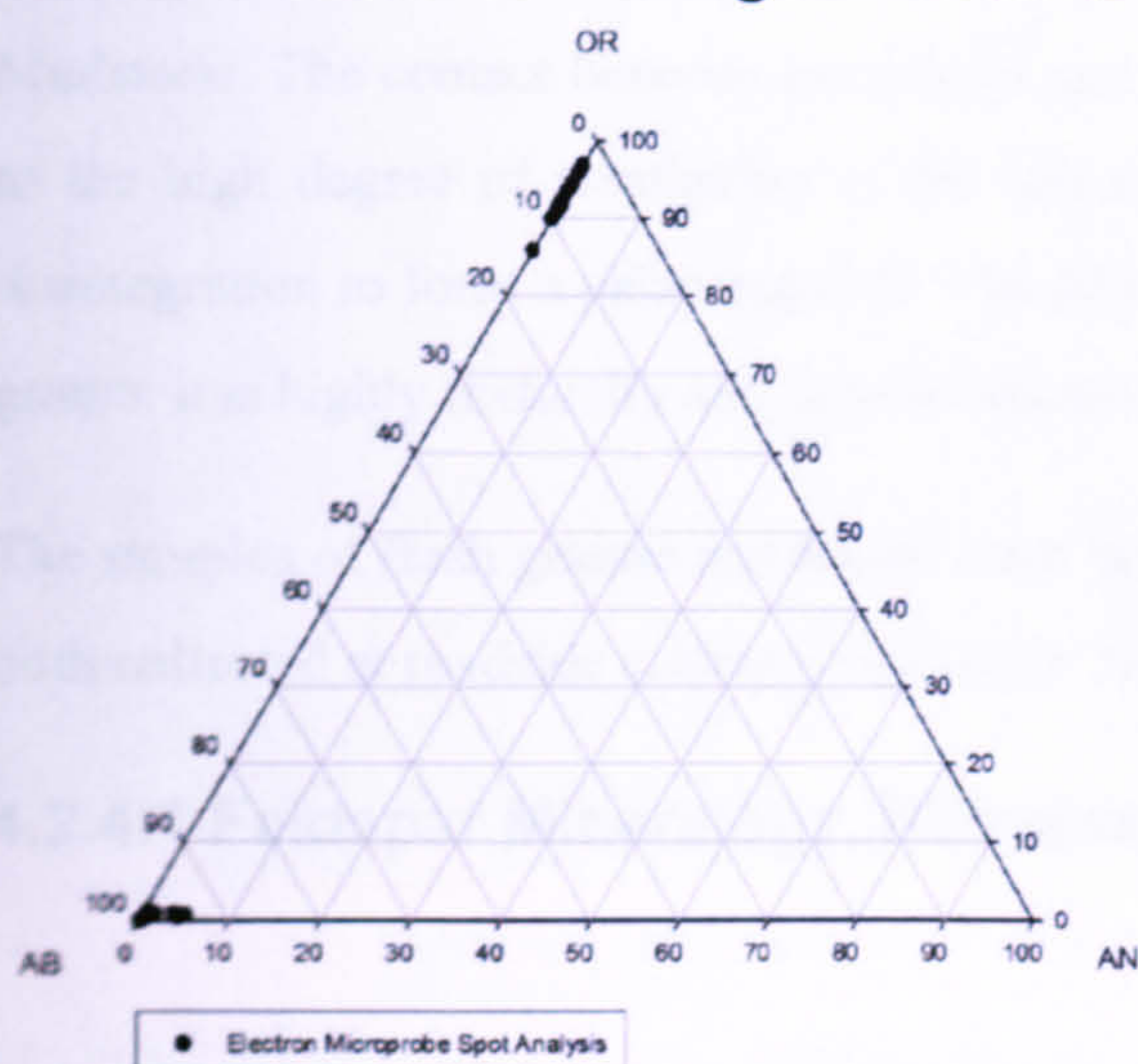
Figure 4.4. Mineralogy, microtexture and composition of fresh Cairngorm granite feldspars (CG1).

The alkali feldspar is a microcline patch microperthite that is predominantly blue in CL. The coarser patches and veins of plagioclase luminesce green or red, indicating that two generations of albite are present. The samples are a mixture of alkali and plagioclase feldspar with very little contamination by quartz.

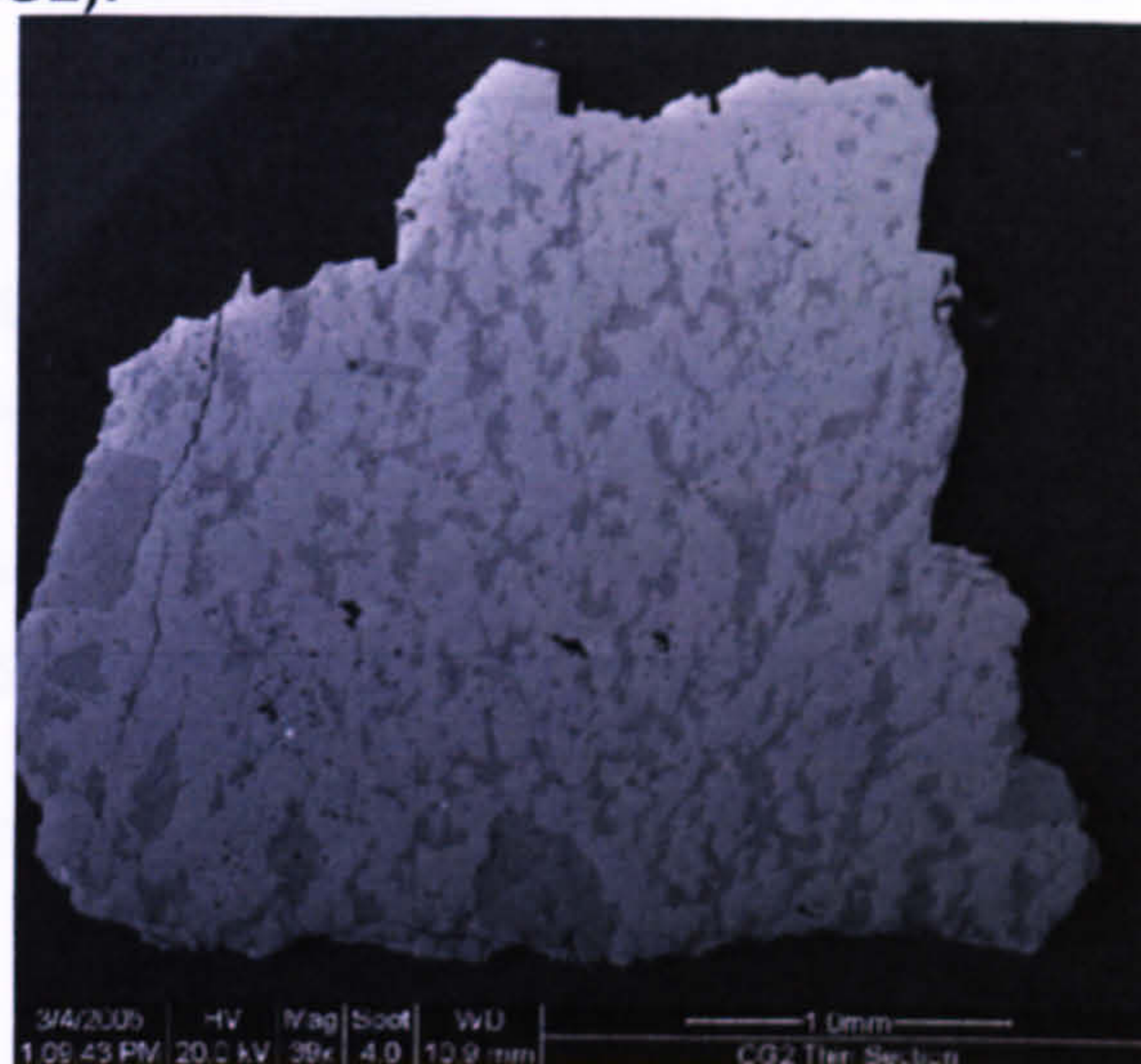
4.2.4 The Cairngorm Batholith

The Cairngorm batholith is a large, irregularly shaped mass of granitic rock that covers an area of about 400 km². It is composed of a mixture of alkali and plagioclase feldspar, quartz, and mica. The batholith is characterized by a complex microtexture, including a network of veins and patches of different mineral compositions. The batholith is surrounded by a zone of altered rock, which is composed of a mixture of alkali and plagioclase feldspar, quartz, and mica. The batholith is a good example of a large-scale igneous intrusion.

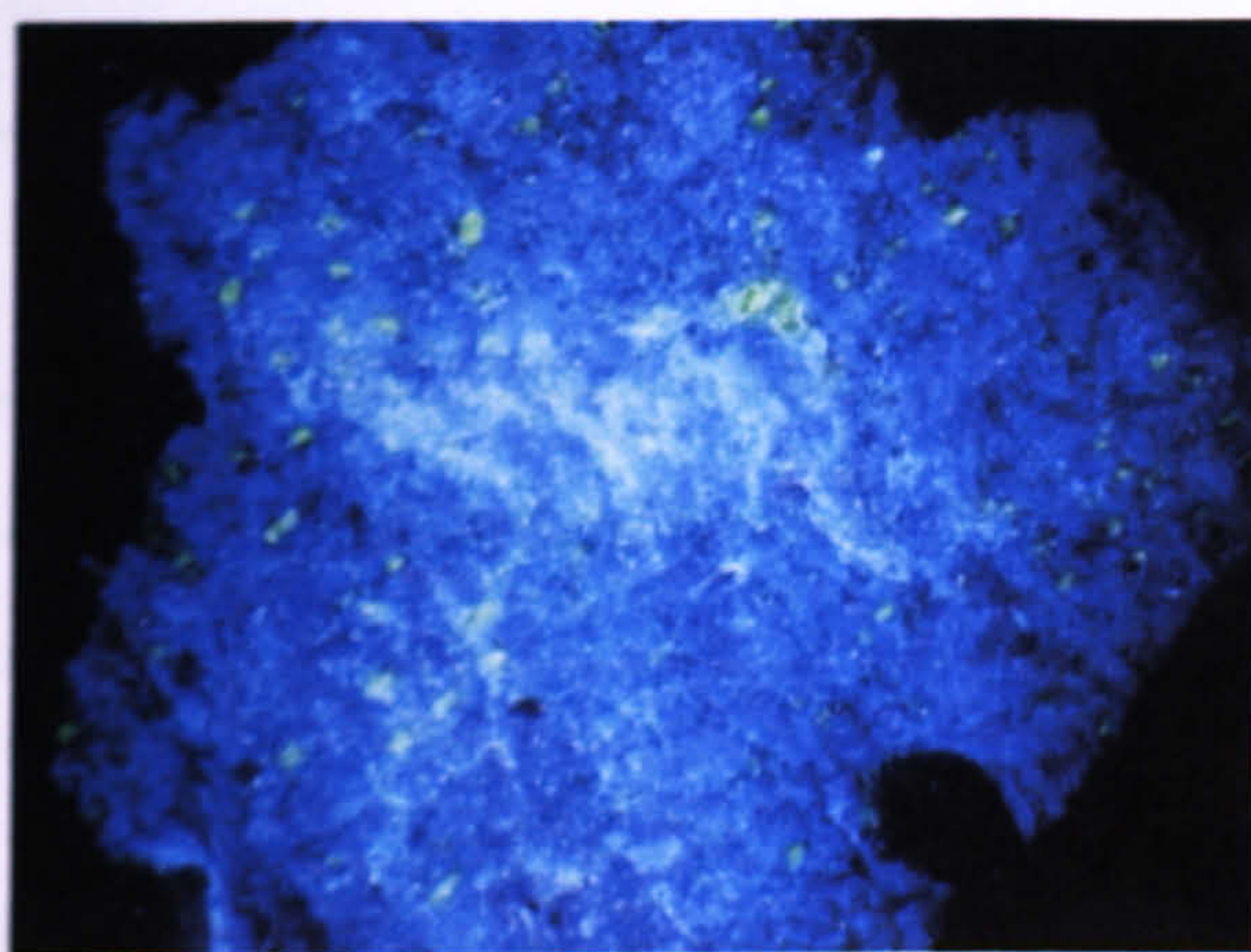
4.2.3.2 Weathered Cairngorm Granite (CG2).



Feldspar chemical compositions



Backscattered electron SEM image (grain mount)



Optical CL image (grain mount)

SPT fraction (g/cm ³)	Mineralogy
<2.62	---
2.52-2.58	---
2.58-2.62	A ₅₀ P ₄₅ Q ₅
2.62-2.74	A ₅ P ₅ Q ₉₀
>2.74	---
Not SPT separated	---

Mineralogy of the density fractions

Figure 4.5. Mineralogy, microtexture and composition of weathered Cairngorm granite feldspars (CG2).

In common with alkali feldspar from the fresh granite, the weathering feldspar shows a blue luminescing patch microperthite containing green luminescing albite. The separation of alkali and plagioclase feldspar using SPT was relatively ineffective in this sample.

4.2.4 The Helmsdale Samples.

The Caledonian granite at Helmsdale is another of the 'Newer Granites' whose age is between 420 and 400 Ma, depending on the chronometer used (Torsvik *et al.*, 1983). It has intruded into Moinian meta-sedimentary rocks. The granite outcrops over a 100km² area (Tyrell *et al.*, 2006) and consists of an outer zone of pink, coarse grained, porphyritic adamellite surrounding an inner zone of pink, finer grained non-porphyritic adamellite. The granite was uplifted, exposed and partially eroded in the Devonian, giving the opportunity of studying feldspars that crystallized at the same time but have spent most of their subsequent geological history in different lithologies. A Lower Devonian sedimentary rock, the Ousdale Arkose (referred to as Helmsdale arkose (Ark) within this

study), overlies the granite on its eastern margin and passes laterally and vertically into the Ousdale Mudstone. The contact between the granite and the sedimentary rocks is subtle and gradational due to the high degree of weathering of the surface of the igneous rock resulting in *in situ* granular disintegration to form a palaeoregolith. The arkose grades up from this and in the layers close to the granite it is highly texturally and mineralogically immature.

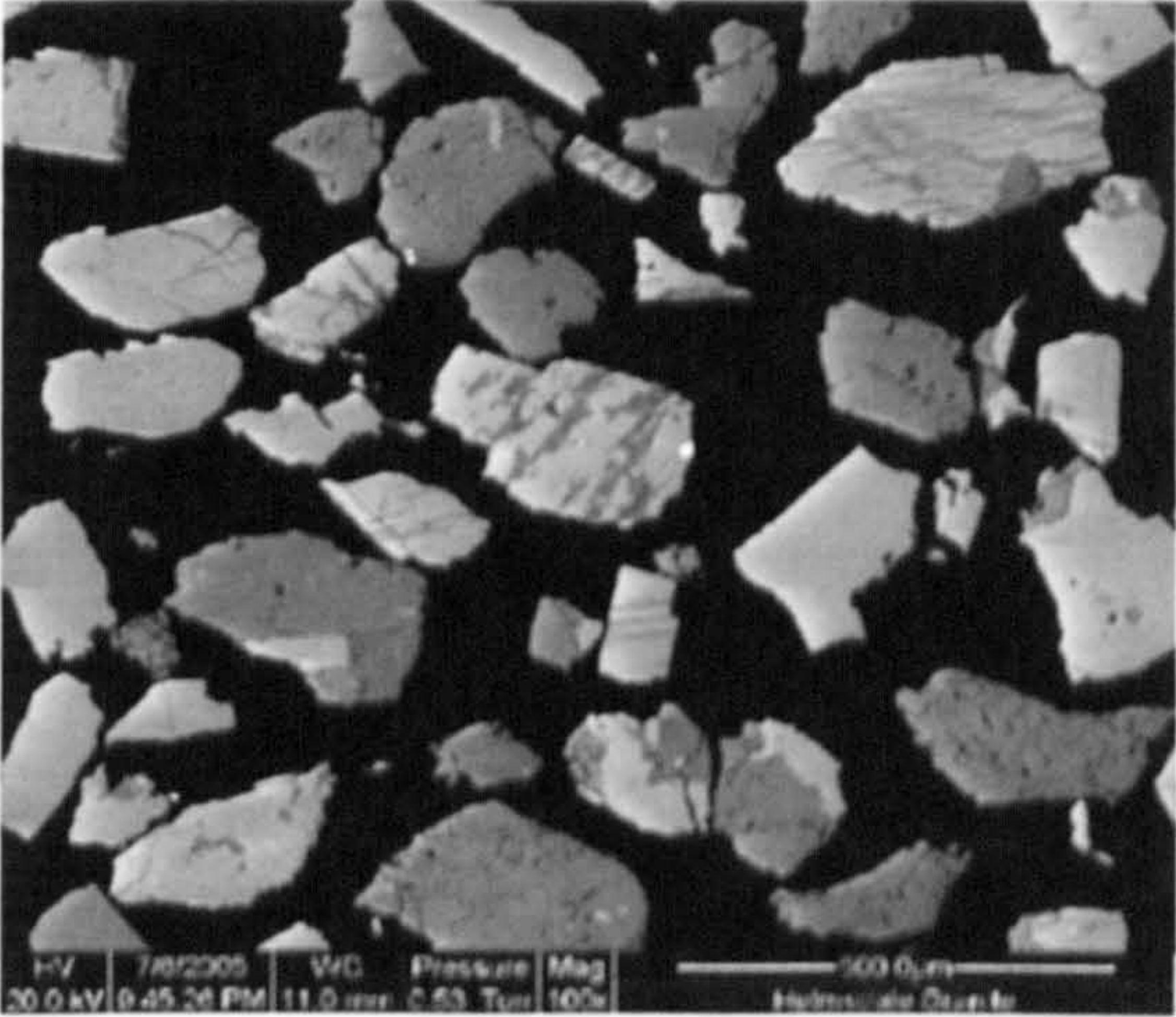
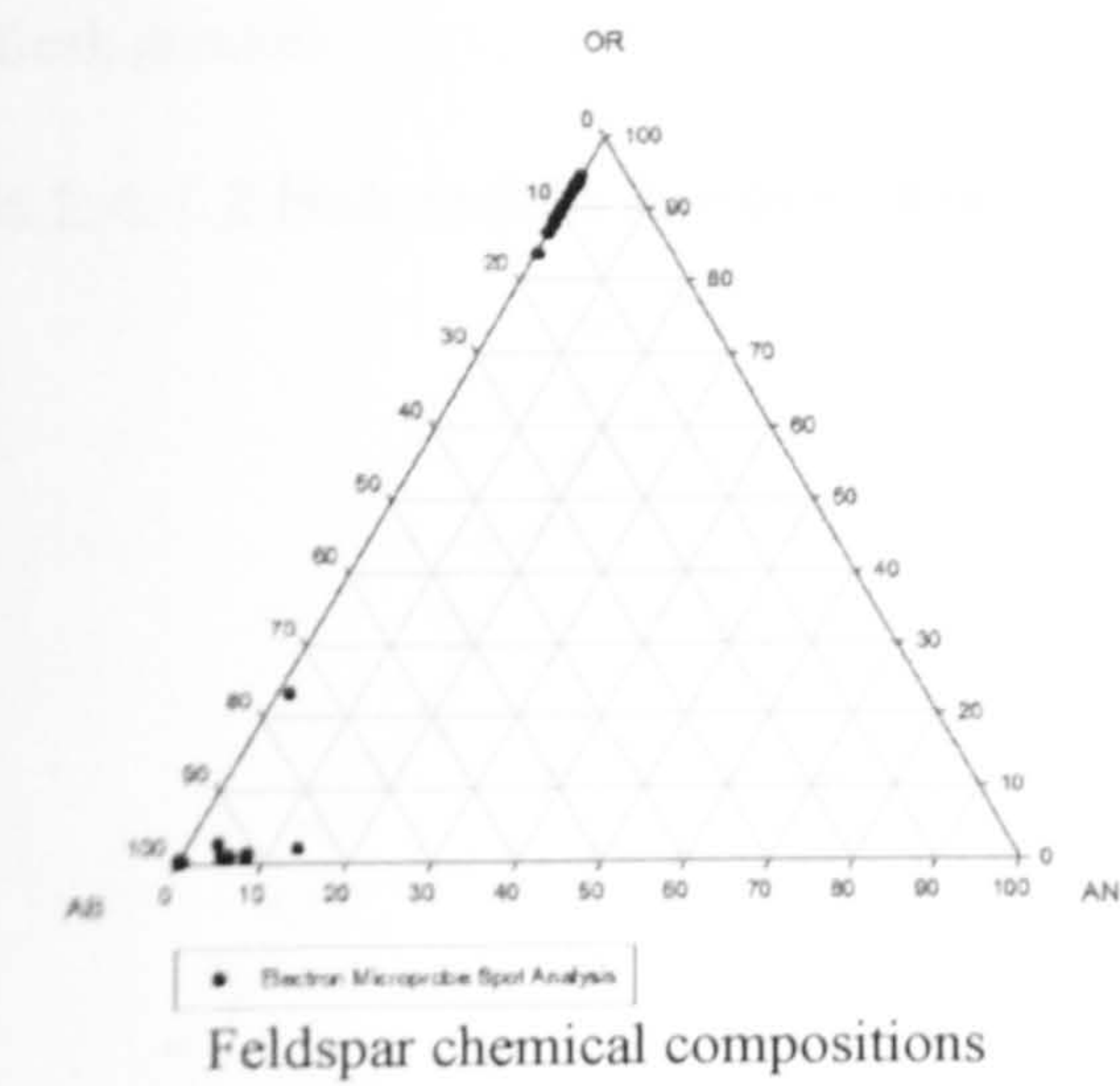
The samples of fresh granite and arkose used in this study were collected by Martin Lee. They were both collected at roadside cuttings, Grid Refs: NC054 181 and NC066 201 respectively.

4.2.4.1 Feldspar Mineralogy, Microtexture and Composition.

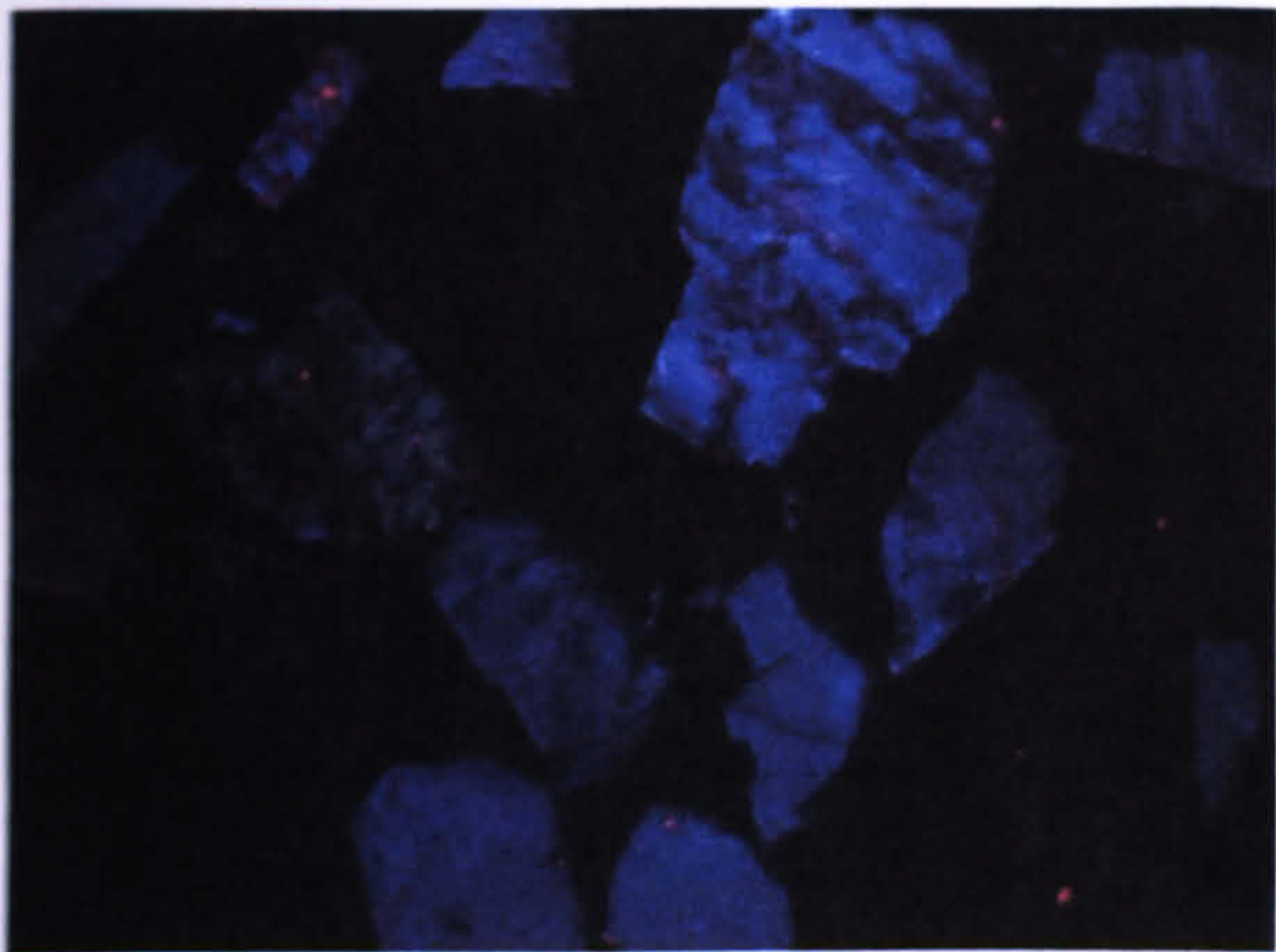
Table 4.5. Chemical compositions of Helmsdale granite feldspars (Mol%).

Sample	Alkali Feldspar			Plagioclase Feldspar		
	Ab	An	Or	Ab	An	Or
Helmsdale Granite (Helms)	10	0	90	96	3	1
Helmsdale Arkose (Ark)	37	3	60	---	---	---

4.2.4.1.1 Helmsdale Granite (Helms).



Backscattered electron SEM image (grain mount)



Optical CL image (grain mount)

SPT fraction (g/cm ³)	Mineralogy
<2.62	A ₁₀₀ P ₀ Q ₀
2.52-2.58	---
2.58-2.62	---
2.62-2.74	---
>2.74	---
Not SPT separated	---

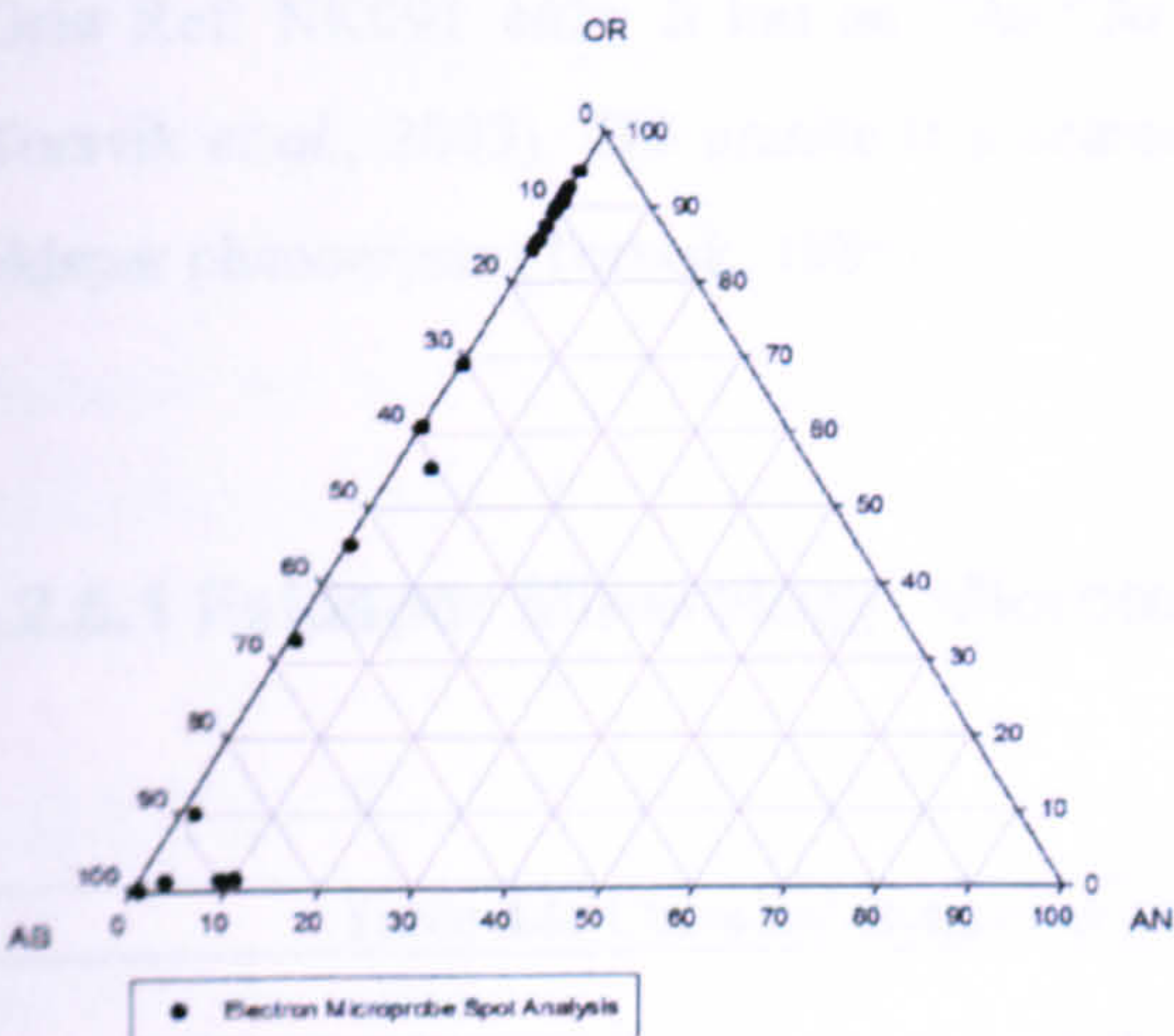
Mineralogy of the density fractions

Figure 4.6 Mineralogy, microtexture and composition of Helmsdale granite feldspars (Helms).

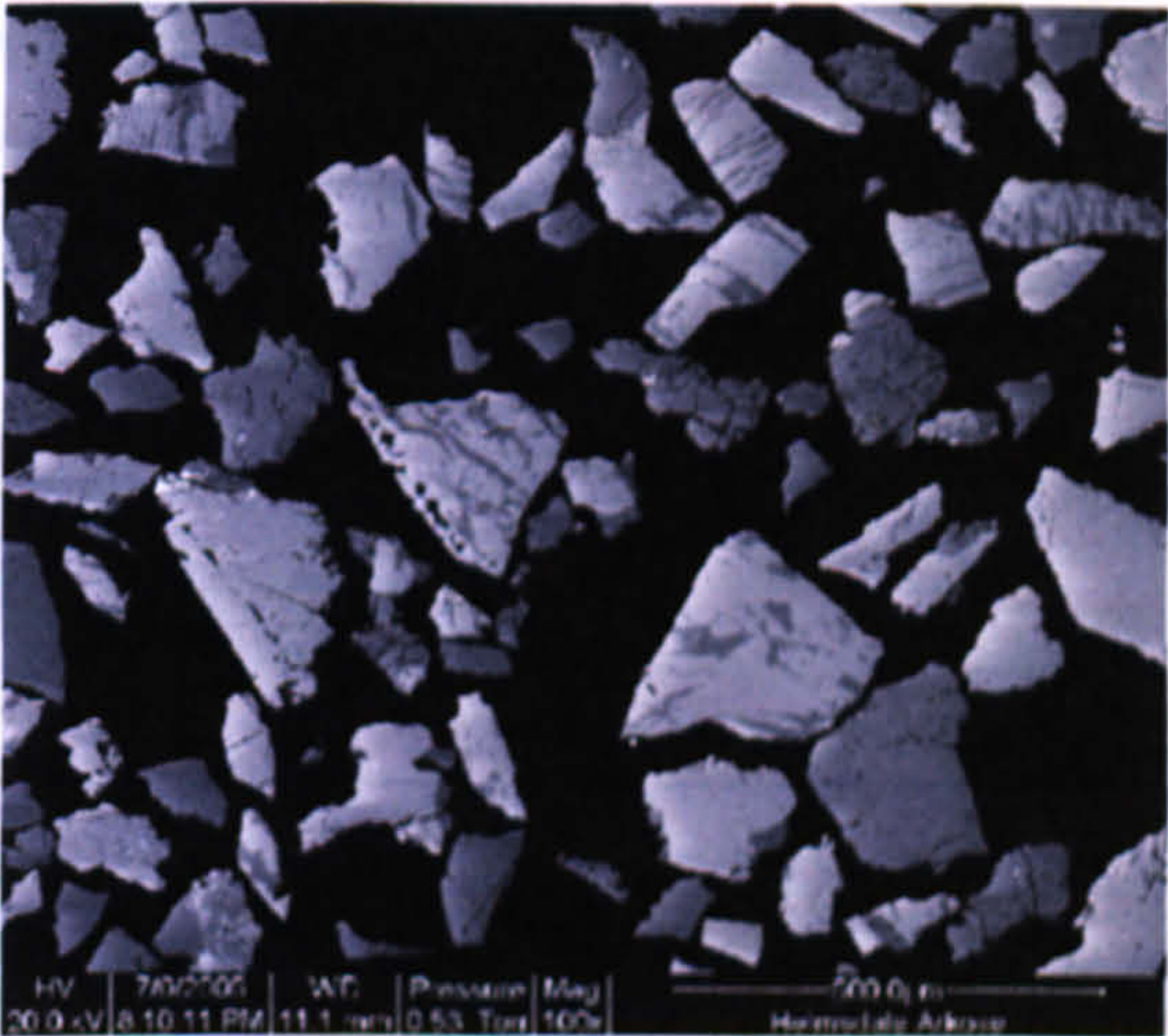
The granite alkali feldspars are orthoclase microperthites within which the K-feldspar has blue CL and the veins of perthitic albite are dull red. The free plagioclase (albite) grains are dull green or dull red in CL. Separation of feldspars from their host granite has been very effective and the one fraction used is near-pure alkali feldspar.

In addition to the fresh granite feldspars, a series of grains were etched in HF acid to simulate natural weathering. Feldspars within these powders are mineralogically comparable to those in the fresh granite.

4.2.4.1.2 Helmsdale Arkose (Ark).



Feldspar chemical compositions



Backscattered electron SEM image (grain mount)



Optical CL image (grain mount)

SPT fraction (g/cm ³)	Mineralogy
<2.62	A ₂₀ P ₈₀ Q ₀
2.52-2.58	---
2.58-2.62	---
2.62-2.74	---
>2.74	---
Not SPT separated	---

Mineralogy of the density fractions

Figure 4.7. Mineralogy, microtexture and composition of Helmsdale arkose feldspars (Ark).

Alkali feldspars from the arkose are also blue luminescent vein microperthites associated with red luminescing albite. These alkali feldspars were much more difficult to separate from the plagioclase than those from the present granite. A series of sub-samples of these feldspars were etched in HF acid to simulate the effects of weathering on luminescence emission and fading. This additional study comparing etched Helmsdale samples with the Shap granite alkali feldspars was carried out after the characterisation work was completed, so relevant images are unavailable.

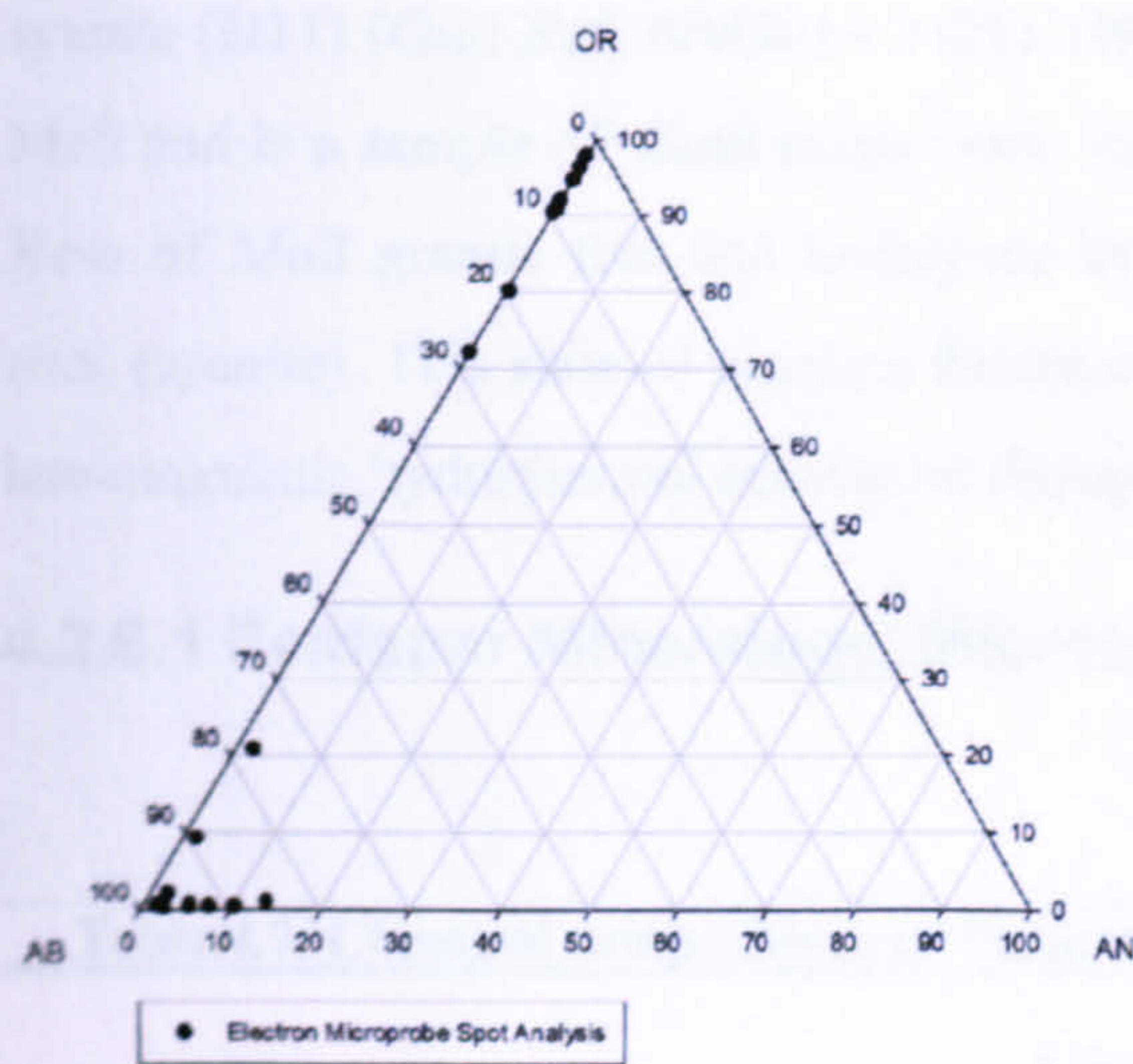
4.2.5 Peterhead Granite (GU3).

The Peterhead Granite is a Newer Granite that outcrops in the NE Grampian Mountains of Scotland (Grid Ref: NK091 462). It has an ⁴⁰Ar-³⁹Ar isotope biotite and K-feldspar age of 432 ± 7 Ma (Torsvik *et al.*, 2003). The granite is a coarsely crystalline pink coloured rock that contains large feldspar phenocrysts (Torsvik, 1985).

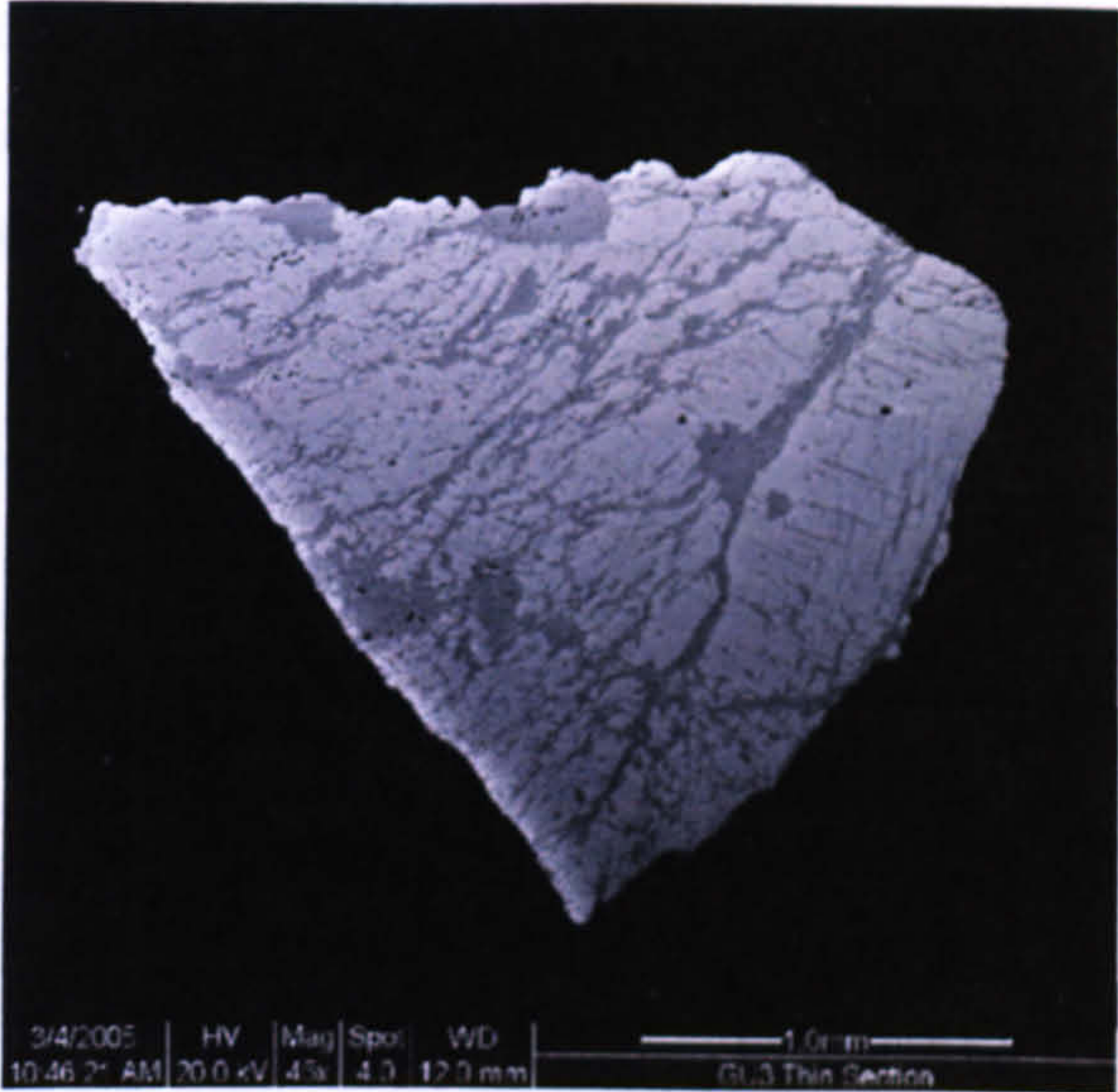
4.2.5.1 Feldspar Mineralogy, Microtexture and Composition.

Table 4.6. Chemical compositions of Peterhead granite feldspars (Mol%).

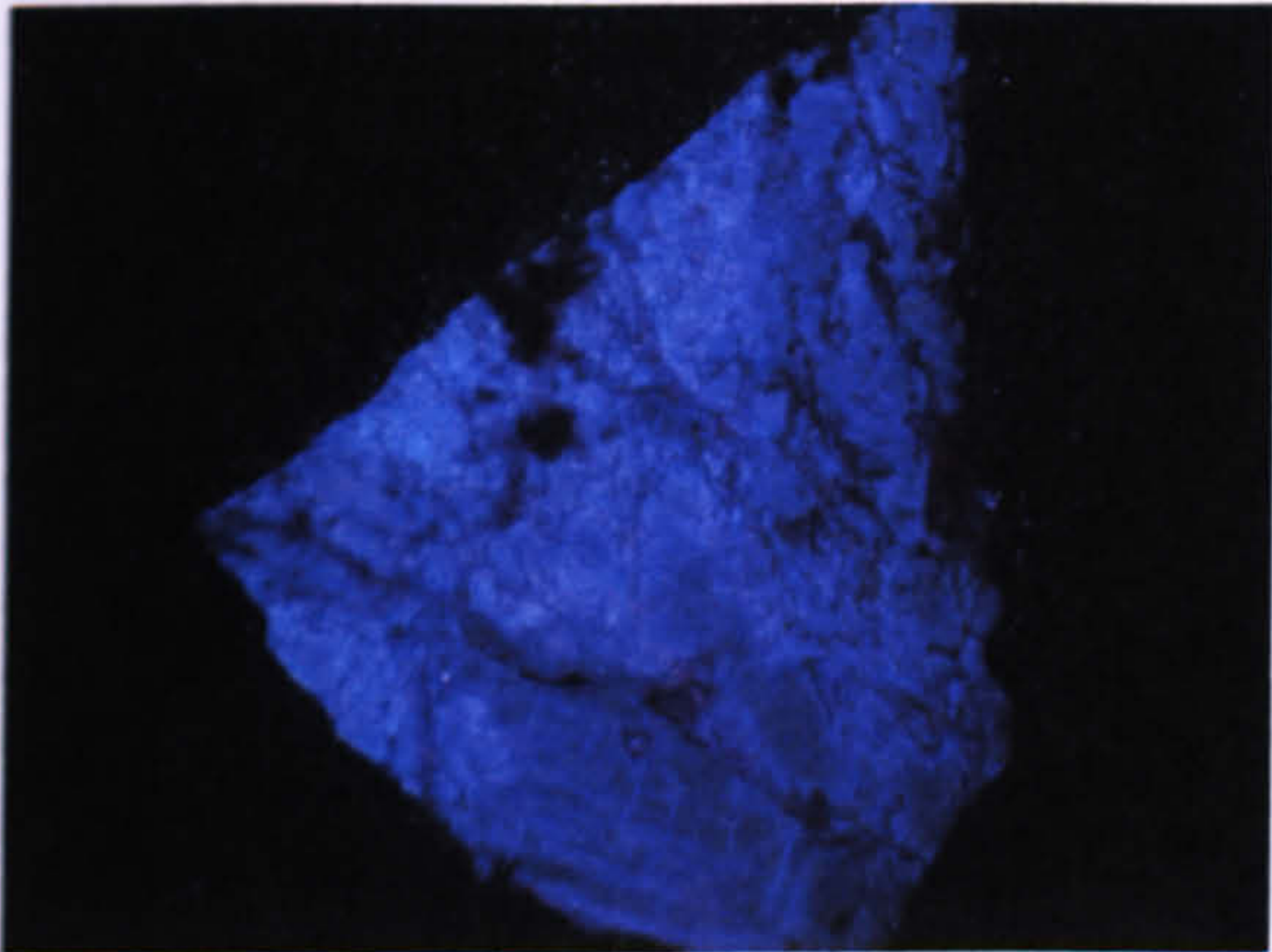
Sample	Alkali feldspar			Free plagioclase feldspar		
	Ab	An	Or	Ab	An	Or
Peterhead Granite (GU3)	7	0	93	94	4	2



Feldspar chemical compositions



Backscattered electron SEM image (grain mount)



Optical CL image (grain mount)

SPT fraction (g/cm ³)	Mineralogy
<2.62	---
2.52-2.58	---
2.58-2.62	A ₇₅ P ₂₅ Q ₀
2.62-2.74	---
>2.74	---
Not SPT separated	---

Mineralogy of the density fractions

Figure 4.8. Mineralogy, microtexture and composition of Peterhead granite feldspars (GU3).

The alkali feldspar is a very fine microperthite containing red luminescent veins of albite that cross-cut the blue luminescent microcline. Larger inclusions of free plagioclase also show red luminescence. Separation of alkali from plagioclase feldspar has been very effective in the one SPT fraction.

4.2.6 The Ross of Mull Granite.

The Ross of Mull Granite contains a group of intrusive igneous rocks that include diorite through to granodiorite and granite (Zaniewski *et al.*, 2006). The granite crops out on the western end of the Ross of Mull peninsula and occupies an onshore area of 70-80km², though this represents only about half of the actual outcrop with the rest stretching offshore. This intrusion has a Caledonian age of ~414Ma (Zaniewski *et al.*, 2006).

Samples were supplied by John Faithfull (Glasgow University) from three exposed lithologies: granite (H9) (Grid Ref: NM352 243), porphyritic granite (H10) (Grid Ref: NM3064 2394) and

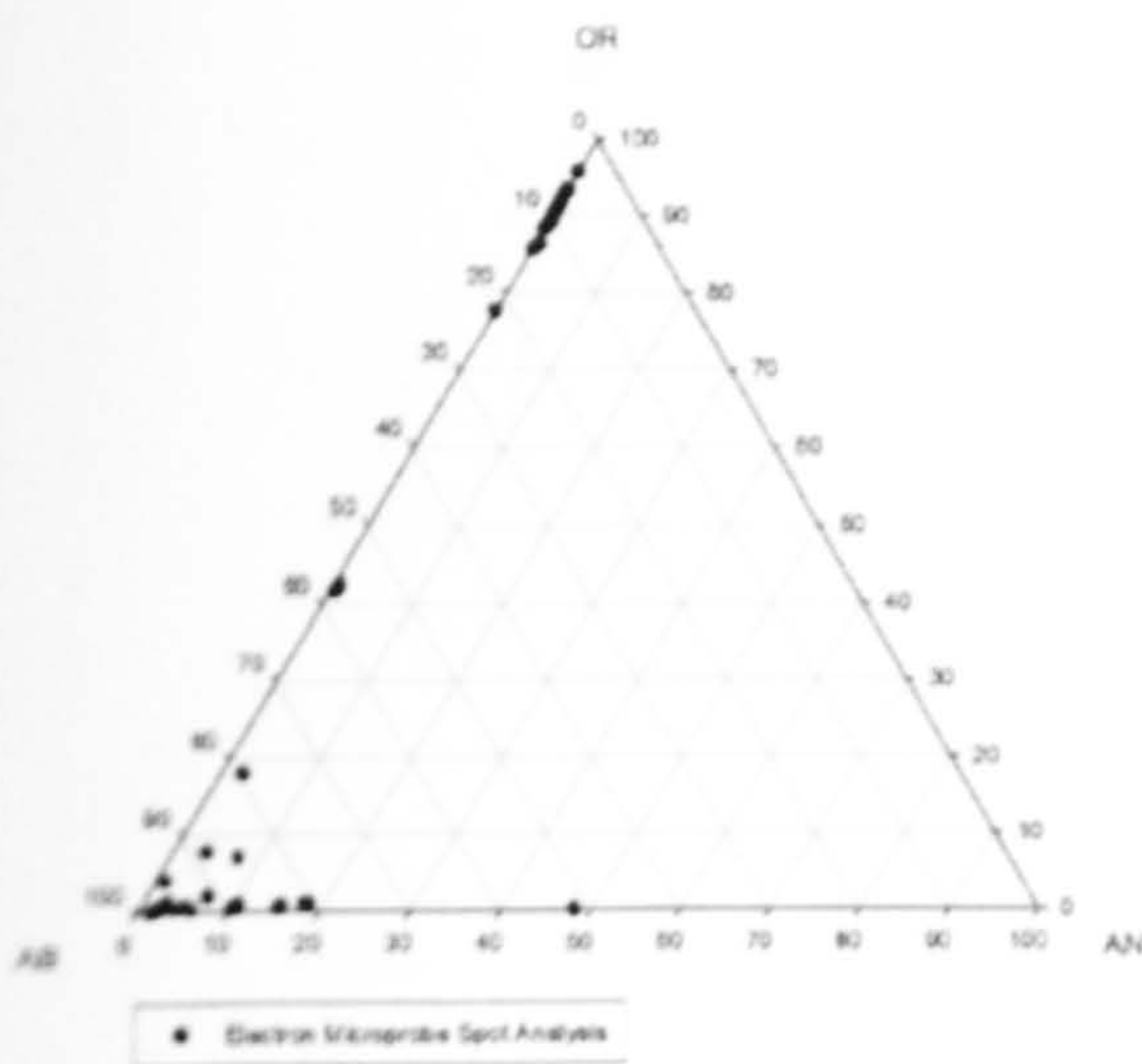
syenite (H11) (Grid Ref: NM3013 2421). H9 and H10 was collected at Fionnphort on the Ross of Mull and is a sample of alkali megacrystic biotitic granite. H11 was collected from a region of the Ross of Mull granite that had undergone hydrothermal alteration to form an alkali feldspar-rich rock (syenite). This suite of samples therefore provides the opportunity to investigate the impact of late-magmatic hydrothermal activity on feldspar luminescence properties.

4.2.6.1 Feldspar Mineralogy, Microtexture and Composition.

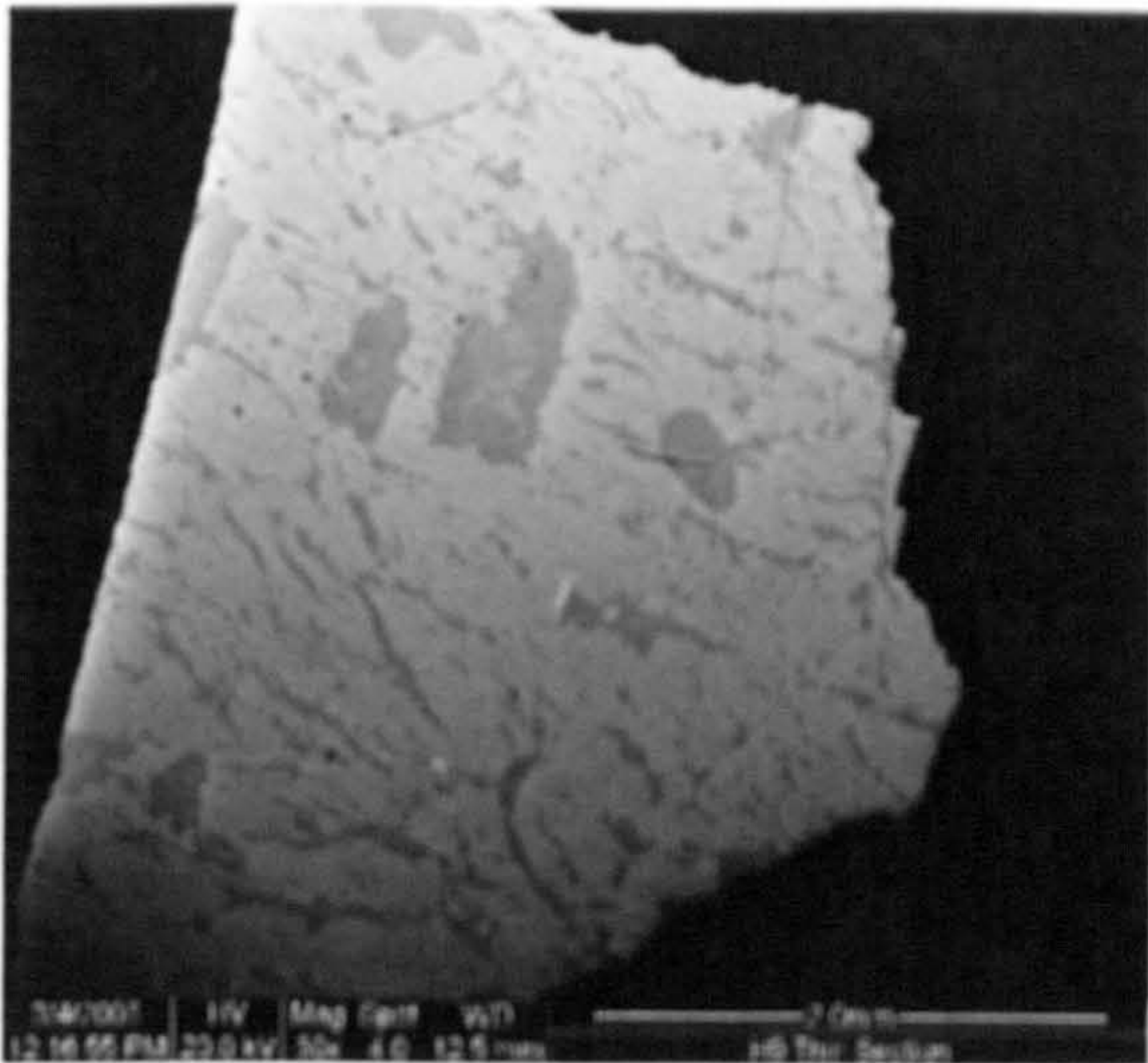
Table 4.7. Chemical compositions of feldspars from the Ross of Mull granite and syenite (Mol%).

Sample	Alkali Feldspar			Free plagioclase feldspar		
	Ab	An	Or	Ab	An	Or
Ross of Mull Granite (H9)	9	0	91	91	7	2
Ross of Mull Granite (H10)	12	0	88	90	8	2
Hydrothermal Syenite (H11)	8	0	92	93	6	1

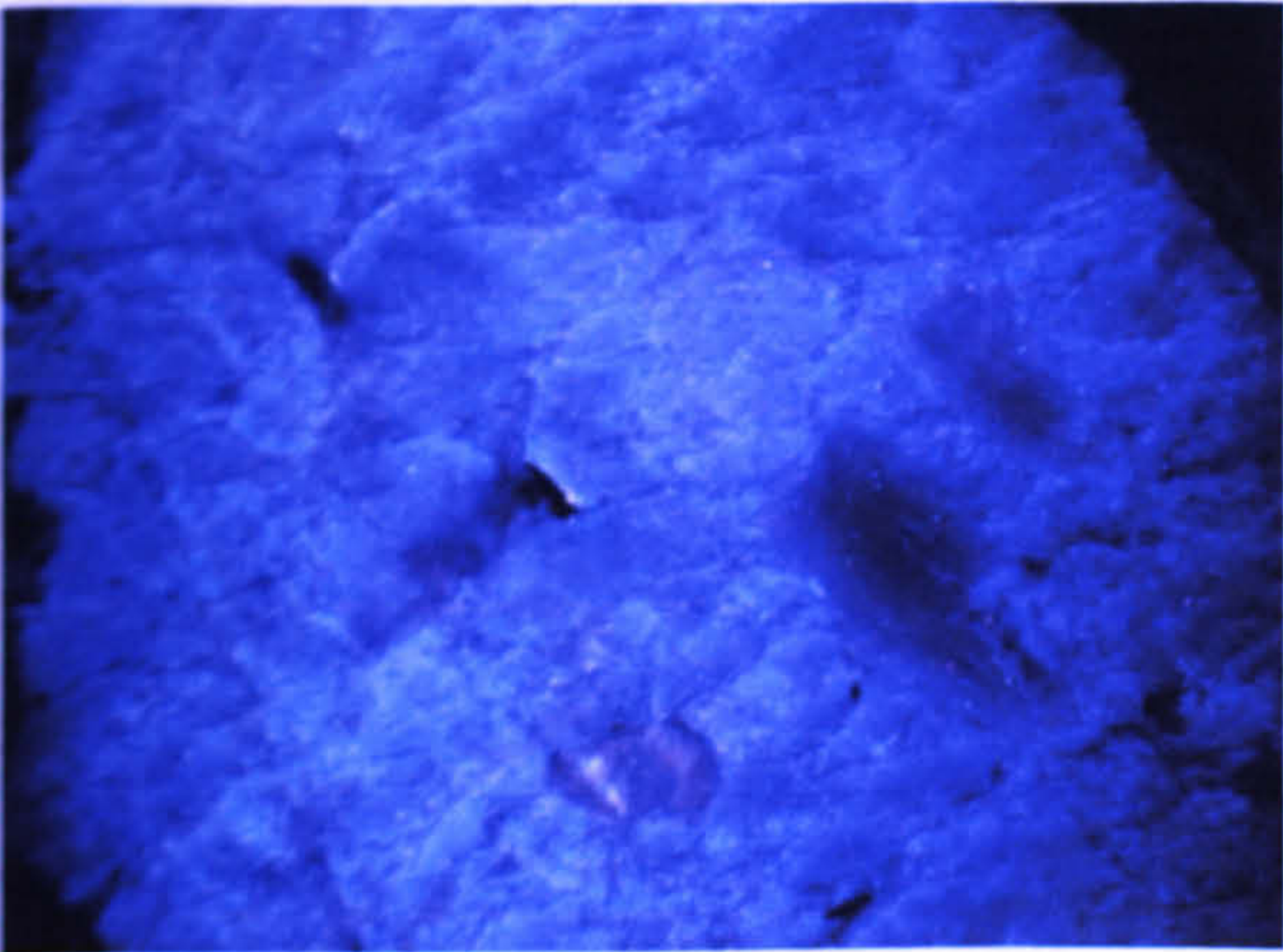
4.2.6.1.1 Ross of Mull Granite (H9).



Feldspar chemical compositions



Backscattered electron SEM image (grain mount)



Optical CL image (grain mount)

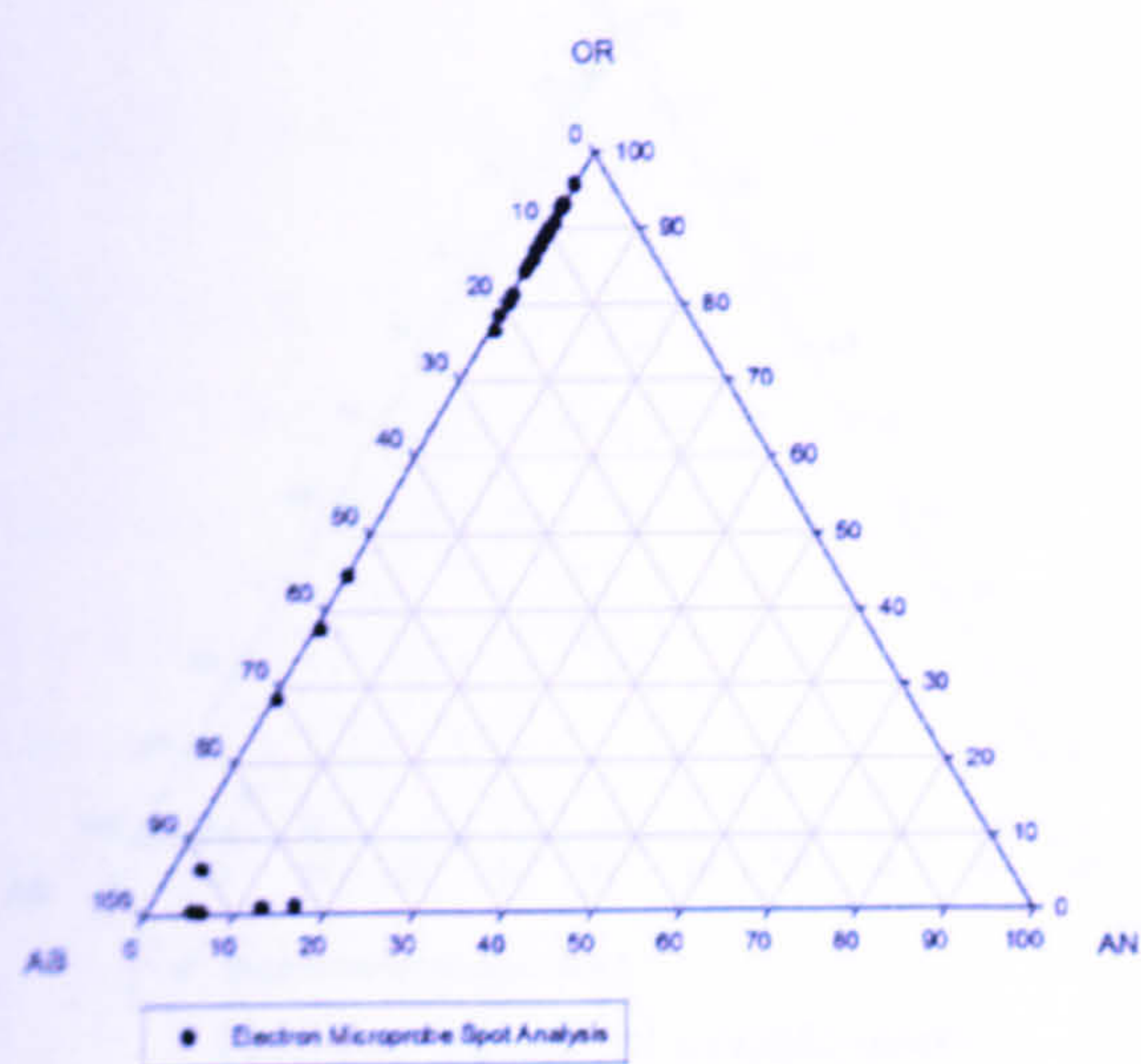
SPT fraction (g/cm ³)	Mineralogy
<2.62	---
2.52-2.58	A ₉₈ P ₂ Q ₀
2.58-2.62	---
2.62-2.74	A ₄₀ P ₅₀ Q ₁₀
>2.74	---
Not SPT separated	---

Mineralogy of the density fractions

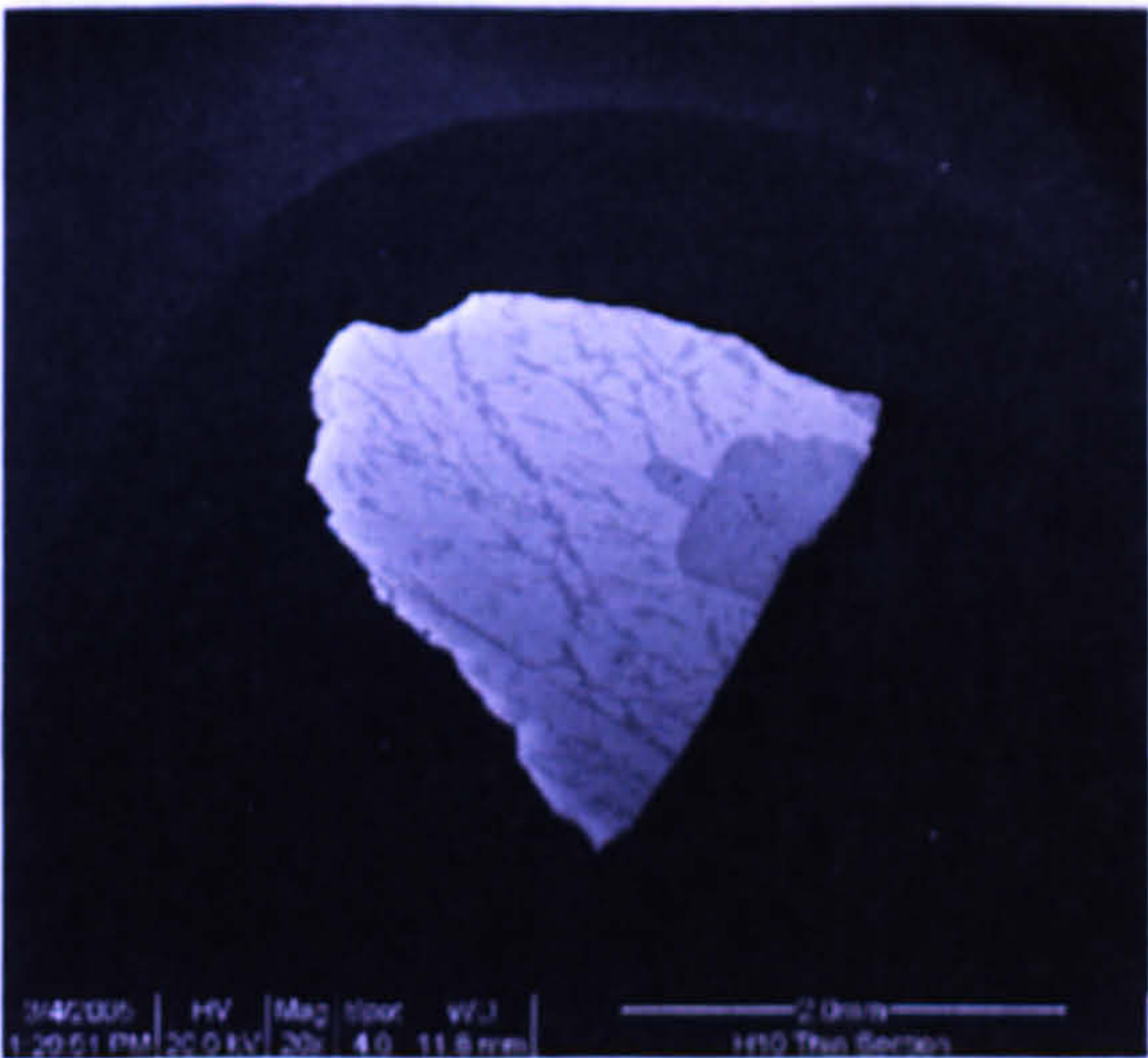
Figure 4.9. Mineralogy, microtexture and composition of Ross of Mull granite feldspars (H9).

The alkali feldspar is a coarse microperthite with red luminescing veins of albite cross-cutting the bright blue luminescent microcline. Inclusions of free plagioclase (albite) also luminesce a medium red. Separation of alkali feldspar from plagioclase and quartz was very effective in the 2.52-2.58g/cm³ SPT fraction.

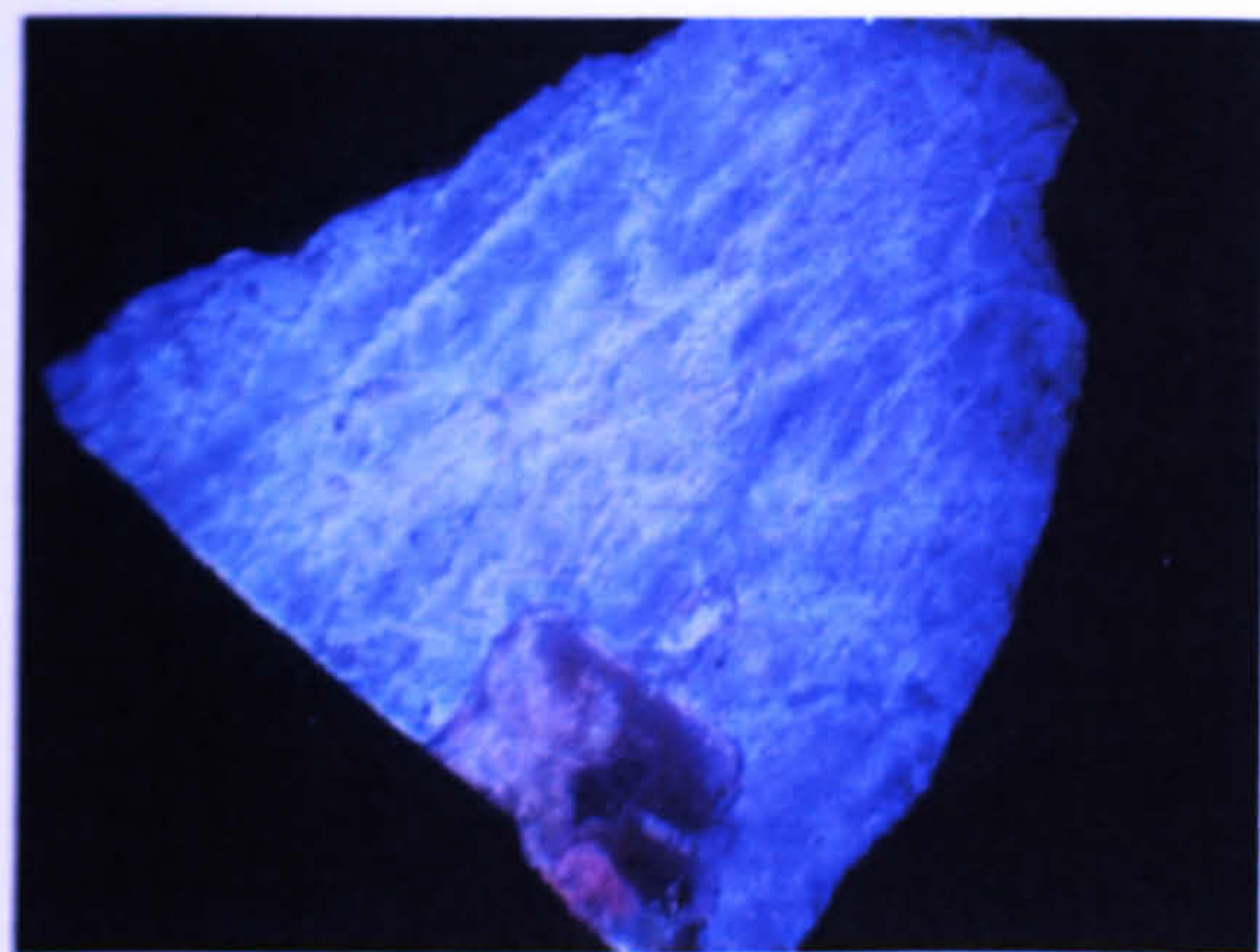
4.2.6.1.2 Ross of Mull Granite (H10).



Feldspar chemical compositions



Backscattered electron SEM image (grain mount)



Optical CL image (grain mount)

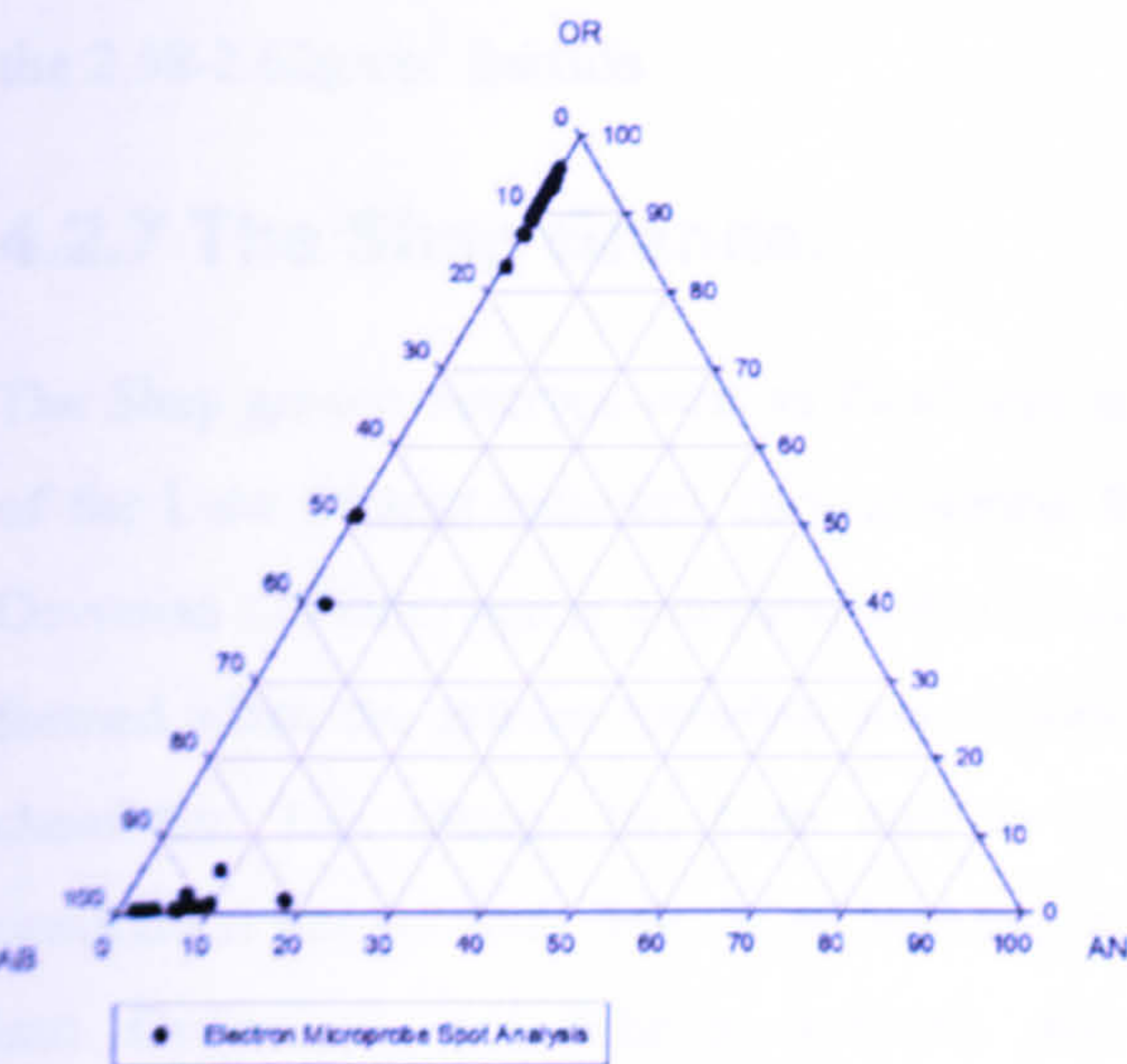
SPT fraction (g/cm ³)	Mineralogy
<2.62	---
2.52-2.58	A ₈₅ P ₁₅ Q ₀
2.58-2.62	---
2.62-2.74	---
>2.74	---
Not SPT separated	---

Mineralogy of the density fractions

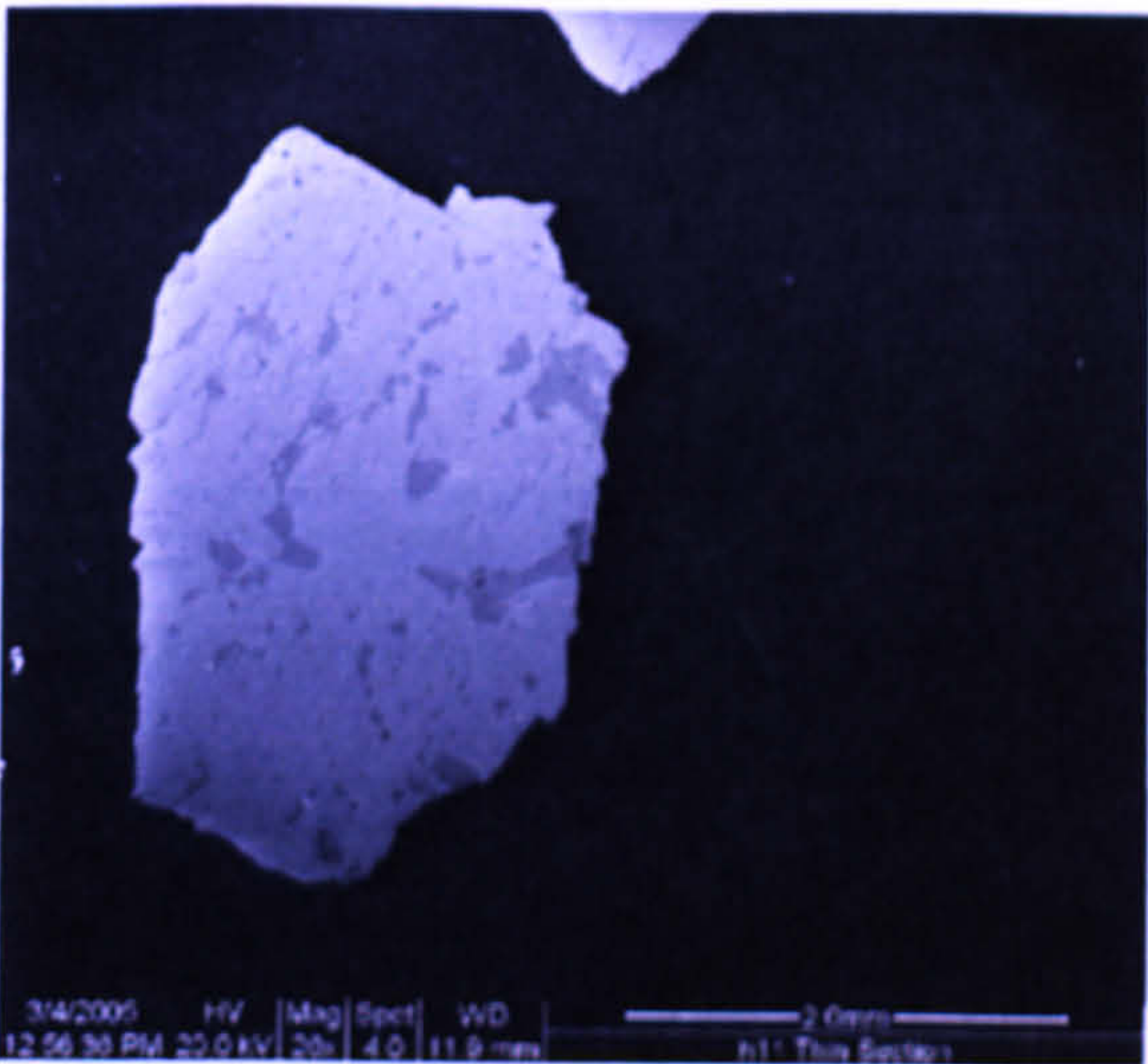
Figure 4.10. Mineralogy, microtexture and composition of Ross of Mull granite feldspars (H10).

The porphyritic Ross of Mull granite is also a coarse microperthite containing dark red luminescing veins and larger crystals of free plagioclase within the bright blue luminescing microcline. Alkali feldspar has again separated well into the light SPT fraction.

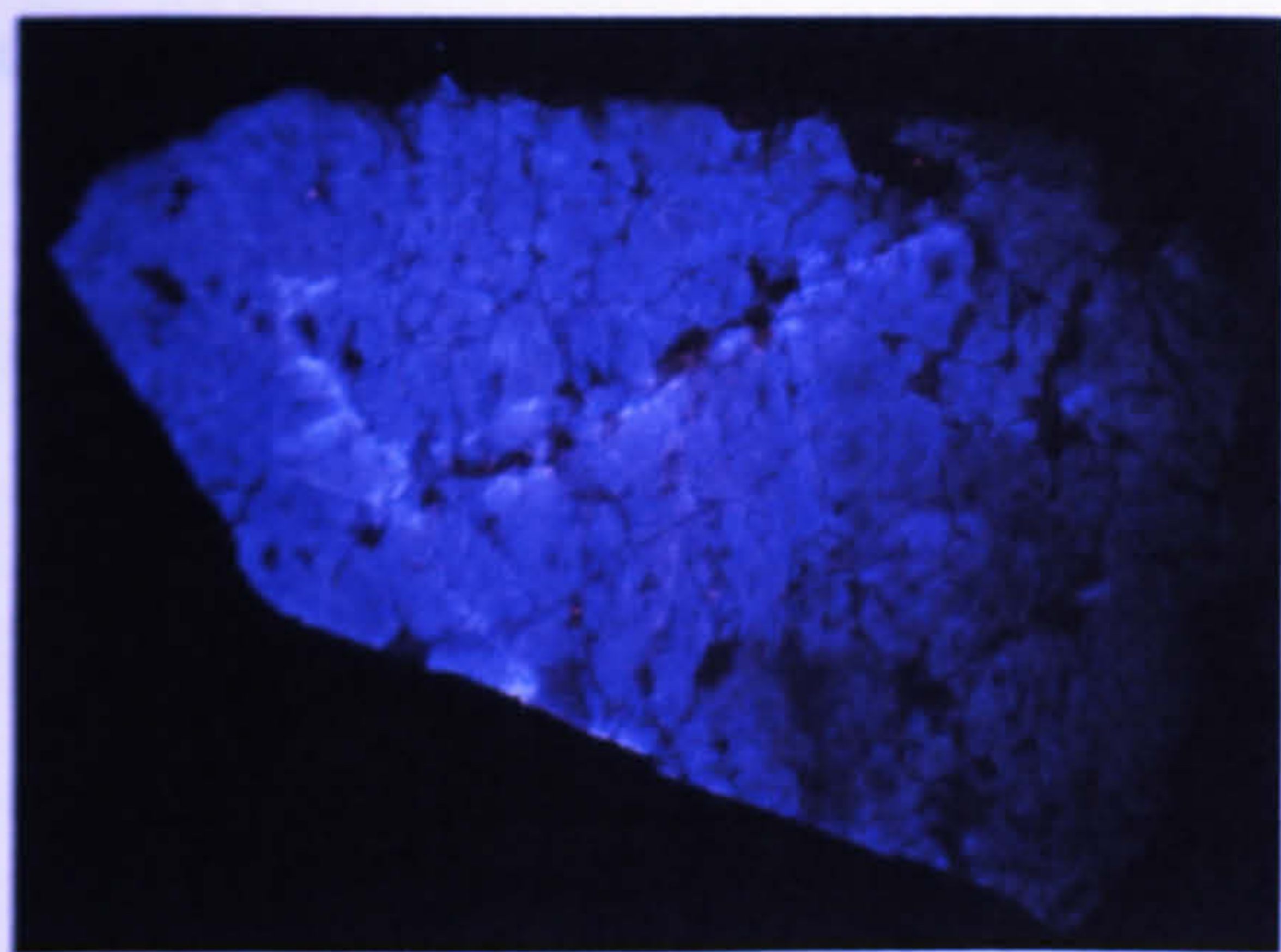
4.2.6.1.3 Ross of Mull Hydrothermal Syenite (H11).



Feldspar chemical compositions



Backscattered electron SEM image (grain mount)



Optical CL image (grain mount)

SPT fraction (g/cm ³)	Mineralogy
<2.62	---
2.52-2.58	---
2.58-2.62	A ₈₀ P ₂₀ Q ₀
2.62-2.74	A ₁₅ P ₈₅ Q ₀
>2.74	---
Not SPT separated	---

Mineralogy of the density fractions

Figure 4.11. Mineralogy, microtexture and composition of feldspars from the Ross of Mull hydrothermal syenite (H11).

In common with the granite samples the hydrothermal syenite is a coarse vein microcline microperthite within which the veins of plagioclase luminesce dark red. Although the K-feldspar luminesces bright blue, it has a red tinge, which may reflect an abundance of very finely intergrown plagioclase. In common with the granite samples, SPT separation of alkali feldspar from plagioclase feldspar was very effective, but in this case the alkali feldspar is concentrated within the 2.58-2.62g/cm³ fraction.

4.2.7 The Shap Granite.

The Shap granite outcrops over an 8km² area at the eastern margin of the Lake District and is part of the Lake District batholith, formed during the third and last phase of its emplacement. Its late Devonian (394Ma) age is comparable to that of the Skiddaw Granite (Duff and Smith, 1992), and formed when the granite batholith was evolving from a tholeiitic, to an increasing calc-alkaline, chemistry. This change has been used to imply magma genesis beneath an evolving arc or continental margin with little or no melting or sedimentary protolith. The Shap Granite intruded into Ordovician and Silurian volcanic and metasedimentary rocks and is an adamellite characterised by distinctive large pink K-feldspar megacrysts.

The fresh Shap (Ditlefsen) and unweathered Shap samples were extracted from hand specimens of the granite collected from the working Shap ‘pink’ quarry (Grid Ref: NY557 083) on the eastern edge of the intrusion. The samples that were etched in HF acid for different lengths of time were also separated from an unweathered hand specimen of the granite. The aim of the HF acid etching was to simulate the effects of natural weathering and Lee and Parsons (1995) have shown that HF acid selectively attacks the same defects that are picked out during natural weathering. Naturally weathered feldspars were extracted from soil formed on the granite and these samples are referred to as ‘Weathered Shap Granite’ (WSH).

4.2.7.1 Feldspar Mineralogy, Microtexture and Composition.

Shap feldspar and chemistry data: Appendix 1

Table 4.8. Chemical compositions of Shap granite feldspars (Mol%).

Sample	Alkali feldspar			Free plagioclase		
	Ab	An	Or	Ab	An	Or
Fresh Shap (Ditlefsen)	9	0	90	94	5	1
Unweathered Shap (UWSH)	16	0	84	93	6	1
Weathered Shap (WSH)	19	0	82	74	1	25
HF Etched Shap 1-15 mins	17	0	83	92	4	4

4.2.7.1.1 Fresh Shap Granite (Ditlefsen).

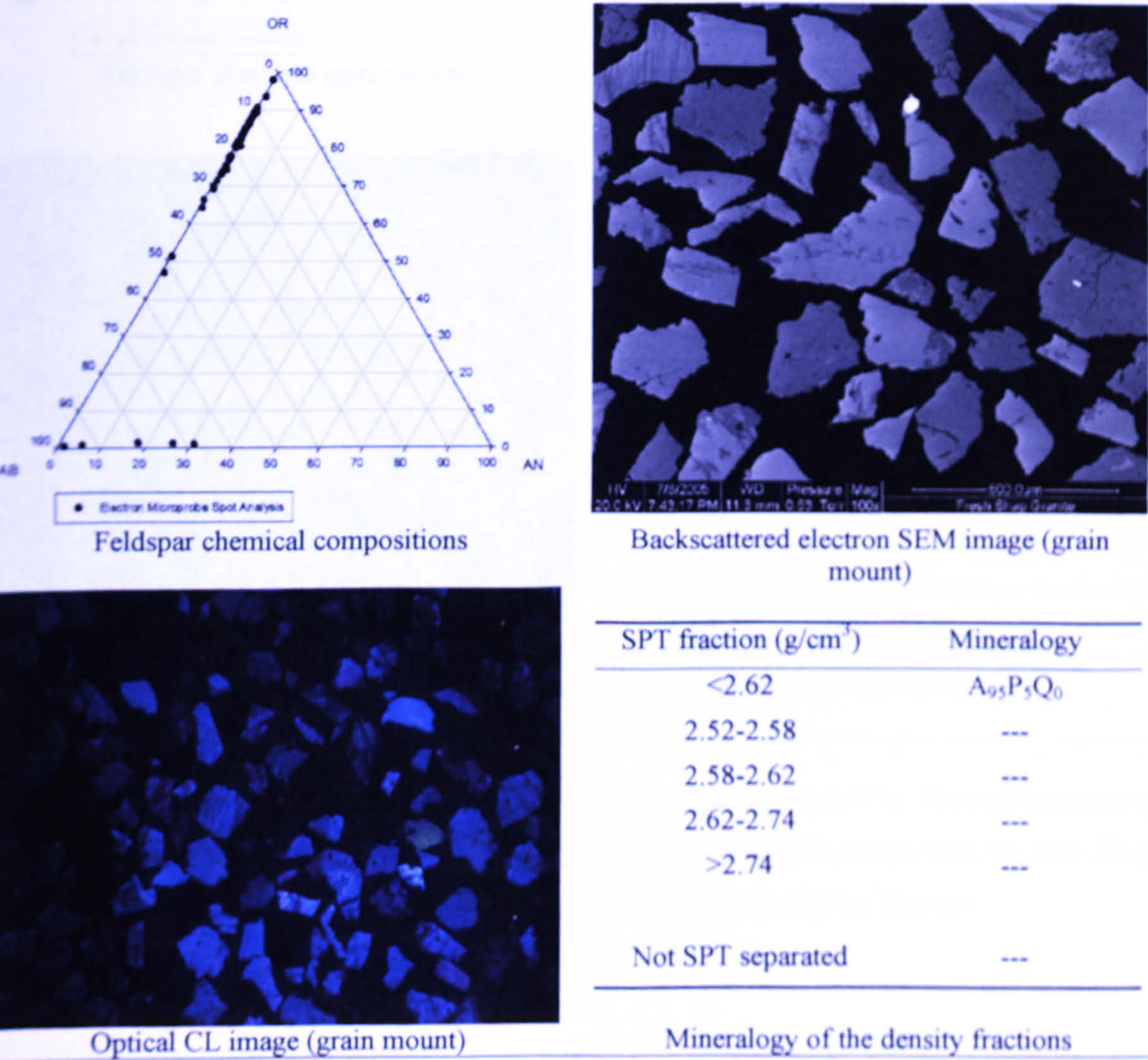
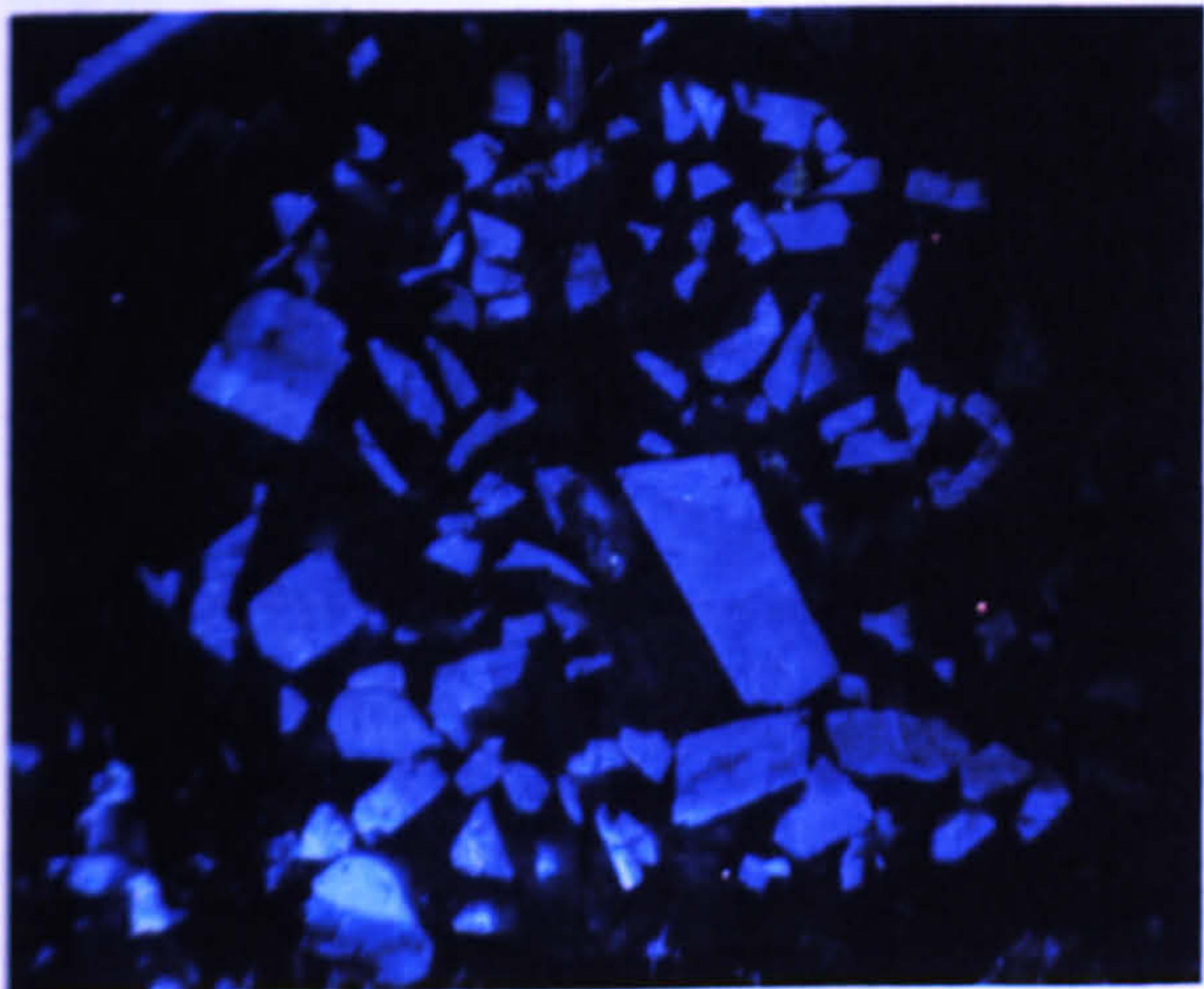
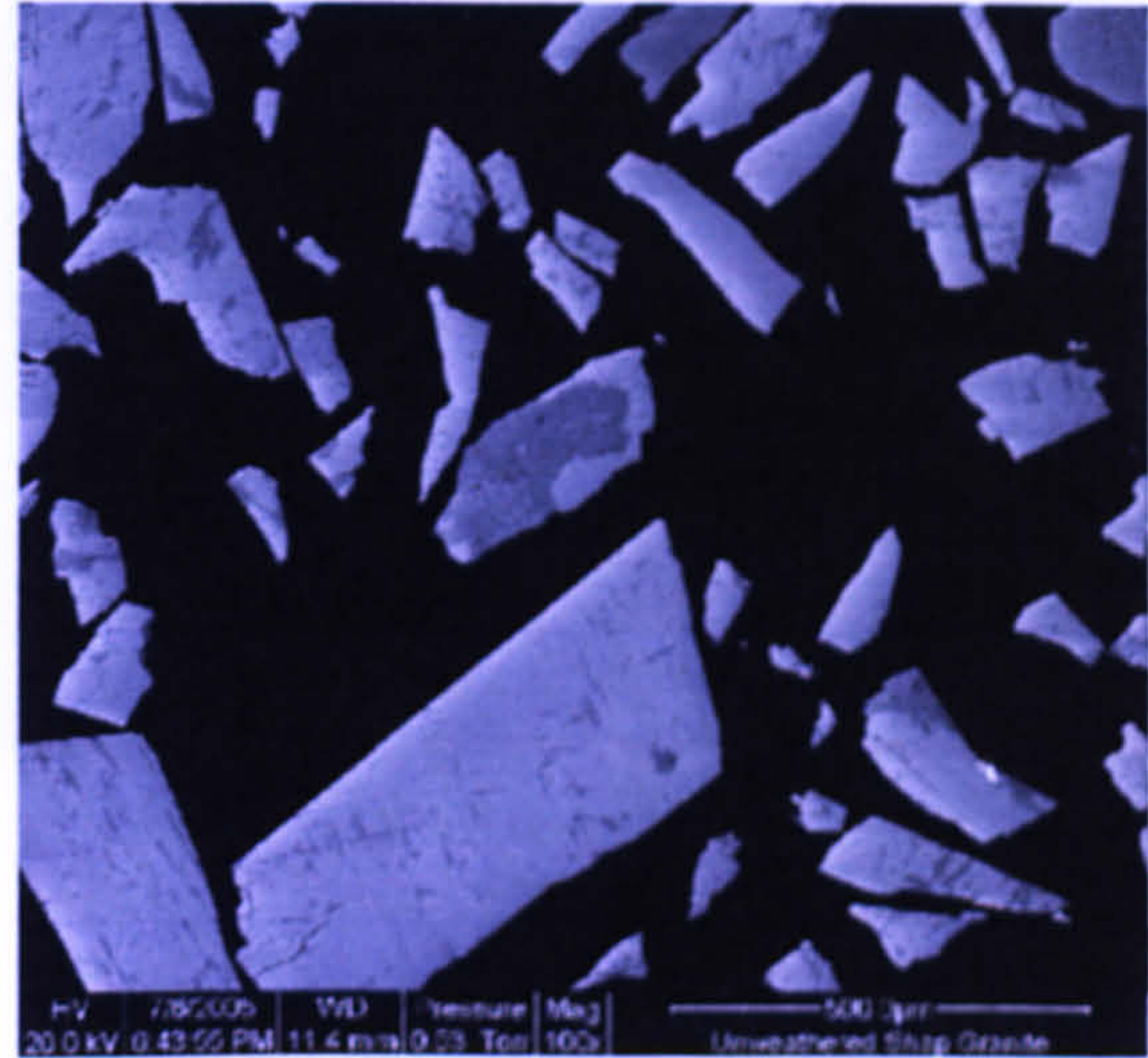
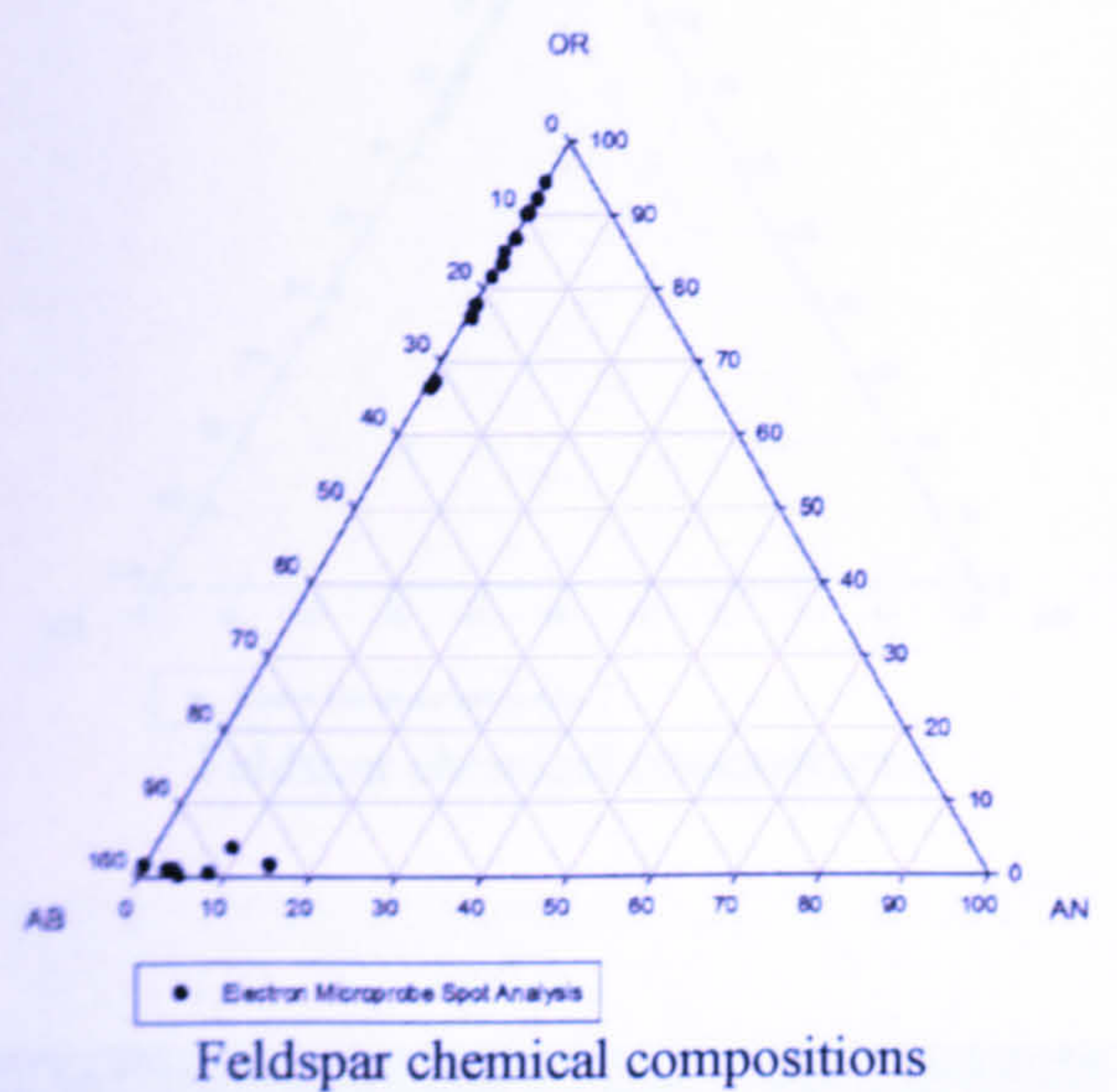


Figure 4.12. Mineralogy, microtexture and composition of the fresh Shap granite feldspars (Ditlefsen).

The alkali feldspars are fine lamellar and vein orthoclase microperthites. The orthoclase has a bright blue CL whereas the albite veins luminesce red. The free plagioclase grains luminesce dull

red or green and their relatively large size means that they have been easy to separate from the alkali feldspar and the single density separate is relatively pure.

4.2.7.1.2 Unweathered Shap Granite (UWSH).



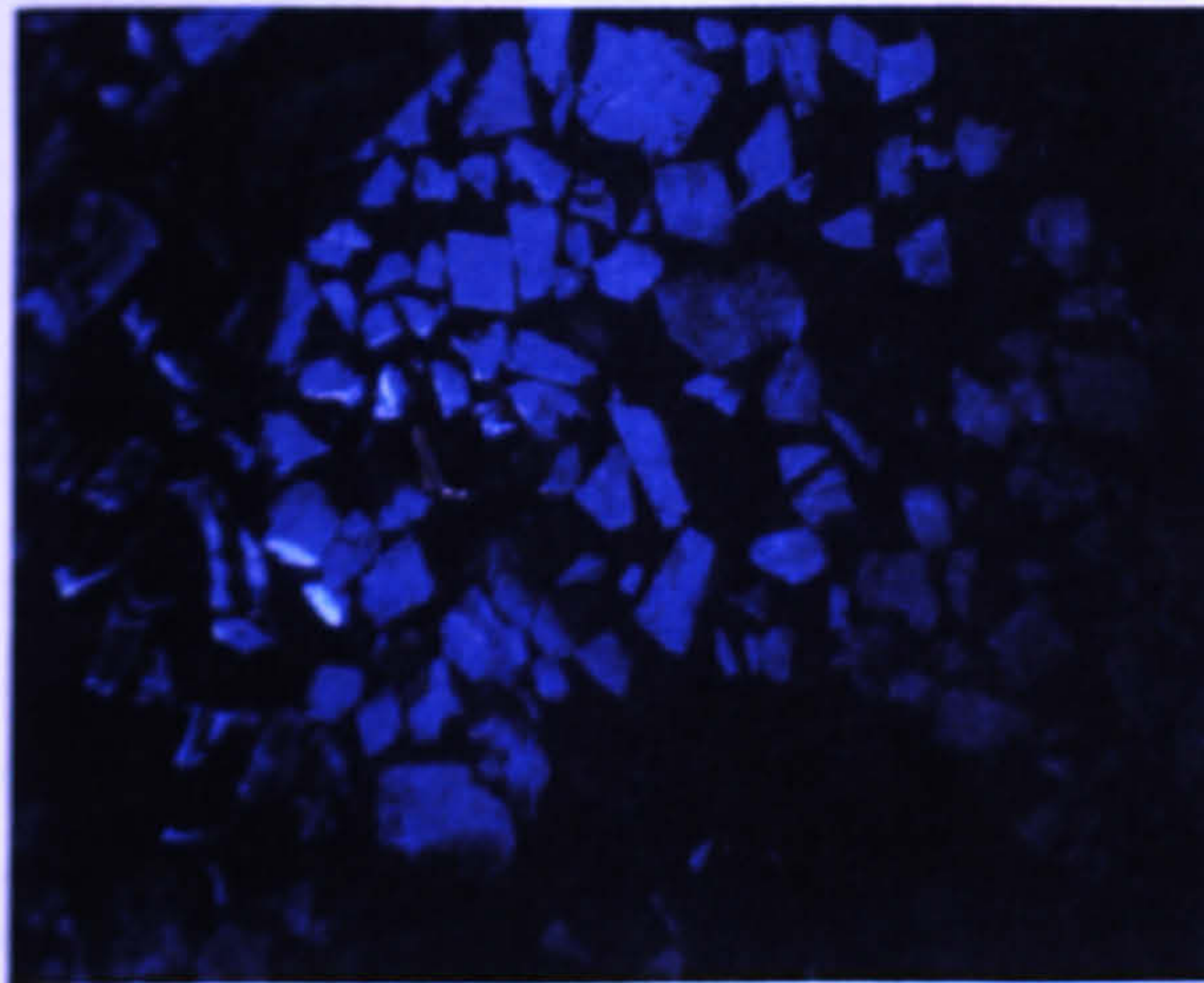
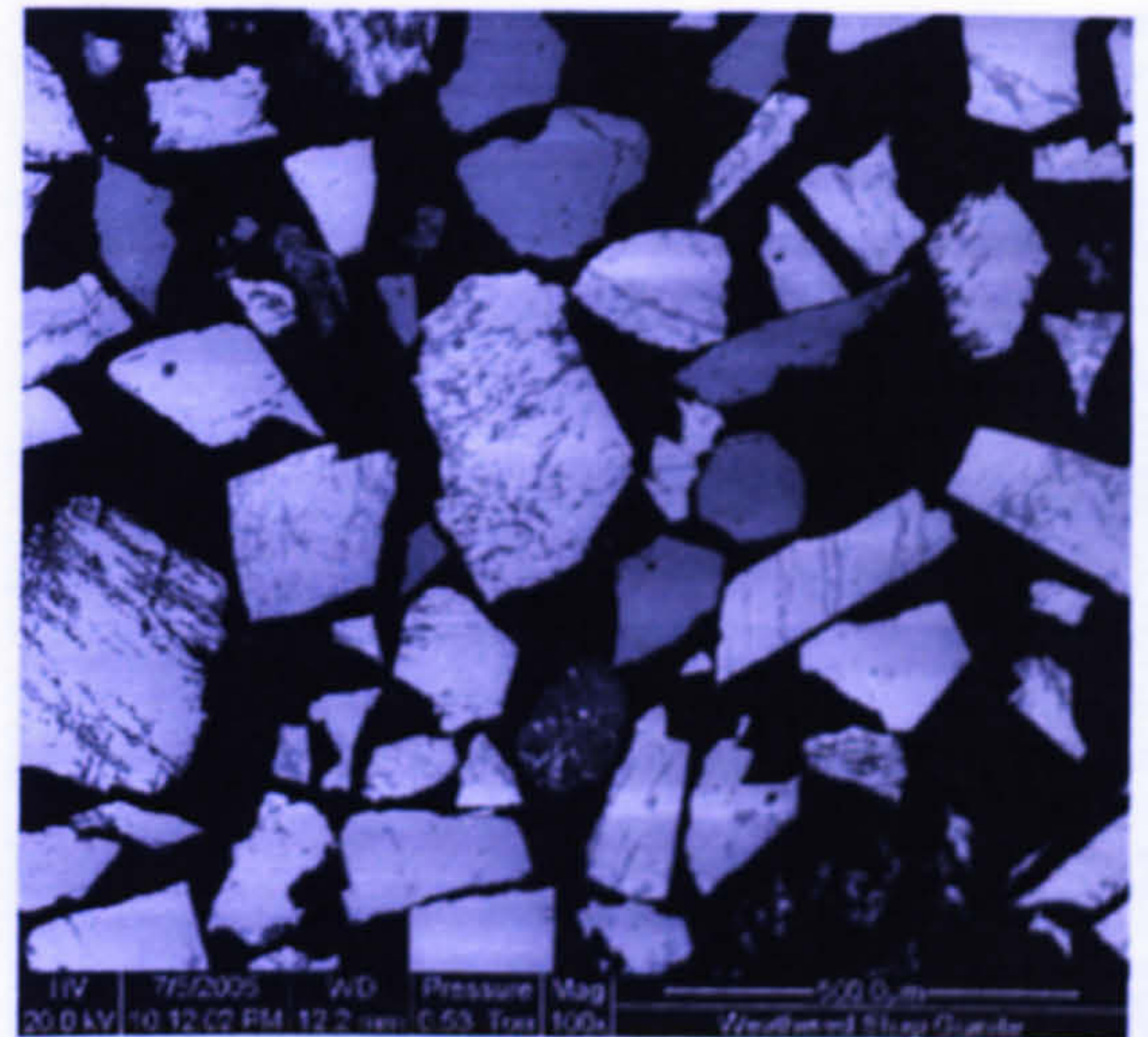
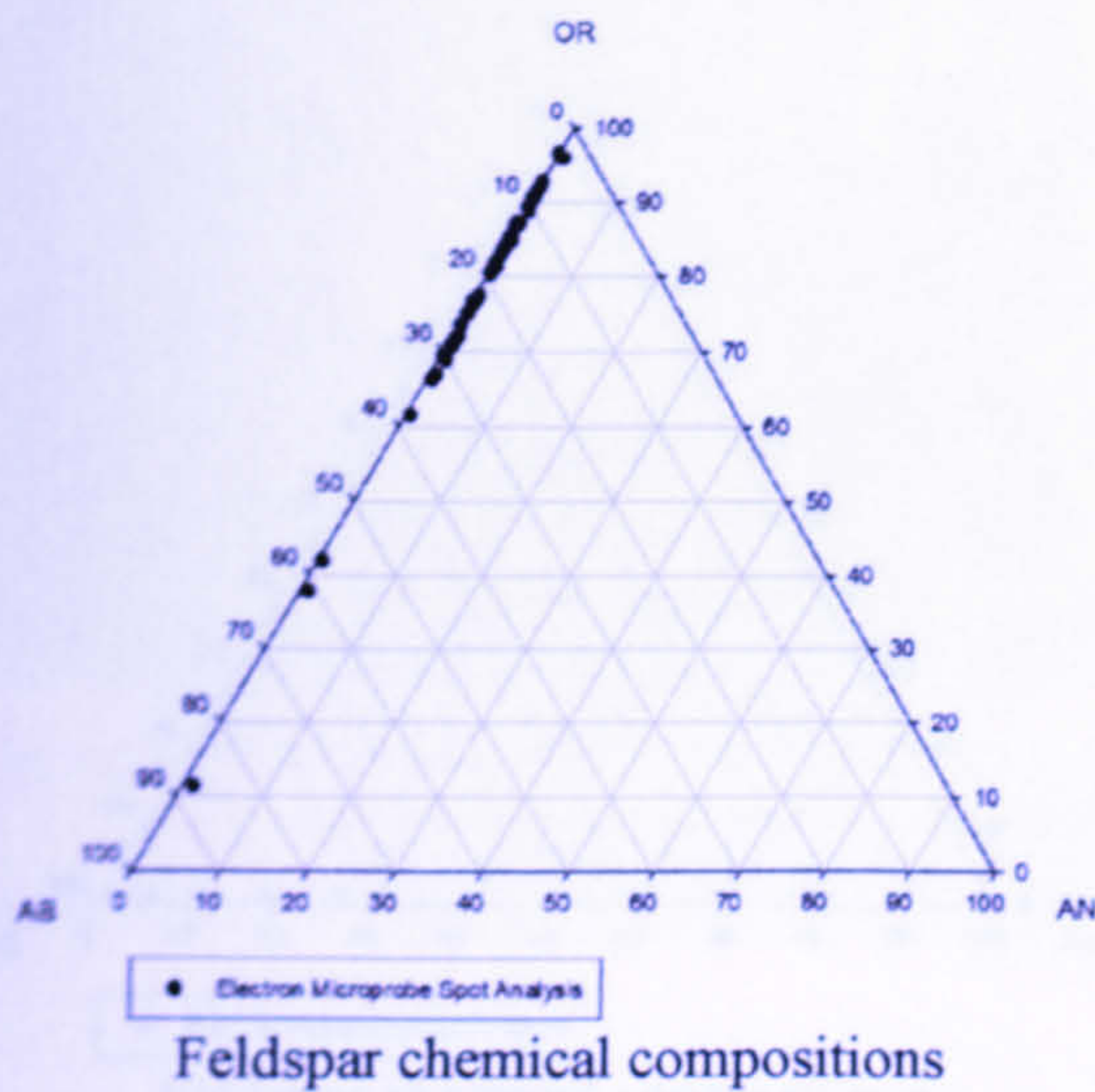
SPT fraction (g/cm ³)	Mineralogy
<2.62	A ₈₅ P ₁₅ Q ₀
2.52-2.58	---
2.58-2.62	---
2.62-2.74	---
>2.74	---
Not SPT separated	---

Mineralogy of the density fractions

Figure 4.13. Mineralogy, microtexture and composition of unweathered Shap granite feldspars (UWSH).

In common with the Fresh Shap sample this is an orthoclase microperthite. The red luminescing vein and free plagioclase is less evident within the grain mount of this sample than the fresh Shap. The alkali feldspar grains have separated relatively well into the <2.62g/cm³ fraction.

4.2.7.1.3 Weathered Shap Granite (WSH).



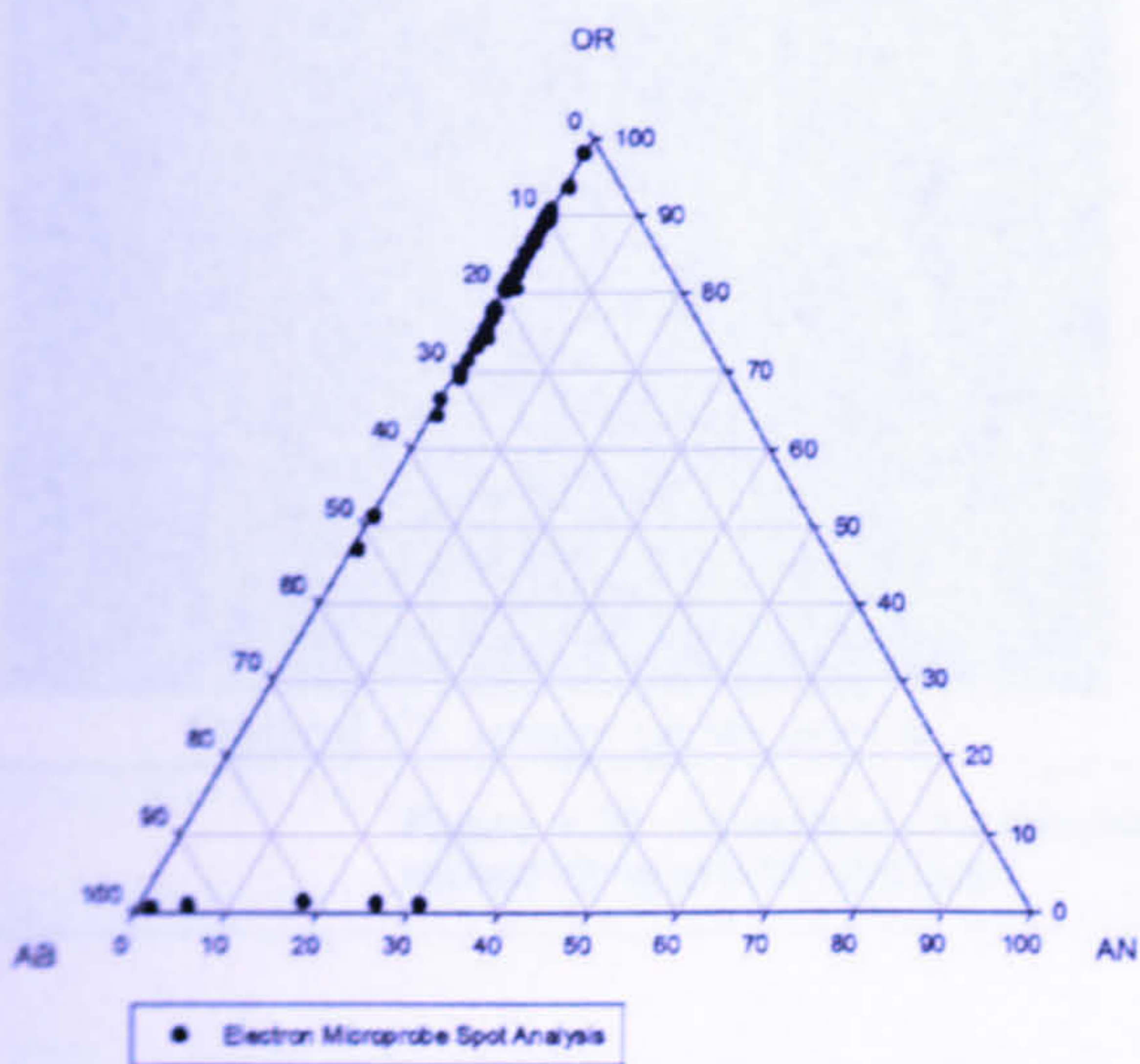
SPT fraction (g/cm ³)	Mineralogy
<2.62	A ₉₅ P ₅ Q ₀
2.52-2.58	---
2.58-2.62	---
2.62-2.74	---
>2.74	---
Not SPT separated	---

Mineralogy of the density fractions

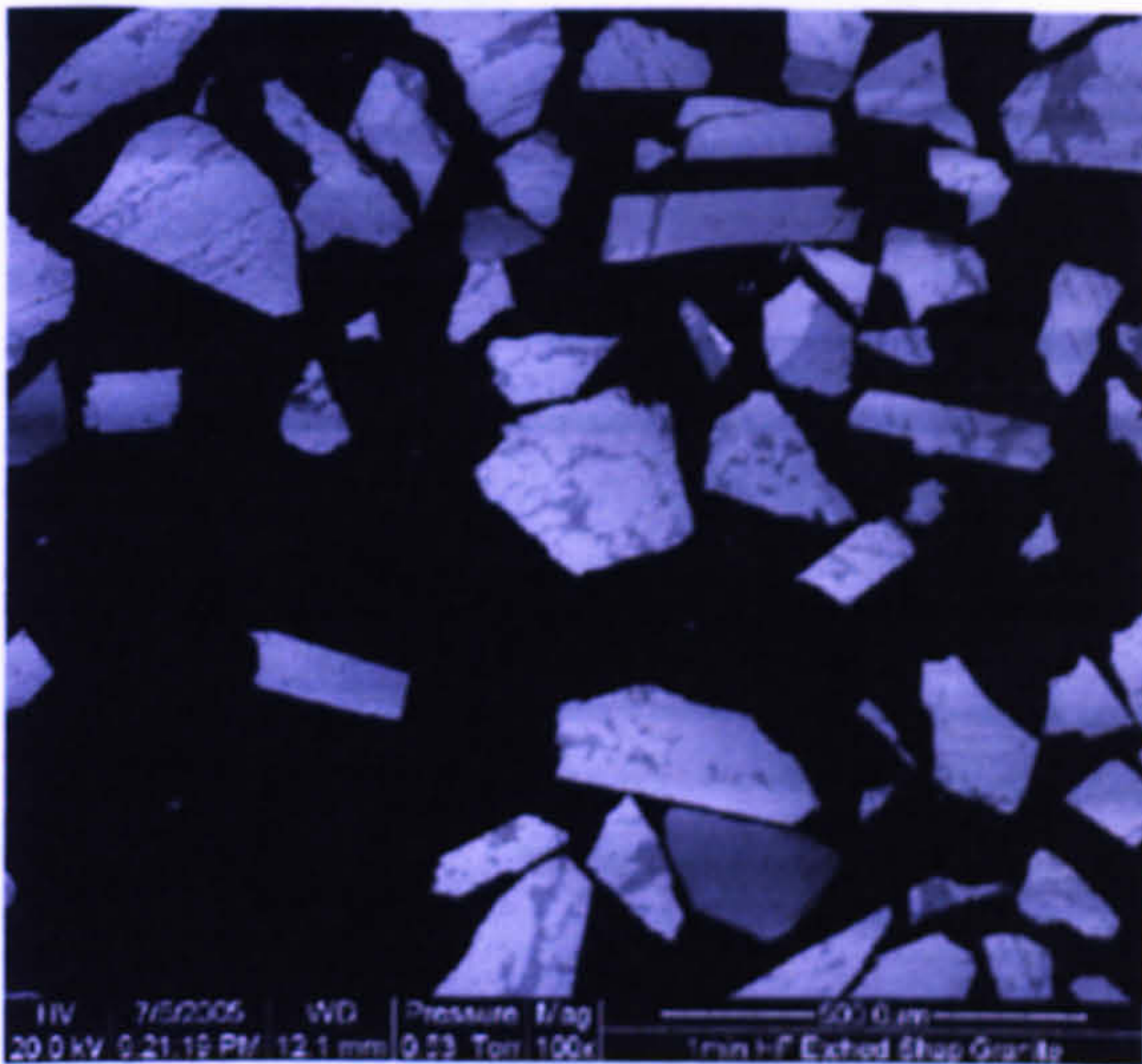
Figure 4.14. Mineralogy, microtexture and composition of weathered Shap granite feldspars (WSH).

Alkali feldspars in the polished grain mount are bright blue luminescent orthoclase microperthites whereas the grains of free plagioclase and quartz are largely non-luminescent. Note in the backscattered electron image that some of the alkali feldspar grains have been heavily weathered to form long and narrow etch pits projecting inwards from the outer edge of the grain. The weathering will also have removed most of the plagioclase so that the medium grey grains in the backscattered image are quartz. The single density separate is again relatively pure alkali feldspar.

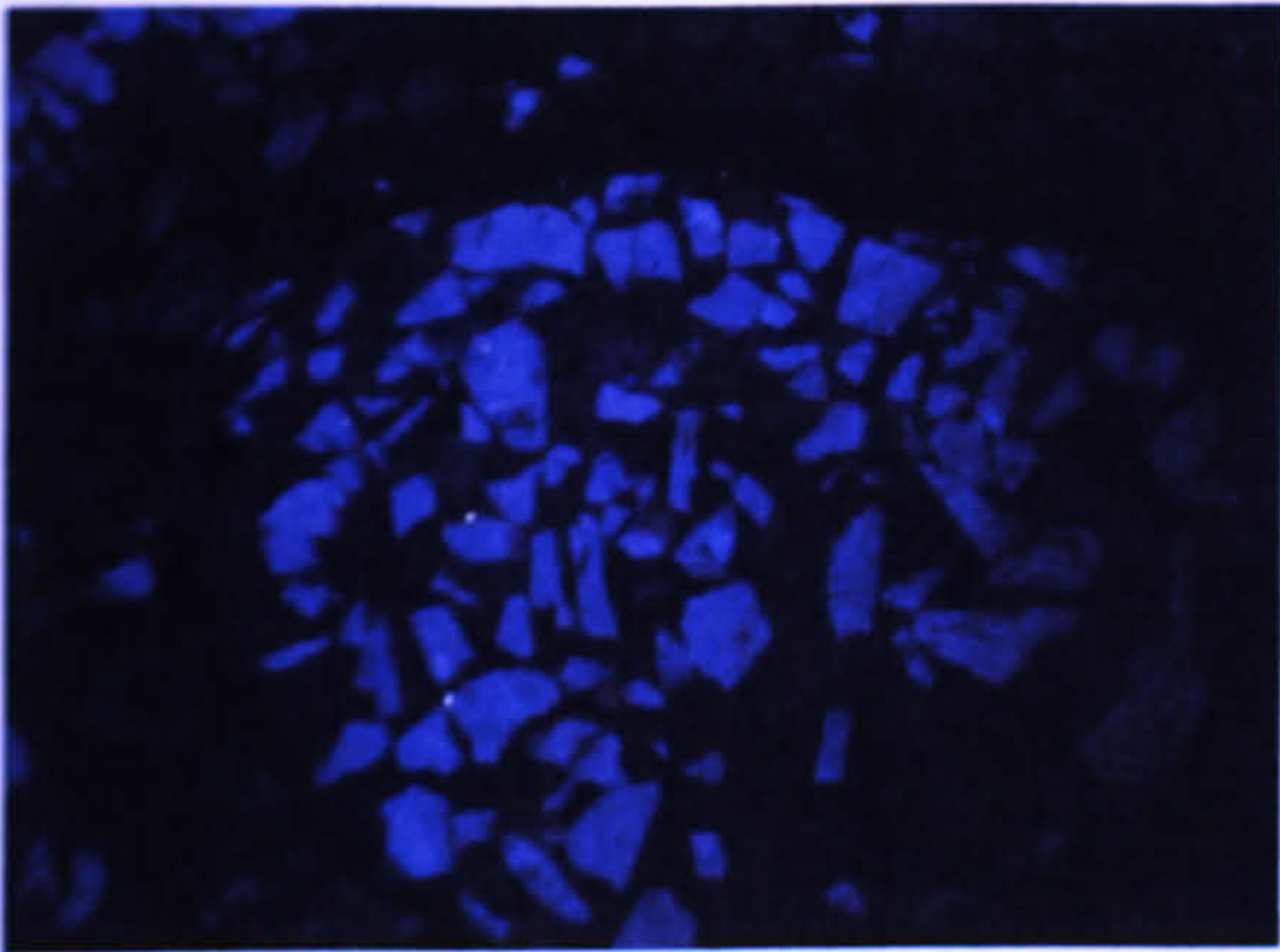
4.2.7.1.4 HF Acid Etched Shap Granite.



Feldspar chemical compositions



Backscattered electron SEM image (grain mount)

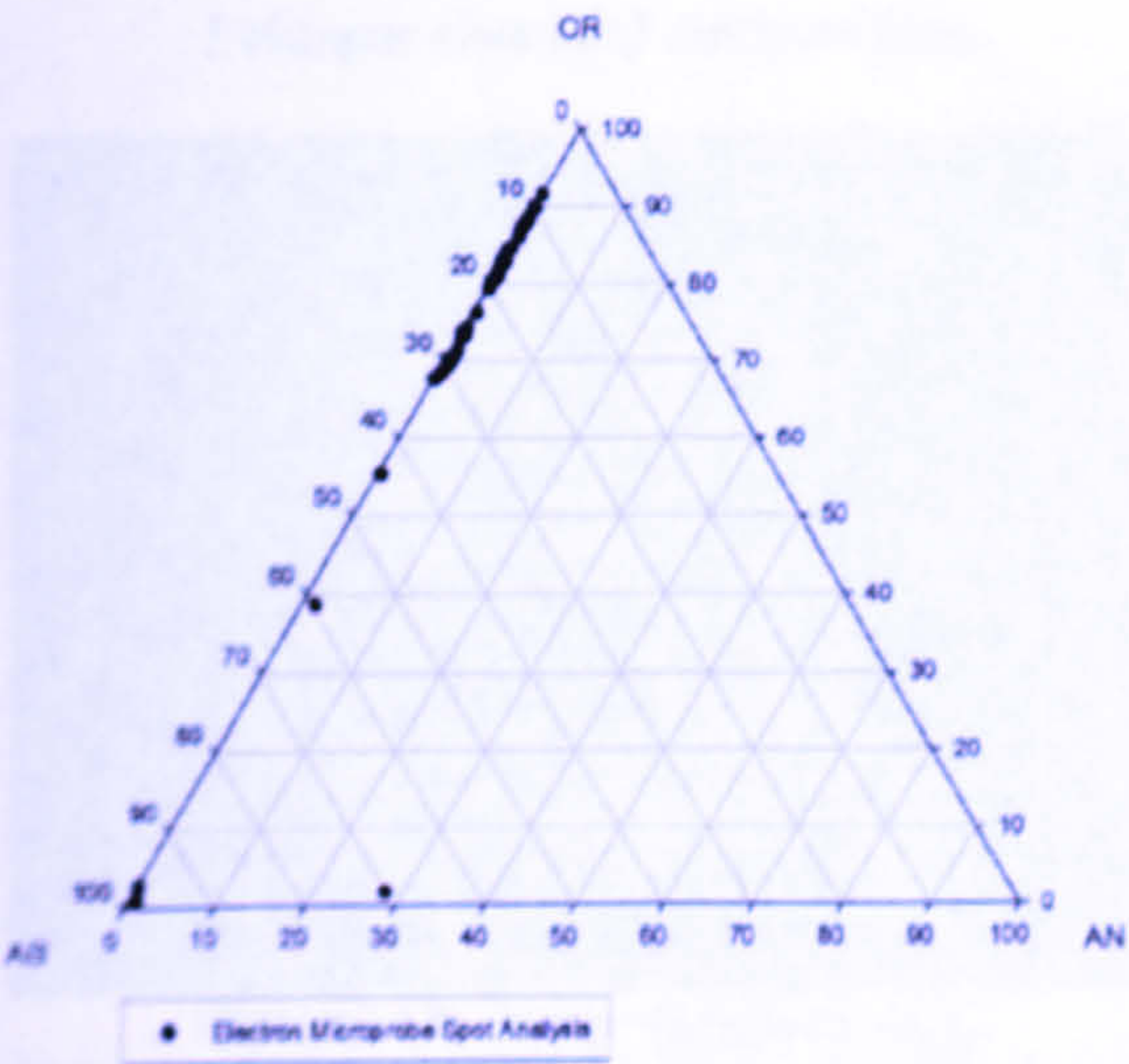


Optical CL image (grain mount)

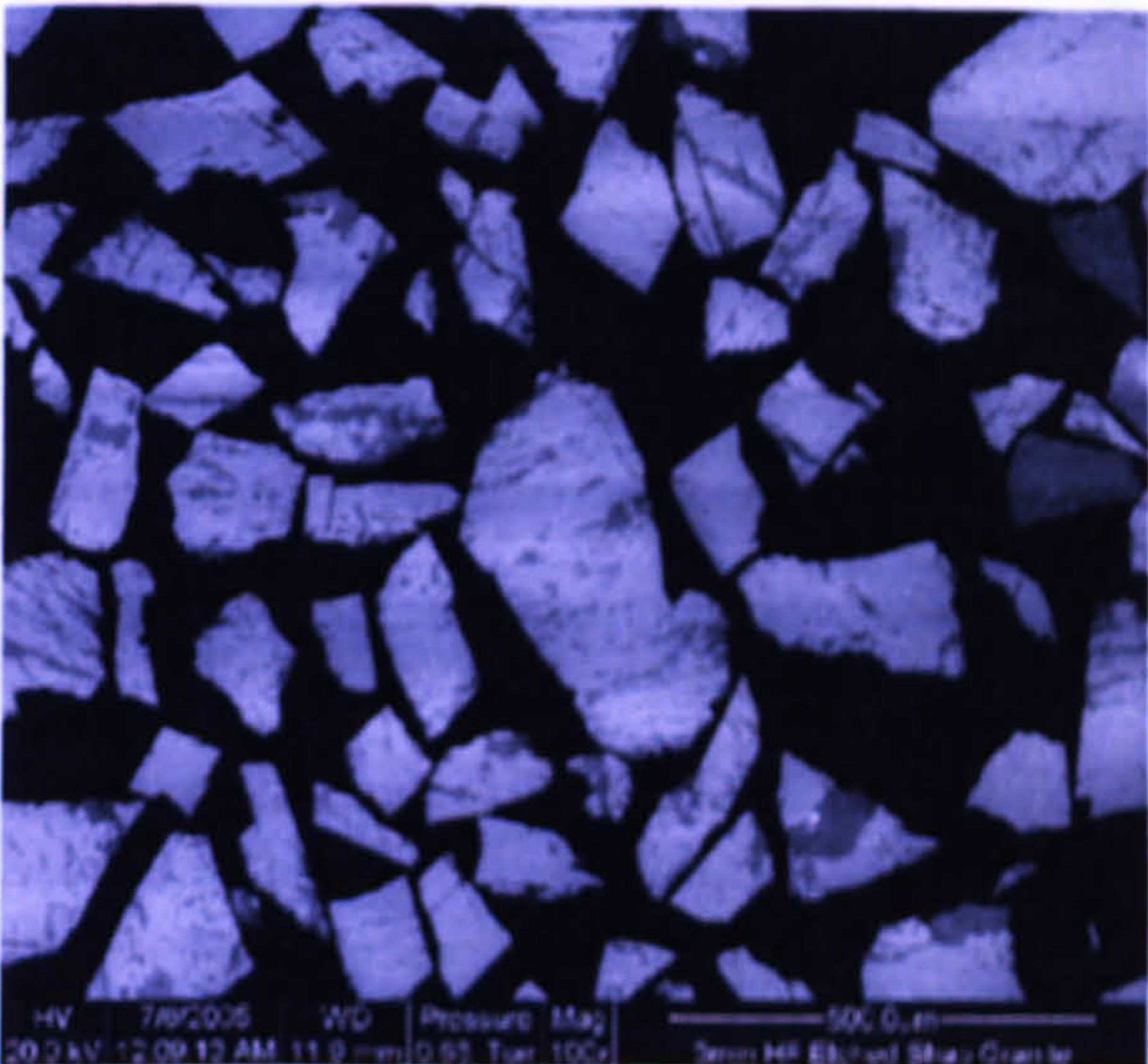
SPT fraction (g/cm ³)	Mineralogy
<2.62	A ₈₀₋₉₀ P ₅ Q ₅₋₁₅
2.52-2.58	---
2.58-2.62	---
2.62-2.74	---
>2.74	---
Not SPT separated	---

Mineralogy of the density fractions

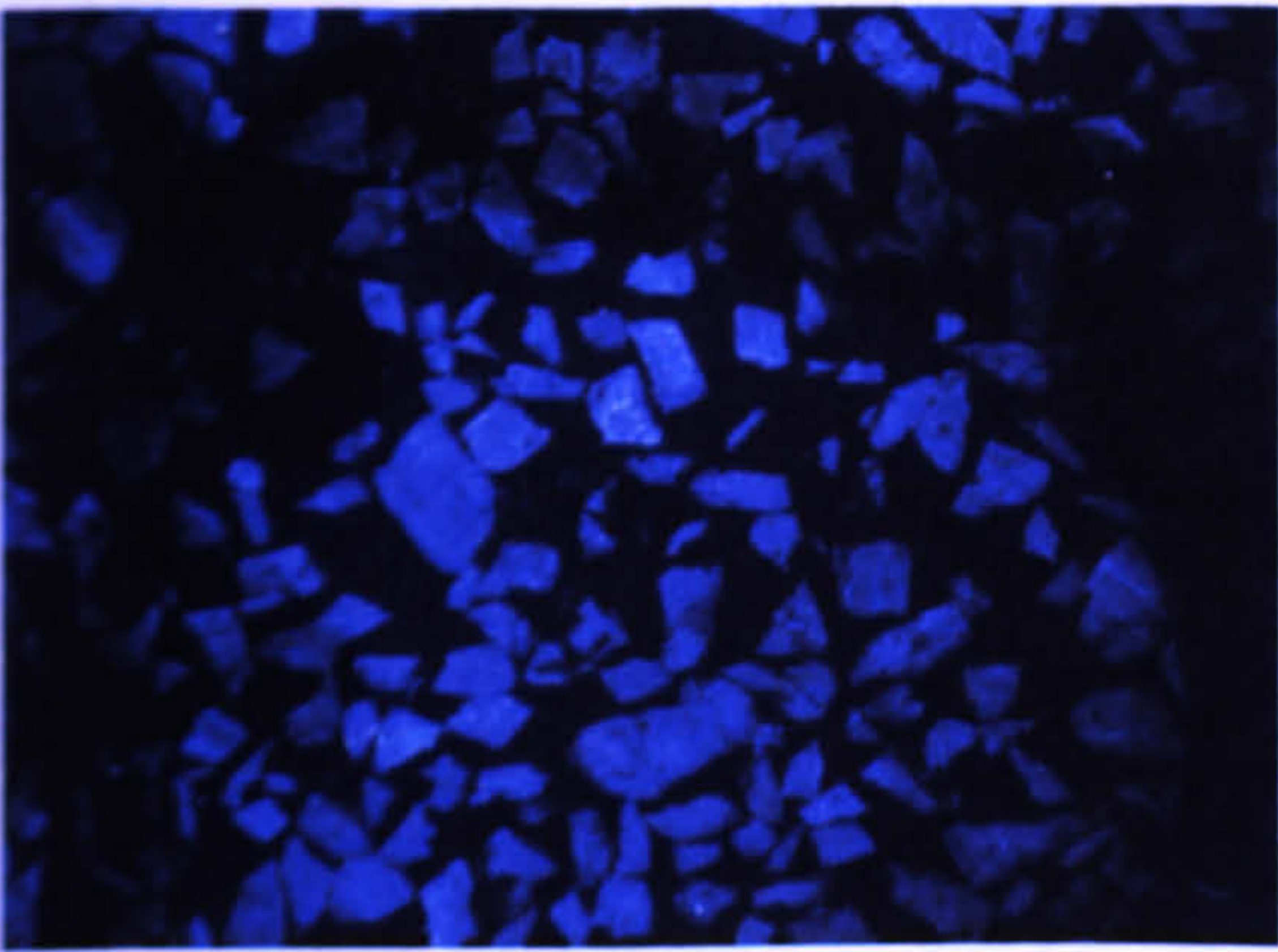
Figure 4.15. Mineralogy, microtexture and composition of 1 minute HF acid etched Shap granite feldspars.



Feldspar chemical compositions



Backscattered electron SEM image (grain mount)



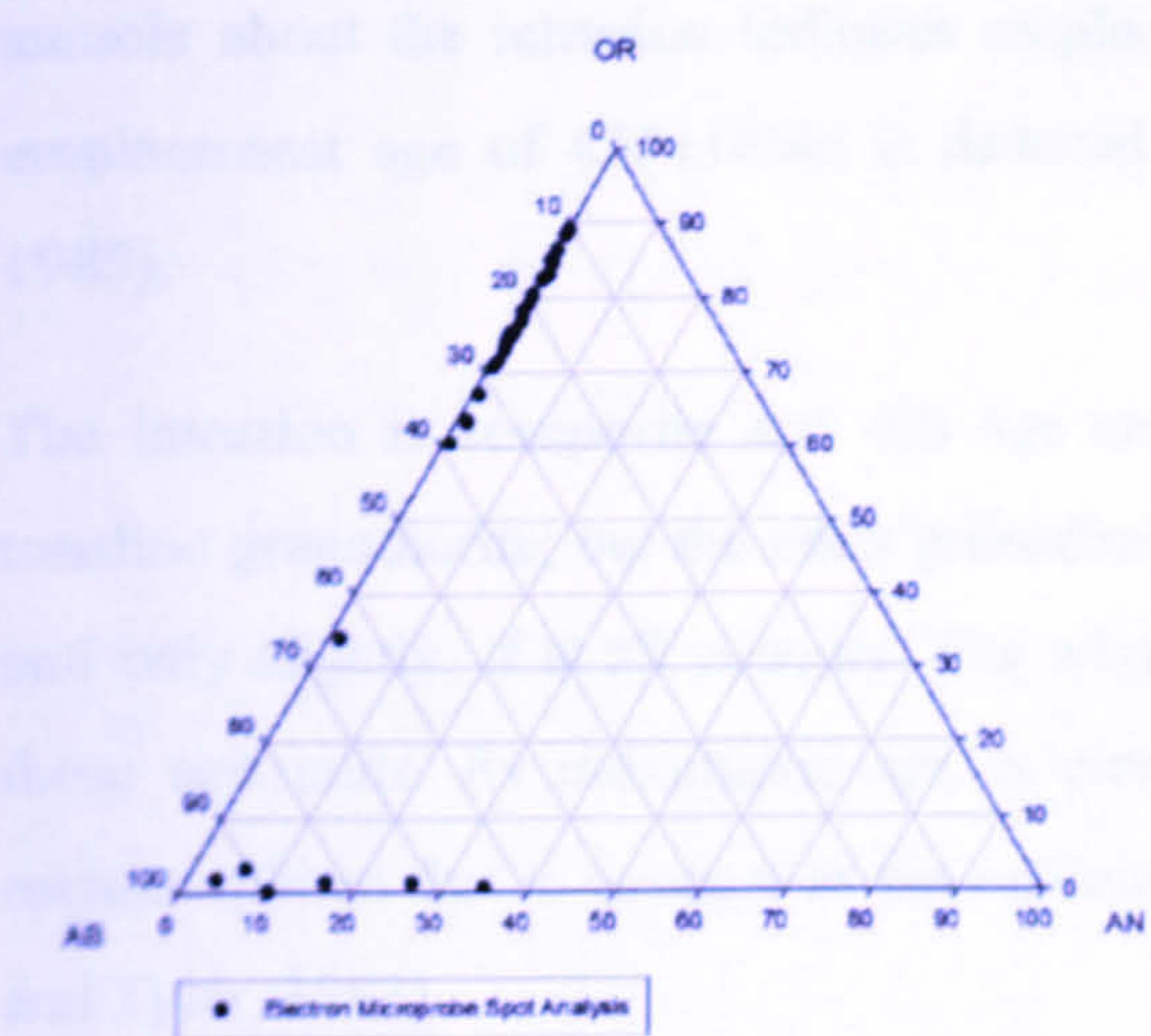
Optical CL image (grain mount)

SPT fraction (g/cm ³)	Mineralogy
<2.62	A ₈₀₋₉₀ P ₅ Q ₅₋₁₅
2.52-2.58	---
2.58-2.62	---
2.62-2.74	---
>2.74	---
Not SPT separated	---

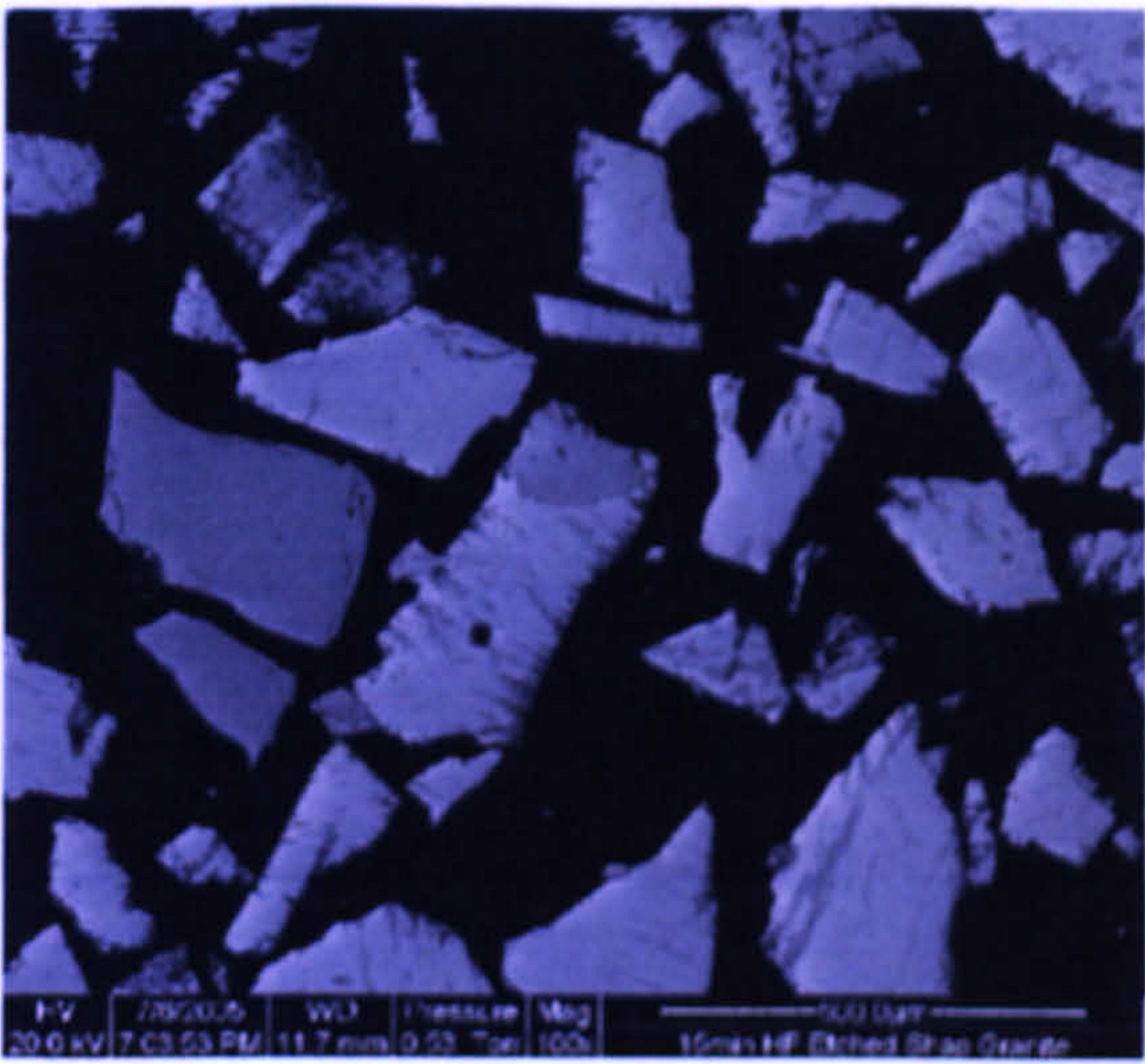
Mineralogy of the density fractions

Figure 4.16. Mineralogy, microtexture and composition of 3 minute HF acid etched Shap granite feldspars.

The country rocks into which the granite was emplaced are a combination of the mafic gabbro, with a history of Permo-Triassic magmatic-hydrothermal modification (Ashworth and Tyler, 1983). The effect of the Caledonian high δ subvolcanism around it is below 467±20Ma. Around 300Ma, the country rock was largely made up of a fine-grained granite about the same as the granite in the gabbro.



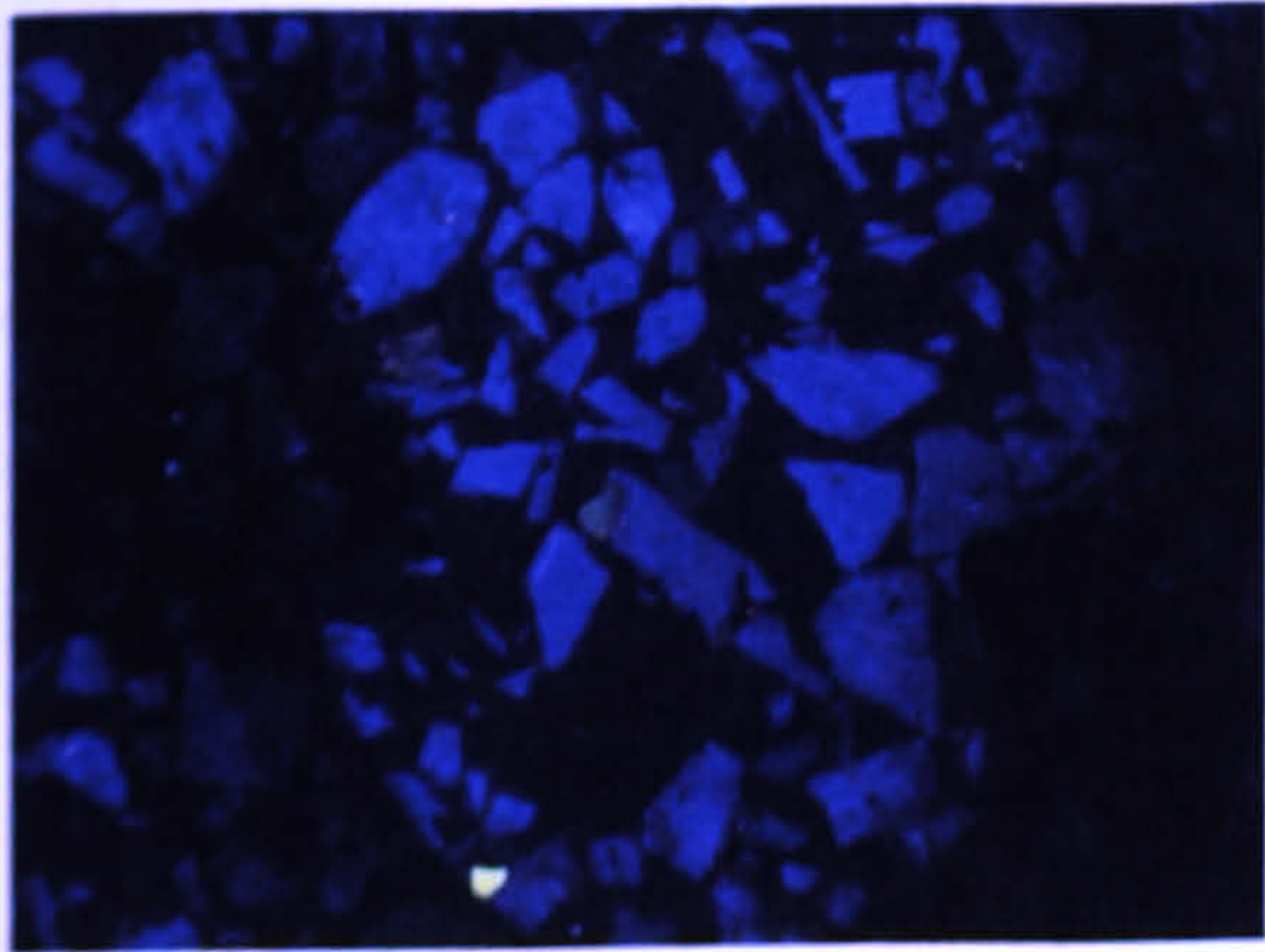
Feldspar chemical compositions



Backscattered electron SEM image (grain mount)

SPT fraction (g/cm ³)	Mineralogy
<2.62	A ₈₀₋₉₀ P ₅ Q ₅₋₁₅
2.52-2.58	---
2.58-2.62	---
2.62-2.74	---
>2.74	---
Not SPT separated	---

Mineralogy of the density fractions



Optical CL image (grain mount)

Figure 4.17. Mineralogy, microtexture and composition of 15 minute HF acid etched Shap granite feldspars.

Feldspars from all of the HF acid etched samples have the same chemical, microtextural and mineralogical properties as those from the fresh and unweathered samples. Only one of the powders used for luminescence measurements was X-ray mapped to determine its mineralogy, but results show that in common with the other Shap samples the $<2.62 \text{ g/cm}^3$ fraction is relatively pure alkali feldspar.

4.2.8 Strontian Granodiorite (H8).

The Strontian Granodiorite is another of the 'Newer Granites' and was emplaced during the Caledonian orogeny. This intrusion has a significant metamorphic aureole that is asymmetric, with broader zones to the east of the intrusion compared to the west.

The country rocks into which the granodiorite was emplaced are metasediments of the western Moine, with a history of Precambrian as well as Caledonian regional metamorphism (Ashworth and Tyler, 1983). The climax of the Caledonian regional metamorphism occurred at or before $467 \pm 20 \text{ Ma}$. Around Strontian, this metamorphism was high grade and the lack of a hornfelsic aureole about the intrusion indicates emplacement while the rocks were still regionally hot. An emplacement age of $435 \pm 10 \text{ Ma}$ is deduced from U-Pb studies of zircon (Ashworth and Tyler, 1983).

The intrusion is composite and this age actually refers to just one unit – the outer tonalite or tonalitic granodiorite; but the other granodiorite unit, the porphyritic granodiorite, is closely related and only slightly, if at all younger. The whole of the northern part of the intrusion is made up of these two units. Its radiometric age is closely comparable with the closing stages of regional metamorphism that is younger in the western Moines than east of the Great Glen Fault (Ashworth and Tyler, 1983).

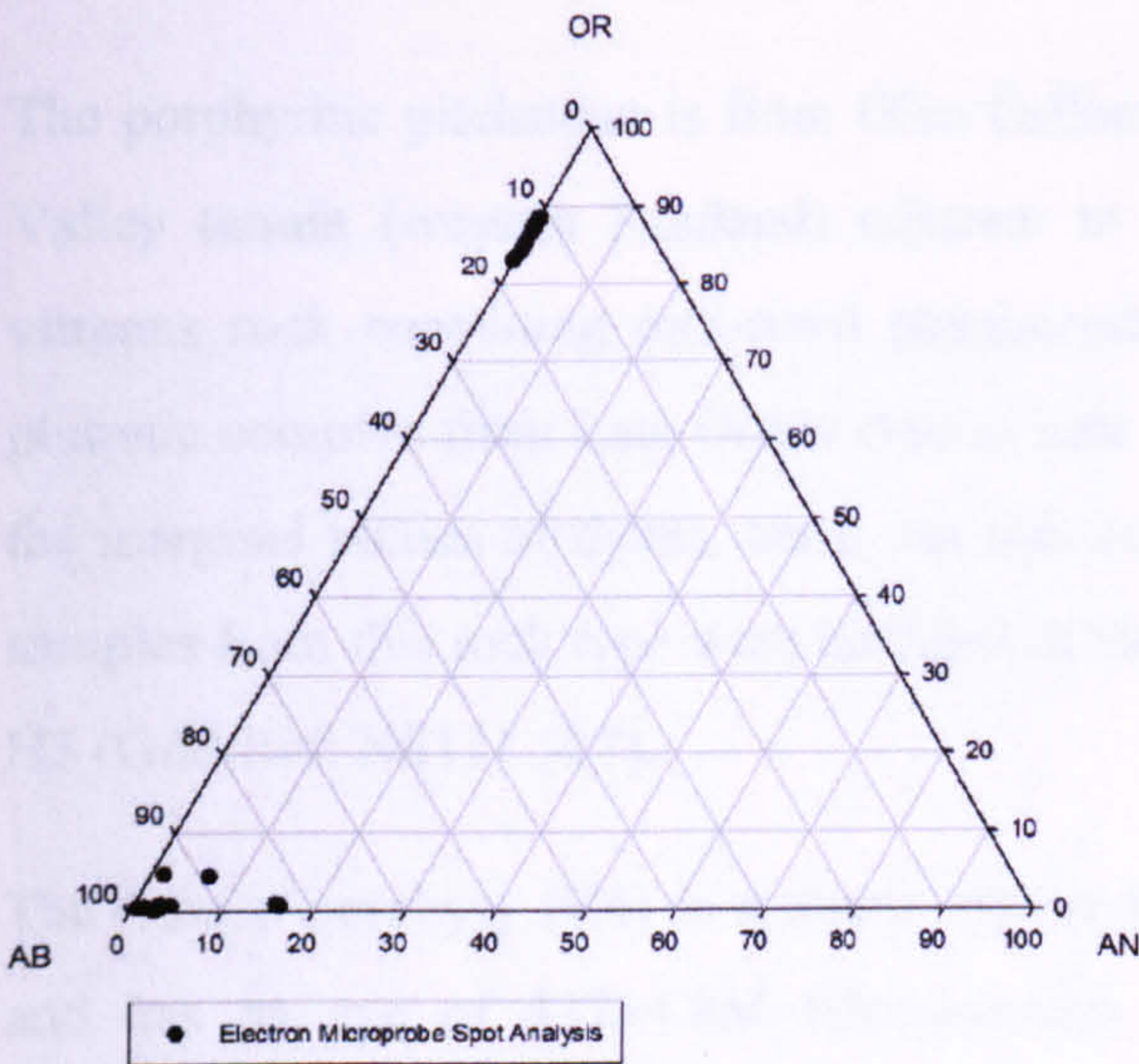
The outer contact of the granodiorite with the country rocks is sharp and consistently dips steeply inwards. Much of the intrusive body is foliated and lineated possibly as a result of deformation, due to expansion during its intrusion. These structures conform to a broad pattern without major discontinuities, suggesting that the intrusive event was a single continuous process.

Samples were supplied by John Faithfull (Glasgow University) and were collected from a road cut in Strontian, NW Scotland (Grid Ref: NM7612 5415). It has an internal reference number of H8.

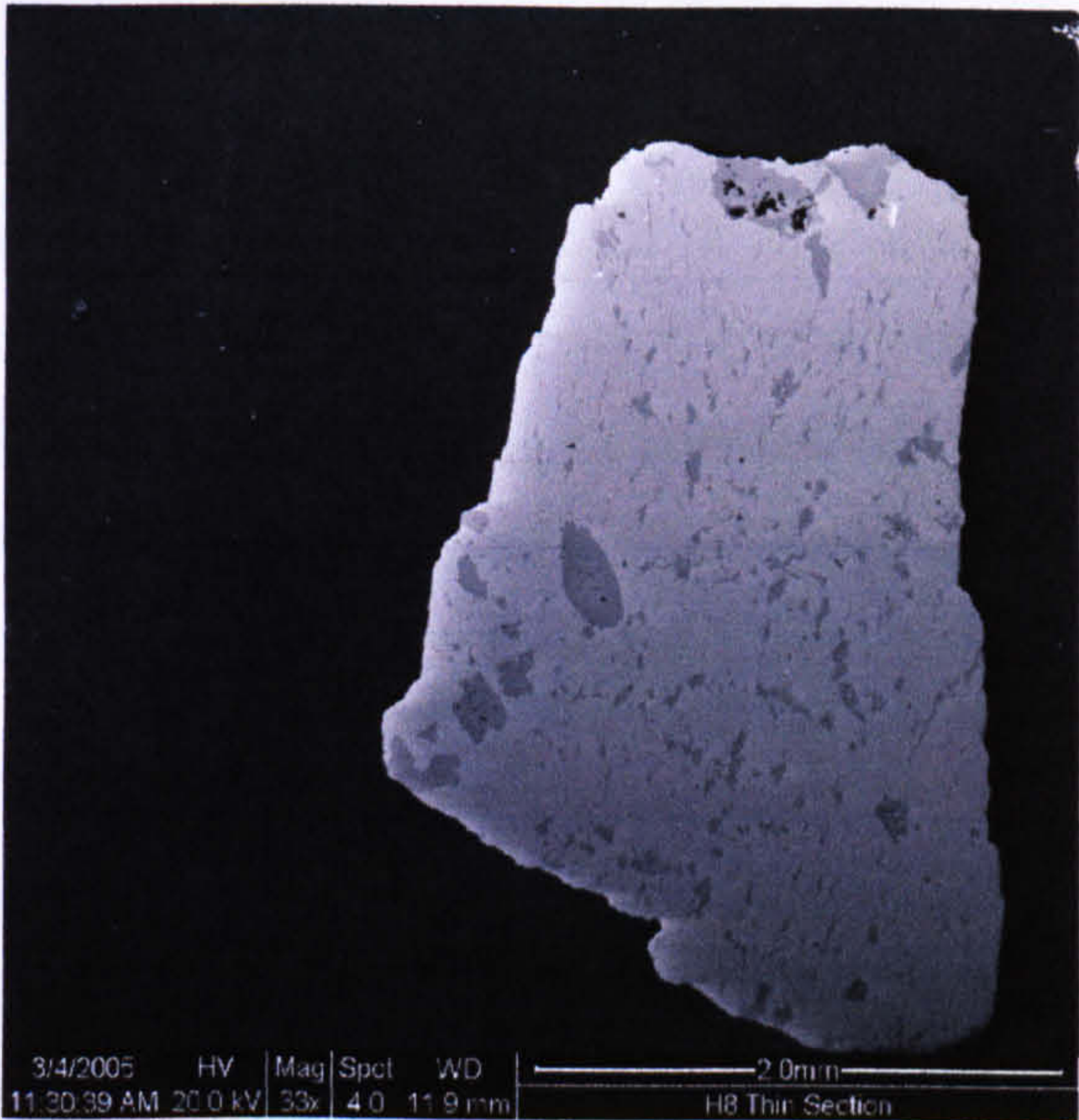
4.2.8.1.1 Feldspar Mineralogy, Microtexture and Composition.

Table 4.9. Strontian granodiorite feldspar chemical compositions (Mol%).

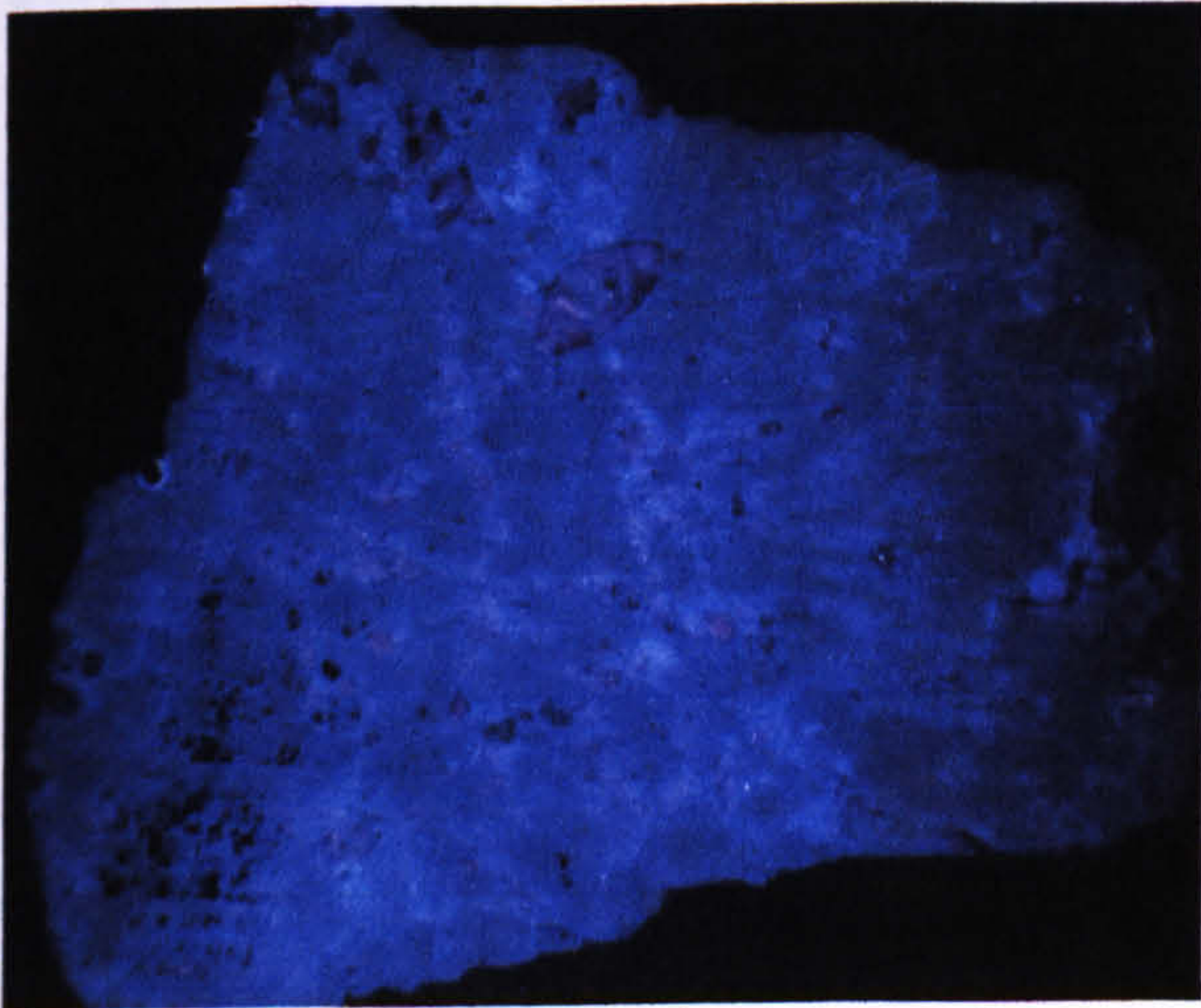
Sample	Alkali Feldspar			Free plagioclase feldspar		
	Ab	An	Or	Ab	An	Or
Strontian Granodiorite (H8)	14	0	86	94	5	1



Feldspar chemical compositions



Backscattered electron SEM image (grain mount)



Optical CL image (grain mount)

SPT fraction (g/cm ³)	Mineralogy
<2.62	---
2.52-2.58	---
2.58-2.62	---
2.62-2.74	A ₉₀ P ₁₀ Q ₀
>2.74	---
Not SPT separated	---

Mineralogy of the density fractions

Figure 4.18. Mineralogy, microtexture and composition of Strontian granodiorite feldspars (H8).

The alkali feldspars are microperthites containing fine patches of red luminescing plagioclase within the bright blue luminescing orthoclase. Unusually, the alkali feldspar has been concentrated in the 2.62-2.74 g/cm³ SPT fraction, but nonetheless the separation from quartz and plagioclase feldspar has been effective.

4.3 Silicic Minor Igneous Intrusions.

This group comprises three samples, two from a porphyritic pitchstone (H2 and H3) and one from a quartz-syenite sill (H4). The importance of these samples for the present study is that they have an acidic composition, but unlike the large igneous intrusions (granites and granodiorites) have cooled relatively rapidly owing to their small size; together these samples therefore may enable the influence on feldspar luminescence and fading rates of crystallization temperature (i.e. similar in the acidic granite and minor intrusions) to be distinguished from cooling rate (much faster in the minor intrusions than the granite).

The porphyritic pitchstone is from Glen Callum in Bute in the north-western area of the Midland Valley terrain (western Scotland) adjacent to the Highland Boundary Fault. It is a dark grey vitreous rock containing mm-sized phenocrysts of feldspar. This area was part of a volcanic-plutonic complex from Late Ordovician to Late Silurian. Pitchstone is usually found in dykes or in the marginal phases of dykes, but it can also occur as thick intrusive sheets as seen on Eigg. Two samples from this rock type were included in the study, designated H2 (Grid Ref: NS111 527) and H3 (Grid Ref: NS111 527).

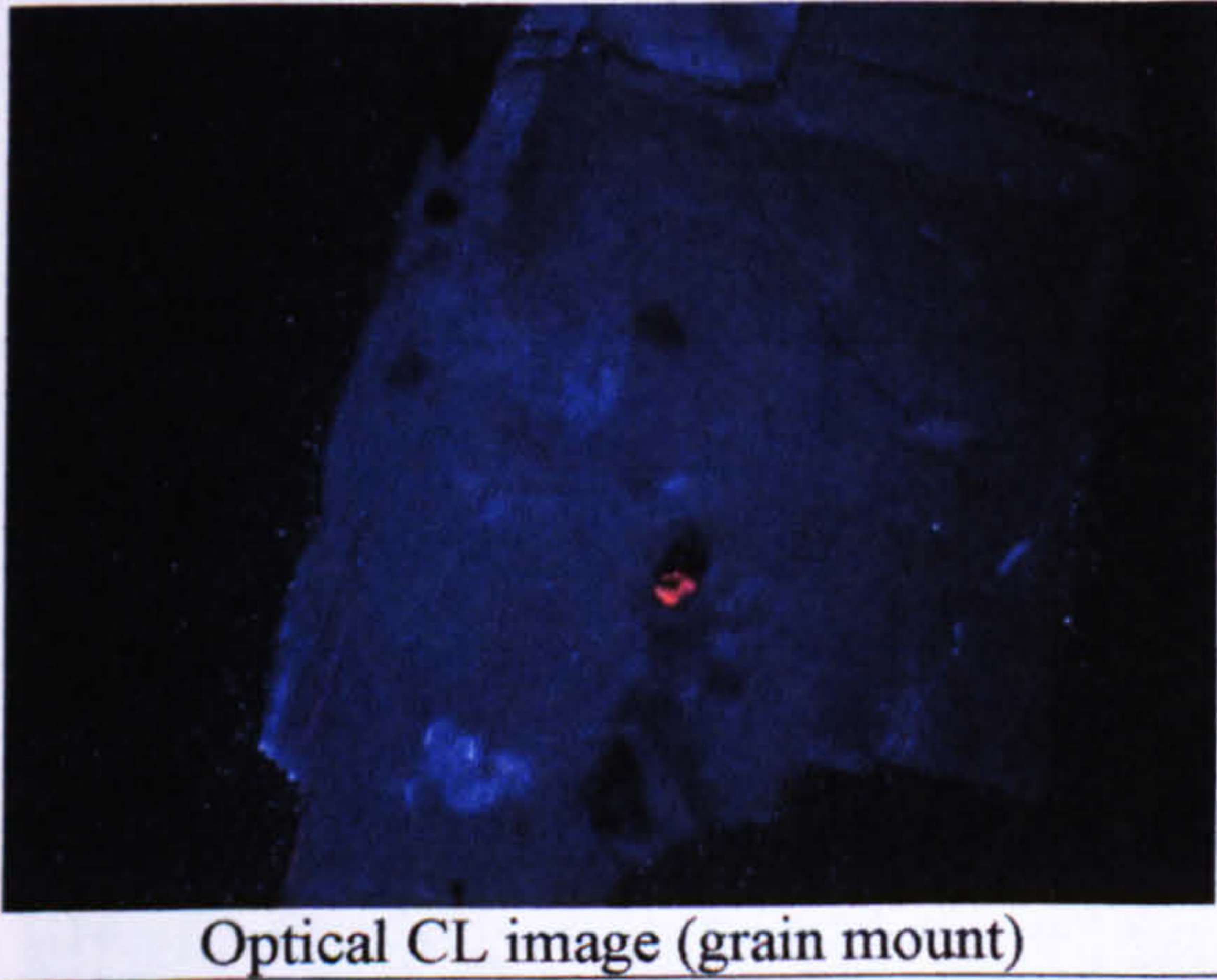
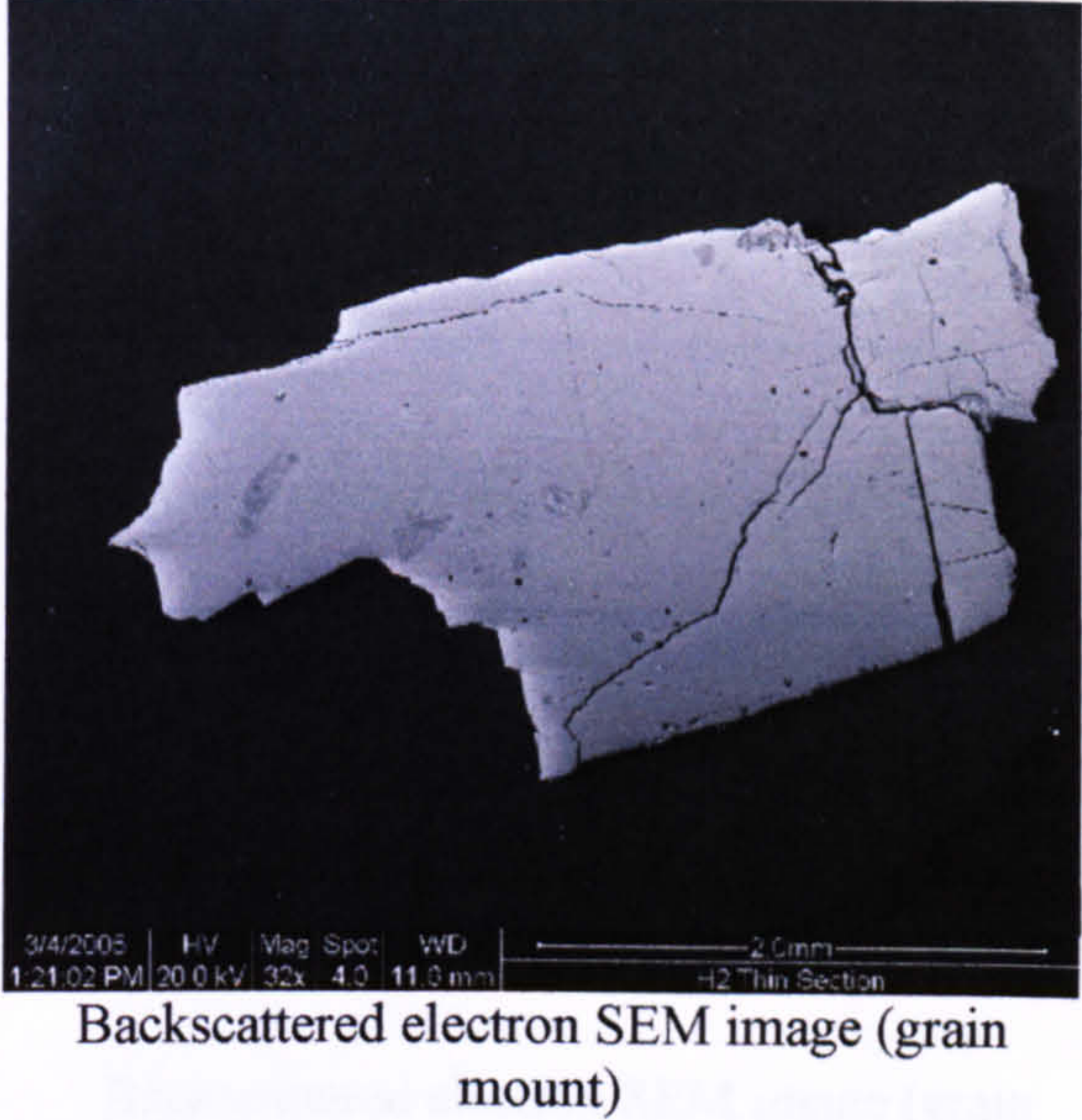
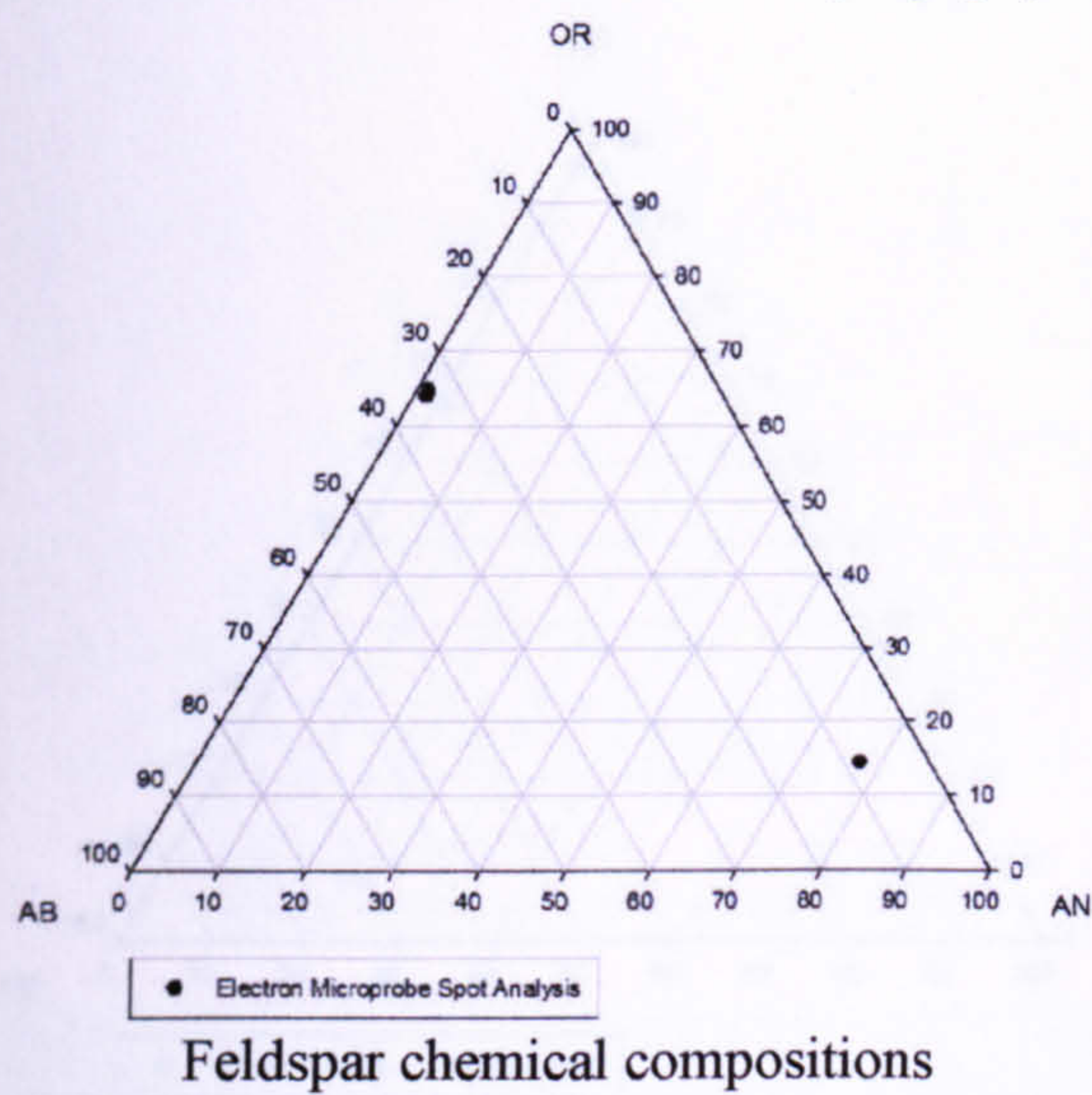
The Canisp porphyry (H4) is a quartz syenite that contains distinctive large feldspar phenocrysts and has an age of 437 ± 4.8 M (Goodenough *et al.*, 2006). The porphyry forms sills within unmetamorphosed Torridonian and Cambrian sedimentary rocks. Material for this study was provided by John Faithfull (Glasgow University) from a weathered exposure on the summit of Canisp in Assynt (Grid Ref: NC203 187).

4.3.1 Feldspar Mineralogy, Microtexture and Composition.

Table 4.10. Chemical composition of pitchstone porphyry feldspars (Mol%).

Samples	Alkali Feldspar			Free plagioclase feldspar		
	Ab	An	Or	Ab	An	Or
Pitchstone porphyry (H2)	34	2	64	8	77	15
Weathered pitchstone porphyry (H3)	32	1	67	8	71	21
Weathered orthoclase, Canisp (H4)	33	0	67	97	2.5	0.5

4.3.1.1 Bute Pitchstone Porphyry (H2).



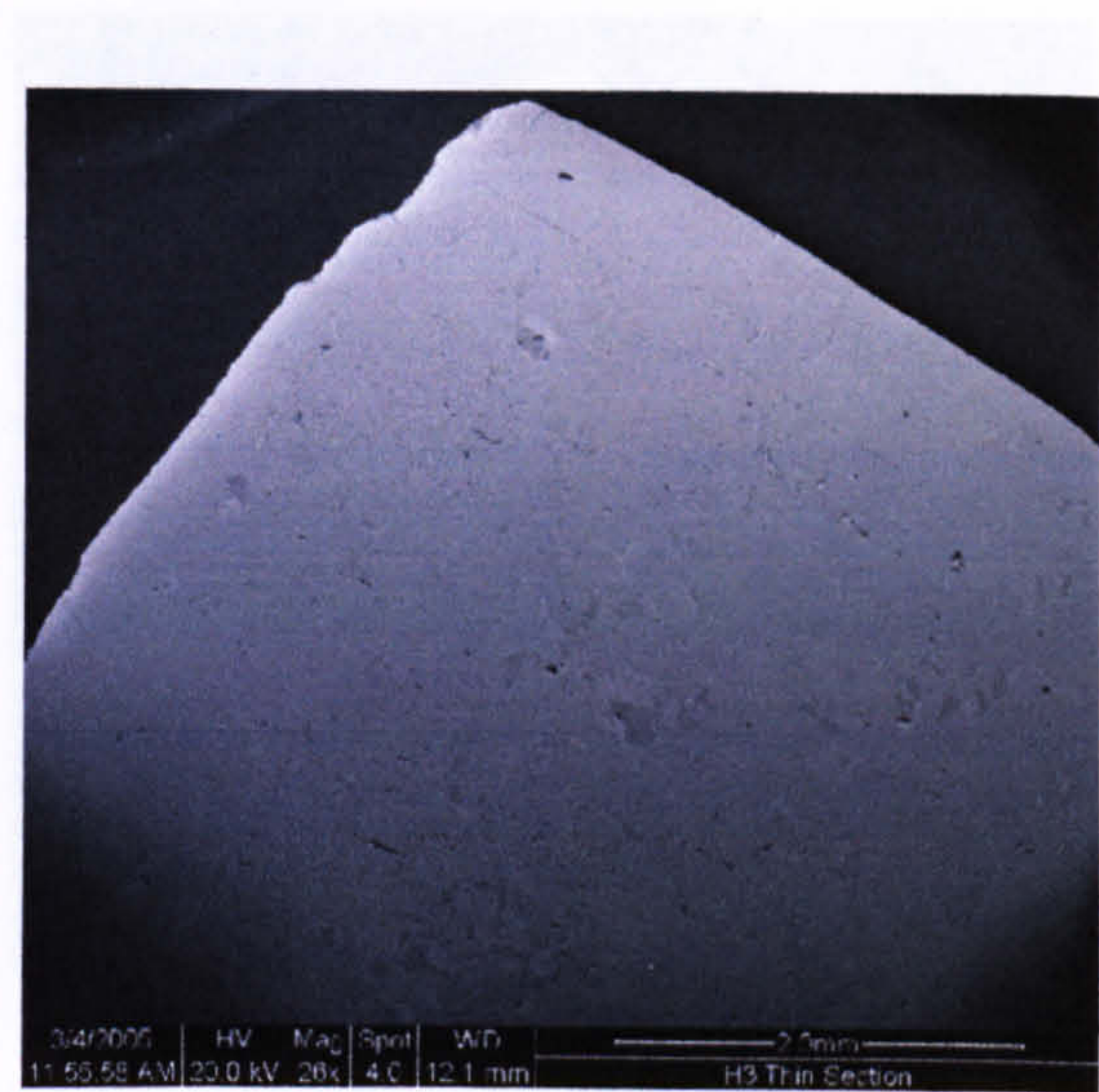
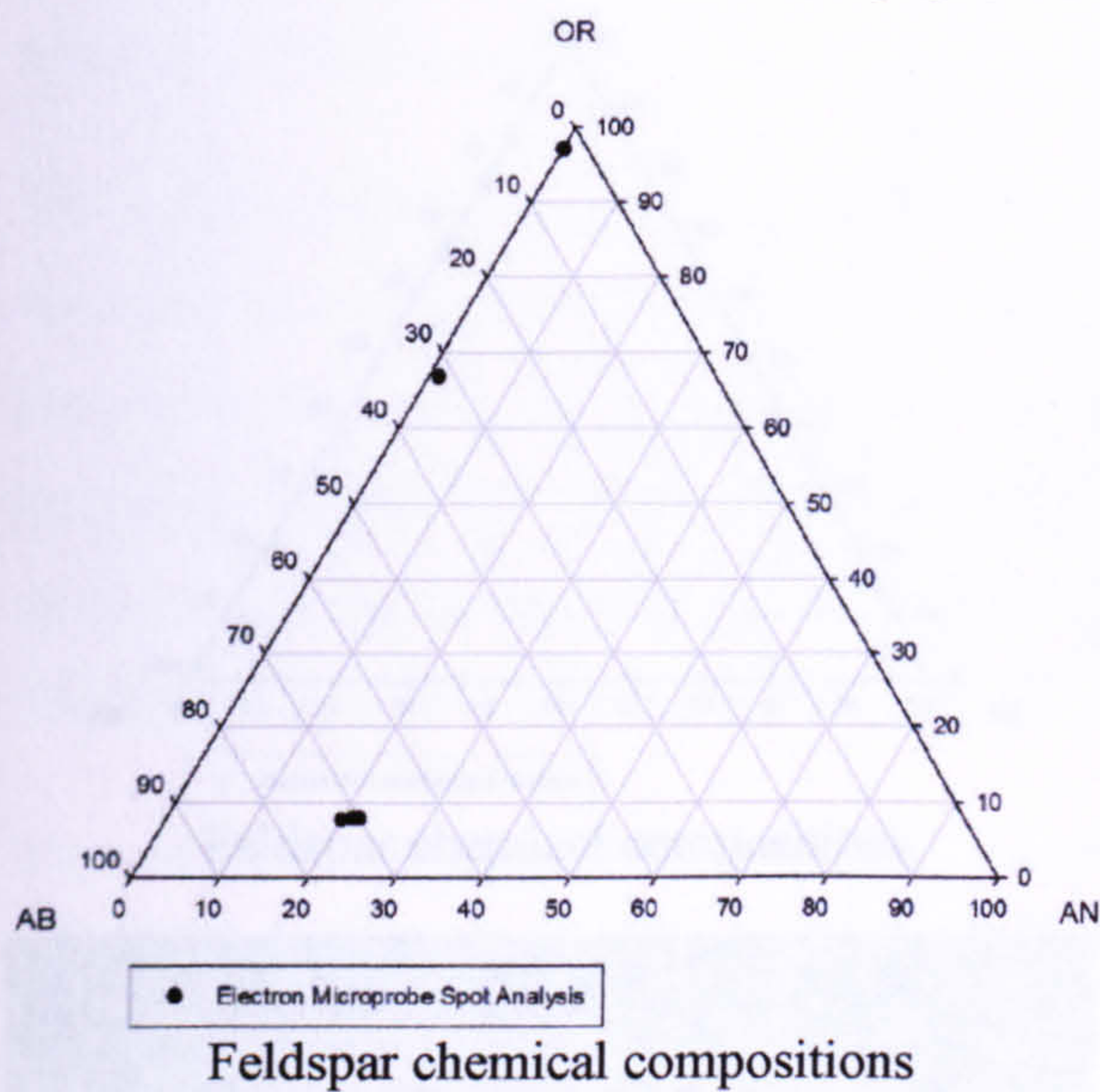
SPT fraction (g/cm ³)	Mineralogy
<2.62	---
2.52-2.58	---
2.58-2.62	---
2.62-2.74	A ₀ P ₅₀ Q ₅₀
>2.74	---
Not SPT separated	---

Mineralogy of the density fractions

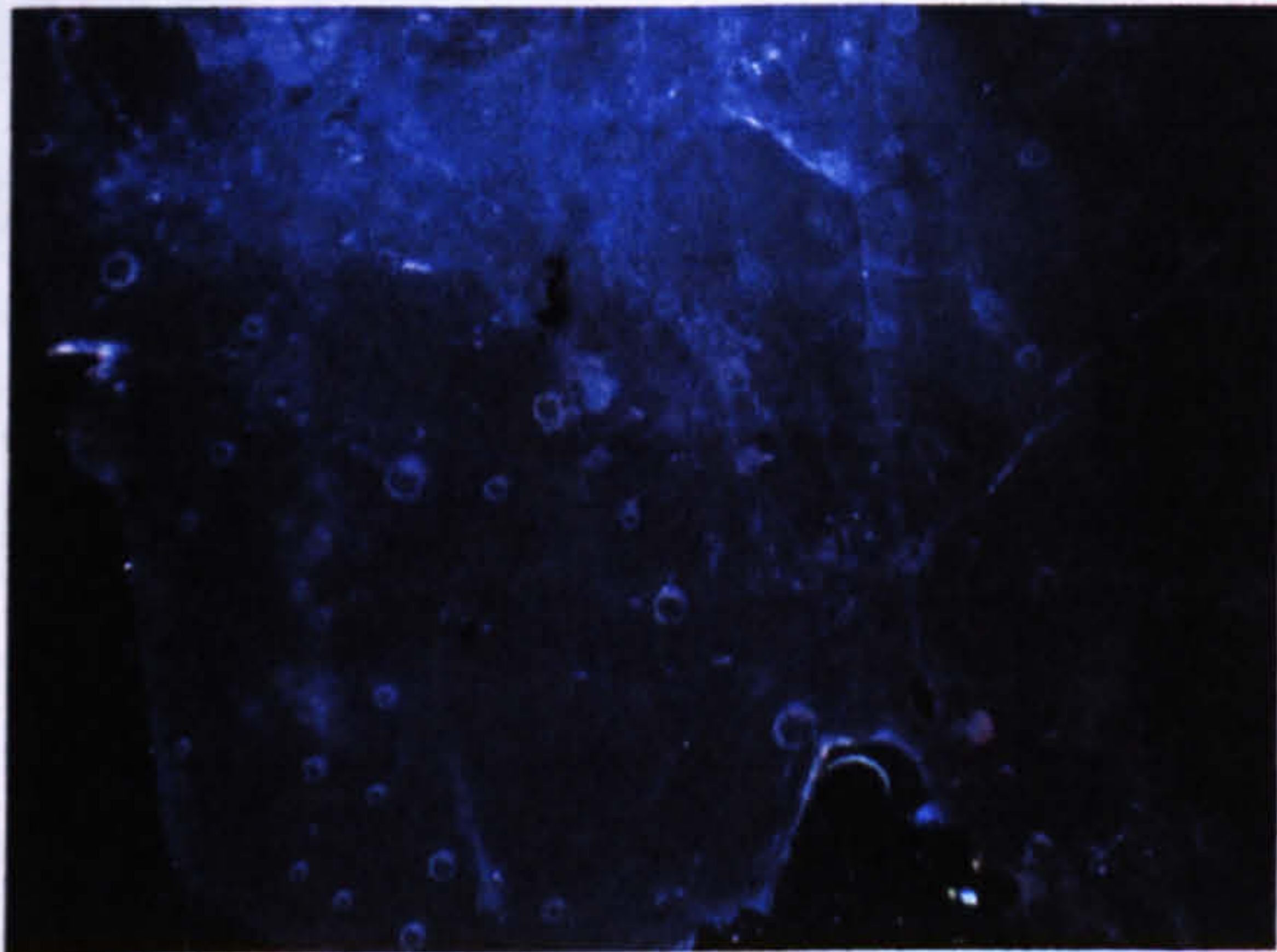
Figure 4.19. Mineralogy, microtexture and composition of pitchstone porphyry feldspars (H2).

The alkali feldspar is a blue luminescing orthoclase with no obvious exsolution lamellae but a strongly developed oscillatory zoning in CL. Small inclusions of plagioclase are anorthite-rich. Note that despite the abundance of alkali feldspar in the grain mount, SPT separation retained the quartz and plagioclase. There was insufficient alkali dominated SPT fraction produced to dispense multiple aliquots for measurements.

4.3.1.2 Bute Pitchstone Porphyry (H3).



Backscattered electron SEM image (grain mount)



Optical CL image (grain mount)

SPT fraction (g/cm ³)	Mineralogy
<2.62	---
2.52-2.58	---
2.58-2.62	A ₅₀ P ₅₀ Q ₀
2.62-2.74	---
>2.74	---
Not SPT separated	---

Mineralogy of the density fractions

Figure 4.20. Mineralogy, microtexture and composition of weathered Pitchstone porphyry feldspars (H3).

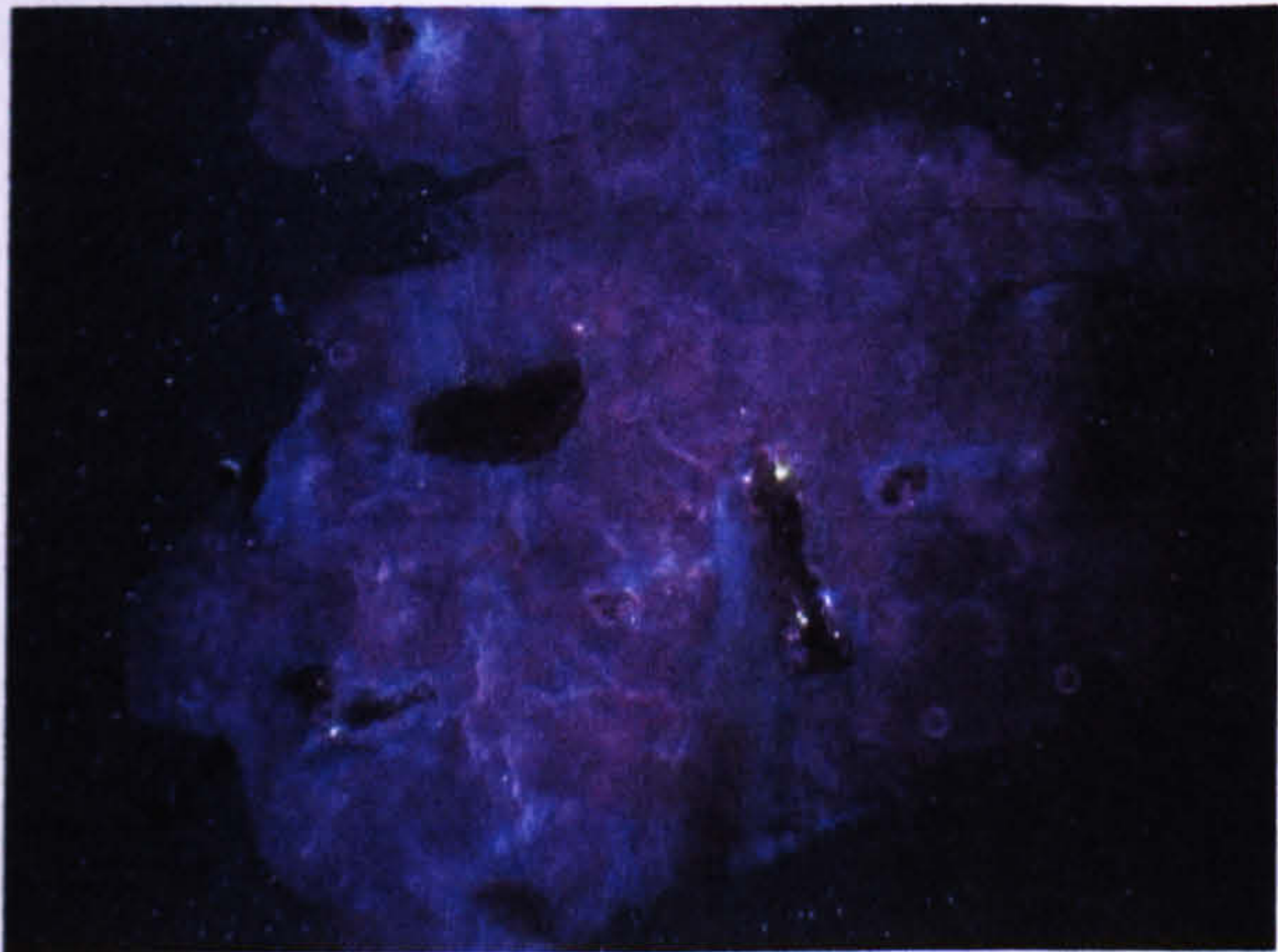
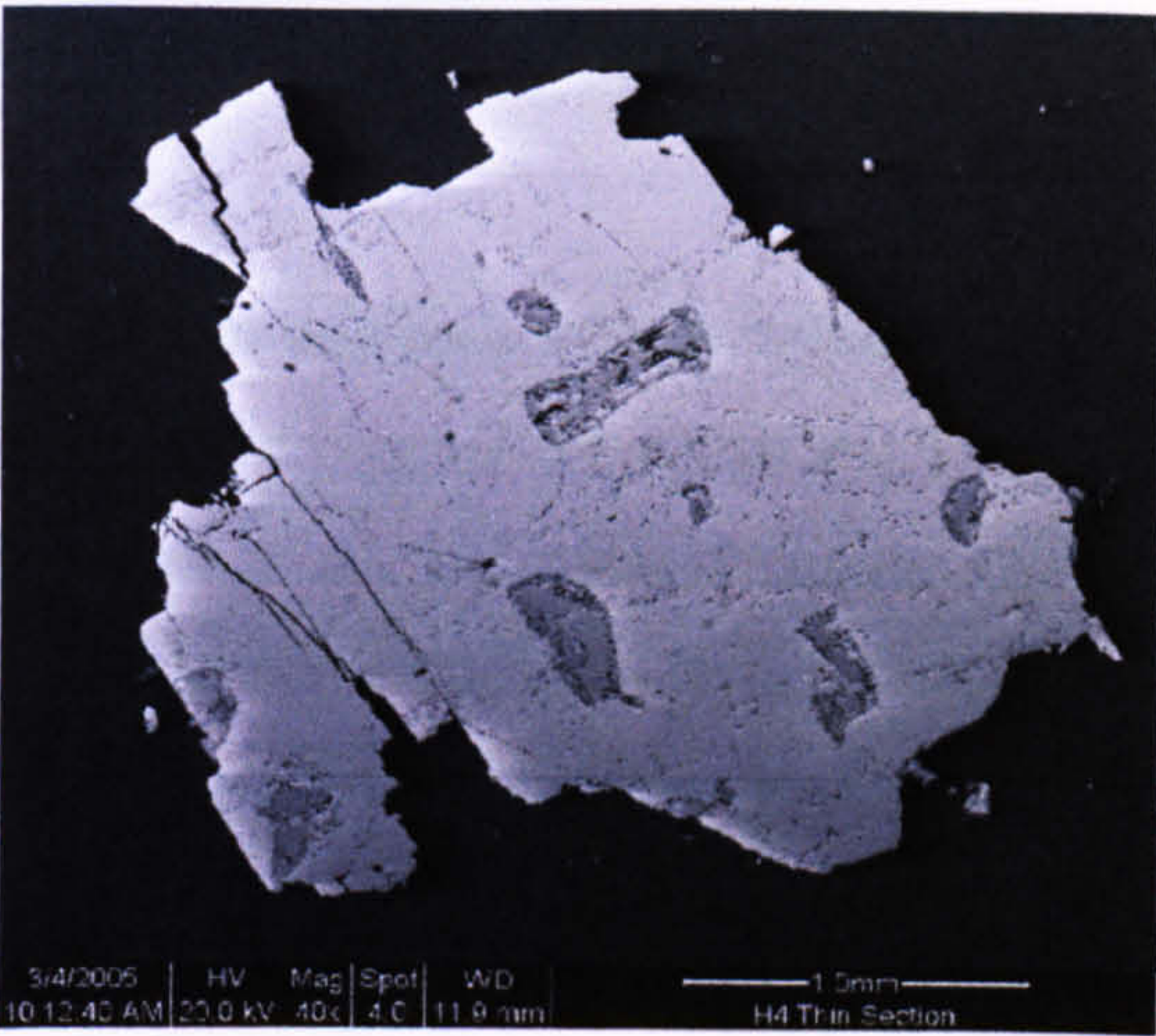
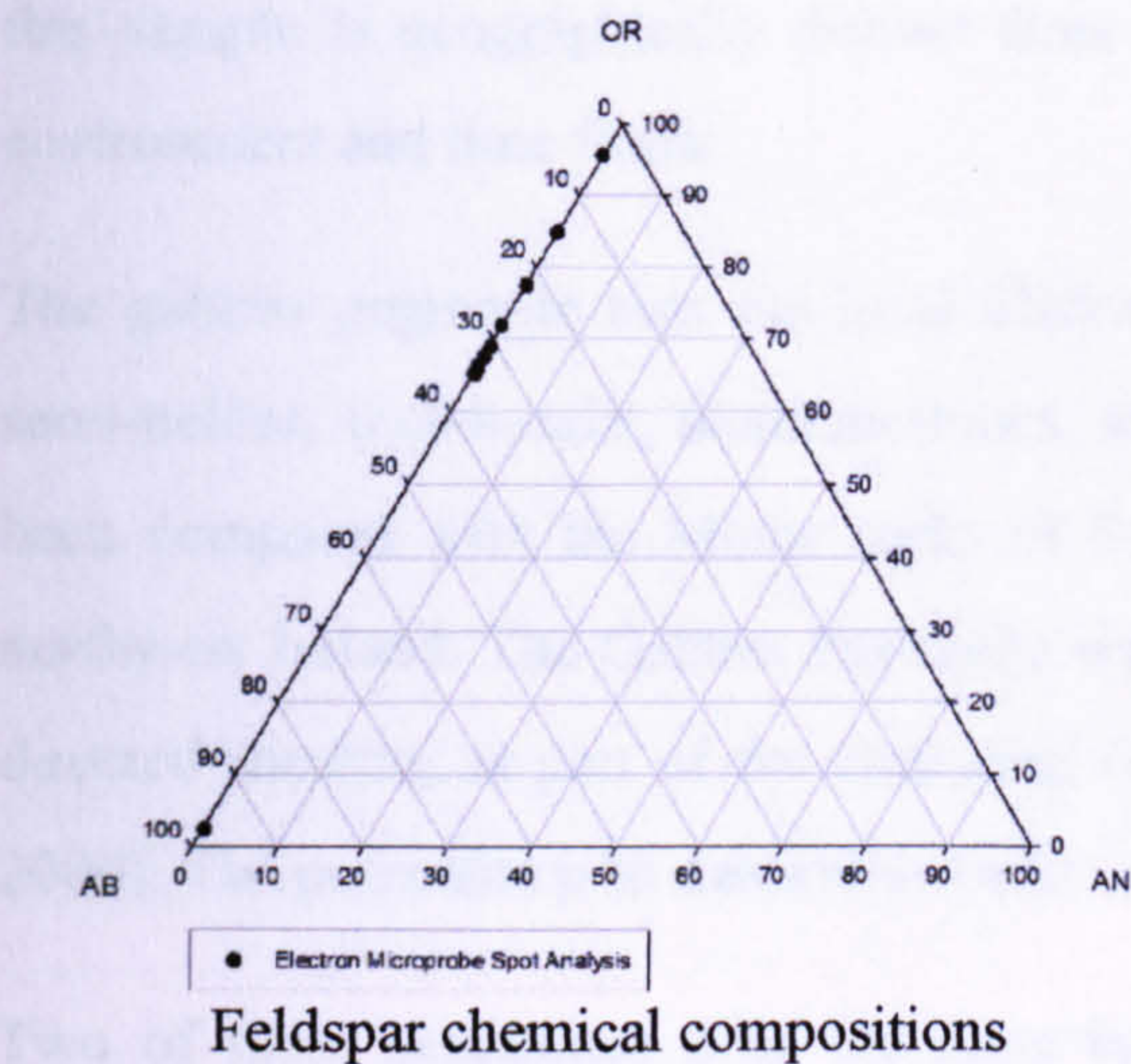
This sample is compositionally and microtexturally comparable to the alkali feldspars of the other pitchstone porphyry (H2). Again, despite the abundance of alkali feldspar line in the H2 grain mount most of the grains in the powder are plagioclase. Canisp Porphyry (H4).

4.4.1 Coonapitok Camp, Nunavut (H1)

The sample is from a small, isolated, and relatively recent volcanic field.

Major deformation and metamorphism is not present.

The Deformation is not well developed and is not well defined.



SPT fraction (g/cm ³)	Mineralogy
<2.62	---
2.52-2.58	---
2.58-2.62	A ₉₅ P ₀ Q ₅
2.62-2.74	A ₀ P ₅₀ Q ₅₀
>2.74	---
Not SPT separated	---

Optical CL image (grain mount)

Mineralogy of the density fractions

Figure 4.21. Mineralogy, microtexture and composition of feldspars from the Canisp porphyry (H4).

The alkali feldspar is a non-perthitic orthoclase with an unusual purple emission in CL. Inclusions of free plagioclase (albite) luminesce a dark red. The SPT separated fractions have isolated alkali feldspars effectively in the less dense fraction but the denser fraction is unrepresentative of the material as a whole.

4.4 Igneous Calcic Plagioclase.

In order to cover the full compositional range of the group of feldspars in this study, a suite of calcic (i.e., An-rich) plagioclase feldspars were studied. These are from a number of different igneous and related rock types.

4.4.1 Connemara Gabbro Pegmatite (H1).

This sample is from Ireland’s Grampian Orogenic Belt (Sample Locality: 53:33:59N, 9:55:20W). Major deformation and metamorphism under greenschist to amphibolite facies conditions affected the Dalradian rocks of northwestern Ireland and Scotland in the Caledonian orogeny. Even though

this sample is geographically distinct from the Scottish localities it is from a similar geological environment and time frame.

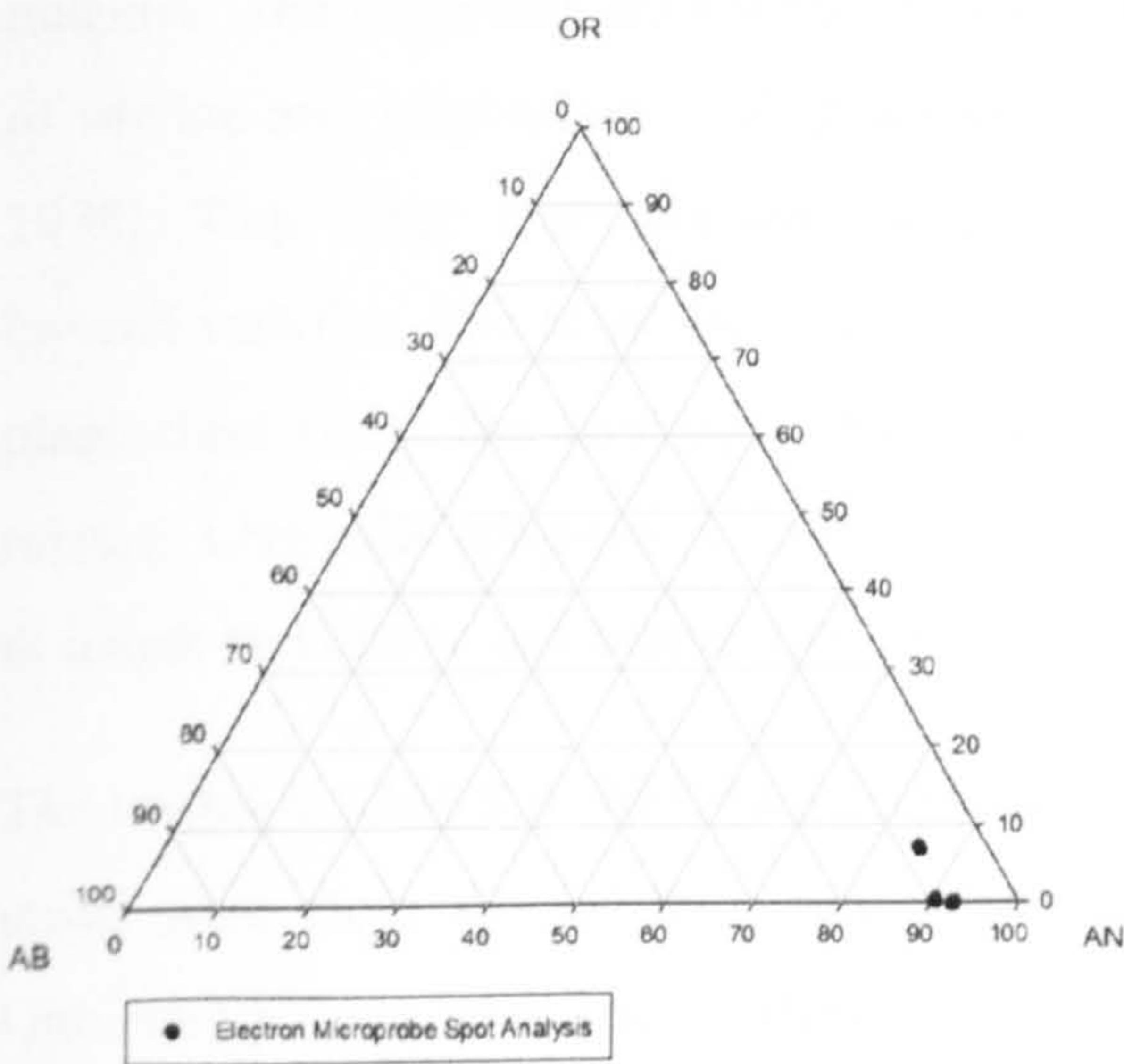
The gabbro pegmatite cuts the local Sliswood Division, a sequence of psammites with minor semi-pelites, metabasalts, metalimestones, serpentinites, and metagranitoid intrusions. These have been compared with the Moine rocks of Scotland as well as the Dalradian Grampian Group in northwest Ireland. The Gabbro Pegmatite was juxtaposed with the Dalradian during south-easterly directed shearing as part of the Grampian Orogeny D3 phase of deformation. (Flowerdew *et al.*, 2000). The pegmatite post dates this event.

Two of these pegmatites from the same locality yield Rb-Sr muscovite ages of ~460Ma. It is possible that all the pegmatites are syn-orogenic and yield the same age but their use as deformation time-markers could be misleading as it is possible that they form more than one intrusive suite. Possible sources of this pegmatite material include the Annagh Gneiss Complex, Dalradian Metasediments, Rhinns Complex and the surrounding Sliswood Division.

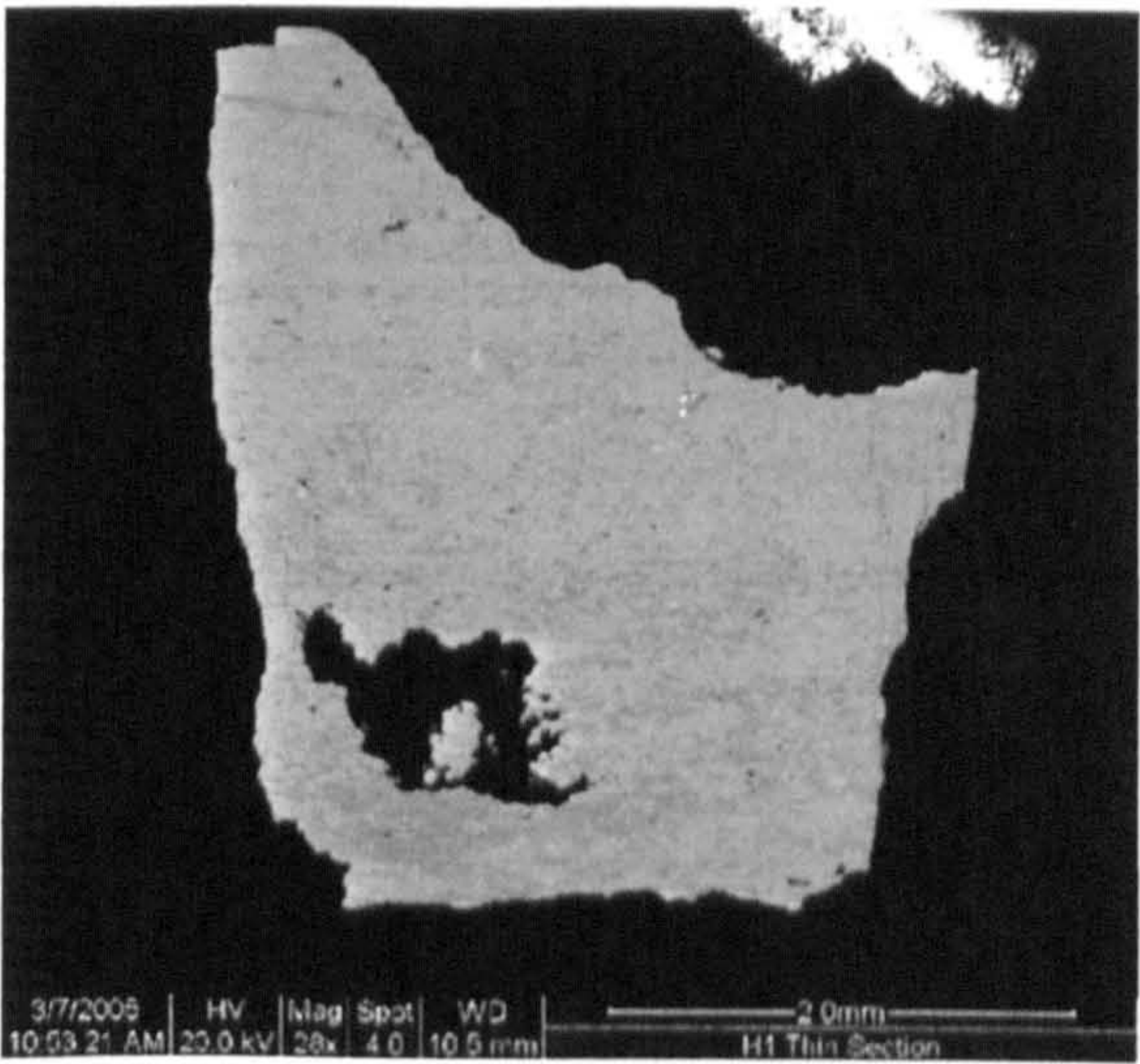
4.4.1.1 Feldspar Mineralogy, Microtexture and Composition.

Table 4.11. Chemical composition of the gabbro pegmatite feldspar (Mol%).

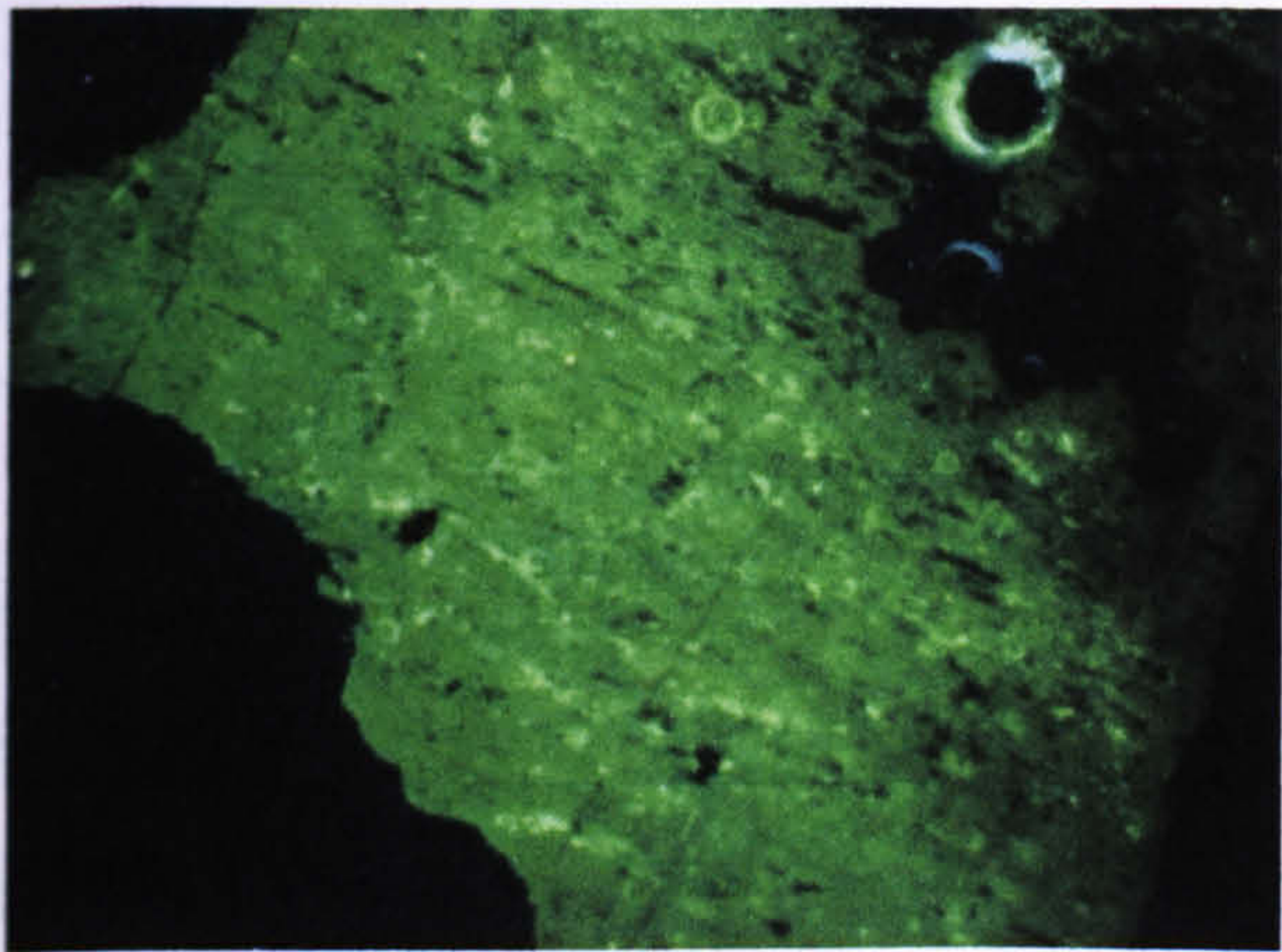
Sample	Alkali Feldspars			Free plagioclase feldspars		
	Ab	An	Or	Ab	An	Or
Gabbro pegmatite (H1)	---	---	---	10	90	0



Feldspar chemical compositions



Backscattered electron SEM image (grain mount)



Optical CL image (grain mount)

SPT fraction (g/cm ³)	Mineralogy
<2.62	---
2.52-2.58	---
2.58-2.62	---
2.62-2.74	---
>2.74	A ₀ P ₁₀₀ Q ₀
Not SPT separated	---

Mineralogy of the density fractions

Figure 4.22. Mineralogy, microtexture and composition of gabbro pegmatite feldspars (H1).

This feldspar is a bright green luminescing plagioclase feldspar. The backscattered electron image reveals compositional heterogeneity on the sub-hundred micron scale, although it has separated to a pure plagioclase sample.

4.4.2 Troctolite Pegmatite and Anorthosite from Hallival (units 1-5), Rum.

The Eastern Layered Series (Daniels *et al.*, 1953) of the Palaeocene (~60 Ma) Rum ultrabasic complex is composed of alternating thick layers of peridotite and feldspar-rich allivulate with subsidiary anorthosite and minor chromite (Bedard *et al.*, 1988). Allivulate is a local term for conformable feldspathic rocks such as troctolite and gabbro. It has been argued that the microlayering resulted from alternating injections of magma that are differentiated at depth. It is believed that the repetition of these layers was the periodic replenishment or basalt or picritic magmas. The troctolites are homogenous and typically contain approximately cotectic proportions of olivine and plagioclase, with pyroxene constituting less than 7% of the node (Bedard *et al.*, 1988). They range from massive equigranular, to massive laminated, to strongly rhythmically layered varieties. The foliation is usually deformed by the preferred orientation of layered-parallel plagioclase laths. The layering is deformed by variations in grain size, mineral proportions and texture. Lenticular schileron of anorthosite to leuco-troctolite are generally few tens of centimetres in length and one or two centimetres thick, though they can be larger locally.

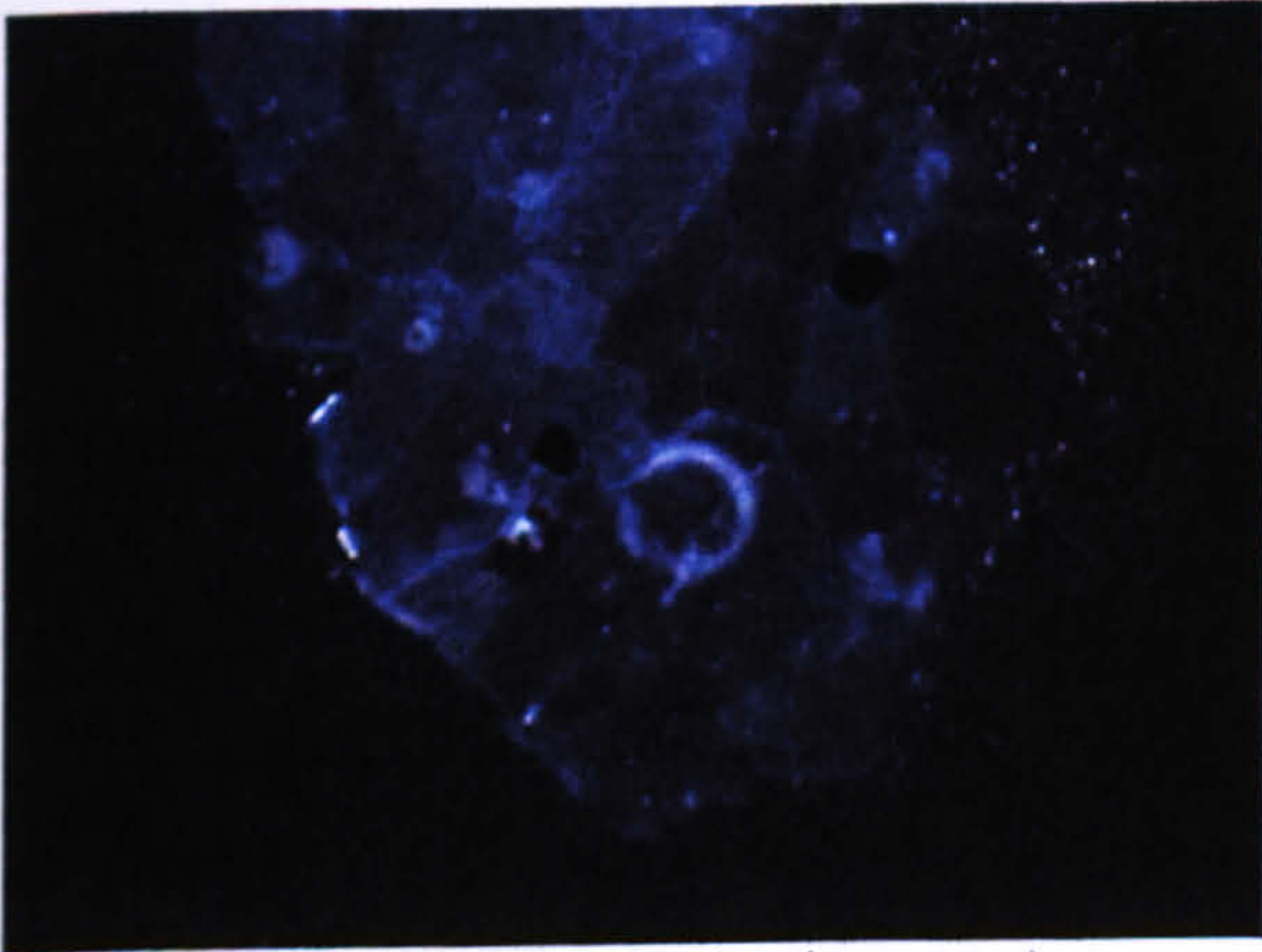
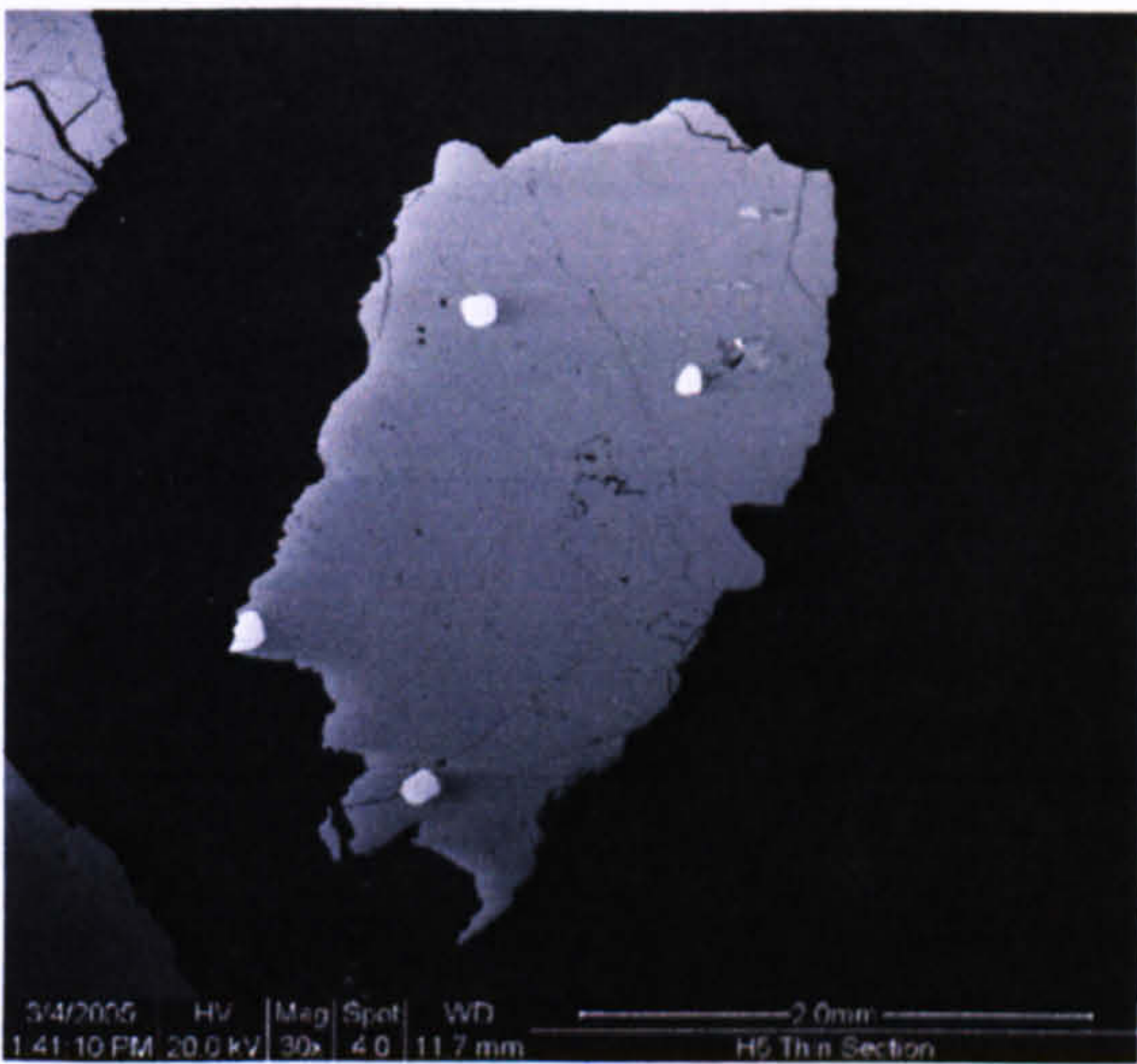
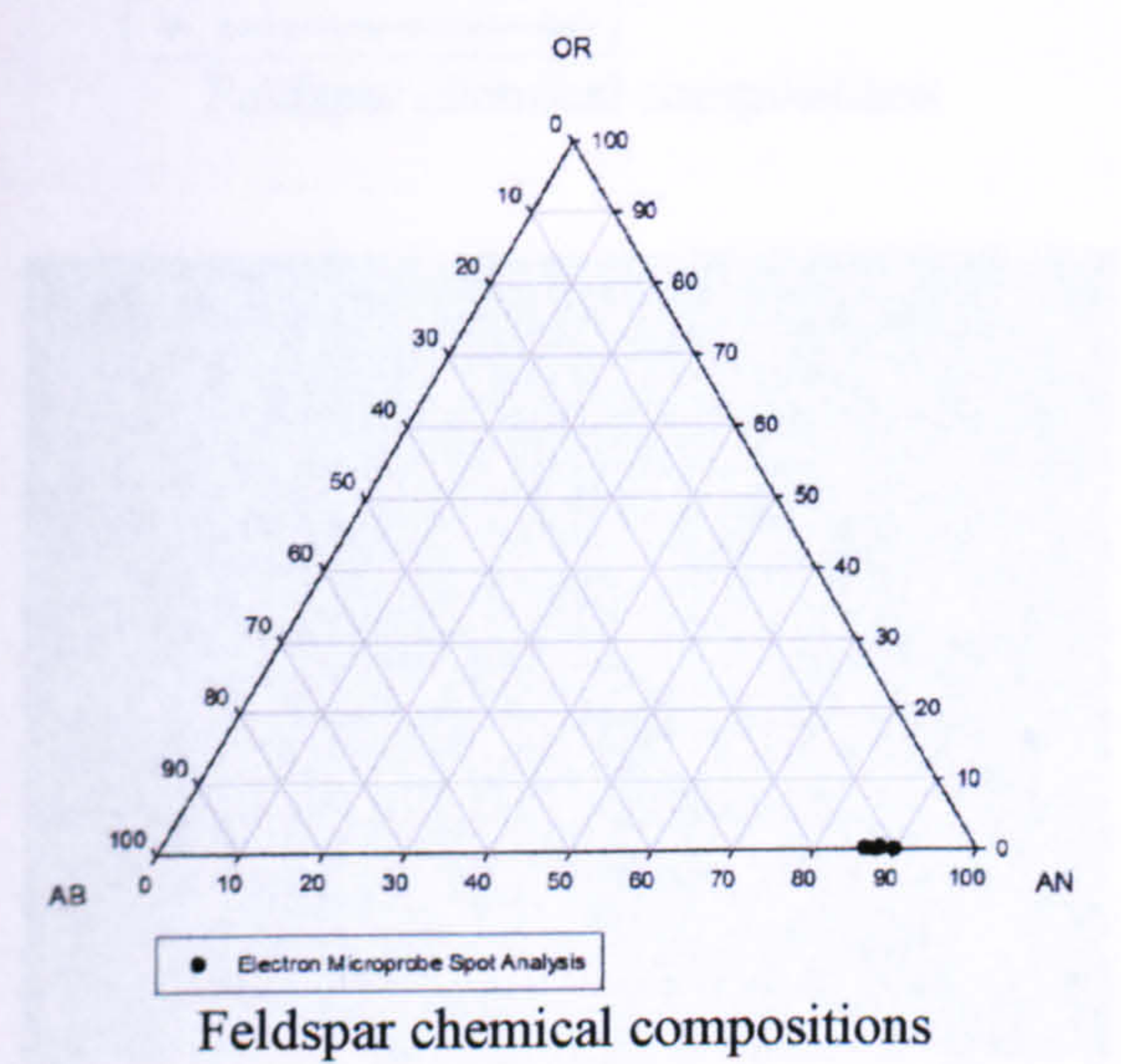
The troctolite (Grid Ref: NM394 964) and anorthosite (Grid Ref: NM394 966) samples used in this study were from one of the larger schilerons and were supplied by John Faithful (Glasgow University). This rock has a finely crystalline granular texture and contains euhedral feldspar phenocrysts, ophitic olivine-plagioclase clasts, subhedral, zoned clinopyroxene and skeletal olivine.

4.4.2.1 Feldspar Mineralogy, Microtexture and Composition.

Table 4.12. Chemical composition of the Hallival sample’s feldspar (Mol%).

Sample	Alkali feldspar			Free plagioclase feldspar		
	Ab	An	Or	Ab	An	Or
Rum anorthosite (H5)	---	---	---	12	88	0
Run troctolite pegmatite (H7)	---	---	---	18	82	0

4.4.2.1.1 Rum Anorthosite (H5).



SPT fraction (g/cm ³)	Mineralogy
<2.62	---
2.52-2.58	---
2.58-2.62	---
2.62-2.74	A ₀ P ₁₀₀ Q ₀
>2.74	---
Not SPT separated	---

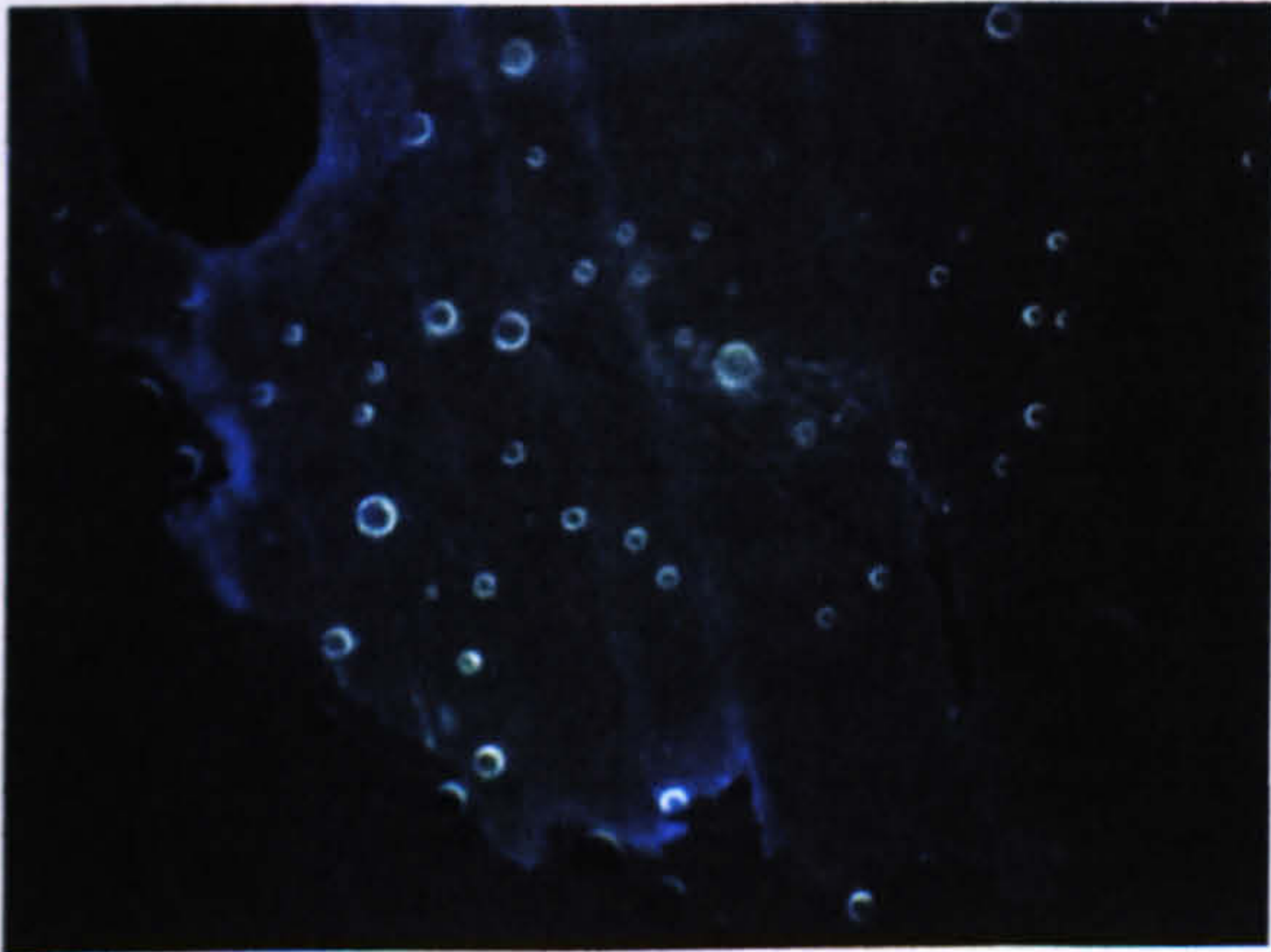
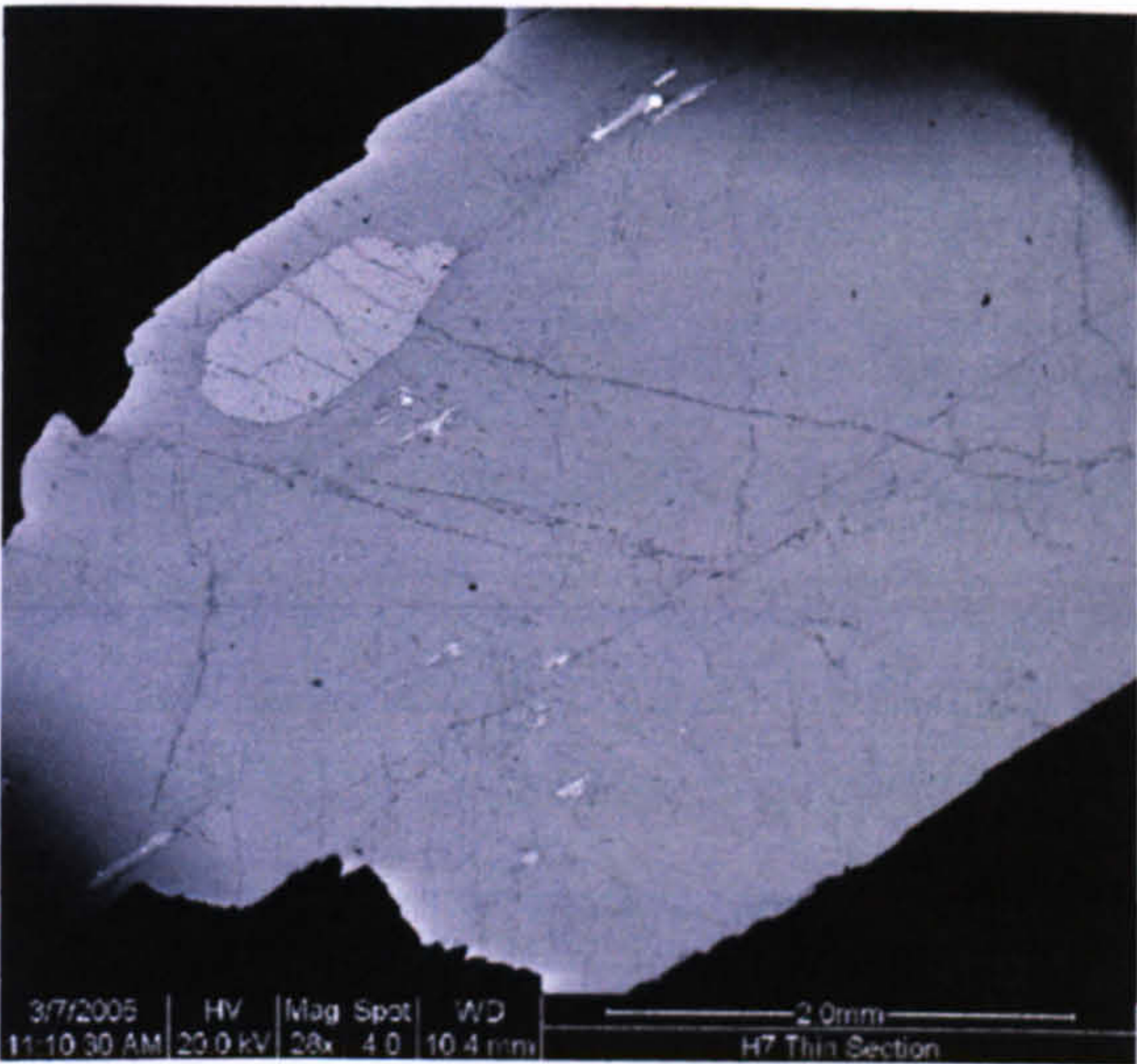
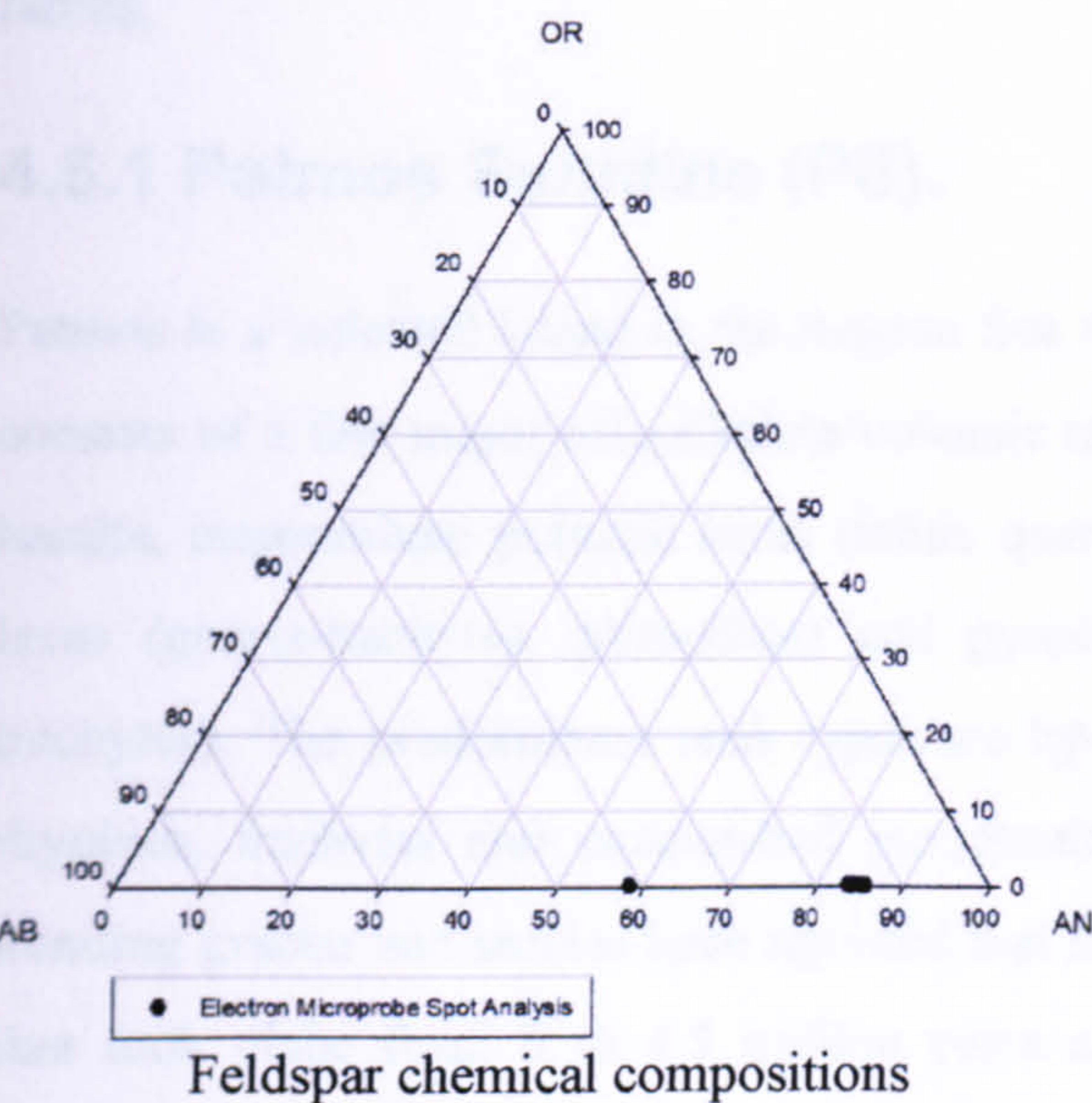
Optical CL image (grain mount)

Mineralogy of the density fractions

Figure 4.23. Mineralogy, microtexture and composition of anorthosite feldspars from Rum (H5).

The crystal in the grain mount is homogeneous, but the CL image reveals the presence of angular domains with slightly different intensities and wavelengths of dull red-purple luminescence. Although the host rock is an anorthosite, has been classified as such by other workers (John Faithful, *pers.com.*), the feldspar itself is a calcite bytownite.

4.4.2.1.2 Rum Troctolite Pegmatite (H7).



SPT fraction (g/cm ³)	Mineralogy
<2.62	---
2.52-2.58	---
2.58-2.62	---
2.62-2.74	---
>2.74	A ₀ P ₉₅ Q ₅
Not SPT separated	---

Optical CL image (grain mount)

Mineralogy of the density fractions

Figure 4.24. Mineralogy, microtexture and composition of Rum troctolite feldspars (H7).

The crystal in the grain mount studied lacks any exsolution microtexture and luminesces a dull green, although edges of the grain are bluer in CL colour. Compositionally the feldspar is a bytownite and has separated to a pure plagioclase powder.

4.5 Extrusive Igneous Rocks.

As noted in the literature review of Chapter 2, feldspars from extrusive igneous rocks, which crystallized rapidly from a high temperature melt, are expected to suffer much more from unexplained loss of signal during storage than feldspars from plutonic rocks, which have cooled slowly at depth within the Earth’s crust. Rapid cooling is believed to promote anomalous fading because it hinders development of an ordered crystal structure (Visocekas *et al.*, 1994; Visocekas *et al.*, 1996; Visocekas *et al.*, 1998; Zink and Visocekas, 1997). Included in the set of samples

described below are grains that other studies have consistently shown to suffer from anomalous fading.

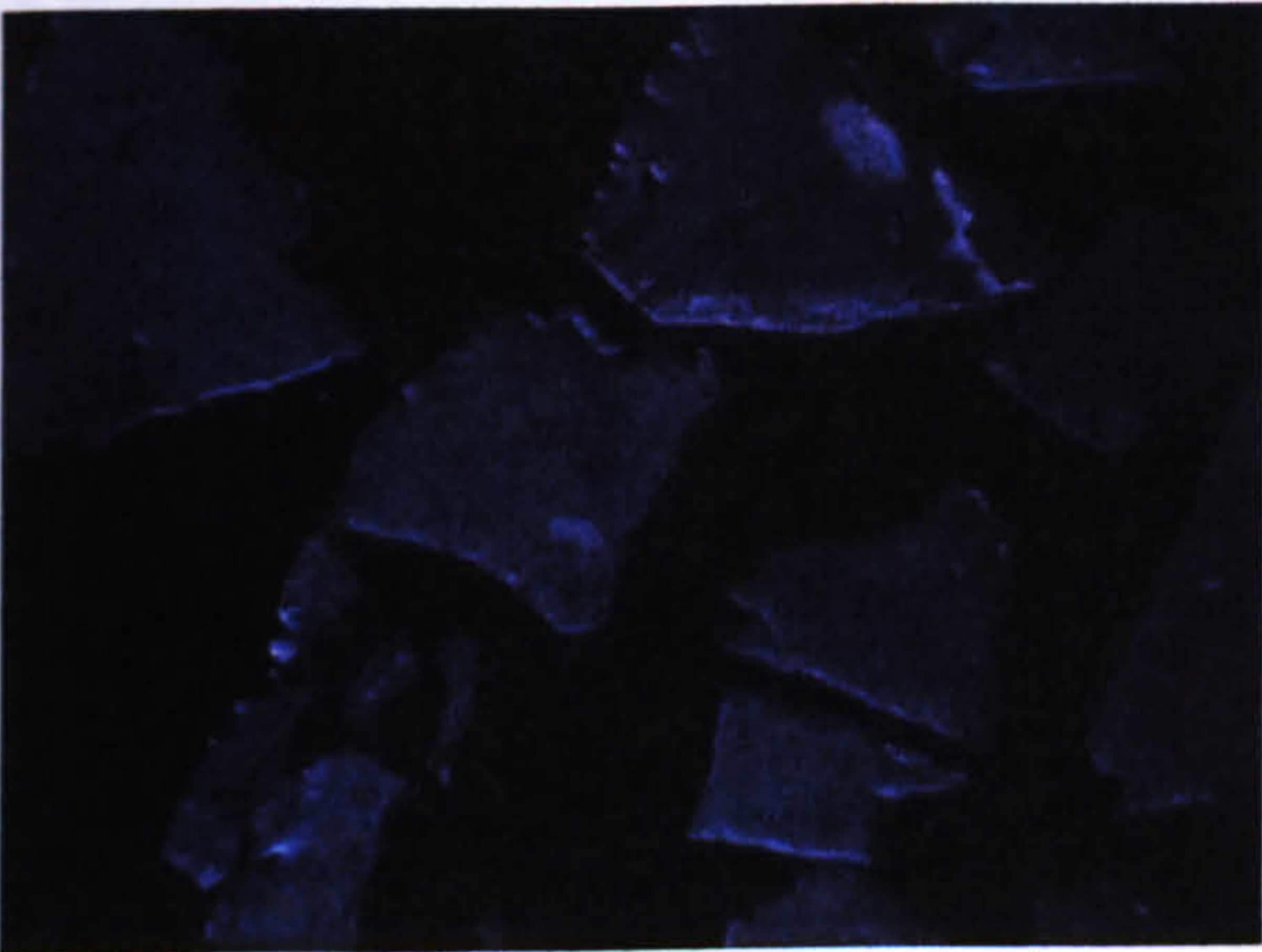
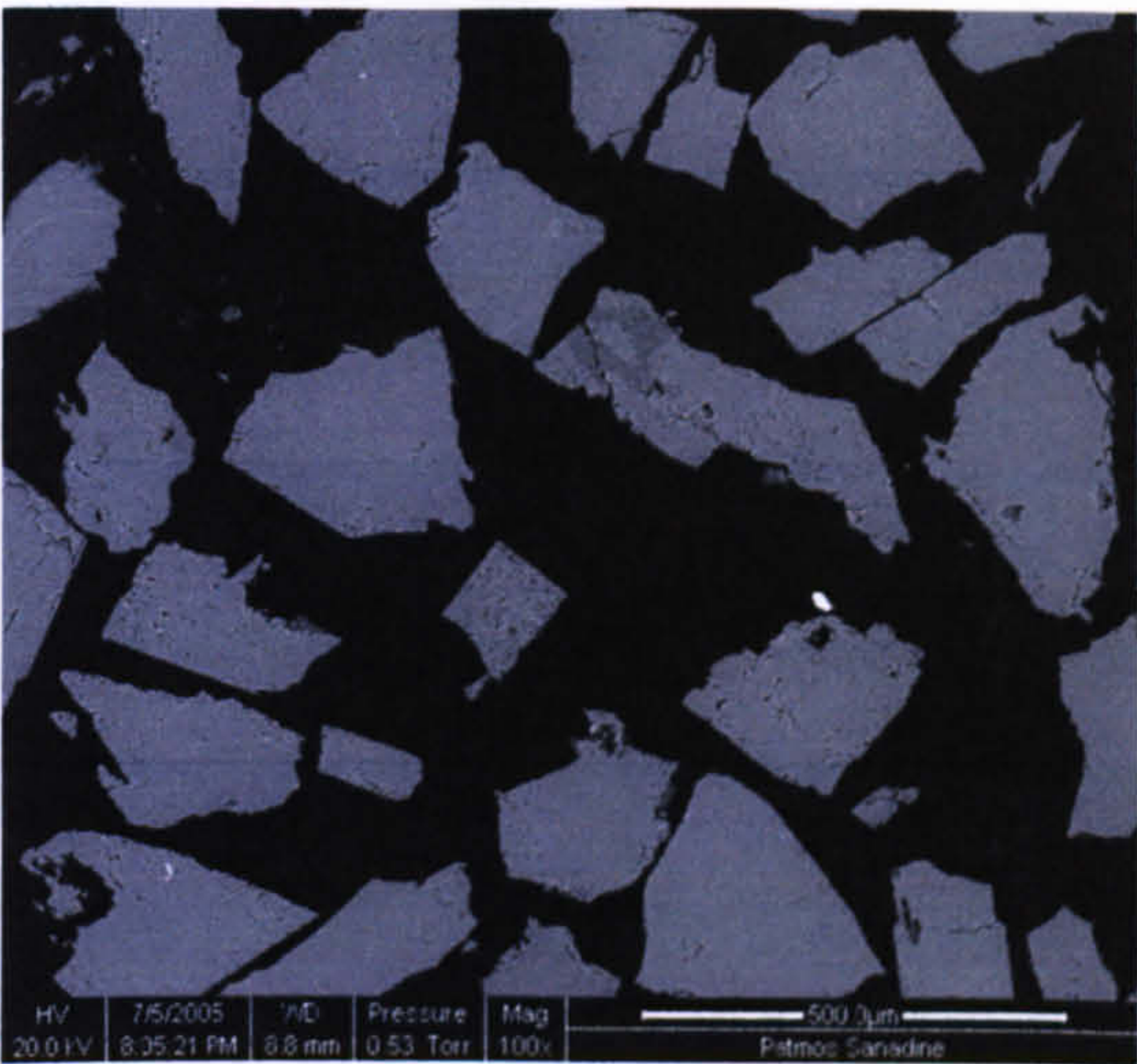
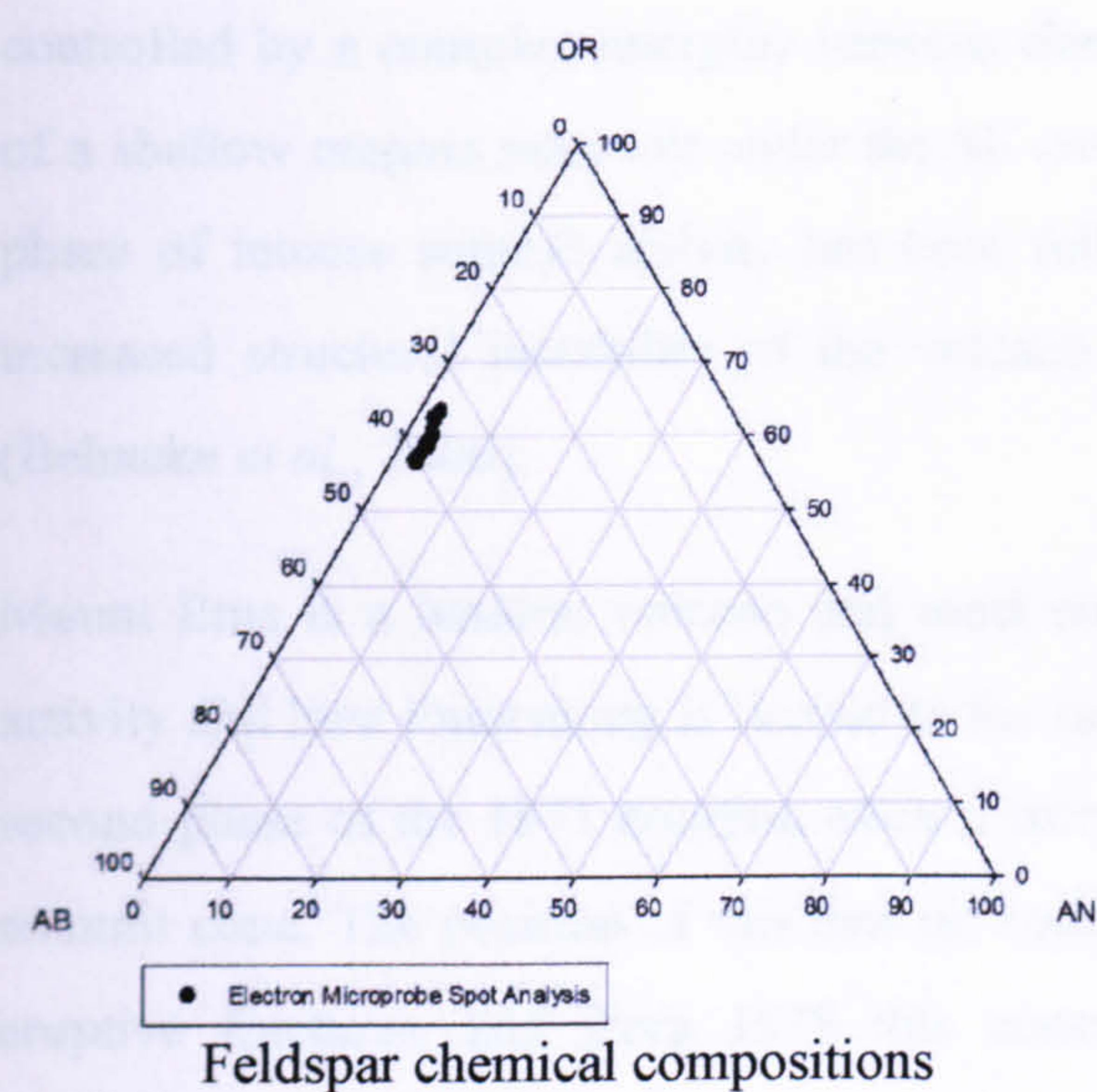
4.5.1 Patmos Sanidine (PS).

Patmos is a volcanic island in the Aegean Sea with an area of approximately 38km². The geology consists of a few major calc-alkaline volcanic regions (Wyres and Barton, 1986): High-K, high-Al basalts, intermediate potassic lavas (latite, quartz-latite, potassic trachytes), quartz-potassic alkali lavas (quartz-trachytes, phonolites) and pyroclastics and sodic alkaline lavas (phonolites and trachytes). The predominant rock types are hy-trachybasalts, hy-trachyandesites and Q-trachytes, rhyolites, trachytes and unclassified pyroclastics. The central part of Patmos lies in a NW-SE trending graben and studies have reported that there were at least two episodes of volcanic activity that took place from 6 to 4.5 million years ago (Wyres and Barton, 1987). Plagioclase is the dominant phenocryst in all of the lavas and they have complex morphologies that are similar to those feldspars from oceanic basalts. A single sanidine phenocryst was supplied to SUERC by Raphael Visocekas.

Sanidine was included in this study as other authors have reported severe fading rates when attempting to date and recover known doses (Visocekas *et al.*, 1994; Wintle, 1973; Zink and Visocekas, 1997). On Patmos, it occurs as reabsorbed xenocrysts in the hy-trachybasalts and as phenocrysts in the trachyandesites and Q-trachytes. The sanidine in the trachyandesites shows some reabsorbtion effects. They range in composition from Or₅₆An₇ to Or₇₅An₁ and individual crystals are normally zoned (i.e., Or decreases and An increases towards the rims). They are thought to be derived from relatively evolved magma involved in the mixing event.

4.5.1.1 Feldspar Mineralogy, Microtexture and Composition.

Table 4.13. Chemical composition of the Patmos sanidine (Mol%).						
Sample	Alkali Feldspar			Free plagioclase feldspar		
	Ab	An	Or	Ab	An	Or
Patmos Sanidine (PS)	38	3	59	---	---	---



SPT fraction (g/cm ³)	Mineralogy
<2.62	A _{>95} P ₀ Q _{<5}
2.52-2.58	---
2.58-2.62	---
2.62-2.74	---
>2.74	---
Not SPT separated	---

Mineralogy of the density fractions

Figure 4.25. Mineralogy, microtexture and composition of Patmos sanidine (PS)

This is a homogenous sanidine, which is expected from a high quality single feldspar grain (whose grinding has produced the powders imaged above). This sample was taken from a large phenocryst and the optical CL is very dull. Given that the sample was a single crystal of feldspar the purity of the SPT fraction is unsurprising.

4.5.2 Etna Basaltic Lava (Etna).

Mount Etna on the island of Sicily is a highly active volcano with four craters on its summit. The south eastern of these craters has been the most active since 1971, and between 1996 and 2001 it experienced exceptional activity and growth. This time period was marked by near continuous activity that has been sub-divided by workers into five distinct phases (Behncke *et al.*, 2006). These were characterised by a wide range of eruptive styles and intensities from quiet non-explosive lava emission to brief, violent lava fountaining episodes. Fluctuations in eruptive styles and rates were

controlled by a complex interplay between changes in the conduit geometry (including the growth of a shallow magma reservoir under the SE crater), magma supply rates and flank instability. This phase of intense summit activity has been followed, since the summer of 2001, by a period of increased structural instability of the volcano marked by a series of important flank eruptions (Behncke *et al.*, 2006).

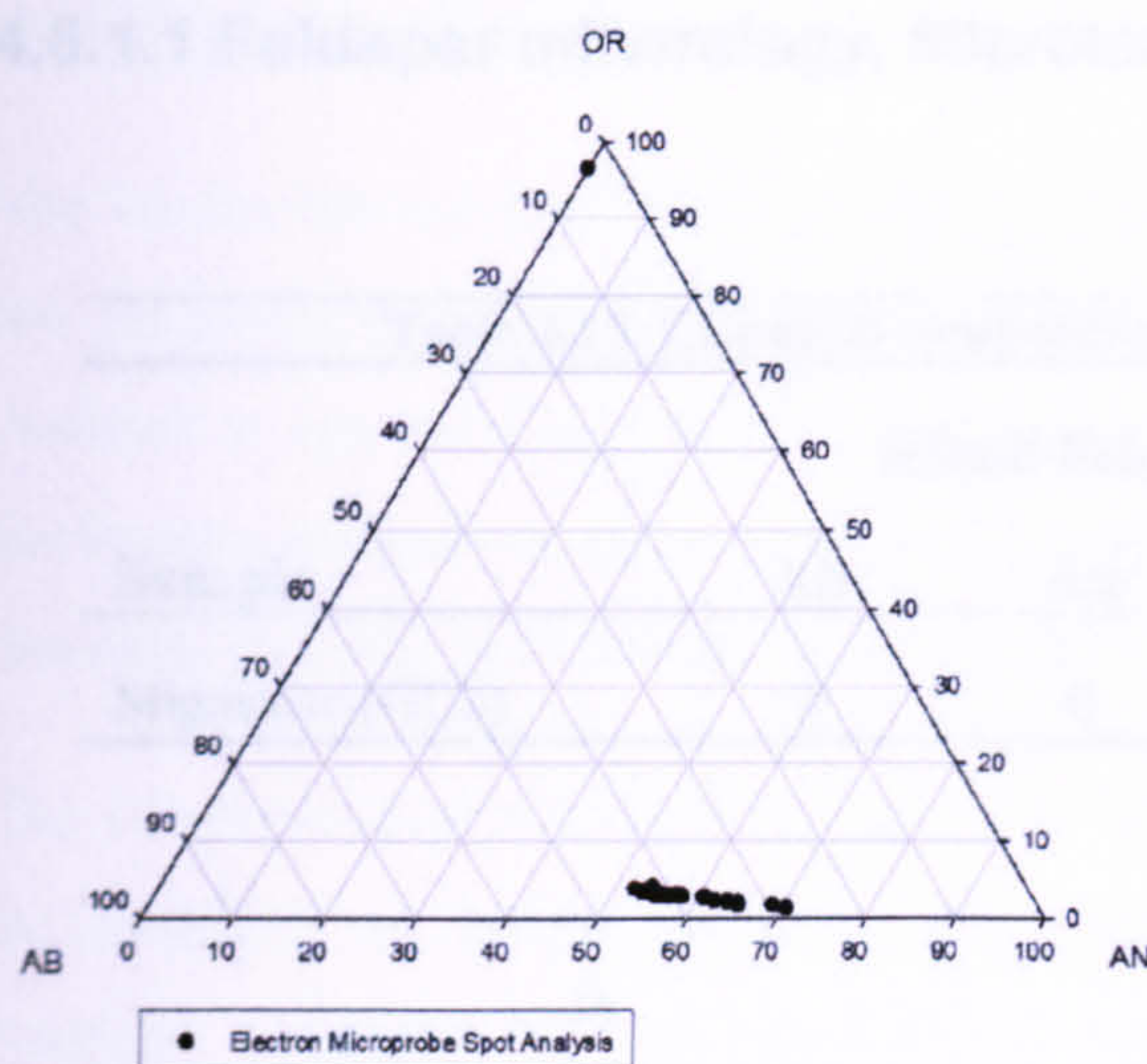
Mount Etna is a basaltic volcano and most eruptions produce voluminous lava flows. Explosive activity and lava fountaining is limited to the summit. The history of the SE crater began during the second phase of the 1971 eruption when it formed as a degassing pit on the SE base of the central summit cone. The position of this new pit coincided with the intersection of two major systems of eruptive fractures, and from 1978 this crater produced frequent flank eruptions. Prior to its reactivation in 1996, it was a relatively simple, saucer shaped depression about 150m wide. Over the next five years its high rate of activity and large amount of lava extrusion controlled the change in its shape and geometry of the summit of this important volcano (Behncke *et al.*, 2006).

The sample used was collected by Martin Lee from close to the summit of the mountain (37.7N, 15.0E, 10,990 feet) in 2001 and will have been erupted as molten rock, cooled and crystallized within the last twenty years. The basalt contained ~1cm sized phenocrysts of plagioclase feldspar in a very finely crystalline groundmass. These feldspars have therefore crystallized rapidly from a high temperature melt. The sample does not appear to have suffered any significant weathering.

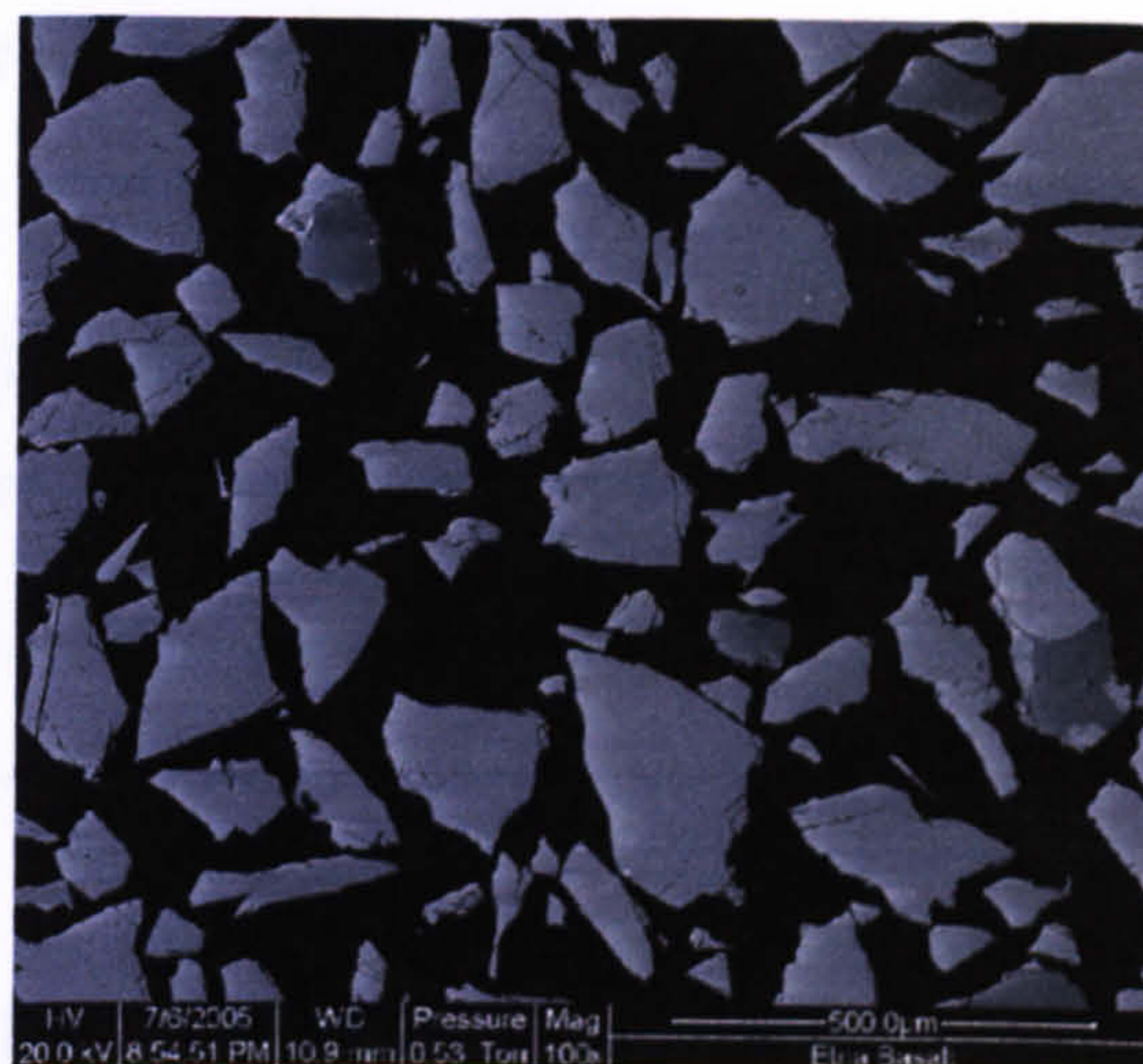
4.5.2.1 Feldspar Mineralogy, Microtexture and Composition.

Table 4.14. Chemical composition of feldspars from the Etna basalt (Mol%).

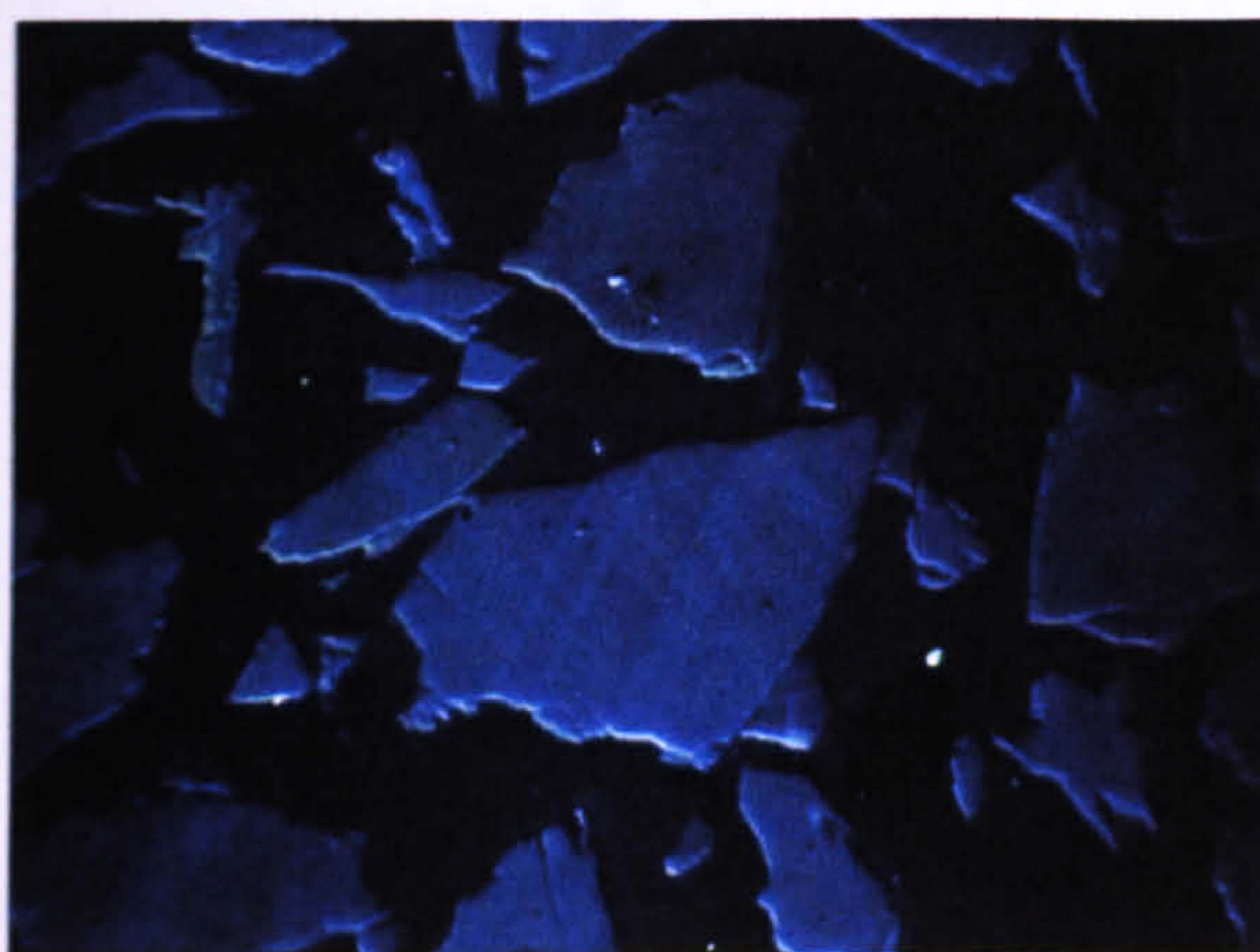
Sample	Alkali Feldspar			Free plagioclase feldspar		
	Ab	An	Or	Ab	An	Or
Etna Basalt (Etna)	—	—	—	39	59	2



Feldspar chemical compositions



Backscattered electron SEM image (grain mount)



Optical CL image (grain mount)

SPT fraction (g/cm ³)	Mineralogy
<2.62	A _{<10} P _{>85} Q _{<5}
2.52-2.58	---
2.58-2.62	---
2.62-2.74	---
>2.74	---
Not SPT separated	---

Mineralogy of the density fractions

Figure 4.26. Mineralogy, microtexture and composition of Etna basaltic lava feldspars (Etna).

The polished grain mount predominantly contains dull blue luminescing homogeneous labradorite. The single density separate is also plagioclase-dominated.

4.6 Metamorphic Rocks.

4.6.1 Glen Tarbert Migmatite (GU2).

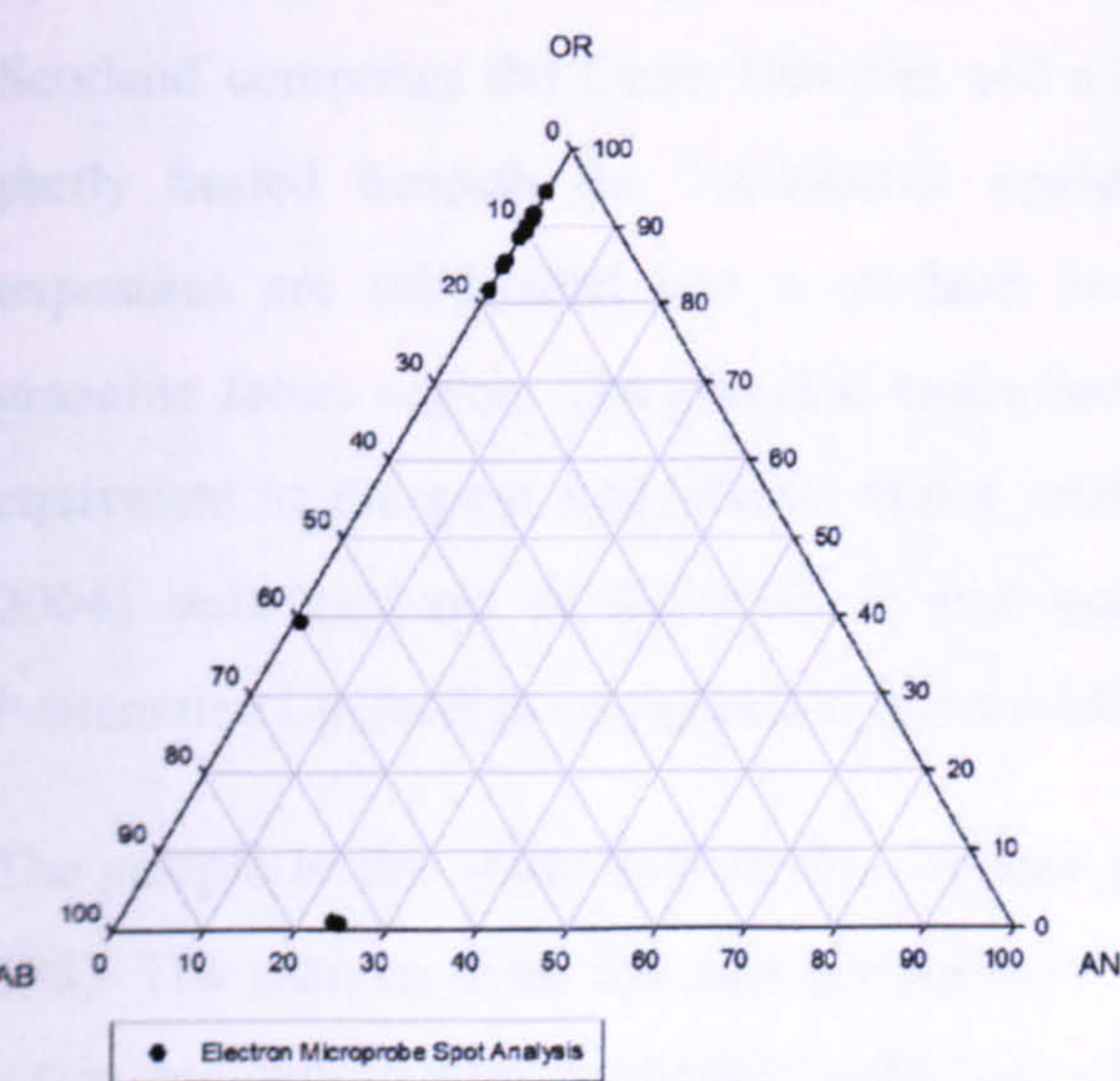
The Glen Tarbert migmatite (Grid Ref: NM880 585) has formed in the cordierite-K-feldspar zone of the aureole surrounding the Strontian granodiorite (Ashworth and Tyler, 1983) and so is comparable in geological age (i.e., 435 ± 10 Ma). Aureole migmatites are found only above the muscovite-out isograd and they are distinguished texturally from the earlier, regional migmatite, and also their thin leucosomes contain quartz and two feldspars, whereas the regional leucosomes are predominantly quartz-plagioclase. In fact migmatization is seen throughout the inner aureole.

This sample was taken from a collection of metamorphic rocks stored at the University of Glasgow and is designated (GU2).

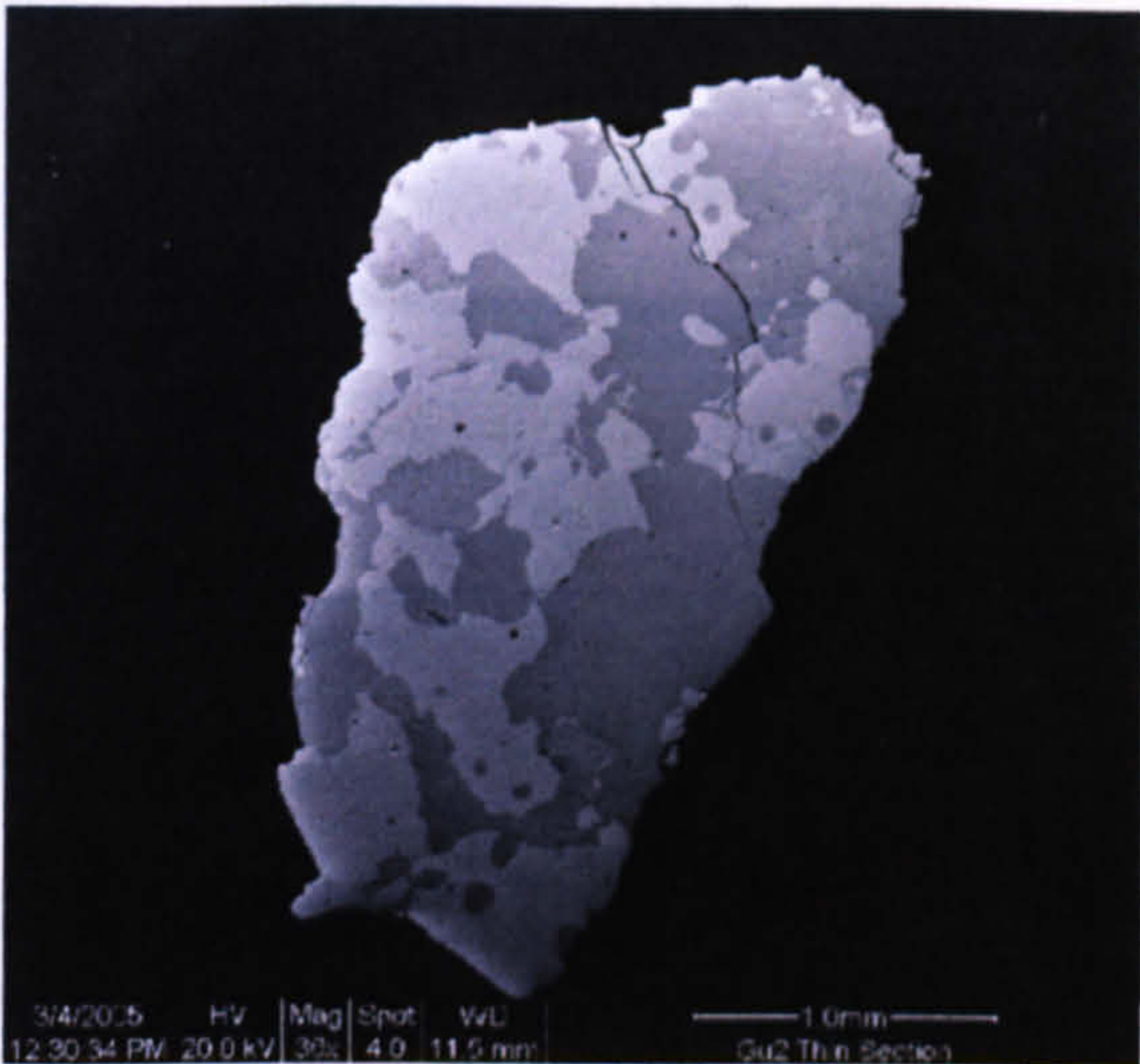
4.6.1.1 Feldspar mineralogy, Microtexture and Composition.

Table 4.15. Chemical composition of the migmatite feldspars (Mol%).

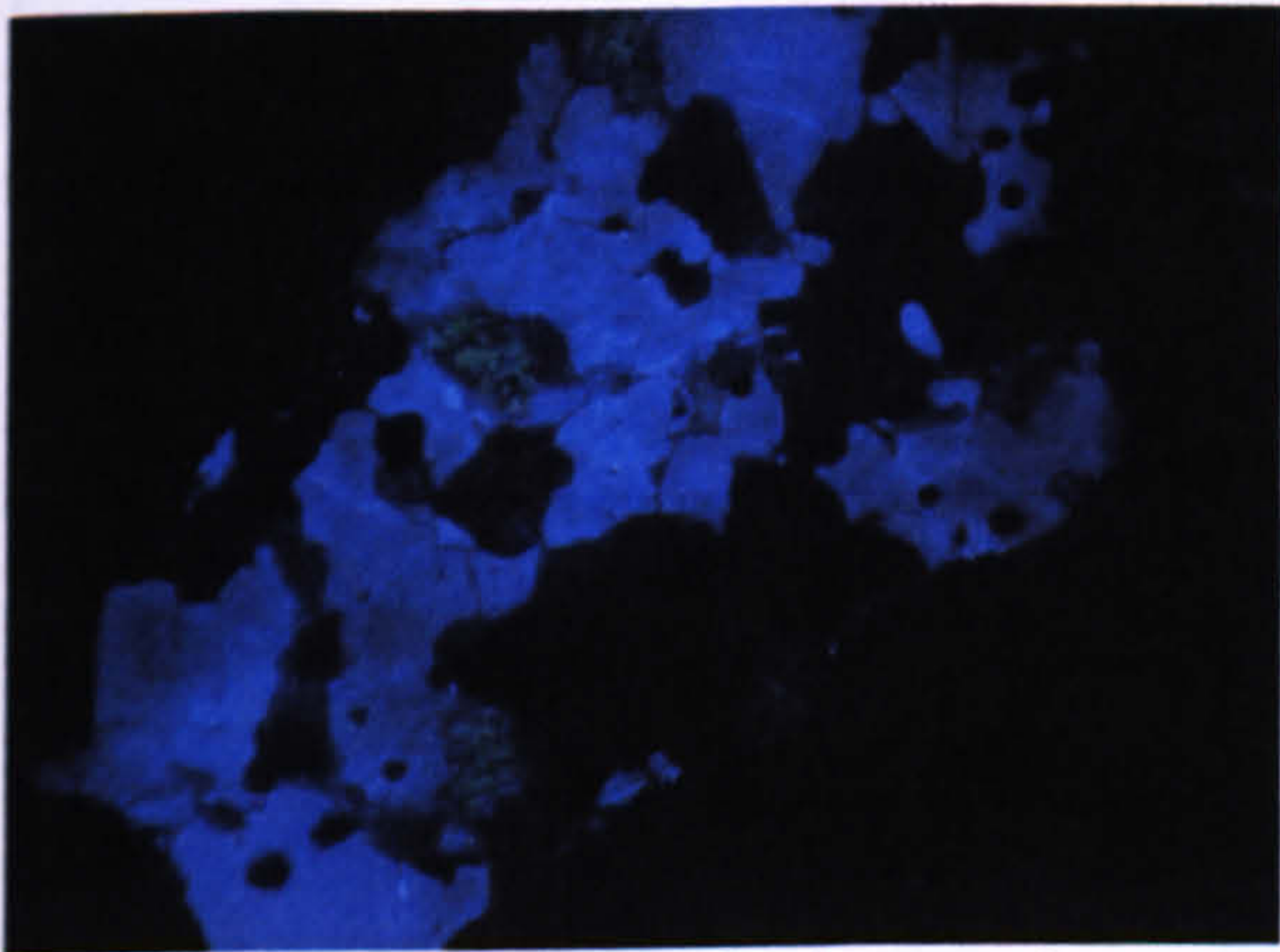
Sample	Alkali Feldspar			Free plagioclase feldspar		
	Ab	An	Or	Ab	An	Or
Migmatite (GU2)	9	0	91	24	75	1



Feldspar chemical compositions



Backscattered electron SEM image (grain mount)



Optical CL image (grain mount)

SPT fraction (g/cm ³)	Mineralogy
<2.62	---
2.52-2.58	---
2.58-2.62	---
2.62-2.74	A ₁₀ P ₂₀ Q ₇₀
>2.74	---
Not SPT separated	---

Mineralogy of the density fractions

Figure 4.27. Mineralogy, microtexture and composition of Glen Tarbet migmatite feldspars (GU2).

Images of the grain mount show that the blue luminescing K-feldspar (Or₉₁Ab₉An₀) contains hundreds of micrometer-sized inclusions of quartz (non-luminescent) and plagioclase (green CL). Possibly because of these complex intergrowths the density separation has been highly inefficient with alkali feldspar constituting only ~10% of the powder.

4.6.2 Lewisian and Torridon Gneiss.

The biotite-bearing hornblende gneiss is found through the Torridon complex and forms much of the landscape around Loch Torridon (Grid Ref: NG906 563) (Friend and Kinny, 2001). It is Archean in age and is one of the oldest rocks in this study. It is the gneisses that form a lot of the landscapes and palaeovalleys that make up the Lewisian gneiss basement rock that is common in this area, and will be described briefly below.

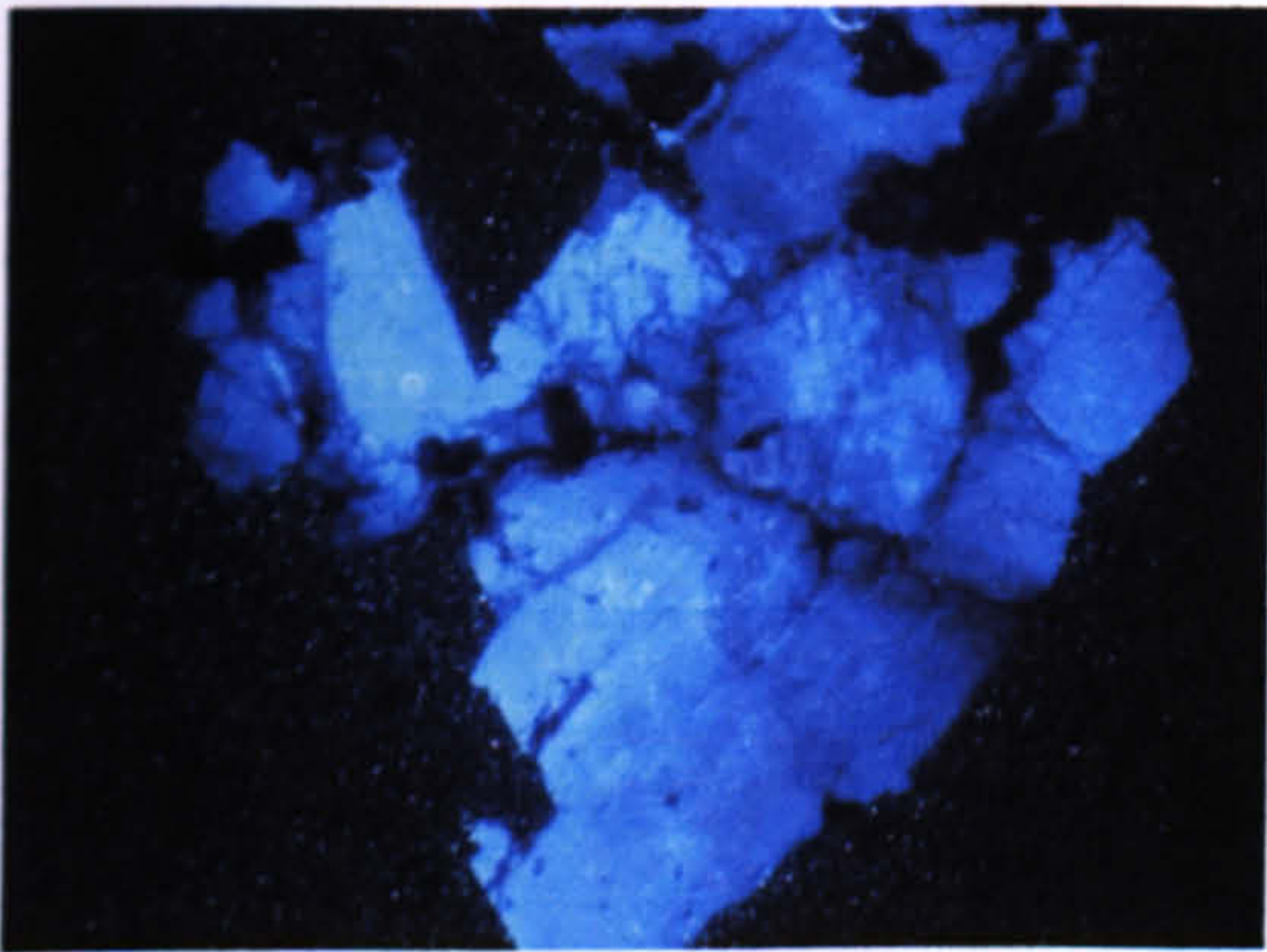
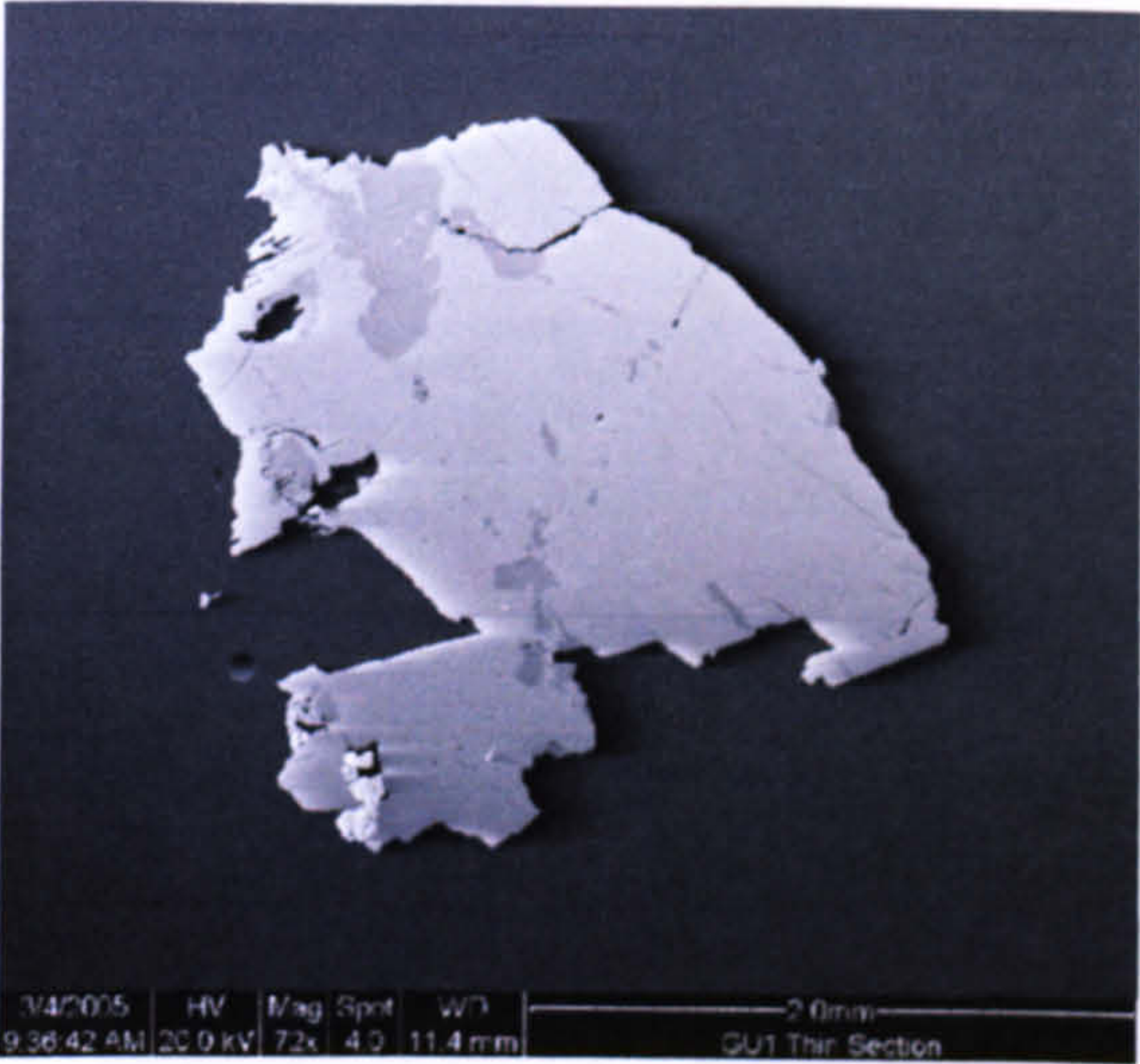
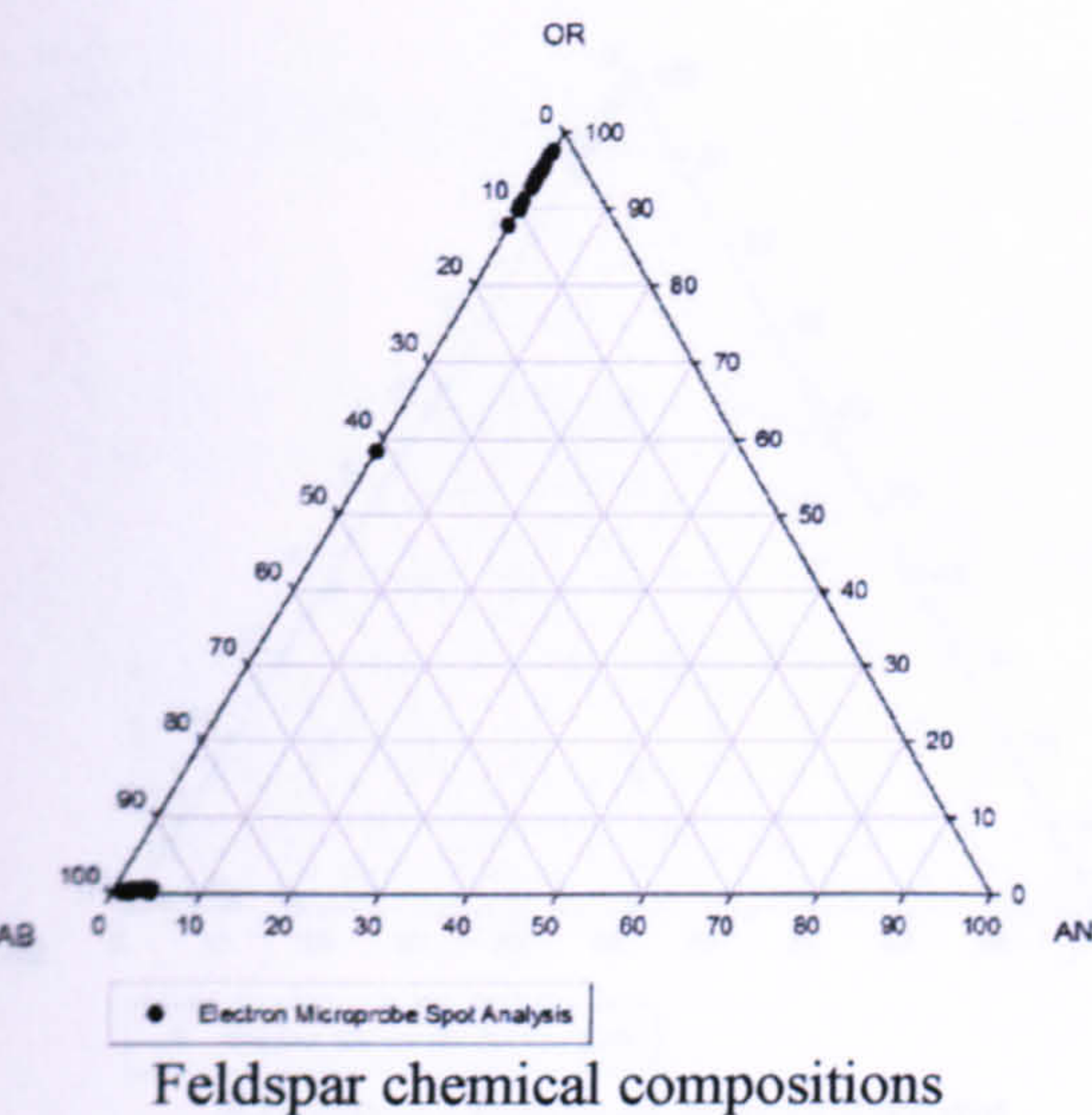
The Lewisian Gneiss Complex is the oldest rock series in Scotland, believed to have been formed by reworking of Archean age rocks during the Proterozoic. The Lewisian Complex of northwest Scotland comprises the Outer Hebrides and a large coastal strip west of the Moine thrust zone, partly buried beneath the Torridonian sandstones (Friend and Kinny, 2001). The mainland exposures are subdivided into a northern and southern amphibolite facies flanking a central granulite facies region. The granulite facies Scourian gneisses of the central region are considered equivalent to the grey, amphibolite facies, tonalite-trondhjemite-granodiorite (Lasaga and Luttge, 2004) suite gneisses of the northern and southern regions that has been strongly affected by Proterozoic Laxfordian retrogression and reworking.

The sample in this study is from the Archean gneiss complex of Lewis-Harris (Grid Ref: NC200 488). The gneisses from this area are typically relatively homogenous, grey tonalitic gneisses with a few thin, sub parallel leucocratic veins over which there has been some late epidote development, particularly along joint surfaces. The rock is medium-grained and largely comprises plagioclase and quartz with a very small amount of interstitial microcline. The mafic phases are biotite and hornblende that has been altered to epidote with a small amount of chlorite. The age range that has been reported from these rocks from a series of ²⁰⁷Pb/²⁰⁶Pb dates is 2700 and 2850Ma (Friend and Kinny, 2001).

4.6.2.1 Feldspar Mineralogy, Microtexture and Composition.

Table 4.16. Chemical compositions of feldspars from the gneiss samples (Mol%).						
Samples	Alkali feldspar			Free plagioclase feldspar		
	Ab	An	Or	Ab	An	Or
Hornblende gneiss (GU1)	5	0	95	97	3	0
Lewisian gneiss (LG)	8	0	92	92	7	1

4.6.2.1.1 Torridon Hornblende Gneiss (GU1).



SPT fraction (g/cm ³)	Mineralogy
<2.62	---
2.52-2.58	A ₅₀ P ₅₀ Q ₀
2.58-2.62	---
2.62-2.74	A ₁₀ P ₃₀ Q ₆₀
>2.74	---
Not SPT separated	---

Mineralogy of the density fractions

Figure 4.28. Mineralogy, microtexture and composition of Torridonian hornblende gneiss feldspars (GU1).

Alkali feldspars within the grain mount are predominantly blue luminescing orthoclase with hundreds of μm sized patches of albite. The density separation was very effective in the 2.52-58g/cm³ fraction, but the denser powder is much more heterogeneous.

4.6.2.1.2 Lewisian Gneiss (LG).

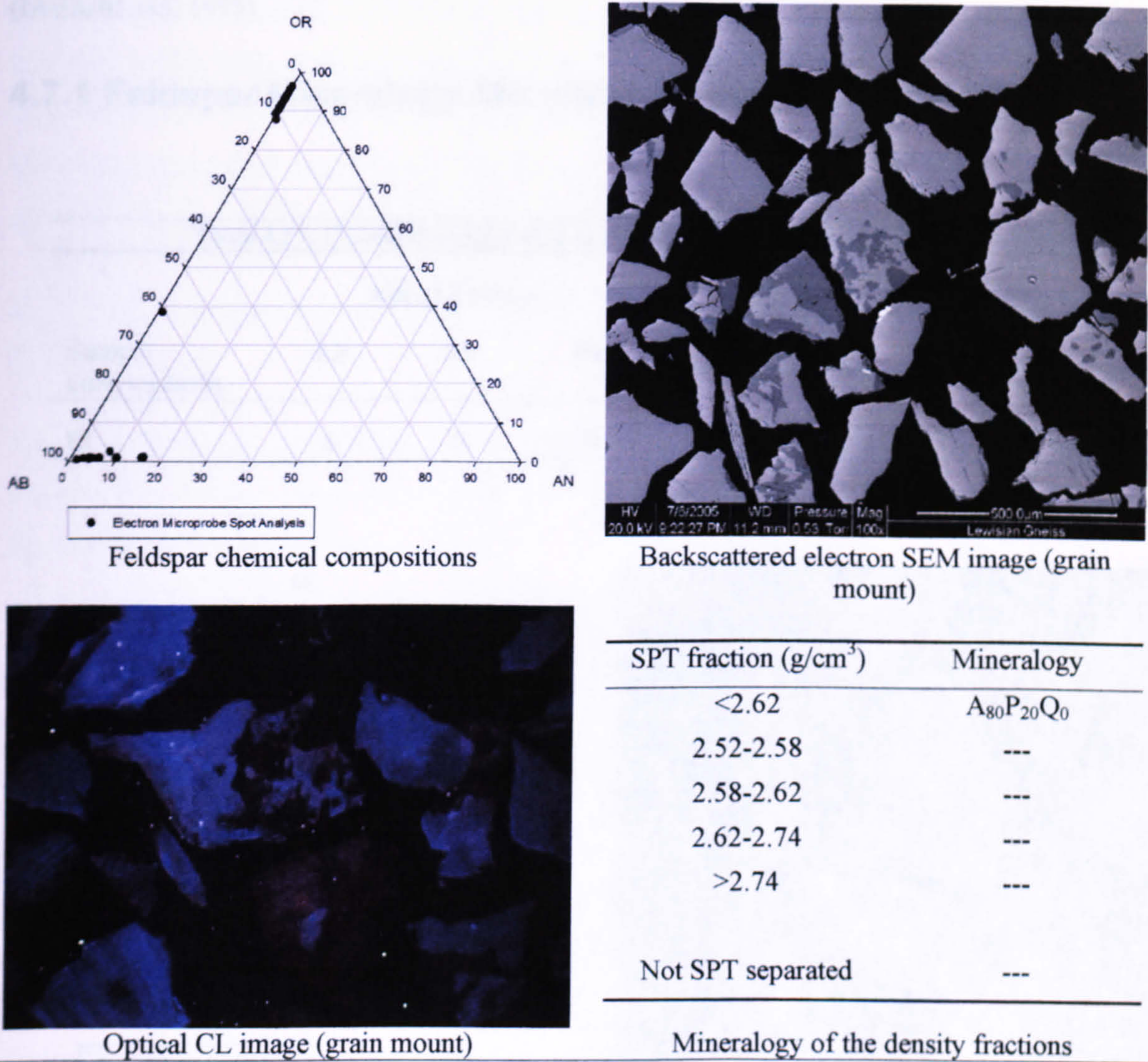


Figure 4.29. Mineralogy, microtexture and composition of Lewisian gneiss feldspars (LG).

The alkali feldspars lack exsolution lamellae and comprise blue luminescing microcline. The orthoclase is intergrown with hundreds of mm-sized patches of dull red or non-luminescent albite. The <2.62g/cm³ fraction is alkali feldspar-rich.

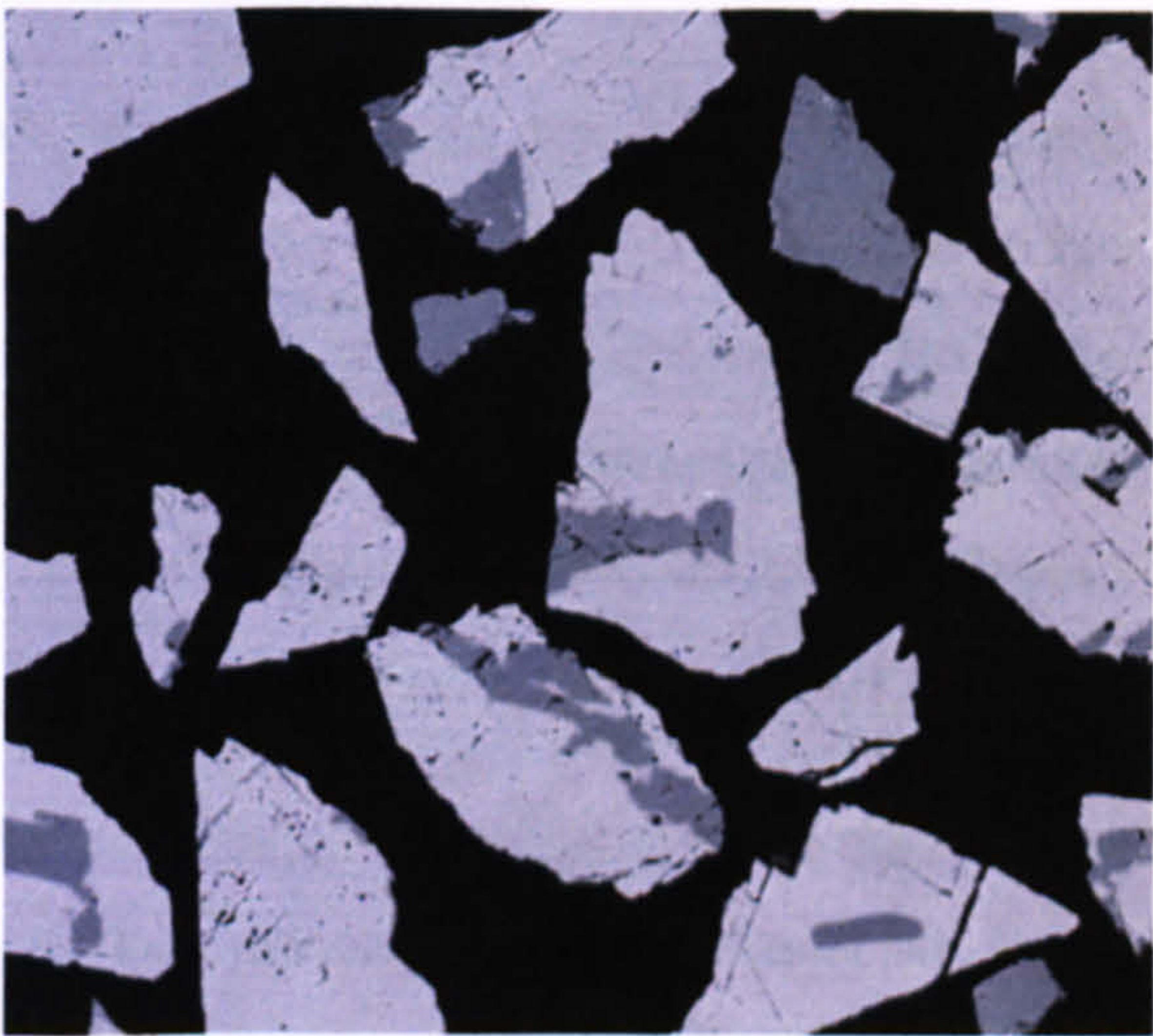
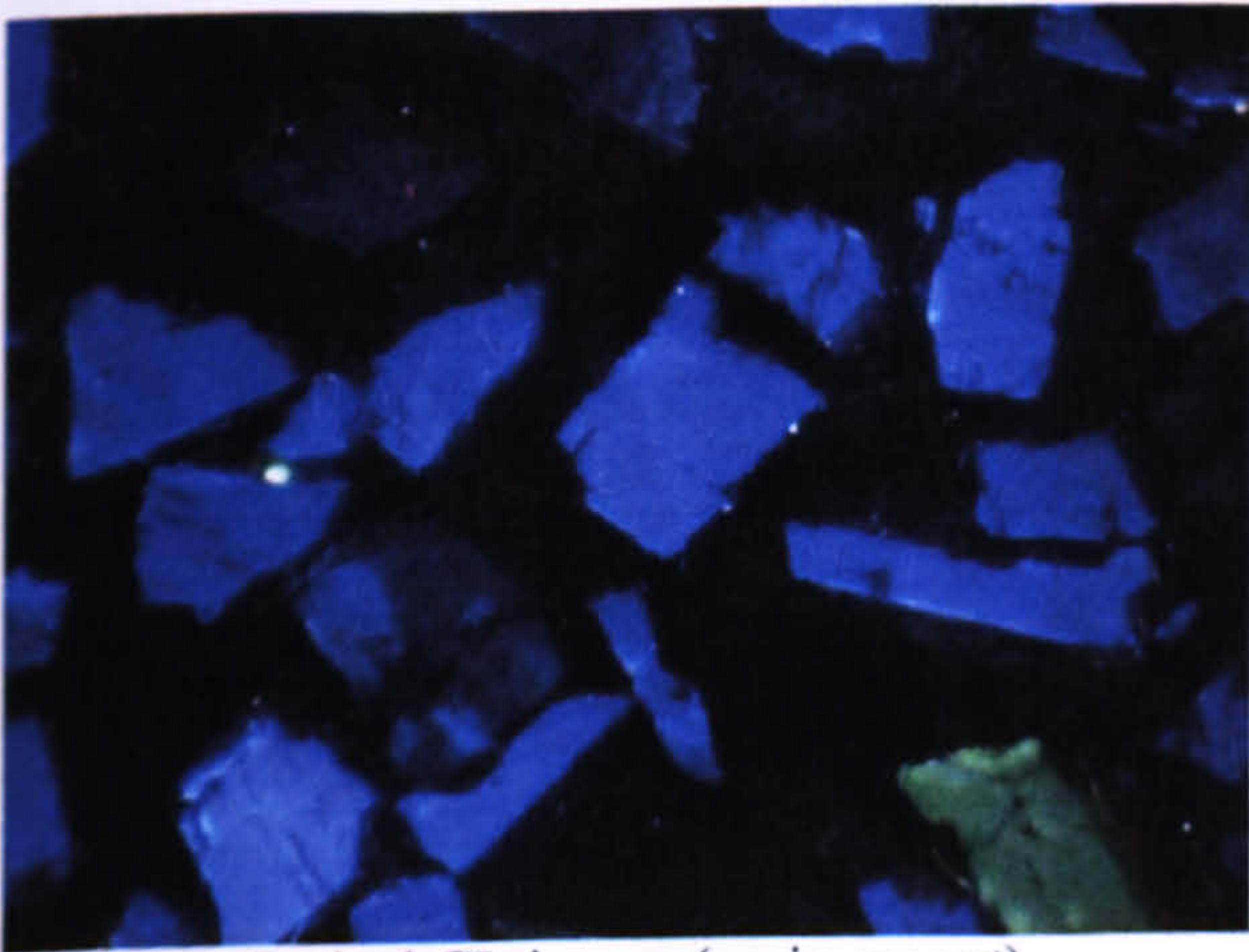
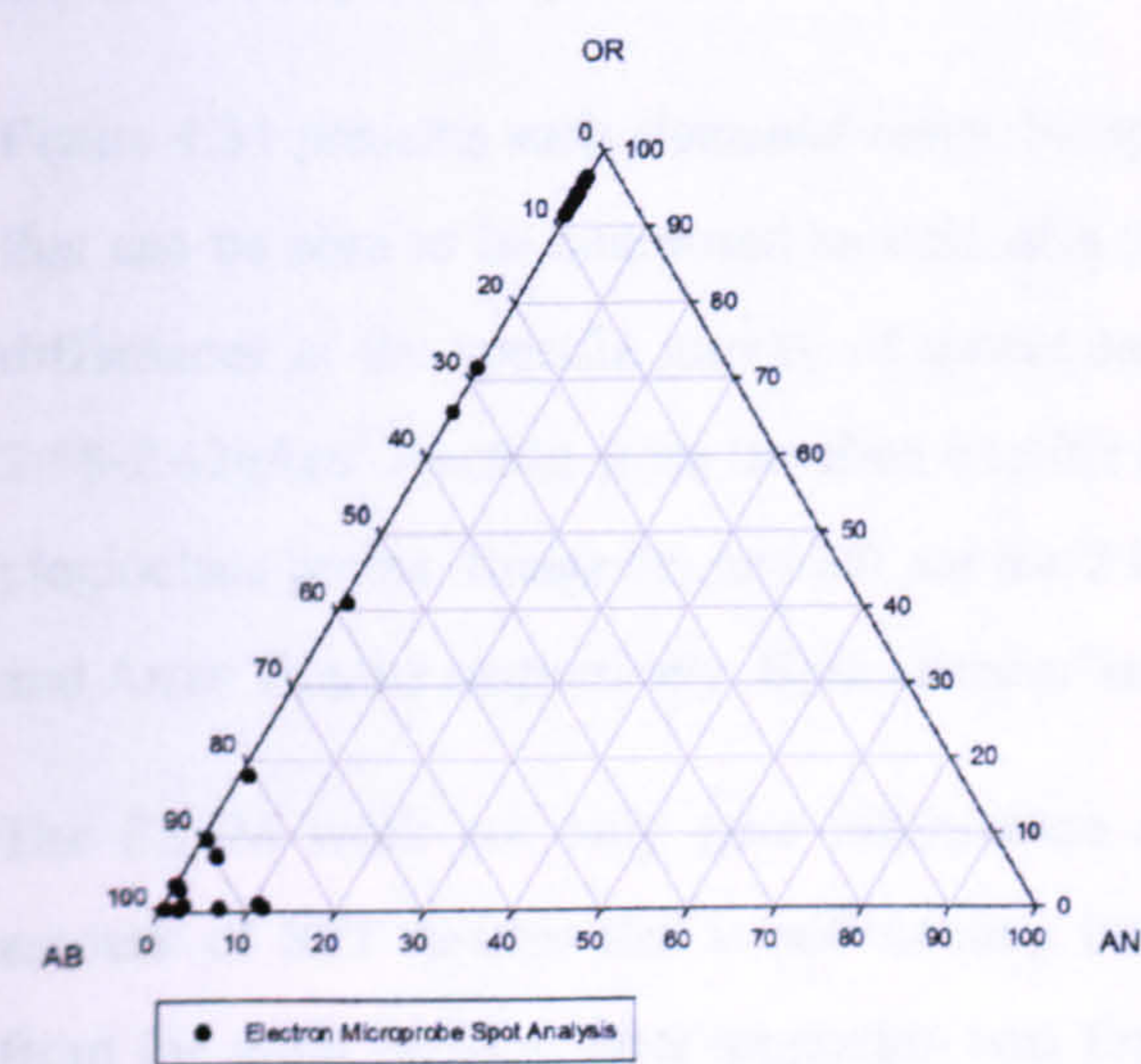
4.7 F1 Laboratory Standard.

F1 is an IAEA potassium feldspar and is used as the main feldspar standard within the SUERC dating laboratories. The source of this material is unknown, but such large volumes of feldspar with consistent chemical and microtextural properties are most likely to have come from a coarsely crystalline pegmatite. The feldspar was supplied to IAEA by the Danish Atomic Energy Commission (Risø) who obtained a bulk chemical composition of 65.2 wt% SiO₂, 19.2 wt% Al₂O₃, 0.07 wt% Fe₂O₃, 0.4 wt% CaO, 12.0 wt% K₂O and 2.8 wt% Na₂O (IAEA/RL/45 1977), which

corresponds to $\text{Or}_{72.3}\text{Ab}_{25.6}\text{An}_{2.0}$. This sample also contains an average of 2.5ppm uranium (IAEA/RL/45, 1977).

4.7.1 Feldspar Mineralogy, Microtexture and Composition.

Table 4.17. Chemical composition of the F1 feldspar standard (Mol%).						
Sample compositions.	Alkali Feldspar			Free plagioclase feldspar		
	Ab	An	Or	Ab	An	Or
F1	6	0	94	93	5	2



SPT fraction (g/cm ³)	Mineralogy
<2.62	---
2.52-2.58	---
2.58-2.62	---
2.62-2.74	---
>2.74	---
Not SPT separated	A ₆₅ P ₃₀ Q ₅

Optical CL image (grain mount)

Mineralogy of the density fractions

Figure 4.30. Mineralogy, microtexture and composition of the F1 standard.

The alkali feldspar is a relatively coarse vein microperthite comprising blue luminescent microcline containing veins of albite that have a low intensity of CL emission. Free plagioclase (albite) is also present and luminesces green. It is notable that this laboratory standard, which was not processed

by SPT density separation techniques, is mineralogically heterogeneous, with a significant abundance of plagioclase (albite) and some quartz. However, given that the sample is used routinely in this form, separation was considered to be undesirable. Note that the bulk molecular composition of F1 calculated using its bulk chemical composition ($\text{Or}_{72.3}\text{Ab}_{25.6}\text{An}_{2.0}$) represents a mixture of approximately 80% microcline ($\text{Or}_{94}\text{Ab}_6\text{An}_0$) with 20% albite ($\text{Or}_2\text{Ab}_{93}\text{An}_5$), in good agreement with proportions in the backscattered electron image of the grain mount above.

4.8 The Problems with SPT Heavy Liquid Separation of Feldspars.

As stated previously each of the density fractions produced by heavy liquid separation of the samples were X-ray mapped using the ESEM. This allowed for a quick and easy quality guide to the mineral separation process.

Figure 4.31 presents such elemental maps. Sample (a) is the $2.52\text{-}58\text{g/cm}^3$ fraction of Arran Granite that can be seen to be composed entirely of a single mineral type, in this case feldspar. Due to the differences in the specific gravity of quartz and feldspar this is to be expected. Image (b) is the $2.58\text{-}2.62\text{g/cm}^3$ fraction from the Etna basaltic lava, the green grain being quartz amongst the blue plagioclase grains. Image (c) and (d) are the $2.62\text{-}2.74\text{g/cm}^3$ fractions of the fresh Ballater Granite and Arran Granite respectively. Both of these have a higher percentage of quartz (yellow).

The ESEM work not only gave information on the mineralogy of the sample but also on the amount of SPT residue that is still coating the grains. Difficulties in removing the heavy liquid from the grain surfaces after separation was first brought to light by Anthony (PhD Thesis, 2003) who discovered that her dating samples were heavily coated with SPT and then carried out a study to assess its impact on luminescence characteristics. She concluded that the SPT residue had a limited impact. The SPT residue that remained on some of the samples used in this study was not a great cause for concern, yet the lack of complete success in its removal despite the rigorous washing protocol used was disappointing. In Figure 4.32 below are examples of the result obtained using the ESEM.

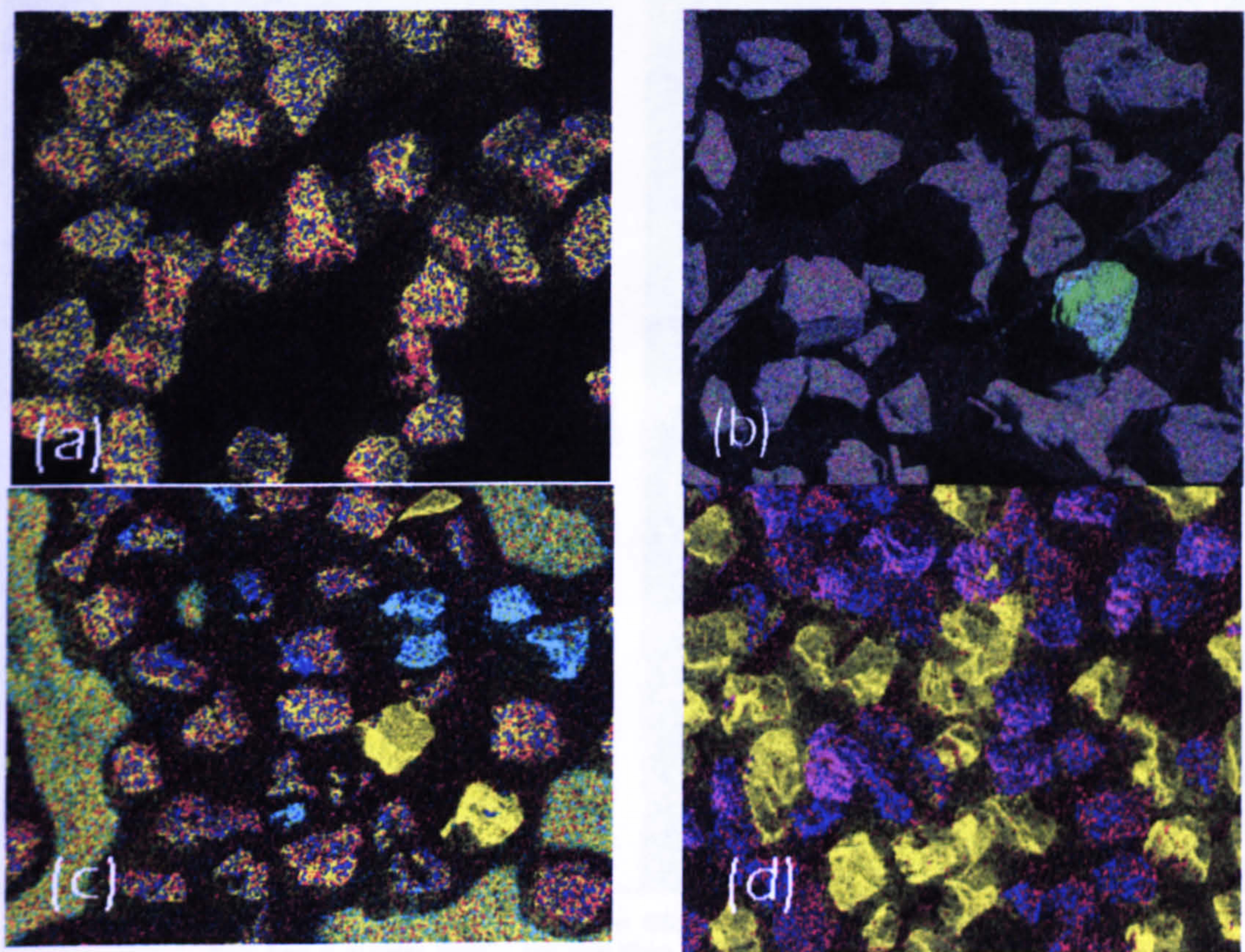


Figure 4.31 Different samples containing different levels of success in obtaining clean feldspar separates. Sample (a) is the 2.52-58g/cm³ fraction of Arran Granite; (b) is the 2.58-2.62g/cm³ fraction from the Etna basaltic lava, the green grain being quartz amongst the blue plagioclase grains. Image (c) and (d) are the 2.62-2.74g/cm³ fractions of the fresh Ballater Granite and Arran Granite respectively. Both of these have a higher percentage of quartz (yellow).

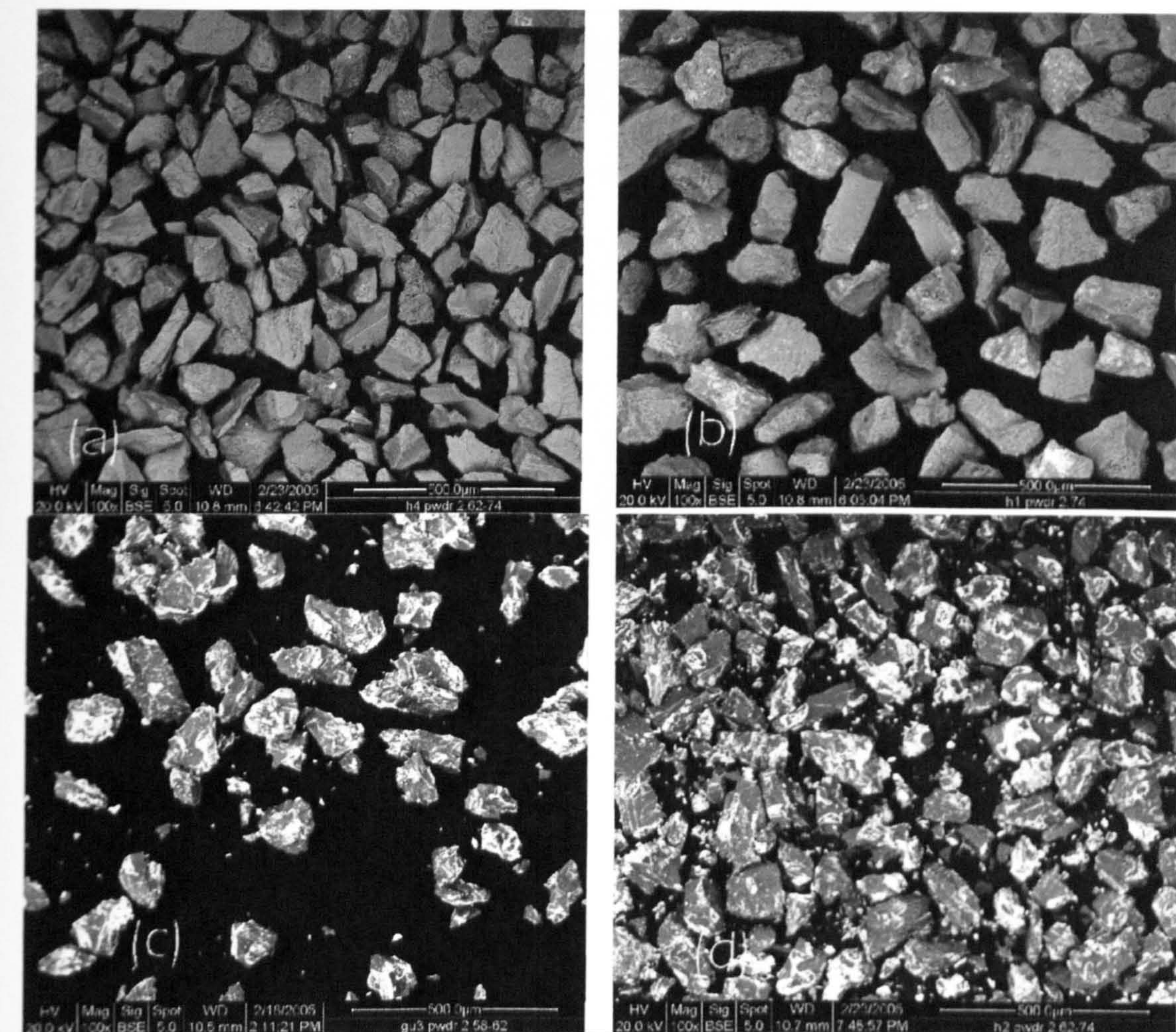


Figure 4.32 Backscattered electron ESEM images of grain separates. SPT has a greater atomic number than the feldspars and so should be white in the images. Image (a) had no SPT residue, whilst (b) had some around a handful of grains. In image (c) there was around 50% of the grains surfaces are coated and in (d) the problem was greater still.

4.9 Summary.

The sample characterisation results presented above will be used in comparison with the remnant luminescence data (Chapter 5) to test the hypothesis that mineralogical, chemical and microtextural properties of the feldspars outlined in this chapter will help in understanding controls on the stability in the measured signals. Within this sample set there are significant variations in age, cooling rate, post-formational alteration, chemistry and exsolution alteration microtextures. Such variables have been hypothesised within the literature (outlined in Chapter 2) to influence the presence and rate of anomalous fading. These samples along with their sampling location and geological context are listed in Table 4.18 below for ease of reference. Table 4.19 is an overview of the success of the SPT technique and should be referred to when density fractions are quoted in relation to the luminescence work. The results obtained in these characterisation methods are compiled and summarised in Table 4.20-4.27.

Table 4.18 The sample set, reference numbers and locality (listed in order of preparation for luminescence work).

Sample	Host Rock	External reference	Location	Geological context
1	Shap Granite (Shap)	N/A	Shap, Northern England (NY557083)	Sample collected from a working quarry in the granite by Dr M. Lee.
2	Helmsdale Granite (Helms)	N/A	Helmsdale, Northeast Scotland. (NC054181)	Sample collected from a roadside exposure of the granite by Dr M. Lee in 1995.
3	Helmsdale Arkose (Ark)	N/A	Helmsdale, Northeast Scotland. (NC066201)	Sample collected from a roadside exposure (the Ousdale cutting) by Dr M. Lee in 1995.
4	Lewisian Gneiss (LG)	N/A	Northwest Scotland (NC200488)	Sample obtained from collections in the Department of Geographical and Earth Sciences, University of Glasgow.
5	Patmos Sanidine (Parsons <i>et al.</i>)	N/A	Patmos, Greece (37N 26E)	Sample was supplied as a museum quality specimen by Dr D. Huntley (Simon Fraser University, Canada).
6	F1	N/A	Laboratory Standard (Unknown)	Unknown (Laboratory standard supplied by the Danish Atomic Energy Commission)
7	Etna Basaltic Lava (Etna)	N/A	Mount Etna lava field (37.7N, 15.0E, 10,990 feet (3,350 m)	Sample collected from a recently erupted lava flow on the summit of Etna by Dr M. Lee in 2001.
8	Gabbro Pegmatite (H1)	M106104	Currywongaun, Connemara, Eire (53:33:59N, 9:55:20W)	Sample is from the syn-tectonic Currywongaun intrusion (ca475Ma). Supplied by Dr John Faithful from the Hunterian Museum collections.
9	Pitchstone Porphyry (H2)	TYR2895	NW of Glen Callum Bay (NS 111527)	Sample is a glassy apophysis from a large Palaeogene quartz porphyry sill. Supplied by Dr John Faithful from the Hunterian Museum collections.

10	Feldspar Crystals (from above) (H3)	106431	NW of Glen Callum Bay (NS 111527)	Sample was taken from the soil above the sill described above. Supplied by Dr John Faithful from the Hunterian Museum collections.
11	Orthoclase Crystals (H4)	M6908	Summit of Canisp, Assynt (NC203187)	Weathered from the "Canisp Porphyry" sill (ca 437Ma). Extracted from the soil at the summit. Supplied by Dr John Faithful from the Hunterian Museum collections.
12	Anorthosite (H5)	111288	Hallival, Rum (NM394 966)	Sample is from the Unit 11/12 Contact of the Eastern layered Series. Supplied by Dr John Faithful from the Hunterian Museum collections.
13	Troctolite Pegmatite (H7)	78	Hallival, Rum (NM394 964)	From Unit 15 of the Eastern Layered Series. Supplied by Dr John Faithful from the Hunterian Museum collections.
14	Strontian Granodiorite (H8)	JF 2003.135	Road cut, Strontian, Scotland (NM7612 5415)	Typical coarse facies of the Strontian Granite Pluton. Supplied by Dr John Faithful from the Hunterian Museum collections.
15	Ross of Mull Granite (H9)	JF 2000.5	Camas Tuath Quarry, Mull (NM352243)	Typical fresh RM1 facies. Supplied by Dr John Faithful from the Hunterian Museum collections.
16	Ross of Mull Granite (H10)	178	Tonmore Quarry, Fionnphort, Mull (NM3046 2394)	Typical fresh RM1 facies. Supplied by Dr John Faithful from the Hunterian Museum collections.
17	Hydrothermal Syenite (H11)	JF93.10A	Just north of pier, Tonmore, Fionnphort, Mull (NM3013 2421)	Late-magmatic metasomatic "syenite" patches in RM1 facies. Supplied by Dr John Faithful from the Hunterian Museum collections.
18	Hornblende Gneiss (GU1)	M8	Torridon, Northwest Scotland (NG906563)	Sample obtained from collections in the Department of Geographical and Earth Sciences, University of Glasgow.

19	Migmatite (GU2)	M15	Glen Tarbet, Invernesshire (NM880585)	Sample obtained from collections in the Department of Geographical and Earth Sciences, University of Glasgow.
20	Peterhead Granite (GU3)	13	Peterhead (Blackhills, NK091462)	Supplied by Dr John Faithful from the Hunterian Museum collections.
21	Ballater Granite (B1)	N/A	Ballater Pass scree slope (NO 36759 97018)	Here cut by late pegmatite sheets, and post magmatic quartz-flourite veins. Collected by Sally Alexander and Dr Martin Lee, 2004.
22	Soil sample of weathered Ballater Granite (B2)	N/A	Ballater Pass scree slope (NO 36759 97018)	Sample taken from soil collected at the base of the above outcrop. Collected by Sally Alexander and Dr Martin Lee, 2004.
23	Cairngorm Granite (CG1)	N/A	Cairngorm Mt road cutting (NH 98780 07165)	Collected by Sally Alexander and Dr Martin Lee, 2004.
24	Weathered Cairngorm Granite (CG2)	N/A	Cairngorm Mt road cutting (NH 98780 07165)	Collected by Sally Alexander and Dr Martin Lee, 2004.
25	Arran Granite (AG1)	N/A	Glen Catacoll, Arran. (NR 924483)	Collected by Dr Martin Lee, 2004.

Table 4.19 The samples and the approximate compositions of the density fractions produced during the various mineral separation procedures outlined in Chapter 3. A=alkali feldspar; P=plagioclase feldspar (non-perthitic); Q=quartz.

Source	Sample name	SPT density fraction (g/cm ³)					Not SPT separated
		<2.62	2.52-2.58	2.58-2.62	2.62-2.74	>2.74	
Arran granite	Arran granite (AG1)	—	A ₁₀₀ P ₀ Q ₀	—	A ₂₅ P ₂₅ Q ₅₀	—	—
Ballater granite	Ballater granite (BG1)	—	A ₂₀ P ₈₀ Q ₂₀	—	A ₁₀ P ₈₀ Q ₁₀	—	—
Cairngorm granite	Cairngorm granite (CG1)	—	A ₁₀₀ P ₀ Q ₀	—	A ₆₀ P ₃₈ Q ₂	—	—
Helmsdale granite	Helmsdale granite (Helms)	—	—	—	—	—	—
Helmsdale arkose	Helmsdale arkose (Ark)	—	—	—	—	—	—
Peterhead granite	Peterhead granite (GU3)	—	—	A ₇₅ P ₂₅ Q ₀	—	—	—
Ross of Mull granite	Ross of Mull granite (H9)	—	A ₉₈ P ₂ Q ₀	—	A ₄₀ P ₅₀ Q ₁₀	—	—
Ross of Mull granite	Ross of Mull granite (H10)	—	A ₈₅ P ₁₅ Q ₀	—	—	—	—
Ross of Mull syenite	Ross of Mull syenite (H11)	—	—	A ₈₀ P ₂₀ Q ₀	A ₁₅ P ₈₅ Q ₀	—	—
Shap granite	Fresh Shap (Ditlefsen)	—	—	—	—	—	—
Shap granite	Unweathered Shap (UWSH)	—	—	—	—	—	—
Strontian granodiorite	Strontian granodiorite (H8)	—	—	—	A ₉₀ P ₁₀ Q ₀	—	—
Bute Pitchstone porphyry	Pitchstone porphyry (H2)	—	—	—	A ₀ P ₅₀ Q ₅₀	—	—
Bute Pitchstone porphyry	Pitchstone porphyry (H3)	—	—	—	A ₅₀ P ₅₀ Q ₀	—	—
Canisp quartz -syenite	Canisp quartz -syenite (H4)	—	—	A ₉₅ P ₀ Q ₅	A ₅₀ P ₀ Q ₅₀	—	—
Gabbro pegmatite	Gabbro pegmatite (H1)	—	—	—	—	A ₀ P ₁₀₀ Q ₀	—
Rum anorthosite	Anorthosite (H5)	—	—	—	A ₀ P ₁₀₀ Q ₀	—	—
Troctolite pegmatite	Troctolite pegmatite (H7)	—	—	—	—	A ₀ P ₉₅ Q ₅	—
Patmos	Patmos sanidine (PS)	—	A ₈₅ P ₀ Q ₁₅	—	—	—	—
Etna basaltic lava	Etna basalt (Etna)	—	A _{<10} P _{>85} Q _{<5}	—	—	—	—
Glen Tarbert migmatite	Glen Tarbert migmatite (GU2)	—	—	—	A ₁₀ P ₂₀ Q ₇₀	—	—
Lewisian gneiss	Lewisian gneiss (LG)	—	—	—	—	—	—
Torridon gneiss	Torridon gneiss (GU1)	—	A ₅₀ P ₅₀ Q ₀	—	A ₁₀ P ₃₀ Q ₆₀	—	—
Ballater granite	Ballater granite weathered (B2)	—	A ₉₀ P ₁₀ Q ₀	—	A ₁₀ P ₈₀ Q ₁₀	—	—
Cairngorm granite	Cairngorm granite weathered (C2)	—	—	A ₅₀ P ₄₅ Q ₅	A ₅ P ₅ Q ₉₀	—	—
Shap granite	Weathered Shap (WSH)	—	—	—	—	—	—
Shap granite	HF etched series	—	—	—	—	—	—
Helmsdale arkose	HF etched series	—	—	—	—	—	—
Helmsdale granite	HF etched series	—	—	—	—	—	—
F1	F1	—	—	—	—	—	A ₆₅ P ₃₀ Q ₅

Table 4.20 Summary of the microtexture, composition and optical-CL colour of the plutonic igneous and associated samples. (NL denotes non-luminescent)

Source	Sample name	Alkali feldspar microtexture	Alkali feldspar composition		Optical-CL colours	K-feldspar mineralogy	Plagioclase composition/ mineralogy	Plagioclase optical-CL colour
			Or-rich	Ab-rich				
Arran granite	Arran granite (AG1)	Fine vein microperthite with a few free plagioclase inclusions	Or ₈₃ Ab ₁₇ An ₀	Or ₉₈ Ab ₂ An ₂	K-feldspar = blue	n/a	n/a	n/a
Ballater granite	Ballater granite (BG1)	Fine microperthite with free plagioclase inclusions	Or ₉₄ Ab ₆ An ₀	Or ₁ Ab ₉₉ An ₃	K-feldspar = blue Free plagioclase = green	Tweed orthoclase	n/a	n/a
Cairngorm granite	Cairngorm granite (CG1)	Patch microperthite	Or ₉₃ Ab ₇ An ₀	Or ₁ Ab ₉₉ An ₄	K-feldspar = blue Perthitic albite = green	Microcline	n/a	n/a
Helmsdale granite	Helmsdale granite (Helms)	Vein microperthite	Or ₉₀ Ab ₁₀ An ₀	Or ₁ Ab ₉₉ An ₃	K-feldspar = blue Perthitic albite = red	Tweed orthoclase	n/a	n/a
Helmsdale arkose	Helmsdale arkose (Ark)	Vein microperthite	Or ₆₀ Ab ₃₇ An ₃	n/a	K-feldspar = blue Perthitic albite = red	Tweed orthoclase	n/a	n/a
Peterhead granite	Peterhead granite (GU3)	Vein microperthite	Or ₉₃ Ab ₇ An ₀	Or ₂ Ab ₉₄ An ₄	K-feldspar = blue Perthitic albite = red	Microcline	n/a	n/a
Ross of Mull granite	Ross of Mull granite (H9)	Vein microperthite with free plagioclase inclusions	Or ₉₁ Ab ₉ An ₀	Or ₉₁ Ab ₇ An ₂	K-feldspar = blue Perthitic albite = red Free plagioclase inclusions = red	Microcline	n/a	n/a
Ross of Mull granite	Ross of Mull granite (H10)	Vein microperthite with free plagioclase inclusions	Or ₈₈ Ab ₁₂ An ₀	Or ₂ Ab ₉₀ An ₈	K-feldspar = blue Perthitic albite = red Free plagioclase inclusions = red	Microcline	n/a	n/a
Ross of Mull syenite	Ross of Mull syenite (H11)	Vein microperthite with free plagioclase inclusions	Or ₉₂ Ab ₈ An ₀	Or ₁ Ab ₉₃ An ₆	K-feldspar = blue Perthitic albite = red Free plagioclase inclusions = NL	Microcline	n/a	n/a
Shap granite	Fresh Shap (Ditlefsen)	Lamellar & vein microperthite	Or ₉₁ Ab ₉ An ₀	Or ₁ Ab ₉₄ An ₅	K-feldspar = blue Perthitic albite = red	Tweed orthoclase	n/a	n/a
Shap granite	Unweathered Shap (UWSH)	Lamellar & vein microperthite	Or ₈₄ Ab ₁₆ An ₀	Or ₁ Ab ₉₃ An ₆	K-feldspar = blue Perthitic albite = red	Tweed orthoclase	n/a	n/a
Strontian granodiorite	Strontian granodiorite (H8)	Fine patch microperthite	Or ₈₆ Ab ₁₄ An ₀	Or ₉₄ Ab ₅ An ₁	K-feldspar = blue Perthitic albite = red	Tweed orthoclase	n/a	n/a

Table 4.21 Summary of the microtexture, composition and optical-CL colour of the silicic minor igneous intrusion samples. (NL denotes non-luminescent)

Source	Sample name	Alkali feldspar microtexture	Alkali feldspar composition		Optical-CL colours	K-feldspar mineralogy	Plagioclase composition/ mineralogy	Plagioclase optical-CL colour
			Or-rich	Ab-rich				
Bute Pitchstone porphyry	Pitchstone porphyry (H2)	Lamellae-free K-feldspar with rare plagioclase inclusions	Or ₆₄ Ab ₃₄ An ₂	Or ₁₅ Ab ₈ An ₇₇	Blue with oscillatory zoning	Tweed orthoclase	n/a	n/a
Bute Pitchstone porphyry	Pitchstone porphyry (H3)	Lamellae-free K-feldspar with plagioclase inclusions	Or ₆₇ Ab ₃₂ An ₁	Or ₂₁ Ab ₈ An ₇₁	Patchy blue-NL	Tweed orthoclase	n/a	n/a
Canisp quartz-syenite	Canisp quartz-syenite (H4)	K-feldspar with inclusions of free plagioclase	Or ₆₇ Ab ₃₃ An ₀	Or ₉₇ Ab _{0.5} An _{2.5}	K-feldspar = blotchy blue-red Free plagioclase = red	Tweed orthoclase	n/a	n/a

Table 4.22 Summary of the microtexture, composition and optical-CL colour of the igneous calcic plagioclase samples. (NL denotes non-luminescent)

Source	Sample name	Alkali feldspar microtexture	Alkali feldspar composition		Optical-CL colours	K-feldspar mineralogy	Plagioclase composition/ mineralogy	Plagioclase optical-CL colour
			Or-rich	Ab-rich				
Gabbro pegmatite	Gabbro pegmatite (H1)	n/a	n/a	n/a	n/a	n/a	Or ₃ Ab ₈ An ₈₉ Labradorite	Green
Rum anorthosite	Anorthosite (H5)	n/a	n/a	n/a	n/a	n/a	Or ₀ Ab ₁₂ An ₈₈ Bytownite	Very dull blue
Rum Troctolite pegmatite	Troctolite pegmatite (H7)	n/a	n/a	n/a	n/a	n/a	Or ₀ Ab ₁₂ An ₈₂ Bytownite	Dull green-blue

Table 4.23 Summary of the microtexture, composition and optical-CL colour of the extrusive igneous samples. (NL denotes non-luminescent)

Source	Sample name	Alkali feldspar microtexture	Alkali feldspar composition		Optical-CL colours	K-feldspar mineralogy	Plagioclase composition/ mineralogy	Plagioclase optical-CL colour
			Or-rich	Ab-rich				
Patmos	Patmos sanidine (PS)	Homogeneous	Or ₅₉ Ab ₃₈ An ₃	n/a	K-feldspar = mottled blue-red	Sanidine	n/a	n/a
Etna basaltic lava	Etna basalt (Etna)	n/a	n/a	n/a	na	n/a	Or ₂ Ab ₃₉ An ₅₉ Labradorite-	NL

Table 4.24 Summary of the microtexture, composition and optical-CL colour of the Metamorphic samples. (NL denotes non-luminescent)

Source	Sample name	Alkali feldspar microtexture	Alkali feldspar composition		Optical-CL colours	K-feldspar mineralogy	Plagioclase composition/ mineralogy	Plagioclase optical-CL colour
			Or-rich	Ab-rich				
Glen Tarbert migmatite	Glen Tarbert migmatite (GU2)	n/a	Or ₉₁ Ab ₉ An ₀	Or ₁ Ab ₂₄ An ₇₅	n/a	Tweed orthoclase	n/a	n/a
Lewisian gneiss	Lewisian gneiss (LG)	Homogeneous K-feldspar with blebs of plagioclase	Or ₉₂ Ab ₈ An ₀	Or ₁ Ab ₉₂ An ₇	K-feldspar = blue Free plagioclase = red	Microcline	n/a	n/a
Torridon gneiss	Torridon gneiss (GU1)	Lamellar cryptoperthite with blebs of plagioclase	Or ₉₅ Ab ₅ An ₀	Or ₀ Ab ₉₇ An ₃	K-feldspar = blue Free plagioclase = red	Microcline	n/a	n/a

Table 4.25 Summary of the microtexture, composition and optical-CL colour of the naturally weathered igneous samples. (NL denotes non-luminescent)

Source	Sample name	Alkali feldspar microtexture	Alkali feldspar composition		Optical-CL colours	K-feldspar mineralogy	Plagioclase composition/ mineralogy	Plagioclase optical-CL colour
			Or-rich	Ab-rich				
Ballater granite	Ballater granite weathered (BG2)	Coarse microperthite with free plagioclase inclusions	Or ₉₃ Ab ₇ An ₀	Or ₁ Ab ₉₈ An ₃	K-feldspar = blue Free plagioclase = green	Tweed orthoclase	n/a	n/a
Cairngorm granite	Cairngorm granite weathered (CG2)	Patch microperthite	Or ₉₃ Ab ₇ An ₀	Or ₁ Ab ₉₇ An ₂	K-feldspar = blue Perthitic albite = green	Microcline	n/a	n/a
Shap granite	Weathered Shap (WSH)	Lamellar & vein microperthite	Or ₈₁ Ab ₁₉ An ₀	Or ₂₅ Ab ₇₄ An ₁	K-feldspar = blue Perthitic albite = red	Tweed orthoclase	n/a	n/a

Table 4.26 Summary of the microtexture, composition and optical-CL colour of the HF acid etched samples. (NL denotes non-luminescent)

Source	Sample name	Alkali feldspar microtexture	Alkali feldspar composition		Optical-CL colours	K-feldspar mineralogy	Plagioclase composition/ mineralogy	Plagioclase optical-CL colour
			Or-rich	Ab-rich				
Shap granite	HF etched series	Lamellar & vein microperthite	Or ₈₃ Ab ₁₇ An ₀	Or ₄ Ab ₉₂ An ₄	K-feldspar = blue Perthitic albite = red	Tweed orthoclase	n/a	n/a
Helmsdale arkose	HF etched series	Vein microperthite	Or ₆₀ Ab ₃₇ An ₃	n/a	K-feldspar = blue Perthitic albite & free plagioclase = red	Tweed orthoclase	n/a	n/a
Helmsdale granite	HF etched series	Vein microperthite	Or ₉₀ Ab ₁₀ An ₀	Or ₁ Ab ₉₈ An ₃	K-feldspar = blue Perthitic albite = red	Tweed orthoclase	n/a	n/a

Table 4.27 Summary of the microtexture, composition and optical-CL colour of the laboratory standard. (NL denotes non-luminescent)

Source	Sample name	Alkali feldspar microtexture	Alkali feldspar composition		Optical-CL colours	K-feldspar mineralogy	Plagioclase composition/ mineralogy	Plagioclase optical-CL colour
			Or-rich	Ab-rich				
F1	F1	Vein microperthite	Or ₉₄ Ab ₆ An ₀	Or ₂ Ab ₉₃ An ₅	K-feldspar = blue Perthitic albite = NL	Microcline	n/a	n/a

5

The Stability of the Remnant Luminescence of Alkali Feldspars.

5.1 Introduction.

The characterisation work in the previous chapter has supplied detailed information about the compositional and microtextural properties of the suite of alkali and plagioclase feldspars. These samples (Table 5.1) were then examined for signs of instability in their luminescence signals with emphasis in the discussion of results on those factors that may determine the development, or otherwise, of anomalous fading. Ultimately these determinants will relate to the identity, density and distribution of lattice defects and these will be controlled directly by variables including: (i) feldspar crystal structure, (ii) feldspar microtexture (both exsolution microtextures and those formed by later deuteric/hydrothermal alteration of the mineral in its parent rock) and (iii) feldspar chemical composition (i.e., trace element substitution can produce defects). These three variables are themselves influenced by factors such as: (i) the geological origin of the feldspar (e.g., bulk composition of parent rock and environment of crystallization of the feldspar, such as rapidly cooled volcanic rocks vs. slowly cooled igneous intrusions) and (ii) post-crystallization history of the feldspar (e.g., partial or complete recrystallisation during metamorphism and deuteric/hydrothermal alteration, weathering, diagenesis in sedimentary rocks). Thus the aim of this chapter is to determine whether anomalous signal loss during storage corresponds with various aspects of geological origin/history of the feldspars and so enables conclusions to be made about the origin and nature of defects that render some feldspars especially susceptible to fading.

Previous studies of anomalous fading have reported signal loss in all feldspars studied, or in a particular sub-group of the samples (Huntley and Lamothe, 2001; Spooner, 1992). Those studies concluding that fading is determined by a particular geological or crystallographic factor enable predictions of possible outcomes of analyses of other feldspars to be made, and these hypotheses can be tested. The attempts to use TL to obtain crystallization ages for volcanic feldspars (Wintle 1979) brought the issue of anomalous fading to the forefront of the luminescence community. The anomalous fading of feldspars that have crystallized rapidly from high temperatures (principally the

K-feldspar sanidine), has lead to the hypothesis of the importance of structurally controlled defect distributions in fading and this model was outlined in Chapter 3. A prediction of this model is that those feldspars that have crystallised rapidly will be disordered and so more prone to fading than feldspars from plutonic rocks such as granites (i.e., microcline and orthoclase). This control on fading by cooling rates has been supported by some workers (Visocekas, 1995) but refuted by others (e.g., Huntley (2001)). Huntley (2006, 2007) has suggested that substitution of Ca into the plagioclase feldspar lattice has an influence on defect distributions with increasing Ca concentrations elevating rates of fading. A prediction of this model is that fading will scale with not only the An content of the plagioclase but also the major element chemistry of the parent rock (which ultimately controls feldspar mineralogy and chemistry). Weathering of feldspar and acid etching of the grains during sample preparation has also been suggested to influence the observed levels of signal instability (Parish, 1994). Spooner (1994) concluded that the successful application of luminescence techniques in sediment dating studies is the result of weathering reducing the effects of anomalous fading on trapped charge. Another possible factor that has been suggested in the literature is age (linked to uranium content) with older samples being more likely to suffer from underestimations due to anomalous fading. All of the above hypotheses can be tested using the sample suite chosen for this study (Table 5.1) which are discussed below in order of their broad geological groups.

The magnitude of anomalous fading of any one sample recorded in the laboratory will be dependant on experimental variables such as its mineralogical purity (if non-feldspar ‘contaminants’ luminesce at a sufficient intensity and at the appropriate wavelengths to be detected), the stimulation source, temperature and duration of storage and laboratory dose. In the present study, the temperature and duration of storage (ambient temperatures for 2 months), dose (10 Gys), dose rate and radiation type (strontium beta sources) and stimulation sources remained constant. The Risø automatic reader used three stimulation sources (IRSL, blue-OSL and TL) and the SUERC manual TL and P-IRSL readers were also used in the hope that the contrasting stimulation sources would sample different defect populations and so provide insight into the identities or affiliations of traps associated with anomalous fading (i.e., variations in signal stability with emission would indicate that some luminescence centres are coupled to stable traps whereas others are not). Yet can such variations be accounted for by current models of luminescence emission? A luminescence signal is the end-product of three processes. Firstly, electrons within traps are stimulated and excited by the addition of heat (TL) or photons (PSL). If the energy level diagrams outlined in Chapter 3 are considered, TL of increasing temperature will stimulate progressively deeper traps whereas the traps stimulated by PSL differ according to stimulation wavelength (lower energy IRSL stimulates shallow traps, UV-blue samples deeper traps). The second stage of this process is transport whereby electrons are excited into the conduction bands

where they migrate until, in the final part of the emission process they relax and retrap in a luminescence centre and emit a photon of light. The wavelength of the emission is characteristic of the recombination centre. These different types of luminescence emissions have been scrutinised significantly as a potential variable in recorded magnitudes of anomalous fading (Fattahi and Stokes, 2003b; Fattahi *et al.*, 2004; Visocekas, 2000; Visocekas and Guerin, 2006; Visocekas *et al.*, 1994; Visocekas *et al.*, 1996; Visocekas *et al.*, 1998; Visocekas and Zink, 1999; Zink and Visocekas, 1996; Zink and Visocekas, 1997; Zink *et al.*, 1995). However, few investigations have been undertaken on the different stability in the effects of the various excitation sources. Traps and centres are coupled spatially, as suggested by proximity models such as tunnelling and localised transitions, therefore if a particular luminescence centre is unstable then so should be its related trap. Therefore if one emission range is more unstable than another then different stimulations sources should also produce different stabilities as they are inherently linked. As noted above different traps are excited by different energies of stimulation so it would be logical to assume that such variations will also be observed between different excitation sources as well as emission spectra. The multistimulation runs carried out in the Risø readers will allow investigations not only of the effect of varying excitation sources but also of charge transfer effects as each excitation source causes charge to migrate into different traps, which can influence results of the subsequent stimulation run. The manual readers allow investigation of excitation effects without such possible influences.

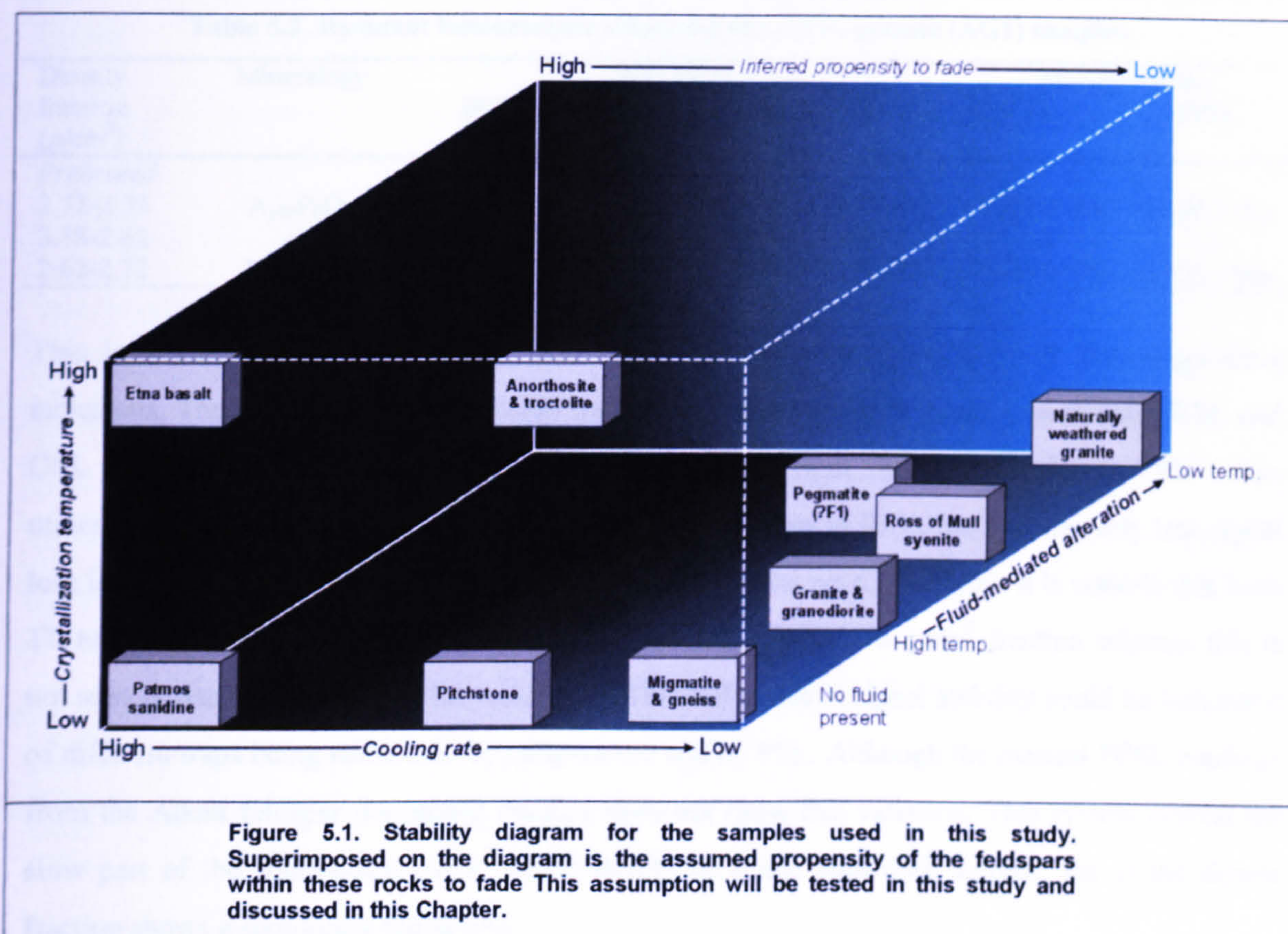
In the following experiments the mineralogy of the powders was also maintained as constant as possible to allow isolation of the various geological and stimulation variables on the stability of feldspar luminescence. Diagnosing a universally reproducible link between specific mineralogical characteristics is important in the field of feldspar luminescence dating, and the variability of such claims has been tested here.

Table 5.1 Sample set by geological association.	
Rock and sample name	Geological age
Plutonic igneous & associated rocks	
Arran Granite	58.5 Ma
Ballater Granite	425–400 Ma
Cairngorm Granite	Silurian-Devonian Boundary
Helmsdale Granite	420–400 Ma
Helmsdale arkose	Lower Devonian
Peterhead Granite	432 ± 7 Ma
Ross of Mull Granite	414 Ma
Ross of Mull Granite	414 Ma
Ross of Mull Syenite	414 Ma
Shap Granite	394 Ma
Strontian Granodiorite	435 ± 10

Silicic minor igneous intrusions	
Bute pitchstone porphyry (H2)	Late Ordovician-Late Silurian
Bute pitchstone porphyry (H3)	Late Ordovician-Late Silurian
Canisp quartz-syenite (H4)	437 ± 4.8 Ma
Igneous calcic plagioclase	
Connemara gabbro pegmatite	460 Ma
Rum anorthosite	~60 Ma
Rum troctolite pegmatite	~60 Ma
Extrusive igneous rocks	
Patmos sanidine	6.5-4 Ma
Etna basalt	Recent
Metamorphic rocks	
Glen Tarbert migmatite	435 ± 10 Ma
Lewisian gneiss	2850-2700
Torridon hornblende gneiss	2850-2700
Naturally weathered igneous	
Ballater Granite	n/a
Cairngorm Granite	n/a
Shap Granite	n/a
HF acid etched igneous & associated rocks	
Shap (1 min, 3 mins, 15 mins)	n/a
Helmsdale arkose (1 min, 3 mins, 15 mins)	n/a
Helmsdale Granite (1 min, 3 mins, 15 mins)	n/a
Laboratory standard	
F1	Unknown

The luminescence results are described in terms of various geological and chemical relationships, such as age difference, purity of sample, the weathered plutonic versus fresh counterparts, formational history, chemistry and also the effect of preheating and HF acid etching. The diagram in Figure 5.1. illustrates qualitatively the relationships between the different samples used in this study in terms of temperature of crystallization, cooling rate, presence of a fluid and inferred propensity of feldspars within these rocks to fade (on the basis of previous work).

5.2.1 Potassium feldspar in the study



5.2 Remnant luminescence results from dark storage

The data below are not values of fading in the strictest sense but rather a comparison of prompt remnant luminescence measurements with measurements after a two-month period of dark storage at ambient temperatures. These figures are the result of a sensitivity normalised (glow 1: glow 3) ratio of prompt (10 discs) to delayed (10 discs) (glow 2: glow 3) measurement cycles of a 10Gy beta irradiation with a 135°C/16hr preheat.

At the start of the study, an initial un-preheated run was carried out and the results of these are also presented as a simple comparison. The lack of any preheating meant that the remnant signal loss measured was a contribution of normal thermal instabilities and, possibly, anomalous fading. Some of the initial measurements on anomalous fading (Wintle, 1973) were made without preheating so these data was included as a point of interest.

An important consideration in these experiments was not to rely on samples that are known to fade and on museum quality specimens but rather on rocks and sediments that would be used in a dating programme. The same was true of the luminescence measurement techniques. For the remnant luminescence measurements the techniques used by the SUERC laboratory when dating feldspar dominated samples were employed.

5.2.1 Plutonic Igneous and Associated Rocks.

Table 5.2. Remnant luminescence values for the Arran granite (AG1) samples.

Density fraction (g/cm ³)	Mineralogy	IRSL	Risø reader OSL	TL	Manual readers TL	PPSL
<i>Preheated</i>						
2.52-2.58	A ₁₀₀ P ₀ Q ₀	0.891 ± 4%	0.833 ± 4%	1.120 ± 4%	1.128 ± 6%	1.130 ± 6%
2.58-2.62	---	---	---	---	---	---
2.62-2.72	A ₂₅ P ₂₅ Q ₅₀	0.824 ± 5%	0.961 ± 4%	1.303 ± 5%	1.408 ± 4%	0.792 ± 2%

This is a Tertiary granite containing fine vein microcline microperthites with free plagioclase inclusions. The alkali feldspar dominated fraction shows a consistent signal loss in both IRSL and OSL after dark storage but signal increase in TL from both readers and also in PPSL. The mineralogically mixed denser fraction again shows signal loss in IRSL but considerably less signal loss in OSL consistent with a contribution from quartz to the net OSL signal. It is notable that both TL techniques show an increase in remnant signal in the 2.52-2.58 g/cm³ fraction whereas this is not seen in data from the two PSL techniques. This difference in signal stability could be indicative of different traps being stimulated by temperature and by PSL. Although the manual PPSL readings from the Alkali feldspar dominated fraction does not show this variation. This system detects the slow part of the shine-down curve, which should be stable with dark storage, yet in the denser fraction shows a significant signal loss.

Table 5.3. Remnant luminescence values for the Ballater granite (BG1) samples.

Density fraction (g/cm ³)	Mineralogy	IRSL	Risø reader OSL	TL	Manual readers TL	PPSL
<i>Preheated</i>						
2.52-2.58	A ₂₀ P ₆₀ Q ₂₀	0.920 ± 3%	0.943 ± 4%	0.875 ± 4%	0.996 ± 3%	0.833 ± 2%
2.58-2.62	---	---	---	---	---	---
2.62-2.72	A ₁₀ P ₈₀ Q ₁₀	0.921 ± 2%	0.911 ± 3%	0.844 ± 5%	0.928 ± 3%	0.849 ± 8%

This granite straddles the Silurian-Devonian boundary and is an adamellite that was volatile-rich during emplacement (Trewin *et al.*, 1987). The alkali feldspars are fine orthoclase microperthites that contain large inclusions of free albite but both SPT fractions are plagioclase-dominated. Notably, results from all stimulation sources show a loss of signal after dark storage for both fractions. Again the PPSL system reveals lower levels of stability than the other stimulation sources in both fractions. The loss of TL signal in the Risø results could be an indication of charge transfer as the value of the remnant signal is lower than in manual TL.

Table 5.4. Remnant luminescence values for the Cairngorm granite (CG1) samples.

Density fraction (g/cm ³)	Mineralogy	IRSL	Risø reader OSL	TL	Manual readers TL	PPSL
<i>Preheated</i>						
2.52-2.58	A ₉₀ P ₁₀ Q ₀	0.998 ± 3%	0.999 ± 3%	0.899 ± 2%	0.910 ± 4%	1.48 ± 32%
2.58-2.62	---	---	---	---	---	---
2.62-2.72	A ₆₀ P ₃₈ Q ₂	0.991 ± 3%	1.089 ± 2%	0.906 ± 3%	1.171 ± 4%	1.086 ± 4%

This I-type Siluro-Devonian granite contains patch microcline microperthite alkali feldspars and the varying green-blue CL emissions from plagioclase (see Figure 4.4) suggest two generations of albite. The less dense fraction is alkali feldspar dominated and shows very good signal retention in IRSL and OSL but there is a consistent ~10 % loss of remnant signal with storage in the TL data. The denser fraction has a greater proportion of plagioclase and shows an increase in the measured remnant signals compared to the 2.52-2.58 g/cm³ fraction.

Table 5.5. Remnant luminescence values for the Helmsdale granite (Helms) samples.

Density fraction (g/cm ³)	Mineralogy	IRSL	Risø reader OSL	TL	Manual readers TL	PPSL
<i>Un-preheated</i>						
<2.62	A ₁₀₀ P ₀ Q ₀	0.611 ± 4%	0.752 ± 5%	0.712 ± 4%	---	---
<i>Preheated</i>						
<2.62	A ₁₀₀ P ₀ Q ₀	1.197 ± 3%	1.083 ± 2%	1.167 ± 4%	---	---

This 420-400 Ma granite contains orthoclase microperthites, which have separated very well into the single fraction. Comparison of unpreheated with preheated data illustrates clearly the inherent thermal instability of stored charge. After preparation of the sample with the long duration/low temperature preheat (16 hrs at 135°C) there is a consistent signal increase following dark storage at ambient temperatures. This sample was not measured using the manual systems.

Table 5.6. Remnant luminescence values for the Helmsdale arkose (Ark) samples.

Density fraction (g/cm ³)	Mineralogy	IRSL	Risø reader OSL	TL	Manual readers TL	PPSL
<i>Unpreheated</i>						
<2.62	A ₂₀ P ₈₀ Q ₀	0.481 ± 5%	0.404 ± 5%	0.690 ± 4%	---	---
<i>Preheated</i>						
<2.62	A ₂₀ P ₈₀ Q ₀	1.052 ± 6%	1.342 ± 4%	1.091 ± 8%	---	---

During the Lower Devonian the Helmsdale granite was uplifted and partially eroded, with its alkali feldspars contributing to form the Helmsdale arkose. In contrast to the Helmsdale Granite sample, the single fraction is plagioclase-rich. Preheating has again removed severe thermal instability of the stored charge (40-60% signal loss over two months) and the preheated fraction shows signal stability or slight signal increase. This sample was not measured using the manual systems.

Table 5.7. Remnant luminescence values for the Peterhead granite (GU3) sample.

Density fraction (g/cm ³)	Mineralogy	IRSL	Risø reader OSL	TL	Manual readers TL	PPSL
<i>Preheated</i>						
2.52-2.58	---	---	---	---	---	---
2.58-2.62	A ₇₅ P ₂₅ Q ₀	1.004 ± 4%	0.970 ± 3%	0.936 ± 7%	1.176 ± 2%	1.185 ± 6%
2.62-2.74	---	---	---	---	---	---

This coarsely crystalline ~432Ma granite contains microcline microperthities and the single density fraction shows consistent stability (within errors) in data from all three stimulation sources. In contrast to the Risø data results, the manual readers measured an increase in signal after storage.

Table 5.8. Remnant luminescence values for the Ross of Mull granite (H9) samples.

Density fraction (g/cm ³)	Mineralogy	IRSL	Risø reader OSL	TL	Manual readers TL	PPSL
<i>Preheated</i>						
2.52-2.58	A ₉₈ P ₂ Q ₀	0.955 ± 3%	1.014 ± 3%	1.064 ± 8%	0.911 ± 3%	1.018 ± 7%
2.58-2.62	---	---	---	---	---	---
2.62-2.72	A ₄₀ P ₅₀ Q ₁₀	0.974 ± 3%	0.960 ± 3%	0.720 ± 4%	1.135 ± 3%	0.816 ± 13%

This 414 Ma granite contains coarse microcline microperthites. The alkali feldspar dominated fraction shows reasonably good stability, although a slight variation with stimulation source; IRSL data reveal fading of ~5% and the manual TL ~9%. The denser fraction is plagioclase dominated and in all results, with the exception of the manual TL data, reveals considerably less stability than the 2.52-2.58 g/cm³ separate.

Table 5.9. Remnant luminescence values for the Ross of Mull granite (H10) sample.

Density fraction (g/cm ³)	Mineralogy	IRSL	Risø reader OSL	TL	Manual readers TL	PPSL
<i>Preheated</i>						
2.52-2.58	A ₈₅ P ₁₅ Q ₀	0.986 ± 3%	0.994 ± 4%	1.500 ± 4%	0.937 ± 3%	0.598 ± 7%
2.58-2.62	---	---	---	---	---	---
2.62-2.72	---	---	---	---	---	---

The sample made from the second Ross of Mull granite is alkali feldspar dominated and shows stability within the Risø IRSL and OSL results (within errors) although the TL exhibits a 50% signal increase. The manual TL and PPSL results show a few percent and ~40% loss of signal respectively; although the latter result (PPSL) has relatively high errors.

Table 5.10. Remnant luminescence values for the Ross of Mull hydrothermal syenite (H11) samples.

Density fraction (g/cm ³)	Mineralogy	IRSL	Risø reader OSL	TL	Manual readers TL	PPSL
<i>Preheated</i>						
2.52-2.58	---	---	---	---	---	---
2.58-2.62	A ₈₀ P ₂₀ Q ₀	0.821 ± 4%	0.798 ± 4%	0.895 ± 2%	1.014 ± 3%	1.144 ± 4%
2.62-2.72	A ₁₅ P ₈₅ Q ₀	0.844 ± 2%	0.895 ± 2%	No Signal	0.861 ± 4%	1.106 ± 3%

This rock formed by hydrothermal alteration of the Ross of Mull Granite. Despite the difference in mineralogy of the two density fractions the IRSL results are comparable within errors and both reveal a very significant signal loss with the greatest magnitude of loss being in the 2.58-2.62 g/cm³ fraction stimulated by Risø OSL. The two fractions show a difference in behaviour in manual TL but show a slight signal increase using the PPSL reader.

Table 5.11. Remnant luminescence values for the fresh and unweathered Shap granite samples.

Density fraction (g/cm ³)	Mineralogy	IRSL	Risø reader OSL	TL	Manual readers TL	PPSL
<i>Un-preheated</i>						
Fresh <2.62	A ₉₅ /P ₅ Q ₀	0.822 ± 6%	0.800 ± 5%	1.029 ± 3%	---	---
<i>Preheated</i>						
Fresh <2.62	A ₉₅ /P ₅ Q ₀	1.010 ± 5%	1.030 ± 5%	1.005 ± 5%	---	---
Unweathered <2.62	A ₈₅ /P ₁₅ /Q ₀	1.024 ± 4%	1.054 ± 6%	1.005 ± 7%	---	---

This Devonian granite is part of the Lake District batholith, and the single separate is dominated by the orthoclase micropertthites. Preheating of the Fresh Shap sample has been successful in removing the thermally unstable signal in IRSL and OSL, although the unpreheated TL result was unexpectedly stable. The Risø TL data have been integrated to omit the initial 140°C part of the TL glow curve and so the unpreheated TL results suggests good thermal stability of traps stimulated at higher temperatures. It is unfortunate that there are no manual TL results for comparison. Results from the preheated Fresh Shap and Unweathered Shap separates both show excellent signal stability. This sample was not measured using the manual systems.

Table 5.12. Remnant luminescence values for the Strontian granodiorite (H8) samples.

Density fraction (g/cm ³)	Mineralogy	IRSL	Risø reader OSL	TL	Manual readers TL	PPSL
<i>Preheated</i>						
2.52-2.58	---	---	---	---	---	---
2.58-2.62	---	---	---	---	---	---
2.62-2.72	A ₉₀ /P ₁₀ Q ₀	1.039 ± 3%	0.998 ± 3%	1.200 ± 3%	1.948 ± 3%	0.942 ± 5%

This Silurian (~435 Ma) granite yielded a single density fraction dominated by orthoclase microperthite. Results show good signal stability for Risø IRSL and OSL, but significant signal increase following dark storage in the Risø TL and manual TL data. The manual PPSL data indicate stability (within errors).

5.2.1.1 Discussion of Results.

Table 5.13 combines results from the plutonic and associated igneous rocks. The unpreheated results have been removed as these will be discussed later (Section 5.6. Table 5.55).

Table 5.13. Remnant luminescence values for feldspars from the fresh plutonic and associated rocks ordered by signal retention in IRSL. Fractions dominated by alkali feldspar are highlighted yellow, plagioclase is clear and quartz is blue.

Sample	Mineralogy	Risø reader				
		IRSL	OSL	TL	Manual readers TL	PPSL
Ross of Mull (H11)	A ₈₀ P ₂₀ Q ₀	0.821 ± 4%	0.798 ± 4%	0.895 ± 2%	1.014 ± 3%	1.144 ± 4%
Arran granite	A ₂₅ /P ₂₅ /Q ₅₀	0.824 ± 5%	0.961 ± 4%	1.303 ± 5%	1.408 ± 4%	0.792 ± 2%
Ross of Mull (H11)	A ₁₅ P ₈₅ Q ₀	0.844 ± 2%	0.895 ± 2%	No Signal	0.861 ± 4%	1.106 ± 3%
Arran granite	A ₁₀₀ P ₀ Q ₀	0.891 ± 4%	0.833 ± 4%	1.120 ± 4%	1.128 ± 6%	1.130 ± 6%
Ballater Granite	A ₂₀ P ₆₀ Q ₂₀	0.920 ± 3%	0.943 ± 4%	0.875 ± 4%	0.996 ± 3%	0.833 ± 2%
Ballater Granite	A ₁₀ P ₈₀ Q ₁₀	0.921 ± 2%	0.911 ± 3%	0.844 ± 5%	0.928 ± 3%	0.849 ± 8%
Ross of Mull (H9)	A ₉₈ P ₂ Q ₀	0.955 ± 3%	1.014 ± 3%	1.064 ± 8%	0.911 ± 3%	1.018 ± 7%
Ross of Mull (H9)	A ₄₀ P ₅₀ Q ₁₀	0.974 ± 3%	0.960 ± 3%	0.720 ± 4%	1.135 ± 3%	0.82 ± 13%
Ross of Mull (H10)	A ₈₅ P ₁₅ Q ₀	0.986 ± 3%	0.994 ± 4%	1.500 ± 4%	0.937±3%	0.598 ± 7%
Cairngorm Granite	A ₆₀ /P ₃₈ /Q ₂	0.991 ± 3%	1.089 ± 2%	0.906 ± 3%	1.171 ± 4%	1.086 ± 4%
Cairngorm Granite	A ₉₀ P ₁₀ Q ₀	0.998 ± 3%	0.999 ± 3%	0.899 ± 2%	0.910 ± 4%	1.48 ± 32%
Peterhead Granite	A ₇₅ P ₂₅ Q ₀	1.004 ± 4%	0.970 ± 3%	0.936 ± 7%	1.176 ± 2%	1.185 ± 6%
Fresh Shap Granite	A ₉₅ P ₅ Q ₀	1.010 ± 5%	1.030 ± 5%	1.005 ± 5%	---	---
UW Shap Granite	A ₈₅ P ₁₅ Q ₀	1.024 ± 4%	1.054 ± 6%	1.005 ± 7%	---	---
Strontian granodiorite	A ₉₀ P ₁₀ Q ₀	1.039 ± 3%	0.998 ± 3%	1.200 ± 3%	1.948 ± 3%	0.942 ± 5%
Helmsdale arkose	A ₂₀ P ₈₀ Q ₀	1.052 ± 6%	1.342 ± 4%	1.091 ± 8%	---	---
Helmsdale Granite	A ₁₀₀ P ₀ Q ₀	1.197 ± 3%	1.083 ± 2%	1.167 ± 4%	---	---

The fresh plutonic igneous samples should, according to previous reported studies (Visocekas *et al.*, 1994; Wintle and Huntley, 1982), show some degree of signal stability due to their slow cooling, thus giving a lower probability of a proximity related tunnelling process in the ordered alkali and plagioclase feldspars. However other studies (Lamothe *et al.*, 2003; Spooner, 1992) suggest that feldspars with these ordered crystal structures will also suffer signal loss.

Table 5.13 illustrates a general stability in the remnant luminescence of feldspars from plutonic and related rocks. Significantly, those fractions that are dominated by plagioclase or quartz show a greater propensity to fade than the alkali feldspar dominated fractions, the exception being the Helmsdale arkose, whose plagioclase dominated fraction suffers no loss of charge with dark storage. In conclusion, while there is the expected stability across these results the variations that are present cannot be easily explained by geology and dominant mineralogy alone.

5.2.2 Silicic Minor Igneous Intrusions.

Table 5.14. Remnant luminescence values for the Bute pitchstone porphyry (H2) samples.

Density fraction (g/cm ³)	Mineralogy	IRSL	Risø reader OSL	TL	Manual readers TL	PPSL
<i>Preheated</i>						
2.52-2.58	---	---	---	---	---	---
2.58-2.62	---	---	---	---	---	---
2.62-2.72	A ₀ P ₅₀ Q ₅₀	1.017 ± 4%	0.988 ± 3%	0.912 ± 2%	0.823 ± 4%	0.779 ± 12%

This sample is from a late Ordovician to late Silurian volcanic-plutonic complex but the separation has yielded only plagioclase feldspar and quartz. The IRSL and OSL results show stability (within errors), whereas both sets of TL data reveal a loss of signal with storage, which is more pronounced in the manual TL results. The PPSL results indicate significant signal instability but the high error on this figure (due to poor signal intensity using this stimulation technique) may account for some of this.

Table 5.15. Remnant luminescence values for the Bute pitchstone porphyry (H3) samples.

Density fraction (g/cm ³)	Mineralogy	IRSL	Risø reader OSL	TL	Manual readers TL	PPSL
<i>Preheated</i>						
2.52-2.58	---	---	---	---	---	---
2.58-2.62	---	---	---	---	---	---
2.62-2.72	A ₅₀ P ₅₀ Q ₀	1.025 ± 3%	0.982 ± 2%	1.129 ± 6%	0.917 ± 3%	1.624 ± 54%

The homogeneous orthoclase has been separated much more effectively in this sample and the Risø results are stable (within errors) but there is considerably more variability in data from the manual readers, but again with high errors in the PPSL results.

Table 5.16. Remnant luminescence values for the Canisp quartz-syenite (H4) samples.

Density fraction (g/cm ³)	Mineralogy	IRSL	Risø reader OSL	TL	Manual readers TL	PPSL
<i>Preheated</i>						
2.52-2.58	---	---	---	---	---	---
2.58-2.62	A ₉₅ P ₀ Q ₅	0.972 ± 3%	0.920 ± 2%	No signal	1.190 ± 6%	1.209 ± 5%
2.62-2.72	A ₅₀ P ₀ Q ₅₀	0.961 ± 3%	0.920 ± 2%	No signal	0.788 ± 9%	1.240 ± 6%

The ~437 Ma orthoclase from this quartz-syenite sill has separated cleanly into the 2.52-2.58 g/cm³ fraction, which exhibits signal loss in both Risø IRSL and OSL, gave insufficient signal for Risø TL and showed minor signal increase in data from the manual readers. The Risø results have reproduced well in the denser and more quartz-rich fraction although data from the manual readers showed significant variability and with large errors.

5.2.2.1 Discussion of Results.

Table 5.17 presents the results of this section as a whole. The unpreheated results have been omitted and will be discussed later (Section 5.6 Table 5.55). Only one powder was alkali feldspar dominated (highlighted yellow in Table 5.17) whereas the other density fractions are more heterogeneous mineralogically. Thus, these density separates are not ideal to use in order to identify any lithologically or mineralogically controlled trends in fading behaviour and perhaps indicate that in such studies such mixed samples should be avoided. However, this type of heterogeneity will be encountered in dating studies and as such have been included as a point of interest.

Table 5.17. Remnant luminescence values for the silicic igneous minor intrusion samples ordered by signal retention in IRSL. Alkali dominated fractions are highlighted yellow and mixed powders are purple.

Sample	Mineralogy	Risø reader				
		IRSL	OSL	TL	Manual readers	
					TL	PPSL
<i>Canisp quartz-syenite</i>	A ₅₀ P ₀ Q ₅₀	0.961 ± 3%	0.920 ± 2%	No signal	0.788 ± 9%	1.240 ± 6%
<i>Canisp quartz-syenite</i>	A ₉₅ P ₀ Q ₅	0.972 ± 3%	0.920 ± 2%	No Signal	1.190 ± 6%	1.209 ± 5%
<i>Bute p'stone p'yry (H2)</i>	A ₀ P ₅₀ Q ₅₀	1.017 ± 4%	0.988 ± 3%	0.912 ± 2%	0.823 ± 4%	0.779 ± 12%
<i>Bute p'stone p'yry (H3)</i>	A ₅₀ P ₅₀ Q ₀	1.025 ± 3%	0.982 ± 2%	1.129 ± 6%	0.917 ± 3%	1.624 ± 54%

The Bute pitchstone samples have relatively stable Risø IRSL and OSL results whereas the quartz-syenite data are unstable. The manual TL results show significant signal loss in three of the samples whereas the PPSL data show a signal increase in three. The variability of the manual TL data is most likely a product of the low intensities resulting with this stimulations source. It can also be observed in Chapter 4 that the optical-CL of these results was also of low intensity. There appears to be no obvious trend within this data set, possibly resulting from the heterogeneity of the samples.

5.2.3 Igneous Calcic Plagioclase.

Table 5.18. Remnant luminescence values for the Connemara gabbro pegmatite (H1) sample.

Density fraction (g/cm ³)	Mineralogy	Risø reader				
		IRSL	OSL	TL	Manual readers TL	PPSL
<i>Preheated</i>						
2.52-2.58	---	---	---	---	---	---
2.58-2.62	---	---	---	---	---	---
2.62-2.72	A ₀ P ₁₀₀ Q ₀	1.147 ± 2%	1.061 ± 3%	No Signal	0.561 ± 4%	1.037 ± 7%

This 460 Ma pegmatite has yielded a pure labradorite powder that has a stable signal in OSL although shows a signal increase after storage in IRSL. There was insufficient signal in Risø TL, which may also explain the signal loss in manual TL. The manual PPSL data also show stability.

Owing to the low TL signal intensities, remnant luminescence values were calculated for five 100°C channels in the glow curves from the manual TL system (Table 5.19). These data show that the best reproducibility of signals disc-to-disc (i.e., lowest errors) is found in the 200-400°C region of the glow curves, but there is no indication of a stable temperature plateau in these groups.

Table 5.19 Remnant manual TL in 100°C groups for the Connemara gabbro pegmatite (H1) sample.

Density fraction (g/cm ³)	Mineralogy	Manual TL stimulation results				
		0-100°C	100-200°C	200-300°C	300-400°C	400-500°C
<i>Preheated</i>						
2.52-2.58	---	---	---	---	---	---
2.58-2.62	---	---	---	---	---	---
2.62-2.72	A ₀ P ₁₀₀ Q ₀	4.794 ± 723%	2.340 ± 37%	0.756 ± 12%	0.426 ± 22%	-31.671 ± 22%

Table 5.20 Remnant luminescence values for the Rum anorthosite (H5) samples.

Density fraction (g/cm ³)	Mineralogy	Risø reader				
		IRSL	OSL	TL	Manual readers TL	PPSL
<i>Preheated</i>						
2.52-2.58	---	---	---	---	---	---
2.58-2.62	---	---	---	---	---	---
2.62-2.72	A ₀ P ₁₀₀ Q ₀	1.030 ± 3%	1.099 ± 3%	1.601 ± 6%	0.792 ± 13%	1.083 ± 14%

This Palaeocene bytownite from the Rum Eastern Layered Series (Daniels *et al.*, 1953) is stable in IRSL and OSL although has some signal increase in Risø TL (Table 5.20). Errors on data from the manual readers are fairly high, probably owing to low luminescence emission intensities, which are also observed when measuring its optical-CL emission. The manual TL data have been broken down into 100°C channels (Table 5.21) and these results again illustrate similar problems resulting from low signal intensities (compare with Table 5.19).

Table 5.21 Remnant manual TL in 100°C groups for the Rum anorthosite (H5) samples.

Density fraction (g/cm ³)	Mineralogy	Manual TL stimulation results				
		0-100°C	100-200°C	200-300°C	300-400°C	400-500°C
<i>Preheated</i>						
2.52-2.58	---	---	---	---	---	---
2.58-2.62	---	---	---	---	---	---
2.62-2.72	A ₀ P ₁₀₀ Q ₀	-1.759 ± 85%	3.312 ± 32%	0.497± 29%	0.314± 63%	22.515 ± 216%

Table 5.22. Remnant luminescence values for the Rum troctolite pegmatite (H7) samples.

Density fraction (g/cm ³)	Mineralogy	Risø reader				
		IRSL	OSL	TL	Manual readers TL	PPSL
<i>Preheated</i>						
2.52-2.58	A ₀ P ₉₅ Q ₅	1.098 ± 3%	1.021 ± 3%	No Signal	No Signal	No Signal
2.58-2.62	---	---	---	---	---	---
2.62-2.72	---	---	---	---	---	---

This other Palaeocene bytownite from Rum is stable in IRSL and OSL but had very low emission intensities in TL and PPSL (Table 5.22). Division of the manual TL data into 100°C channels (Table 5.23) gives a hint of a signal plateau in the 200-400°C range, although again the low signal intensities make clear conclusions difficult to draw.

Table 5.23. Remnant TL in 100°C groups for the Rum troctolite pegmatite (H7) samples.

Density fraction (g/cm ³)	Mineralogy	Manual TL stimulation results				
		0-100°C	100-200°C	200-300°C	300-400°C	400-500°C
<i>Preheated</i>						
2.52-2.58	A ₀ P ₉₅ Q ₅	5.947±904%	2.259±42%	2.423±4 %	-0.08 5±74%	-2.263±186%
2.58-2.62	---	---	---	---	---	---
2.62-2.72	---	---	---	---	---	---

5.2.3.1 Discussion of Results.

Table 5.24. Remnant luminescence values for the igneous calcic plagioclase samples ordered by signal retention in IRSL.

Sample	Mineralogy	IRSL	Risø reader OSL	TL	Manual readers	
					TL	PPSL
<i>Rum anorthosite</i>	A ₀ P ₁₀₀ Q ₀	1.030 ± 3%	1.099 ± 3%	1.601 ± 6%	0.792 ± 13%	1.083 ± 14%
<i>Troctolite pegmatite</i>	A ₀ P ₉₅ Q ₅	1.098 ± 3%	1.021 ± 3%	No Signal	No Signal	No Signal
<i>Gabbro pegmatite</i>	A ₀ P ₁₀₀ Q ₀	1.147 ± 2%	1.061 ± 3%	No Signal	0.561 ± 4%	1.037 ± 7%

Table 5.24 presents results from the calcic plagioclases. As expected these samples have low emission intensities particularly in TL and the high errors on the manual PPSL data are a consequence. The better quality data from the Risø readers show that the signals were stable with storage. Such a result could be of significance because calcium content has been suggested to play a major role in inducing anomalous fading within plagioclase feldspars. Although the very low

signal intensities, after a 16hr at 135°C preheat, could indicate that these calcium dominated samples fade rapidly in a few hours and all the comparisons to produce these data are from very insignificant signals, possibly made mostly of background variation. Further investigation of the potential avoidance of calcic plagioclase from a luminescence dating point of view is needed.

5.2.4 Extrusive Igneous Rocks.

Table 5.25. Remnant luminescence values for the Patmos sanidine samples.

Density fraction (g/cm ³)	Mineralogy	Risø reader		Manual readers		
		IRSL	OSL	TL	TL	PPSL
<i>Unpreheated</i>						
<2.62	A _{>95} P ₀ Q _{<5}	0.717 ± 5%	0.533 ± 7%	0.332 ± 2%	---	---
<i>Preheated</i>						
<2.62	A _{>95} P ₀ Q _{<5}	0.964 ± 2%	0.975 ± 2%	2.070 ± 30 %	---	---

Preheating of this geologically young sanidine removes most of the instability of the unpreheated samples (Table 5.25). The preheated alkali feldspar has a few percent signal loss in IRSL and OSL, but much less than expected from previous work on volcanic sanidines. The TL results show a doubling of signal with storage and whether this is a consequence of the high levels of instability within the TL stimulated traps or is an instrumental artefact is discussed below.

Table 5.26. Remnant luminescence values for the Etna basaltic lava (Etna) samples.

Density fraction (g/cm ³)	Mineralogy	Risø reader			Manual readers	
		IRSL	OSL	TL	TL	PPSL
<i>Unpreheated</i>						
<2.62	A<10P>85Q<5	0.766 ± 2%	0.876 ± 4%	1.050 ± 5%	---	---
<i>Preheated</i>						
<2.62	A<10P>85Q<5	1.149 ± 3%	1.162 ± 2%	1.022 ± 30%	---	---

This Recent labradorite has a thermally unstable signal in IRSL and OSL, but significantly not in Risø TL. After preheating the plagioclase feldspar has a much greater stability and in fact shows a small degree of signal increase with storage.

5.2.4.1 Discussion of Results.

Table 5.27. Remnant luminescence values for the extrusive igneous samples ordered by signal retention in IRSL. Alkali dominated fractions are highlighted yellow and plagioclase clear.

Sample	Mineralogy	Risø reader		Manual readers		
		IRSL	OSL	TL	TL	PPSL
<i>Patmos sanidine</i>	A _{>95} P ₀ Q _{<5}	0.964 ± 2%	0.975 ± 2%	2.070 ± 30 %	---	---
<i>Etna basalt</i>	A _{<10} P _{>85} Q _{<5}	1.149 ± 3%	1.162 ± 2%	1.022 ± 30%	---	---

Table 5.27 presents the results of this section; the unpreheated results will be discussed elsewhere (Section 5.6, Table 5.55). Feldspars from extrusive igneous rocks have been predicted to be particularly susceptible to anomalous fading due to the disordered lattice owing to rapid cooling from high temperatures of crystallization (see Chapter 2), but results in Table 5.27 are not in agreement with these predictions. The Patmos sanidine especially is predicted to experience severe anomalous fading with dark, ambient temperature storage (Huntley and Lamothe, 2001; Visocekas, 1979; Visocekas *et al.*, 1998). The results in Table 5.27 demonstrate only a few percent signal loss following the long/low temperature preheat regime. The high errors on the TL results are due to low signal intensities and should be treated as erroneous. Therefore when comparisons are made between the volcanic and the plutonic samples above there is no evidence of the differences predicted as a result of rate of crystallization and both sets of samples exhibit comparable levels of stability.

5.2.5 Metamorphic Rocks.

Table 5.28. Remnant luminescence values for the migmatite (GU2) samples.

Density fraction (g/cm ³)	Mineralogy	Risø reader			Manual readers	
		IRSL	OSL	TL	TL	PPSL
<i>Preheated</i>						
2.52-2.58	---	---	---	---	---	---
2.58-2.62	---	---	---	---	---	---
2.62-2.72	A ₁₀ P ₂₀ Q ₇₀	0.856 ± 2%	0.920 ± 3%	0.913 ± 3%	1.079 ± 3%	0.769 ± 16%

Alkali feldspar has separated poorly from this metamorphic rock, which formed in the thermal aureole surrounding the Strontian granodiorite. The Risø results show a consistent signal loss while there is considerable variation in the manual systems; the TL is stable and the PPSL severely unstable with high errors (Table 5.28).

Table 5.29. Remnant luminescence values for the Lewisian gneiss (LG) samples.

Density fraction (g/cm ³)	Mineralogy	Risø reader			Manual readers	
		IRSL	OSL	TL	TL	PPSL
<i>Unpreheated</i>						
<2.62	A ₈₀ P ₂₀ Q ₀	0.858 ± 5%	0.744 ± 6%	0.804 ± 2%	---	---
<i>Preheated</i>						
<2.62	A ₈₀ P ₂₀ Q ₀	0.947 ± 2%	0.935 ± 3%	0.880 ± 8%	---	---

The Archean orthoclase in the single density separate is unstable prior to preheating but also shows considerable instability across all stimulation sources after preheating (Table 5.29).

Table 5.30. Remnant luminescence values for the Torridonian hornblende gneiss (GU1) samples.

Density fraction (g/cm ³)	Mineralogy	Risø reader				
		IRSL	OSL	TL	Manual readers	
					TL	PPSL
<i>Preheated</i>						
2.52-2.58	A ₅₀ P ₅₀ Q ₀	0.918 ± 3%	0.933 ± 4%	0.895 ± 2%	1.468 ± 4%	1.200 ± 10%
2.58-2.62						
2.62-2.72	A ₁₀ P ₃₀ Q ₆₀	0.973 ± 2%	0.974 ± 5%	0.905 ± 8%	1.079 ± 3%	0.853 ± 8%

This Precambrian hornblende gneiss has separated variably, with both fractions being mineralogically heterogeneous. Risø results from the 2.52-2.58 g/cm³ fraction show a ~10% signal loss with storage, but the luminescence emission was more stable when measured using the manual readers. The denser fraction is quartz-dominated and surprisingly shows a loss of stored signal in all but the manual TL data (Table 5.30). The manual TL results have been investigated further by grouping the data into 100°C integrals (Table 5.31). In the alkali feldspar dominated sample, there is a distinct plateau in the region of the glow curve used to calculate results in Table 5.30. The glow curves of the 2.58-2.62 g/cm³ fraction are more reproducible than for the quartz-dominated denser separate.

Table 5.31. Remnant manual TL in 100°C groups for the Torridonian hornblende gneiss (GU1) samples.

Density fraction (g/cm ³)	Mineralogy	Manual TL stimulation results				
		0-100°C	100-200°C	200-300°C	300-400°C	400-500°C
<i>Preheated</i>						
2.52-2.58						
2.58-2.62	A ₅₀ P ₅₀ Q ₀	-1.079± 42%	1.064± 33%	1.491± 4%	1.461± 5%	2.769± 210%
2.62-2.72	A ₁₀ P ₃₀ Q ₆₀	-1.693± 17%	1.254± 59%	1.060± 3%	1.210± 3%	0.011± 89%

5.2.5.1 Discussion of Results.

Table 5.32. Remnant luminescence values for the metamorphic samples ordered by signal retention in IRSL. Alkali feldspar dominated fractions are highlighted yellow, quartz blue and mineralogically mixed fractions are purple.

Sample	Mineralogy	Risø reader			Manual readers	
		IRSL	OSL	TL	TL	PPSL
<i>Glen Tarbert Migmatite</i>	A ₁₀ P ₂₀ Q ₇₀	0.856 ± 2%	0.920 ± 3%	0.913 ± 3%	1.079 ± 3%	0.769 ± 16%
<i>Hornblende gneiss</i>	A ₅₀ P ₅₀ Q ₀	0.918 ± 3%	0.933 ± 4%	0.895 ± 2%	1.468 ± 4%	1.200 ± 10%
<i>Lewisian gneiss</i>	A ₈₀ P ₂₀ Q ₀	0.947 ± 2%	0.935 ± 3%	0.880 ± 8%	---	---
<i>Hornblende gneiss</i>	A ₁₀ P ₃₀ Q ₆₀	0.973 ± 2%	0.974 ± 5%	0.905 ± 8%	1.079 ± 3%	0.853 ± 8%

Table 5.32 presents the results of this section as a whole; the unpreheated results are discussed elsewhere (Section 5.6, Table 5.55). These density fractions are heterogeneous with only the Lewisian gneiss yielding an alkali feldspar dominated powder. However, the majority of results show some signal loss with dark storage. The variation again lies in the results of the manual

systems and the high errors in the PPSL results suggest caution must be used in interpretation, although within errors these data show similar levels of signal stability to the Risø PSL sources. The manual TL results are stable and more so than the Risø TL results. If we concentrate on the Risø results initially it can be seen that metamorphism appears to promote the propensity of feldspars to fade across the three stimulation techniques. In the manual readers the signals are mostly stable although there are two results that show signal loss with storage the Hornblende Gneiss PPSL reader results being comparable with those from the Risø. The Migmatite result from the same reader shows more loss but has a significant error margin that could account for this difference.

5.2.6 The Laboratory Standard.

Table 5.33. Remnant luminescence values for the laboratory standard (F1) sample.

Density fraction (g/cm ³)	Mineralogy	Risø reader				
		IRSL	OSL	TL	Manual readers TL	PPSL
<i>Unpreheated</i>						
Not density separated	A ₆₅ P ₃₀ Q ₅	0.617 ± 8%	0.604 ± 5%	0.520 ± 7%	---	---
<i>Preheated</i>						
Not density separated	A ₆₅ P ₃₀ Q ₅	1.010 ± 3%	1.016 ± 2%	1.062 ± 5%	---	---

The origin and age of these microcline microperthites is unknown. This sample again shows the value of preheating in removing the instabilities (~50% of the stored signal) within this sample. The signal in the preheated sample is entirely stable across the three Risø stimulation sources (Table 5.33).

5.2.6.1 Discussion of Results.

The stability of this standard with storage after being treated with the long and low temperature preheat was expected and demonstrates clearly the effectiveness of the experimental protocols used in this study.

5.2.7 Naturally Weathered Igneous.

Table 5.34. Remnant luminescence values for the Ballater granite (BG2) samples.

Density fraction (g/cm ³)	Mineralogy	Risø reader				
		IRSL	OSL	TL	Manual readers TL	PPSL
<i>Preheated</i>						
2.52-2.58	A ₉₀ P ₁₀ Q ₀	0.911 ± 2%	0.959 ± 2%	1.007 ± 5%	0.941 ± 5%	0.936 ± 33%
2.58-2.62	---	---	---	---	---	---
2.62-2.72	A ₁₀ P ₈₀ Q ₁₀	1.302 ± 2%	1.641 ± 3%	1.000 ± 4%	0.975 ± 5%	1.097 ± 6%

The 2.52-2.58 g/cm³ fraction of the weathered Ballater orthoclase microperthites is stable (within errors) in the TL but shows some loss in both IRSL and OSL data. For the denser plagioclase dominated sample there is no signal loss in any of the results, although the IRSL and OSL data show some signal increase after storage (Table 5.34).

Table 5.35. Remnant luminescence values for the Cairngorm granite (CG2) samples.

Density fraction (g/cm ³)	Mineralogy	Risø reader		Manual readers		
		IRSL	OSL	TL	TL	PPSL
<i>Preheated</i>						
2.52-2.58	---	---	---	---	---	---
2.58-2.62	A ₅₀ P ₄₅ Q ₅	1.002 ± 2%	1.011 ± 3%	0.966 ± 1%	1.205 ± 3%	1.054 ± 6%
2.62-2.72	A ₅ P ₅ Q ₉₀	0.927 ± 5%	0.957 ± 5%	0.915 ± 6%	1.034 ± 4%	1.086 ± 4%

The alkali and plagioclase feldspar dominated 2.58-2.62 g/cm³ fraction is stable, within error for the Risø TL. The quartz-dominated denser fraction shows a greater loss of signal in the Risø results but not in data from the manual readers (Table 5.35).

Table 5.36. Remnant luminescence values for the Shap granite (WSH) samples.

Density fraction (g/cm ³)	Mineralogy	Risø reader		TL	Manual readers	
		IRSL	OSL		TL	PPSL
<i>Unpreheated</i>						
<2.62	A ₉₅ P ₅ Q ₀	0.842 ± 7%	0.782 ± 4%	0.824 ± 6%	---	---
<i>Preheated</i>						
<2.62	A ₉₅ P ₅ Q ₀	1.000 ± 2%	1.010 ± 3%	0.946 ± 3%	---	---

The impact of natural weathering on Shap Granite alkali feldspars has been studied in detail by Lee *et al* (1995). Results of this work have demonstrated that weathering is selective to high energy sites on the grain surface, especially the outcrops of edge dislocations along albite exsolution lamellae (Fig. 5.2). Thus, progressive weathering should remove defects, which are sites in the lattice where charge may potentially be stored.

Preheating has removed the ~20% unstable signal in these weathered orthoclase microperthites from the two PSL stimulation sources. The TL results however still exhibit a few percent loss even after preheating (Table 5.36).

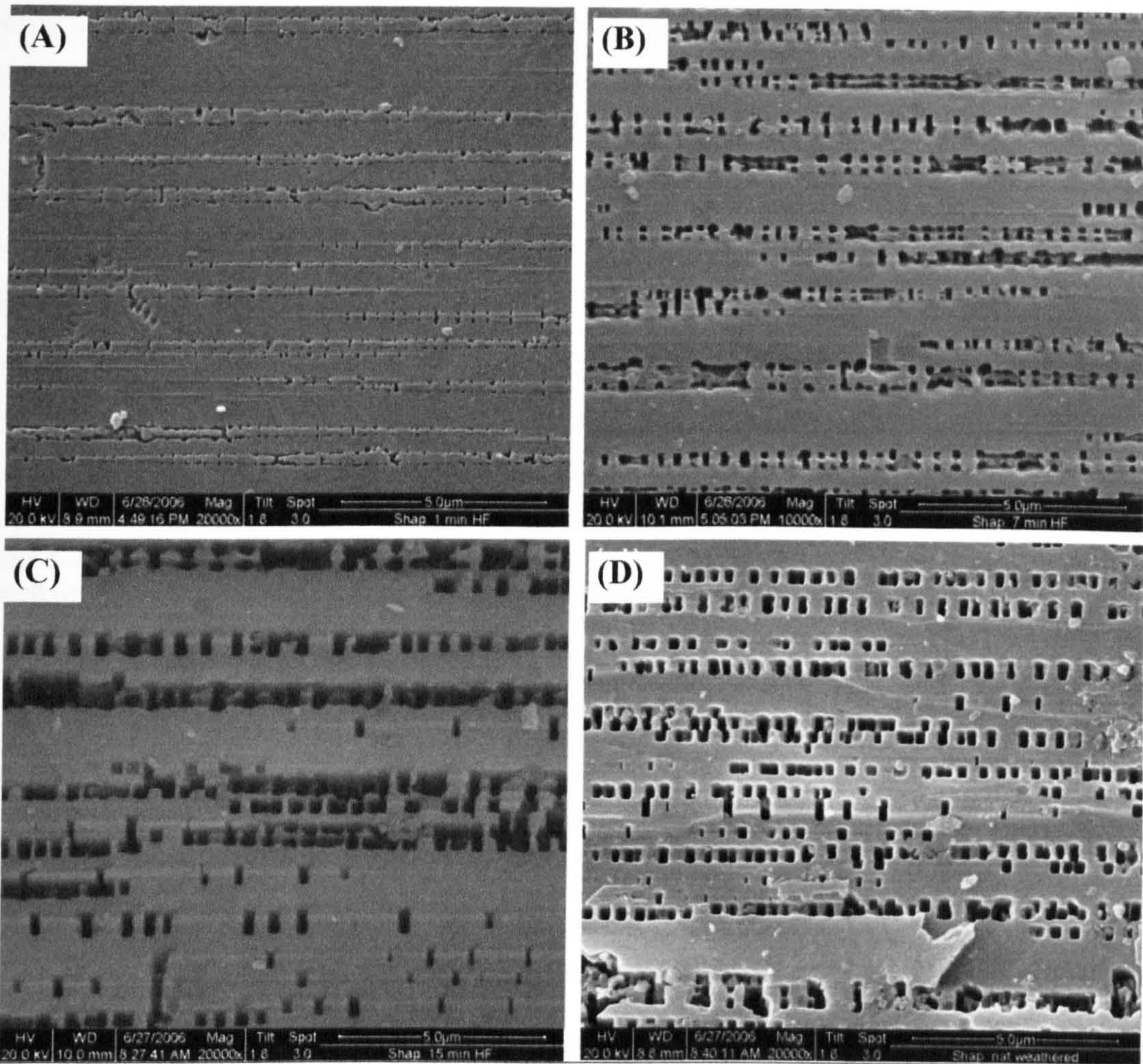


Figure 5.2. Secondary electron ESEM images of Shap Granite alkali feldspars that have undergone HF acid etching for different lengths of time (a-c) and also grains that have been naturally weathered. Acid etching is selective to the sites where edge dislocations along albite exsolution lamellae intersect the grain surface, producing lines of etch pits. Natural weathering (d) is also selective to dislocation outcrops and the images in (c) and (d) are very similar.

5.2.7.1 Discussion of the Influence of Weathering.

There is a broad agreement within the luminescence community that weathering can modify mineral luminescence properties and Parish (1994) suggested that this process can in fact induce anomalous fading. However, Spooner (1994) showed that documented cases of laboratory fading in sediment dating studies are less common than would be expected from the claimed ubiquitous nature of anomalous fading. He speculated that feldspars likely to exhibit fading are disproportionately absent from the sediment record because they are prone to elimination through weathering owing to disorder in their lattice. One way in which to test these suggestions is to compare the luminescence properties of feldspars extracted from fresh granites with their weathered equivalents.

Table 5.37 compares the fresh and weathered Ballater granite samples. If differences in the mineralogy of the powders are disregarded then these results suggest that weathering has no

consistent impact on the stability of the luminescence signal during dark storage. Comparison of the three plagioclase dominated fractions shows that the two separates from the fresh granite fade in Risø IRSL, OSL and TL whereas plagioclase from the weathered granite sample is stable in the Risø results or displays some signal increase with dark storage. Thus, it could be argued that weathering does induce stability, at least in the case of plagioclase feldspars from this granite. Possible support for this explanation comes from the alkali feldspar dominated weathered granite sample whereby weathering has not induced stability, possibly because the weathering rate of alkali feldspar is much slower than plagioclase and so a given duration of weathering may have less impact on the luminescence properties of the orthoclase microperthite than the albite.

Table 5.37. Remnant luminescence for the fresh vs. naturally weathered Ballater granite samples ordered by signal retention in IRSL. Alkali feldspar dominated fractions are highlighted yellow and plagioclase is clear.

Sample	Mineralogy	Risø reader				
		IRSL	OSL	TL	Manual readers TL	PPSL
Weathered granite	A ₉₀ P ₁₀ Q ₀	0.911 ± 2%	0.959 ± 2%	1.007 ± 5%	0.941 ± 5%	0.936 ± 33%
Fresh granite	A ₂₀ P ₆₀ Q ₂₀	0.920 ± 3%	0.943 ± 4%	0.875 ± 4%	0.996 ± 3%	0.833 ± 2%
Fresh granite	A ₁₀ P ₈₀ Q ₁₀	0.921 ± 2%	0.911 ± 3%	0.844 ± 5%	0.928 ± 3%	0.849 ± 8%
Weathered granite	A ₁₀ P ₈₀ Q ₁₀	1.302 ± 2%	1.641 ± 3%	1.000 ± 4%	0.975 ± 5%	1.097 ± 6%

Table 5.38 presents results of natural weathering on the luminescence behaviour of the Cairngorm samples. The impact of weathering is difficult to discern because the fresh alkali feldspars are stable in IRSL and OSL. Data from Risø TL are less stable and it could be argued that weathering again increases stability in the case of the TL signal.

Table 5.38. Remnant luminescence for the fresh vs. naturally weathered Cairngorm granite samples ordered by signal retention in IRSL. Alkali feldspar dominated fractions are highlighted yellow and quartz is blue.

Sample	Mineralogy	Risø reader				
		IRSL	OSL	TL	Manual readers TL	PPSL
Weathered granite	A ₅ P ₅ Q ₉₀	0.927 ± 5%	0.957 ± 5%	0.915 ± 6%	1.034 ± 4%	1.086 ± 4%
Fresh granite	A ₆₀ P ₃₈ Q ₂	0.991 ± 3%	1.089 ± 2%	0.906 ± 3%	1.171 ± 4%	1.086 ± 4%
Fresh granite	A ₉₀ P ₁₀ Q ₀	0.998 ± 3%	0.999 ± 3%	0.899 ± 2%	0.910 ± 4%	1.482 ± 32%
Weathered granite	A ₅₀ P ₄₅ Q ₅	1.002 ± 2%	1.011 ± 3%	0.966 ± 1%	1.205 ± 3%	1.054 ± 6%

Table 5.39 presents results comparing the effects of weathering on the Shap granite feldspar samples. The results are reproducible within errors and provide no information on the impact of weathering on signal loss during storage, to the extent that it induces or removes fading. Rather it suggests that weathering has no impact on Shap granite.

Table 5.39. Remnant luminescence for the fresh vs. naturally weathered Shap granite samples ordered by signal retention in IRSL. Alkali feldspar dominated fractions are highlighted yellow.

Sample	Mineralogy	IRSL	Risø reader OSL	TL	Manual readers	
					TL	PPSL
Weathered Shap	A ₉₅ P ₅ Q ₀	1.000 ± 2%	1.010 ± 3%	0.946 ± 3%	---	---
Fresh Shap	A ₉₅ P ₅ Q ₀	1.010 ± 5%	1.030 ± 5%	1.005 ± 5%	---	---
Unweathered Shap	A ₈₅ P ₁₅ Q ₀	1.024 ± 4%	1.054 ± 6%	1.005 ± 7%	---	---

5.2.8 HF Acid Etched Igneous and Associated Rocks.

Table 5.40. Remnant luminescence values for the HF acid etched Shap granite samples.

Density fraction (g/cm ³)	Mineralogy	IRSL	Risø reader OSL	TL	Manual readers TL PPSL	
<i>Unpreheated</i>						
<2.62						
1 min. etched	A ₈₀₋₉₀ P ₅ Q ₅₋₁₅	0.306 ± 4%	0.308 ± 5%	0.638 ± 3%	---	---
3 mins etched	A ₈₀₋₉₀ P ₅ Q ₅₋₁₅	0.708 ± 5%	0.654 ± 5%	0.706 ± 3%	---	---
15 mins etched	A ₈₀₋₉₀ P ₅ Q ₅₋₁₅	0.727 ± 3%	0.653 ± 7%	0.735 ± 4%	---	---
<i>Preheated</i>						
<2.62						
1 min. etched	A ₈₀₋₉₀ P ₅ Q ₅₋₁₅	1.007 ± 2%	0.991 ± 3%	1.505 ± 7%	---	---
3 mins etched	A ₈₀₋₉₀ P ₅ Q ₅₋₁₅	1.020 ± 4%	0.998 ± 4%	1.020 ± 4%	---	---
15 mins etched	A ₈₀₋₉₀ P ₅ Q ₅₋₁₅	1.069 ± 5%	1.025 ± 3%	1.017 ± 4%	---	---

As illustrated in Figure 5.1, HF acid etching of alkali feldspars is selective to the sites where edge dislocations along albite exsolution lamellae intersect the grain surface, producing etch pits. With progressive etching these pits deepen and widen by dissolution of surrounding orthoclase and albite. Results in Table 5.40 show that progressive acid etching increases the magnitude of the signal retained in the unpreheated powders and this effect is especially noticeable in the IRSL and OSL data. Preheating removes the entire thermally unstable signal and there is little variation between samples etched for different durations; the high error in the TL data for the 1 minute etched sample is due to the low intensity of TL.

Table 5.41. Remnant luminescence values for the HF acid etched Helmsdale arkose samples.

Density fraction (g/cm ³)	Mineralogy	IRSL	Risø reader OSL	TL	Manual readers	
					TL	PPSL
<i>Unpreheated</i>						
<2.62						
1 min. etched	A ₂₀ P ₈₀ Q ₀	0.113 ± 5%	0.521 ± 6%	0.308 ± 8%	---	---
3 mins etched	A ₂₀ P ₈₀ Q ₀	0.064 ± 5%	0.450 ± 2%	0.106 ± 5%	---	---
15 mins etched	A ₂₀ P ₈₀ Q ₀	0.075 ± 4%	0.067 ± 5%	0.075 ± 8%	---	---
<i>Preheated</i>						
<2.62						
1 min. etched	A ₂₀ P ₈₀ Q ₀	1.359 ± 4%	1.176 ± 3%	0.952 ± 6%	---	---
3 mins etched	A ₂₀ P ₈₀ Q ₀	0.916 ± 3%	0.910 ± 5%	0.713 ± 5%	---	---
15 mins etched	A ₂₀ P ₈₀ Q ₀	1.072 ± 3%	1.157 ± 3%	1.187 ± 6%	---	---

In contrast to the Shap samples the Helmsdale arkose powders are plagioclase-rich and show a dramatic reduction in the magnitude of remnant signal in the unpreheated fractions with etching (Table 5.42). By contrast, the data from the preheated samples are far more stable although there is a considerable range of results from any one stimulation source between the samples etched for different lengths of time.

Table 5.42. Remnant luminescence values for the acid etched Helmsdale granite samples.

Density fraction (g/cm ³)	Mineralogy	Risø reader			Manual readers	
		IRSL	OSL	TL	TL	PPSL
<i>Unpreheated</i>						
<2.62						
1 min. etched	A ₈₀ P ₂₀ Q ₀	0.931 ± 2%	0.768 ± 6%	0.406 ± 7%	---	---
3 mins etched	A ₈₀ P ₂₀ Q ₀	0.963 ± 4%	0.962 ± 5%	0.961 ± 6%	---	---
15 mins etched	A ₈₀ P ₂₀ Q ₀	1.107 ± 5%	1.098 ± 4%	0.956 ± 8%	---	---
<i>Preheated</i>						
<2.62						
1 min. etched	A ₈₀ P ₂₀ Q ₀	1.279 ± 4%	1.226 ± 3%	1.244 ± 7%	---	---
3 mins etched	A ₈₀ P ₂₀ Q ₀	1.302 ± 4%	1.286 ± 3%	1.052 ± 5%	---	---
15 mins etched	A ₈₀ P ₂₀ Q ₀	1.036 ± 2%	1.103 ± 2%	1.029 ± 5%	---	---

In common to the Shap samples the magnitude of remnant signal in the unpreheated samples increases with the duration of etching and this effect is especially noticeable in OSL and TL; 15 minutes of etching stabilises the alkali feldspar signal. Etching has little impact overall on the magnitude of the remnant signal in the preheated samples, although there is an indication that the amount of signal increase after dark storage decreases with acid etching.

5.2.8.1 Discussion of the Influence of HF Acid Etching.

Results from the unpreheated samples will be discussed first, then the preheated acid etched grains. The unpreheated alkali feldspar rich Shap and Helmsdale Granite powders both show an increase in remnant signal with duration of etching. In the Helmsdale case the most highly etched samples are essentially stable, whereas the Shap micropertthites retain a considerable component of thermally unstable signal even after 15 minutes of etching. The clear implications of these results are that acid etching selectively destroys thermally unstable traps, or at least destroys the thermally unstable traps at a greater rate than the stable ones. These traps may well correspond to the dislocations that are picked out by the HF treatment. Unpreheated plagioclase feldspars from the Helmsdale arkose show the opposite effect, with loss of stored charge increasing with the duration of acid etching. This difference in behaviour between the alkali and plagioclase feldspar rich samples cannot be an instrumental artefact because the Helmsdale arkose measurements were undertaken on the same carousel and between the Shap and Helmsdale granite discs. It is likely that the plagioclase feldspars are far more susceptible to acid etching than alkali feldspars and etching is selective to the traps that should retain the stored charge.

Results from the preheated powders all show no real change in signal stability with duration of exposure to HF acid, although there is a hint of increased stability in OSL results from Shap granite alkali feldspars. Thus although the grains have been acid etched, thermally stable defects that can retain stored charge remain in sufficient abundance to yield a measurable signal with low errors. Results of the Helmsdale granite give no additional information as they are all consistently stable. Plagioclase from the Helmsdale arkose has an unusual behaviour as the 1 and 15 minutes results are in good agreement with each other yet the 3 minute etched plagioclase exhibits a ~10% loss of stored charge in IRSL and OSL and ~30% in TL.

In common with natural weathering, there is little evidence that HF acid etching decreases stability of the stored signal, contrary to the claims by Parish (1994), and most likely has little impact on the thermally stable traps, as suggested by Spooner (1994). In the case of the Shap granite the 15 minutes duration of etching creates more stable remnant signals than the natural weathering, supporting Spooner (1994). The acid etching results and their good relationship with those of the naturally weathered samples do supply information about the unstable traps responsible for fading. The acid will have attacked points of high energy on lattice surface and with the removal of these the stability of the signal is improved. This indicates that the fading traps are high energy points of weakness in the crystal in comparison to the low energy stable defects. Yet the HF acid has in fact created a higher level of stability in this study than the majority of the natural. This could be the result of the acid being more powerful over a shorter period of time than the natural weathering processes. Such differences are often the case when attempting to recreate natural processes over geologically instantaneous timescales in the laboratory. Weathering still has the potential to induce stability but a further etching phase introduced into sample preparation techniques may be needed.

5.3 Testing Previous Models of Anomalous Fading in Feldspars.

The luminescence results and brief discussions above provide some clues to the mineralogical and geological factors that may have a role in determining the likelihood of feldspar from a given rock to display anomalous fading. Before these factors can be discussed in more detail, the main models that have been previously proposed to explain the susceptibility of various types of feldspars to anomalous fading will be tested using data acquired in this study.

5.3.1 Cooling Rate and Order-Disorder of Alkali Feldspars.

In this study luminescence measurements were undertaken on samples containing alkali feldspars that themselves contain one of three polymorphs of KAlSi_3O_8 : sanidine (monoclinic with Al atoms distributed randomly between two lattice sites), orthoclase (monoclinic K-feldspar with a

‘stranded’ tweed microtexture and intermediate ordering) and microcline (triclinic and the lowest temperature form of K-feldspar) (Deer, 1996). Previous work (Visocekas, 1995; Visocekas *et al.*, 1996) have suggested that the degree of fading of a K-feldspar is a function of Si,Al ordering, itself related to cooling rate of the feldspar crystal’s host rock. Table 5.43 lists the remnant luminescence values of alkali feldspar-rich samples containing the three polymorphs of K-feldspar. These samples have been selected owing to the reproducibility and so reliability of luminescence results (a number of fresh, naturally weathered and acid-etched Shap samples were measured and F1 is the SUERC laboratory standard); only one sanidine was studied, but previous work (Smith 1998) has also shown this to fade during dark storage. These three were chosen as a sampling window to test this hypothesis as the Sanidine is classically unstable while the ordered Microcline of the F1 is recognised to be stable.

Table 5.43. Remnant luminescence values for three alkali feldspar-rich samples arranged by degree of K-feldspar disorder.						
K-feldspar polymorph	Sample	IRSL	Risø reader OSL	TL	Manual readers TL	PPSL
Sanidine	Patmos	0.964 ± 2%	0.975 ± 2%	2.070 ± 30 %	---	---
	Fresh Shap	1.010 ± 5%	1.030 ± 5%	1.005 ± 5%	---	---
Orthoclase	Unweathered Shap	1.024 ± 4%	1.054 ± 6%	1.005 ± 7%	---	---
Microcline	F1	1.010 ± 3%	1.016 ± 2%	1.062 ± 5%	---	---

Results in Table 5.43 show that the disordered sanidine suffers ~3-4% signal loss after 2 months dark storage, as measured by the two PSL techniques whereas the orthoclase, with an intermediate ordering and the fully ordered microcline shows no signal loss by any technique. The conclusion from this simple comparison is that there is evidence that complete Si,Al disorder may promote signal loss during storage, but this principal does not extend to intermediate ordered orthoclase. It is important however to note that the Patmos sample is heterogeneous and Ab-rich (Or₅₉Ab₃₈An₃) whereas the Shap and F1 samples are both perthitic and the K-feldspar is closer to an end-member chemical composition (Or₈₅₋₉₀Ab₁₀₋₁₅An₀ and Or₉₄Ab₆An₀ respectively). These very significant compositional and microtextural contrasts between the alkali feldspars may be more significant than ordering as a determinant of defect distributions and so anomalous fading. This is in agreement with Spooner (1994) who reported that the only unambiguously non-fading signals originate from highly ordered end-members of the alkali feldspar series.

5.3.2 Calcium Concentration of Plagioclase Feldspars.

The chemistry of the feldspars being studied has been recognised as an important influence on the fading rates by other workers, in particular Huntley *et al* (2007). Building on previous work, he presented data showing a positive correlation between fading rate and calcium content in plagioclase feldspars. However, it was initially concluded (Huntley and Lian, 2006) that while

there is evidence that fading rates do increase with calcium content, the calcium ion may not in fact be the centre to which an electron tunnels, but rather the centre is the result of the replacement of sodium by calcium or the replacement of aluminium by silicon. So rather than the calcium itself being the cause of fading it is rather the strain placed on the lattice by such substitutions that is important. However, even within Huntley’s own data set there are samples that do not follow this trend (with IRSL short shine stimulation), indicating the presence of other determining factors, and it is informative to test the effects of calcium content on the results obtained within this study (Table 5.44).

Table 5.44. Remnant luminescence values for plagioclase feldspar-rich samples ordered by calcium content (percentage content of An).

Percentage content of An.	Sample	IRSL	Risø reader OSL	TL	Manual readers	
					TL	PPSL
90	Gabbro	1.147 ± 2%	1.061 ± 3%	No Signal	0.561 ± 4%	1.037 ± 7%
	pegmatite					
88	Rum	1.030 ± 3%	1.099 ± 3%	1.601 ± 6%	0.792 ± 13%	1.083 ± 14%
	anorthosite					
82	Troctolite	1.098 ± 3%	1.021 ± 3%	No Signal	No Signal	No Signal
	pegmatite					
59	Etna basalt	1.149 ± 3%	1.162 ± 2%	1.022 ± 30%	---	---
3	Ballater	0.921 ± 2%	0.911 ± 3%	0.844 ± 5%	0.928 ± 3%	0.849 ± 8%
	Granite					
3	Ballater	1.302 ± 2%	1.641 ± 3%	1.000 ± 4%	0.975 ± 5%	1.097 ± 6%
	Granite					
	(weathered)					

Results of comparison of An content with remnant luminescence values reveal no correlation between the two as measured by IRSL or OSL and the signal from all samples is relatively stable. The Risø TL data also show no clear trends, although there is a suggestion in the manual TL results that the An-rich plagioclases do fade to a greater extent than the granitic albites. The PPSL data again show no clear trends. It should be noted that although the powders used are fairly pure (80% plagioclase), much of the signal from the Ballater samples may be from the minor alkali feldspar component. It is also important to note that plagioclase from the Etna basalt does not fade more rapidly than plagioclase from the much more slowly cooled and geologically older igneous intrusions. In conclusion, these data give no support to the model for Ca control on luminescence stability and corroborate the theory that it is not the calcium itself but possibly the act of lattice substitution that is important.

5.3.3 Natural Weathering and Laboratory Etching.

The reasons for this discussion of this model and the results obtained in the present study have been discussed extensively in the sections above. The relative stability in samples studied here has made it difficult to corroborate or refute either of the two models, proposed by Parish (1994) and Spooner (1994) conclusively. The results presented above indicate that weathering, both artificial and

natural does not induce instabilities in the previously stable ‘fresh’ alkali feldspars. The implications of this conclusion is that, as Parish suggested, HF etching does mirror in some way natural chemical weathering (although not in the way that was suggested by this early work) but to what extent requires further investigation. HF etching does attack thermally unstable traps selectively, and possibly this process could be used as a means of preparing samples for luminescence work in situations where application of a preheat is undesirable.

5.3.4 Geological age.

Table 5.45. Remnant luminescence values for plagioclase feldspar-rich samples ordered by age.						
Age (Ma)	Sample	IRSL	Risø reader OSL	TL	Manual readers	
					TL	PPSL
2850-2700	Lewisian gneiss	0.947 ± 2%	0.935 ± 3%	0.880 ± 8%	---	---
420-400	Helmsdale Granite	1.197 ± 3%	1.083 ± 2%	1.167 ± 4%	---	---
435±10	Strontian granodiorite	1.039 ± 3%	0.998 ± 3%	1.200 ± 3%	1.948 ± 3%	0.942 ± 5%
432±7	Peterhead Granite	1.004 ± 4%	0.970 ± 3%	0.936 ± 7%	1.176 ± 2%	1.185 ± 6%
414	Ross of Mull Granite (H9)	0.955 ± 3%	1.014 ± 3%	1.064 ± 8%	0.911 ± 3%	1.018 ± 7%
414	Ross of Mull Granite (H10)	0.986 ± 3%	0.994 ± 4%	1.500 ± 4%	0.937 ± 3%	0.598 ± 7%
~410	Cairngorm Granite	0.998 ± 3%	0.999 ± 3%	0.899 ± 2%	0.910± 4%	1.48± 32%
394	Fresh Shap Granite	1.010 ± 5%	1.030 ± 5%	1.005 ± 5%	---	---
394	Unweathered Shap Granite	1.024 ± 4%	1.054 ± 6%	1.005 ± 7%	---	---
58.5	Arran Granite	0.891 ± 4%	0.833 ± 4%	1.120 ± 4%	1.128 ± 6%	1.130 ± 6%
These data include only alkali feldspar-rich separates from acidic igneous or metamorphic rocks.						

Some previous work suggested that the geological age of feldspars can influence the amount of anomalous fading, with older samples fading to a greater extent than geologically young grains (Huntley and Lamothe, 2001). The explanation is that older samples have undergone longer irradiation, particularly from alpha particles from the decay of uranium and thorium, that may enhance disorder and/or form defects in feldspars. Such a trend is not observable in the results of the sample suite measured in this study. The Precambrian Lewisian gneiss is significantly older than the other samples in Table 5.45 and at first glance does appear to have a greater level of instability (~12% over two months in TL) than the Palaeozoic granites. However the Tertiary Arran sample experiences greater level of instabilities in the Risø IRSL and OSL than the metamorphic gneiss.

The release of energy from the decay of uranium has also been proposed to cause fading and a link has been suggested between rates of signal lost during dark storage and uranium concentration

(Lamothe *pers. com.*). It is therefore a possibility that the geologically young Arran granite has undergone high levels of irradiation damage despite its age, but without knowing the relative levels of environmental and internal radiation doses of the two samples (Arran granite and Lewisian gneiss) firm conclusions cannot be made. Such measurements would have been made if luminescence dating was being carried out but such readings were beyond the scope of this study. It is pertinent to note that the Ross of Mull hydrothermal syenite that fades significantly when measured using the Risø and does not have high levels of uranium (John Faithful *personal communication*). Therefore, it must be concluded that results from the present sample suite do not support the predicted age related trends.

5.4 Controls on Anomalous Fading in the Present Sample Set.

5.4.1 The Impact on Fading Rates of Specific Stimulation Sources.

The varying excitation sources were used in this study as a means of evaluating the possibility that different trap populations exhibit a measurable variation in stability. Such behaviour has been suggested by the reported differences of fading rates between luminescence centres (the red emission in comparison with the blue). If traps and centres are coupled as proximity models imply then varying excitation energies should yield luminescence emissions of varying stabilities. Tables 5.46-5.51 explore the impact of different stimulation on alkali feldspars from different geological settings. The tables are divided into a comparison of Risø IRSL and OSL, and the two TL stimulation techniques. The manual PPSL system is excluded for this comparison as it produced some inaccurate results due to low sensitivity.

Table 5.46. Alkali feldspar samples that do not fade in IRSL or OSL after dark storage ordered by signal retention in IRSL.				
Sample	Remnant luminescence		Alkali feldspar microtexture	K-feldspar polymorph
	IRSL	OSL		
Ross of Mull Granite (H10)	0.986 ± 3%	0.994 ± 4%	Coarse vein microperthite	Microcline
Cairngorm Granite (fresh)	0.998 ± 3%	0.999 ± 3%	Patch microperthite	Microcline (shows strain in BSE)
Shap Granite (weathered)	1.000 ± 2%	1.010 ± 3%	Lamellar and vein microperthite	Orthoclase
Cairngorm Granite (weathered)	1.002 ± 2%	1.011 ± 3%	Patch microperthite	Microcline
Shap Granite (1 min. HF etched)	1.007 ± 2%	0.991 ± 3%	Lamellar and vein microperthite	Orthoclase

Peterhead Granite	$1.004 \pm 4\%$	$0.970 \pm 3\%$	Fine vein microperthite	Microcline (shows strain in BSE)
F1 laboratory standard	$1.010 \pm 3\%$	$1.016 \pm 2\%$	Patch microperthite	Microcline
Shap Granite (fresh)	$1.010 \pm 5\%$	$1.030 \pm 5\%$	Lamellar and vein microperthite	Orthoclase
Shap Granite (3 mins HF etched)	$1.020 \pm 4\%$	$0.998 \pm 4\%$	Lamellar and vein microperthite	Orthoclase
Bute pitchstone (H3)	$1.025 \pm 3\%$	$0.982 \pm 2\%$	Homogeneous	Orthoclase
Helmsdale Granite (15 mins HF etched)	$1.036 \pm 2\%$	$1.103 \pm 2\%$	Vein microperthite	Orthoclase (shows strain in BSE)
Strontian Granodiorite	$1.039 \pm 3\%$	$0.998 \pm 3\%$	Fine patch microperthite	Orthoclase
Shap Granite (15 mins HF etched)	$1.069 \pm 5\%$	$1.025 \pm 3\%$	Lamellar and vein microperthite	Orthoclase
Helmsdale Granite	$1.197 \pm 3\%$	$1.083 \pm 2\%$	Vein microperthite	Orthoclase
Helmsdale Granite (1 min. HF etched)	$1.279 \pm 4\%$	$1.226 \pm 3\%$	Vein microperthite	Orthoclase
Helmsdale Granite (3 mins HF etched)	$1.302 \pm 4\%$	$1.286 \pm 3\%$	Vein microperthite	Orthoclase

The feldspars in Table 5.46 are all from acidic igneous intrusions (although the origin of F1 is unknown) and would have cooled relatively slowly. Therefore their stability is expected in terms of the expected model in the literature for explaining fading. The presence of orthoclase and microcline has no effect on fading rate, nor does the nature of the exsolution microtexture.

Table 5.47. Alkali feldspar samples that fade in IRSL or OSL during dark storage ordered by signal retention in IRSL.

Sample	Remnant luminescence		Alkali feldspar microtexture	K-feldspar polymorph
	IRSL	OSL		
Ross of Mull syenite (H11)	0.821 ± 4%	0.798 ± 4%	Coarse vein microperthite	Microcline
Arran Granite	0.891 ± 4%	0.833 ± 4%	Fine vein microperthite	Microcline
Ballater Granite (weathered)	0.911 ± 2%	0.959 ± 2%	Fine microperthite	Orthoclase
Lewisian gneiss	0.947 ± 2%	0.935 ± 3%	Coarse patch microperthite	Microcline
Patmos sanidine	0.964 ± 2%	0.975 ± 2%	Homogenous	Sanidine
Canisp porphyry	0.972 ± 3%	0.920 ± 2%	Homogeneous	Orthoclase

There is no consistency of geological background within the results in Table 5.47. The group includes plutonic, volcanic igneous and metamorphic rocks. It also includes two granites, which were well represented in the non-fading group above. It is important to note that the most severely fading sample has formed by hydrothermal alteration of the Ross of Mull Granite, whose feldspars are stable in IRSL and OSL. Again there is no obvious trend with mineralogy or microtexture, although the two worst offending samples contain microcline, which should if Si, Al disorder results in proximity effects, show stability.

Table 5.48. Alkali feldspar samples that do not fade in Riso TL during dark storage ordered by signal retention.

Sample	Remnant TL	Alkali feldspar microtexture	K-feldspar polymorph
Peterhead Granite	0.936 ± 7%	Fine vein microperthite	Microcline
Fresh Shap Granite	1.005 ± 5%	Lamellar and vein microperthite	Orthoclase
Unweathered Shap Granite	1.005 ± 7%	Lamellar and vein microperthite	Orthoclase
Ballater Granite (naturally weathered)	1.007 ± 5%	Fine microperthite	Orthoclase
Shap Granite (15 mins HF etched)	1.017 ± 4%	Lamellar and vein microperthite	Orthoclase
Shap Granite (3 mins HF etched)	1.020 ± 4%	Lamellar and vein microperthite	Orthoclase
Helmsdale Granite (15 mins HF etched)	1.029 ± 5%	Vein microperthite	Orthoclase
Helmsdale Granite (3 mins HF etched)	1.052 ± 5%	Vein microperthite	Orthoclase
Ross of Mull Granite (H9)	1.064 ± 8%	Coarse vein microperthite	Microcline

Arran Granite	1.120 ± 4%	Fine vein microperthite	Microcline
Helmsdale Granite	1.167 ± 4%	Vein microperthite	Orthoclase
Strontian granodiorite	1.200 ± 3%	Fine patch microperthite	Orthoclase
Helmsdale Granite (1 min. HF etched)	1.244 ± 7%	Vein microperthite	Orthoclase
Ross of Mull Granite (H10)	1.500 ± 4%	Coarse vein microperthite	Microcline
Shap Granite (1 min. HF etched)	1.505 ± 7%	Lamellar and vein microperthite	Orthoclase

Excludes data with large errors (e.g. Patmos sanidine). Only samples with >75% alkali feldspar have been included.

In Table 5.48 all the samples are from plutonic rocks and will have cooled slowly and are expected to be stable with storage. There is a greater probability for signal enhancement in post-PPSL TL opposed to those that have exhibited stability with IRSI and OSL excitation, possibly due to some charge transfer mechanisms occurring throughout the multistimulation technique.

Table 5.49. Alkali feldspar samples that fade in Riso TL during dark storage ordered by signal retention.

Sample	Remnant TL	Alkali feldspar microtexture	K-feldspar polymorph
Lewisian gneiss	0.880 ± 8%	Coarse patch microperthite	Microcline
Ross of Mull syenite (H11)	0.895 ± 2%	Vein microperthite	Microcline
Cairngorm Granite	0.899 ± 2%	Patch microperthite	Microcline
Shap Granite (naturally weathered)	0.946 ± 3%	Lamellar and vein microperthite	Orthoclase

Excludes data with large errors (e.g. Patmos sanidine). Only samples with >75% alkali feldspar have been included.

In Table 5.49 there is again no geological or mineralogical consistency with fading in TL. The group contains metamorphic, plutonic and hydrothermally altered rocks. The same lack of controlling trend is shown by the microtexture and the polymorphs.

Table 5.50. Alkali feldspar samples that do not fade in manual TL during dark storage ordered by signal retention.

Sample	Remnant TL	Alkali feldspar microtexture	K-feldspar polymorph
Ross of Mull syenite (H11)	1.014 ± 3%	Vein microperthite	Microcline
Canisp quartz-syenite	1.190 ± 6%	Homogeneous	Orthoclase
Arran Granite	1.128 ± 6%	Fine vein microperthite	Microcline

Peterhead Granite	1.176 ± 2%	Fine vein microperthite	Microcline
Strontian granodiorite	1.948 ± 3%	Fine patch microperthite	Orthoclase
Only samples with >75% alkali feldspar have been included.			

Table 5.51. Alkali feldspar samples that fade in manual TL during dark storage ordered by signal retention.

Sample	Remnant TL	Alkali feldspar microtexture	K-feldspar polymorph
Cairngorm Granite	0.910 ± 4%	Patch microperthite	Microcline
Ross of Mull Granite (H9)	0.911 ± 3%	Coarse vein microperthite	Microcline
Ross of Mull Granite (H10)	0.937 ± 3%	Coarse vein microperthite	Microcline
Ballater Granite (weathered)	0.941 ± 5%	Fine microperthite	Orthoclase
Only samples with >75% alkali feldspar have been included.			

It is pertinent to discuss the manual TL results, those that do not experience fading (Table 5.50) and those that do fade (Table 5.51) together. There is possibly an effect of the scale of the microtextures on the stability of the TL signals. The stable samples have finer textures than those that lose their signal with storage. Such correlations were not observable in the Risø TL results and the influence of charge transfer is a possible reason. The previous stimulation of the sample by both IRSL and OSL can affect the TL emissions of the samples. The most obvious effect is the shifting of charge into shallow traps and this can be observed on glow curves as a low temperature ‘shoulder’. The difference in scale of these microtextures is important to models of anomalous fading and may shed some light on the mechanisms behind the claimed stability of feldspars from slowly cooled plutonic and the instability of the rapidly cooled extrusive igneous rocks. Crystals that form under high strain will have coarse exsolution textures and vice versa. These larger scale perthitic features cause defects to form in very close proximity to each other, in essence there are ‘walls’ of defects at the phase boundaries. The larger the phase boundary the greater the clustering of defects that is an essential feature for proximity models such as tunnelling to occur. Therefore, it is plausible that the amount of strain under which the feldspar forms and the resulting microtextures exert a control on fading. Possible avenues for investigating this model will be outlined in section 5.7.

5.4.2 Discussion of Results.

With the exception of the manual TL results there does not appear to be a relation between extent of anomalous fading, geological background, mineralogy and stimulation source. The stand alone

TL stimulation results indicate that the strain on the crystal at perthite interfaces has an influence on clustering of defects and coarse microtextures may promote proximity effects such as tunnelling. Defect rich walls of perthite microtextures are areas of high energy and as has been described above (Section 5.2.8.1) both natural weathering and HF etching specifically attack these sites at the grain surface and this link between scale of microtexture and its relation to instabilities levels has been observed in the limited fresh vs. weathered granite set already discussed. The Cairngorm and Shap granites show less variation in stability with weathering and etching than the Ballater sample. These both exhibit exsolution microtexture on a smaller scale than the Ballater granite which supports the mineralogical controls suggested by the manual TL results. Taking into account the limited data set a plausible explanation for the observed influences are that the texturally controlled spatially related high energy defect regions are preferentially removed by weathering and etching and are the population that is excited by TL. The existence and possible subsequent removal of these features controls fading rates observed in the TL results.

5.5 The Impact on Fading Rates of Specific Geological Variables.

5.5.1 Erosion and Deposition.

As described briefly in Chapter 4 the Helmsdale granite was uplifted, exposed and eroded in the Devonian and this process led to the formation of the Ousdale arkose (designated Helmsdale arkose here). This sedimentary rock allows investigation of the effect lithification into a new rock and the evolution from granite to arkose after the lack of comprehensive trends out of formational environment and weathering. This sample has allowed an investigation a step further along in the life of a feldspar mineral. The results of the remnant luminescence measurements made on these rocks are combined in Table 5.52.

Table 5.52. A comparison of remnant luminescence values for the Helmsdale granite and its related sedimentary arkose.

Sample	Mineralogy	Risø reader			Manual readers	
		IRSL	OSL	TL	TL	PPSL
<i>Granite</i>						
<i>Unpreheated</i>	$A_{100}P_0Q_0$	$0.611 \pm 4\%$	$0.752 \pm 5\%$	$0.712 \pm 4\%$	---	---
<i>Preheated</i>		$1.197 \pm 3\%$	$1.083 \pm 2\%$	$1.167 \pm 4\%$	---	---
<i>Arkose</i>						
<i>Unpreheated</i>	$A_{20}P_{80}Q_0$	$0.481 \pm 5\%$	$0.404 \pm 5\%$	$0.690 \pm 4\%$	---	---
<i>Preheated</i>		$1.052 \pm 6\%$	$1.342 \pm 4\%$	$1.091 \pm 8\%$	---	---

The results presented in Table 5.42 compare the remnant signals of the Helmsdale granite and its associated arkose. The SPT separate from the granite is pure alkali feldspar but the arkose sample is dominated by plagioclase. There is a clear difference in the unpreheated results with the

sedimentary plagioclase-rich sample showing ~20-30% more instability than the igneous alkali feldspar-rich fraction. However, after the long and low thermal pre-treatment the remnant measurements become very similar. Given the similar nature of the exsolution features (vein microperthites) and the lack of manual TL it is impossible to associate these results with the evolving hypothesis that the microtextures present predict the amount of lattice strain and subsequent rate of fading observed.

5.5.2 Hydrothermal Alteration.

Table 5.53. Remnant luminescence for alkali feldspar-rich samples from the Ross of Mull granite samples and its associated hydrothermal syenite.					
Sample	Risø reader		TL	Manual readers	
	IRSL	OSL		TL	PPSL
<i>Syenite</i>	0.821 ± 4%	0.798 ± 4%	0.895 ± 2%	1.014 ± 3%	1.144 ± 4%
<i>H9 granite</i>	0.955 ± 3%	1.014 ± 3%	1.064 ± 8%	0.911 ± 3%	1.018 ± 7%
<i>H10 granite</i>	0.986 ± 3%	0.994 ± 4%	1.500 ± 4%	0.937 ± 3%	0.598 ± 7%

Table 5.53 presents results from the two Ross of Mull granite samples and its associated hydrothermal syenite. The alkali dominated fractions from the granite (2.52-2.58 g/cm³) exhibit very similar results from the three Risø stimulation sources and the manual TL. All show signal stability except the latter. These alkali dominated fractions can be compared with a mineralogically similar powder from the syenite. This fraction exhibits much lower levels of stability in the Risø results yet the manual readers have produced stable signals.

5.5.3 Metamorphism.

Table 5.54. Remnant luminescence for the Strontian granodiorite and associated Glen Tarbert migmatite.					
Sample	Risø reader		TL	Manual readers	
	IRSL	OSL		TL	PPSL
Strontian granodiorite	1.039 ± 3%	0.998 ± 3%	1.200 ± 3%	1.948 ± 3%	0.942 ± 5%
Glen Tarbert migmatite	0.856 ± 2%	0.920 ± 3%	0.913 ± 3%	1.079 ± 3%	0.769 ± 16%

Table 5.54 presents a comparison of the alkali feldspars from Strontian granodiorite and from the migmatite in its metamorphic aureole. The metamorphic rock shows signal instability across the Risø results and the manual PPSL. It is difficult to apply the strain model to the manual TL results in Table 5.54 as the granodiorite shows no signal loss. The conclusion from this simple comparison is that metamorphism may be important in making a feldspar susceptible to fading although a much larger sample set is needed to investigate this link further and make solid conclusions.

5.6 The Influence of Preheating.

The stability shown by many of the samples discussed in the results presented in this Chapter may well be due to the successful application of the long duration low temperature preheat. The pre-treatment of the samples to 16hrs at 135°C has been successful in removing sometimes severe signal losses in all but two of the samples (Table 5.55).

Table 5.55. Remnant luminescence values for unpreheated vs. preheated samples. Ordered by change in stability with IRSL.					
Sample	Mineralogy	IRSL	Risø reader OSL	TL	Alkali feldspar microtexture
Helmsdale granite					
<i>Unpreheated</i>	A ₁₀₀ P ₀ Q ₀	0.611 ± 4%	0.752 ± 5%	0.712 ± 4%	Vein microperthite
<i>Preheated</i>	A ₁₀₀ P ₀ Q ₀	1.197 ± 3%	1.083 ± 2%	1.167 ± 4%	
Helmsdale arkose					
<i>Unpreheated</i>	A ₂₀ P ₈₀ Q ₀	0.481 ± 5%	0.404 ± 5%	0.690 ± 4%	Vein microperthite
<i>Preheated</i>	A ₂₀ P ₈₀ Q ₀	1.052 ± 6%	1.342 ± 4%	1.091 ± 8%	
F1 feldspar					
<i>Unpreheated</i>	A ₆₅ P ₃₀ Q ₅	0.617 ± 8%	0.604 ± 5%	0.520 ± 7%	Patch microperthite
<i>Preheated</i>	A ₆₅ P ₃₀ Q ₅	1.010 ± 3%	1.016 ± 2%	1.062 ± 5%	
Etna basalt					
<i>Unpreheated</i>	A _{<10} P _{>85} Q _{<5}	0.766 ± 2%	0.876 ± 4%	1.050 ± 5%	N/A
<i>Preheated</i>	A _{<10} P _{>85} Q _{<5}	1.149 ± 3%	1.162 ± 2%	1.022 ± 30%	
Patmos sanidine					
<i>Unpreheated</i>	A _{>95} P ₀ Q _{<5}	0.717 ± 5%	0.533 ± 7%	0.332 ± 2%	Homogenous
<i>Preheated</i>	A _{>95} P ₀ Q _{<5}	0.964 ± 2%	0.975 ± 2%	2.070 ± 30 %	
Fresh Shap					
<i>Unpreheated</i>	A ₉₅ P ₅ Q ₀	0.822 ± 6%	0.800 ± 5%	1.029 ± 3%	Lamellar and vein microperthite
<i>Preheated</i>	A ₉₅ P ₅ Q ₀	1.010 ± 5%	1.030 ± 5%	1.005 ± 5%	
Weathered Shap					
<i>Unpreheated</i>	A ₉₅ P ₅ Q ₀	0.842 ± 7%	0.782 ± 4%	0.824 ± 6%	Lamellar and vein microperthite
<i>Preheated</i>	A ₉₅ P ₅ Q ₀	1.000 ± 2%	1.010 ± 3%	0.946 ± 3%	
Lewisian gneiss					
<i>Unpreheated</i>	A ₈₀ P ₂₀ Q ₀	0.858 ± 5%	0.744 ± 6%	0.804 ± 2%	Coarse patch microperthite
<i>Preheated</i>	A ₈₀ P ₂₀ Q ₀	0.947 ± 2%	0.935 ± 3%	0.880 ± 8%	

The samples in Table 5.55 are listed by decreasing removal of IRSL signal loss with preheating. There is no clear relationship between rock type or dominant feldspar mineralogy and the amount of signal loss before preheating, although plagioclase-rich samples are disproportionately abundant in these results. There is also a slight trend with stimulation source, although the results are limited

to the Risø multistimulation. With the exception of F1, there is a hint of microtextural control on the amount of instability removed by preheating, although, these results are inconsistent with the trends in the manual TL data. Stability seems to increase with the scale of microtextures. This could be the result of the IRSL and OSL exciting different trap populations to that of the TL. The Risø TL itself is too varied in Table 5.55 to be informative; although the greater the proportion of alkali feldspar the more stable the emitted luminescence before preheating with the exception of the Patmos sample whose TL result is significantly different to all the others although it is important to note that it has large errors. Preheating does seem at this point to be the most effective method of inducing stabilisation in feldspar luminescence.

5.6.1 Preheating Induced Anti-fading.

In Table 5.55 both Helmsdale samples exhibit a signal enhancement with storage, the opposite to the signal loss expected with anomalous fading, with the granite experiencing signal enhancement in IRSL and OSL and the arkose in OSL only. Similar results have been found in other studies (Smith 1998) and charge transfer has been suggested as a possible explanation. In this process charge released from shallow traps, most probably due to thermal processes, are re-trapped by deeper (stable) traps. Work carried out by Hout and Lamothe (2003) suggested that such a signal increase could be due to the timing of the preheat regime in the measurement cycles. The results described in this chapter were measured with the thermal pre-treatment carried out after storage whereas the fading test described by Auclair *et al* (2003) recommended it be carried out before, directly after irradiation as is the case in the prompt glows. If charge transfer is the reason behind this signal increase after storage then the cause may be delayed preheating. During the storage period the trapped charge has the opportunity to detrap and recombine in more stable traps. If the preheating had been carried out prior to storage then the shallow unstable traps would have been empty and such transfer would have had less probability of occurring. Therefore, a sample with a strong thermal transfer and temperature dependence may give erroneous ages that are not accounted for by loss but rather migration of charge.

5.7 Discussion and Conclusions.

Fading rates over an extended period of time have been measured from a series of well characterised feldspars with varying ages, compositions and formational histories. The effects of different stimulation and detection methods on measured fading rates have been examined, including an assessment of extended pre-heating. The effects of weathering, chemistry, formational history, age of formation and presence of alteration and exsolution microtextures on fading have also been examined.

Perhaps surprisingly, given the extensive and frequently repeated literature statements to the contrary, results of this work show little evidence of substantial fading in most feldspars after extensive preheating. Variations in excitation and emission spectra are not easily observable within these results, most probably due to the very small levels of instabilities within the sample group as a whole. The IRSL and OSL results are very similar even though the energy models that the luminescence process is based upon describes them as exciting different trap populations. It is possible that this is the case, but nonetheless different traps have similar levels of stability.

The increasing stability of luminescence signals with weathering was expected as it has long been known to have an influence, and is due to weathering preferentially destroying unstable traps (Spooner 1994). Similar effects were also observed in the HF acid etched samples although caution is advised when directly comparing these results to those obtained through natural processes.

The metamorphic samples were the other group where post formational alteration appeared to influence signal stability. This time the opposite effect was obtained to that of weathering and these samples experienced the only consistent remnant signal losses of the sample suite. There appeared to be no conclusive trends based on stimulation source, detection wavelength or sample chemistry. There was no certain evidence to support Huntley's (2007; 2006) conclusions that increased calcium content in plagioclase induces fading although detection problems were encountered due to low emission intensities of the calcic samples included here.

Further work to test the affects of weathering and metamorphism is required. For example the Ross of Mull syenite sample could be acid etched to test whether the signal stability of its parent granite samples (H9 and H10) could be reproduced. Also a greater variety of metamorphic samples could be measured to attempt to narrow down any mineralogical variables within these rock types that explain these instabilities.

Overall it was the manual TL results that proved to be the most informative about the nature of the defects responsible for anomalous fading. The results of this study suggest that anomalous fading, investigated here as a function of remnant signal levels, is linked to lattice strain effects, which can be characterised by the scale of the exsolution textures of the alkali feldspars. Further investigation of this is required and a technique similar to that used to investigate annealing of apatite by hydrothermal fluids is suggested. A suggested approach would be to investigate a rock type that has been exposed to hydrothermal alteration in large veins, possibly fault zones, and measure the stability of the feldspars using the manual TL approach used here at varying distances away from this altered zone. The hydrothermal fluids should have significantly altered the feldspars in close proximity to the fluid conduit and to a lesser degree further away.

The information gleaned by the manual TL system has highlighted the importance of investigating different trap populations. The lack of significant variations from these conventional systems suggests that more novel excitation instrumentation should be employed to unravel the effects of proximity models and the role of coupling of traps and centres in anomalous fading in greater detail. Also the success of the preheating regime should be investigated further by application in an actual dating context where its potential for leaving only stable datable emissions can be properly ascertained.

6

Exploring Other Luminescence Techniques.

6.1 Introduction.

As described in Chapter 5, luminescence measurements by conventional techniques show some differences in fading with varying excitation sources without preheating but most are removed with extensive thermal pre-treatment, with the exception of sanidine and feldspars from metamorphic rocks. These findings are encouraging for luminescence studies and the future role of feldspars as dating tools. Therefore this chapter concludes with a case study to assess whether stability over a 10^{12} second period (~40Ka) (e.g. archaeological samples) can be achieved using the preheating regime defined in Chapter 3 and used to great success in Chapter 5.

To comprehensively overcome the hurdle of anomalous fading, further understanding of its mechanisms are required beyond those obtainable using conventional excitation systems, which gave promising stability results in Chapter 5. Therefore this chapter will begin by presenting work on extending the range of the luminescence methods in an attempt to investigate any variations in signal stability within a single emission using a combination of IR-red band detection and slow pulsed (high repetition rate) stimulation. As noted in Chapter 2 the early work by Visocekas and co-workers (Visocekas and Guerin, 2006; Visocekas *et al.*, 1994; Visocekas *et al.*, 1998; Visocekas and Zink, 1999; Zink and Visocekas, 1996; Zink and Visocekas, 1997; Zink *et al.*, 1995) together with the experimental studies of Fattahi and Stokes (2000; 2003a; 2003b; 2003c; 2004b; 2004a) had suggested that the red emission of feldspar may be more stable than other emission bands. Also, following from work by Clark and Sanderson (Clark, 1992; Clark *et al.*, 1997; Sanderson and Clark, 1994) and Tsukamoto (2006), it was pertinent to investigate the properties of the slow relaxation of the luminescence process, which was made possible by using pulsed diode stimulation. These techniques will compliment work already carried out in this study and help to investigate further the role of stimulation source on remnant luminescence and also look at time dependence, which may help in the understanding of the controls on the amount of signal loss observed.

6.2 Near-IR TL.

6.2.1 Introduction.

Typically, TL glow curve analysis is undertaken from 0-500°C using UV-blue transmission filters in front of the PMT. TL glow curves of laboratory-irradiated feldspars display a composite wide curve extending from 50-500°C. The nature of the TL peaks varies slightly between samples, reflecting their mineralogy and structural characteristics. The far-red band has a Gaussian spectrum in the near IR (~700-710nm) with a maximum at 1.7eV (c.710nm) which has been attributed to Fe^{3+} substituting for Al^{3+} in the feldspar lattice (Bos *et al.*, 1994; Krbetschek *et al.*, 1997). This near-IR emission is a prominent component of TL spectra from many feldspars and is often the most intense in those of materials such as sanidine or intermediate K-Na or Na-Ca feldspars (Krbetschek *et al.*, 1997). After laboratory storage of 'fading' alkali feldspars, this near-IR emission is observed to 'fade' much less than the 'blue' TL emission (Zink *et al.*, 1995).

Although the level of stability during dark storage of the samples used in this study is reasonably good, the recent near-IR research by workers in France and Oxford is of huge significance to all involved in the field of feldspar luminescence dating. Volcanic feldspars have been associated in the literature with fading (Fattahi and Stokes, 2003b; Wintle, 1973) and the possibility of being able to measure a relatively stable signal from such unstable samples would be a significant development. Having already compared the influence of various stimulation techniques on magnitudes of fading and observing little variation, the ability to measure different emission wavelengths, especially one that may behave so differently to others stimulated and measured by conventional techniques, would be an advantage to this work.

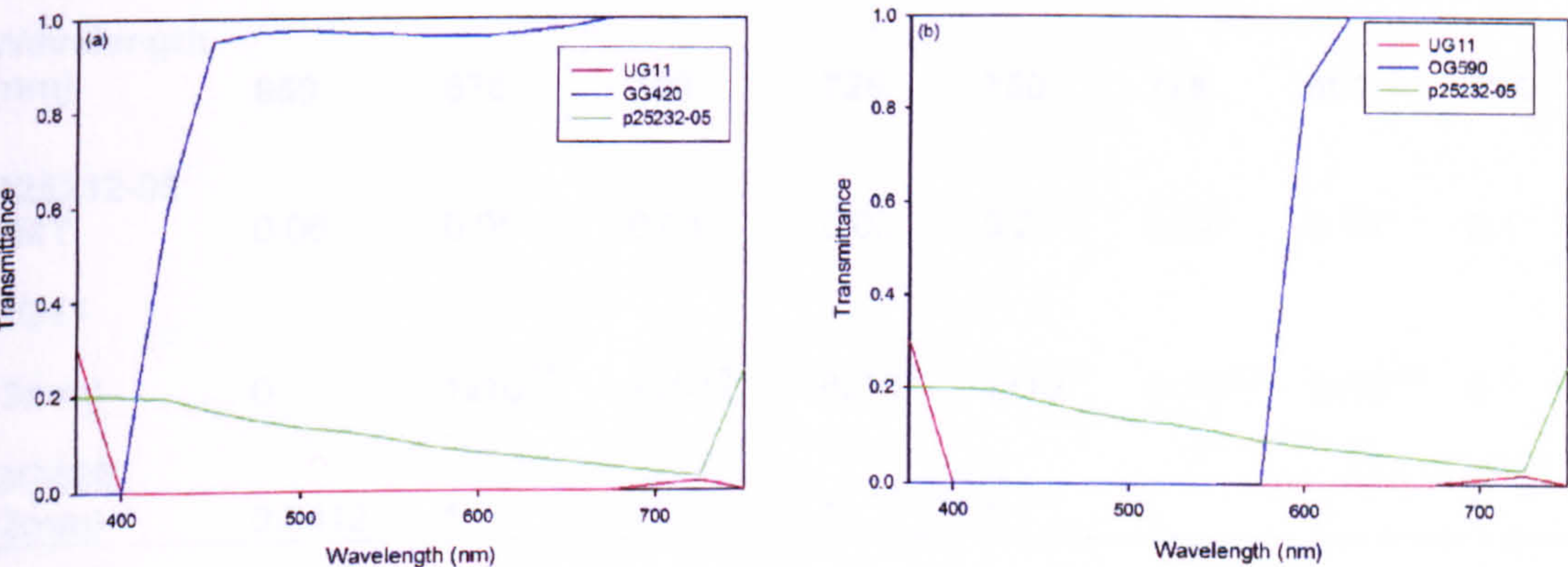
Measurements of IR luminescence emissions were outside the scope of the main body of this study as they are beyond the detection limits of common PMT modules. For this study a p25232-05 red sensitive module was purchased from Electron Tubes and subsequently used to measure a subsection of the sample set with the SUERC Manual TL system being used as a stimulation source. As described in Chapter 2, different workers have had varying degrees of success when attempting to measure the supposedly stable 710nm-centred emission peak using TL. Visocekas and co-workers have indicated success measuring low temperature near-IR TL, but have had difficulty isolating a higher temperature signal from the thermal background (Visocekas, 2000; Visocekas and Guerin, 2006; Visocekas *et al.*, 1994; Zink and Visocekas, 1997). The Oxford group (Stokes and Fattahi, 2003d) have reported success in dating what they term red-TL in both volcanic feldspars and quartz although there are differences, possibly significant, between the methods and instrumentation used by these groups.

The French researchers used a system based around a RCA C31034 PMT with a GaAs photocathode that had a verified extensive (200-900nm) spectral sensitivity (Visocekas and Zink, 1999). Fattahi and Stokes carried out their research using a different system (Fattahi *et al.*, 2004a). They explored the relative merits of a series of Electron Tubes systems including bialkali, extended green bialkali and S20 photocathode systems, sited in a cooled housing attached to a Risø reader. Due to problems with the thermal background encountered during earlier work by Visocekas and co-workers, Fattahi and Stokes shifted the detection window slightly away from the 710nm peak maximum to <700nm. This change of detection window helped with the background-to-signal ratio, diminishing it enough to produce a measurable high temperature feldspar red-TL emission (Stokes and Fattahi, 2003d); however, it must be noted that the possibility of using this near-IR TL as a convenient luminescence dating tool is still unresolved. Thus, an attempt was made within this project to use a ‘red sensitive’ PMT in conjunction with a routine TL reader to measure such an emission from feldspars and the results of this investigation are presented below.

6.2.2 Results of Investigating the near-IR TL of Feldspars.

The initial stage of this work was evaluating the success of various optical filter combinations with the p25232-05 PMT using the F1 alkali feldspar with a logarithmically increased dose (10Gys, 100Gys and 1Kgy). The discs were not preheated before measurements were made as the work outlined in this section was designed not to characterise luminescence stability, but rather to ascertain the ability of various optical filters to attenuate the thermal incandescence and record sample derived signals. The filter combinations and their respective transmissions are presented in Figure 6.1.

6.2.2.1 Initial RTL work on the P25232-05 PMT with different combination of optical filters.



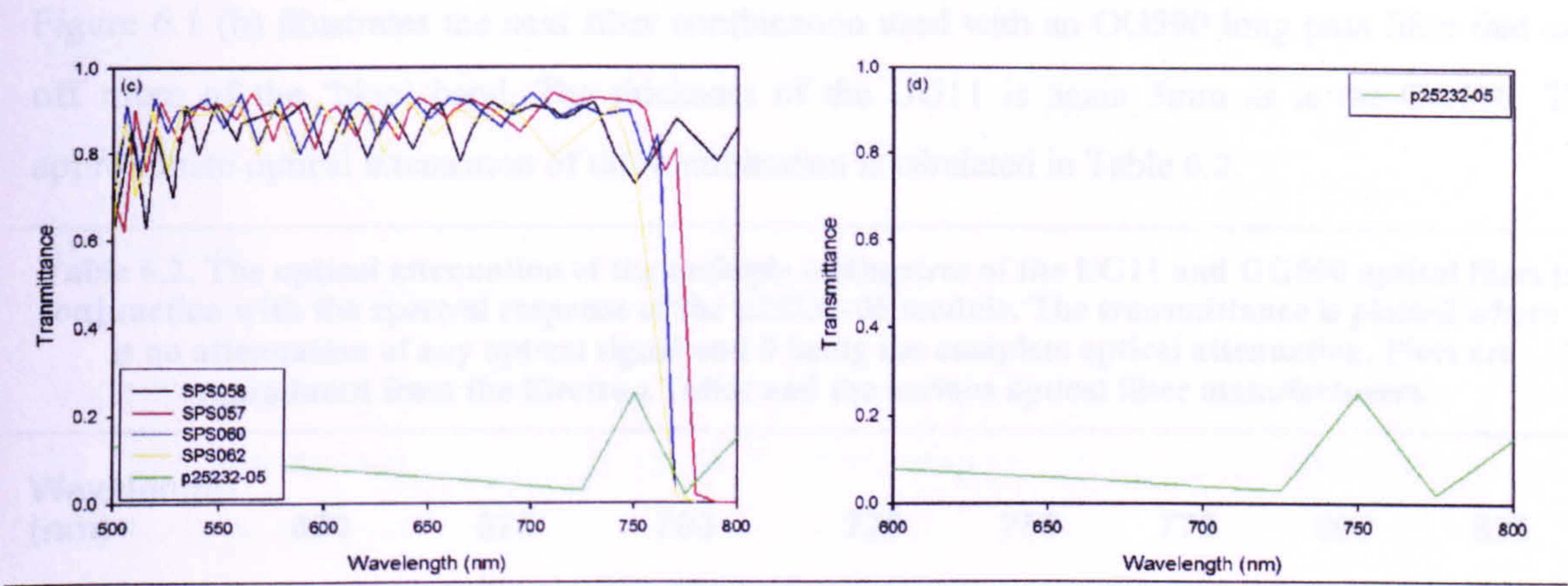


Figure 6.1 Plots of the spectral response of the photodetector module and the various optical filter combinations that were used in the initial part of the near-IR work. The transmittance is plotted where 1 is no attenuation of any optical signal and 0 being the complete optical attenuation. Plots are reproduced from the Electron Tubes and the various optical filter manufacturers.

Figure 6.1 (a) illustrates the estimated transmittance of the UG11 and GG420 optical filters, as well as the spectral response of the P25232-05 electron tubes PMT. These data were taken directly from the Electron Tubes and various filter manufacturers catalogues and should act only as a guide. The curves are also representative of the optical transmittance of only 1mm of these filters. In fact in this configuration there was 3mm of GG420 and 3mm of UG11. As stated, the band of interest is centred on the 700-720nm region of the spectral range. The UG11 gave a small window in this area with the GG420 blocking everything below 420nm. Even though the response of the PMT diminishes in the required region it is still capable of detecting this ~710nm band. The approximate optical attenuation of this arrangement is calculated in Table 6.1.

Table 6.1. The optical attenuation of the multiple millimetres of the UG11 and GG420 optical filers in conjunction with the spectral response of the p25232-05 module. The transmittance is plotted where 1 is no attenuation of any optical signal and 0 being the complete optical attenuation. Plots are reproduced from the Electron Tubes and the various optical filter manufacturers.

Wavelength (nm)	650	675	700	725	750	775	800	825
P25232-05 PMT	0.06	0.05	0.04	0.03	0.25	0.02	0.15	0.1
UG11 (3mm)	0	1x10 ⁻¹⁵	1x10 ⁻⁶	8x10 ⁻⁶	1x10 ⁻⁹	1x10 ⁻¹²	1x10 ⁻¹⁵	0
GG420 (3mm)	0.9412	1	1	1	1	1	1	1
Optical Attenuation	0	5x10 ⁻¹⁷	4x10 ⁻⁸	2x10 ⁻⁷	2x10 ⁻¹⁰	2x10 ⁻¹⁴	1x10 ⁻¹⁶	0

Figure 6.1 (b) illustrates the next filter combination used with an OG590 long pass filter that cuts off more of the ‘blue’ band. The thickness of the UG11 is again 3mm as is the OG590. The approximate optical attenuation of this combination is tabulated in Table 6.2.

Table 6.2. The optical attenuation of the multiple millimetres of the UG11 and OG590 optical filers in conjunction with the spectral response of the p25232-05 module. The transmittance is plotted where 1 is no attenuation of any optical signal and 0 being the complete optical attenuation. Plots are reproduced from the Electron Tubes and the various optical filter manufacturers.

Wavelength (nm)	650	675	700	725	750	775	800	825
P25232-05 PMT	0.06	0.05	0.04	0.03	0.25	0.02	0.15	0.1
UG11 (3mm)	0	1x10 ⁻¹⁵	1x10 ⁻⁶	8x10 ⁻⁶	1x10 ⁻⁹	1x10 ⁻¹²	1x10 ⁻¹⁵	0
OG590 (3mm)	1	1	1	1	1	1	1	1
Optical Attenuation	0	5x10 ⁻¹⁷	4x10 ⁻⁸	2x10 ⁻⁷	2x10 ⁻¹⁰	2x10 ⁻¹⁴	1x10 ⁻¹⁶	0

Figure 6.1 (c) shows the internal transmittance of the interference filters that were manufactured for the SUERC luminescence laboratories for use in conjuncture with the PMT. They are 2mm thick, so each additional filter to the ‘stack’ will attenuate the signal further. These filters were designed to cut out signal above ~775nm including a significant proportion of the thermal incandescence from the heater plate and disc leaving the luminescence signal from the sample to make up the majority of the detected emission. The approximate optical attenuation of this filter stack is tabulated in Table 6.3.

Table 6.3. The optical attenuation of the multiple millimetres of the UG11 and the complete set of interference optical filers in conjunction with the spectral response of the p25232-05 module. The transmittance is plotted where 1 is no attenuation of any optical signal and 0 being the complete optical attenuation. Plots are reproduced from the Electron Tubes and the various optical filter manufacturers.

Wavelength (nm)	625	650	675	700	725	750	775	800
P25232-05 PMT	0.07	0.06	0.05	0.04	0.03	0.25	0.02	0.15
SP057 (4mm)	0.81	0.8372	0.8336	0.7225	0.8556	0.8464	0.1560	0
SP058 (4mm)	0.8281	0.7225	0.81	0.81	0.8281	0.81	0.5329	0.64
SP062 (2mm)	0.64	0.7056	0.7569	0.3025	0.4290	0.5776	0.0004	0

SP060

(2mm)	0.84	0.88	0.9	0.94	0.91	0.86	0.01	0
Optical Attenuation.	0.0252	0.0225	0.0230	0.0067	0.0083	0.0851	6x10 ⁻⁹	0

In the last stage of this experiment the 100Gy and 1Kgy F1 discs were measured with the P25232-05 PMT without any additional optical filtration (Figure 6.1 (d)). The approximate optical attenuation of this arrangement is calculated in Table 6.4.

Table 6.4. The spectral response of the p25232-05 module in the spectral range of interest. The transmittance is plotted where 1 is no attenuation of any optical signal and 0 being the complete optical attenuation. Plots are reproduced from the Electron Tubes and the various optical filter manufacturers.

Wavelength (nm)	650	675	700	725	750	775	800	825	850	875
P25232-05	0.06	0.05	0.04	0.03	0.25	0.02	0.15	0.1	0.05	0

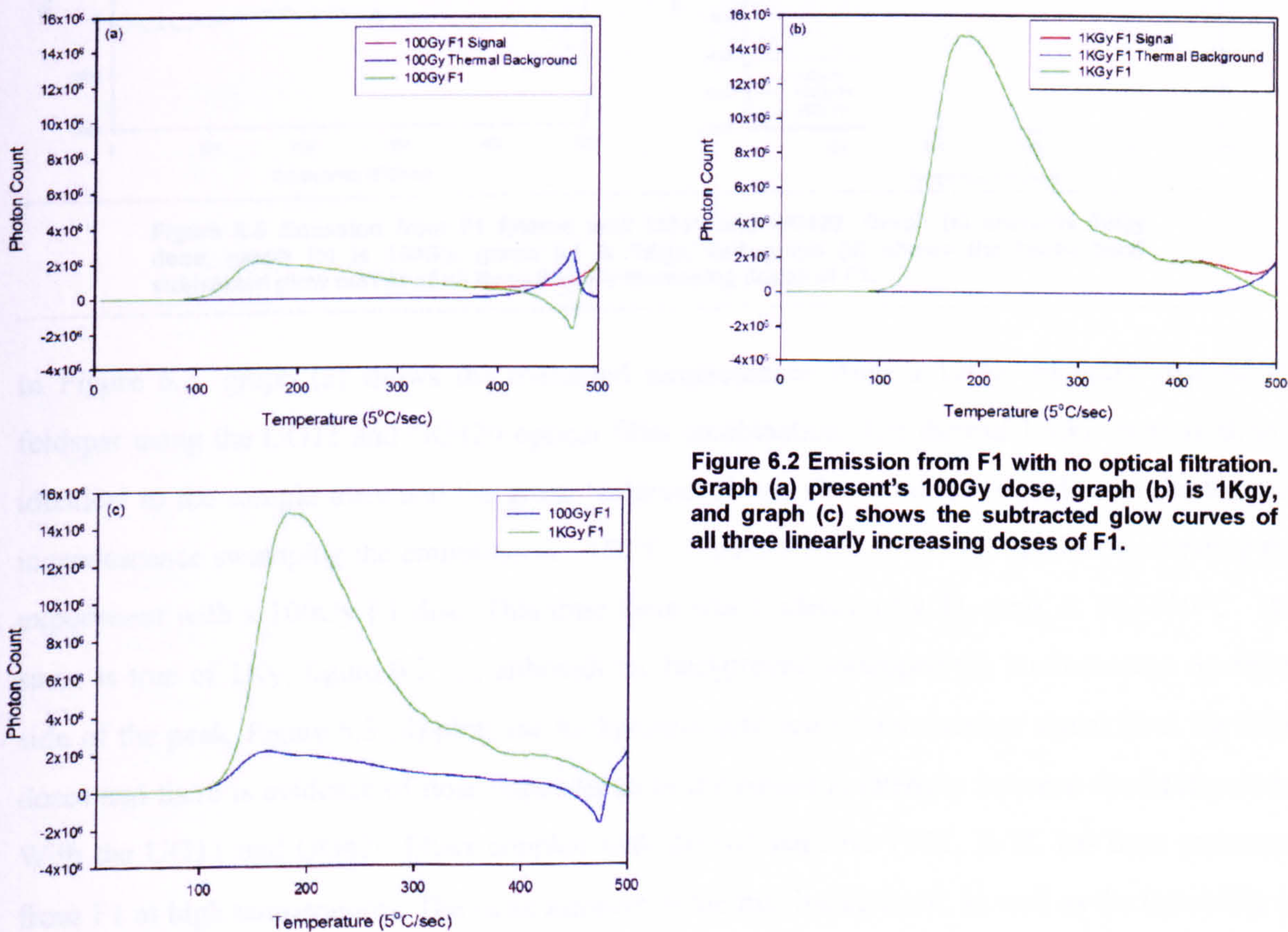


Figure 6.2 Emission from F1 with no optical filtration. Graph (a) present's 100Gy dose, graph (b) is 1Kgy, and graph (c) shows the subtracted glow curves of all three linearly increasing doses of F1.

In Figure 6.2, graphs (a) and (b) the F1 discs had a large measurable signal over background. The photodetector module was unfiltered and this peak was therefore a measure of all the emitted TL peaks from feldspar within the 275-875nm detection window of the p25232-05 PMT. These data demonstrate that the red system can in fact measure TL with a high background level in this emission range and when the detection window is not narrowed by optical filtration. The next stage was to narrow down the detection wavelength to the $\sim 710\text{nm}$ peak of interest.

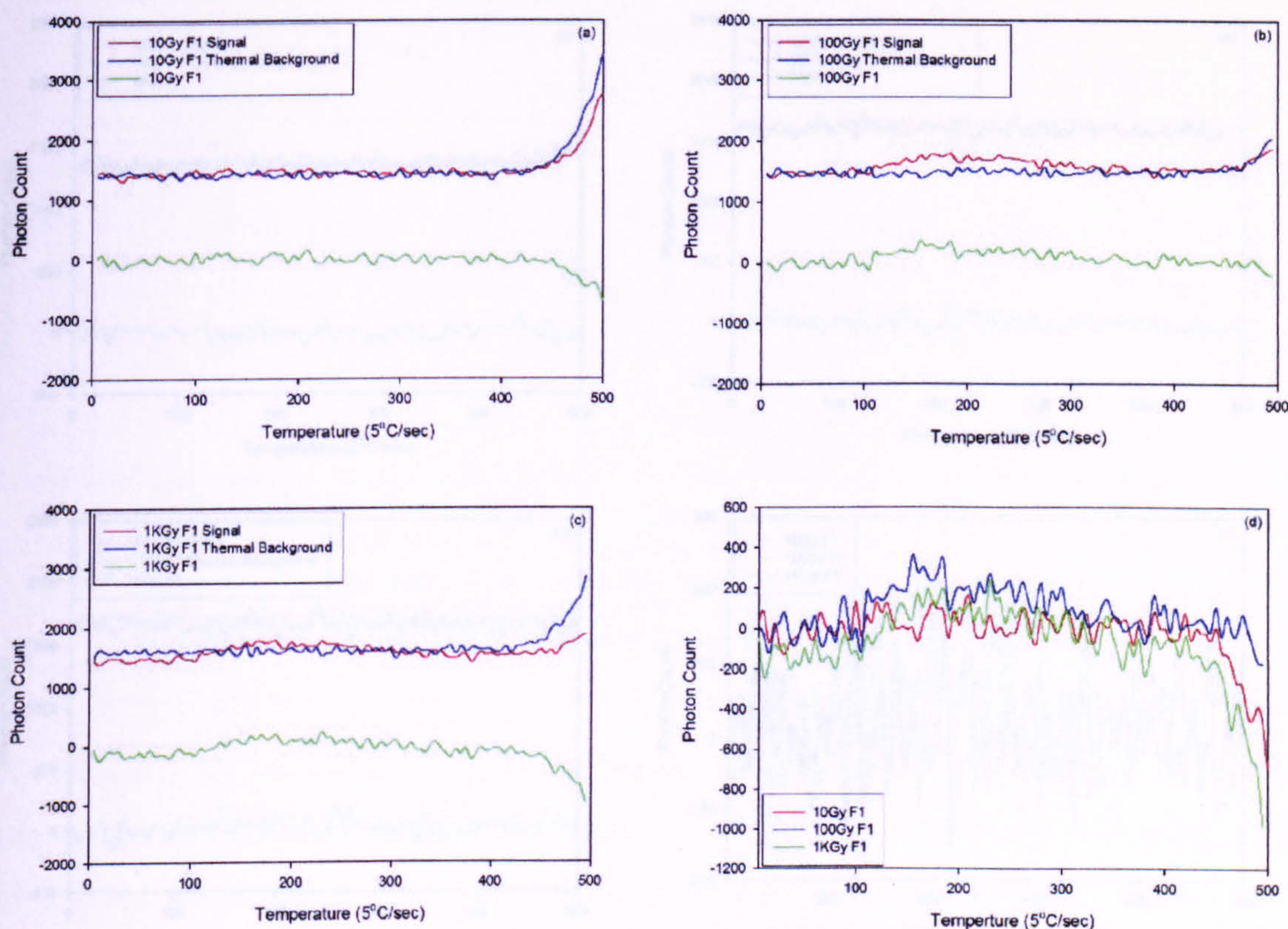


Figure 6.3 Emission from F1 filtered with UG11 and GG420. Graph (a) presents 10Gy dose, graph (b) is 100Gy, graph (c) is 1KGy, and graph (d) shows the background subtracted glow curves of all three linearly increasing doses of F1.

In Figure 6.3, graph (a) shows the measured luminescence from a 10Gy irradiated disc of F1 feldspar using the UG11 and GG420 optical filter combination. The thermal background is almost identical to the sample trace and the green 'subtracted' line shows no real signal, with the thermal incandescence swamping the emissions at $\sim 450^\circ\text{C}$. Figure 6.3 (b) shows the results of repeating the experiment with a 100Gy F1 disc. This time there was evidence of a TL peak at 100-350°C. The same is true of 1Ky, figure 6.3 (c), although the background swamped the luminescence on either side of the peak. Figure 6.3 (d) plots the background subtracted luminescence signal from the three doses and there is evidence of dose dependence of the emission intensity between the three curves. With the UG11 and GG420 filters coupled with the red sensitive PMT, R-TL has been measured from F1 at high temperatures. The large increase in thermal background, as well as the instability in the heating rate at the high end of the stimulation is obvious in the $>450^\circ\text{C}$ data (Figure 6.3). Also, the lack of reproducibility of this thermal background across the three measurements, with it being

much higher in Figure 6.3 (a), is evidence of instability within the system. Promisingly, where the thermal background was at its lowest level (Figure 6.3 (c)) a peak is observed. Within graph (d) in Figure 6.3 there are slight peaks present between 100-300°C in all three of the discs although their peak has only ~300cts/sec and the thickness of UG11 (3mm) has possibly attenuated the signal to a high degree. The results from the UG11 and GG420 filter combination (Table 6.1) are highly promising as it has been able to measure the increasing intensities with dose.

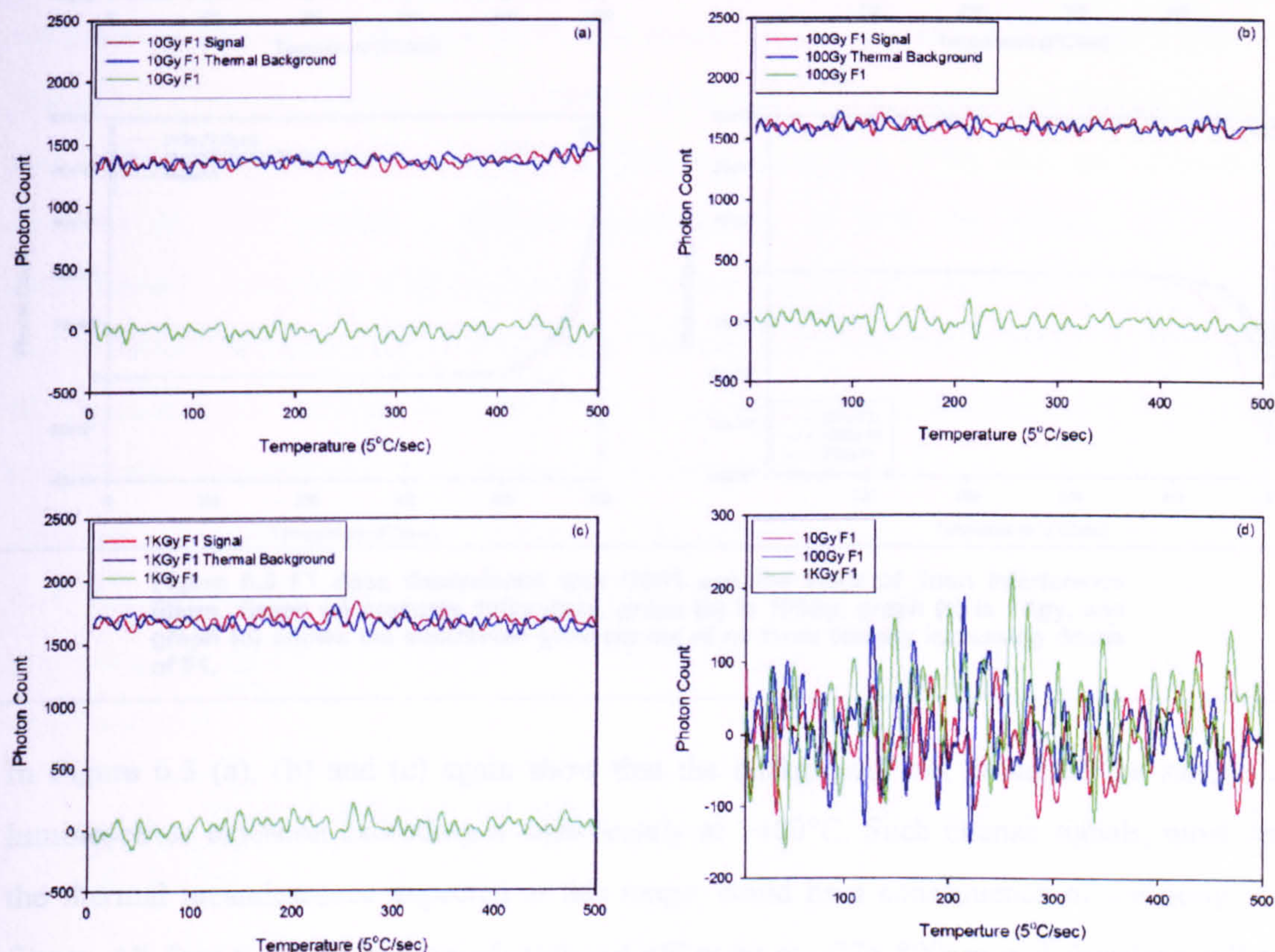


Figure 6.4 F1 dose dependence with UG11 and OG590. Graph (a) presents 10Gy dose, graph (b) is 100Gy, graph (c) is 1Kgy, and graph (d) shows the subtracted glow curves of all three linearly increasing doses of F1.

With the filter combination outlined in Table 6.2 (P25232-05 PMT, UG11 (3mm) and OG590 (3mm)) there was no detectable TL signal from any of the doses applied to F1 feldspar (Figure 6.4), with a signal recorded that was equivalent to thermal background in all cases. The lack of shape change at the high temperature end of these curves (>400°C) indicates that only the thermal background was being measured. In this set however there was an increasing trend in the measured thermal signal. This could have been due to a number of factors, one of the most likely being a rise in the ambient temperature of the sample chamber, which could also cause an increase in the temperature of the detector module, and in turn the PMT's internal dark count.

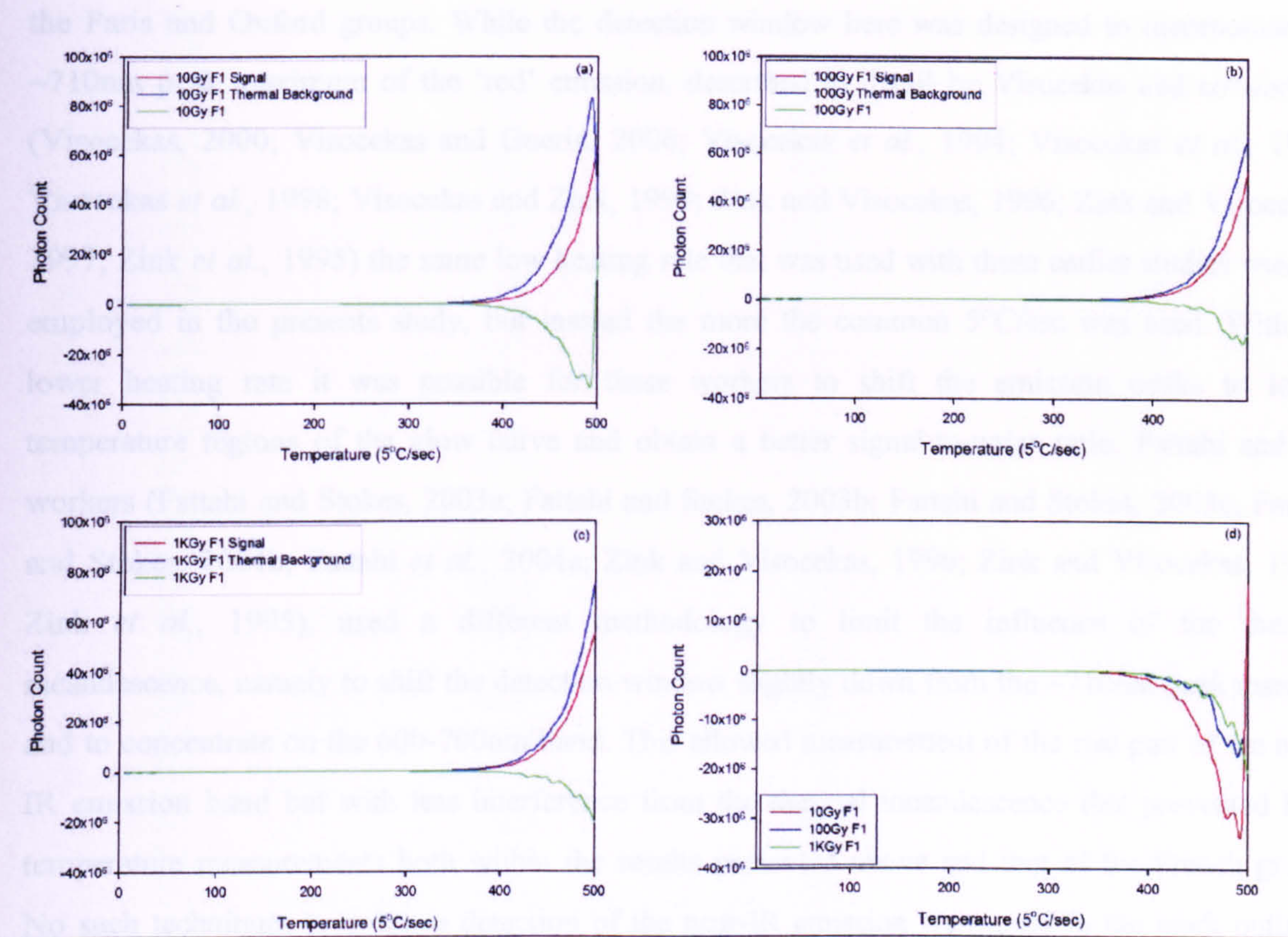


Figure 6.5 F1 dose dependence with UG11 and the stack of 1mm interference filters. Graph (a) presents 10Gy dose, graph (b) is 100Gy, graph (c) is 1KGy, and graph (d) shows the subtracted glow curves of all three linearly increasing doses of F1.

In Figure 6.5 (a), (b) and (c) again show that the background has swamped the sample derived luminescence emission exceeding it significantly at $>400^{\circ}\text{C}$. Such intense signals, most definitely the thermal incandescence expected at this range, could be a consequence of the design of these filters. All four types have a wavelength cut off point at $\sim 775\text{-}800\text{nm}$ and therefore still transmit the thermal incandescence emissions below this. The flat trace observed in the graphs presented in Figure 6.4 are a function of these high intensity $>400^{\circ}\text{C}$ background emissions, however, the raw data (Table 6.5) of the curves from Figure 6.4 show that minor peaks are present within the ‘flat’ low temperature region, hidden in Figure 6.4 due to the intensity of the high temperature background signals. With 10Gy F1 there is a small low temperature peak between $100\text{-}230^{\circ}\text{C}$; this peak is at a temperature below that used in TL dating but its intensity is higher than those seen with the previous filter combination (Figures 6.2 and 6.3). In the 100Gy sample the peak was more pronounced, stretching from $85\text{-}250^{\circ}\text{C}$, and at 1kGys it spans $80\text{-}300^{\circ}\text{C}$. The low temperature rises are due to a lack of preheating but the higher temperature signals measured in the 100Gy and 1kGy signals are promising. These temperature ranges are similar to those shown by Zink and Visocekas (1997) to contain IR signals that may circumvent fading. The weak but measurable TL signal from the F1 discs appeared only below 300°C with all emission above this temperature being lost within the intense thermal incandescence. The signals measured here are of particular importance because the system specification, stimulation regime and detection window differ from those used by both

the Paris and Oxford groups. While the detection window here was designed to incorporate the ~710nm peak maximum of the ‘red’ emission, described in detail by Visocekas and co-workers (Visocekas, 2000; Visocekas and Guerin, 2006; Visocekas *et al.*, 1994; Visocekas *et al.*, 1996; Visocekas *et al.*, 1998; Visocekas and Zink, 1999; Zink and Visocekas, 1996; Zink and Visocekas, 1997; Zink *et al.*, 1995) the same low heating rate that was used with these earlier studies was not employed in the presents study, but instead the more the common 5°C/sec was used. With the lower heating rate it was possible for these workers to shift the emission peaks to lower temperature regions of the glow curve and obtain a better signal-to-noise ratio. Fattahi and co-workers (Fattahi and Stokes, 2003a; Fattahi and Stokes, 2003b; Fattahi and Stokes, 2003c; Fattahi and Stokes, 2004b; Fattahi *et al.*, 2004a; Zink and Visocekas, 1996; Zink and Visocekas, 1997; Zink *et al.*, 1995), used a different methodology to limit the influence of the thermal incandescence, namely to shift the detection window slightly down from the ~710nm peak maxima and to concentrate on the 600-700nm band. This allowed measurement of the rise part of the near-IR emission band but with less interference from the thermal incandescence that prevented high temperature measurements both within the results presented above and that of the French group. No such techniques to enhance detection of the near-IR emission were used in the work outlined here but results obtained using the interference filters and the p25232-05 module are highly promising for the future development of such a system at the SUERC luminescence laboratories and elsewhere.

Table 6.5 Raw data (with background subtraction) for Figure 6.4 (d).

Temp (°C)	10Gy F1	100Gy F1	1kGy F1
50	-37	32	99
55	-36	60	122
60	-16	167	116
65	78	195	301
70	53	262	469
75	56	325	781
80	42	733	1282
85	130	1007	1944
90	234	1478	2984
95	360	2028	4594
100	462	2913	7303
105	551	3740	10659
110	709	4593	15568
115	807	5440	21994
120	920	5836	30519
125	1160	6431	40930
130	1019	6373	52348
135	923	6299	63918
140	1020	6070	74962
145	975	5959	82619
150	1032	5651	88084
155	900	5457	90502
160	807	4962	89616
165	816	4694	87026
170	627	4454	82463
175	714	4142	78311
180	719	3846	72290
185	530	3762	66054
190	546	3701	61290
195	450	3313	57626
200	509	3137	54191

205	423	3062	50281
210	392	2832	47045
215	336	2590	43528
220	200	2387	38910
225	113	2142	34767
230	-176	2094	32104
235	-252	1915	29373
240	-440	1708	26574
245	-624	1494	23987
250	-1126	1194	22644
255	-1693	848	19672
260	-2897	610	17384
265	-3172	548	16497
270	-4131	-105	14539
275	-5145	-600	12725
280	-6833	-2530	10773
285	-9926	-2673	8959
290	-14539	-2308	6816
295	-19169	-3757	5822
300	-23411	-5753	5257
305	-34901	32	-811
310	-34023	60	-2612
315	-51501	167	-5393
320	-58094	195	-13685
325	-76860	262	-23176
330	-91954	325	-21498
335	-102854	733	-49714
340	-141084	1007	-72027
345	-161773	1478	-73368
350	-233988	2028	-105561

6.2.3 Discussion.

The results in this section show that with the addition of a red sensitive PMT a conventional TL reader can be adapted to measure the near-IR TL at high temperatures. UG11 (3mm) with GG420 (3mm) was the optimum filtration combination and despite low signal intensities dose dependence can be measured. To increase the signal intensity one option would be to reduce the optical attenuation by decreasing the thickness of the UG11. The addition of a short pass filter to reduce the background from the thermal incandescence could also be investigated. Another possibility is to add lenses to increase the effective size of the PMT window thus increasing the sensitivity of the PMT to the feldspar luminescence. The other filter combinations appeared to be less promising but there is another factor to consider. As can be seen in Figure 6.3 (c) there is over-subtraction of the dark count that has removed the dose dependency of the 1kGy and made the increasing emission intensity with dose less conclusive in Figure 6.3 (d). The red sensitive PMT is small and heats up rapidly when in contact with the sample chamber. This then causes an increased dark count within the tube, which in conjunction with thermal incandescence can render the signal undetectable when heated to high temperatures. A possible remedy could be to add a collar taking the PMT further away from the sample chamber or the addition of a cooled housing around the PMT.

Therefore, despite all the advantages of this seemingly non-fading near-IR TL band in comparison with the conventionally used 'blue' emission, there is a significant detection problem that has yet to be completely overcome. For temperatures greater than 350°C, the incandescence of the sample

and heater plate has an intense emission at wavelengths of $>790\text{nm}$ and it is the rise part of this emission that has restricted effective measurements to temperatures below 350°C (Zink and Visocekas, 1996; Zink and Visocekas, 1997).

In conclusion this system filtered using UG11 and therefore taking advantage to its secondary transmittance in the region of interest (700-720nm), Fe^{3+} associated R-TL can be authenticated to $\sim 300^\circ\text{C}$. Further investigation of UG11 thickness, lenses and cooled housing may increase the temperature range of this system.

6.3 Pulsed Photostimulated Luminescence.

6.3.1 Introduction.

The above work on the RTL of feldspars has highlighted the problems of signal-to-background ratios and the current difficulties in obtaining routine measurements of feldspar near-IR TL. However, there are other luminescence stimulation techniques that are designed to measure asynchronous luminescence, which is the sample-derived emissions after or between stimulation and may reduce significantly, or even eliminate, signal-to-background problems. Thus, having encountered exactly such problems when using TL a logical step was to use such an asynchronous technique, in this case pulsed photostimulated luminescence or PPSL.

Here an array of IR diodes was pulsed on and off to stimulate the sample discs. Firstly measurements were carried out on the entire sample suite using a 'UV-blue' detection system working on the hypothesis that such a technique could be used to develop a single aliquot single irradiation fading test, some of the results of which are discussed below. This technique was then taken a stage further with the construction of a red-sensitive system complete with cooled housing. The preliminary results from this new system are also outlined below along with recommended further work.

6.3.2 Pulsed 'Blue' IRSL.

The advantages of using pulsed light for stimulation as opposed to CW techniques, have been outlined in Section 3.4.1.5. One of these advantages discussed was time domain analysis. Using this technique it was possible to measure the timescale and underlying physical processes of charge transport and luminescence recombination following stimulation (Sanderson and Clark, 1994). This early study used pulse widths on a timescale related to that of charge carrier dynamics, e.g. of microseconds (Clark 1992), with the delay between pulses being sufficiently long to allow the system to return to equilibrium before the next pulse. This technique measured within-pulse and post-pulse luminescence on a short repeatable timescale (Clark, 1992; Sanderson and Clark, 1994).

A similar system was used in this study and although the size of the pulses employed here was too large to measure charge movement dynamics, a comparison of the broad fast and slow components was carried out.

Within the scope of this study the main use of the ‘blue’ pulsed IRSL (P-IRSL) technique was linked to a suggestion made during previous work on time resolved OSL using $\alpha\text{-Al}_2\text{O}_3\text{:C}$ (Markey *et al.*, 1995). It was stated that pulse widths of 10-100ms are short enough that the entire trapped charge population is not depleted in one measurement (each excitation pulse samples only a fraction of the radiation-induced trapped charge population). Such a technique therefore gives the ability to reread the OSL signal many times. For the samples with very small doses and luminescence intensities, signal averaging can be performed to detect weak signals, while samples with larger doses the samples may be stored for future readings and for multiple subsequent checks in the case of questionable results.

Limited bleaching from stimulation could allow for a single aliquot, single irradiation, fading test thus removing the need for normalisation. Such a technique could possibly overcome potential problems due to sensitivity changes over repeated irradiation and stimulation cycles. Each sample from the feldspar suite used in this study was put through such a fading run to test whether this approach is a viable future option. A representative set of the results is described and discussed below.

6.3.2.1 Equipment and Experimental Design.

The basic equipment used in this initial pulsed work has already been outlined in Section 3.4.1.1. The 9883QB PMT that is used on all the SUERC manual readers was again utilized here, this time with 8.5mm of BG39. The internal transmittance of the optical filters and the spectral response of the PMT are outlined in Figure 6.6 and Table 6.6.

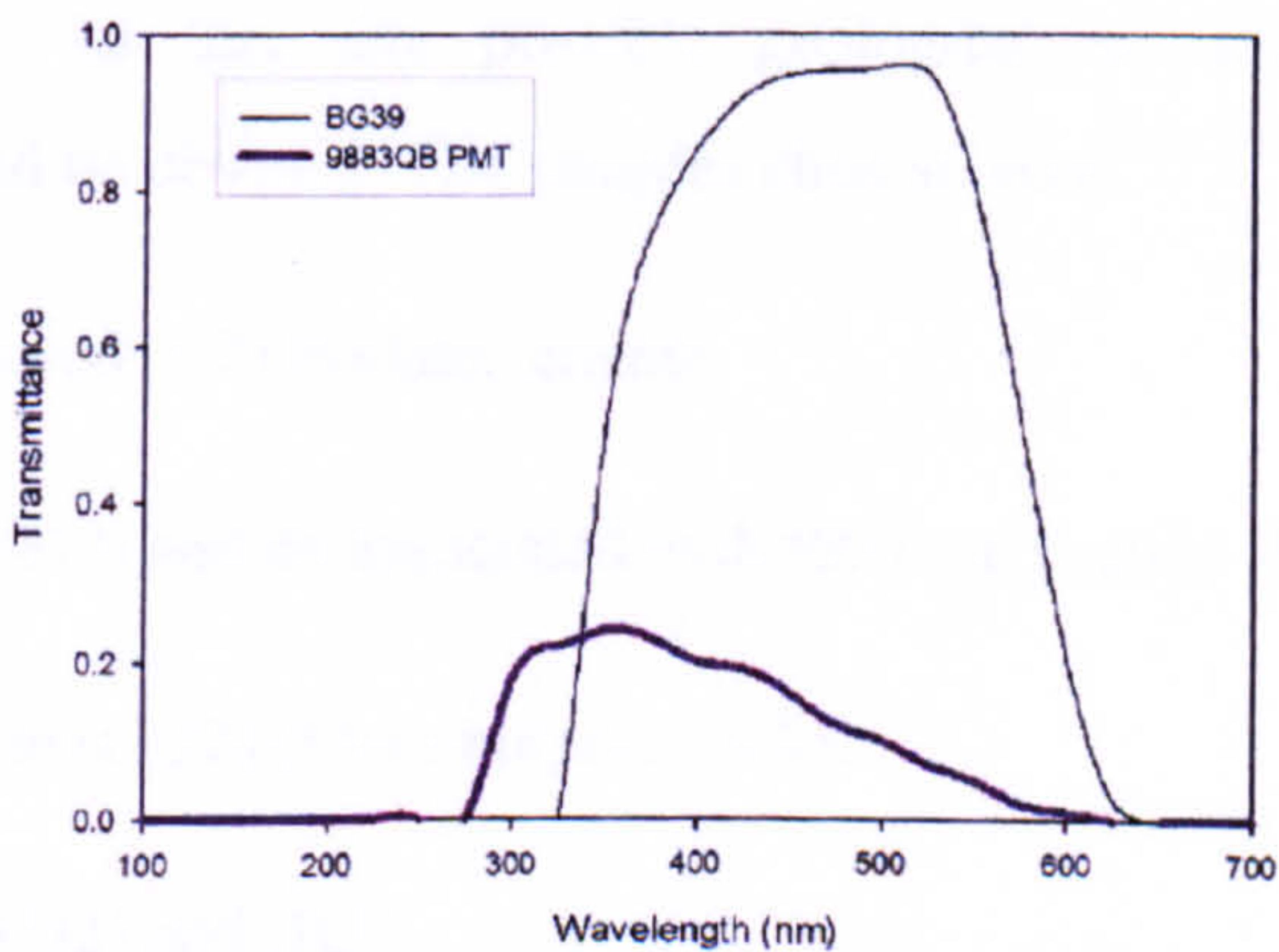


Figure 6.6 The typical Spectral Response of BG39 (1mm) and 9883QB PMT.

Table 6.6 Optical attenuation of the luminescence signal by a combination of optical filtration and the SUERC blue-PPSL system’s PMT. The transmittance is plotted where 1 is no attenuation of any optical signal and 0 being the complete optical attenuation. Plots are reproduced from the Electron Tubes and the various optical filter manufacturers. The figure is a multiplication of the transmittance of the filters and the PMT’s.

Wavelength (nm)	400	425	450	475	500	525	550	575	600
9883QB PMT	0.24	0.23	0.2	0.19	0.16	0.12	0.1	0.07	0.05
BG39 (8.5nm)	0.2775	0.5155	0.6466	0.6761	0.7068	0.6466	0.1501	0.0028	1x10 ⁻⁶
Optical Attenuation.	0.055	0.098	0.104	0.081	0.071	0.045	0.008	6x10 ⁻⁵	1x10 ⁻⁸

To test the hypothesis that microsecond pulses can stimulate a luminescence signal without significantly bleaching the disc, each single aliquot of the samples was given a 100Gy dose and a short sharp preheat (200°C/60secs). The end of this preheat is taken to be the 0 second mark. These laboratory irradiated discs were then measured at 100 seconds after preheating, then at 1000, 10 000, and finally 100 000 seconds. The next stage was to give the discs a long and low temperature preheat, of the type employed in the initial stages of this project. The 0 seconds stage is taken at 16 hours after irradiation so this is an extra factor that must be taken into consideration when comparing these two results. Any rapid short-term fading that may be apparent in the first set will not be in the second as it will have taken place during the 16hr preheat.

The pulsing module was set to deliver a pulse width of 20µs and was triggered externally by the multi channel scalar (MCS) software. The frequency of the pulse used was 1460µs (14ms). On the MCS the dwell time of each channel was 10µs, the first two channels recording the within-pulse luminescence plus signal from the stimulation source.

The results presented below are taken from feldspar samples representative of the main geological groups of samples studied, so that any possible geological or mineralogical controls on luminescence properties would be obvious. The samples chosen were:

- Fresh (B1) and weathered (B2) Ballater granite.
- Ross of Mull granite (H9) and its associated hydrothermal syenite (H11).
- Glen Tarbert migmatite (GU2) (Metamorphic rock).
- Pitchstone porphyry, (H2) and (H3).
- Patmos sanidine and Etna as representatives of the extrusive igneous rocks.

- Helmsdale arkose (Ark) (Sedimentary rock).
- Rum anorthosite (H2) (Calcic plagioclase).

6.3.2.2 Results.

The results of these measurements are outlined in Figure 6.7 and Table 6.7. They are divided into three parts: prompt (the first 30 μ s) and delayed (the last 1430 μ s) and the entire curve summed together. These widths were chosen as most of the luminescence signal emitted under this stimulation regime was found within this first 30 μ s time period, which also encompasses the pulse, while the remaining was mostly dark count in the tail, especially in the long and low preheated samples. The dark count has been subtracted from all of these values and within the preheated (PH) samples the delayed results have very little to no signal. The errors are large as they are simple counting errors. The sample is defined by internal reference numbers and their average mineralogy after SPT separation. Both the preheated and unpreheated (UPH) results are tabulated (Figure 6.7) and then plotted (Table 6.7) against time to investigate any time dependence on signal decreases. For this investigation of time dependence the results are treated as one and are not divided by mineralogical factors.

Tsukamoto (2006) and Clark (1992) both concluded that it is the slow component of photostimulated luminescence that is more stable, in comparison with the fast component, and that it has potential as a dating method circumventing the issue of anomalous fading.

Figure 6.7 (a), (c) and (d) presents data investigating the time dependence of signal loss after extensive preheating (135°C/16hrs) as a function of the fast (a) slow (c) components and the emission as a whole (e). The fast (0-30 μ s) signal (a) shows no time dependence while the slow signal (c) (30-1450 μ s) exhibits a slight increase in loss with time. When all the channels are summed together (e) this trend is repeated. This result is contrary to the model proposed by Tsukamoto et al (2006) and Clark (1992). Figure 6.7 (b), (d) and (f) show the results of the same measurements carried out without the preheating and the expected decrease in signal with time as a result of phosphorescence is observed. The majority of the signal is present in the slow here, which is the opposite of the preheated.

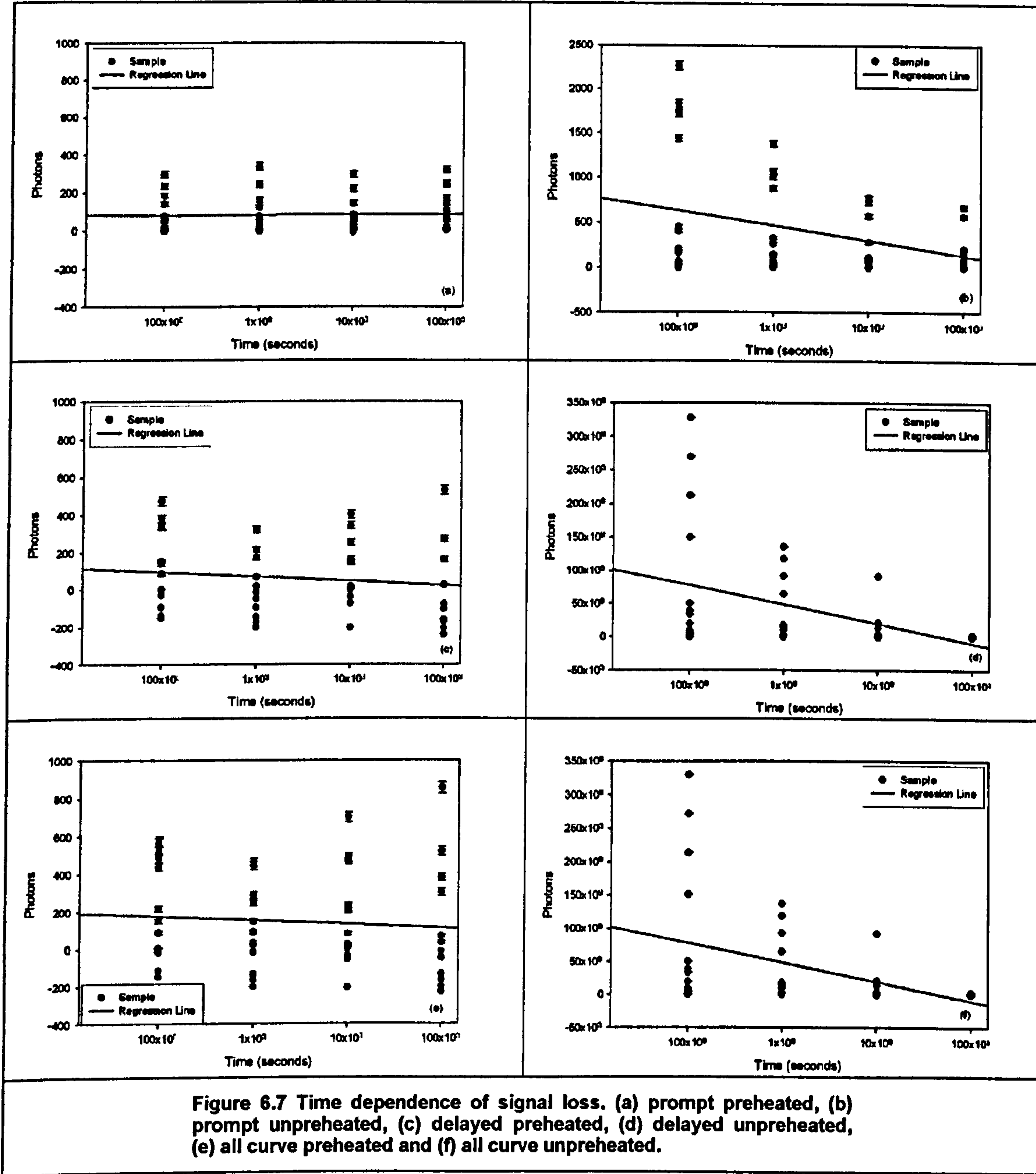


Table 6.7 Time dependence on signal loss, with and without preheating, on a sub set of the feldspar sample suite. PH = with preheating. UPH = without preheating. The time is quoted after the end of preheating in the PH results and after the completion of irradiation in the UPH results. The data is resented as a summation of counts per time; prompt = 30μs, delayed the following 1430μs and all is equivalent to the complete 1460μs pulse cycle. Samples are presented after preheating before and unpreheated following below. The samples are arranged in decreasing alkali feldspar component.

Sample. <i>Preheated.</i>	10 ¹ seconds			10 ² seconds			10 ³ seconds			10 ⁴ seconds		
	Prompt	Delayed	All	Prompt	Delayed	All	Prompt	Delayed	All	Prompt	Delayed	All
PS PH	5±2	0.8±0.8	6±2	4±2	-143	-139	3±1	-38	-35	---	---	---
A ₉₃ P ₀ Q _{<5}												
B2 PH	185±13	382±19	568±24	159±12	-12	147±12	69±8	146±12	216±14	172±13	-104	68±8
A ₉₀ P ₁₀ Q ₀												
H3 PH	77.2±8	-94	-17	24±4	66±8	91±9	25±5	-2.2	23±5	23±4	-159	-136
A ₅₀ P ₅₀ Q ₀												
H9 PH	22±4	-138	-116	77±8	-94	-17	64±8	15±3	80±8	66±8	-78	-12
A ₄₀ P ₅₀ Q ₁₀												
B1 PH	68±8	148±12	216±15	74±9	172±13	246±16	86±9	142±12	228±15	107±10	273±17	380±20
A ₂₀ P ₆₀ Q ₂₀												
ArK PH	298±17	139±11	438±20	337±18	-48	289±17	297±17	403±20	701±26	323±17	532±23	856±29
A ₂₀ P ₈₀ Q ₀												
H11 PH	14±3	-28	-14	7±2	-172	-165	16±4	-72	-56	9±3	-208	-199
A ₁₅ P ₈₅ Q ₀												
GU2 PH	47±6	475±21	523±22	51±7	-16	35±5	41±6	162±12	204±14	58±7	-104	-46
A ₁₀ P ₂₀ Q ₇₀												
B1 PH	140±11	345±18	486±22	122±11	322±18	445±21	142±12	342±18	485±22	141±11	161±12	303±17
A ₁₀ P ₈₀ Q ₁₀												
B2 PH	235±15	339±18	575±23	244±15	214±14	459±21	220±14	252±15	473±21	246±15	273±16	520±22
A ₁₀ P ₈₀ Q ₁₀												
Etna PH	-2	152±12	151±12	10.2±3	-145	-135	-2	1.8±1	0±0	11±3	23±4	35±5
A _{<10} P _{>85} Q _{<5}												
H2 PH	3±1	85±9	89±9	4±2	17±4	22±4	6±2	4±2	11±3	10±3	-239	-229
A ₀ P ₅₀ Q ₅₀												
H5 PH	3±1	-150	-147	-1	-201	-202	-4	-204	-209	6±2	-171	-165
A ₀ P ₁₀₀ Q ₀												

<i>Unpreheated</i>												
PS UPH	178±13	33520±183	33699±183	65±8	12088±109	12154±110	13±3	1529±39	1543±39	5±2	261±16	267±16
A _{>95} P ₀ Q _{<5}												
B2 UPH	1833±42	269869±51 ₉	271703±52	1067±32	117992±34 ₃	119060±14 ₇	570±23	21261±145	21832±147	169±13	146±12	316±17
A ₉₀ P ₁₀ Q ₀												
H3 UPH	35±5	5640±75	5676±75	27±5	2098±45	2126±46	15±3	236±15	252±15	19±4	-43	-24
A ₅₀ P ₅₀ Q ₀												
H9 UPH	155±12	20043±141	20199±142	128±11	13811±117	13940±118	69±8	4387±66	4457±66	51±7	512±22	564±23
A ₄₀ P ₅₀ Q ₁₀												
B1 UPH	1722±41	212271±46 ₂	213993±46 ₂	879±29	92053±303	92932±304	775±28	92053±303	92828±304	211±14	2471±49	2682±51
A ₂₀ P ₆₀ Q ₂₀												
Ark UPH	2266±47	327376±57 ₂	329643±57 ₄	1383±37	135737±36 ₈	137121±37 ₀	759±27	21781±147	22541±150	669±25	2423±49	3093±55
A ₂₀ P ₈₀ Q ₀												
H11 UPH	205±14	19917±141	20123±141	148±12	9931±99	10080±100	110±10	1955±44	2066±45	85±9	140±11	226±15
A ₁₅ P ₈₅ Q ₀												
GU2 UPH	403±20	39095±197	39499±198	259±16	16271±127	16531±128	96±9	2924±54	3021±54	97±9	296±17	384±19
A ₁₀ P ₂₀ Q ₇₀												
B1 UPH	445±21	49822±223	50268±224	324±18	17920±133	18245±135	279±16	5136±71	5416±73	201±14	1215±34	1417±37
A ₁₀ P ₈₀ Q ₁₀												
B2 UPH	1440±37	150038±38 ₇	151479±38 ₉	1008±31	64129±253	65138±255	725±26	14055±118	14781±121	572±23	3518±59	4091±63
A ₁₀ P ₈₀ Q ₁₀												
Ema UPH	73±8	9883±99	9957±99	32±5	4244±65	4277±65	16±4	779±27	796±28	9±3	86±9	96±9
A _{<10} P _{>85} Q _{<5}												
H2 UPH	22±4	3329±57	3352±57	15±4	1246±35	1262±35	12±3	53±7	66±8	3±1	-154	-151
A ₀ P ₅₀ Q ₅₀												
H5 UPH	-2	272±16	270±16	3±1	-3	0±0	-4	-172	-177	---	---	---
A ₀ P ₁₀₀ Q ₀												

6.3.2.3 Discussion.

The pulsed blue system has the ability to measure time dependence of the loss of remnant signal in feldspars as this sample of the results has shown. The potential of such a system for undertaking single aliquot and single dose measurements has been established and with further research and development this system has the ability to become a very powerful investigative tool. The intensities of the 'fast' component were lower than was wished but this could be increased by speeding up the rate of repetition and possibly increasing the pass count during each measurement, although the potential for bleaching the signal should be ascertained with all these developments. Also as the ability to investigate time dependence has been authenticated the investigation of mineralogical controls on fading behaviour (Chapter 5) can be continued.

The terms 'fast' and 'slow' in the above discussion is one of convenience rather than accuracy. Clark (1992) defines the 'fast' component as 2-10 μ s, and Tsukamoto <20 μ s and in Figure 6.7 the division has been placed at 30 μ s. Using a pulsed diode array to produce the high repetition rate has influenced this designation and shorter components can be stimulated using a nitrogen dye laser (Clark 1992) but the number of pulses possible is lower. However, using this system in conjunction with the laser would allow for an investigation of the time domain of different mineralogical factors covered by the sample suit used in this study.

Given the success of the preliminary investigation of this system and that reported in previous work detecting feldspar red TL, a logical step was to bring the two systems together and use the asynchronous luminescence capabilities, with the resulting reduction or even elimination of signal-to-background issues, to investigate the red IRSL of feldspars.

6.3.3 Pulsed 'Red' IRSL

The feldspar emission in the near-IR region is important to feldspar anomalous fading research as it is supposedly stable (Stokes and Fattahi, 2003d; Zink and Visocekas, 1997). In order to study further this phenomenon a Hammamatsu red sensitive PMT was purchased together with a thermoelectrically cooled housing (Section 3.4.2.1.). IRSL can be used to stimulate the red and near-IR emissions from feldspars (Fattahi *et al.*, 2004a) although the technique has been largely unexplored. However, IRSL is close to the detection window and again the signal-to-background ratio when using CW stimulation could be an issue. For this reason the good preliminary results in the 'blue' pulsed system has allowed for a natural progression to investigate the use of PIRSL as a viable alternative.

The recently reported results of Tsukamoto *et al* (2006) have explored time-resolved IRSL techniques, building on previous work by Sanderson (1994) and Clark (1997), to stimulate signals

from K- and Na-feldspars extracted from sediments. Their study (Tsukamoto *et al.*, 2006) involved a comparison of UV, blue and red P-IRSL that enabled separation and measurement of the short and long-lived components from the samples. From comparisons of the natural/regenerated and prompt/delayed signals, they postulate that long lifetime components are immune from anomalous fading (Tsukamoto *et al.*, 2006). If this pulsed technique can indeed measure a non-fading red emission then the issues with synchronous stimulation/detection techniques such as near- IR TL may have been overcome. Described below are results of a study to assess the ease of separating and measuring a convincing near-IR PIRSL signal from a variety of the feldspars.

6.3.3.1 Equipment and Experimental Design.

Due to the signal-to-background issues that have been described previously, it was first necessary to experiment with different optical filters in CW IR-IRSL mode to find the optimum combination for this prototype near-IR system. Those tested are listed in Table 6.8 below.

Table 6.8 The different filter combinations tested with the R2257 red sensitive PMT.					
Optical Combination	Number of Diodes	Filter Type	Thickness (mm)	PMT Dark Count (cts/sec)	Diode Break Through (cts/sec ⁵)
A	3	RG850 (in front of diodes)	3	14 200	125
		KG1	6		
		SP057	2		
		RG695	3		
B	3	RG850 (in front of diodes)	3	13 000	90
		KG1	6		
		SP057	2		
		RG695	3		
		UG5	4.7		
C	3	RG850 (in front of diodes)	3	13 000	90
		RG650	3		
		BG39	6		
D	3	RG850 (in front of diodes)	6	13 500	60
		KG1	6		
		SP057	2		
		RG695	3		
		UG5	4.7		
E	3	RG1000 (in front of diodes)	3	14 000	0.3
		KG1	6		
		SP057	2		
		RG695	3		
		UG5	4.7		

F	3	RG850 (in front of diodes) KG1 SP057 SP058 SP062 SP060	6 6 4 4 4 2	143 000	21
G	2	RG850 (in front of diodes) KG1 SP057 SP058 SP062 SP060	6 6 4 4 4 2	58 036	21
H	1	RG850 (in front of diodes) KG1 SP057 SP058 SP062 SP060	6 3 4 4 4 2	16 000	12
I	1	RG850 (in front of diodes) KG1 SP057 SP058 SP062 SP060	6 6 4 4 4 2	16 000	1.6
J	1	RG850 (in front of diodes) KG1 SP057 SP058 SP062 SP060	6 6 2 2 2 2	16 000	2
K	1	RG850 (in front of diodes) KG1 SP057 SP058 SP062 SP060	6 6 4 4 2 2	16 000	1.6
L	1	RG850 (in front of diodes) KG1 SP057 SP058 SP062 SP060	12 6 4 4 2 2	16 000	1.2

M	1	RG850 (in front of diodes)	14	9 000	0.3
		KG1	6		
		SP057	4		
		SP058	4		
		SP062	2		
		SP060	2		
N	1	RG850 (in front of diodes)	14	10 000	9
		KG1	3		
		SP057	4		
		SP058	4		
		SP062	2		
		SP060	2		
O	1	RG850 (in front of diodes)	18	24 000	0.5
		KG1	3		
		SP057	4		
		SP058	4		
		SP062	2		
		SP060	2		
		RG695	3		
		GG420	3		

The large diode breakthrough in combination A suggested ill-fitting filters in this original diode collar. This problem was repeated in combinations B and C (Table 6.8) despite different filters being combined. The slight drop in breakthrough was probably due to the very high counts affecting the PMT rather than any filtration changes.

To test for rim leaks around the filters, set B was reinstated and the number of RG850s in front of the diode was doubled (D) and there was an observable drop in breakthrough (Table 6.8). The diodes are described by the manufacturer to have an emission peak at ~940nm. The RG850s should have attenuated the lower rise of this peak and to test the range of the stimulating emission they were swapped for 3mm of RG1000 in combination E. This filter cuts off most of the diode's signal but there was still a measurable breakthrough. This suggested a wide and bright rise and tail around the 940nm peak.

The UG5 was removed and a set of interference filters were added in their place. To deal with the issue of rim leaks that were evident in the previous results a new collar was machined entirely out of a solid block of aluminium, reducing the available pathways for the light to reach the PMT. This new collar had a greater diameter (50mm) filter recess that allowed for a better fitting filter stack. The aluminium surface had also to be blackened to reduce reflectivity. The elevated dark count (F) indicates a light leak in the system that was remedied. Even with this leak there was already a significant decrease in the diode breakthrough showing that the new collar was a success. Rather

than add more filters at this juncture, due to the inability to reduce the breakthrough to manageable level, one of the three diodes was removed (G) (Table 6.8).

The lack of difference in the breakthrough between three and two diodes led to a second diode being removed leaving just the one ~940nm LED to stimulate the sample. To test the stimulating ability of this single diode an F1 disc was irradiated to 100Gys. When measurement took place by CW IRSL the luminescence appeared to be swamped by the breakthrough. At this point the IRSL was changed from CW to PPSL, and this allowed measurement of sample luminescence to a level of 5000cts/sec.

The next stage in setting up the red-sensitive system was to further decrease the diode breakthrough without significantly attenuating signal in the 710nm region reaching the PMT. 3mm of the KG1 filter was removed as it is known to have a high attenuation factor in the desired detection region (H). This KG1 filter was then reinstated (I) due to the increase in breakthrough and half the interference filters were removed instead (J) (doubling the filter thickness does not always affect the breakthrough). The interference filters were then replaced one at a time until the initial 160000cts/sec breakthrough was attained (K) (Table 6.8).

To try and reduce breakthrough further the number of long pass filters in front of the diode was doubled to 12mm (L). Now that the diode power had been decreased by the extra RG850s the thickness of KG1 was again halved (N). Having this direct comparison between 6 and 3mm of KG1 allowed the use of its transmittance curve to diagnose where on the spectrum the breakthrough sits; around 755nm (M). In an attempt to shift the breakthrough further up the spectrum another 6mm RG850 was added to the front of the diode and 3mm of RG695 was added to the stack inside the collar. The last of the rim leaks were eliminated by inserting a GG420. It was taped to the base of the collar thus blocking the last possible path along the edges of these filters (O) (Table 6.8).

Having arrived at the best filter combination and the least diode breakthrough, the next stage was to decrease the PMT's internal dark count. This was done by inserting the PMT into a thermoelectrically cooled housing. The effectiveness of cooling the PMT and subsequently decreasing the dark count was then measured (Table 6.9). To do this a measurement at ambient room temperature was made and then measured as the temperature was decreased in 5°C intervals. Due to the length of time the system takes to cool the MCS was set to a channel dwell time of five seconds.

To help the efficiency of the thermoelectric cooler the mains water was passed from the tap through a large coil of rubber tubing that was submerged in icy water (a bucket filled with water and ice packs which were changed every two hours during measurement).

Table 6.9 The decrease in PMT dark count and diode breakthrough (cts/sec) with decrease in thermoelectric cooling system setting.

Thermoelectric Cooler Temperature (°C)	PMT Dark Count (cts/sec)	Diode Breakthrough (cts/sec)
+ 26 (ambient mains water temperature)	120000	250000
-5	1400	85000
-10	1200	80000
-15	900	75000
-20	700	70000

With the filter combination outlined above and the cooler set to -10°C the system had a working background of:

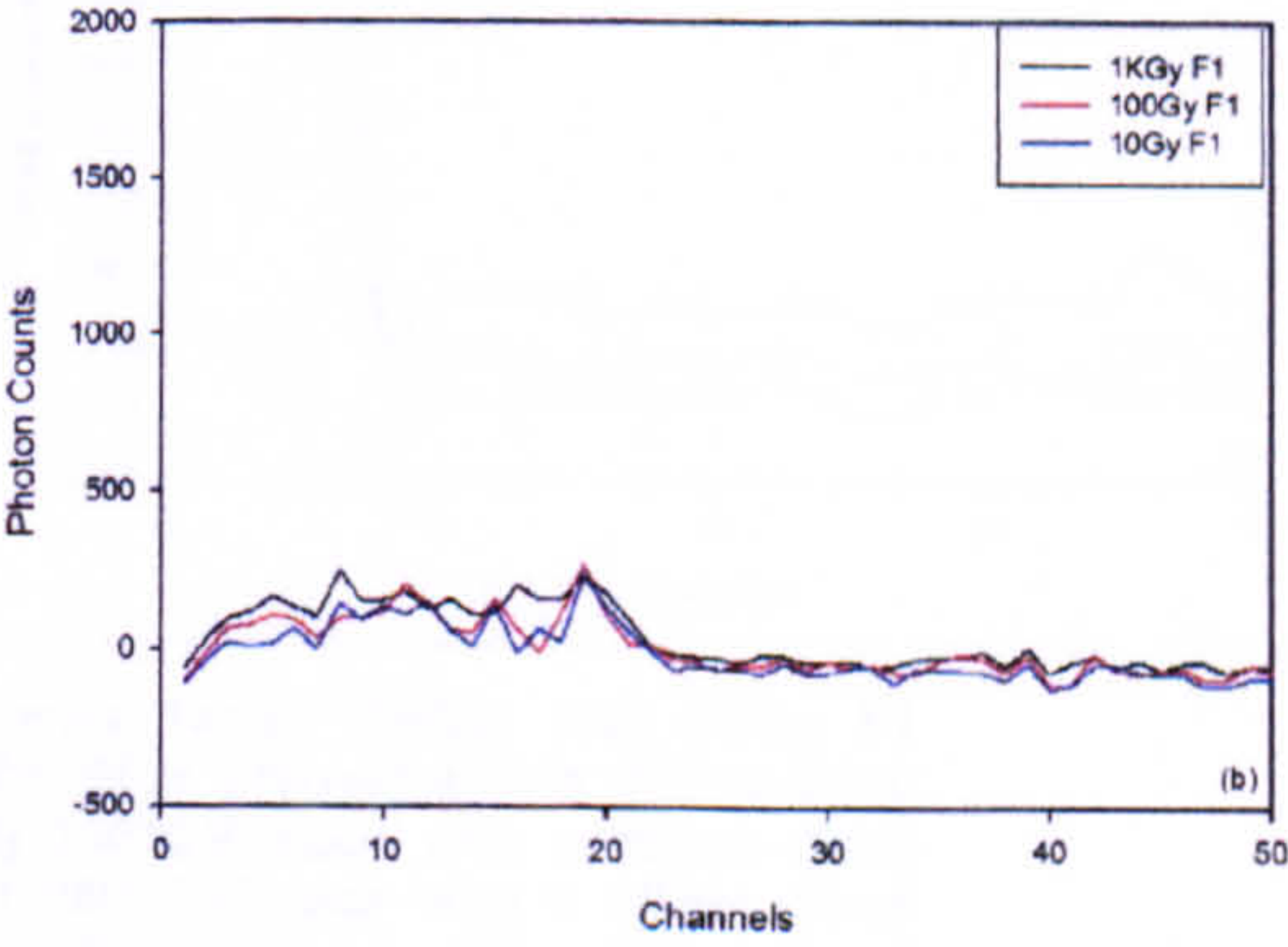
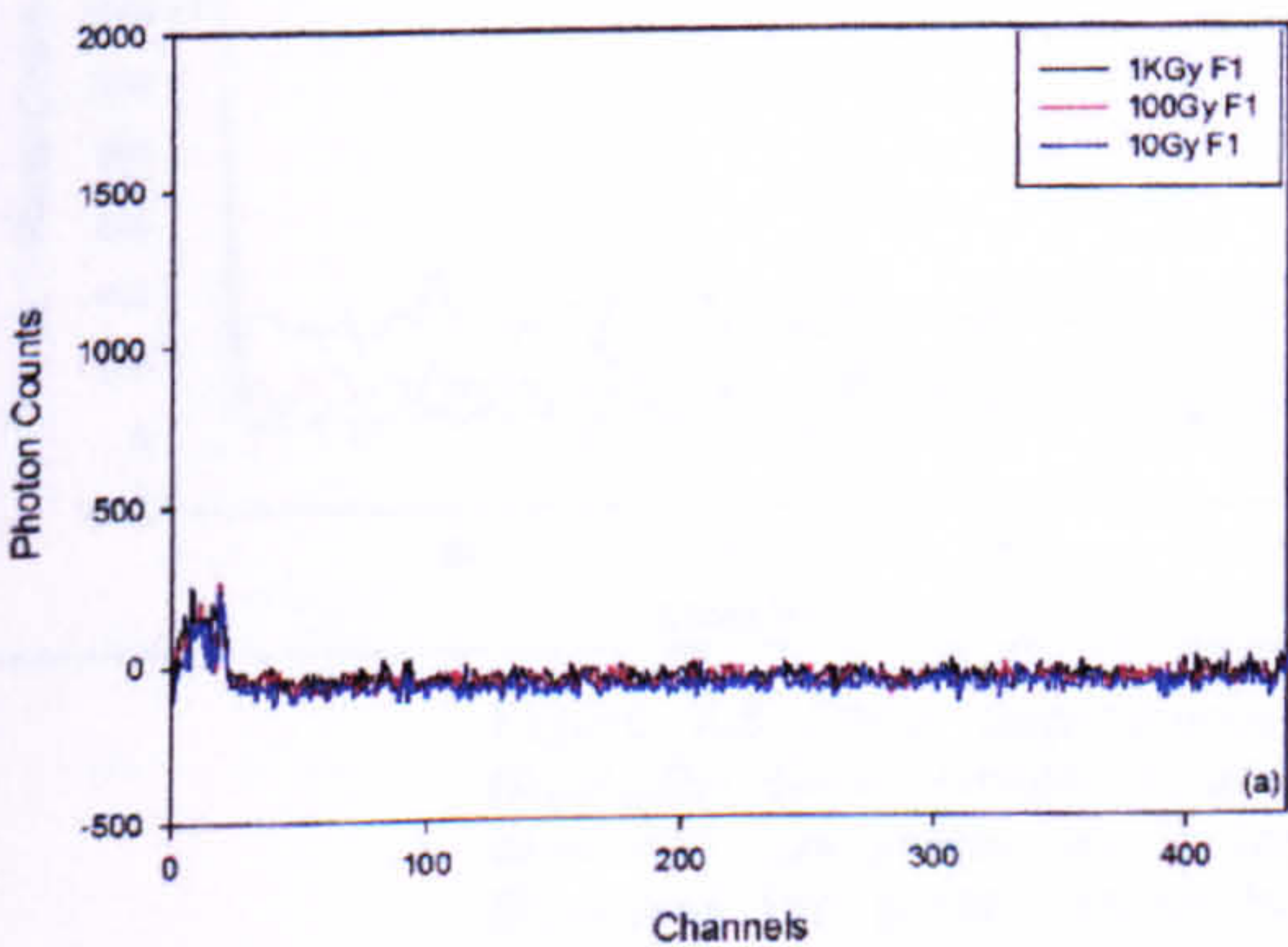
PMT Dark Count: 180 cts/sec
Diode Breakthrough: 17 000 cts/sec

This near-IR pulsed work utilised a different MCS system than the blue (see Section 3.4.2.1), allowing for smaller channel dwell times. The pass length was also less constrained and the pass count could be set as high as desired. The pulse was set at 1µs, the smallest this module could produce, with a frequency of 88µs. The pass count was set to 3 000 000 channels/pulse cycle.

6.3.3.2 Results.

The results below are presented as raw glow curves as the features being described and instrumentally investigated are best defined in this format.

6.3.3.2.1 Measuring Dose Dependence.



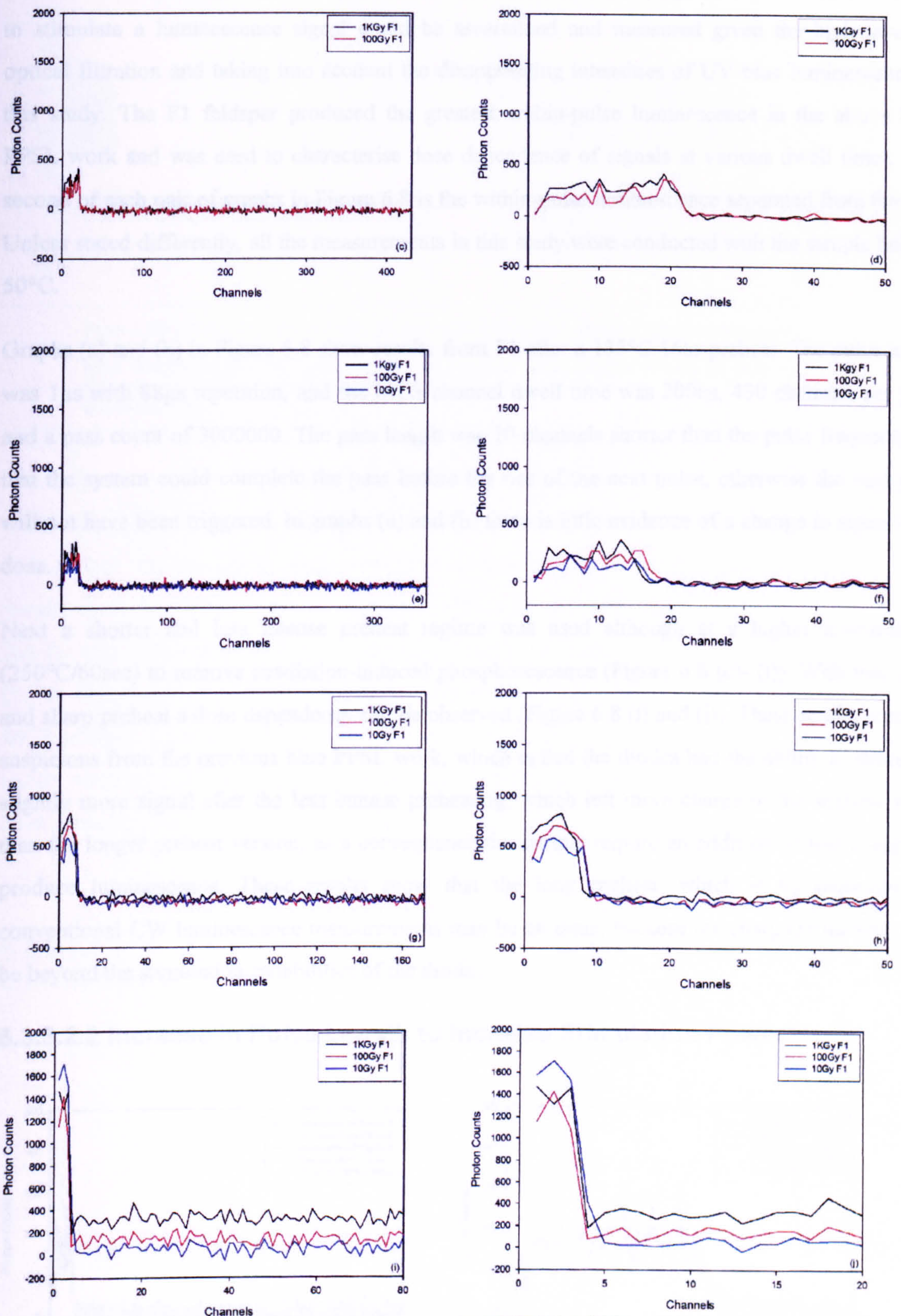


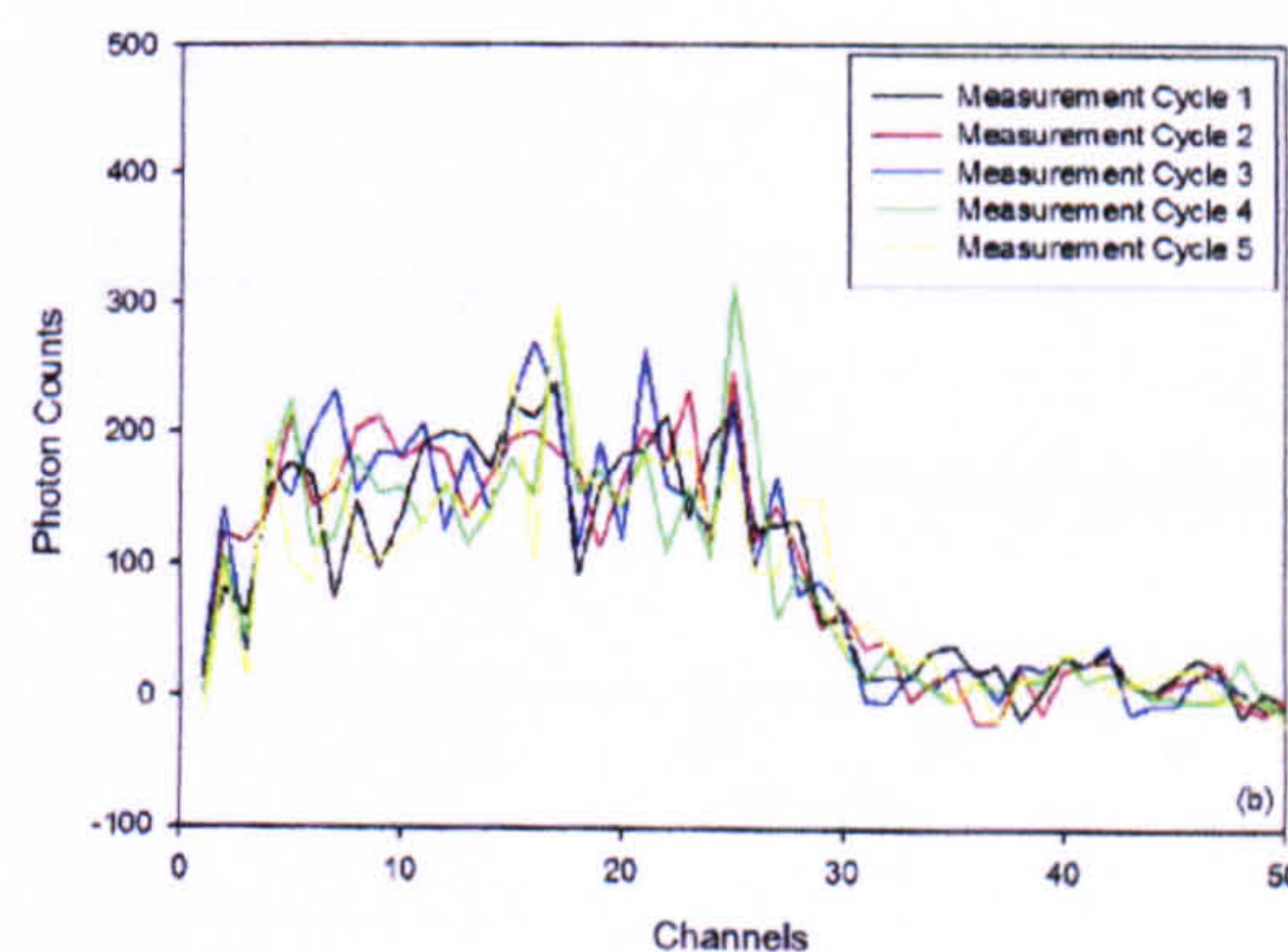
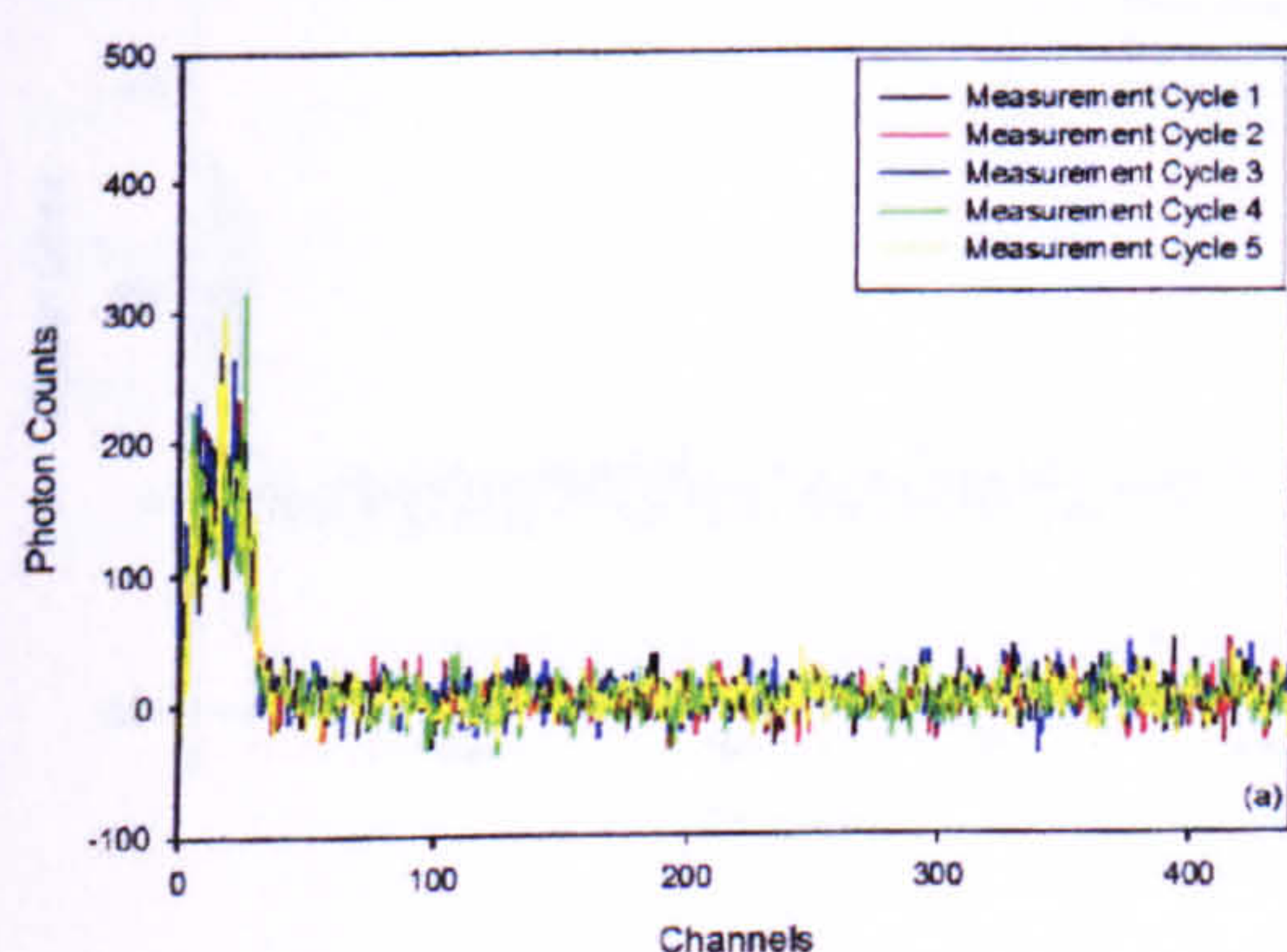
Figure 6.8 Dose dependence study with 1kgy, 100Gy, and 10Gy F1 ($A_{65}P_{30}Q_5$) discs. Graph (a) and (b) 135°C/16hr preheat with a 200ns dwell time and 1 μ s pulse. Graph (c) and (d) 250°C/60secs with a 200ns dwell time and 1 μ s pulse. Graph (e) and (f) 250°C/60secs with a 250ns dwell time and 1 μ s pulse. Graph (g) and (h) 250°C/60secs with a 500ns dwell time and 1 μ s pulse. Graph (i) and (j) 250°C/60secs with a 1 μ s dwell time and 1 μ s pulse. Graphs (a), (c), (e), (g) and (i) show the full shine down curve while (b), (d), (f), (h) and (j) show the first 20 channels.

After the cooled red system was operational and the diode breakthrough at a low level, the ability to stimulate a luminescence signal could be ascertained and measured given the high level of optical filtration and taking into account the disappointing intensities of UV-blue luminescence in this study. The F1 feldspar produced the greatest within-pulse luminescence in the above blue PPSL work and was used to characterise dose dependence of signals at various dwell times. The second of each pair of graphs in Figure 6.8 is the within-pulse luminescence separated from the tail. Unless stated differently, all the measurements in this study were conducted with the sample held at 50°C.

Graphs (a) and (b) in Figure 6.8 show results from F1 after a 135°C/16hr preheat. The pulse width was 1µs with 88µs repetition, and the MCS channel dwell time was 200ns, 430 channels per pass and a pass count of 3000000. The pass length was 10 channels shorter than the pulse frequency so that the system could complete the pass before the rise of the next pulse, otherwise the next pass will not have been triggered. In graphs (a) and (b) there is little evidence of a change in signal with dose.

Next a shorter and less intense preheat regime was used although at a higher temperature, (250°C/60sec) to remove irradiation-induced phosphorescence (Figure 6.8 (c)- (j)). With this short and sharp preheat a dose dependency can be observed (Figure 6.8 (i) and (j)). These results confirm suspicions from the previous blue PPSL work, which is that the diodes had the ability to stimulate slightly more signal after the less intense preheating, which left more charge in the shallow traps than the longer preheat version; as a consequence the sample require an addition of less energy to produce luminescence. These results show that the long preheat, which is so successful in conventional CW luminescence measurements may be an issue, because the charge remaining may be beyond the stimulation capabilities of the diodes.

6.3.3.2.2 Increase in Pulse Length to Increase Stimulation Power.



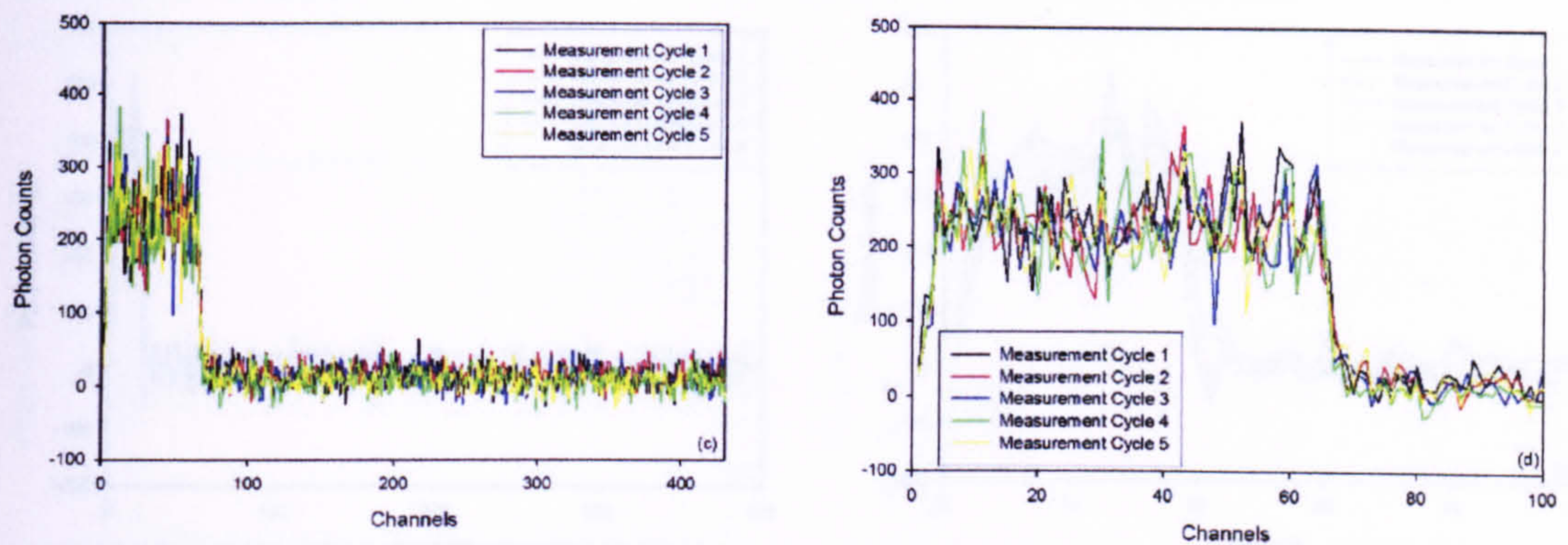
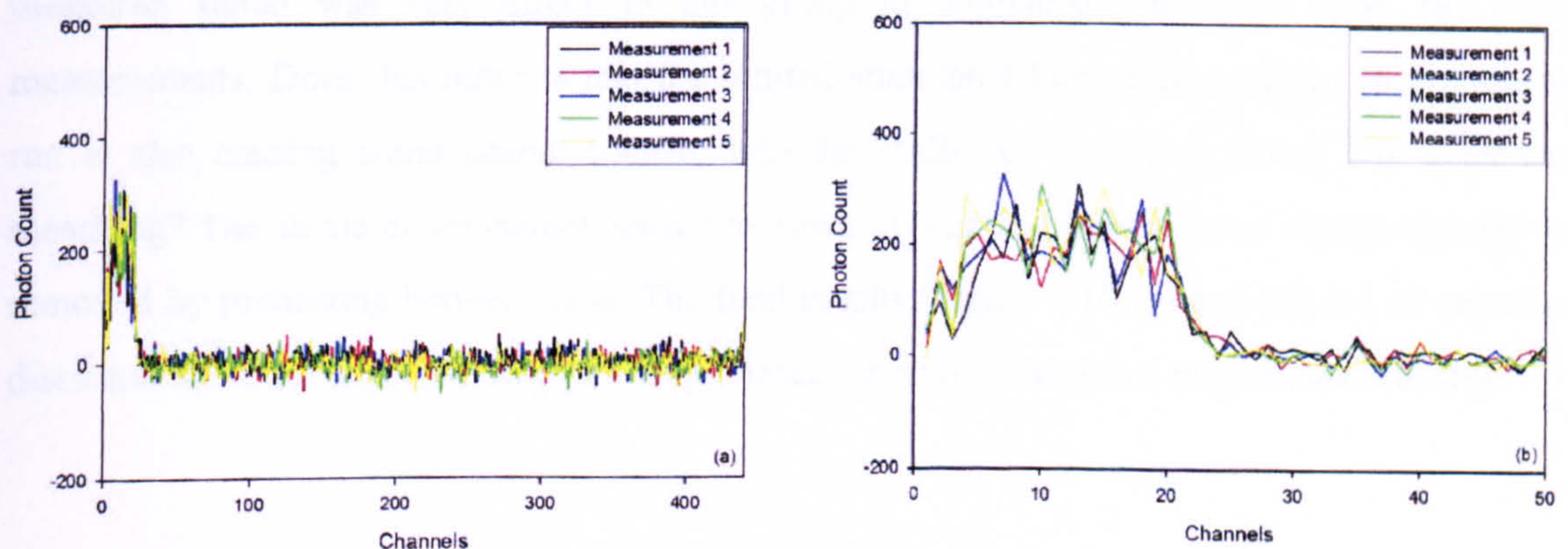


Figure 6.9 Increasing pulse length to increase stimulation power. All measurements made using a 1Kgy F1 ($A_{65}P_{30}Q_5$) disc with a 250°C/60secs preheat and a 200ns dwell time. Graphs (a) and (b) 2µs pulse, (c) and (d) 10µs pulse. Graphs (a) and (c) present the complete shine down curve, (b) the first 50 channels of (a) and (d) the first 100 channels of (c).

The ability to measure differences in dose response in the previous runs (Figure 6.8 (i) and (j)) was encouraging. Also the single ~940nm diode can clearly stimulate some luminescence emission, but is it enough that repeated measurements would show a decrease in the signal produced? In other words, could the diode bleach the signal? In Figure 6.9 the pulse width was doubled from 1µs to 2µs for stimulation of the 1Kgy disc and again there was no sign of signal bleaching in either (a) or (b). In Figure 6.22 (c) and (d) the pulse width was 10µs with the same 87µs repetition time and MCS settings. There is a hint of a signal decrease in the 1Kgy F1 disc with this pulse width but the results were inconclusive. If the diode was insufficiently intense to bleach the signal, the question must again be asked, how much of the pulsed signal is derived from luminescence of the feldspar.

6.3.3.2.3 The Affects of Preheating – Testing Phosphorescence vs. Luminescence.



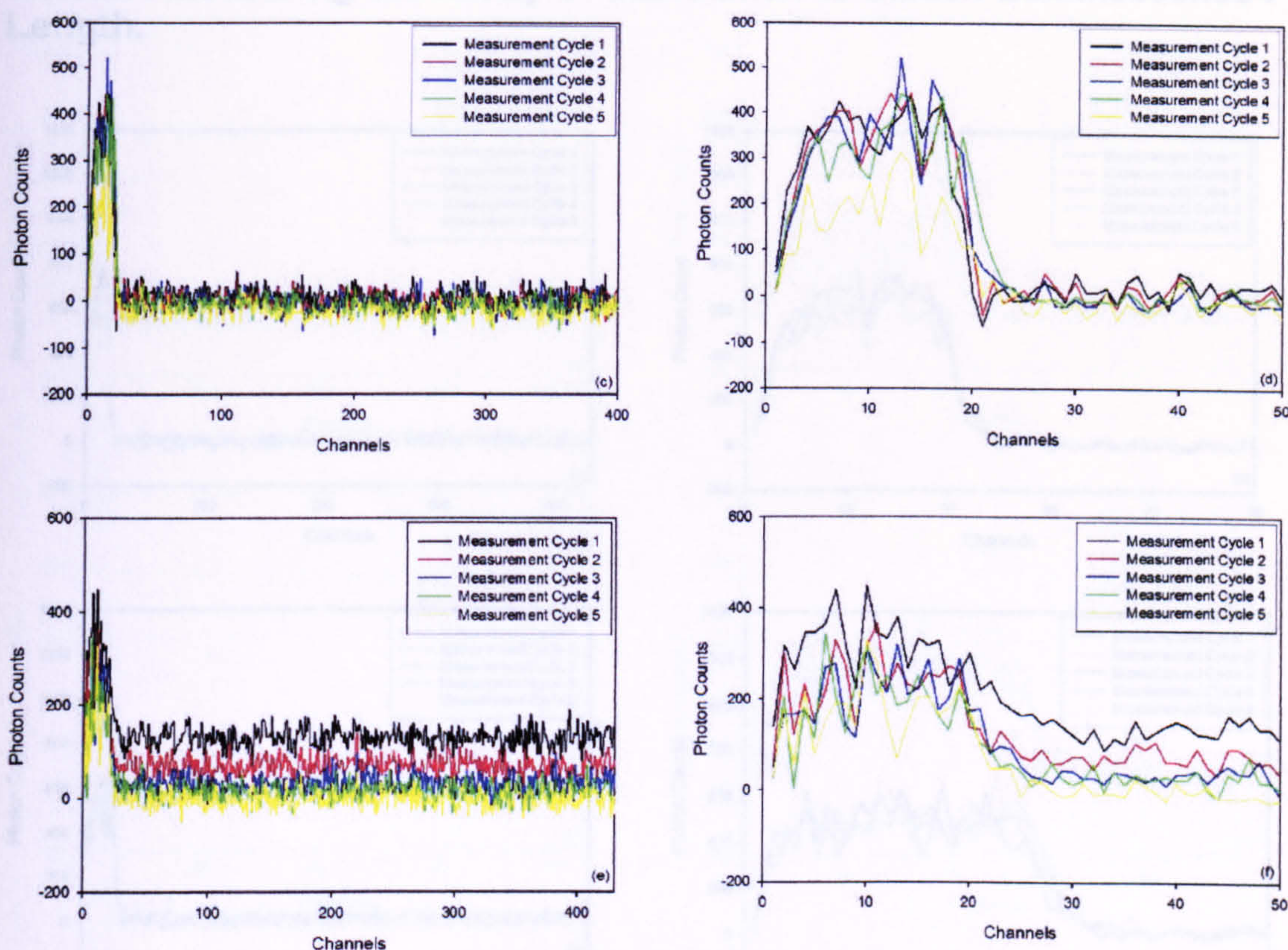


Figure 6.10 Phosphorescence Vs. luminescence. How does preheating affect detectable signal? All measurements carried out using a 1Kgy F1 ($A_{65}P_{30}Q_5$) disc and a 200ns dwell time with 5 consecutive measurement cycles. Graphs (a) and (b) show the signals after a 250°C/60secs preheat at the start of the measurement, (c) and (d) the same preheat regime between each of the five cycles, (e) and (f) has no preheat. Graphs (a), (c) and (e) show the complete shine down curve, while (b), (d) and (f) show the first 50 channels.

Figure 6.10 shows results of a three disc run to study how preheating and consecutive measurements influence the signals produced. Figure 6.10 (a) and (b) used the standard 250°C/60secs initial preheat directly after irradiation of the disc. Figure 6.10 (c) and (d) show the effects of undertaking the preheating between each of the five runs (i.e. four preheats). The drop in measured signal was very minor in this group in comparison to those from the previous measurements. Does this indicate that the limited stimulated luminescence from each consecutive run is also causing some charge transfer into the shallower traps and hiding any evidence for bleaching? The single diode cannot cause bleaching proper, but maybe some charge transfer that is removed by preheating between runs. The final graphs (Figure 6.10 (e) and (f)) are of unpreheated discs and show the expected drop in phosphorescence with consecutive measurement cycles.

6.3.3.2.4 Measuring the Ability of Stimulation to Bleach Luminescence-Pulse Length.

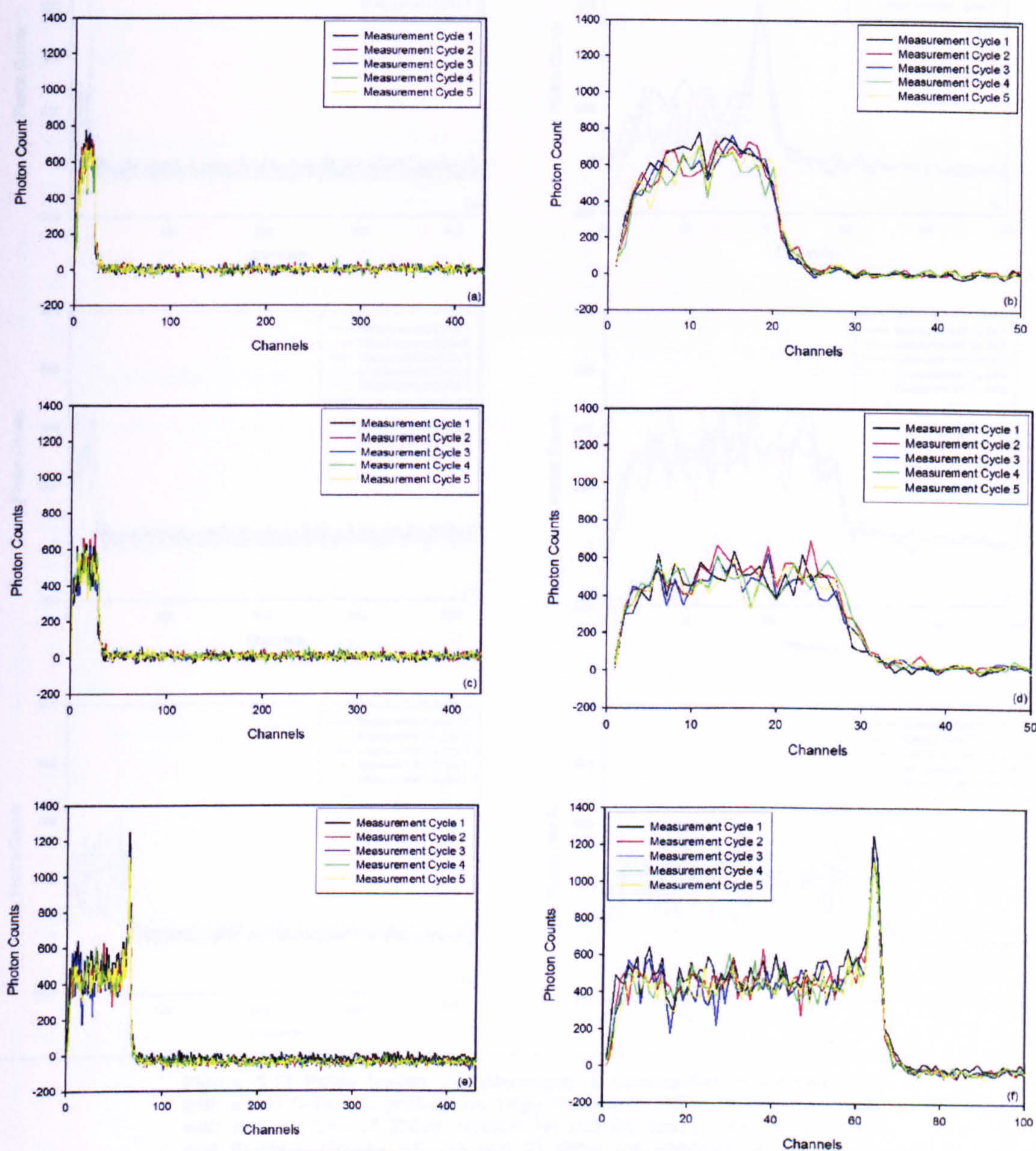


Figure 6.11 Pulse length Vs. Bleaching. 5 consecutive measurements with a 250°C/60secs preheat on 1Kgy F1 ($A_{65}P_{30}Q_5$) discs with a dwell time of 200ns. Graphs (a) and (b) 1μs, (c) and (d) 2μs, (e) and (f) 10μs pulse length. In graphs (b), (d) and (f) the number of channels plotted are reduced to investigate the within-pulse signals.

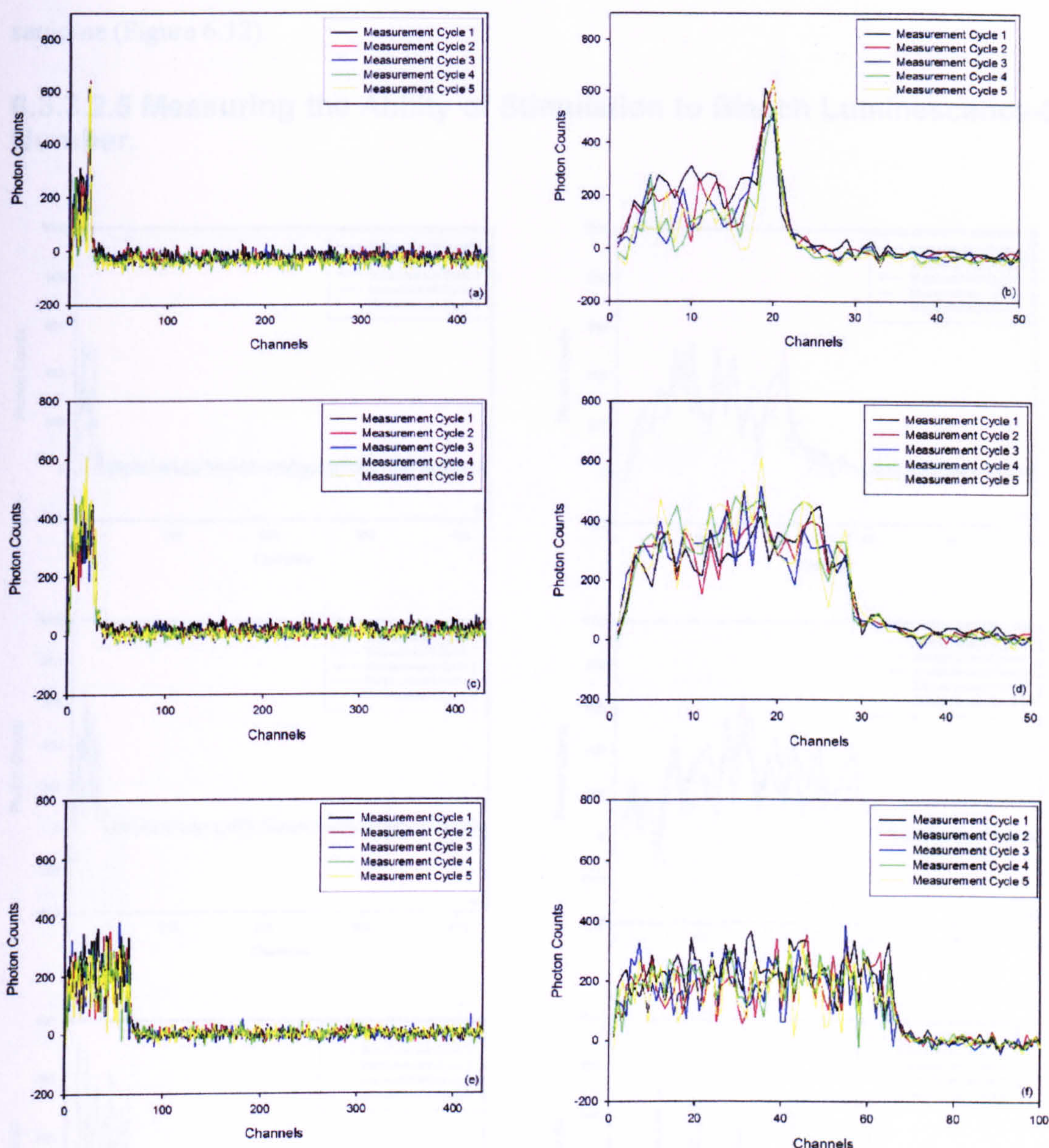


Figure 6.12 Pulse length Vs. Bleaching. 5 consecutive measurements with a 250°C/60secs preheat on 1Kgy Patmos sanidine ($A_{95}P_{0.5}Q_{5}$) discs with a dwell time of 200ns. Graphs (a) and (b) 1 μ s, (c) and (d) 2 μ s, (e) and (f) 10 μ s. Graphs (b), (d) and (f) show the within-pulse signal but decreasing the number of channels plotted.

The consecutive bleaching measurements were carried out using different pulse lengths and the results are presented in Figures 6.11 and 6.12. There was no difference in bleaching with the three lengths of 1 μ s Figure 6.11 (a) and (b), 2 μ s Figures 6.11 (c) and (d), and 10 μ s Figures 6.11 (e) and (f) of the 1kgy F1 disc. Note that in the last pulse measurement there was a spike at the end of the pulse is due to a stability problem in the power that drives the module (i.e. a noise spike appearing when the diodes were switched off). The instability appeared because the pulsing module was set at the far ends of its capabilities. The same spike appeared in the 1Kgy Patmos sanidine disc (Figure 6.12), at the end of the 1 μ s pulse. This 1Kgy Patmos measurement was carried out directly after the 10 μ s F1 measurement and adds credence to the hypothesis that the spikes are a system artefact.

Again there was little to no evidence of a signal decrease by repetitive measurements in the Patmos sanidine (Figure 6.12).

6.3.3.2.5 Measuring the Ability of Stimulation to Bleach Luminescence-Diode Number.

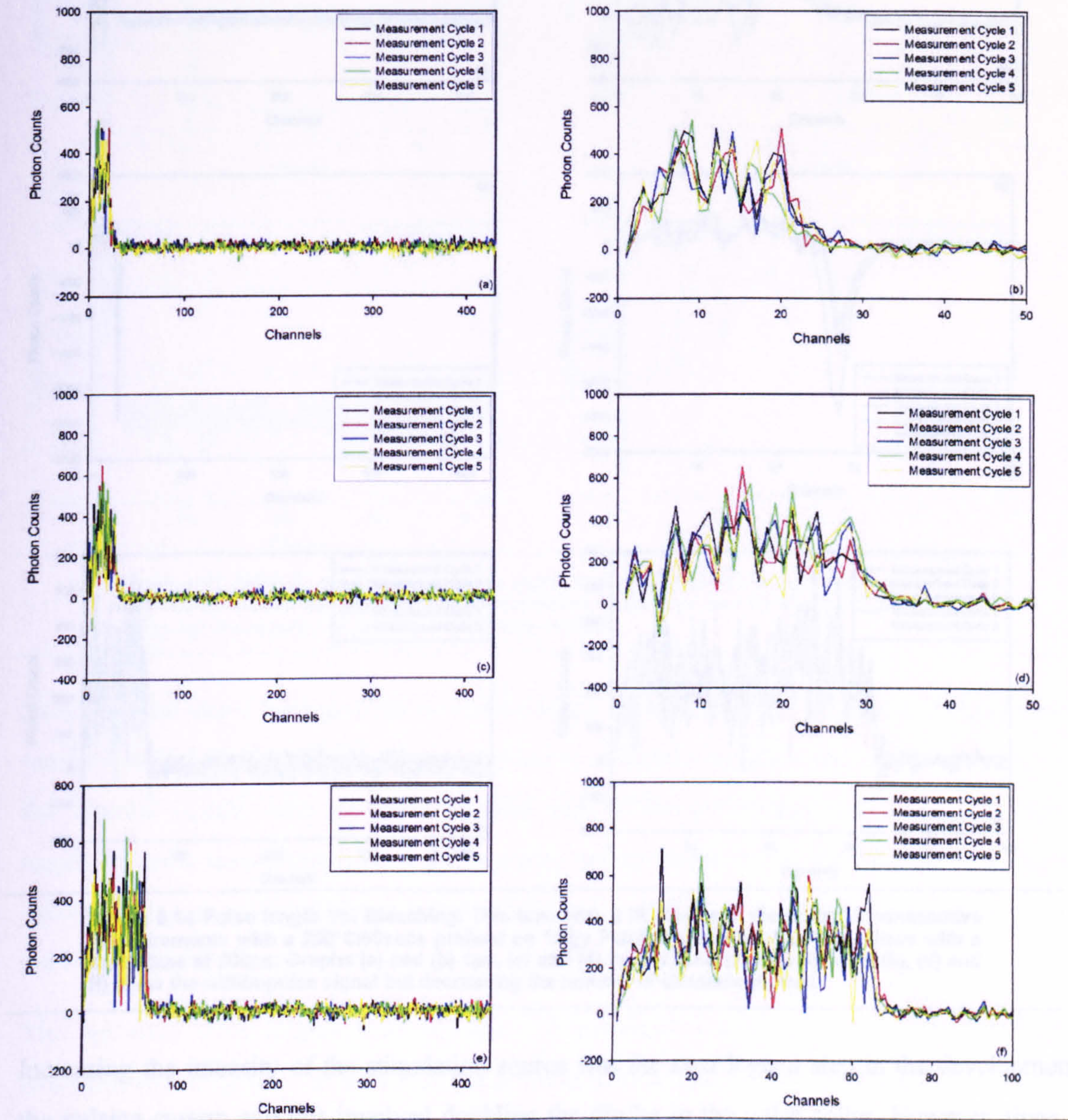


Figure 6.13 Pulse length Vs. Bleaching. This time with 2 IR diodes in the collar. 5 consecutive measurements with a 250°C/60secs preheat on 1Kgy F1 (A₆₅P₃₀Q₅) discs with a dwell time of 200ns. Graphs (a) and (b) 1μs, (c) and (d) 2μs, (e) and (f) 10μs. Graphs (b), (d) and (f) show the within-pulse signal but decreasing the number of channels plotted.

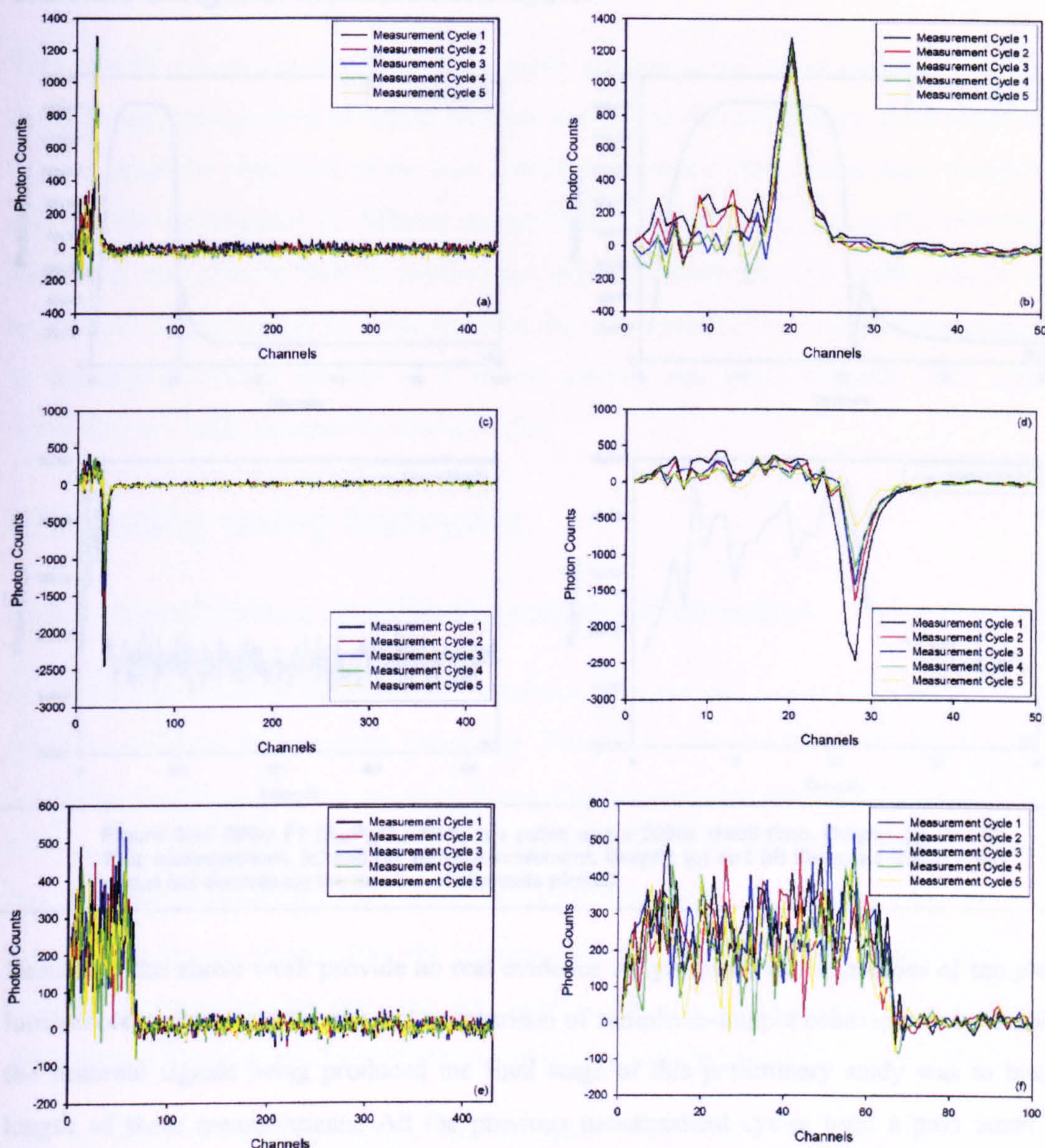


Figure 6.14 Pulse length Vs. Bleaching. This time with 2 IR diodes in the collar. 5 consecutive measurements with a 250°C/60secs preheat on 1Kgy Patmos sanidine ($A_{95}P_{0.5}Q_{0.5}$) discs with a dwell time of 200ns. Graphs (a) and (b) 1μs, (c) and (d) 2μs, (e) and (f) 10μs. Graphs (b), (d) and (f) show the within-pulse signal but decreasing the number of channels plotted.

Increasing the intensity of the stimulation source was the next logical step in the development of the pulsing system and this involved doubling the diodes in the pulse collar. However, there was little difference in the 1kGy F1 signal intensity across the three pulse lengths (Figure 6.13). In the Patmos sanidine there was much evidence of system instability in relation to the pulsing (Figure 6.14). The only stimulation run without these spikes was the 10μs pulse (Figure 6.13 (e) and (f)), and this showed no bleaching. The second diode was removed at the end of these measurements.

6.3.3.2.6 Length of Measurement Cycle.

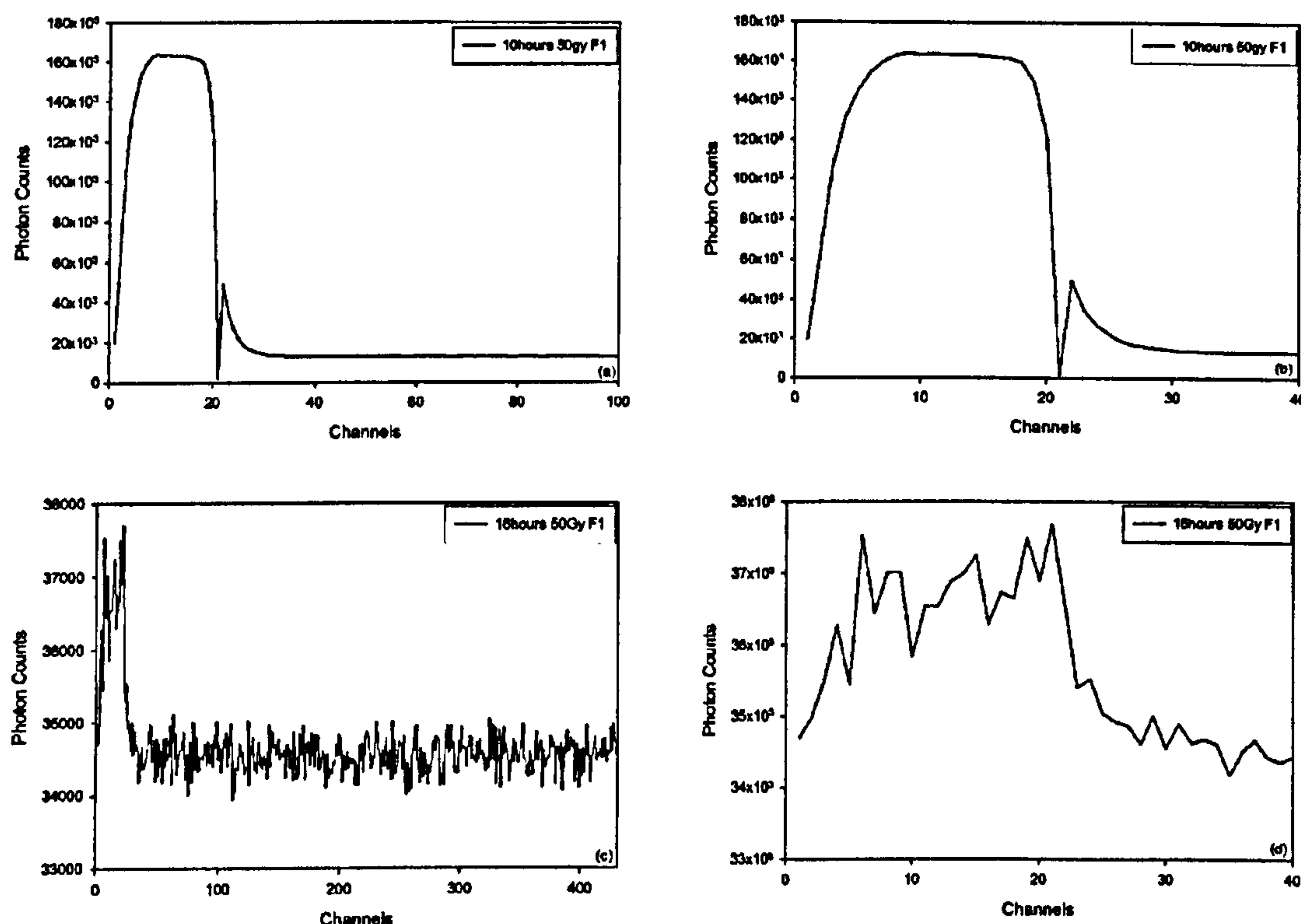


Figure 6.15 50Gy F1 ($A_{65}P_{30}Q_5$) disc, 1 μ s pulse and a 200ns dwell time. Graphs (a) and (b) 10hr measurement, (c) and (d) 16hr measurement. Graphs (b) and (d) show the within-pulse signal but decreasing the number of channels plotted.

Results of the above work provide no real evidence for production of intensities of sample derived luminescence sufficient for any real comparison of sample-to-sample behaviour to be made. Due to the minimal signals being produced the final stage of this preliminary study was to increase the length of these measurements. All the previous measurement cycles used a pass count of three million. This was increased for two discs of 50Gy F1, the first was measured for the equivalent of ten hours and the second sixteen hours.

The ten hour cycle (Figure 6.15 (a) and (b)) exhibited a peak after the pulse but this was unfortunately not present in the sixteen hour cycle so it is hard to classify whether it was a sample derived signal or not. The measured signals were much higher in intensity, as would be expected, and there was no indication that other than measuring more background due to longer pass counts there was any change in within-pulse peak shape. The shape of the ten hour curve indicates that it was not a good measurement, although there was an interesting trend in the peak in the sixteen hour data, Figure 6.15 (d). The shape of the within-pulse signal had changed with the latter part of the peak showing a rise. This was at the end of the pulse and if it was just diode breakthrough the opposite results would be expected.

6.3.3.3 Discussion.

This near-IR system has the ability to measure a signal in its current operating conditions but a single diode and high level of optical filtration has limited the applicability of the results to feldspar dating. Again the adaptation of the laser stimulation source to this system may provide an answer and also the investigation of different unconventional optical filers, such as the interference filters used here, may provide clues to improve the operating conditions. This system also has the ability to measure TL and should be combined with the UG11 and RG520 combinations suggested above to investigate whether the use of a cooled housing and larger diameter PMT will improve sensitivity to a level adequate for dating studies.

6.4 Dating using feldspars.

6.4.1 Introduction and Background Information.

Given the high levels of signal stability (obtained from the sample suit characterised in Chapter 4) using conventional luminescence techniques (Chapter 5), the possibility of using the successfully applied preheating regime to an actual dating situation was investigated. The samples chosen for this investigation were part of a larger international NERC funded EFCHED (Environmental Factors in the Chronology of Human Evolution and Dispersal) project, involving dating of middle Palaeolithic sites in Russia and the Ukraine. The overall aim of this project is to investigate whether present chronological data are biasing the current perceptions of the relative cold adaptation of Neanderthals and modern humans in the Ukraine (Burbidge *et al.*, In press).

The two samples that were chosen for this study were from the Kostienki-14 site. They were samples 1579 and 1580 (SUERC internal reference numbers), the former being taken from below a tefra layer and the later above. Kostienki 14 is a silty colluvial site located near the River Don at Voronezh. The site has relatively good independent age control on Early Upper Palaeolithic archaeological levels (Burbidge *et al.*, In press). For simplicity the layers have been numbered 1-11 in this EFCHED study rather than traditional Kostienki system. The upper part (1-2) includes a tephra layer that has been associated with the “Campanian Ignimbrite/Y5” constrained to an approximate age of 39.3Ka. It is this layer that is straddled by the samples described here (Pyle *et al.*, 2006).

Table 6. 10 Estimated mineral percentages of samples 1579 and 1580.

Sample	Mineralogy
1579	A ₁₀ P ₅₀ Q ₄₀
1580	A ₄₅ P ₁₅ Q ₄₅

Despite the high levels of quartz in these samples the feldspar emission is of an intensity that is orders of magnitude greater and is expected to constitute the vast majority of the detected signal.

6.4.2 Results.

The sample preparation techniques and measurement regime has been outlined in sections 3.5.2 and 3.5.2.1.

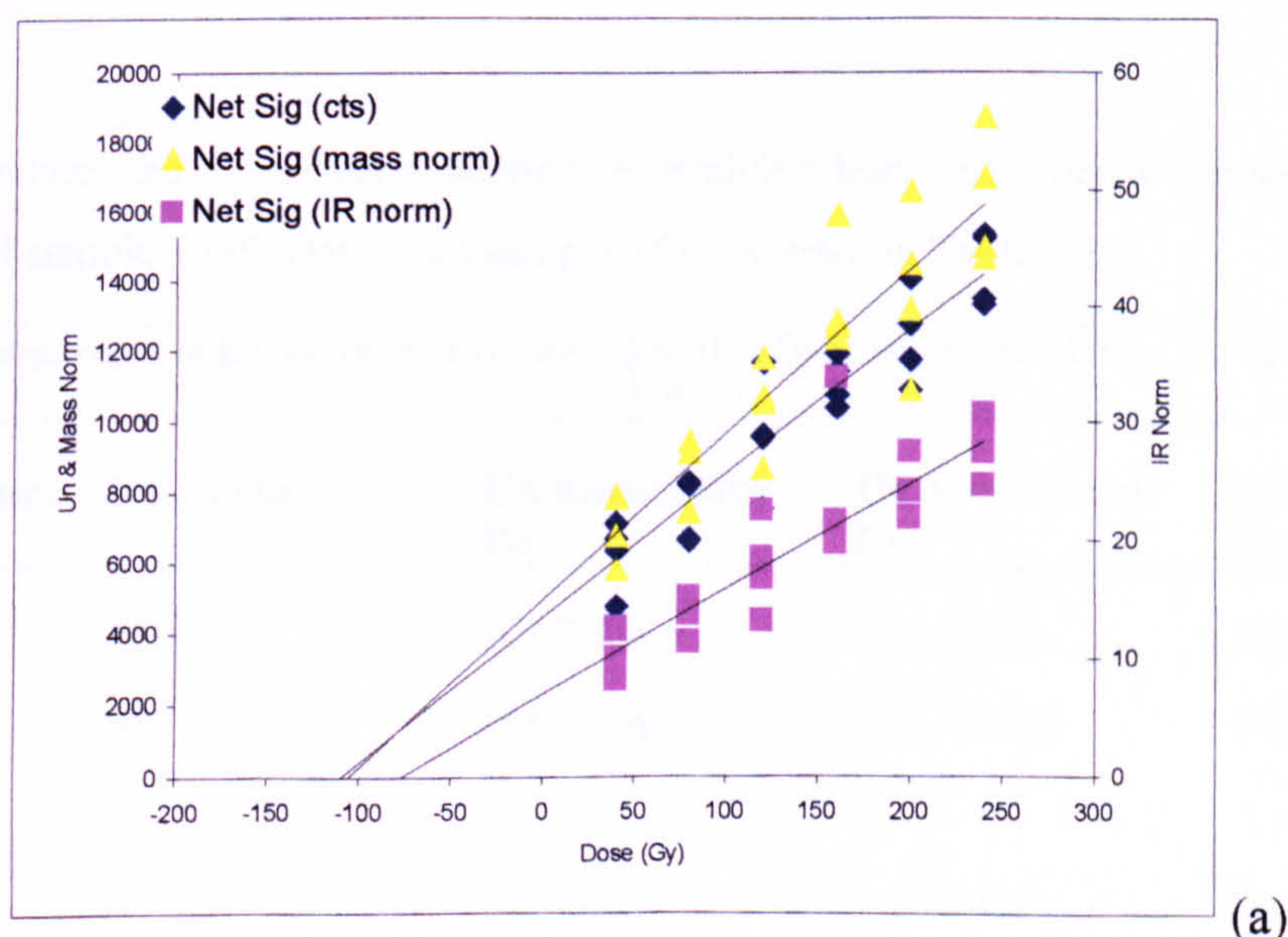
6.4.2.1 Sample 1579.

The natural and regenerative dose measurements (cts/sec) were inserted into a spreadsheet and two sets of normalisation carried out, IR signal normalised and mass normalised. These data were then compared with un-normalised data to obtain estimated dose values (D_e). The IR normalised data was the net count of each of the discs when irradiated, divided by the net of the 2 second natural signal measurement. Mass normalised means that the net signal of the irradiated disc is divided by the sample weight. This was carried out to reduce scatter that could be caused by the differences in sensitivity (IR or signal normalisation) and the amount of sample on each disc (mass normalised). The results were plotted up with a best fit line (Figure 6.16). This is a line of regression and where the three lines cross the 0 counts on the x-axis is the D_0 point and this gives the D_e of each data set.

To give a more accurate D_e these numbers were inserted into a sigma plot worksheet and using the functions within this programme a linear regression line was plotted using the following formula:

$$Y=y_0+ax$$

[6.1]



6.4.2.2 Sample 1579

The aluminium discs were irradiated in a ⁶⁰Co source and the net signal was measured. The stainless steel discs were irradiated in a ⁶⁰Co source and the net signal was measured. The net signal was measured for each disc and the net signal was measured for each disc.

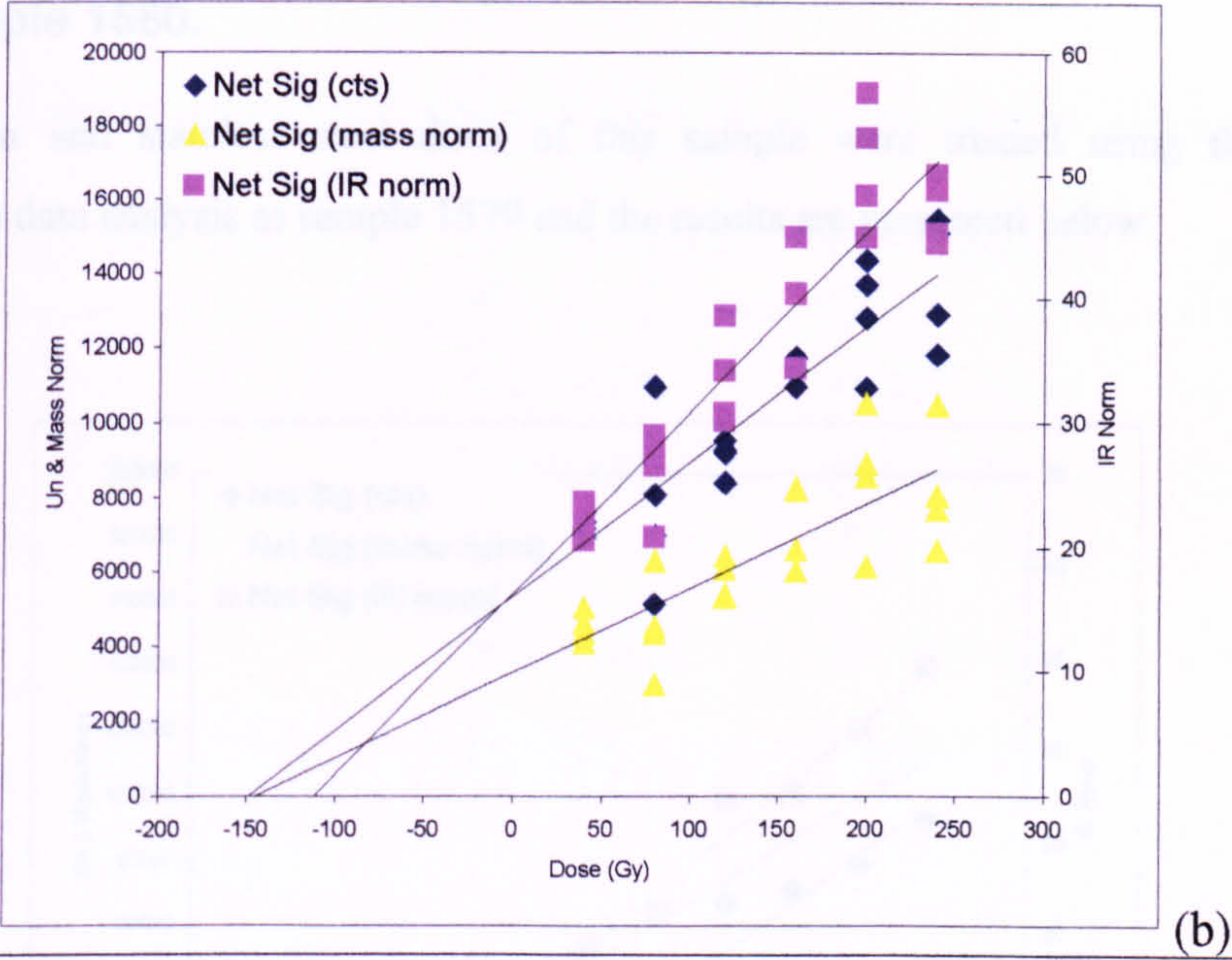


Figure 6.16 Aluminium (a) and Stainless Steel (b) discs groups for 1579 with fit lines to give the De values.

However, it is accepted that the growth of signal with dose is non-linear and if the saturation point is taken into account the regression line is in fact also non-linear. As a result the De has also been evaluated using an estimated saturation point of 1kGy. The formula used was:

$$Y=a*(1-\exp(-(x-x0)/1000))$$

[6.2]

With ‘a’ being the saturation value and x0 representing where the y axis crosses 0 on the x axis (the D₀).

Table 6.11 tabulates the De values generated by applying both line types to the same data set. In this case that of sample 1579. Data from sample 1580 is listed in Table 6.12.

Table 6.11 Comparison of linear vs. non-linear regression lines when calculating De values for sample 1579.

Regression Line.	Disc Type	Un-normalised De	IR Normalised De	Mass Normalised De
Linear	Al	109.7±13Gy	57.3±77Gy	105.8±18Gy
	SS	148±16Gy	111.7±16Gy	144.1±24Gy
Non-linear	Al	86.3±19Gy	41.3±111Gy	82.1±25Gy
	SS	115.7±22Gy	86.3±22Gy	112.1±33Gy

6.4.2.2 Sample 1580.

The aluminium and stainless steel discs of this sample were treated using the exact same procedures and data analysis as sample 1579 and the results are presented below.

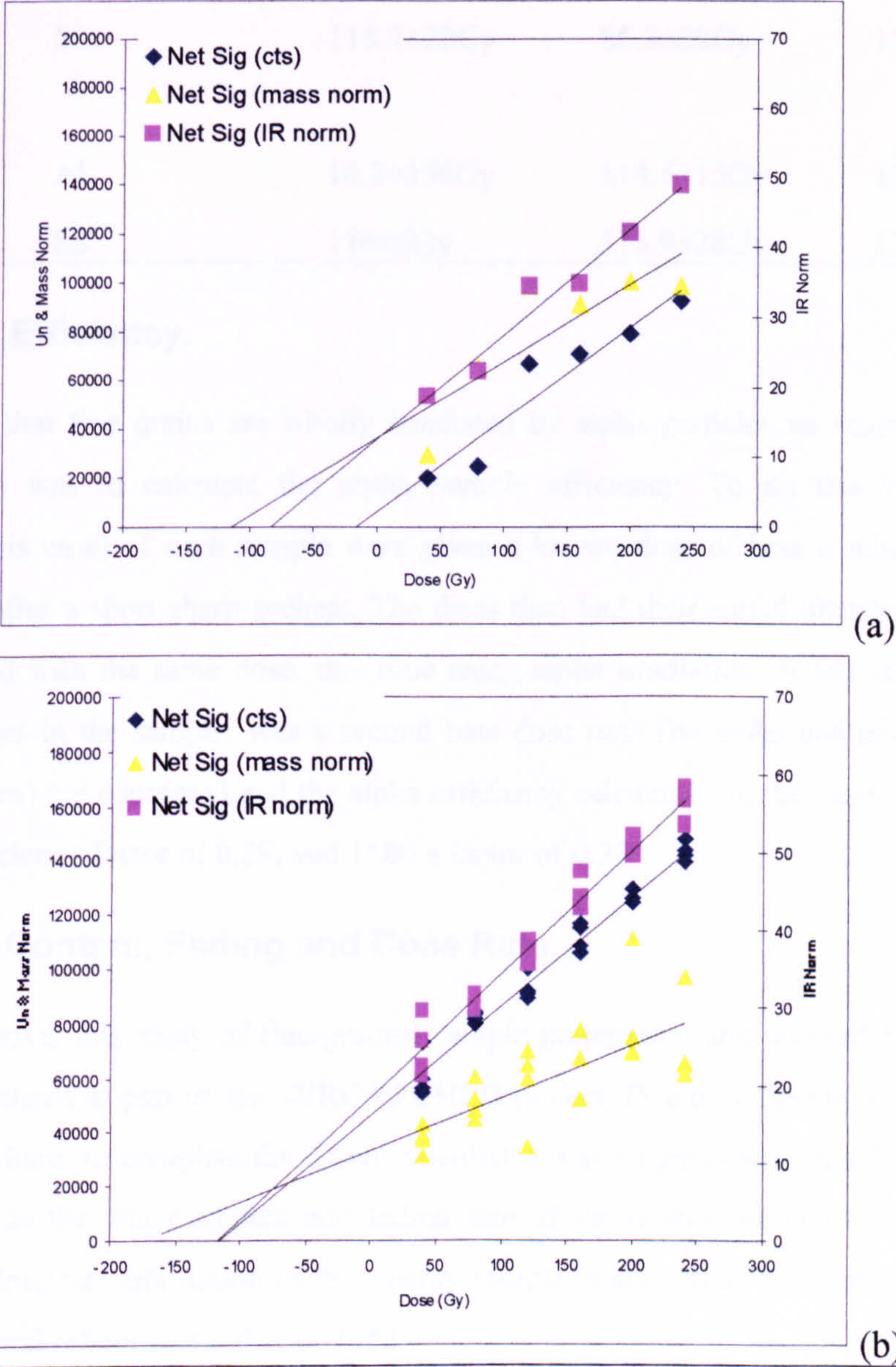


Figure 6.17 Aluminium (a) and Stainless Steel (b) discs groups for 1580 with fit lines to give the De values.

Table 6.12 Comparison of linear vs. non-linear regression lines when calculating De values for sample 1580.

Regression Line.	Disc Type	Un-normalised De	IR Normalised De	Mass Normalised De
Linear	Al	86.3±19Gy	41.3±111Gy	82.1±25Gy
	SS	115.7±22Gy	86.3±22Gy	112.1±33Gy
Non-linear	Al	16.2±156Gy	114.5±15Gy	115±55Gy
	SS	116±6Gy	116.9±28Gy	173.3±28Gy

6.4.2.3 Alpha Efficiency.

Due to the fact that fine grains are wholly irradiated by alpha particles an essential part of this dating technique was to calculate the alpha particle efficiency. To do this six of the discs (aluminium in this case) of each sample were given a known dose of beta irradiation and the IR signal read out after a short sharp preheat. The discs then had their signal bleached using TL and were re-irradiated with the same dose, this time using alpha irradiation. A last step, to check for sensitivity changes in the sample, was a second beta dose run. The alpha and beta (corrected for sensitivity changes) are compared and the alpha efficiency calculated. In this case the 1579 sample had an alpha efficiency factor of 0.29, and 1580 a factor of 0.33.

6.4.2.4 Water Content, Fading and Dose Rate.

As mentioned above, this study of fine-grained sample preparation and adapted SARA technique has since been utilised as part of the NERC EFCHED project. Due to the exploratory nature of the results presented here, to complete the dating calculation some figures from this later project have been used, such as the water content and fading rate of the nearest sample to 1579 and 1580. Importantly the dose rate calculation of this nearby sample is also used. This sample is from Layer 3 and has an internal reference number of 1653.

6.4.2.5 Apparent Ages.

In the table below are presented the apparent age estimates from this preliminary study on the adapted SARA technique and an equivalent age estimate from the 1653 EFCHED Layer 3 sample.

Table 6.13 Apparent ages (Ka) from 1579 and 1580 compared to the age from 1653. (al =aluminium, ss = stainless steel).

Sample	Un norm (ka)	Err	%Err	IR Norm (ka)	Err	%Err	Mass Norm (ka)	Err	%Err
1579 Al	57	11	20	28	31	112	55	14	25
1579 SS	77	17	22	58	13	22	75	25	33
1580 Al	4	15	331	58	13	22	56	42	74
1580 SS	59	5	9	59	6	9	87	33	38
1653 (Al)	-----	-----	-----	-----	-----	-----	39	3	8

6.4.3 Discussion.

Disappointingly, the ages of these two preliminary samples are much greater than the equivalent EFCHED sample, which is in agreement with external age controls (the tephra layer). There are a few possible reasons for this, the most obvious being the large errors on the data from this preliminary study in comparison with the EFCHED results. These larger errors are possibly the result of the dose normalisation that the NERC results have been calculated with. This involves a final irradiation of the disc after having the signals bleached by TL and then the highest dose point is repeated (240Gys) and the results are normalised to this. This normalisation was not carried out in this preliminary study.

Another possible explanation for this age discrepancy is unrelated to the measurement or normalisation techniques but due to the site itself. There is evidence from the fieldwork observations of reworking of the section and this would account for the older ages found at the top of the site. The samples taken for the EFCHED study are all below the two measured here. Reworking is therefore the most likely explanation as even those results with good errors, such as the 1580 stainless steel results all suffered overestimation compared to their nearest EFCHED neighbour.

Despite this overestimation the technique developed as part of this study has been used successfully as part of the NERC EFCHED project and ages have been produced within this larger study that

are in good agreement with external controls (Figure 6.18). The fading tests carried out by Burbidge (In prep) used the long and low temperature preheat that was observed to be a success within this study, and his results are promising with the majority exhibiting no fading and those that do have been partly explained by uncertainties (*pers. comm.*). The results of these fading tests are reproduced in Figure 6.19 as a demonstration of the successful application of this technique within a large international dating study.

Figure 6.19 presents the prompt/delayed responses to 100Gy beta irradiation for all the EFCHED samples. Six prompt and six delayed disks were measured for each sample and signals from each disk were dose normalised using their response to a separate cycle of irradiation and readout. The average of the six normalised prompt responses was then divided by the average of the six delayed responses. Each disk was preheated for 16 hrs at 135 °C prior to pulsed IRSL measurement for 20s at room temperature. The Kostienki samples are SUTL 1652-1656 and delays were between 3.1 to 5.0 x10⁶s. As can be observed there was no apparent trend with delay time. The mean prompt/delayed value is 0.980±0.006 (Std.Dev. = 0.034) (Burbidge *Pers. comm.*).

8.5 Alternative Dating Techniques

8.5.1 Introduction

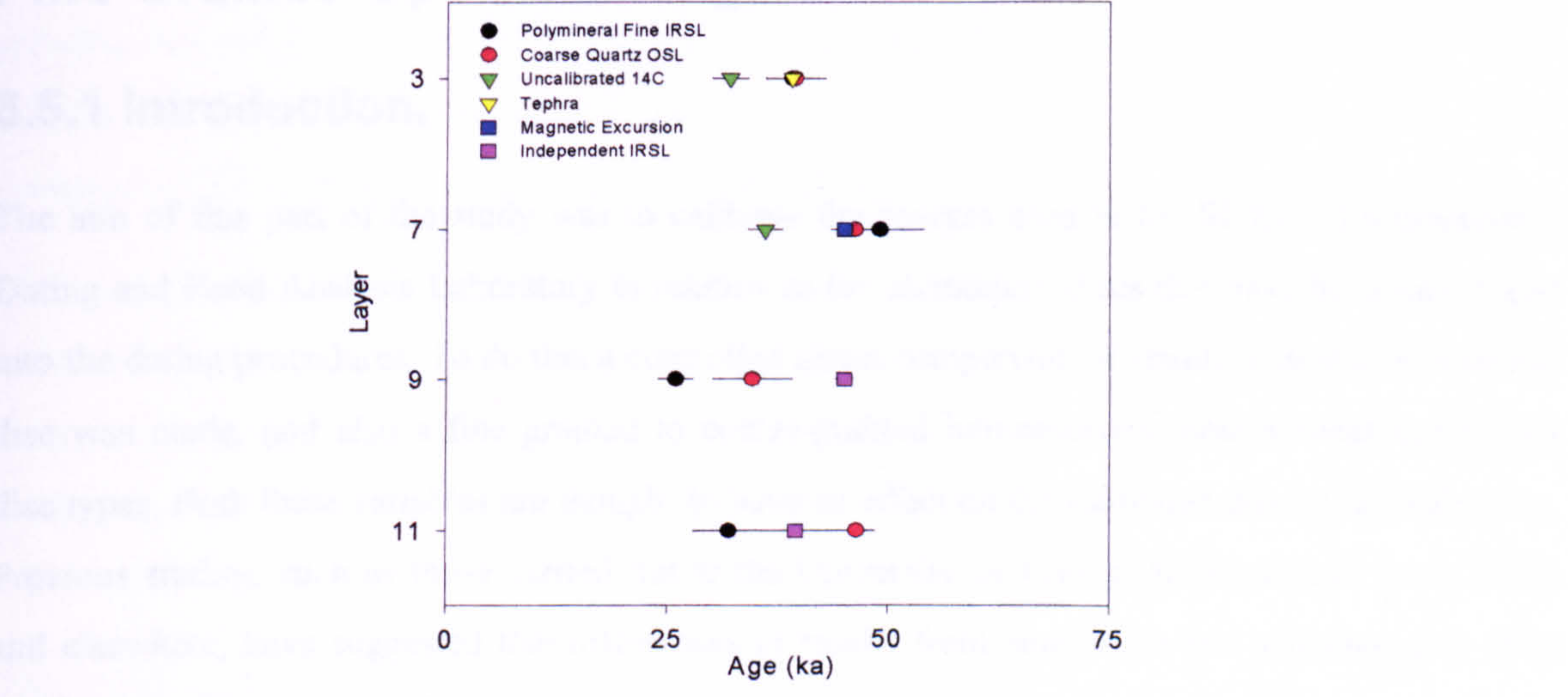


Figure 6.18. Redrawn from Burbidge *et al* (In Prep). Coarse quartz OSL equivalent doses were obtained from 200µm etched quartz grains on steel disks using the SAR (Single Aliquot Regenerative) protocol. Polymineal fine IRSL equivalent doses were obtained from 4-11µm grains on aluminium disks using the MAAD (Multiple Aliquot Additive Dose) protocol. Dose rates for age calculation were estimated using field and high resolution gamma spectrometry, and thick source beta counting. Uncalibrated 14C values are averages for each layer. Tephra age from Pyle *et al.* (2006).

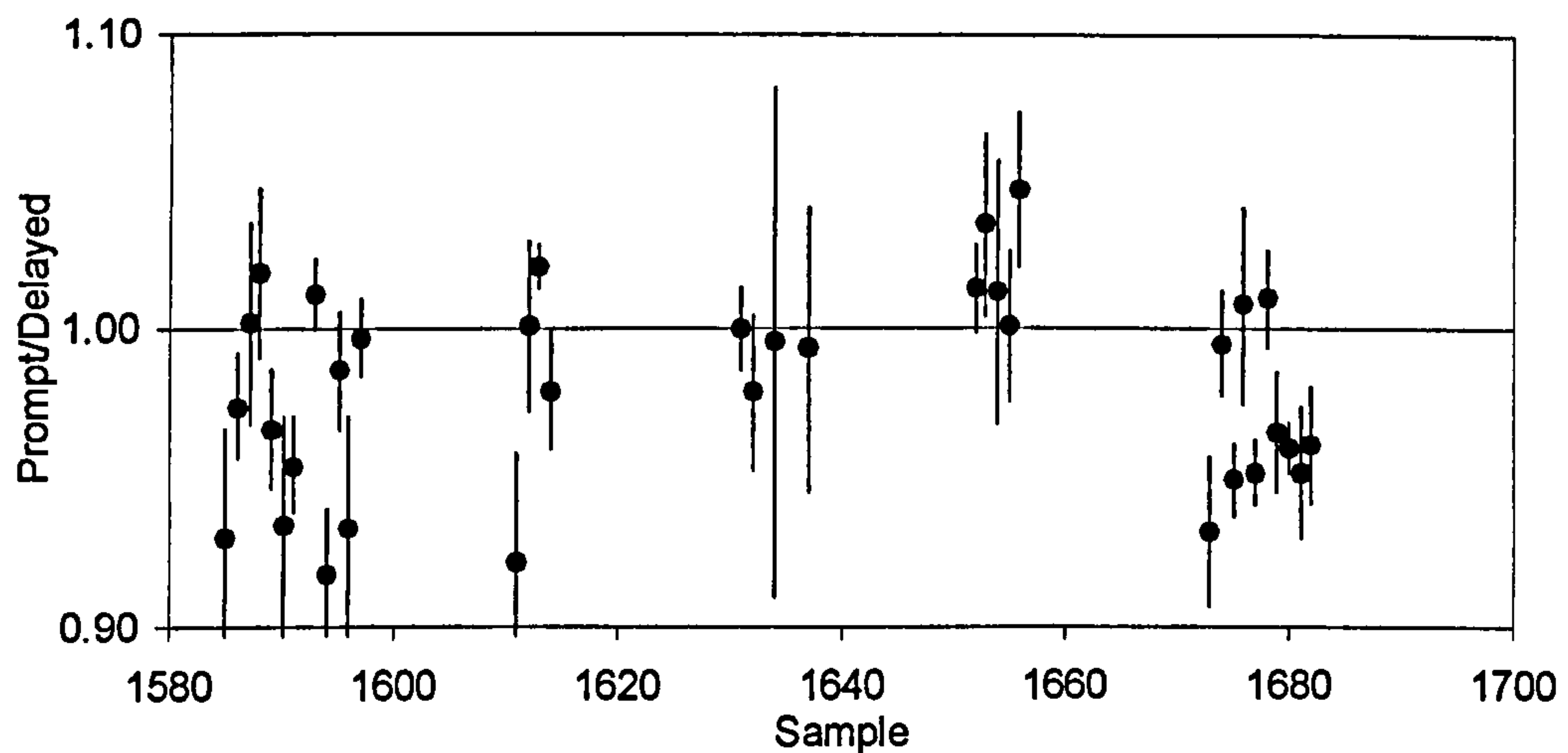


Figure 6.19. Results of fading tests conducted as part of the NERC EFCHED dating study. Redrawn from Burbidge *et al* (In Prep).

6.5 Aluminium (Al) Versus Stainless Steel (SS) Discs in Fine Grained Optical Dating.

6.5.1 Introduction.

The aim of this part of the study was to calibrate the sources used in the SUERC Luminescence Dating and Food Analysis Laboratory in relation to the aluminium discs that have been introduced into the dating procedures. To do this a controlled direct comparison of stainless steel to aluminium disc was made, and also a fine grained to coarse-grained luminescence measurement using both disc types. Both these variables are thought to have an effect on the estimated dose (D_e) evaluation. Previous studies, such as those carried out at the University of Liverpool (Mauz and Lang 2004) and elsewhere, have suggested that differences in results from aluminium and stainless steel discs are reproducible between laboratories.

The figures and differences described by Mauz and Lang (2004) between aluminium and steel discs are consistent with the discrepancies reported elsewhere and will be outlined in Section 6.5.4. A calibration protocol was devised due to the fact that the aluminium discs are twice the thickness of the traditional stainless steel discs and also within the SUERC luminescence laboratories a variety of irradiation sources are used, both beta and gamma, highlighting the need to calibrate the discs to each source because of the different source geometries and dose rates.

6.5.2 Experimental Design.

The calibration medium was a sample of laboratory standard quartz sand (BDA acid washed) obtained from the laboratory suppliers VWR Ltd. The first stage in the process was to anneal the quartz for an hour at 800°C in a furnace to remove the fast component of the luminescence signal. The sand was then processed to obtain the two-size fractions that are used in the dating procedures within SUERC. The quartz sand was given a brief and low intensity grinding using a pestle and mortar before dry sieving the powder through a set of nylon meshes to give a coarse grain fraction (100-200µm) and a fine grain fraction (~ 4-11µm). These fractions were then gamma irradiated at the Beatson Clinic (University of Glasgow). For transportation and irradiation the samples were secured within a light tight black polythene bag after being sealed within two separate plastic Petri dishes. The samples were gamma irradiated side-by-side within a box, thus avoiding backscattering from the floor beneath.

Back at SUERC and under dark light conditions the samples were dispensed onto pre-weighed aluminium and stainless steel discs. This was a simple procedure using the coarse grain fraction, but the fine-grained sample required a little more attention as the initial pre-irradiation rough grinding had produced a very broad grain size distribution. Before the discs could be dispensed the powder was settled through acetone as outlined in Aitken (1985). This procedure left a sample comprising grains in the 3-11µm region that was then dispensed onto the discs (see Section 3.14).

The number of discs dispensed was 24 of each calibration component (i.e. 24 coarse grain stainless steel and aluminium discs, and 24 fine-grained stainless steel and aluminium discs). The number used in the actual experiment was only 20; the 4 additional discs per set were to allow for any scratching or dropping during the weighing procedure but to leave a sufficiently large aliquot for a representative set of results.

The actual sequence used in this calibration method was as follows. As the sample had already received a 10Gy gamma dose the initial step was to preheat each disc at 200°C/10secs (a regime widely used in the quartz dating community). This was then followed by stimulation and recording of the OSL signal with the inbuilt blue LED's in the Risø machine. They were run at 60% power for 100 seconds, with a readout temperature of 125°C. The next stage was to give the discs a lower dose using the Risø's own strontium beta source as a measurement of any sensitivity change that may occur as a result of continuous irradiation and stimulation. This normalisation dose is always significantly less than the dose being measured (1Gy dose in this instance). The pre-heat stage was then repeated and whilst it is usual to use a lower temperature at this point, it was decided to retain the same settings throughout the measurements. For the actual calibration study the discs were then given an equivalent irradiation dose to that of the initial gamma dose (10Gy's).

Repeating the experiment using both the ELSEC beta irradiator and the Risø machine’s beta source enables an estimate of the affect of the backscatter created by the different source geometries on the different disc media, both of which are supposed to have a large influence on the estimated dose (De). The backscatter would be specific to the irradiator used and therefore may be lab specific, thus being one source of disagreement with the universal claim on the figures from Mauz and Lang (2004).

6.5.3 Results.

Results of the study of the variations in source geometry are listed in Table 6.14 below.

Table 6.14 Results of gamma to Risø and ELSEC beta sources. Comparisons utilise coarse and fine grained quartz on aluminium and stainless steel discs.							
Comparison of a 10Gy beta source (ELSEC) recovery and a 10Gy gamma source (Beatson clinic) recovery on the Risø automatic reader.							
Disc and sample medium.	Irradiation source/ Risø	Net Mean	Std Dev	Std Err	Err Mean	Std Dev	Std Err
Coarse grains on stainless steel discs.	ELSEC/ Risø	10.26	0.39	0.12	0.3	0.16	0.05
	GAMMA /Risø	10.61	0.63	0.2	0.31	0.14	0.04
Coarse grains on aluminium discs	ELSEC/ Risø	10.22	0.19	0.06	0.16	0.02	0
	GAMMA /Risø	11.44	0.4	0.13	0.18	0.02	0
Fine grains on stainless steel discs	ELSEC/ Risø	10.47	0.13	0.1	0.15	0.01	0
	GAMMA/ Risø	10.07	0.33	0.1	0.16	0.01	0
Fine grains on aluminium discs	ELSEC/ Risø	10.51	0.24	0.07	0.16	0.01	0
	GAMMA /Risø	11.92	0.23	0.07	0.18	0.01	0
Ratio of 10Gy gamma dose recovery from different disc media using the Risø reader (1.00 being an exact match):							
Gamma source on the Risø reader					Ratio		
Coarse grain Al/SS					1.07843		
Fine grain SS/SS					1.07637		
Fine grain Al/Coarse grain SS					1.12381		
Fine grain SS/Coarse grain SS					1.04407		
Ratio of 10Gy beta dose recovery from different disc media using the Risø reader (1.00 being an exact match):							
ELSEC beta source on the Risø reader					Ratio		
Coarse grain Al/SS					0.99613		
Fine grain SS/Al					1.00466		
Fine grain Al/Coarse grain SS					1.02519		
Fine grain SS/Coarse grain SS					1.02044		

6.5.4 Discussion.

Data in Table 6.14 differ considerably from those of Mauz and Lang (2005), who found an induced dose rate difference of around 16% between disc media and ~11% between grain size (i.e. coarse versus fine). The results from the work presented here have 5% for sample size and 8% on the disc

substrate, well below the other studies. In the interests of calibrating the SUERC laboratory equipment, the ELSEC Automatic irradiator was compared with the Risø beta irradiator producing a difference of 2% due to grain size and 1-2% due to substrate. These differences between laboratory sources are most likely due to source geometry; the ELSEC is further from the sample than the Risø. The ELSEC manual readers are designed so that the source geometry can be set, to an extent, by the user. The height of the source from the sample can be altered by the insertion of one or two sets of rods. The SUERC ELSEC irradiator has one set of custom-made rods in position and the source-to-sample distance is ~15mm.

In light of these initial results a larger number of variables were measured, including the proportion of the disc surface covered by that the sample and the thickness of the discs. The latter is especially important as the new aluminium discs are twice the thickness of the original stainless steel discs. Therefore, results based on varying the substrate, 5% compared to around 12% of other authors, are not only due to the different radiative characteristics of the metal but also the additional 0.5mm in thickness alters the source geometry. Tables 6.15 and 6.16 present the results of this set of calibration experiments.

Table 6.15 The results of doubling the stainless steel discs to remove variations in source geometry due to disc thickness. (CG = coarse grain).

Comparison of 10Gys dose recovery from ELSEC beta source and gamma source by the Risø automatic reader:							
Medium	Irradiation source/ Risø	Mean Net	Std Dev	Std Err	Mean Error	Std Dev	Std err
Coarse grain on Double SS	ELSEC/ Risø	9.92	0.23	0.07	0.22	0.05	0.02
	Gamma/ Risø	9.49	0.33	0.11	0.20	0.04	0.01
Comparison of 10Gys dose recovery from ELSEC beta source and gamma source, by the Risø automatic reader:							
Coarse Grain on Al	ELSEC/ Risø	10.32	0.52	0.16	0.24	0.05	0.02
	Gamma/ Risø	11.30	0.56	0.18	0.26	0.05	0.02
Ratio of 10Gy beta dose recovery from different disc mediums using the Risø reader (1.00 being an exact match):							
ELSEC/Risø				Ratio			
Al/SS				1.04			
SS/Al				0.96			
Ratio of 10Gy gamma dose recovery from different disc mediums using the Risø reader (1.00 being an exact match):							
Gamma/Risø				Ratio			
Al/SS				1.19			
SS/Al				0.84			

Table 6.16 Results of comparing the sample coverage of the two discs.

Comparison of 10Gys dose recovery from ELSEC beta source and gamma source by the Risø automatic reader:							
Medium	Irradiation source/ Risø	Mean Net	Std Dev	Std Err	Mean Err	Std Dev	Std Err
Coarse Grain on Double SS Discs	ELSEC/ Risø	10.33	0.15	0.05	0.07	0.01	0.00
	Gamma/ Risø	9.64	0.20	0.06	0.07	0.01	0.00
Coarse Grain on Single SS Discs	ELSEC/ Risø	10.28	0.12	0.04	0.08	0.01	0.00
	Gamma/ Risø	10.60	0.21	0.04	0.08	0.01	0.00
Coarse Grain on Single Al Discs	ELSEC/ Risø	10.27	0.13	0.04	0.07	0.01	0.00
	Gamma/ Risø	11.44	0.16	0.05	0.08	0.01	0.00
Ratio of 10Gy gamma dose recovery from different disc mediums using the Risø reader (1.00 being an exact match):							
GAMMA/Risø					Ratio		
Al/Double SS					1.19		
Al/Single SS					1.08		
Double SS/Al					0.84		
Single SS/Al					0.93		
Double SS/Single SS					0.91		
Single SS/Double SS					1.10		
Ratio of 10Gy beta dose recovery from different disc mediums using the Risø reader (1.00 being an exact match):							
ELSEC/Risø					Ratio		
Al/Double SS					0.99		
Al/Single SS					1.00		
Double SS/Al					1.01		
Single SS/Al					1.00		
Double SS/Single SS					1.00		
Single SS/Double SS					1.00		

6.5.5 Discussion.

First to be examined is the percentage difference in recoverable doses between the gamma irradiated samples and the same samples re-irradiated using the Risø internal beta source. The coarse grain aluminium to single stainless steel disc comparison gave an 8% difference in dose rate, whereas the double thickness of stainless steel discs that are compared in thickness to the aluminium discs, give a 20% difference in dose rate.

Differences in the proportion of the disc covered by the sample may also affect the recovered dose on the two thicknesses of stainless steel discs. This possibility was considered because Mauz and Lang (2004) were very specific about the disc coverage whereas other authors do not quantify it. In this experiment one set of ten discs was used with the sample in a 4.5-5mm diameter spot in the centre, which is the usual for SUERC samples, and also another set of ten with the sample covering 7-7.5mm diameter, as used by Mauz and Lang (2004). When results from the small centred sample are compared with the double and single discs a 12% difference is found, which is directly related to the 0.5mm difference in source geometry caused by the extra disc. The broader sample coverage

leads to a smaller difference of 9%. Thus the difference in sample dispensing adds a further 3% between discs and this is shown further when the different sample widths on just the single stainless steel discs are compared and the difference is only 2%.

Comparison of the above results with those from a similar experiment using a 10Gy dose delivered by exposure to the ELSEC and irradiation by the Risø reader, there is a stark difference. The slight change in source geometry (i.e. the decrease in sample/source distance of 0.5mm) caused a 12% difference in the Risø/gamma results, but only 2% in the ELSEC/Risø results. Therefore it can be concluded that the dose given by the ELSEC manual irradiator is almost four times less sensitive to changes in source geometry than that of the Risø reader.

6.5.6 Conclusions of this Calibration Investigation.

The second part of this calibration study indicates that when using dose rate comparisons, for either substrates or sample grain size differences, figures obtained in other laboratories on other equipment should be used with care. It has been illustrated above how the newer luminescence equipment, in which the source-to-sample distance has been reduced, is highly sensitive to even the slightest variation in the media used. It is recommended that each laboratory carry out its own calibration, on all the sources and substrates that are routinely used in dose determination exercises.

6.6 Conclusions.

Within this Chapter it has been shown that a working R-TL system has been constructed and measuring high temperature regions of the glow curve is a possibility. Suggestions have been included to increase the sensitivity and decrease the background interference of such measurements using this experimental arrangement.

The results investigating the time dependence of signal loss from feldspars have been presented and suggested future applications of this technique, in conjunction with results from this study, have been outlined.

A cooled red sensitive near-IR PPSL system has been constructed and the further research and development required for completion of the evolution of this system into a routine dating tool has been discussed. Stimulation and detection issues have been discussed and accounted for.

Using the preheating regime applied in the remnant measurements (Chapter 5) a technique for feldspar dating has been put forward and subsequently successfully used to obtain accurate ages for an important international dating study.

7

Discussion.

7.1 Introduction.

This study has investigated past and current explanations for anomalous fading and has tested each model using a geologically well constrained and mineralogically well characterised set of samples. Other explanations of signal loss with storage have been proposed and possible techniques to circumvent the problem of anomalous fading in feldspar luminescence dating have been discussed. Here the study concludes with a critical assessment of fading models and mechanisms of circumvention of the problem by drawing on results obtained.

7.2 The Mechanisms of Anomalous Fading in Alkali Feldspars.

Within the extensive literature on the subject there is little consensus about the factors that control whether a feldspar sample experiences anomalous fading and the magnitude of signal loss with storage. Within this study emphasis has been placed on the geological controls, or those defined by the nature of the sample itself and how they can be used to predict the occurrence of this important process.

7.2.1 Tunnelling Models.

The most widely accepted model to describe non-radiative signal loss is thermally assisted quantum mechanical tunnelling. Tunnelling is one of two competing models that rely on the trap and centre being in close proximity so that the probability of charge tunnelling through the energy barrier is high (Section 2.6.3). However, as discussed in Chapter 2 (Section 2.6.4) neither of these competing processes has been able to account for all the results and variations of anomalous fading that have been reported. There is adequate evidence for both models, yet tunnelling has been widely accepted as the cause of the signal loss. Due to differences in thermal dependence of the two fading mechanisms it is possible that both could act on a single feldspar grain under different circumstances. If this were the case then those feldspars that react well to preheating and produce stable signals as a result (Sanderson 1988), could be prone to signal loss by localised transitions.

Those feldspars that fade significantly after thermal pre-treatment could be more strongly influenced by quantum mechanical tunnelling.

7.2.2 Geological and Mineralogical Controls on Fading Behaviour.

One difficulty with understanding the fading problem has been making the link between the sub atomic scale processes of storage and movement of charge within the crystal lattice and the properties of the highly imperfect and typically polycrystalline feldspar crystals that are used for routine luminescence work. There have been many theories put forward to explain why some feldspars fade and others are stable, or in the case of Huntley and Lamothe (2001), why all feldspars fade but some more than others.

7.2.2.1 Geological Age.

Huntley and Lamothe (2001) have made a link with the geological age of the feldspar and have suggested that older feldspars have relatively highly damaged crystal structures owing to longer durations of exposure to environmental radiation. This conclusion has lead to construction of a map of North America outlining relative stabilities of feldspathic sediments (Fig. 7.1).

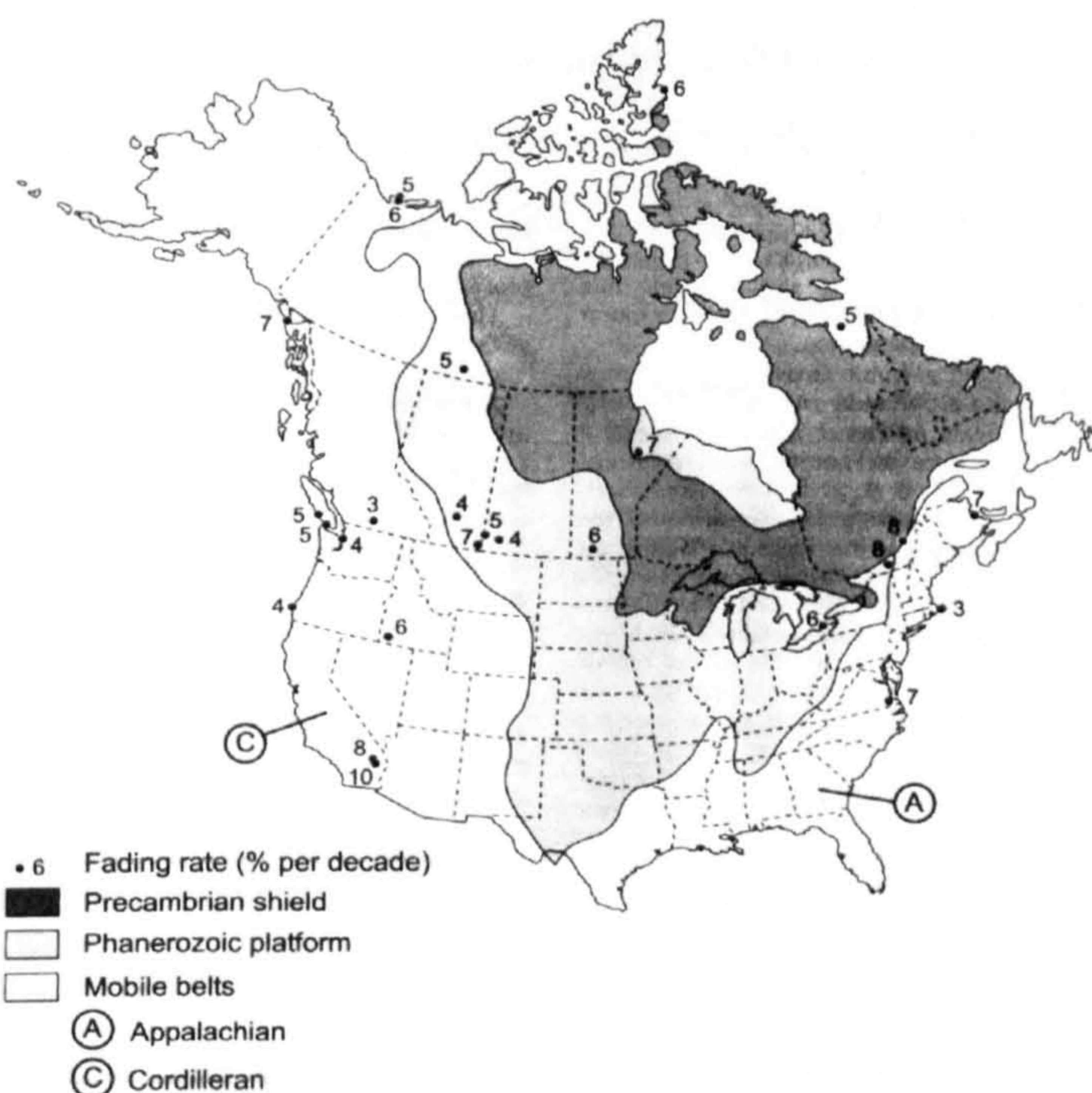


Figure 7.1. Map showing the main geological domains in northern North America, sample provenances and measured rates of anomalous fading. An average value is shown when two or more samples have similar provenances. The broken lines are provincial and state boundaries (reproduced from Huntley and Lamothe 2001)

There has also been a link suggested with the concentration of uranium in the feldspar's source area to explain fading in geologically young feldspars. Thus, this model is not necessarily about geological age but rather the extent of exposure to environmental radiation and this process may be

of more importance to feldspars that are close to their saturation point. The difficulties with Huntley and Lamothe's (2001) model is that the sediments they analysed will contain feldspars from a wide variety of rocks of different geological ages and with contrasting uranium concentrations. A proportion of the sediment grains are also likely to have been eroded and deposited a number of times, each episode of which will have a different impact on stored charge and defects. Results from the present study provided little evidence that geological age is a significant determinant of signal stability. The two oldest alkali feldspars in the group (the Archean gneisses) do fade but so do alkali feldspars from the Tertiary Arran granite and the even younger Patmos sanidine.

The absolute age of a feldspar sample is inferred to be possibly less important to luminescence properties than what has happened to the mineral during this time. If this age control is a function on the amount of exposure to environmental radiation then it may be better to focus on that control to describe differences in fading rates between these minerals. With a possible model that samples taken from a region with a high environmental dose rate may be more prone to fading.

7.2.2.2 Si,Al Order-Disorder.

Ordering of Al and Si in K-feldspar has gained acceptance within the luminescence community as being a major factor in fading, and this idea has been championed by the Paris group. It has been one of the few general consensuses since the work of Wintle (1973) thrust the subject of anomalous fading into the spotlight. Visocekas *et al* (1998) suggest that differences in the magnitude of fading between feldspars relates to the conditions under which they crystallise and they focus on cooling rate and its relationship to lattice disorder. Like Huntley and Lian (2006), Visocekas *et al* (1998) use the structural differences between high sanidine and low microcline to explain the relative amounts of fading from each, with the differences between the radiative energy storage and the decay processes being explained solely by the crystal structure. The disorder of sanidine is claimed to cause a clustering of defects and so increases the probability of the charge tunnelling to a nearby centre. However there is a counter claim that the ordered feldspars have clustered defects as the regular repetition of the tetrahedra brings defects that sit at its edges into close proximity. Therefore if crystal structure is indeed the main control on fading then it is still unresolved as to which feldspar structure, ordered or disordered, promotes signal loss. It could simply be the case that they both do in some way. In order to examine these possibilities further data from two previous fading studies have been re-examined.

Table 7.1. Comparison of the results gained by measuring fading rates of alkali feldspars of Spooner (1994) and Huntley and Lian (2006)						
Spooner (1994)			Huntley and Lian (2006)			
K-feldspar polymorph (sample identifier)	% remnant signal after 2 months dark storage at 10°C		K-feldspar polymorph (sample identifier)	K/Na	% Fe	^g (%/decade) IRSL
	IRSL	OSL				
Sanidine (Patmos)	51	40	Sanidine (?) (PLTF)	1.2	0.59	34.5 ± 4.2
			Sanidine (BRS)	6.5	0.29	16.7 ± 0.6
			Sanidine (WCRS)	4.1	0.37	10.1 ± 0.6
Orthoclase (Z6)	90	102	Orthoclase (K3)	3.1	0.08	8.2
			Orthoclase (K11)	3.3	0.77	23.4 ± 0.9
			Orthoclase (K12)	---	---	10.0 ± 1.2
Microcline (3062)	105	99	Microcline (K7)	1.4	0.24	12.2 ± 0.6
Microcline (Z5)	47	43	Microcline (K13)	5.8	0.07	5.0 ± 0.3
Microcline (Dup(C))	90	95	Microcline (K10)	3.4	0.04	4.4 ± 0.2
			Microcline (K9)	3.3	0.06	3.9 ± 0.3
			Microcline perthite (K8)	3.2	0.19	2.8 ± 0.2
			Microcline (K6)	2.9	0.10	0.9 ± 0.3

Data in Spooner (1994) show that sanidine does fade significantly, although the proportion of remnant signal remaining after two months (40% and 51%) is less than one of the three microcline samples Z5, (47% and 43%). The orthoclase, which is partially ordered, is relatively stable after three months of storage. Unfortunately, information on the mineralogy and chemical composition of the feldspars was not supplied by Spooner (1994) and so the degree to which these data can be used to extend results from the present study is limited. Alkali feldspar fading data from Huntley and Lian (2006) are also mixed (Table 7.1). There is some evidence for the partially ordered orthoclase fading at a rate intermediate between that of disordered sanidine and ordered microcline, but the fading rate of one sanidine is less than a number of orthoclase and microcline samples. Huntley and Lian (2006) state that: “..sanidines generally have higher fading rates than orthoclases and microclines. These feldspars only differ in the arrangement of the Al and Si atoms” and so link ordering directly with the propensity to fade. However, the statement made by Huntley and Lian is entirely incorrect. If it is homogeneous, sanidine will contain K, Na and Ca in solid solution, which will influence significantly the crystal structure parameters, whereas in orthoclase and microcline almost all of the Na and Ca will have exsolved to form lamellae of plagioclase. The boundaries of these microtextures contain a wealth of defects such as dislocations (Lee *et al.*, 1995). In addition, orthoclase has a very fine-scale ‘tweed’ microtexture formed during ordering and microcline is pervasively twinned, typically on a variety of spatial scales. Lastly, most of the sanidines used in luminescence studies are likely to come from geologically young rocks (e.g. the 6-4Ma Patmos sanidine), whereas the orthoclase and microcline are more likely to be from older rocks that have undergone a variety of geological processes (e.g. hydrothermal alteration and tectonic

deformation). Any or all of these microtextures and microstructures may influence luminescence properties.

It is also very important to note that most if not all of the “orthoclase” and “microcline” samples used by Huntley and Lian (2006) will have been perthitic, although insufficient imaging or compositional data were provided for the microtexture of any of the samples to be determined. The K/Na values for these samples were however listed and most are low, consistent with considerable volumes of albite intergrown with the K-feldspar (assuming that the compositions in Huntley and Lian (2006) are from bulk chemical analyses, but none of the analytical procedures have been described). One interesting correlation from these data is the relationship between % Fe and fading rate (g). These data were not discussed together by Huntley and Lian (2006), but Table 7.1 reveals a positive correlation between % Fe and g for orthoclase and microcline. The majority of the Fe will be present as inclusions, predominantly Fe-oxides, which form during deuteritic/hydrothermal alteration of the feldspar whilst still within its parent rock (Worden *et al.*, 1990). Thus, Fe will not play a direct role in the luminescence phenomenon, but may be an indicator of the extent of deuteritic/hydrothermal alteration that the feldspar has experienced (sanidine is not included in this discussion as it is very unlikely to have undergone deuteritic or hydrothermal alteration). The correlations discussed above may support tentative conclusions from the present study that the extent of deuteritic/hydrothermal alteration is an important factor in determining the propensity of alkali feldspar to fade by influencing the nature and abundance of defects within the crystal. Sanidine does not fit with this model, but owing to its very significant difference in crystal structure and geological history such a mismatch is unsurprising. In addition, even though sanidines fade it is very unlikely that it will be a large contributor to the luminescence emission used to generate De’s for a dating study.

Taking into account the above caveats regarding sample microtextures the ability to test the influence of ordering solely on fading is difficult. There are simply too many variables that could affect any comparisons that could be made. One possible way forward is to use laboratory techniques where the level of lattice ordering of a single feldspar grain can be manipulated, so replicating the transition between K-feldspar polymorphs. It is easy by these procedures to gradually anneal away perthite microtextures and so gradually destroy defect populations (Fitz Gerald *et al.*, 2006). Such techniques involve heating the crystal and then quenching it at different speeds and at different rates.

7.2.2.3 Lattice substitutions

Lattice substitutions have also been reported as a possible cause of non-radiative signal loss. Huntley and Lian (2006) have demonstrated that there is a link between increased Fe and Ca

content in plagioclase feldspars and the amount of fading observed. However, even within this very paper they conclude that the difference in fading rates may not actually be due to the presence of these atoms themselves but rather the substitution process. They use the argument that the centres to which electrons tunnel are not impurities but structural defects and the centres are themselves the result of the replacement of Na with Ca, or Al with Si. So it must be concluded that it is simply not possible to make a sweeping generalisation about certain impurities and their control on the amount of fading observed. Again Huntley *et al* (2007) state that Ca-poor plagioclase (albite) does not fade measurably and so may be used for optical dating of up to 1 million years. However, most of the samples they used were pegmatites and so atypical of feldspars in sediments; end-member albite is rare and most plagioclase in acidic igneous rocks is oligoclase. However, this study does highlight the importance of exsolution microtextures in promoting fading, so making a link with structure.

7.2.2.4 Weathering.

Spooner (1994) commented on the differences in the fading rates observed in studies comparing single feldspar crystals with feldspars separated from sediments and this was also discussed by Huntley and Lian (2006). The findings of the present study are that natural weathering preferentially removes thermally unstable traps and defects as they form areas of high energy where they intersect the grain surface. Therefore the question must be asked, if weathering removes fading and sediments are being dated successfully why are feldspar luminescence processes being treated with such suspicion and scepticism?

Investigating just how stabilising a process weathering is on feldspar luminescence emission should be investigated further and the discussion of the weathering results in Chapter 5 have touched on some possibilities already. A study to determine whether luminescence emissions of the Ross of Mull syenite could be stabilised in common with their parent granite is one such suggestion. On a larger scale it would be helpful to take feldspars that are known to fade significantly such as the Patmos sanidine, which is a convenient example, and expose it to various durations of HF acid etching to recreate natural weathering even if acid etching has no impact, that would provide important information on the nature of the unstable traps.

The results of this study suggest that fading is actually controlled by a host of different factors and that the models that have been put forward in the literature to account for the phenomenon may all have an impact on the observed rate of signal loss. The variations in the rate of such losses reported in previous studies may be the result of a multifaceted model. If lattice strain and its control on defect structuring is the key then within one sample there may a number of these models working at the same time. As a result the ability to predict a sample's propensity to fade is not likely.

7.3 Solutions to Anomalous Fading in Feldspars.

7.3.1 Using Conventional Measurement Systems.

The results obtained from the conventional measurement systems within this study have showed very good levels of signal stability. The Risø data are especially encouraging for the future use of feldspars as accurate dosimeters. No stimulation source was better than another in yielding a stable signal, although given the advantages of IRSL in isolating the feldspar emission from a polymineral sediment, this may be the preferred stimulation source for feldspar luminescence dating in the future.

The ability of the long duration low temperature preheating of the samples to remove unstable signal, both thermal and anomalous, has been clearly demonstrated within this study and it has been subsequently used with a high level of success within the EFCHED project discussed in Chapter 6. However, problems remain with signal increase following storage, which is a possible result of the timing of the preheating process, and this requires further study and clarification. Such an investigation should focus on comparing the results of a preheat before storage with one afterwards (as in this study). If the enhanced signal is the result of charge migration during storage then feldspar dating may continue to be problematic as such movement of charge can cause inaccurate De's to be calculated.

7.3.2 Further Development of Experimental Measurement Techniques.

There are many directions in which this work may be taken, both in the development of more pertinent and informative techniques for the study of the processes behind feldspar luminescence, and the further investigation of the geological influences on fading in feldspars. A technique not addressed in this study but that warrants a mention as a tool in measuring or circumventing fading is the scanning laser systems that are currently within the research and development stage in the SUERC dating laboratories. Such systems create a detailed image of the luminescence emission from either a thin section of rock or a disc of powder. The system treats the sample area as a grid and each 'square' is stimulated in turn, therefore producing a map of variation in luminescence emission between areas of the sample. If such a system could be adapted to measure the fading rates of individual grains, then the technique has potential as a screening process of fading grains within a sample, with the possibility of calculating De values from populations of non-fading grains.

Many other possibilities have been suggested in the previous Chapters and two, the red system and mineralogical classification, will be discussed in greater detail here including their advantages and disadvantages for moving the research field forward and its future application.

7.3.2.1 Development of the Far Red Feldspar Emission and Related Techniques.

Without a doubt the work already carried out on the red to far-red part of the feldspar emission spectrum is immensely important to the field of luminescence dating. Fattahi and Stokes (2000; 2003a; 2003b) have shown that TL dating volcanically derived feldspars is possible with this emission. They have also shown preliminary successes in OSL techniques using IR as both the stimulation and detection wavelengths. Tsukamoto *et al* (2006) have had similar success in the same wavelength range but using pulsed stimulation.

The red techniques have not become widely accepted within the luminescence community and this is partly due to the significant difficulties in isolating this band using 'conventional' luminescence readers. Within the present study two red systems were tested and the ease with which they could be implemented was evaluated. The success of both was somewhat inconsistent. The RTL system was successful, albeit on the rise part of the glow peak, but thermal incandescence both from the sample chamber and its heating system was a significant problem. The limitations on these measurements were consistent with the original work by Visocekas and Zink (1999), who were unable to acquire TL data at temperatures of more than 300°C. Fattahi and Stokes have described results from the high temperatures, albeit using a slightly shorter wavelength emission range (Fattahi and Stokes, 2003b).

Given that the RTL system briefly investigated within the present study was quite basic in its construction and the only 'specialist' equipment utilised was the electron tubes p25232-05 PMT, the limited level of detection obtained was unsurprising. There are a number of different avenues that could be further investigated with this system, some already used by others. In the present study the same heating regime as the 'every day' TL runs (5°C/sec) was implemented but reducing the speed of the temperature ramping will move the TL glow peaks to lower temperatures. This would allow a stable dating signal to be obtained therefore avoiding some of the interference from the high thermal background. Such a technique was used by Visocekas and Zink (1999) and is relatively easily achievable with the system used here. Fattahi and Stokes (2003b) took a different track to deal with black body radiation. They shifted the detection window away from the 700-720nm Fe³⁺ peak to a ~600nm window. The rationale behind this is that black body radiation is at its strongest in the region of the Fe³⁺ peak. By shifting the detection window away from this region the cross-talk is reduced and the detectable signal is greater. However, neither of these approaches will bring us closer to the goal of detecting high temperature TL from the ~710nm emission. Given the

fact that the Paris group have failed to get close to measuring this despite their highly specialised and purpose built instrumentation, is it better to follow the path of the Oxford group and move towards an emission range that is easier to detect with more commonplace equipment, as long as it can be comprehensively shown to measure stable luminescence signals.

It must be pointed out that recent work (Huntley *et al.*, 2007) has importantly suggested that this promising red signal is highly prone to thermal quenching and the red tunnelling signal that has been touted as being diagnostic of fading may in fact be the t^{-1} phosphorescence remaining due to the lack of preheating. If this is the case then it may very well be prudent to concentrate the focus of the future work on far red PSL techniques. Such an approach was investigated in the present study and the preliminary results have been presented and discussed in Chapter 6. The cooled red PSL system was constructed as a direct attempt to counter problems with thermal background. This was a much more complex system and was well outside the realm of 'conventional' techniques. The use of the cooled housing around the PMT was similar to that used by the Paris and Oxford groups and pulsing of the stimulation source was devised by Clark and Sanderson (Clark, 1992; Clark *et al.*, 1997; Sanderson and Clark, 1994) and tied in with the recent work of Tsukamoto *et al* (2006) at Risø, where pulsing generated stable long lifetime signals from both alkali and plagioclase feldspars.

To get to the same level of signal detection as was reported by these previous workers both the filtration and stimulation problems encountered with the IR-PPSL system in the present study (Chapter 6) will have to be solved. An important question that should be raised once these issues have been overcome is what is the practical application of such a system in both research terms and in the commercial application of the technique? Pulsed time-domain analysis has the potential to be highly informative about the processes behind the production of luminescence signals from minerals (Clark, 1992; Clark *et al.*, 1997; Sanderson and Clark, 1994) and as shown by Tsukamoto *et al* (2006), allows for detection of a stable signal that has been used for dating. The ability to study the luminescence processes of a variety of fading and non-fading (or relatively stable) feldspars could provide an insight into the variations that promote such signal instabilities. Pulsing in this way could also be a hugely important diagnostic tool for the further work on post-formational alteration and its impact on both removing and inducing anomalous fading suggested by the present study. Pulsing would give an insight into changes in the movement of trapped charge caused by both weathering and metamorphism. An emission spectrometer could be attached to the IR-PPSL system and the recommissioning of SUERC stimulation spectrometer could add a further dimension to understanding the processes behind variations in stability across both detection and emission systems reported in the literature. The IR-PPSL system in its current form also has the

ability to carry out TL measurements and also to cool the sample below room temperature adding to the diagnostic capabilities of this promising system.

Technological advantages have been one of the keys to the success of luminescence dating. The IR-PPSL system described in Chapter 6 and its possible future applications provide a useful diagnostic tool but as is ever common in work on anomalous fading such developments have little cross-laboratory application. Given the specialised nature of not only the instrumentation but also the measurements made such work would have value to the luminescence community from an academic standpoint but may have little relevance to commercial dating projects. Expensive equipment and time consuming measurements of a mineral with the luminescent reputation of feldspars would be a hard sell given the popularity of quartz at present, especially as the risk of having very sample specific results is as ever a potential problem.

7.3.2.2 Understanding the Mineralogical Controls and Atomic-scale Processes Underlying Anomalous Fading.

In the context of the original aims of the present project, another emphasis of future work should be to investigate further the broad geological influences on the propensity of a feldspar to fade, whether this be the formational environment and its influence on crystal lattice disorder, or post-formational alteration through weathering, lithification of sediments, metamorphism and hydrothermal alteration. However, one of the most interesting, and maybe pertinent theories in the recent literature (Huntley *et al* 2007), which was also hinted at in the results within Chapter 5, is the influence on fading of lattice disruption, in particular at the phase boundaries that are ubiquitous in the majority of feldspar minerals.

The influence of crystal structure on fading is a topic that requires significant further work within the luminescence community if the processes behind anomalous fading are to be completely understood. It has been suggested that substitution of certain impurity elements and the associated lattice strain has an influence on a feldspar's propensity to fade (Huntley *et al.*, 2007; Huntley and Lian, 2006). When these theories are coupled with the weathering results in this study strain at feldspar phase boundaries becomes potentially even more important. It has been shown that both weathering and acid etching attack points of high strain energy within the lattice and preferentially removes them, which in turn has an effect luminescence stabilities, the true extent of which is yet to be understood. Above, further work on studying the effects of changing the nature of perthite micro textures, both experimentally and naturally, has been suggested but it is also highly pertinent to investigate further the phase boundaries themselves. If these regions of high energy are important to fading then in depth knowledge of the chemistry and crystal structure of these boundaries is essential. Investigating these regions on an atomic level requires high-resolution and high sensitivity techniques such as TEM and Electron Spin Resonance (ESR). XRD was used in

the present study to characterise sub-samples of the complete sample set, but the results were so complex as to be uninformative. This was due to the high level of heterogeneity within the individual powdered samples, even when broken down into SPT fractions. However to do in depth TEM or ESR analysis would require a reduction in the number of samples and movement towards analysis of a small number, or even a single number of grains, and such results may be unrepresentative. The further work on instrument development and mineralogy outlined above both require a narrowing of the focus of the investigation. One of the main initial aims of the present project was to determine whether a broad geological control on fading could be identified using the models that have been presented in the literature. Such a direction was taken because previous work has focused on one type of feldspar, or samples from a single geographical region, so that the results, and sometimes correction techniques, are potentially inapplicable elsewhere. This was particularly true of the extensive work on fading in sanidine (Visocekas *et al.*, 1994) which has been described by Parsons and Lee (2005) as a rare feldspar with unusual physical properties. However, the lack of any significant variation in the degree of fading found within the sample set used for the present study may indicate that finding a link between broad geological history and signal instability is too optimistic for anomalous fading and research must concentrate on the atomic structure, micro-textures and chemistry of individual fading and non-fading grains. It may be that to understand the bigger picture the fine details need to be investigated and understood first. From the model suggested from the manual TL work in this study it cannot be disputed that only an understanding of the atomic scale features of the regions of lattice high energies will move us closer to answering the questions raised. Table 7.2 lists these future avenues and discusses their future potential in the field of feldspar luminescence dating.

Table 7.2 A brief outline of the potential of each technique/approach in future work on overcoming the fading problem.

Technique/Approach	Potential to understand and overcome anomalous fading?
Geological context of feldspars	Good. There is much to suggest that the geological context of a feldspar mineral at both a macro- and micro-scale influences the minerals propensity to fade. Further work on the atomic level of specifically chosen samples needs to be carried out.
PPSL	Potentially Excellent. Work by previous authors outlined in this thesis have shown

that pulsed luminescence does not only provide valuable information on the movement of trapped charge during the luminescence process but has also been used to produce a stable dating signal. To further enhance the potential of this technique the pulsed laser system needs to be recommissioned to overcome stimulation problems.

TL

Good. This study has shown that it may have the ability to be more accurate in diagnosing variations in fading rates than PSL stimulation techniques. This needs to be further tested using a specifically chosen sample set.

RTL

Potentially high. Issues with thermal background needs to be overcome so increasing the ability to detect the high temperature end of the glow curve.

IR-PSL

Potentially good. Has been shown by Fattahi and Stokes (2003a) to produce accurate dates for volcanically derived samples, although the specialised nature of the equipment needed poses a hurdle for its universal acceptance.

IR-PPSL

Potentially high. This technique combines the success of the PPSL work and the IR work. It also allows the issue of interference from the stimulation source to be controlled. The system constructed within this study requires further work on filter combination and a stronger

simulation source. Again may be limited by the specialist equipment that is required.

Emission and Stimulation Spectrometry

Potentially high. Such a technique would be valuable for investigating further the link between stimulation and detection wavelengths that has been suggested by workers in both the Oxford and the Paris groups. This system can also heat and cool the sample, and enables quick and simple changing of PMT. This allows for integration with the cooled red system described in Chapter 6.

Scanning Laser system.

Potentially good. Has the potential to separate a signal from a population of non-fading grains out of a powder prepared for dating. This system requires more research and development of the laser stimulation source and detection system. (Such work is currently ongoing at the SUERC dating laboratory.)

7.4 The Future of Feldspar Luminescence Dating.

It is possible that anomalous fading may never be truly understood or conquered but recent advances in the techniques and equipment that has made measuring stable feldspar emissions possible the future role of the mineral in luminescence dating is becoming ever more assured. Given the problems that exist within quartz techniques and the desirable luminescence characteristics of feldspar, resolving the issue of anomalous fading (if only to the extent where it can be systematically circumvented) is not only important for the future role of feldspars within luminescence dating but also to the field as a whole.

The conclusions from this study are promising because fading within the sample set used is not ubiquitous nor is it the domain of feldspars from rapidly cooled rock types. Fading is present but within a small subset. Whilst the goals of finding a universal model describing the process and a

technique that circumvents it have not been truly attained it has been demonstrated that dating of samples that contain feldspar emission is possible using conventional luminescence techniques. The investigation of the red emissions and the pulsed work is currently filling an important role in diagnosing fading processes but such techniques are not currently within the scope of most luminescence dating laboratories.

References.

- Aitken, M.J., 1985, Thermoluminescence Dating., Academic Press, 359 p.
- Aitken, M.J., 1992, Optical Dating: Quaternary Science Reviews, v. 11, p. 127-131.
- Aitken, M.J., 1994, Optical Dating - a Nonspecialist Review: Quaternary Science Reviews, v. 13, p. 503-508.
- Aitken, M.J., 1998, An Introduction to Optical Dating: The Dating of Quaternary Sediments by the Use of Photo-stimulated Luminescence., Oxford University Press, 267 p.
- Anthony, I.M.C., 2003, Luminescence Dating of Scottish Burnt Mounds: New Investigations in Orkney and Shetland Glasgow, University of Glasgow.
- Ashworth, J.R., and Tyler, I.M., 1983, The distribution of metamorphic temperatures around the Strontian Granodiorite: Geological Magazine, v. 120, p. 281-290.
- Auclair, M., *et al.*, 2003, Measurement of anomalous fading for feldspar IRSL using SAR: Radiation Measurements, v. 37, p. 487-492.
- Bailiff, I.K., and Mikhailik, V.B., 2003, Spatially-resolved measurement of optically stimulated luminescence and time-resolved luminescence: Radiation Measurements, v. 37, p. 151-159.
- Balescu, S., *et al.*, 2003, Luminescence chronology of Pleistocene loess deposits from Romania: testing methods of age correction for anomalous feldpars: Quaternary Science Reviews, v. 22, p. 967-973.
- Becker, K., 1974, On the Discovery of TL.: Health Physics, v. 27, p. 321-322.
- Bedard, J.H., *et al.*, 1988, Peridotite sills and metasomatic gabbros in the Eastern Layered Series of the Rhum Complex: Journal of the Geological Society, London, v. 145, p. 207-224.
- Behncke, B., *et al.*, 2006, The exceptional activity and growth of the Southeast Crater, Mount Etna (Italy), between 1996 and 2001: Bulletin of Volcanology, v. 69, p. 149-173.
- Bishop, P., *et al.*, 2005, Age-dating of tsunami deposits: Lessons from the December 26 2004 tsunami in Thailand. : Geographical Journal, v. 171 p. 374-378.
- Bos, A.J.J., *et al.*, 1994, Thermoluminescence Emission Spectra and Optical Bleaching of Oligoclase.: Radiation Measurements, v. 23, p. 349-353.
- Botter-Jensen, L., *et al.*, 2003, Developments in radiation, stimulation and observation facilities in luminescence measurements: Radiation Measurements, v. 37, p. 535-541.
- Boyle, R., 1664, Experiments and considerations upon colours with observations on a diamond that shines in the dark: London, Henry Harrington.
- Burbidge, C.I., *et al.*, In press, Survey of Palaeolithic sites by luminescence profiling, a case study from Eastern Europe: Quaternary Geochronology.

- Chen, R., and HagYahya, A., 1997, A new possible interpretation of the anomalous fading in thermoluminescent materials as normal fading in disguise: *Radiation Measurements*, v. 27, p. 205-210.
- Chen, R., *et al.*, 2000, Apparent anomalous fading of thermoluminescence associated with competition with radiationless transitions: *Radiation Measurements*, v. 32, p. 505-511.
- Chithambo, M.L., and Galloway, R.B., 2000, A Pulsed Light-Emitted-Diode System for Stimulation of Luminescence: *Meas. Sci. Technol.*, v. 11, p. 418-424.
- Clark, R.J., 1992, Photostimulated Luminescence as an Archaeological Dating Tool: Glasgow, University of Glasgow.
- Clark, R.J., *et al.*, 1997, A Preliminary Study of Time-Resolved Luminescence in Some Feldspars: *Radiation Measurements*, v. 27, p. 211-220.
- Clarke, M.L., and Rendell, H.M., 1997, Infra-red stimulated luminescence spectra of alkali feldspars: *Radiation Measurements*, v. 27, p. 221-236.
- Daniels, F., *et al.*, 1953, *Science*, v. 117, p. 343.
- Deer, W.A., *et al.*, 1996, *An Introduction to the Rock-Forming Minerals* Prentice Hall, 712 p.
- Deer, W.A., Howie, R.A, & Zussman, J., 1996, *An Introduction to the Rock-Forming Minerals* Prentice Hall, 712 p.
- Ditlefsen, C., 1992, Bleaching of K-Feldspars in Turbid Water Suspensions - a Comparison of Photoluminescence and Thermoluminescence Signals: *Quaternary Science Reviews*, v. 11, p. 33-38.
- Duff, P.M.D., and Smith, A.J., 1992, *Geology of England and Wales*, The Geological Society, p. 651.
- Duller, G.A.T., 1992, Comparison of Equivalent Doses Determined by Thermoluminescence and Infrared Stimulated Luminescence for Dune Sands in New- Zealand: *Quaternary Science Reviews*, v. 11, p. 39-43.
- Duller, G.A.T., 1994a, Luminescence Dating of Sediments Using Single Aliquots - New Procedures: *Quaternary Science Reviews*, v. 13, p. 149-156.
- Duller, G.A.T., 1994b, Luminescence Dating Using Feldspars - a Test-Case from Southern North-Island, New-Zealand: *Quaternary Science Reviews*, v. 13, p. 423-427.
- Duller, G.A.T., 1997, Behavioural studies of stimulated luminescence from feldspars: *Radiation Measurements*, v. 27, p. 663-694.
- Duller, G.A.T., 2003, Distinguishing quartz and feldspar in single grain luminescence measurements: *Radiation Measurements*, v. 37, p. 161-165.
- Fattahi, M., and Stokes, S., 2000, Extending the Time Range of Luminescence Dating Using Red TL (RTL) from Volcanic Quartz: *Radiation Measurements*, v. 32, p. 479-485.

- Fattahi, M., and Stokes, S., 2003a, Dating volcanic and related sediments by luminescence methods: a review: *Earth-Science Reviews*, v. 62, p. 229-264.
- Fattahi, M., and Stokes, S., 2003b, Red luminescence from potassium feldspar for dating applications: a study of some properties relevant for dating: *Radiation Measurements*, v. 37, p. 647-660.
- Fattahi, M., and Stokes, S., 2003a, Photomultiplier and Filter Combinations for the Detection of Relatively Long Wavelength (>600nm) Luminescence Emissions from Feldspar.: *Ancient TL*, v. 21, p. 25-34.
- Fattahi, M., and Stokes, S., 2003b, Dating volcanic and related sediments by luminescence methods: a review: *Earth-Science Reviews*, v. 62, p. 229-264.
- Fattahi, M., and Stokes, S., 2003c, Red luminescence from potassium feldspar for dating applications: a study of some properties relevant for dating: *Radiation Measurements*, v. 37, p. 647-660.
- Fattahi, M., and Stokes, S., 2004b, Absorbed dose evaluation in feldspar using a single-aliquot regenerative-dose (SAR) infrared-stimulated red luminescence protocol: *Radiation Measurements*, v. 38, p. 127-134.
- Fattahi, M., *et al.*, 2004, Red Luminescence Emission from Potassium Feldspars Stimulated by Infrared: *Ancient TL*, v. 22, p. 35-44.
- Fattahi, M., *et al.*, 2004a, Red Luminescence Emission from Potassium Feldspars Stimulated by Infrared: *Ancient TL*, v. 22, p. 35-44.
- Fisk, S., and Sanderson, D.C.W., 1999, Chernobyl-derived radiocesium in heather honey and its dependence on deposition patterns.: *Health Physics*, v. 77, p. 431-435.
- Fitz Gerald, J.D., *et al.*, 2006, Nanotunnels and pull-aparts: defects of exsolution lamellae in alkali feldspars. : *American Mineralogist*, v. 91, p. 772-783.
- Flowerdew, M.J., *et al.*, 2000, Isotopic dating of overthrusting, collapse and related granitoid intrusion in the Grampian orogenic belt, northwestern Ireland: *Geological Magazine*, v. 137, p. 419-435.
- Friend, C.R.L., and Kinny, P.D., 2001, A reappraisal of the Lewisian Gneiss Complex: geochronological evidence for its tectonic assembly from disparate terranes in the Proterozoic: *Contributions to Mineralogy and Petrology*, v. 142, p. 198-218.
- Garlick, G.F.J., and Gibson, A.F., 1948, The electron trap mechanism of luminescence in sulphides and silicate phosphors: *Proc. Phys. Soc.*, v. 60, p. 574-590.
- Garlick, G.F.J., and Robinson, I., 1972, The thermoluminescence of lunar samples: Dordrecht, International Astronomers Union.
- Godfrey-Smith, D.J., and Cada, M., 1996, IR Stimulation Spectroscopy of Plagioclase and Potassium Feldspars, and Quartz: *Radiation Protection Dosimetry*, v. 66, p. 379-385.
- Goodenough, K.M., *et al.*, 2006, Constraining the maximum age of movements in the Moine Thrust Belt: dating the Canisp Porphyry.: *Scottish Journal of Geology*, v. 42, p. 77-81.

- Guibert, P., *et al.*, 2001, Luminescence dating of burnt materials: effects of preheat treatment on OSL and consequences for dating procedures: *Radiation Measurements*, v. 33, p. 439-444.
- Hong, D., *et al.*, 2003, Determination of Sedimentation Rate of a Recently Deposited Tidal Flat, Western Coast of Korea, Using IRSL Dating.: *Quaternary Science Reviews*, v. 22, p. 1185-1189.
- Hoogenstraten, W., 1958, Electron Traps in Zinc-Sulphide Phosphors: *Philips Res. Rep.*, v. 13, p. 515-518.
- Huntley, D.J., 1985a, On the zeroing of thermo-luminescence of Sediments: *Physics and Chemistry of Minerals*, v. 12, p. 122-127.
- Huntley, D.J., 1997, A proposal for dealing with anomalous fading: *Ancient TL*, v. 15, p. 28-29.
- Huntley, D.J., *et al.*, 2007, Tunnelling in Plagioclase Feldspars: *Journal of Physics D-Applied Physics*, v. In press.
- Huntley, D.J., *et al.*, 1985b, Optical Dating of Sediments: *Nature*, p. 105-107.
- Huntley, D.J., and Lamothe, M., 2001, Ubiquity of anomalous fading in K-feldspars and the measurement and correction for it in optical dating: *Canadian Journal of Earth Sciences*, v. 38, p. 1093-1106.
- Huntley, D.J., and Lian, O.B., 2006, Some Observations on Tunnelling of Trapped Electrons in Feldspars and their Implications for Optical Dating.: *Quaternary Science Reviews*.
- Huot, S., and Lamothe, M., 2003, Variability of infrared stimulated luminescence properties from fractured feldspar grains: *Radiation Measurements*, v. 37, p. 499-503.
- Hutt, G., *et al.*, 1988, Optical Dating: K-Feldspars Optical Response Stimulation Spectra: *Quaternary Science Reviews*, v. 7, p. 381-386.
- Hutt, G., *et al.*, 2001, Photoionization of radiation-induced traps in quartz and alkali feldspars: *Applied Radiation and Isotopes*, v. 54, p. 175-182.
- Huxtable, J., *et al.*, 1972, Thermoluminescent dating of baked clay balls of poverty point culture: *Archaeometry* v. 14, p. 269.
- IAEA/RL/45, 1977, Final Report on the Intercomparison of Potassium Feldspar F-1.
- Jain, M., and Singhvi, A.K., 2001, Limits to depletion of blue-green light stimulated luminescence in feldspars: implications for quartz dating: *Radiation Measurements*, v. 33, p. 883-892.
- Krbetschek, M.R., *et al.*, 1997, Spectral Information from Minerals Relevant for Luminescence Dating: *Radiation Measurements*, v. 27, p. 695-748.
- Krbetschek, M.R., and Rieser, U., 1995, Luminescence Spectra of Alkalifeldspars and Plagioclases: *Radiation Measurements*, v. 24, p. 473-477.
- Lamothe, M., and Auclair, M., 1999, A solution to anomalous fading and age shortfalls in optical dating of feldspar minerals: *Earth and Planetary Science Letters*, v. 171, p. 319-323.

- Lamothe, M., *et al.*, 2003, Towards a prediction of long-term anomalous fading of feldspar IRSL: *Radiation Measurements*, v. 37, p. 493-498.
- Lasaga, A.C., and Luttge, A., 2004, Mineralogical Approaches to Fundamental Crystal Dissolution Kinetics: *American Mineralogist*, v. 89, p. 527-540.
- Lee, M.R., *et al.*, 1995, Exsolution and alteration microtextures in alkali feldspar phenocrysts from the Shap granite.: *Mineralogical Magazine*, p. 63-78.
- Markey, B.G., *et al.*, 1995, Time-resolved Optically Stimulated Luminescence from α -Al₂O₃:C.
- Mauz, B., and Lang, A., 2004, The Dose Rate of Beta Sources for Optical Dating Applications: A Comparison Between Fine Silt and Fine Sand Quartz.: *Ancient TL*, v. 22, p. 45-48.
- McKeever, S.W.S., 1985, *Thermoluminescence of Solids*, Cambridge University Press.
- Mejdahl, V., 1983, Felspar Inclusion Dating of Ceramics and Burnt Stones: *PACT*, v. 9, p. 351-364.
- Parish, R., 1994, Chapter 15: The Influence of Feldspar Weathering on Luminescence Signals and the Implications for Luminescence Dating of Sediments, *in* Robinson, D.A., and Williams, R. B.G., ed., *Rock Weathering and Landform Evolution*, John Wiley & Sons Ltd, p. 243-258.
- Parsons, I., and Lee, M.R., 2005, Minerals Are Not Just Chemical Compounds: *The Canadian Mineralogist*, v. 43, p. 1879-1911.
- Poolton, N.R.J., *et al.*, 1995, Thermal quenching of luminescence processes in feldspars: *Radiation Measurements*, v. 24, p. 57-66.
- Poolton, N.R.J., *et al.*, 2003, Luminescence excitation characteristics of Ca-, Na- and K- aluminosilicates (feldspars), in the stimulation range 20-500 eV: optical detection of XAS: *Journal of Physics D-Applied Physics*, v. 36, p. 1107-1114.
- Prescott, J.R., and Robertson, G.B., 1997, Sediment Dating by Luminescence: A Review: *Radiation Measurements*, v. 27, p. 893-922.
- Pyle, D.M., *et al.*, 2006, Wide dispersal and deposition of distal tephra during the Pleistocene 'Campanian Ignimbrite/Y5' eruption, Italy.: *Quaternary Science Reviews*, v. 25, p. 2713-2728.
- Randall, J.T., and Wilkins, M.H.F., 1945, Phosphorescence and Electron Traps: I. The Study of Trap Distributions, II. The Interpretation of Long-Term Phosphorescence.: *Proc. Roy. Soc. London.*, v. 184, p. 366-407.
- Rendell, H.M., and Clarke, M.L., 1997, Thermoluminescence, Radioluminescence and Cathodoluminescence Spectra of Alkali Feldspars: *Radiation Measurements*, v. 27, p. 373-372.
- Richardson, C.A., 2005, *Luminescence Dating of Sediments from Clyde, Washington State, USA*: Glasgow, SUERC, p. 30.
- Roque, C., *et al.*, 2004, Changes in luminescence properties induced by thermal treatments; a case study at Sipan and Trujillo Moche sites (Peru): *Radiation Measurements*, v. 38, p. 119-126.

- Sanderson, D.C.W., 1988, Fading of Thermo-Luminescence in Feldspars - Characteristics and Corrections: Nuclear Tracks and Radiation Measurements, v. 14, p. 155-161.
- Sanderson, D.C.W., and Clark, R.J., 1994, Pulsed Photostimulated Luminescence of Alkali Feldspars: Radiation Measurements, v. 23, p. 633-639.
- Schilles, T., and Habermann, J., 2000, Radioluminescence dating: the IR emission of feldspar: Radiation Measurements, v. 32, p. 679-683.
- Smith, D.J., 1998, Fading and Tunnelling in Luminescence Dating of Volcanic Feldspars.: Glasgow, SUERC, p. 67.
- Spencer, J.Q., 1996, The Development of Luminescence Methods to Measure Thermal Exposure in Lithic and Ceramic Materials: Glasgow, University of Glasgow.
- Spencer, J.Q., and Owen, L.A., 2004, Optically Stimulated Luminescence Dating of Late Quaternary Glaciogenic Sediments in the Upper Hunza Valley: Validating the Timing of Glaciation and Assessing Dating Models.: Quaternary Science Reviews, v. 23, p. 175-191.
- Spooner, N.A., 1992, Optical Dating - Preliminary-Results on the Anomalous Fading of Luminescence from Feldspars: Quaternary Science Reviews, v. 11, p. 139-145.
- Spooner, N.A., 1994, The Anomalous Fading of Infrared-Stimulated Luminescence from Feldspars: Radiation Measurements, v. 23, p. 625-632.
- Stokes, S., and Fattahi, M., 2003d, Red emission luminescence from quartz and feldspar for dating applications: an overview: Radiation Measurements, v. 37, p. 383-395.
- Sutton, S.R., and Zimmerman, D.W., 1978, Attempts to Circumvent Anomalous Fading: Ancient TL, v. 3, p. 10-12.
- Templer, R.H., 1986, The Localised Transition Model of Anomalous Fading: Radiation Protection Dosimetry, v. 17, p. 493-497.
- Torsvik, T.H., 1985, Paleomagnetic results from the Peterhead Granite, Scotland; implication for regional late Caledonian magnetic overprinting: Physics of the Earth and Planetary Interiors, v. 39, p. 108-117.
- Torsvik, T.H., *et al.*, 2003, Palaeomagnetism and geochronology of four Laurentian (Scottish) granites with implications for Iapetus Ocean closure models., EGS - AGU - EUG Joint Assembly.
- Torsvik, T.H., *et al.*, 1983, Multicomponent Magnetization in the Helmsdale granite, North Scotland - Geotectonic Implication.: TECTONOPHYSICS, v. 98, p. 111-129.
- Trautmann, T., *et al.*, 2000, A systematic study of the radioluminescence properties of single feldspar grains: Radiation Measurements, v. 32, p. 685-690.
- Trewin, N.H., 2002, The Geology of Scotland: London, The Geological Society, p. 576.
- Trewin, N.H., *et al.*, 1987, Excursion Guide to the Geology of the Aberdeen Area, Scottish Academic Press, p. 299.

- Trowbridge, P.D., and Burbank, J.E., 1898, Art VIII - Phosphorescence Produced by Electrification: *Am. J. Sci. Series 4*, v. 5, p. 55-56.
- Tso, M.-Y.W., *et al.*, 1996, Determination of Lifetime of Infrared Stimulated Signals from Potassium and Sodium Feldspars: *Radiation Protection Dosimetry*, v. 66, p. 387-389.
- Tsukamoto, S., *et al.*, 2006, Time-resolved Luminescence from Feldspars: New Insight Into Fading: *Quaternary Science Reviews*, v. In Press.
- Tyrell, S., *et al.*, 2006, The Use of the Common Pb Isotope Composition of Detrital K-Feldspars Grains as a Provenance Tool and its Application to Upper Carboniferous Paleodrainage, Northern England: *Journal of Sedimentary Research*, v. 76, p. 324-345.
- Visocekas, R., 1979, Miscellaneous Aspects of Artificial TL of Calcite: Emission Spectra, Athermal Detrapping and Anomalous Fading: *PACT*.
- Visocekas, R., 2000, Monitoring anomalous fading of TL of feldspars by using far-red emission as a gauge: *Radiation Measurements*, v. 32, p. 499-504.
- Visocekas, R., & Zink, A., 1995, Tunnel Afterglow and Point Defects in Feldspars: *Radiation Effects and Defects in Solids*, v. 134.
- Visocekas, R., *et al.*, 1976, Tunnelling Processes in Afterglow of Calcite: *Phys. Stat. Sol.*, v. 35, p. 315-327.
- Visocekas, R., and Guerin, G., 2006, TL Dating of Feldspars Using Their Far-Red Emission to Deal with Anomalous Fading: *Radiation Measurements*, v. In Press.
- Visocekas, R., *et al.*, 1994, Tunnel Afterglow, Fading and Infrared-Emission in Thermoluminescence of Feldspars: *Radiation Measurements*, v. 23, p. 377-385.
- Visocekas, R., *et al.*, 1996, Trap Spectroscopy and TSL in Feldspars: *Radiation Protection Dosimetry*, v. 66, p. 391-394.
- Visocekas, R., *et al.*, 1998, Trap spectroscopy and tunnelling luminescence in feldspars: *Radiation Measurements*, v. 29, p. 427-434.
- Visocekas, R., and Zink, A., 1995, Tunnel Afterglow and Point Defects in Feldspars: *Radiation Effects and Defects in Solids*, v. 134.
- Visocekas, R., and Zink, A., 1999, Use of the far red TL emission band of alkali feldspars for dosimetry and dating: *Quaternary Science Reviews*, v. 18, p. 271-278.
- Wallinga, J., and Duller, G.A.T., 2000, The effect of optical absorption on the infrared stimulated luminescence age obtained on coarse-grain feldspar: *Quaternary Science Reviews*, v. 19, p. 1035-1042.
- Wallinga, J., *et al.*, 2000, The single-aliquot regenerative-dose (SAR) protocol applied to coarse-grain feldspar: *Radiation Measurements*, v. 32, p. 529-533.
- Ward, S., *et al.*, 2003, Optical dating of quartz from young samples and the effects of pre-heat temperature: *Radiation Measurements*, v. 37, p. 401-407.

- Whittle, E.H., 1975a, Thermoluminescent Dating of Egyptian Predynastic Pottery from Hemamieh and Qurna-Tarif: *Archaeometry*, v. 17, p. 119-122.
- Whittle, E.H., and Arnaud, J.M., 1975b, Thermoluminescent Dating of Neolithic and Chalcolithic Pottery from Sites in Central Portugal: *Archaeometry*, v. 17, p. 5-24.
- Wick, F.G., 1924, A Spectroscopic Study of the Cathodo-luminescence of Fluorite: *Phys. Rev.*, v. 24, p. 272-282.
- Wick, F.G., and Slattery, M.K., 1927, The Effect of Exposure to X-rays upon the Thermoluminescence of some Synthetically Prepared Materials: *J. Opt. Soc. Am.*, v. 14, p. 125-132.
- Wick, F.G., and Slattery, M.K., 1928, Thermoluminescence Excited by X-rays, Further Experiments upon Synthetically Prepared Minerals: *J. Opt. Soc. Am.*, v. 16, p. 398-408.
- Wiedemann, E., and Schmidt, G.C., 1895, Ueber Luminescenz: *Ann. Phy. Chem. Neue Folge*, v. 54, p. 604-625.
- Wintle, A., 1973, Anomalous Fading of Thermoluminescence in Mineral Samples: *Nature*, v. 245, p. 143-144.
- Wintle, A., 1985, Stability of the TL signal in fine grains from loess: *Nuclear Tracks and Radiation Measurements*, v. 10.
- Wintle, A., 1990, A review on the current research of TL dating of loess: *Quaternary Science Reviews*, v. 9, p. 385-397.
- Wintle, A.G., 1974, Anomalous Fading: *PACT*.
- Wintle, A.G., and Huntley, D.J., 1978, Preliminary Thermoluminescence Dates for a Core from North Pacific: *Transactions-American Geophysical Union* v. 59, p. 235.
- Wintle, A.G., and Huntley, D.J., 1982, Thermoluminescence Dating of Sediments: *Quaternary Science Reviews*, v. 1, p. 31-53.
- Worden, R.H., *et al.*, 1990, Development of microporosity, diffusion channels and deuteric coarsening in perthitic alkali feldspars.: *Contributions to Mineralogy and Petrology*, v. 104, p. 507-515.
- Wyres, G.P., and Barton, M., 1986, Petrology and Evolution of Transitional Alkaline- Sub Alkaline Lavas from Patmos, Dodecanesos, Greece: Evidence for Fractional Crystallization, Magma Mixing and Assimilation.: *Contributions to Mineralogy and Petrology*, v. 93, p. 297-311.
- Wyres, G.P., and Barton, M., 1987, Geochemistry of a transitional ne-trachybasalt — Q-trachyte lava series from Patmos (Dodecanesos), Greece: further evidence for fractionation, mixing and assimilation.: *Contributions to Mineralogy and Petrology*, v. 97.
- Zaniewski, A., *et al.*, 2006, Field Relationships and Emplacement of the Caledonian Ross of Mull Granite.: *Scottish Journal of Geology*, v. 42, p. 179-189.

Zhou, L.P., and Wintle, A.G., 1994, Sensitivity Change of Thermoluminescence Signals after Laboratory Optical Bleaching - Experiments with Loess Fine Grains: *Quaternary Science Reviews*, v. 13, p. 457-463.

Zink, A., and Visocekas, R., 1996, Dosimetry with Feldspars and Their Infrared Emission Band: *Radiation Protection Dosimetry*, v. 66, p. 399-402.

Zink, A., and Visocekas, R., 1997, Datability of Sanidine Feldspars Using the Near-Infrared TL Emission: *Radiation Measurements*, v. 27, p. 251-256.

Zink, A., *et al.*, 1995, Comparison of Blue and Infrared-Emission Bands in Thermoluminescence of Alkali Feldspars: *Radiation Measurements*, v. 24, p. 513-518.

A

Appendix A.

A.1 Introduction.

This appendix contains the albite, anorthite and orthoclase molecular proportions from the individual electron microprobe spot analyses, and a backscattered electron image of the grains that were chemically analysed. These results were calculated from the raw oxide proportions collected by the electron probe and used to plot the ternary diagrams presented in Chapter 4. All the analysis producing totals of $< \sim 98.5$ and > 101 wt% oxide were disregarded as were inadvertent analysis of quartz. All electron probe work was carried out on polished grain mounts that were carbon coated. In each of the images presented in this appendix the light grey areas are alkali feldspar and the medium grey is albite.

A.2 Plutonic Igneous and Associated Rocks.

A.2.1 Arran Granite.

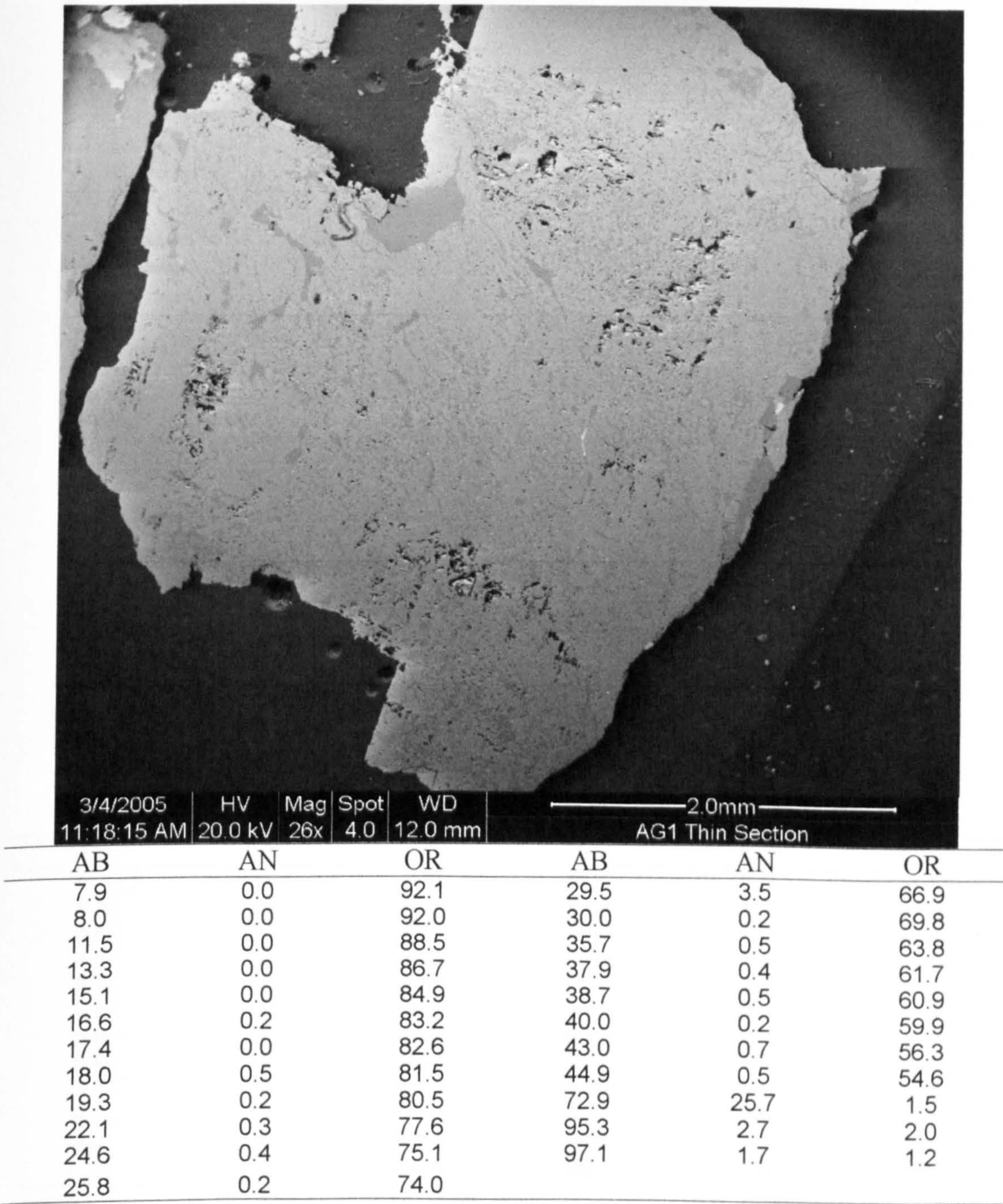
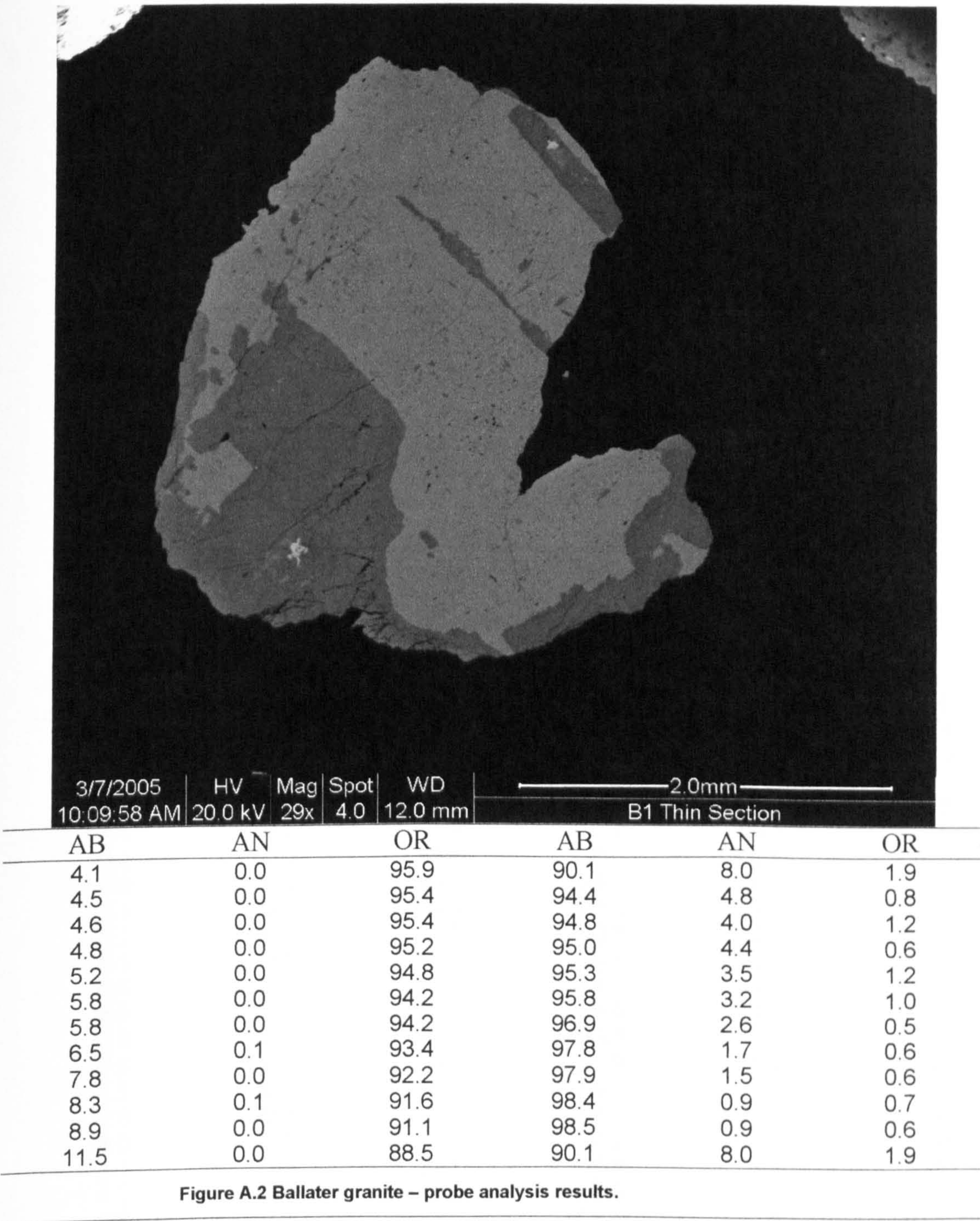


Figure A.1 Arran granite – probe analysis results.

A.2.2 Ballater Granite.



A.2.3 Cairngorm Granite.

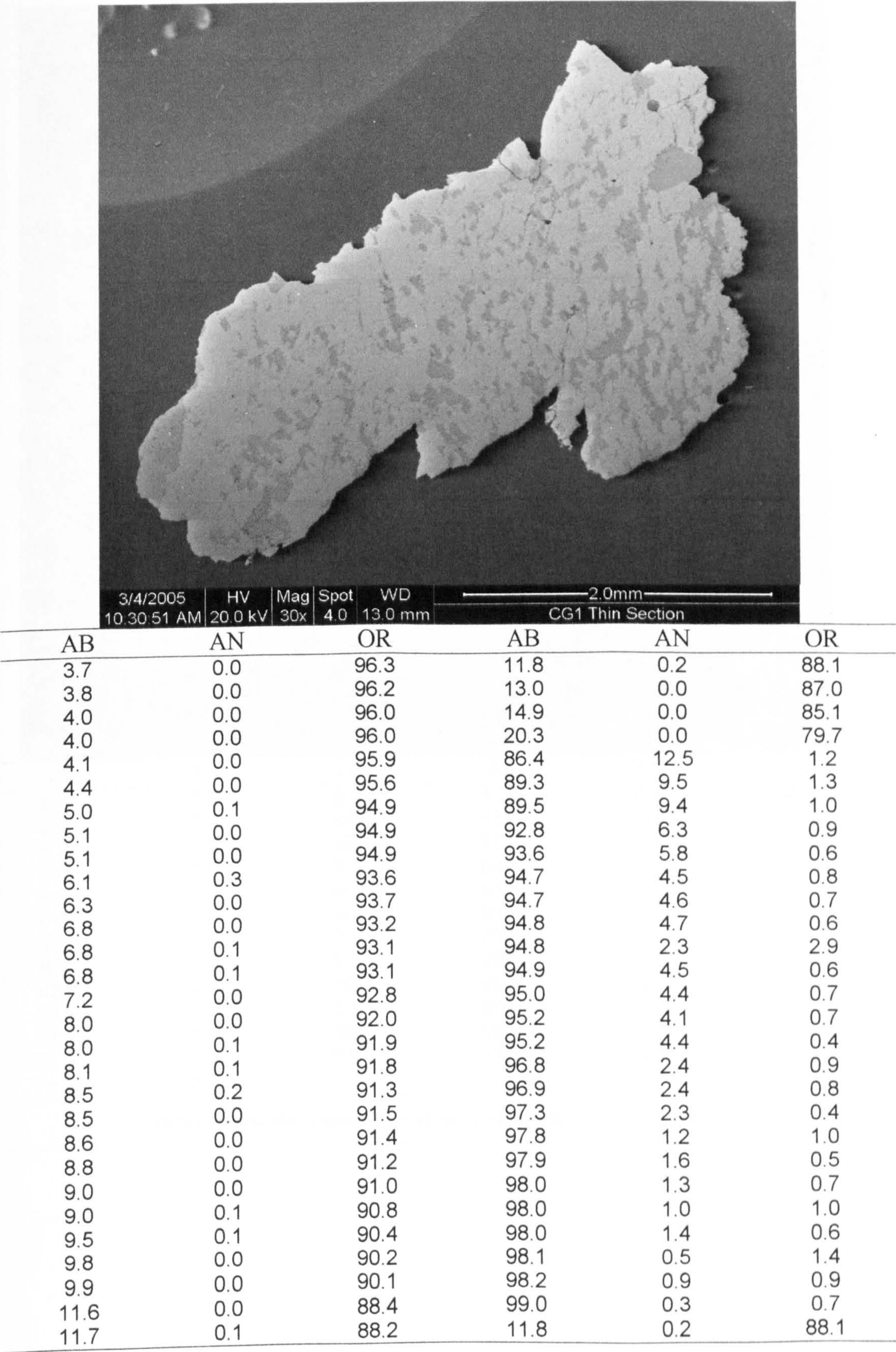


Figure A.3 Cairngorm granite – probe analysis results.

A.2.4 Helmsdale Granite.

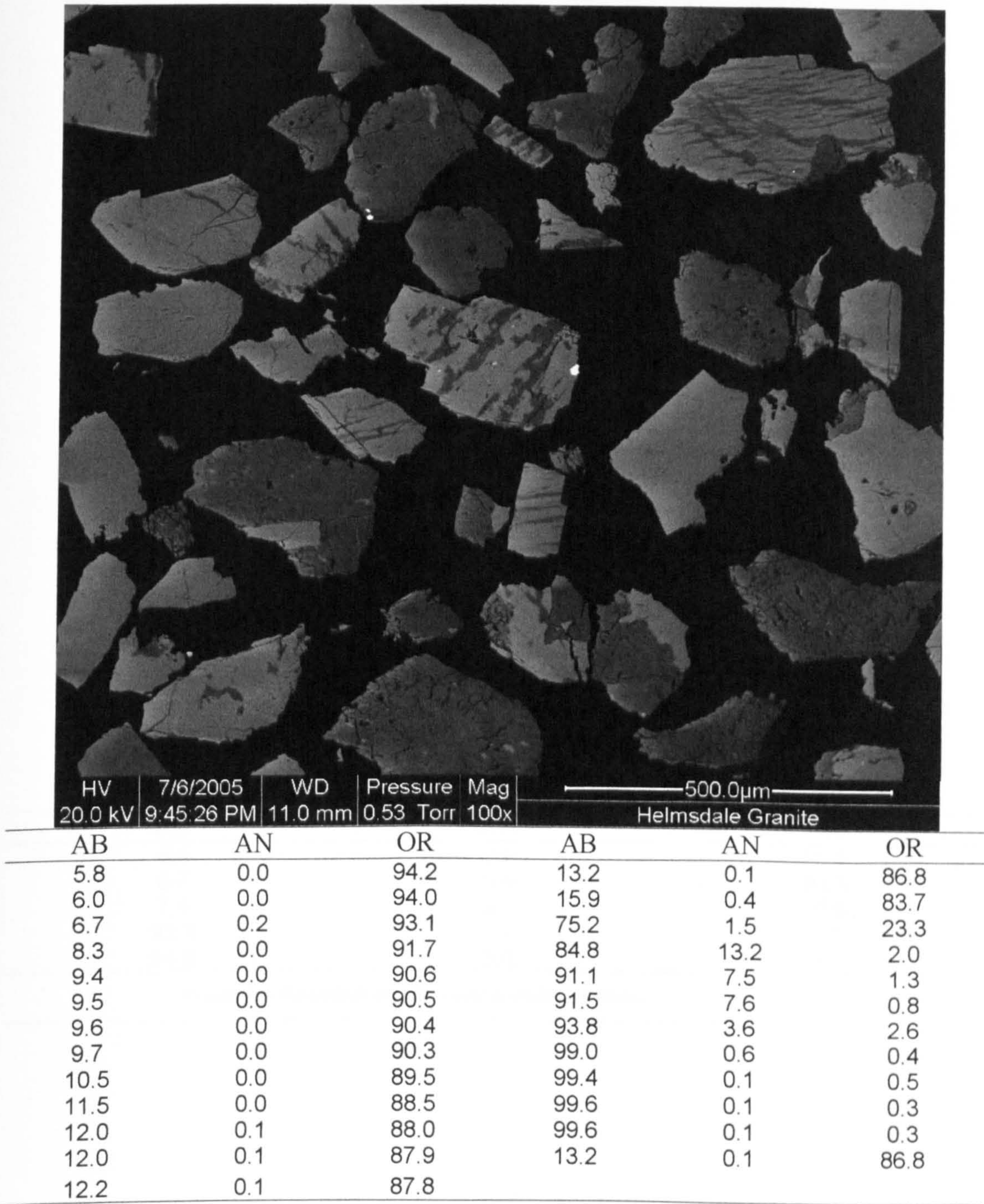
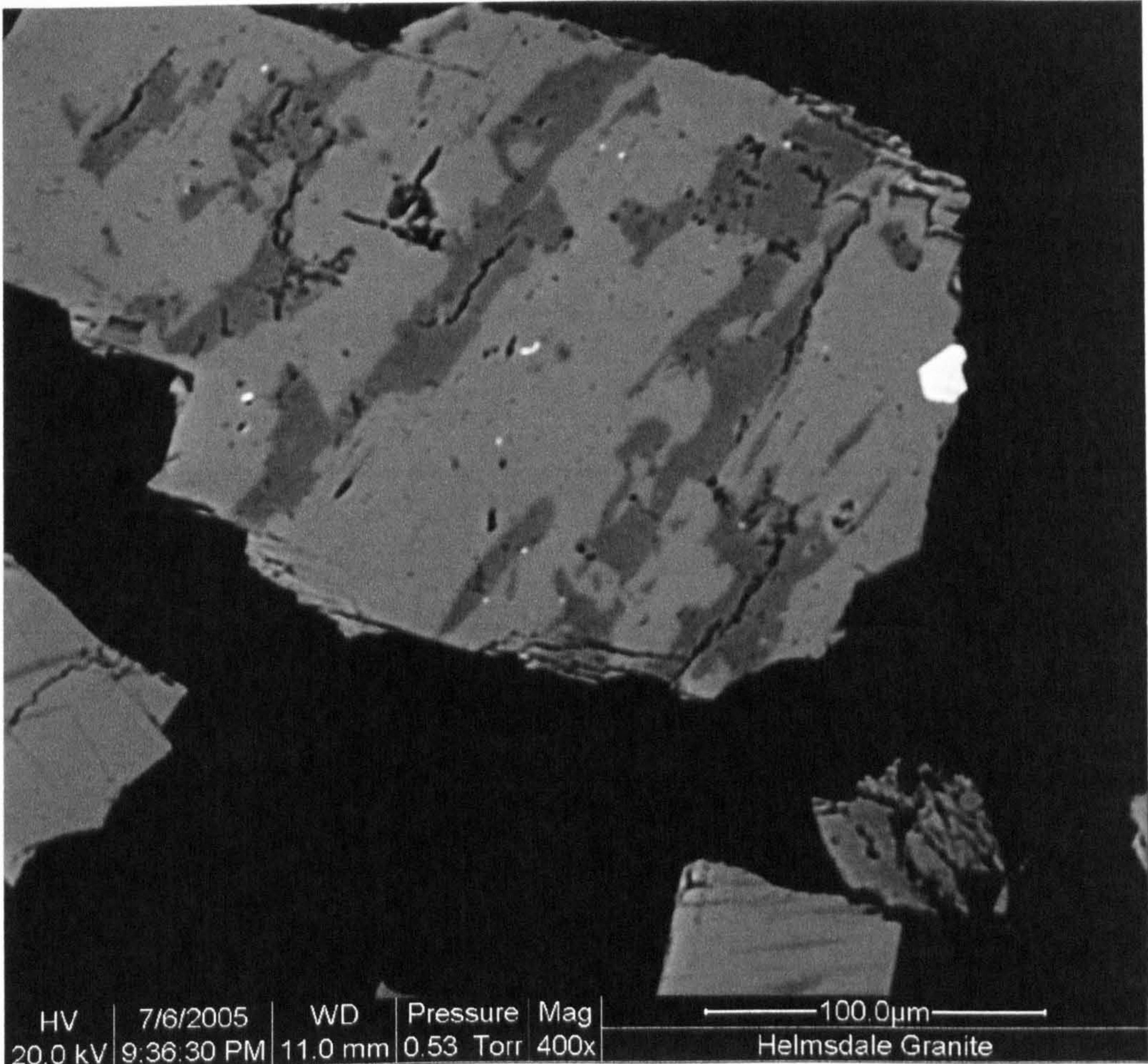


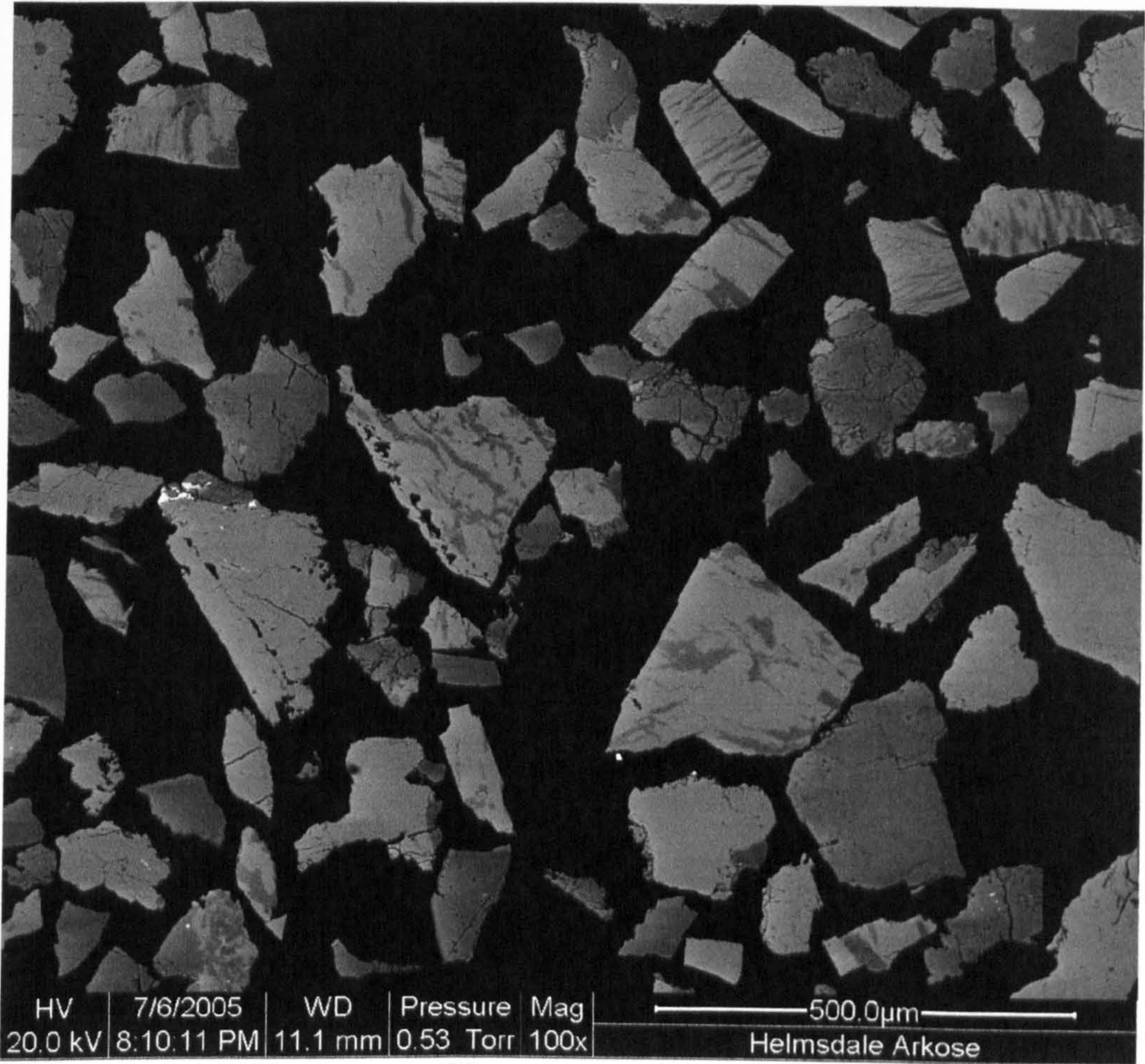
Figure A.4 Helmsdale granite – probe analysis results.



AB	AN	OR
5.4	0.0	94.6
6.7	0.0	93.3
7.4	0.0	92.6
93.3	5.7	1.0
94.3	5.0	0.7

Figure A.5 Helmsdale granite – probe analysis points.

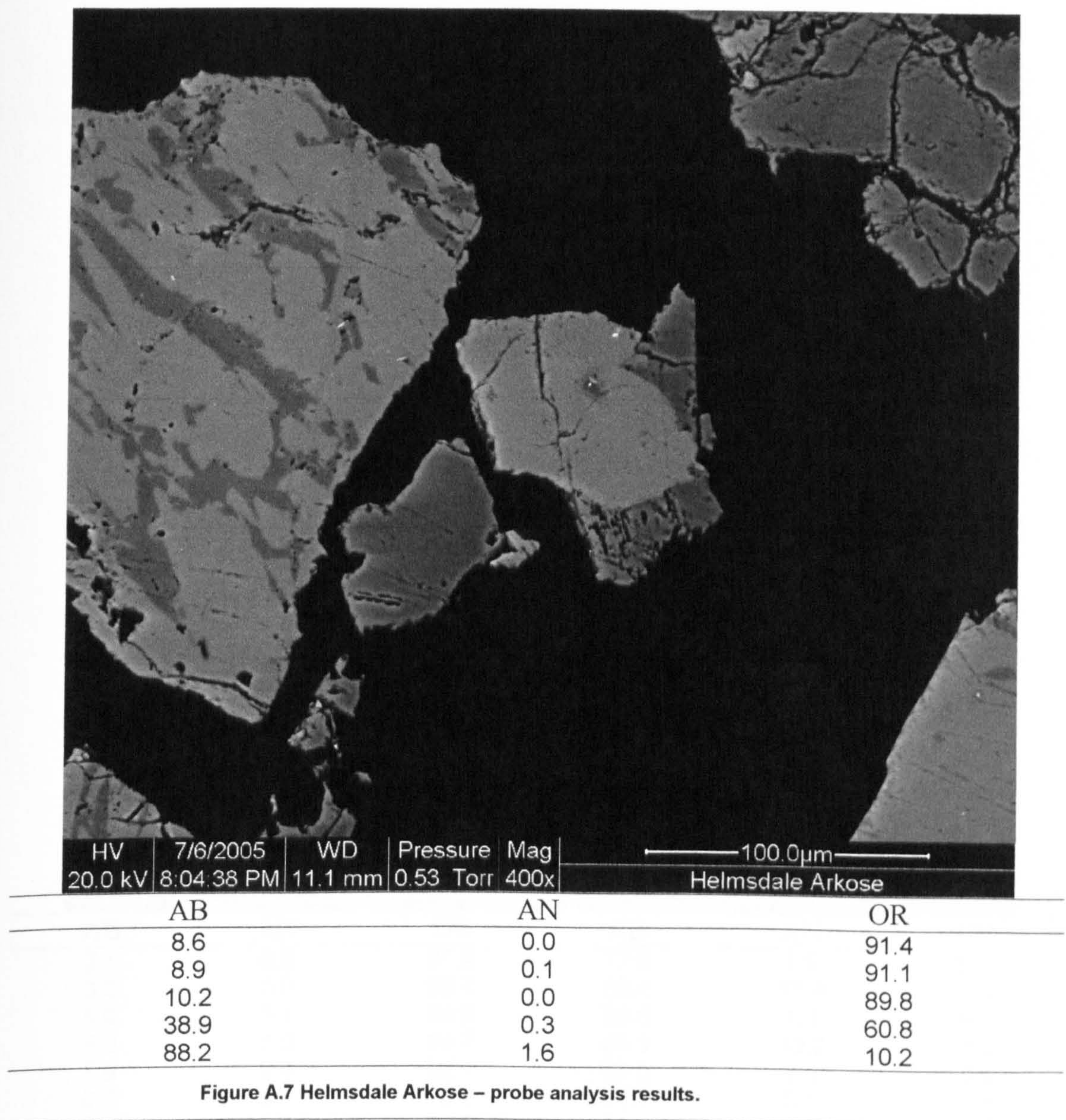
A.2.5 Helmsdale Arkose.



AB	AN	OR	AB	AN	OR
5.2	0.0	94.8	5.2	0.0	94.8
7.4	0.0	92.6	7.4	0.0	92.6
7.5	0.0	92.5	7.5	0.0	92.5
8.8	0.3	90.9	8.8	0.3	90.9
9.0	0.0	91.0	9.0	0.0	91.0
9.0	0.2	90.8	9.0	0.2	90.8
9.7	0.1	90.2	9.7	0.1	90.2
10.2	0.1	89.8	10.2	0.1	89.8
10.2	0.0	89.8	10.2	0.0	89.8
10.9	0.0	89.1	10.9	0.0	89.1
12.5	0.1	87.4	12.5	0.1	87.4
14.2	0.2	85.6			

Figure A.6 Helmsdale arkose – probe analysis results.

A.2.2 Helmsdale Arkose



A.2.6 Peterhead Granite.

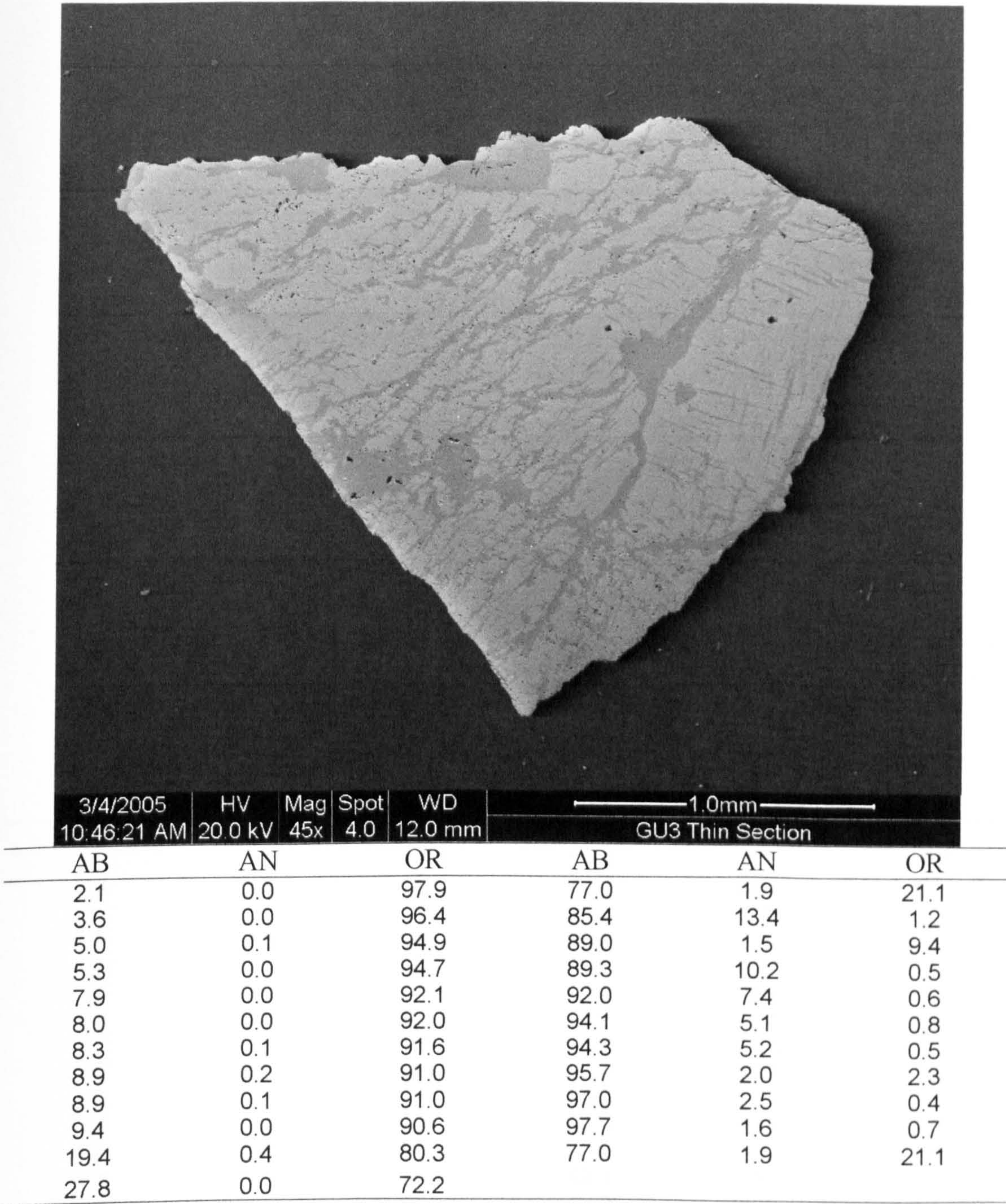


Figure A.8 Peterhead granite – probe analysis results.

A.2.7 Ross of Mull Granite.

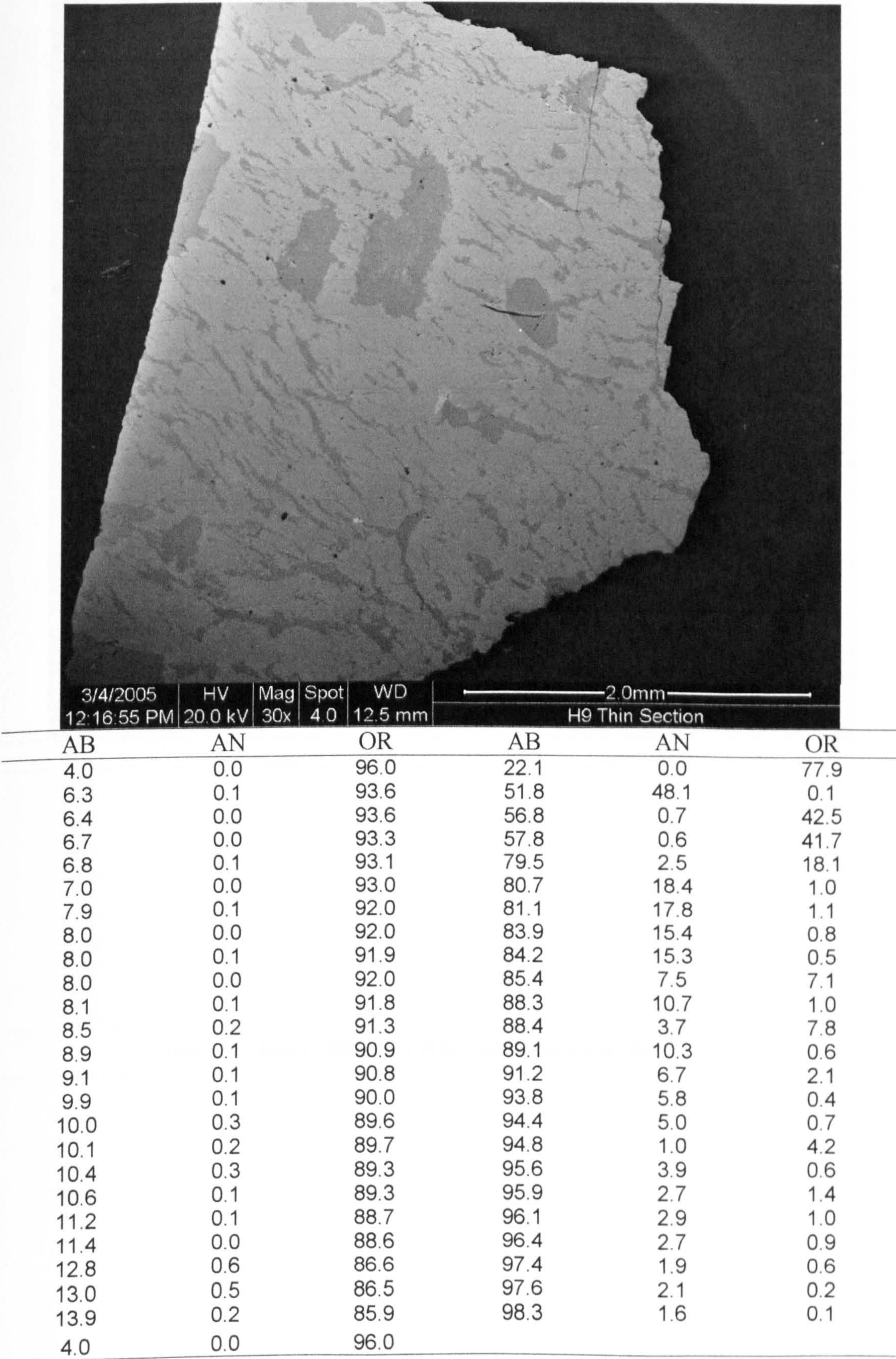


Figure A.9 Ross of Mull granite (H9) – probe analysis results.

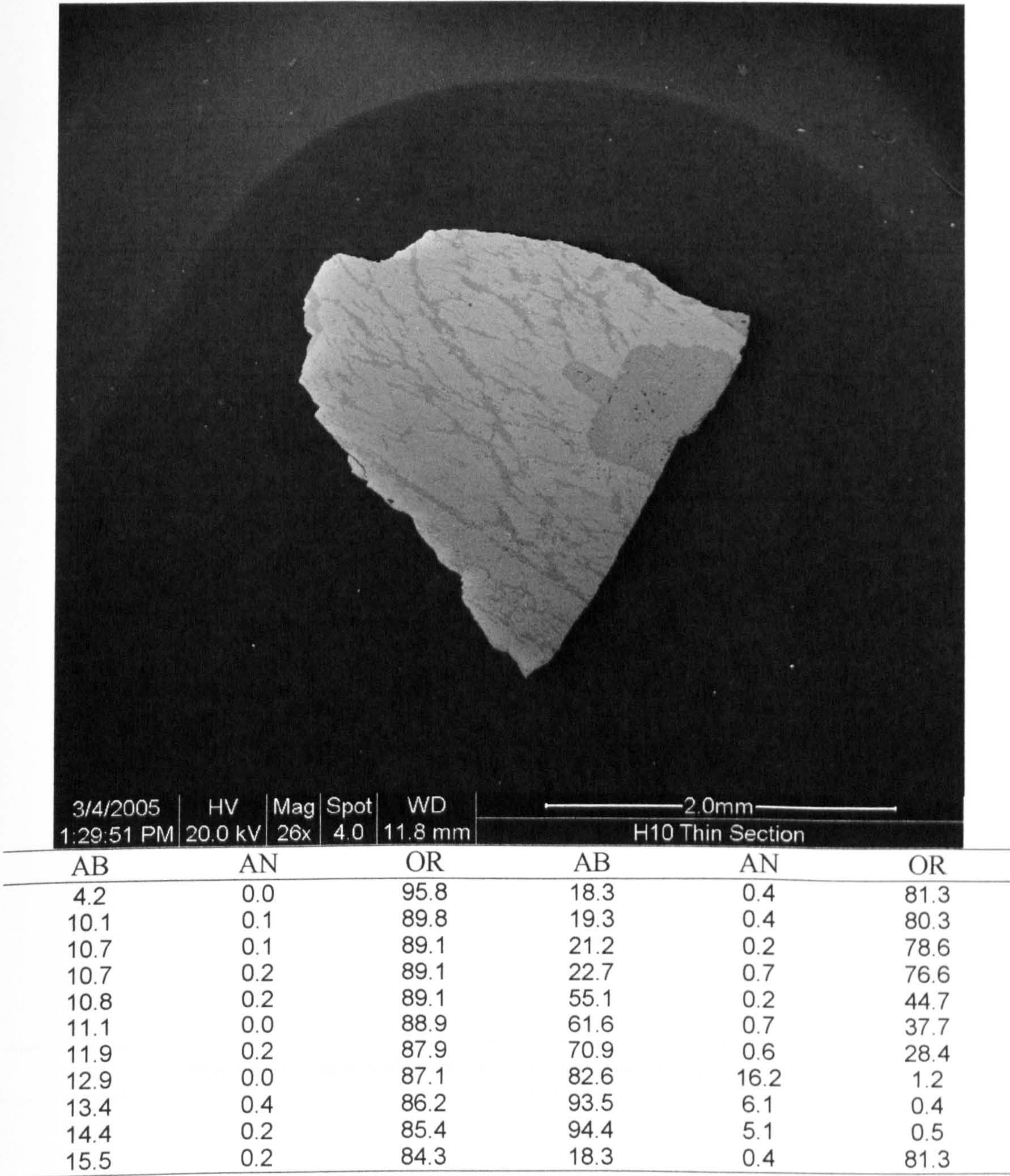


Figure A.10 Ross of Mull granite (H10) – probe analysis points.

A.11 Ross of Mull granite (H10) – probe analysis results

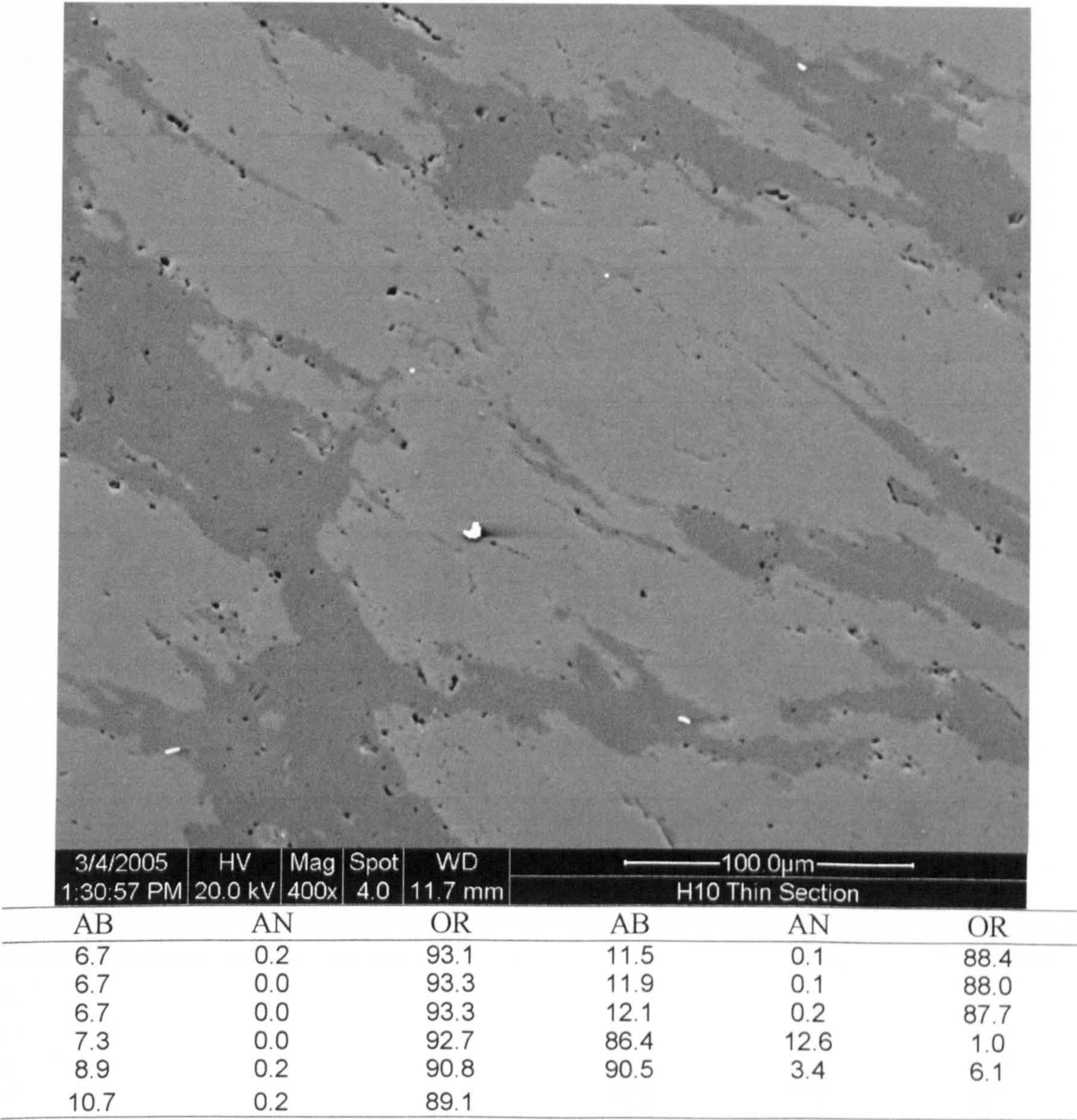


Figure A.11 Ross of Mull granite (H10) – probe analysis results.

A.2.8 Ross of Mull Hydrothermal Syenite.

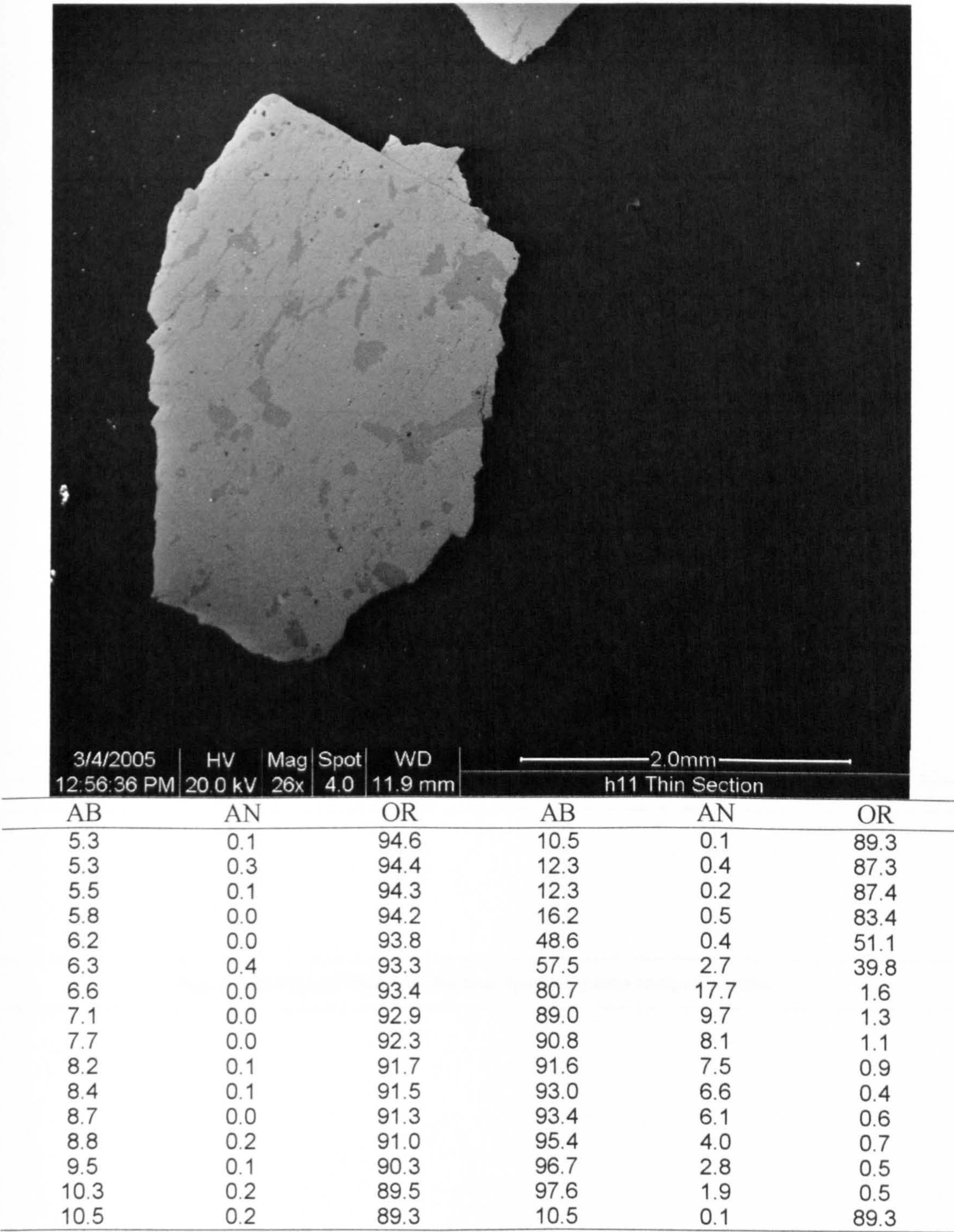
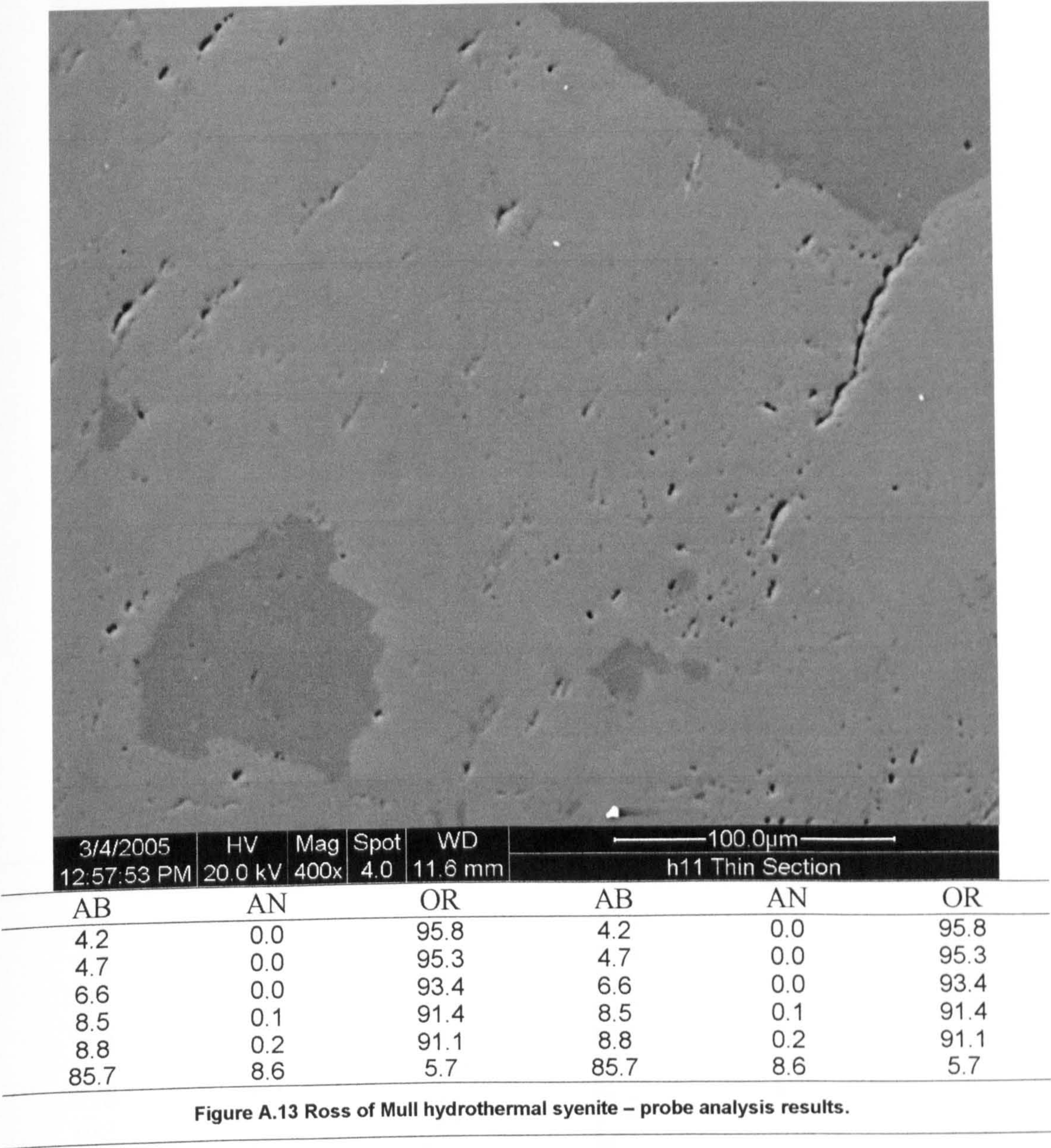


Figure A.12 Ross of Mull hydrothermal syenite – probe analysis results.

A.25 Symplocarite

A.25.1



A.2.9 Shap Granite.

A.2.9.1 Fresh Shap Granite.

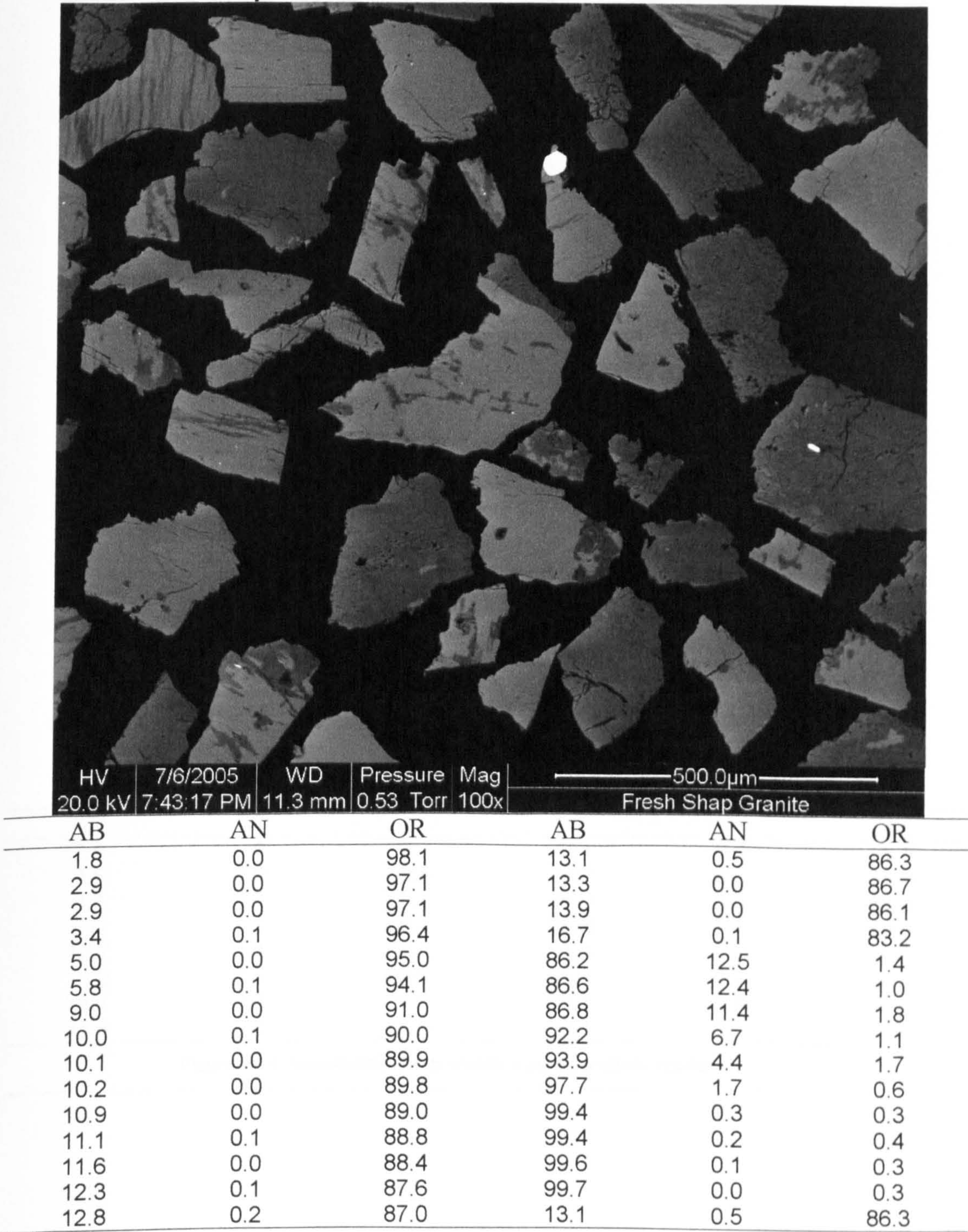
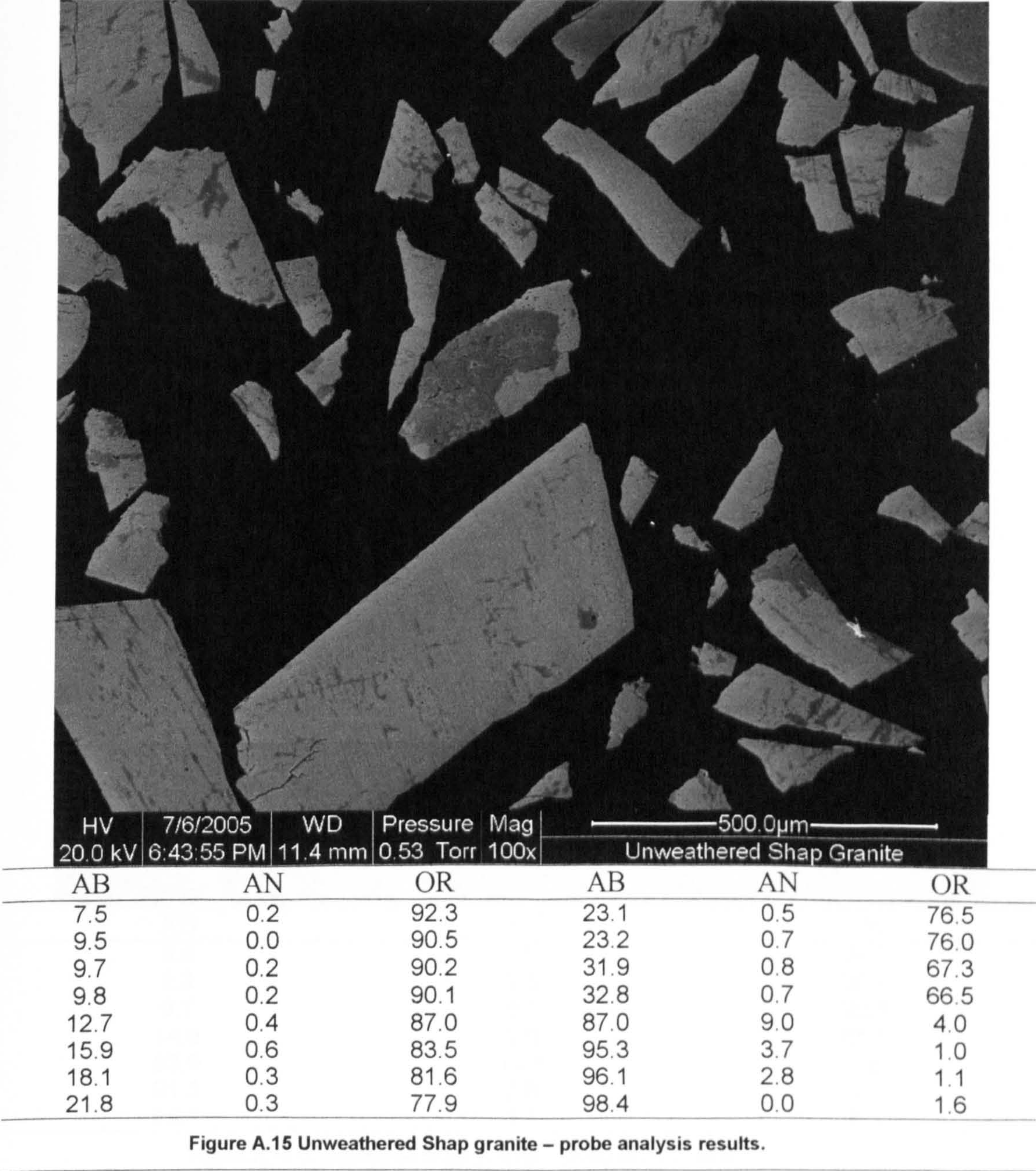
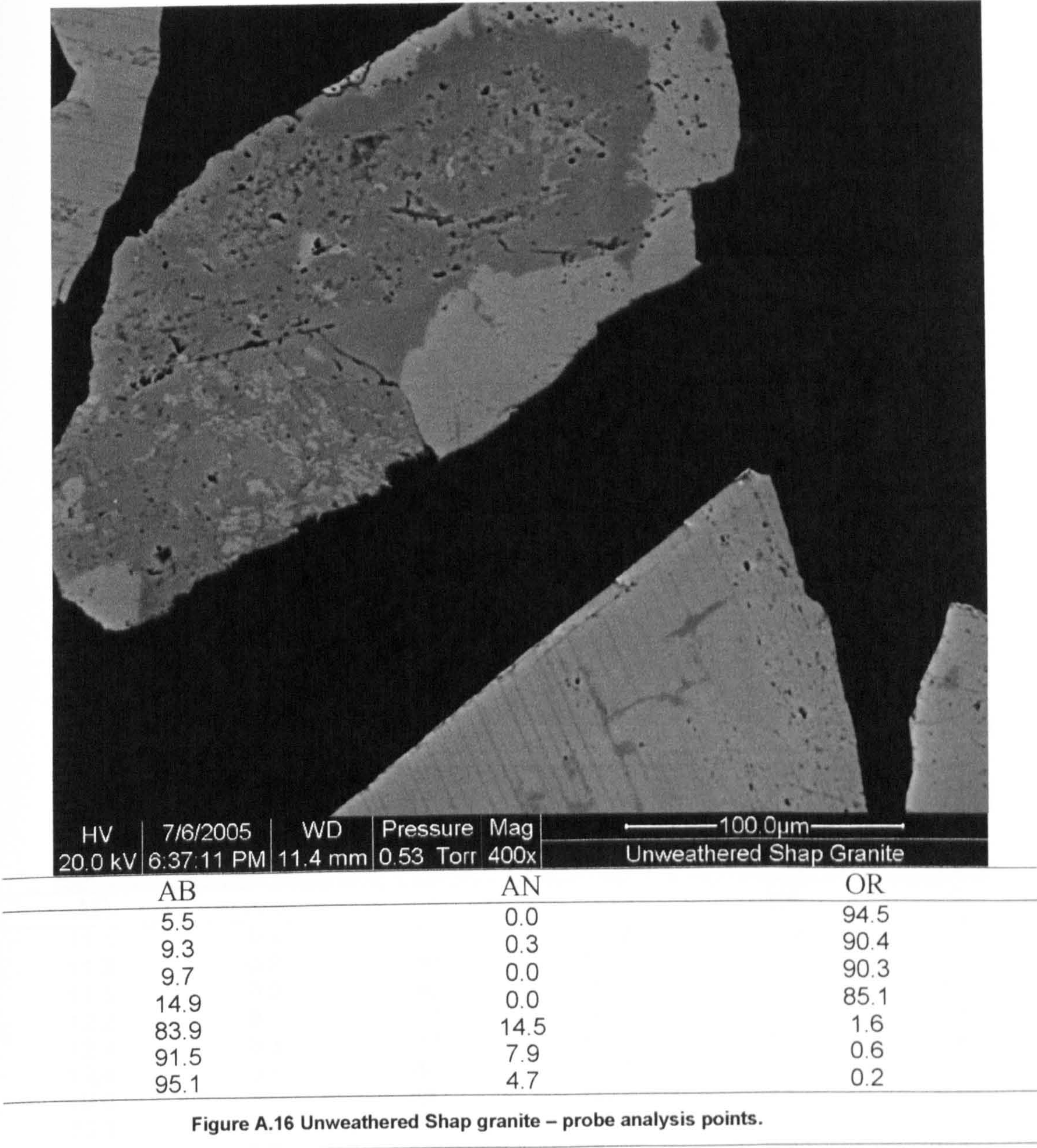


Figure A.14 Fresh Shap granite – probe analysis results.

A.2.9.2 Unweathered Shap Granite.



A.210 Shap Granite



A.2.10 Strontian Granodiorite.

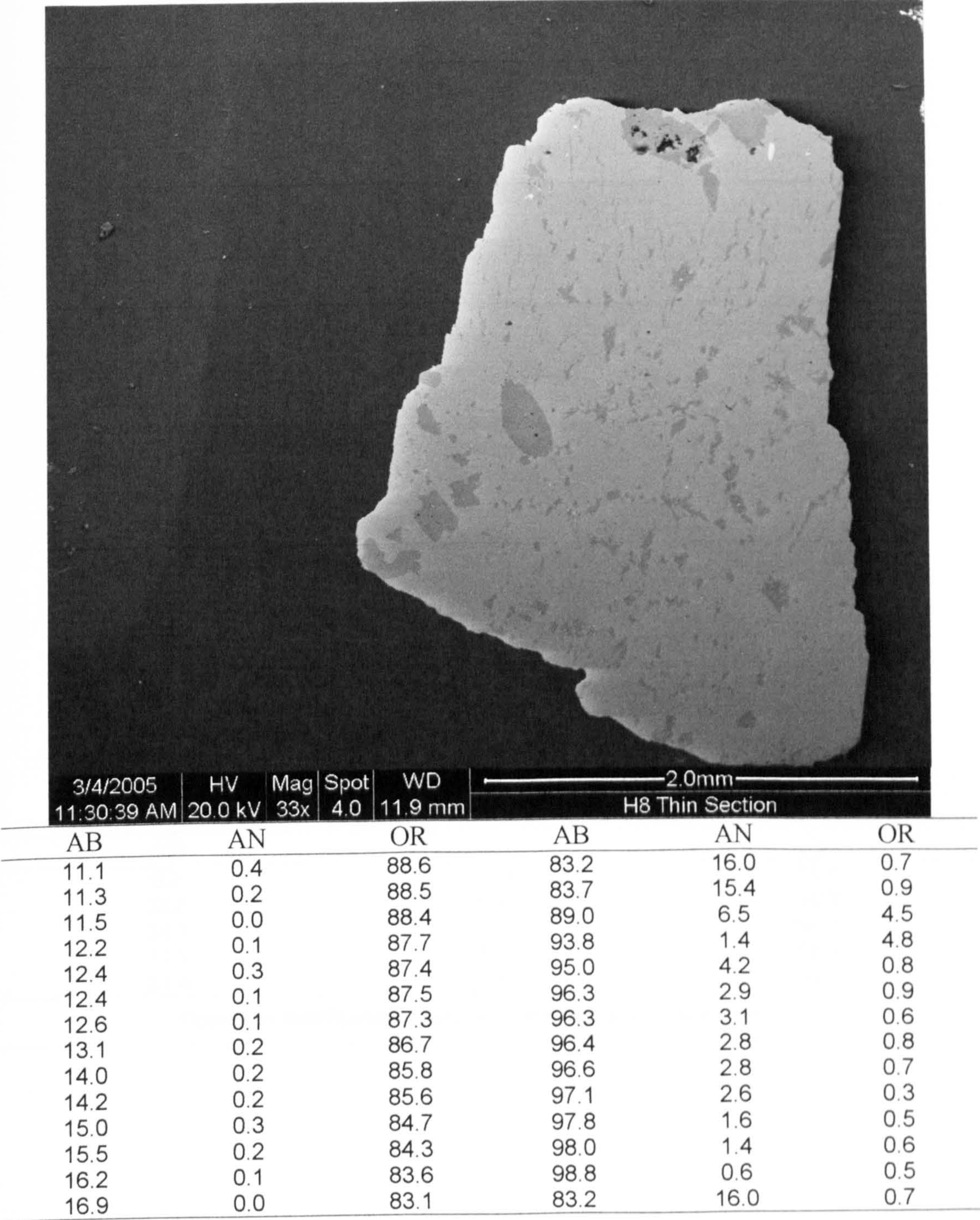
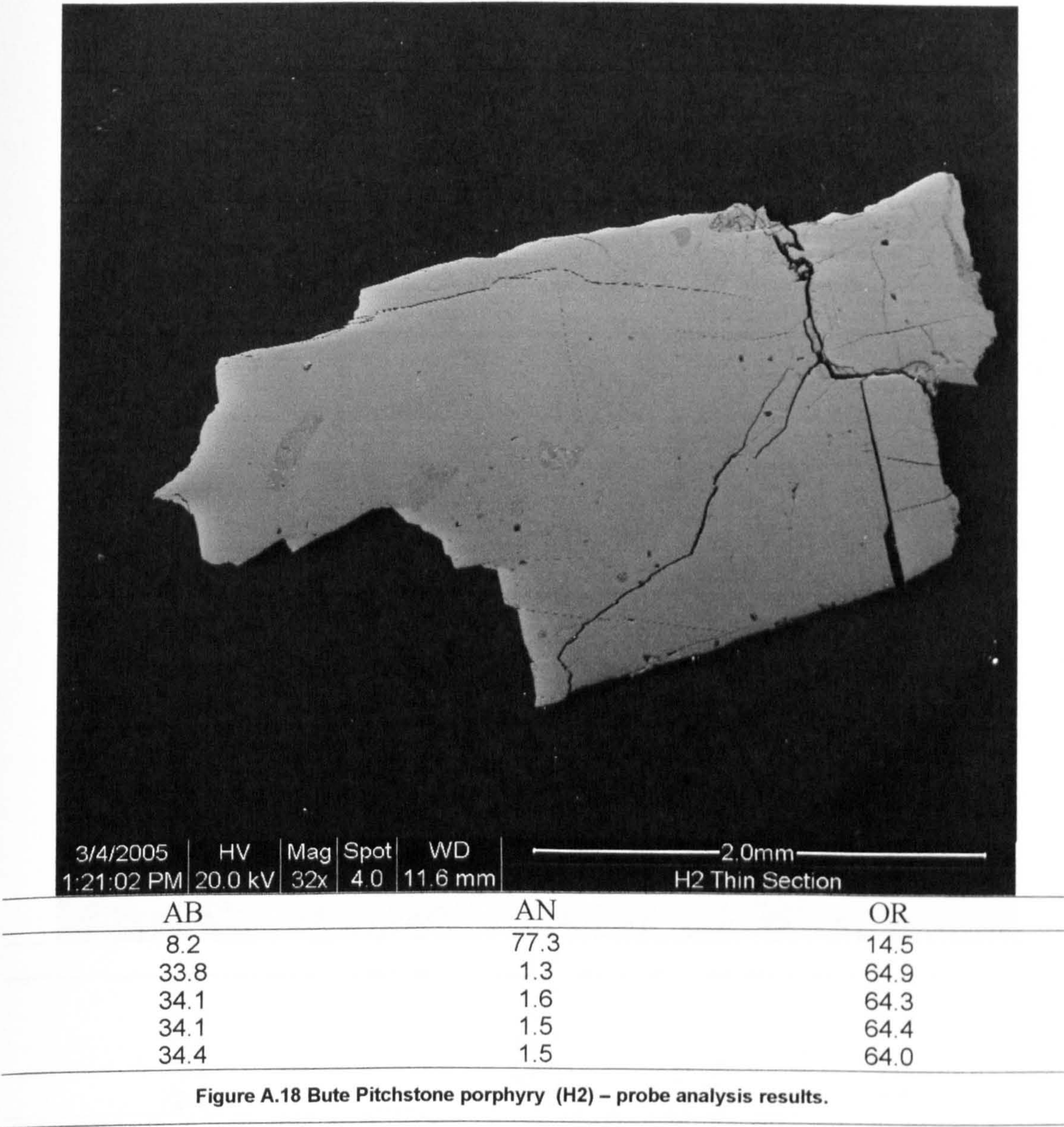
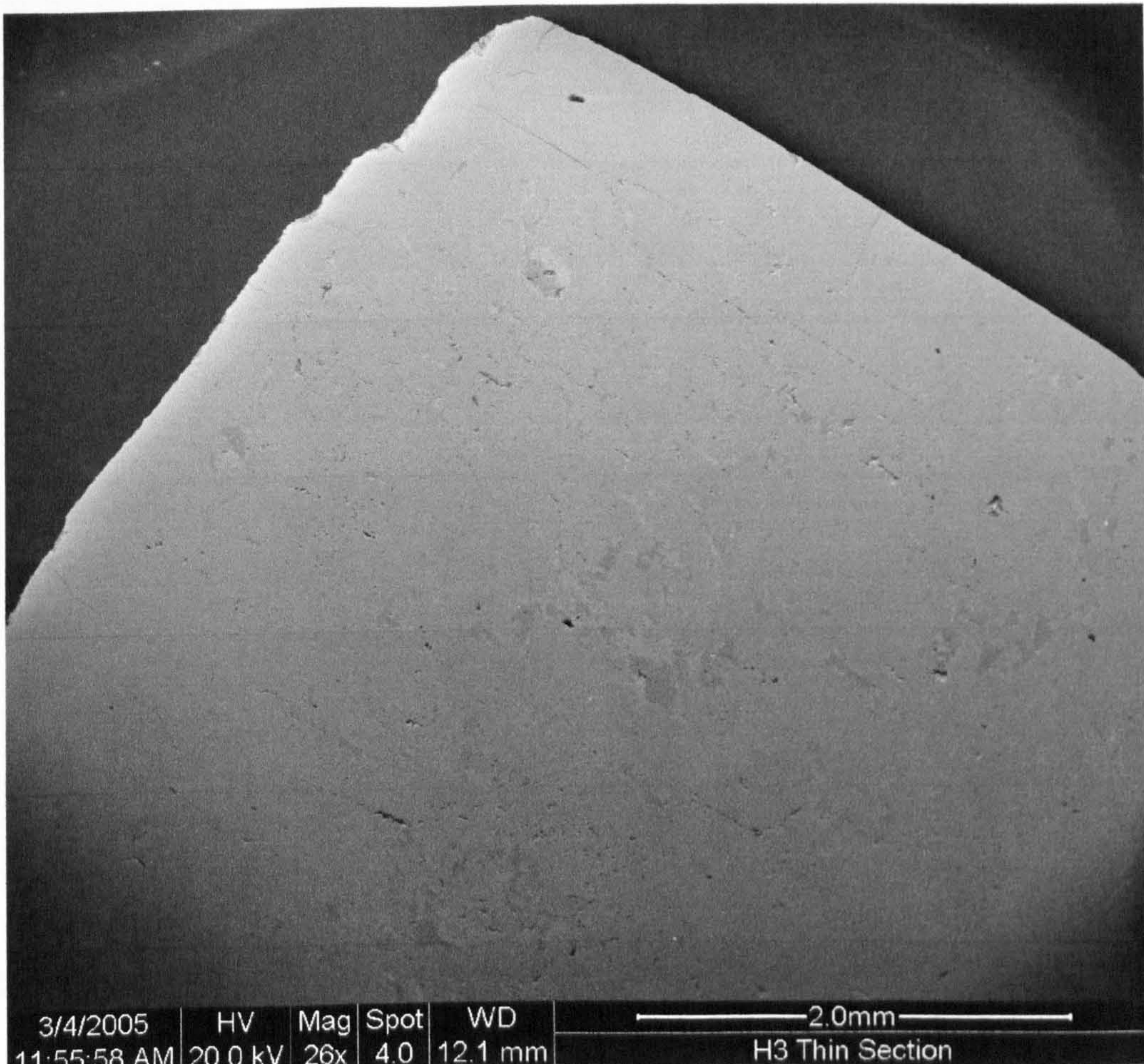


Figure A.17 Strontian granodiorite – probe analysis results.

A.3 Silicic Minor Igneous Intrusions.

A.3.1 Bute Pitchstone Porphyry.

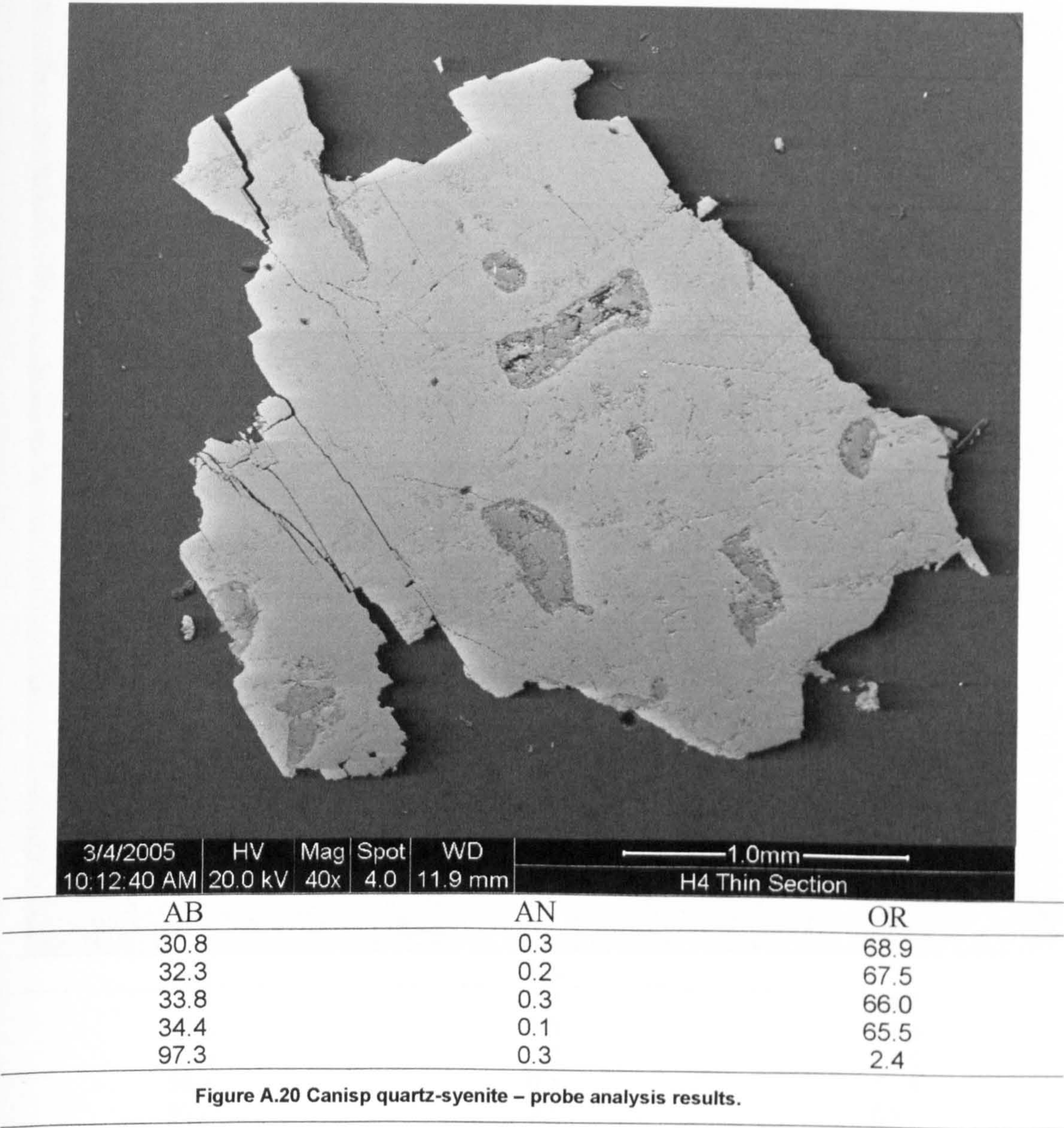




AB	AN	OR
2.6	0.2	97.2
31.9	1.3	66.8
70.0	22.0	8.0
70.8	21.3	7.9
72.2	20.0	7.7

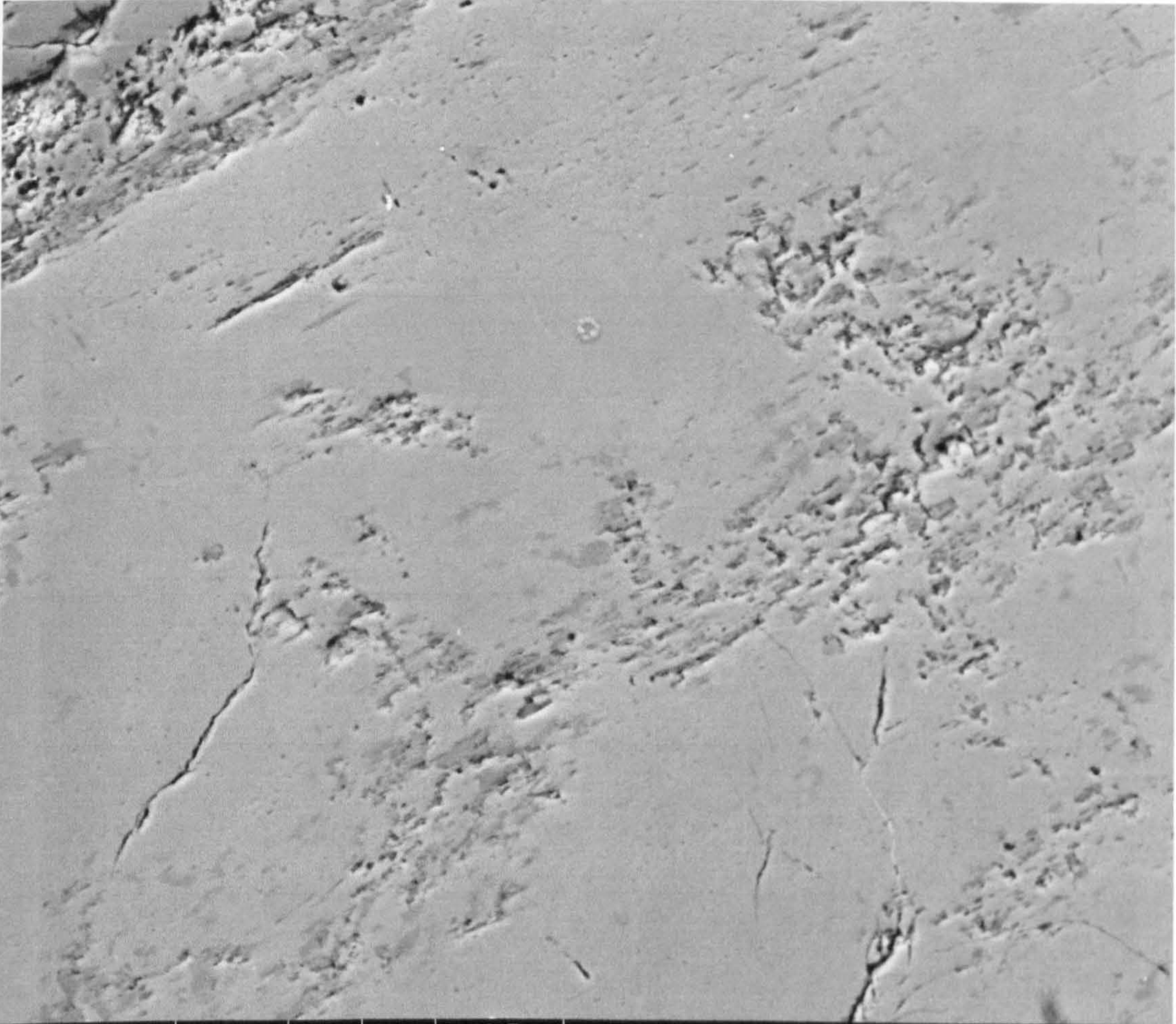
Figure A.19 Bute Pitchstone porphyry – probe data results.

A.3.2 Canisp quartz-syenite.



A.4 Igneous Rocks: Diorite

A.4.5 Canisp Gneiss Foliation



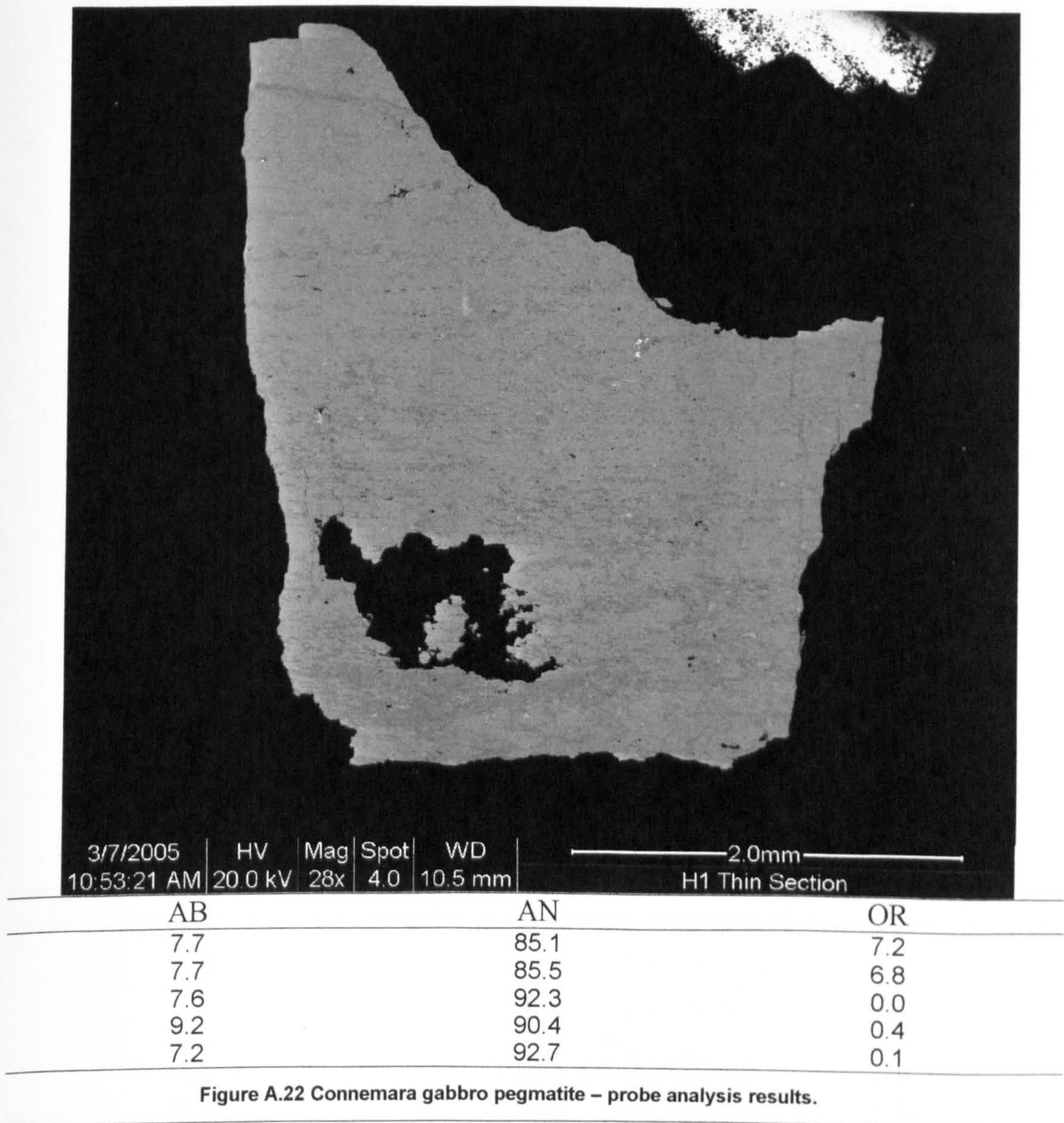
3/4/2005	HV	Mag	Spot	WD	100.0μm
10:02:07 AM	20.0 kV	800x	4.0	11.9 mm	H4 Thin Section

AB	AN	OR
4.4	0.0	95.6
15.1	0.0	84.8
22.3	0.2	77.5
28.1	0.1	71.9
33.8	0.1	66.1

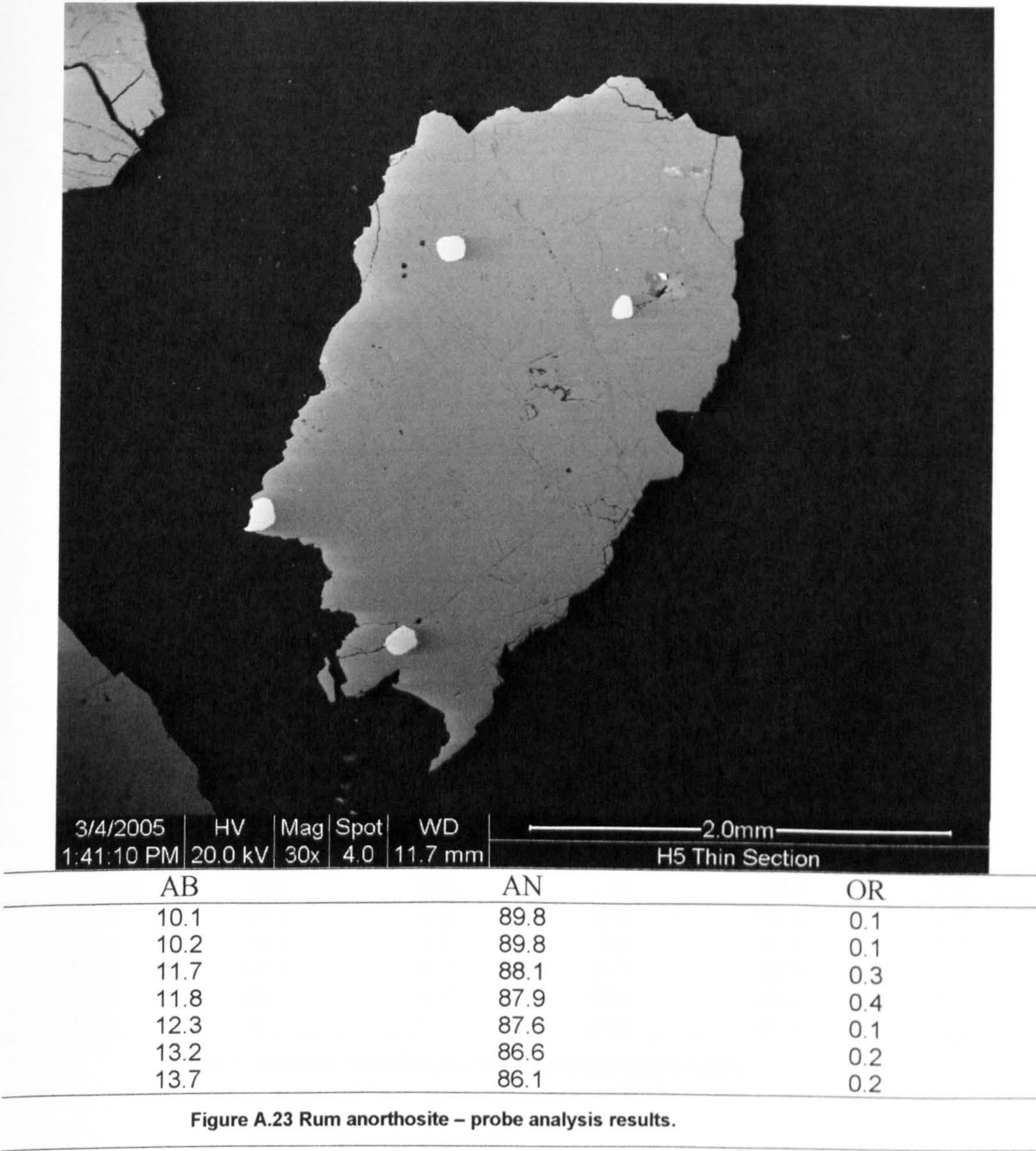
Figure A.21 Canisp quartz-syenite – probe analysis results.

A.4 Igneous Calcic Plagioclase.

A.4.1 Connemara Gabbro Pegmatite.

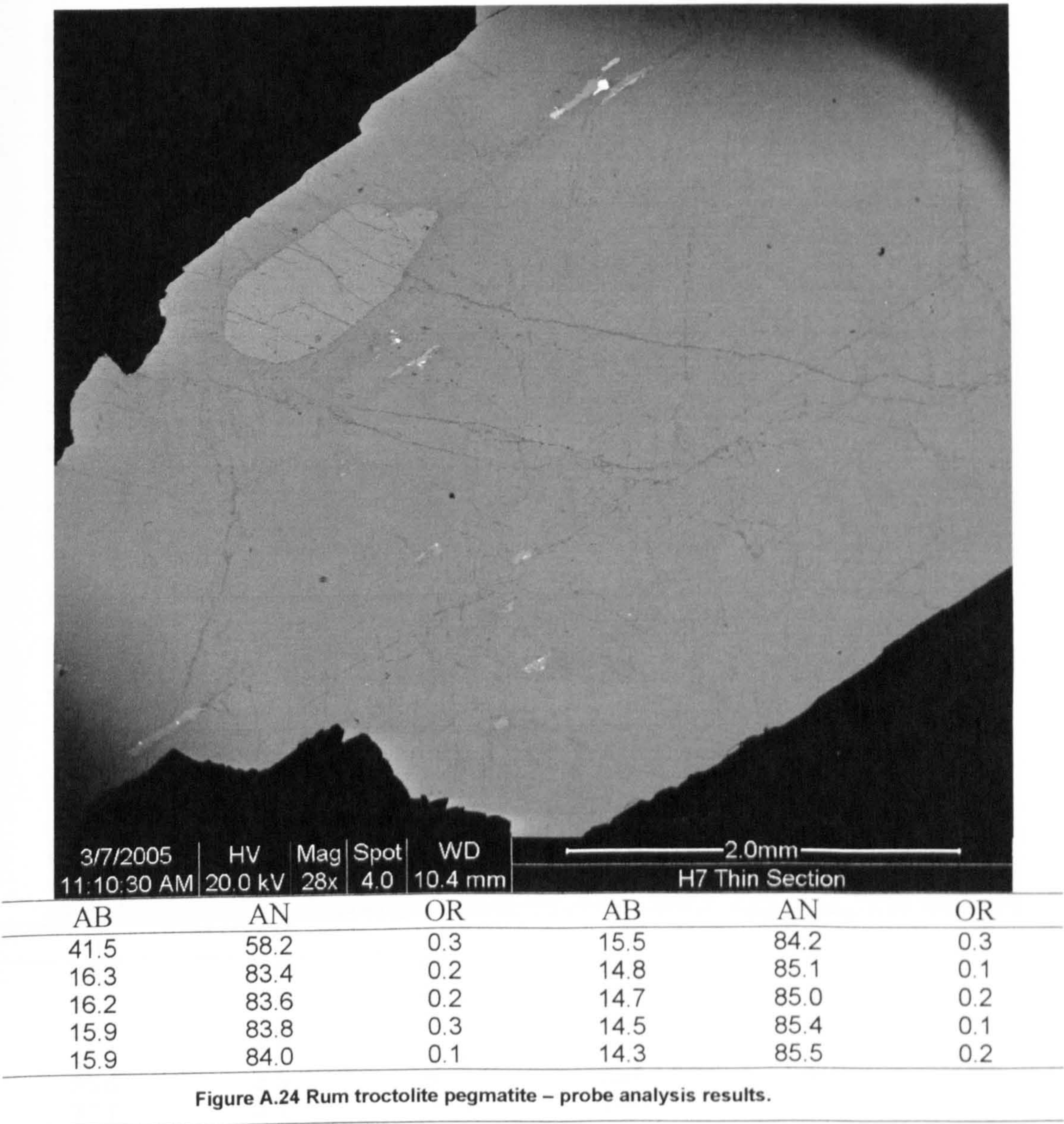


A.4.2 Rum Anorthosite.



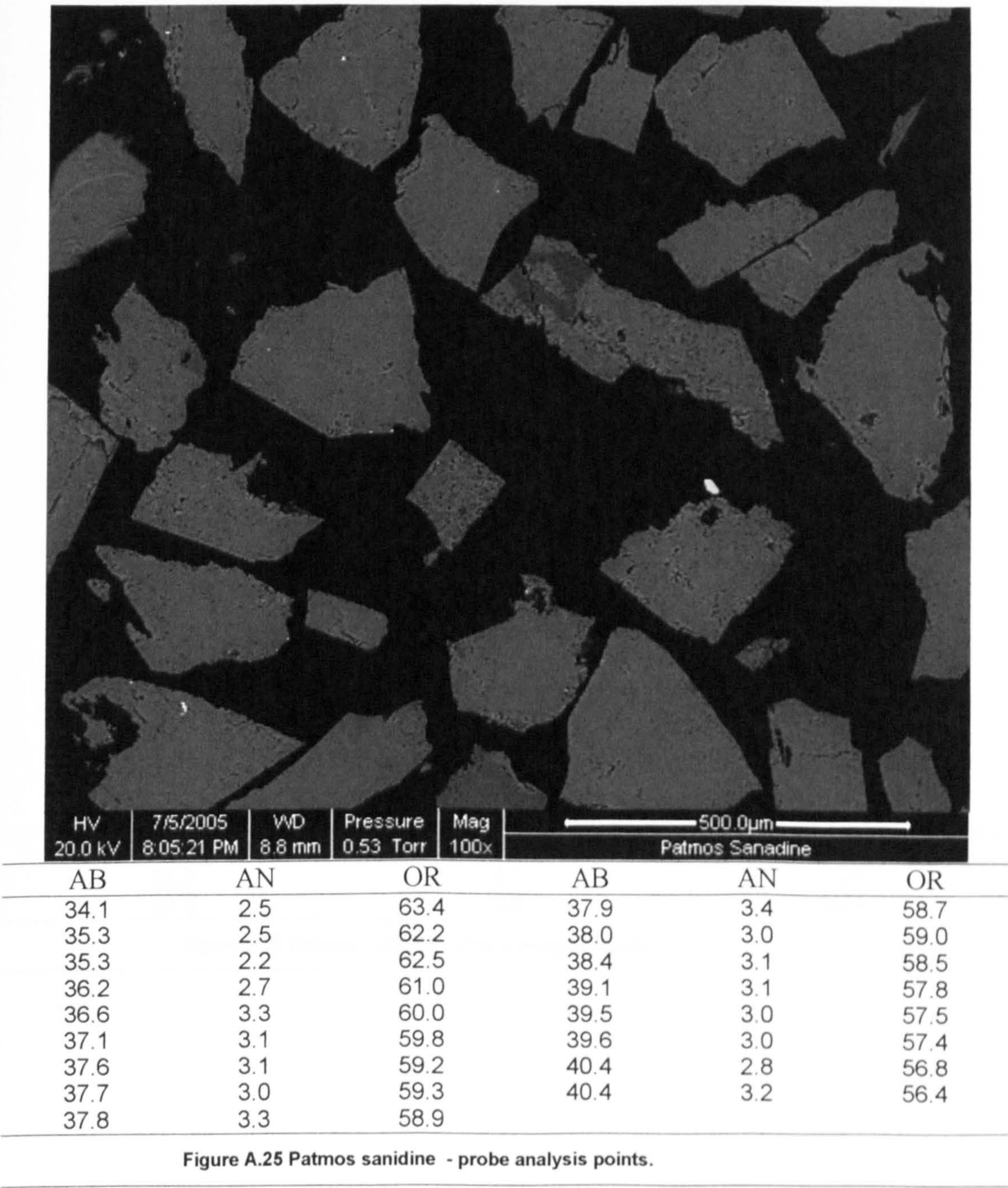
A.5 RUM TROCTOLITE PEGMATITE

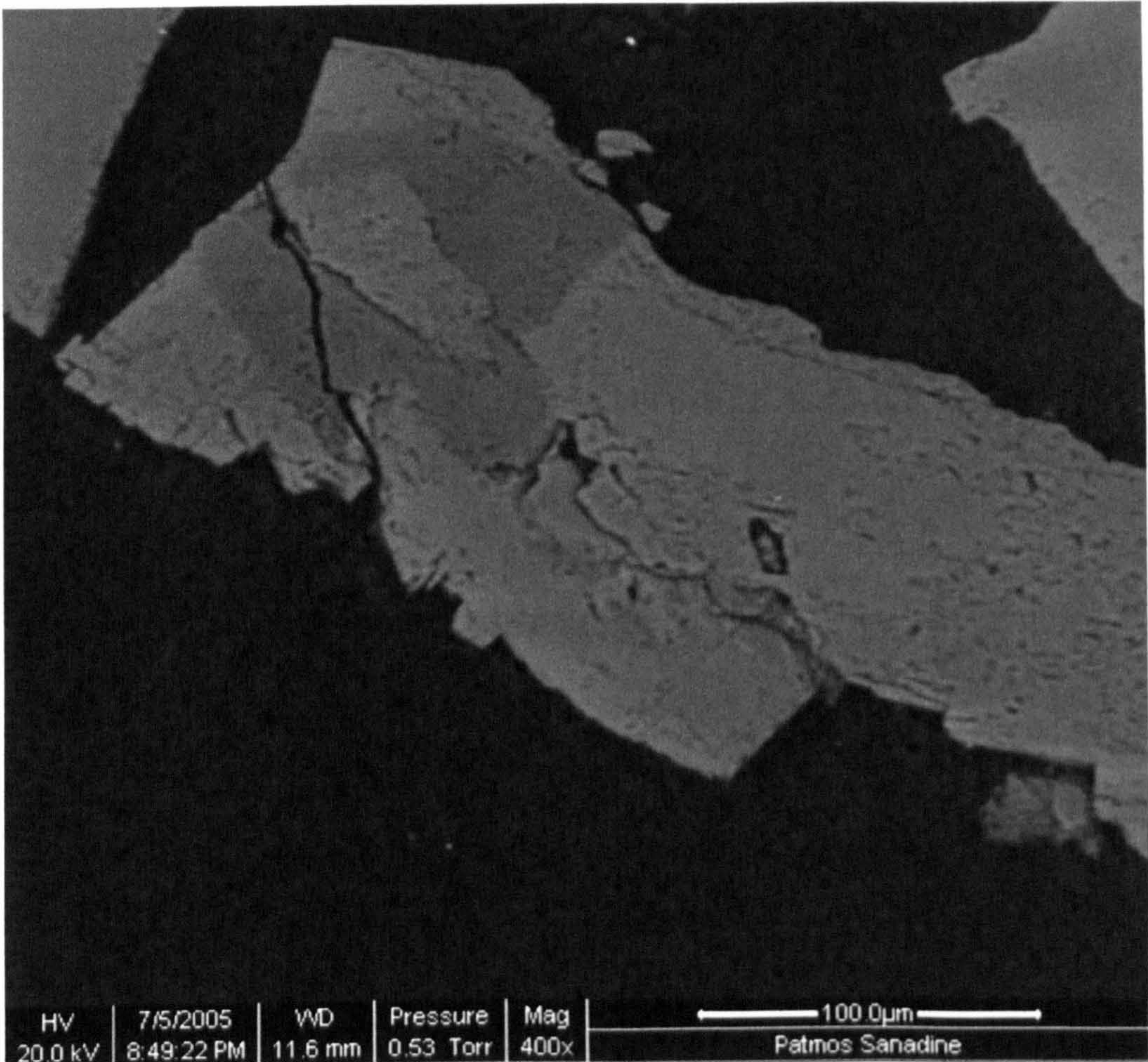
A.4.3 Rum Troctolite Pegmatite.



A.5 Extrusive Igneous Rocks.

A.5.1 Patmos Sanidine.



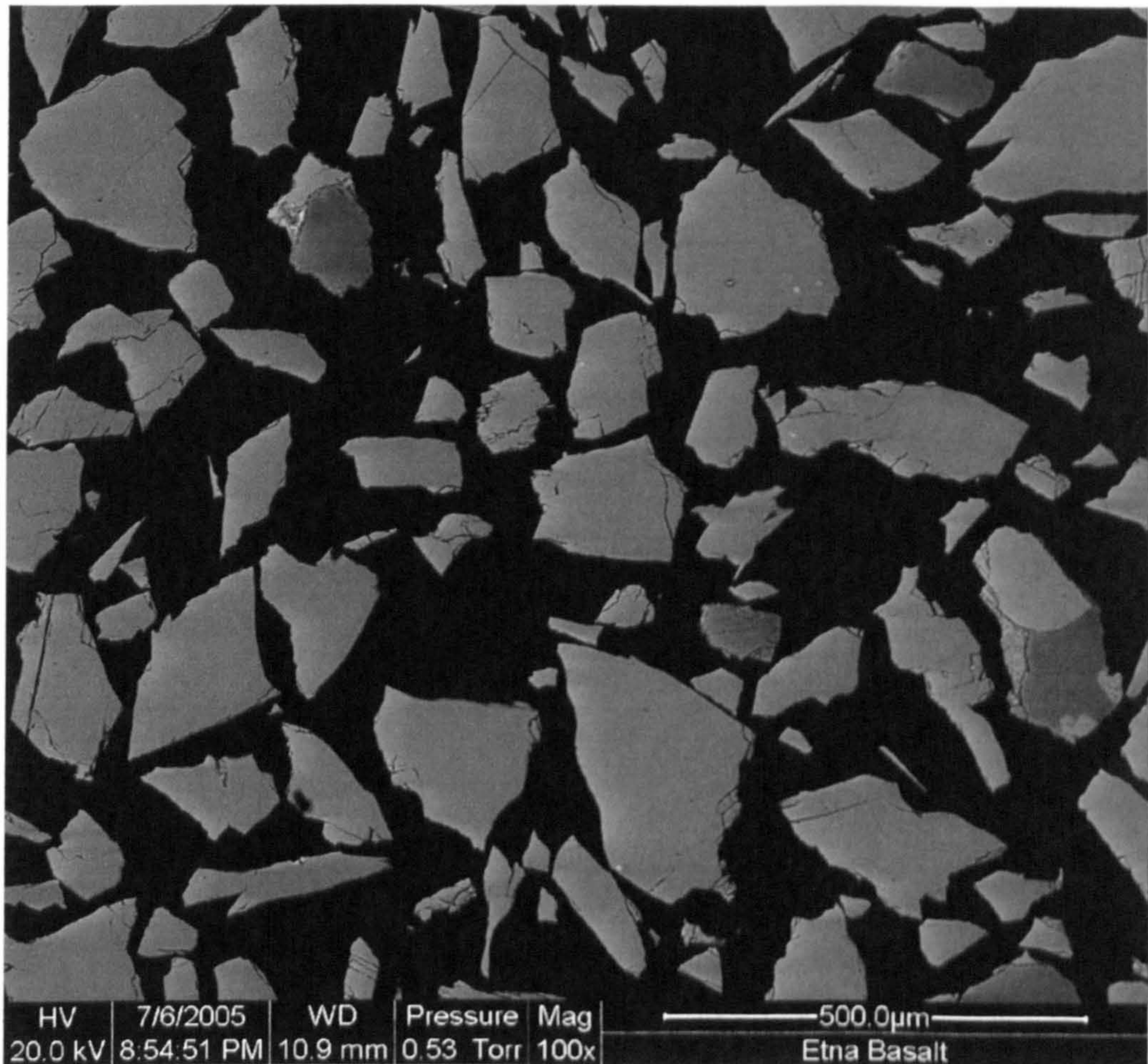


AB	AN	OR
36.5	3.1	60.3
40.5	3.0	56.5

Figure A.26 Patmos sanidine – probe analysis results.

A.5 Petrography and

A.5.2 Etna Basaltic Lava.



AB	AN	OR	AB	AN	OR
3.4	0.0	96.6	40.3	56.9	2.8
3.5	0.0	96.5	41.1	56.0	2.9
28.3	70.4	1.3	41.2	55.8	3.0
29.5	68.7	1.7	41.5	55.7	2.8
33.3	64.8	1.9	41.8	54.2	4.1
33.3	64.8	1.8	41.8	55.2	2.9
34.5	63.5	2.1	41.9	55.1	2.9
35.8	62.0	2.2	42.2	54.5	3.3
36.8	60.6	2.7	42.5	54.1	3.3
39.1	58.1	2.9	43.3	53.4	3.3
39.5	57.4	3.1	43.9	52.3	3.8
39.7	57.5	2.8	40.3	56.9	2.8

Figure A.27 Etna basaltic lava – probe analysis results.

A.6 Metamorphic Rocks.

A.6.1 Glen Tarbert Migmatite.

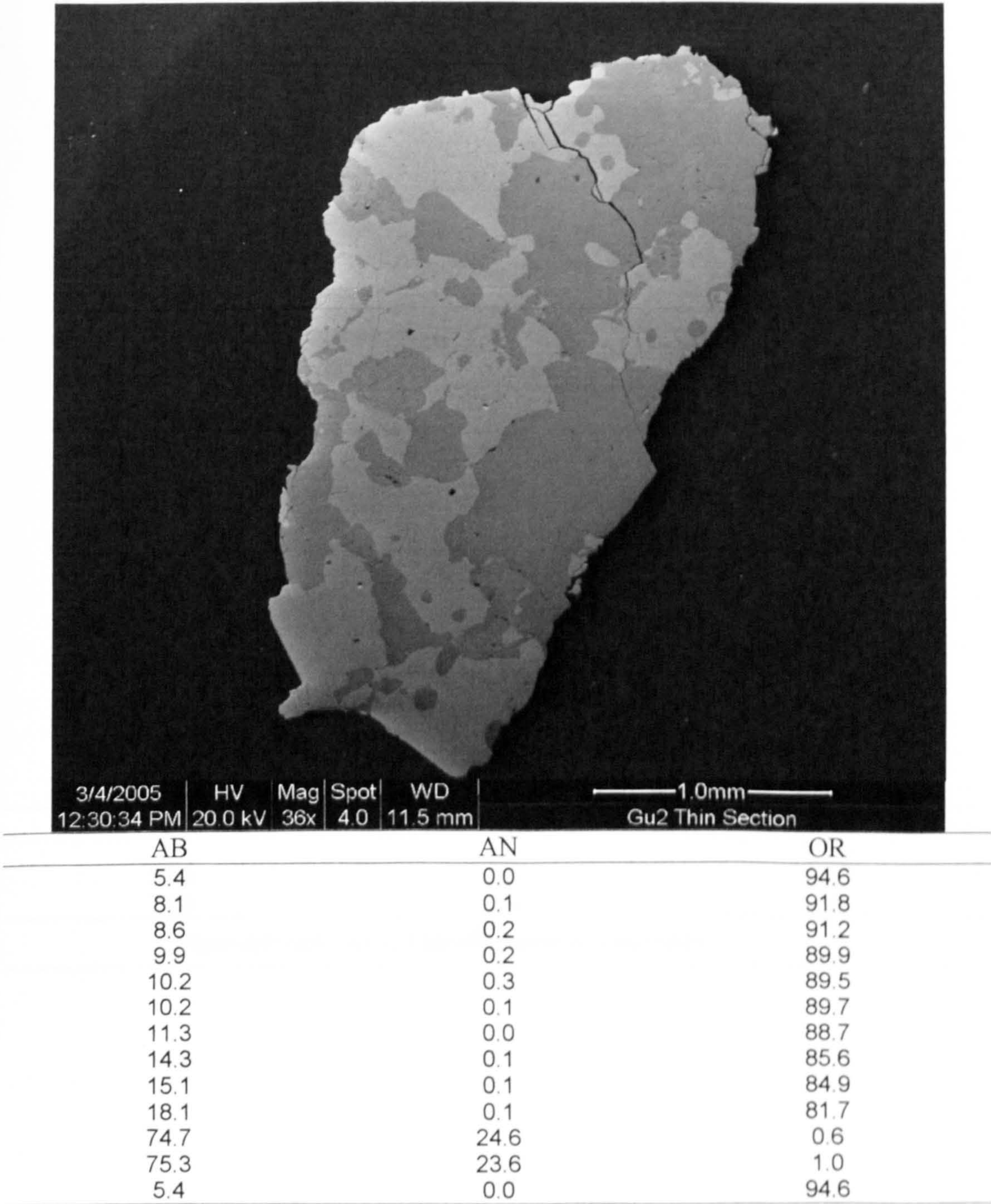
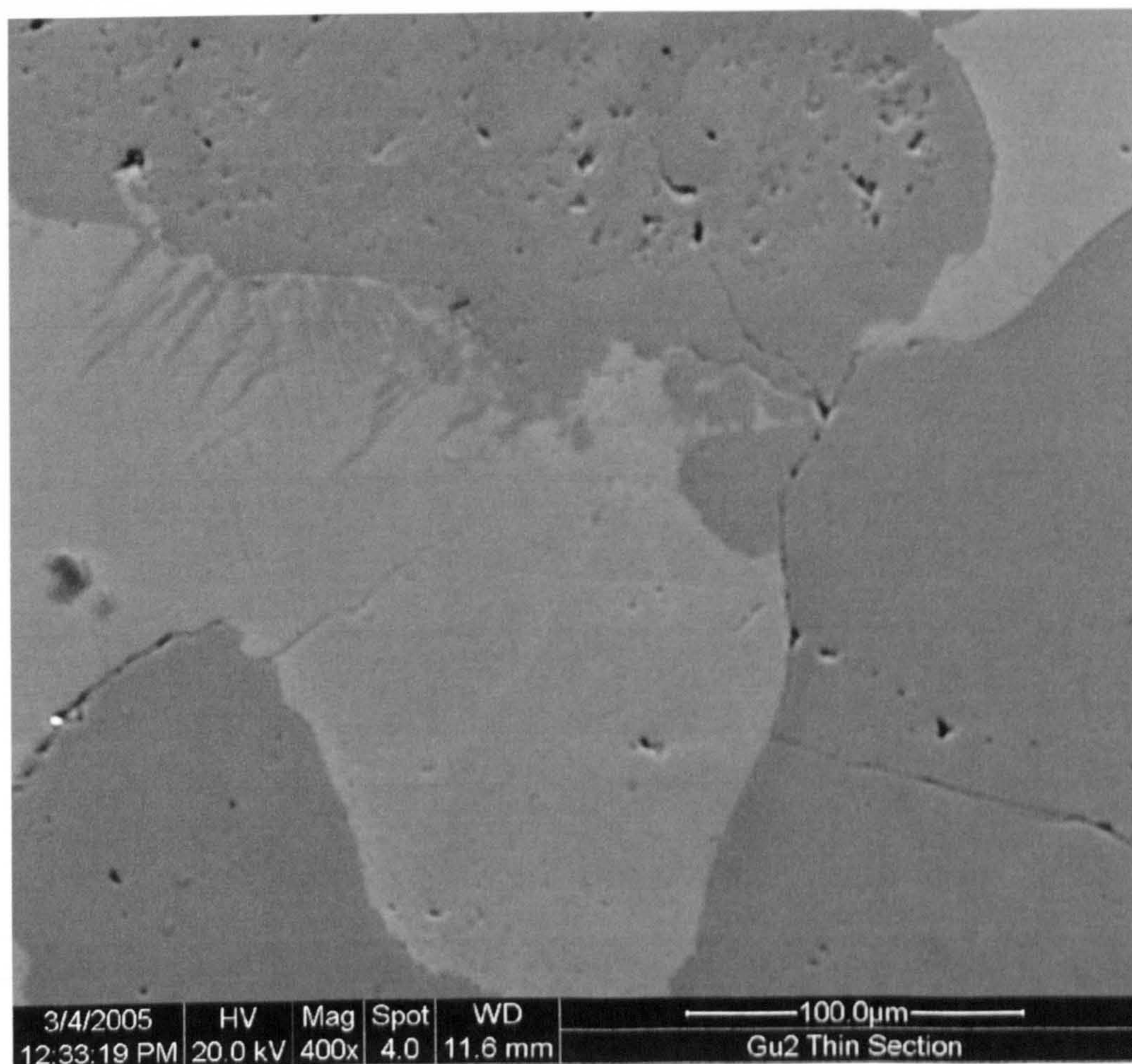


Figure A.28 Glen Tarbert migmatite – probe analysis results.



AB	AN	OR
8.5	0.0	91.5
59.9	0.8	39.3
74.8	24.4	0.8

Figure A.29 Glen Tarbert migmatite – probe analysis results.

A.6.2 Lewisian Gneiss.

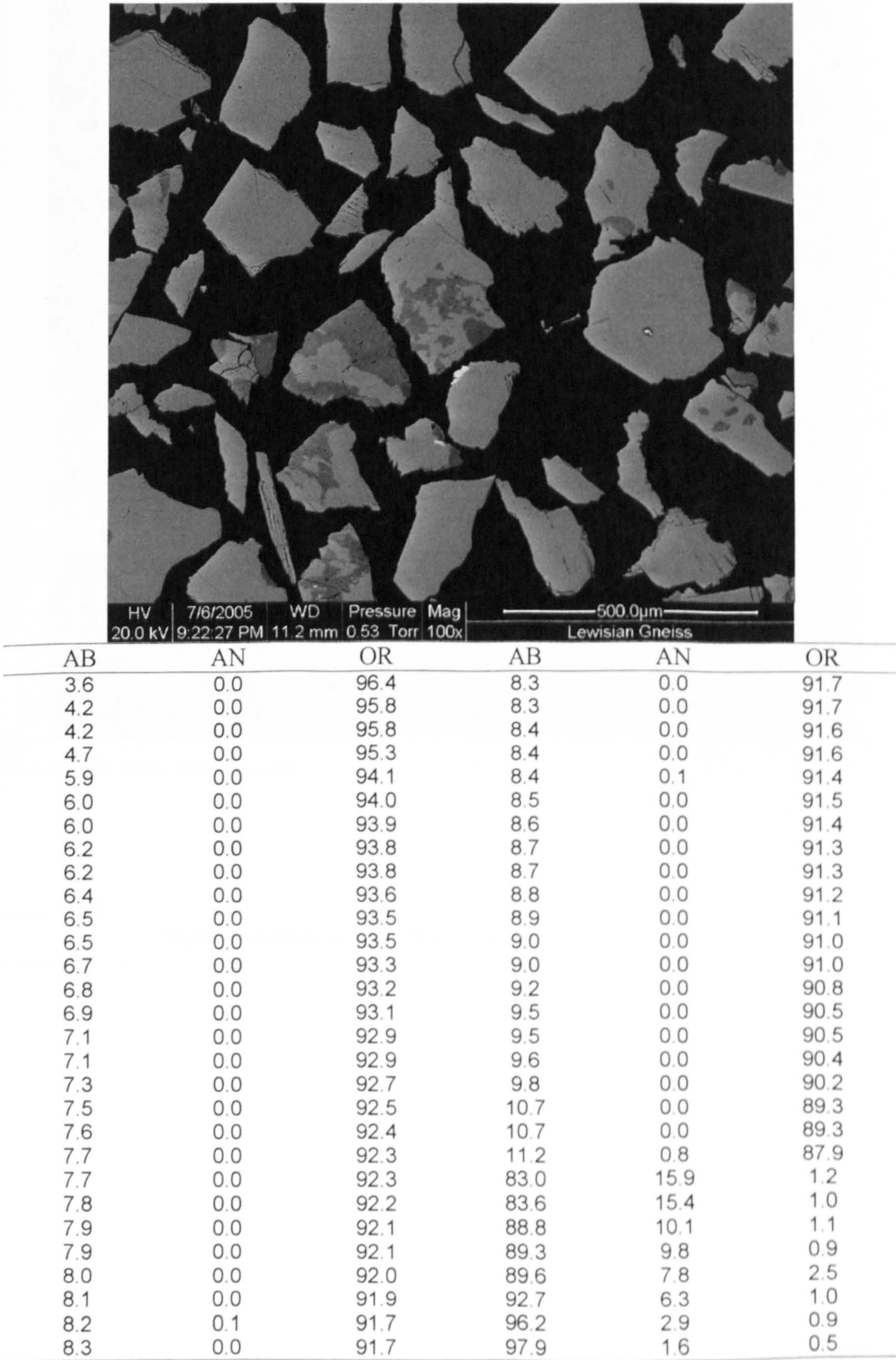


Figure A.30 Lewisian gneiss – probe analysis results.

A.31 Lewisian Gneiss

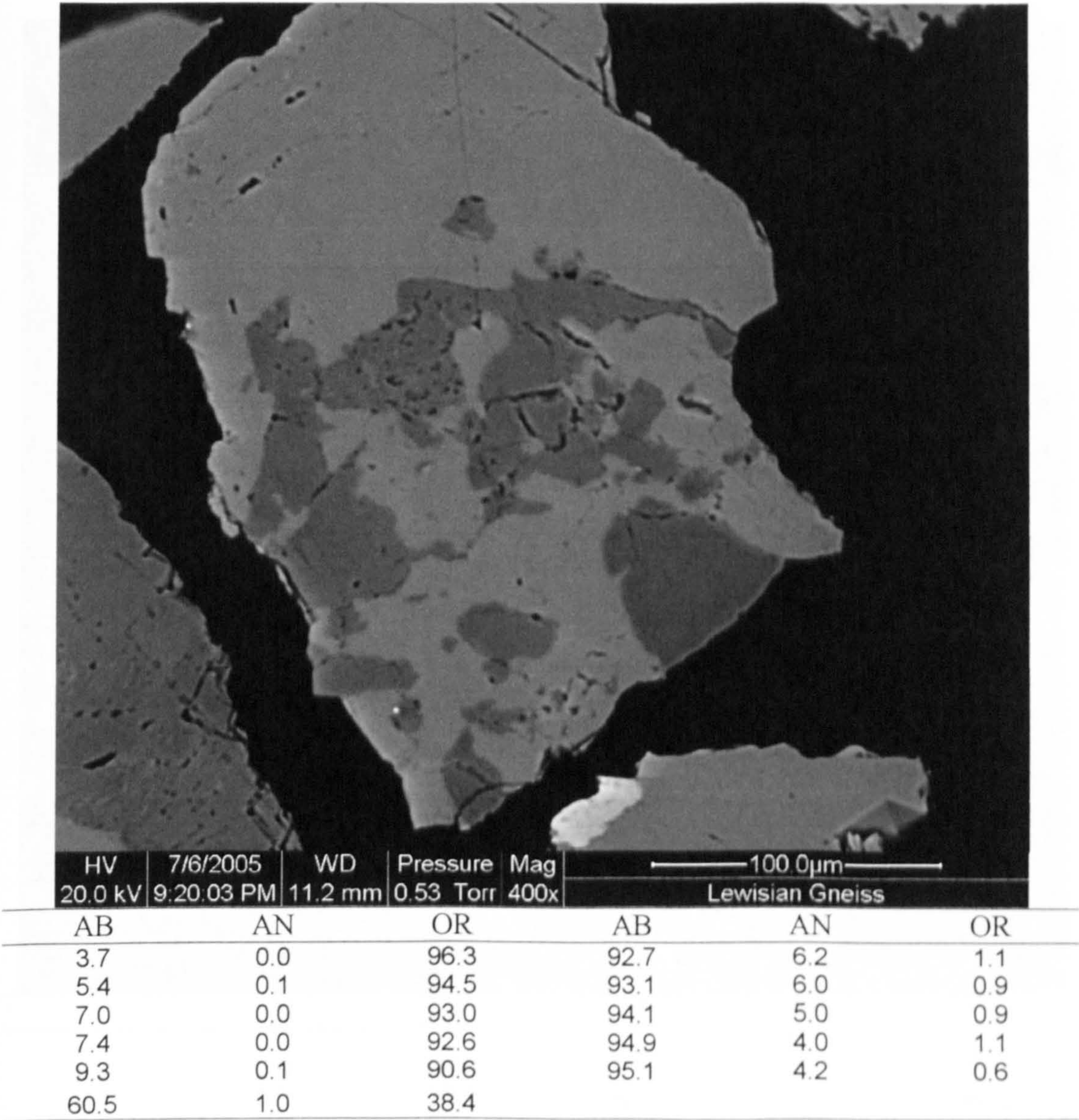


Figure A.31 Lewisian gneiss – probe analysis results.

A.6.3 Torridonian Hornblende Gneiss.

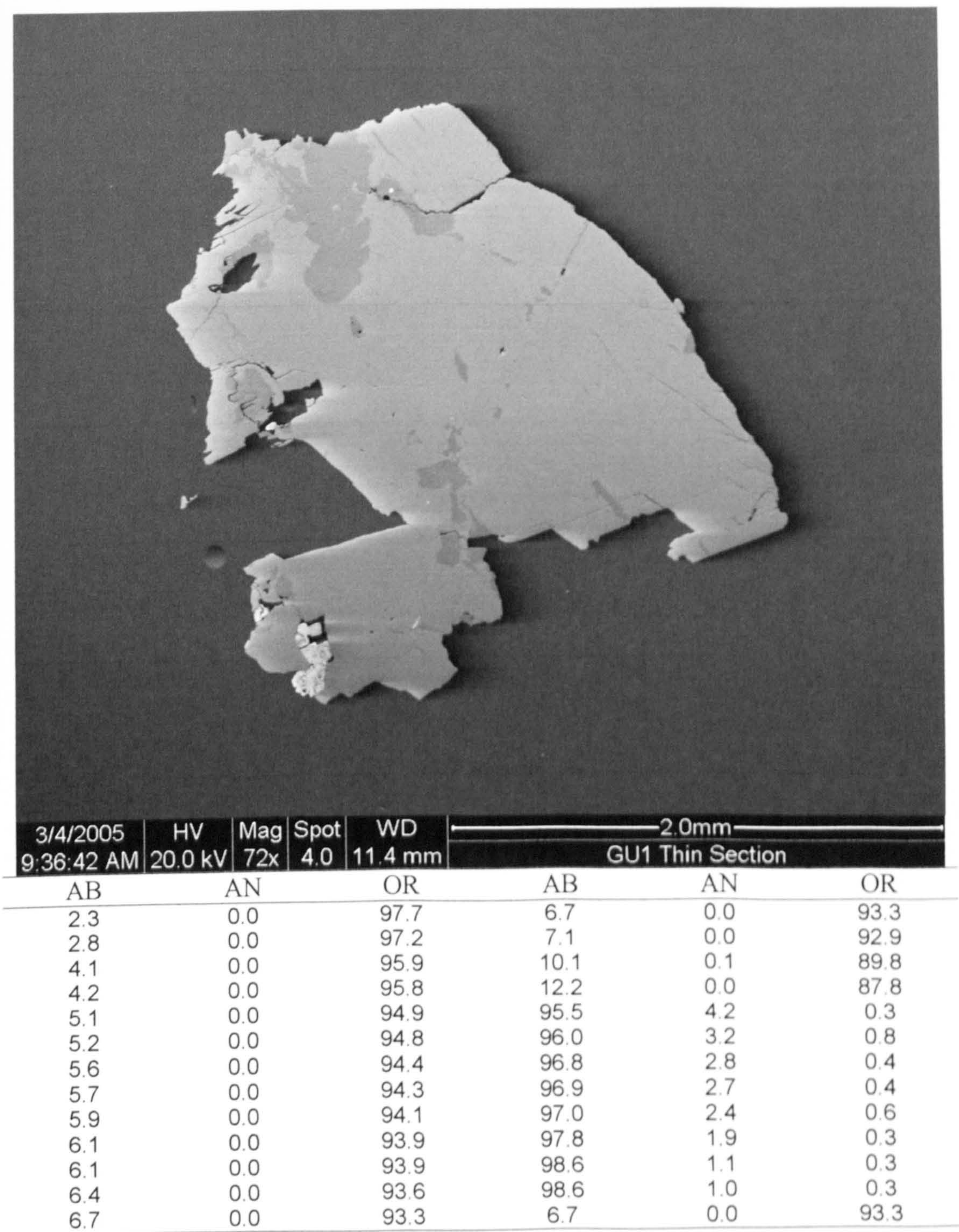


Figure A.32 Torridonian hornblende gneiss – probe analysis results.

A.7 Naturally Weathered Igneous Rocks.

A.7.1 Naturally Weathered Ballater Granite.

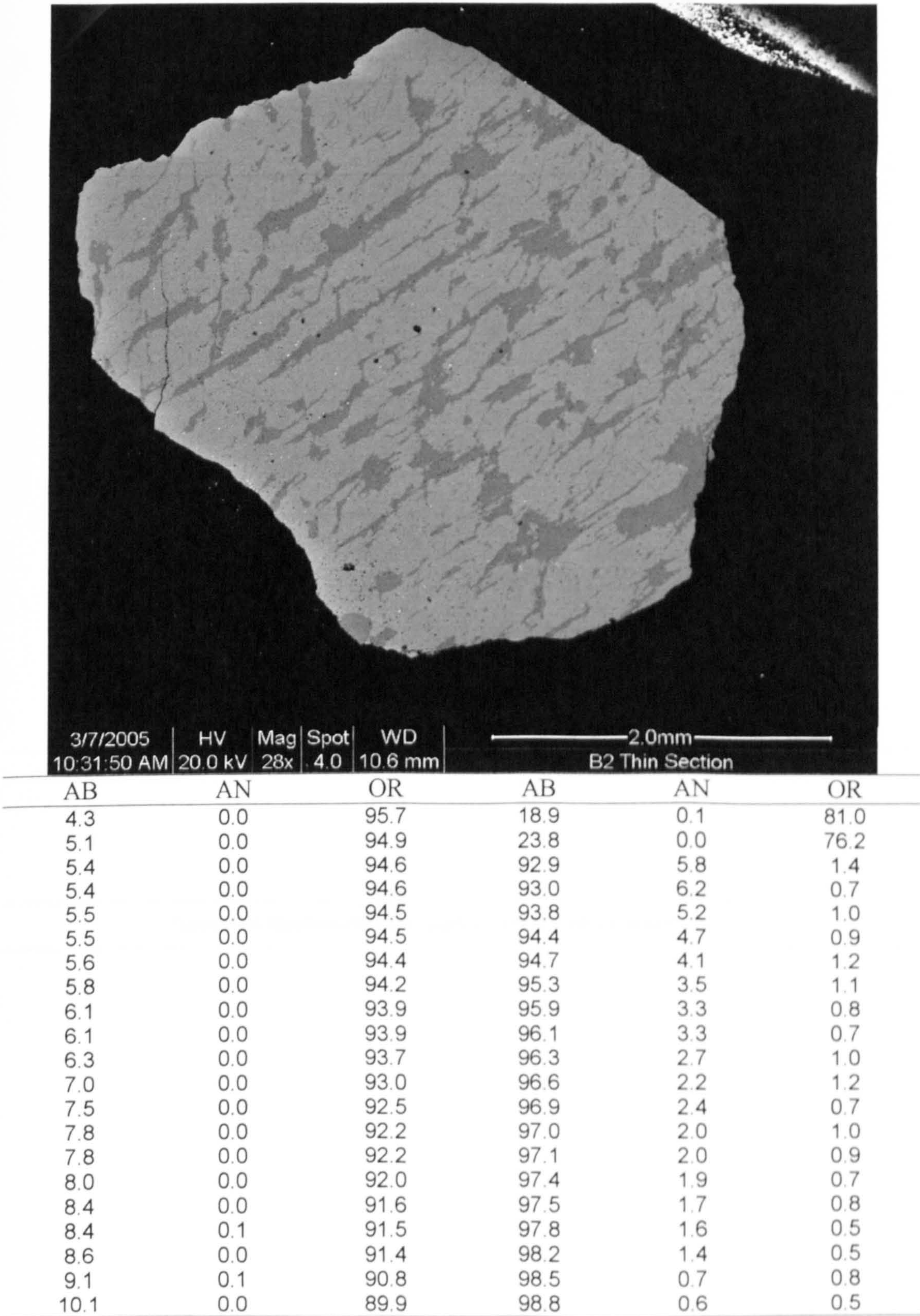


Figure A.33 Ballater granite – probe analysis results.

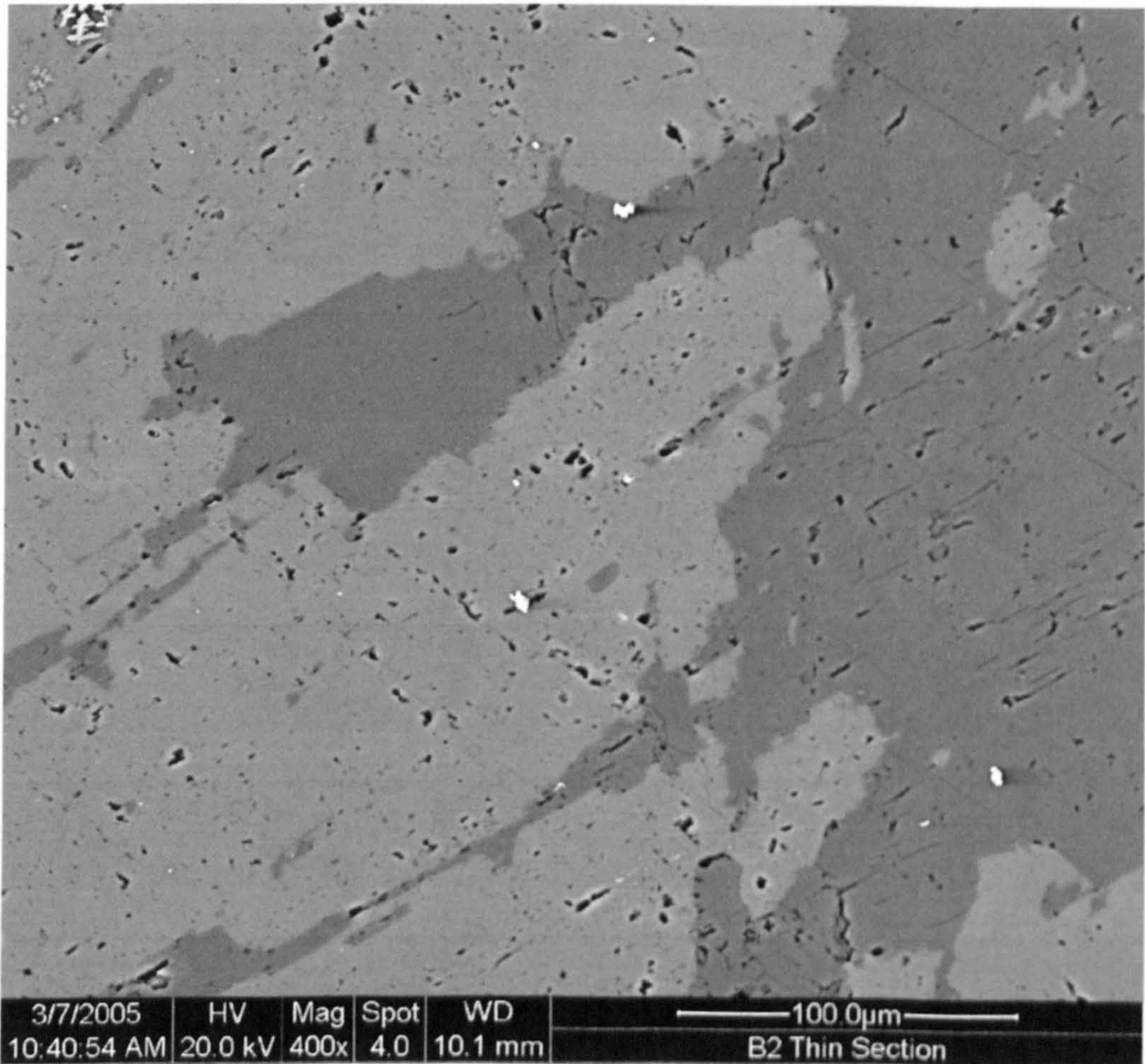
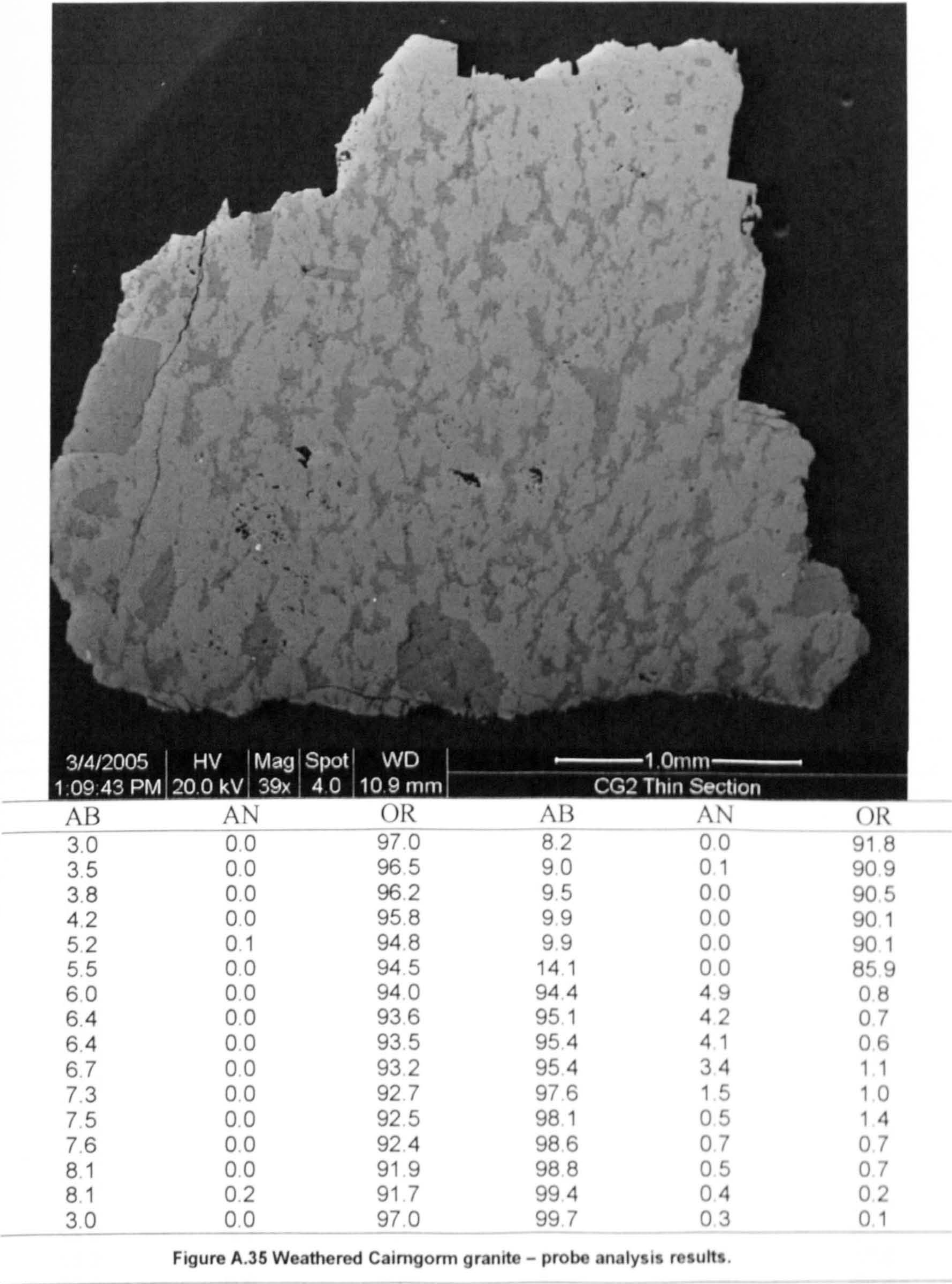


Figure A.34 Weathered Ballater granite – probe analysis points.

A.7.2 Naturally Weathered Cairngorm Granite.



A.5.1 Weathered Shap Granite

A.7.3 Naturally Weathered Shap Granite.

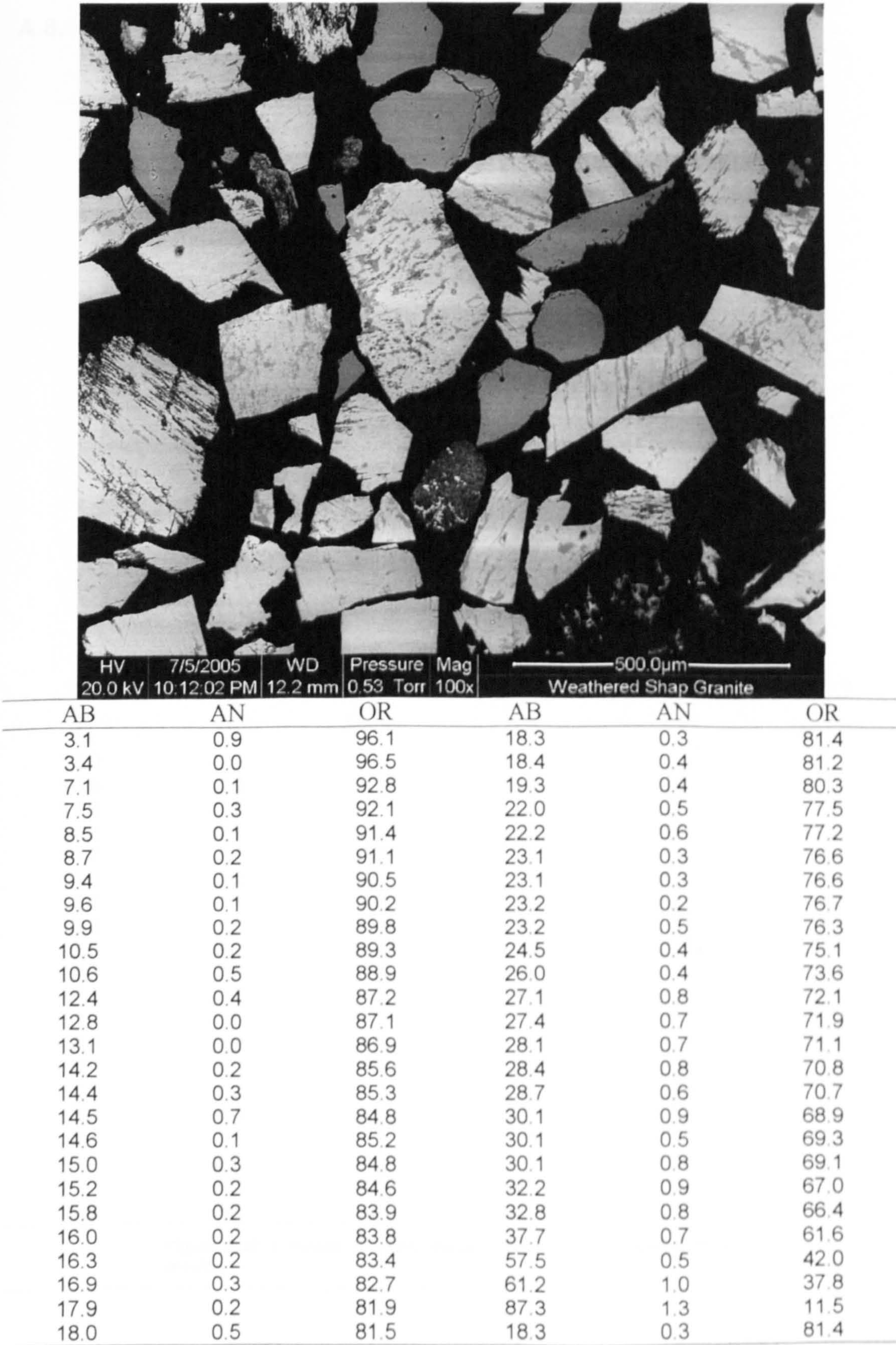


Figure A.36 Weathered Shap granite – probe analysis results.

A.8 HF Acid Etched Igneous and Associated Rocks.

A.8.1 Shap Granite.

A.8.1.1 1 Minute HF Acid Etched.

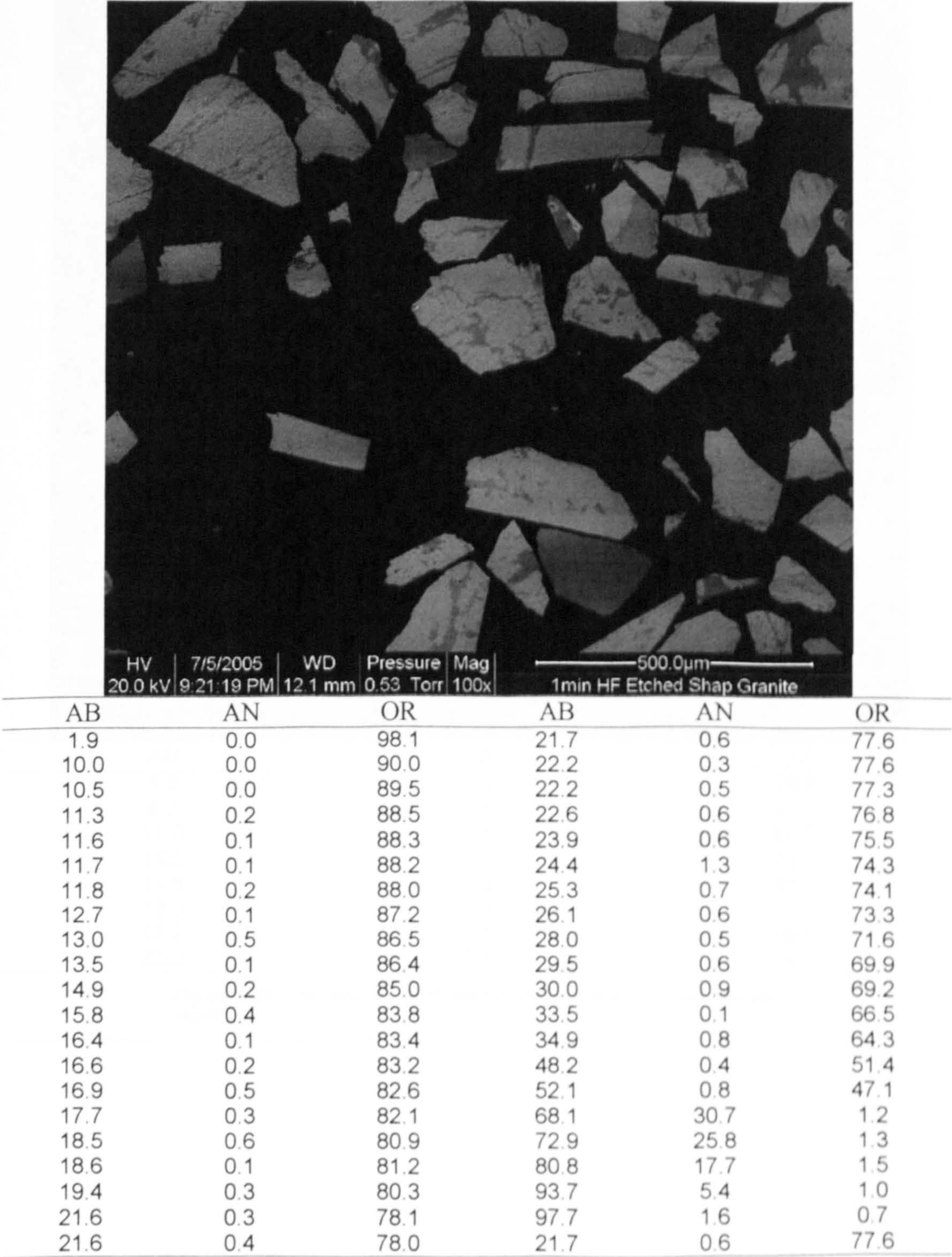
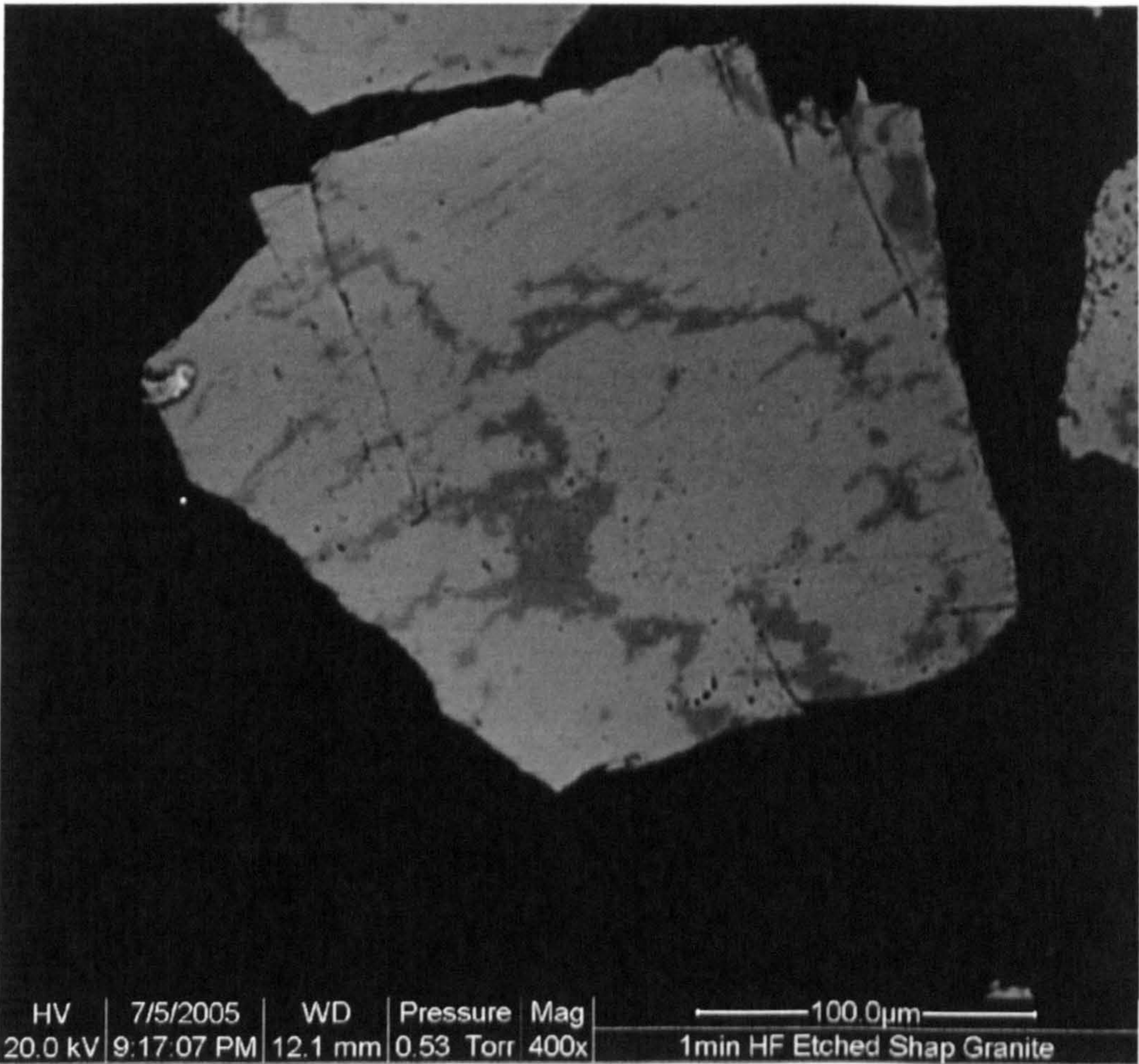


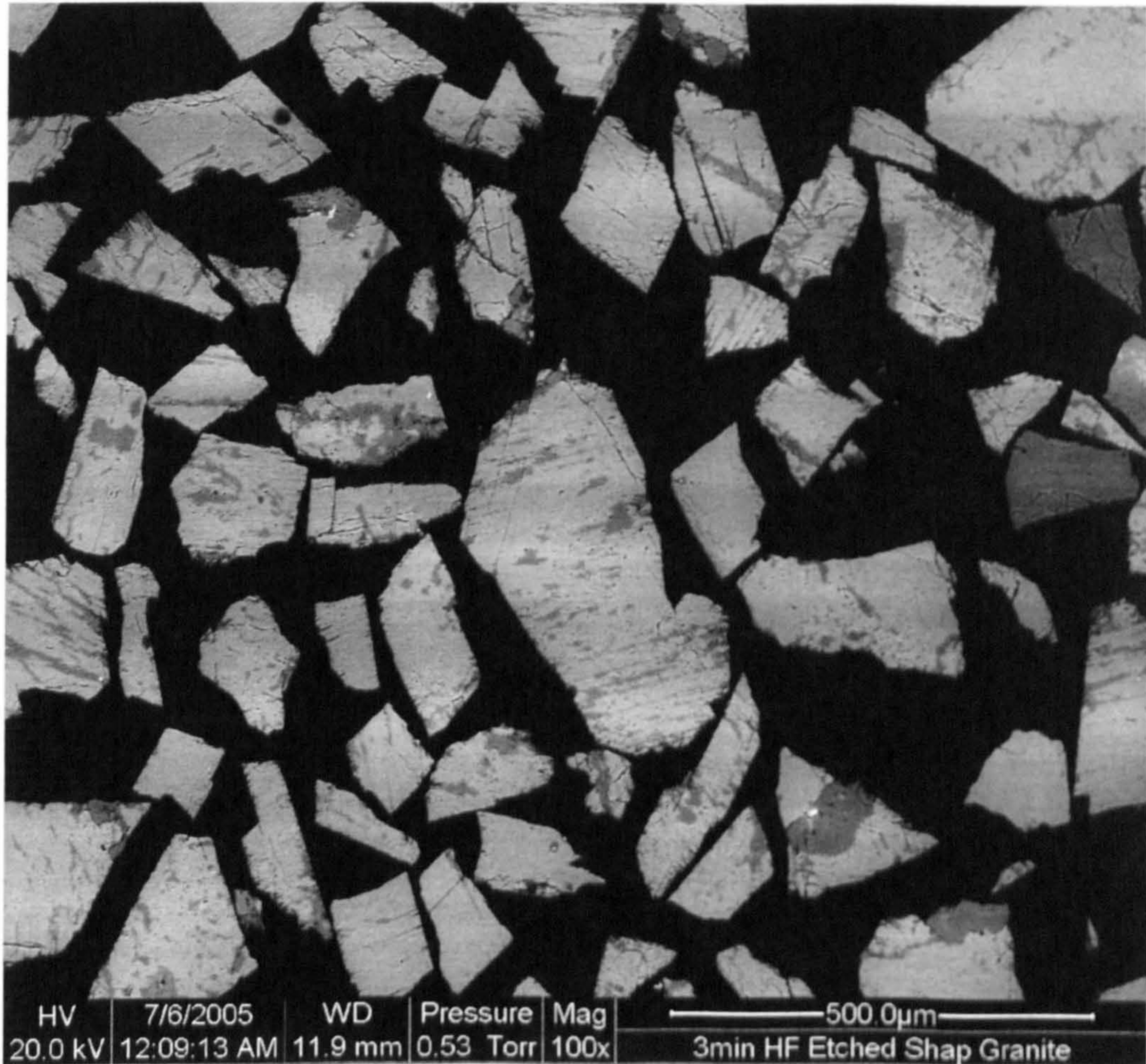
Figure A.37 1 minute HF acid etched shap granite – probe analysis results.



AB	AN	OR
5.8	0.6	93.6
9.2	0.1	90.7
10.0	0.5	89.5
14.0	0.3	85.7
14.8	0.0	85.2
18.0	0.2	81.9
18.2	1.3	80.5
25.3	0.6	74.1

Figure A.38 1 minute HF acid etched shap granite – probe analysis results.

A.8.1.2 3 Minutes HF Acid Etched.



AB	AN	OR	AB	AN	OR
8.2	0.1	91.7	20.2	0.4	79.4
9.8	0.2	90.0	23.1	0.6	76.4
10.7	0.1	89.2	25.1	0.5	74.4
11.3	0.2	88.5	25.4	0.6	73.9
11.8	0.3	87.9	25.7	0.5	73.8
12.6	0.3	87.1	25.8	0.7	73.5
12.7	0.2	87.1	26.0	0.2	73.7
12.7	0.0	87.2	26.0	0.7	73.2
13.0	0.1	86.9	26.4	0.6	72.9
13.5	0.4	86.1	27.6	0.9	71.5
15.1	0.3	84.6	28.7	0.9	70.3
15.6	0.0	84.4	29.2	0.5	70.4
16.2	0.2	83.6	29.5	0.6	70.0
16.6	0.5	83.0	29.5	1.0	69.5
16.7	0.1	83.2	30.9	0.6	68.5
16.9	0.2	82.9	32.0	0.2	67.8
17.3	0.4	82.3	44.1	0.5	55.4
17.4	0.1	82.5	59.6	1.7	38.7
17.8	0.4	81.8	70.3	28.0	1.7
18.0	0.2	81.9	96.8	0.3	2.8
18.3	0.4	81.3	98.1	0.9	1.0
18.7	0.4	80.9	20.2	0.4	79.4

Figure A.39 3 minutes HF acid etched Shap granite - probe analysis results.

A.8.1.3 15 Minutes HF Acid Etched.

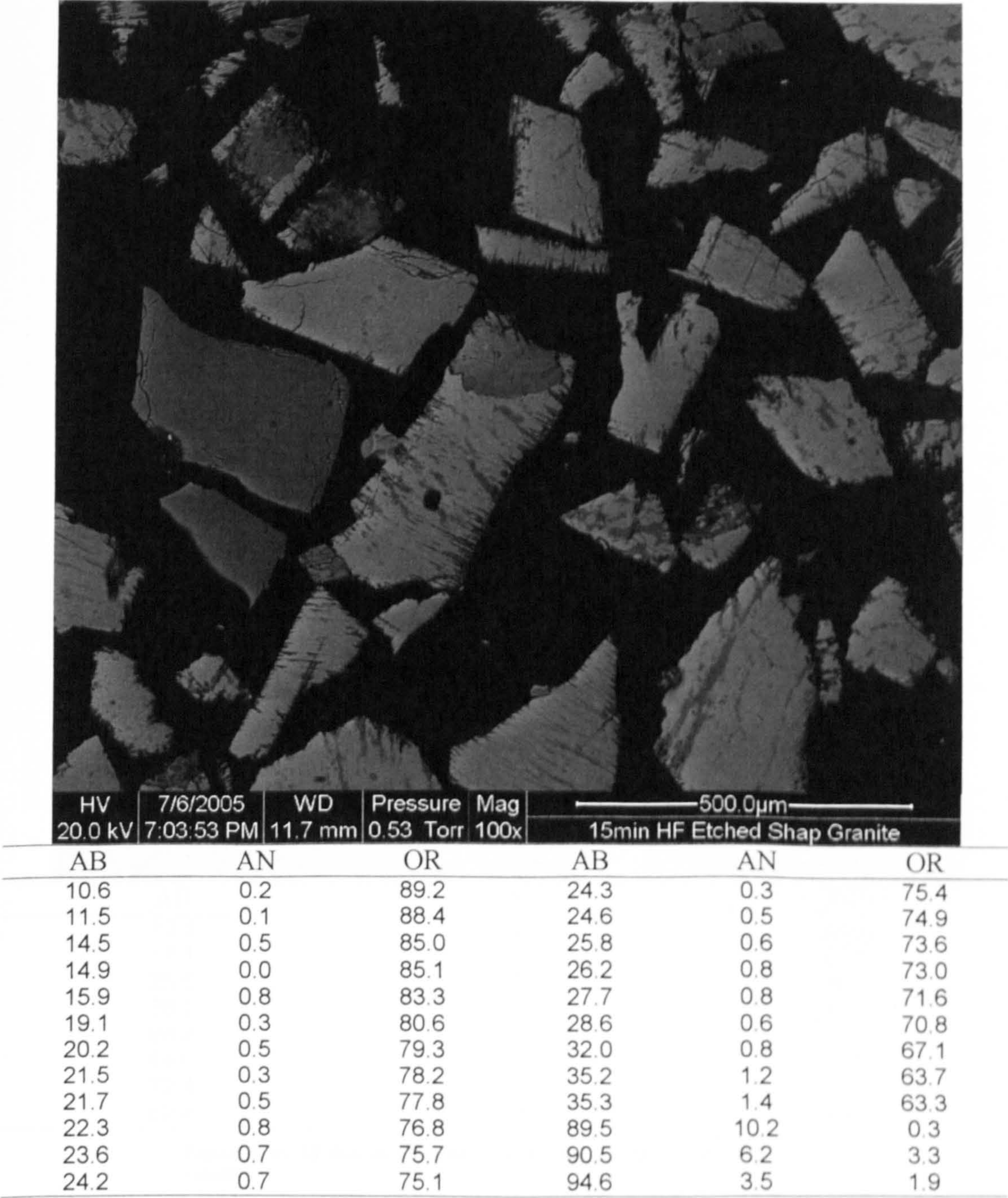
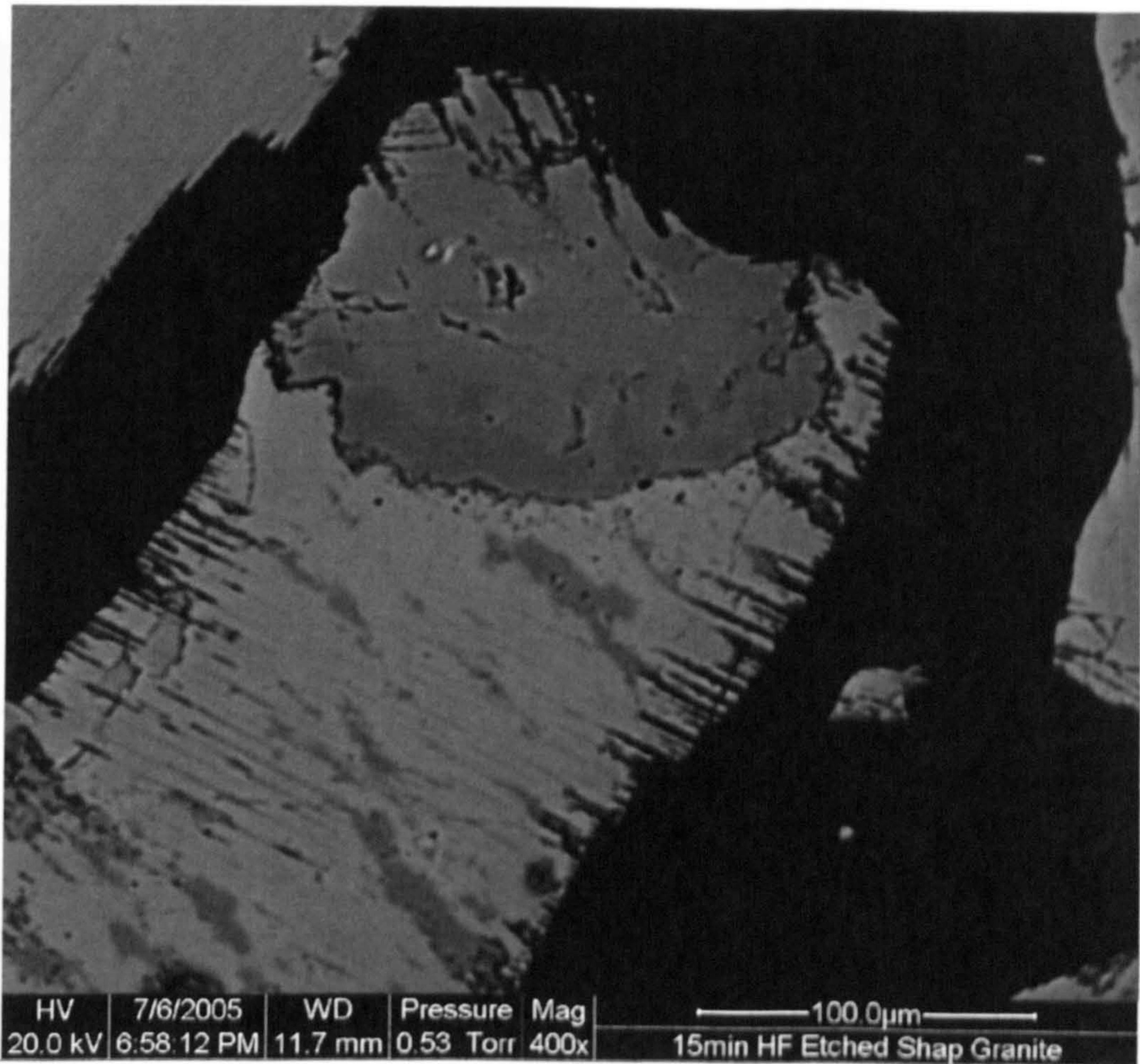


Figure A.40 15 minute HF acid etched Shap granite – probe analysis results.

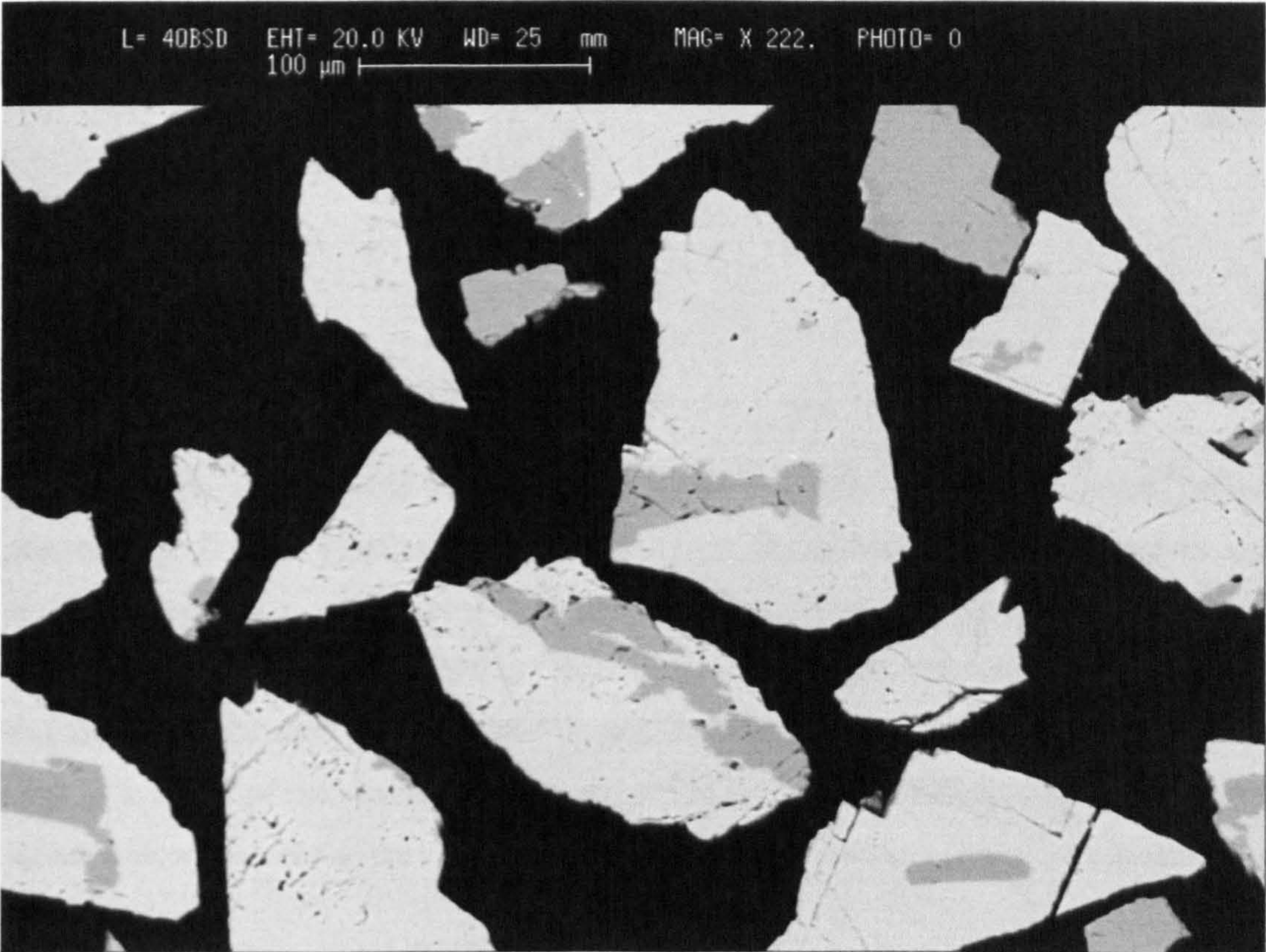


AB	AN	OR
13.3	0.2	86.5
17.1	0.4	82.5
25.0	0.4	74.6
38.7	0.8	60.5
64.4	34.8	0.8
64.6	1.5	34.0
72.4	26.2	1.4
82.4	16.1	1.5

Figure A.41 15 minute HF acid etched Shap granite – probe analysis results.

A.9 Laboratory Standard.

A.9.1 F1.



AB	AN	OR	AB	AN	OR
3.5	0.0	96.5	7.4	0.0	92.6
4.0	0.0	96.0	8.4	0.0	91.6
4.4	0.0	95.6	8.6	0.0	91.4
4.9	0.0	95.1	28.3	0.0	71.7
5.2	0.0	94.8	34.0	0.2	65.8
5.4	0.0	94.6	58.3	0.8	40.9
5.5	0.0	94.5	80.7	1.1	18.1
5.6	0.0	94.4	87.9	11.6	0.5
5.7	0.0	94.3	88.1	11.2	0.6
5.9	0.0	94.1	88.2	10.8	1.0
5.9	0.0	94.1	89.7	2.8	7.5
5.9	0.0	94.1	89.7	0.6	9.8
6.0	0.0	94.0	92.8	6.6	0.5
6.2	0.0	93.8	96.0	0.9	3.1
6.3	0.0	93.7	96.0	0.2	3.8
6.3	0.0	93.7	96.7	2.4	0.9
6.4	0.1	93.5	97.5	2.1	0.4
6.9	0.0	93.1	98.8	0.6	0.6
7.3	0.0	92.7	7.4	0.0	92.6
7.3	0.0	92.7			

Figure A.42 F1 – probe analysis results.

B

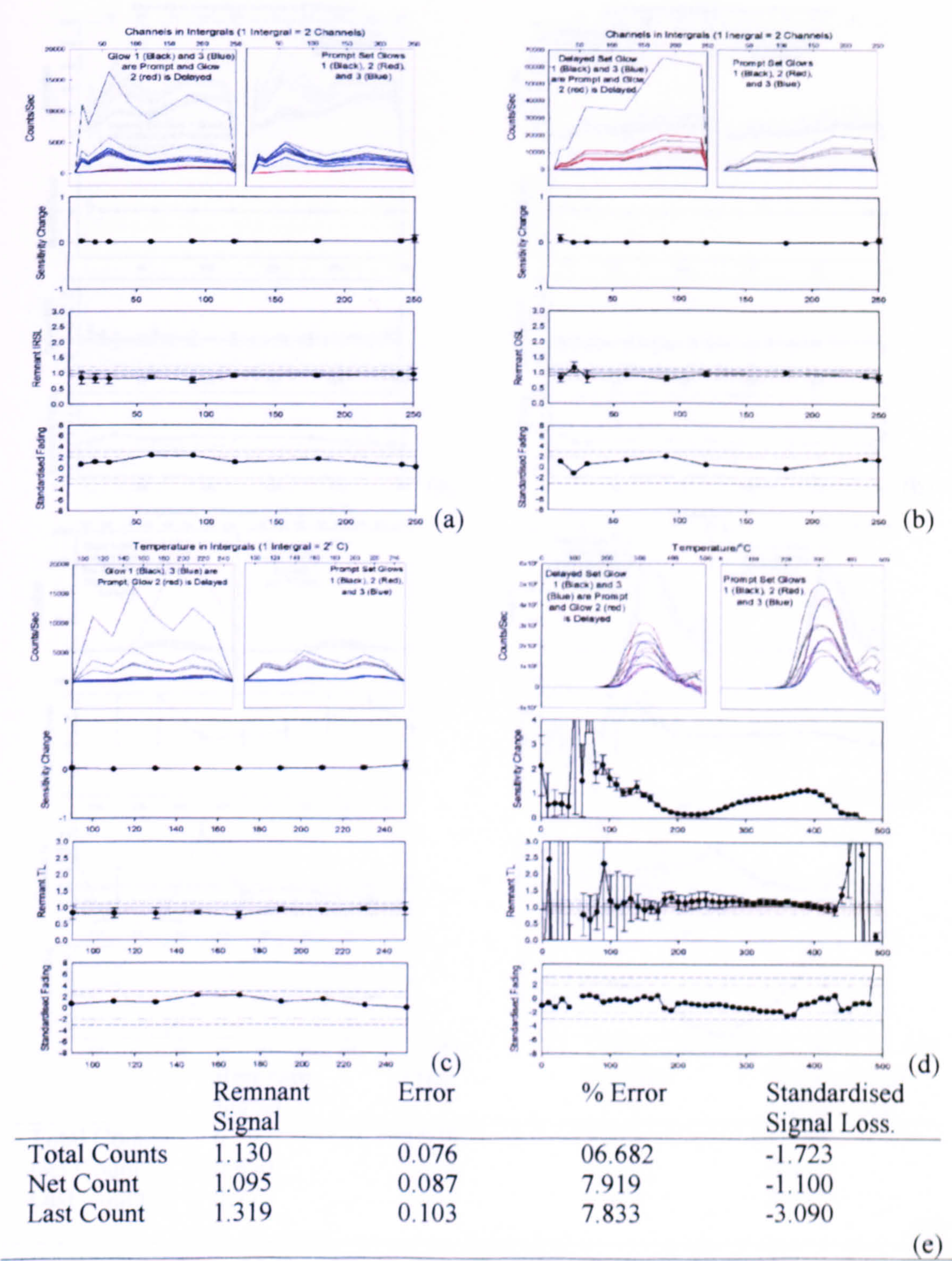
Appendix B.

B.1 Introduction.

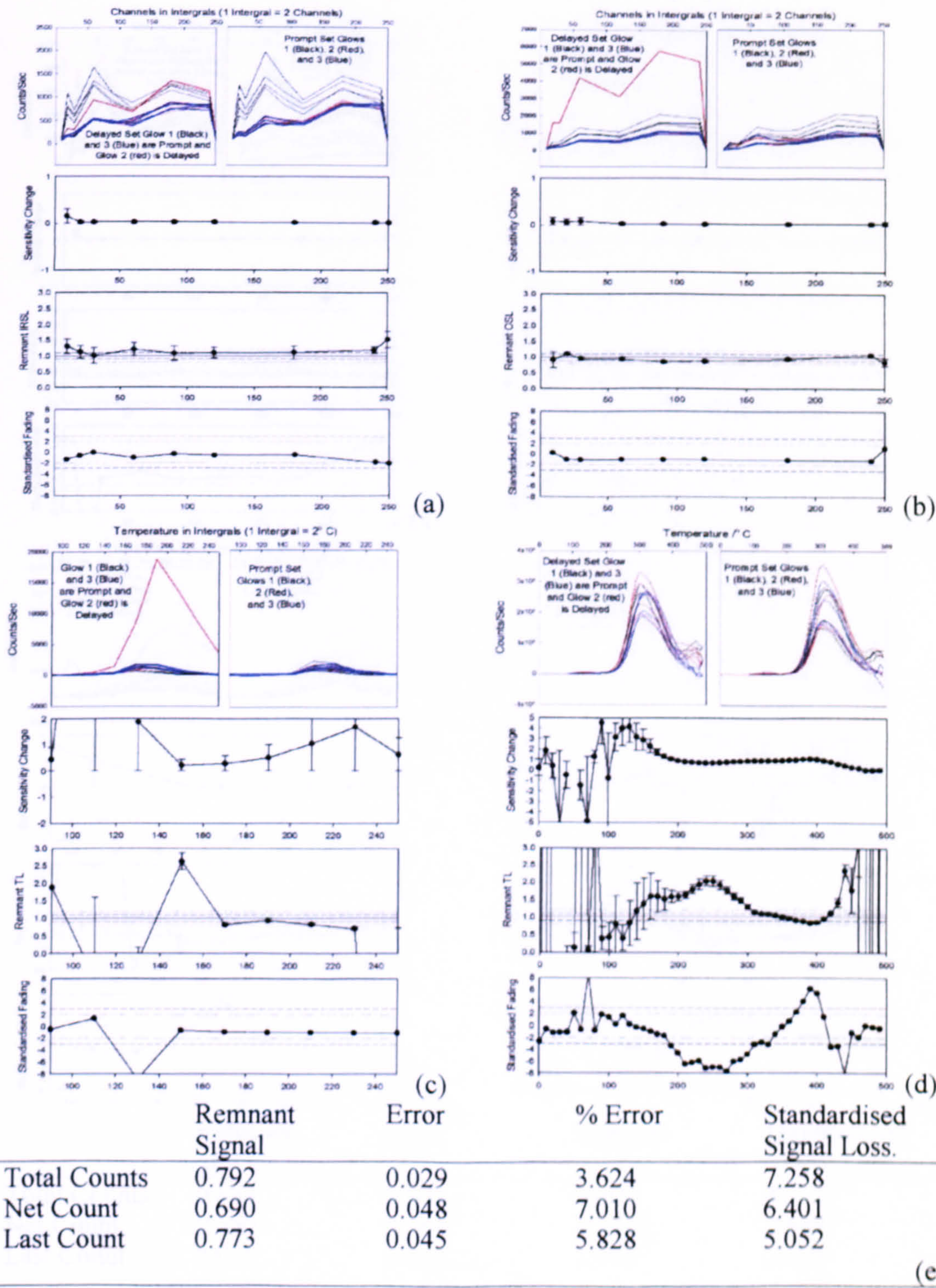
In this section luminescence results from each of the samples and their related subsets are presented. Each figure contains the results obtained by the individual stimulation sources and these are subdivided into a set of graphs. The individual measurements of each disc are plotted as curves of the integrated channels (not glow curves or shine down curves), one presenting the prompt group and the second the delayed. Below that the sensitivity change, remnant signal and its standardised error as averages of each integral are presented. The data for the manual PPSL is tabulated for the summed glows, presenting the total counts the net count and the last count of each measurement.

B.2 Plutonic Igneous and Associated Rocks.

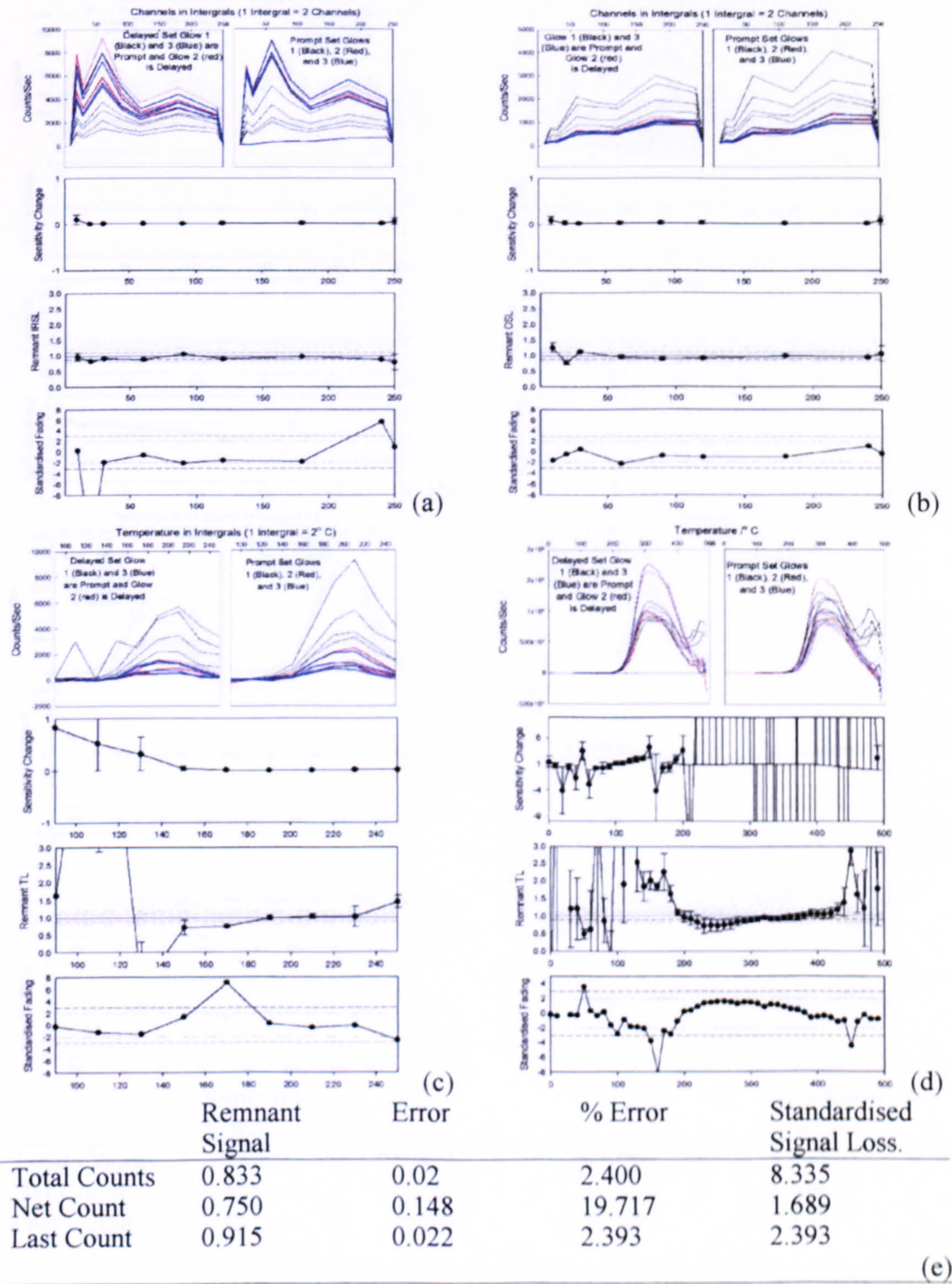
B.2.1 Arran Granite.



B.2.2 Balator Granite



B.2.2 Ballater Granite.



B.2.3 Colmorm Grains

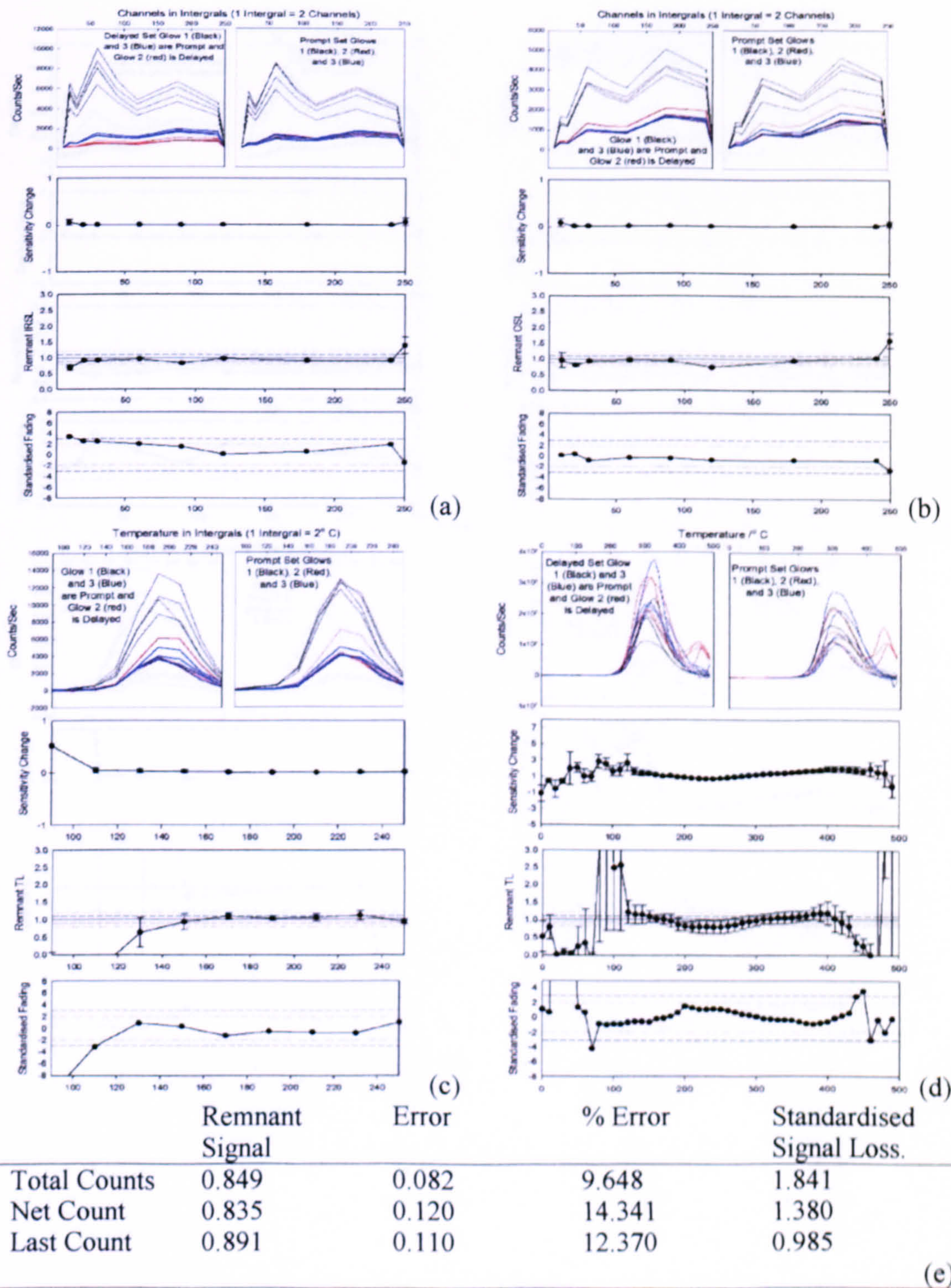


Figure B.4 Risø IRSL (a), Risø OSL (b), Risø TL (c), Manual TL (d), Manual PPSL (e) for the Ballater granite A₁₀P₈₀Q₁₀ (2.62-2.74g/m³ SPT fraction).

B.2.3 Cairngorm Granite.

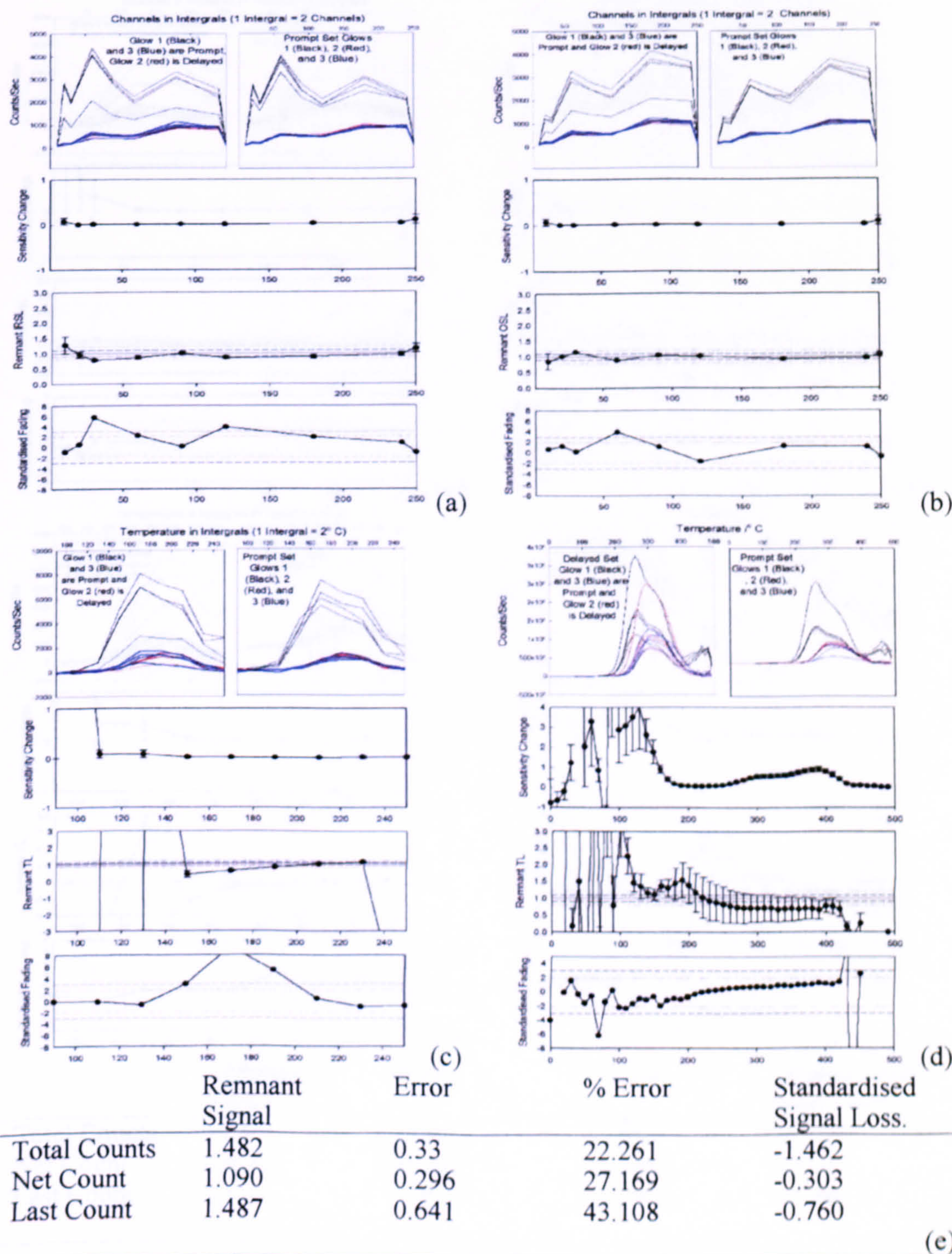


Figure B.5 Risø IRSI (a), Risø OSL (b), Risø TL (c), Manual TL (d), Manual PPSI (e) for the Cairngorm granite A₆₀P₃₈Q₂ (2.52-2.58g/m³ SPT fraction).

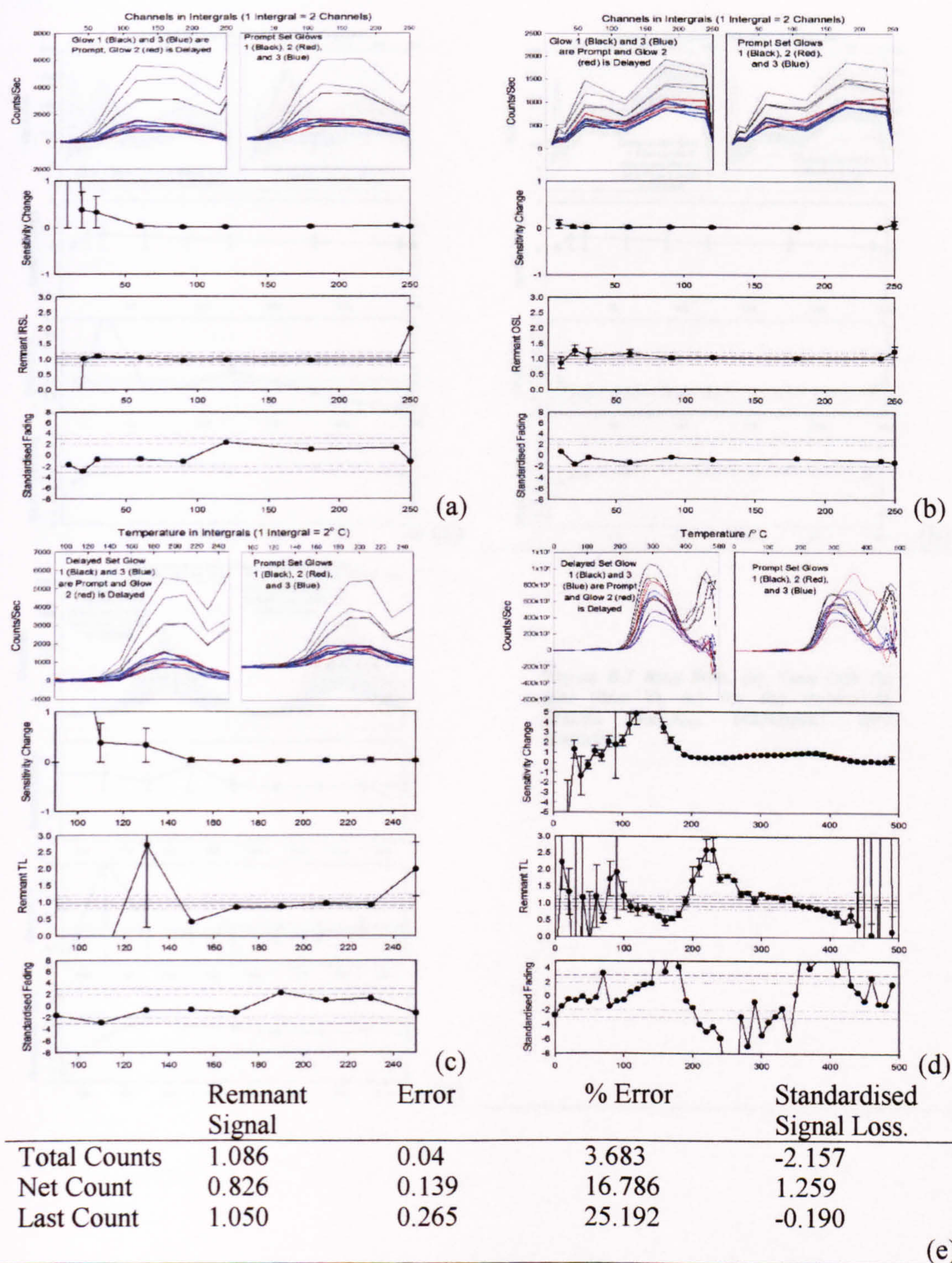


Figure B.6 Risø IRSI (a), Risø OSL (b), Risø TL (c), Manual TL (d), Manual PPSI (e) for the Cairngorm granite A₅P₅Q₉₀ (2.62-2.74g/m³ SPT fraction).

B.2.4 Helmsdale Granite.

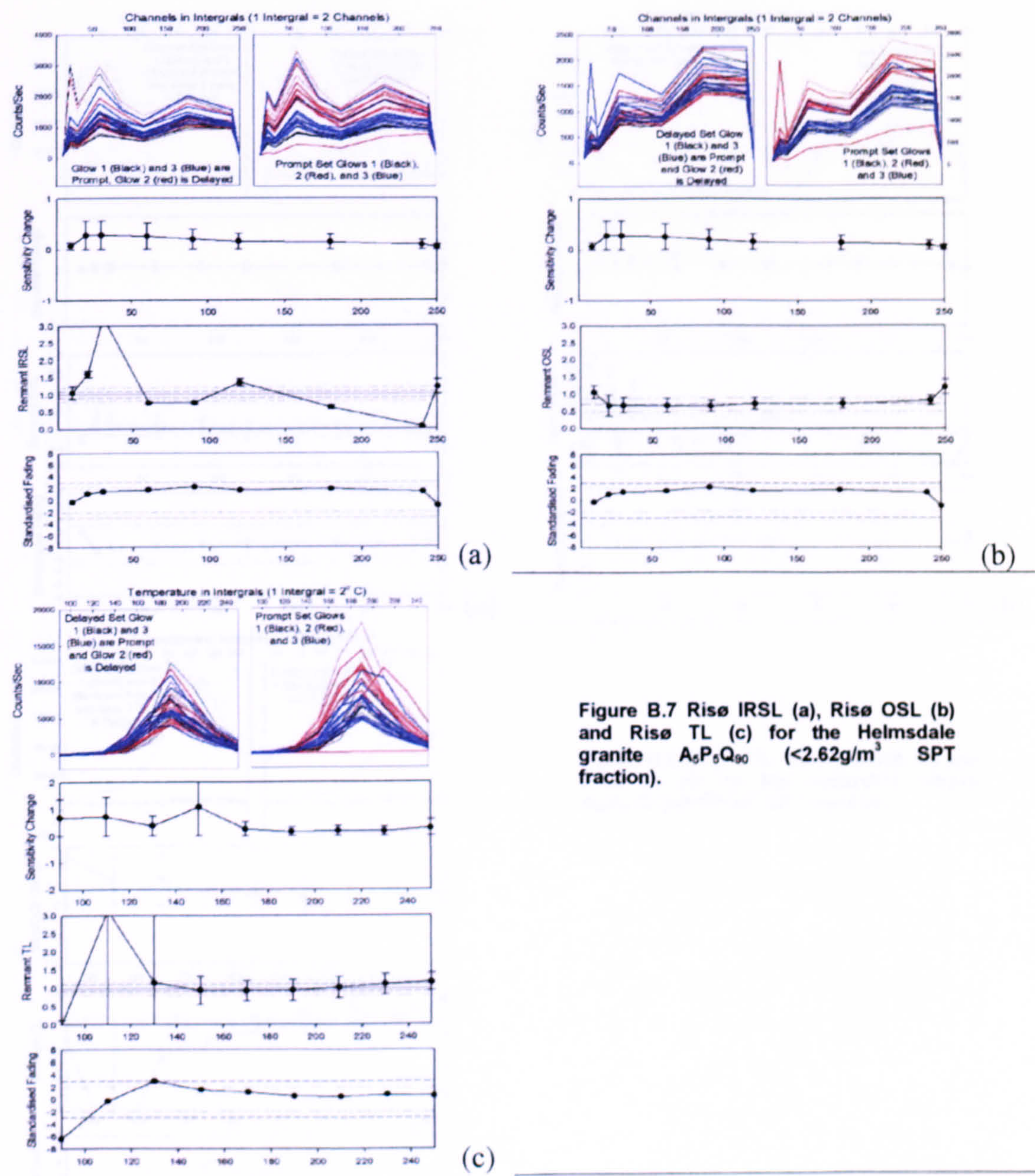


Figure B.7 Risø IRSL (a), Risø OSL (b) and Risø TL (c) for the Helmsdale granite $A_5P_5Q_{90}$ ($<2.62\text{g/m}^3$ SPT fraction).

B.2.5 Helmsdale Arkose.

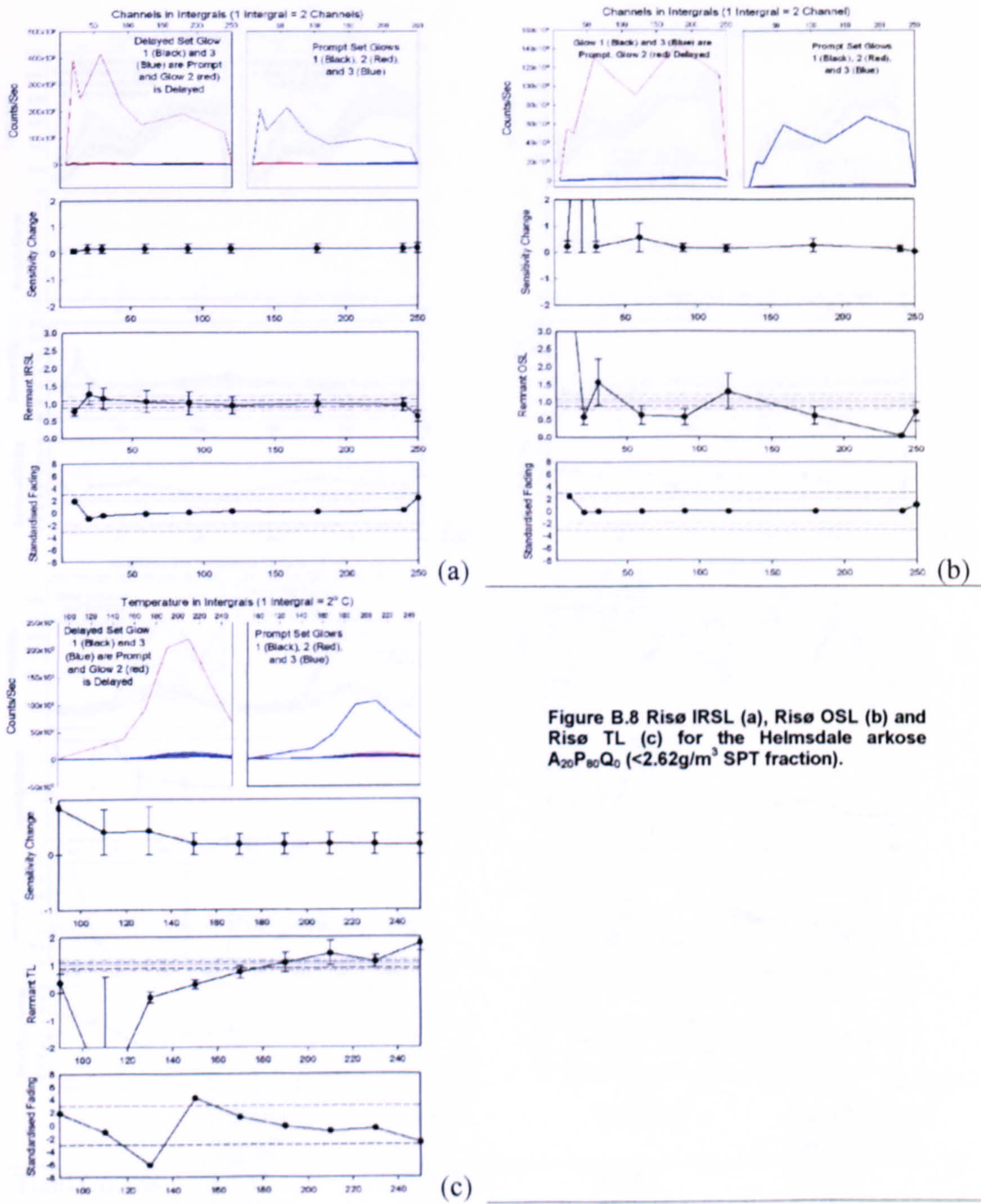


Figure B.8 Risø IRSL (a), Risø OSL (b) and Risø TL (c) for the Helmsdale arkose $A_{20}P_{80}Q_0$ ($<2.62\text{g/m}^3$ SPT fraction).

B.2.6 Peterhead Granite.

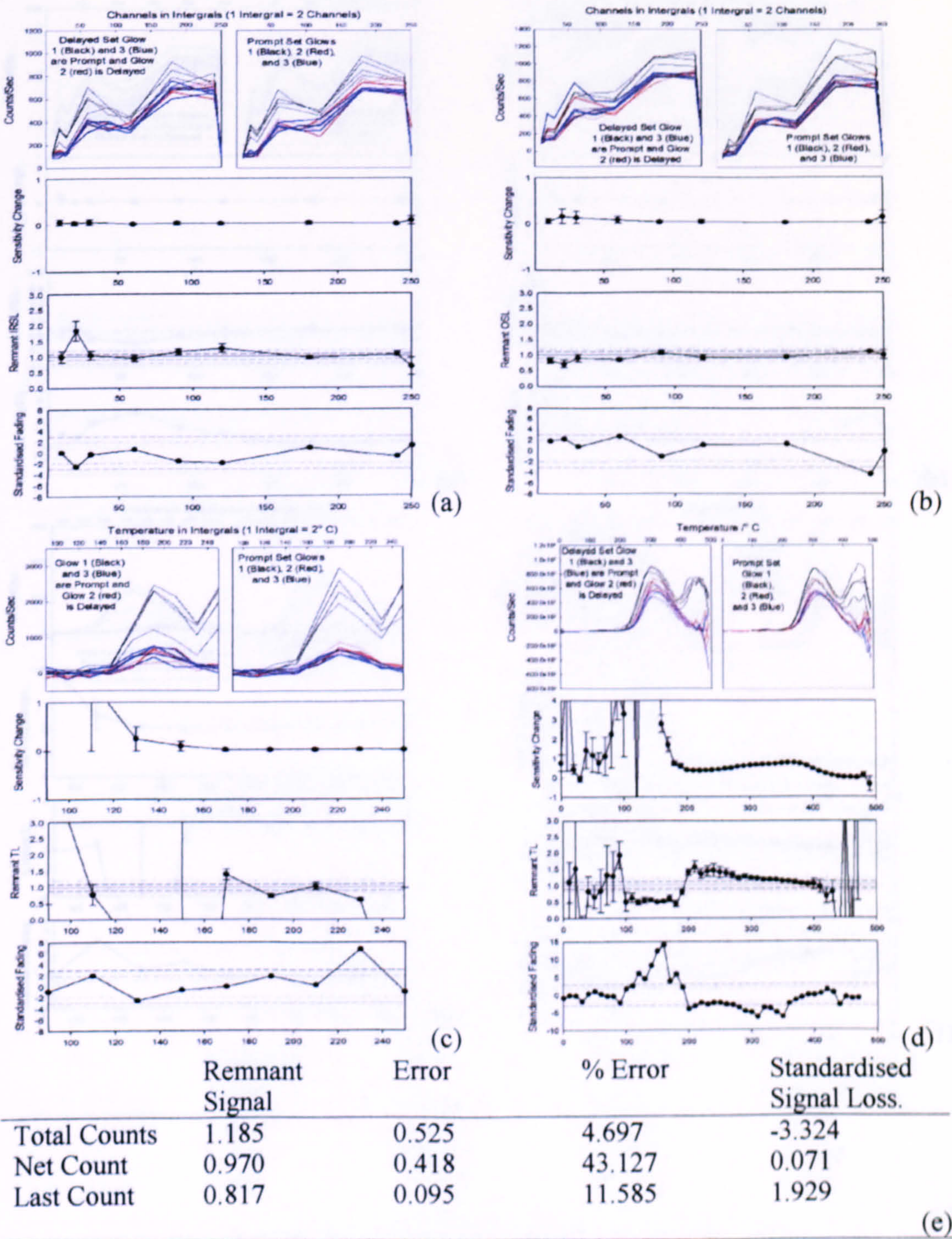
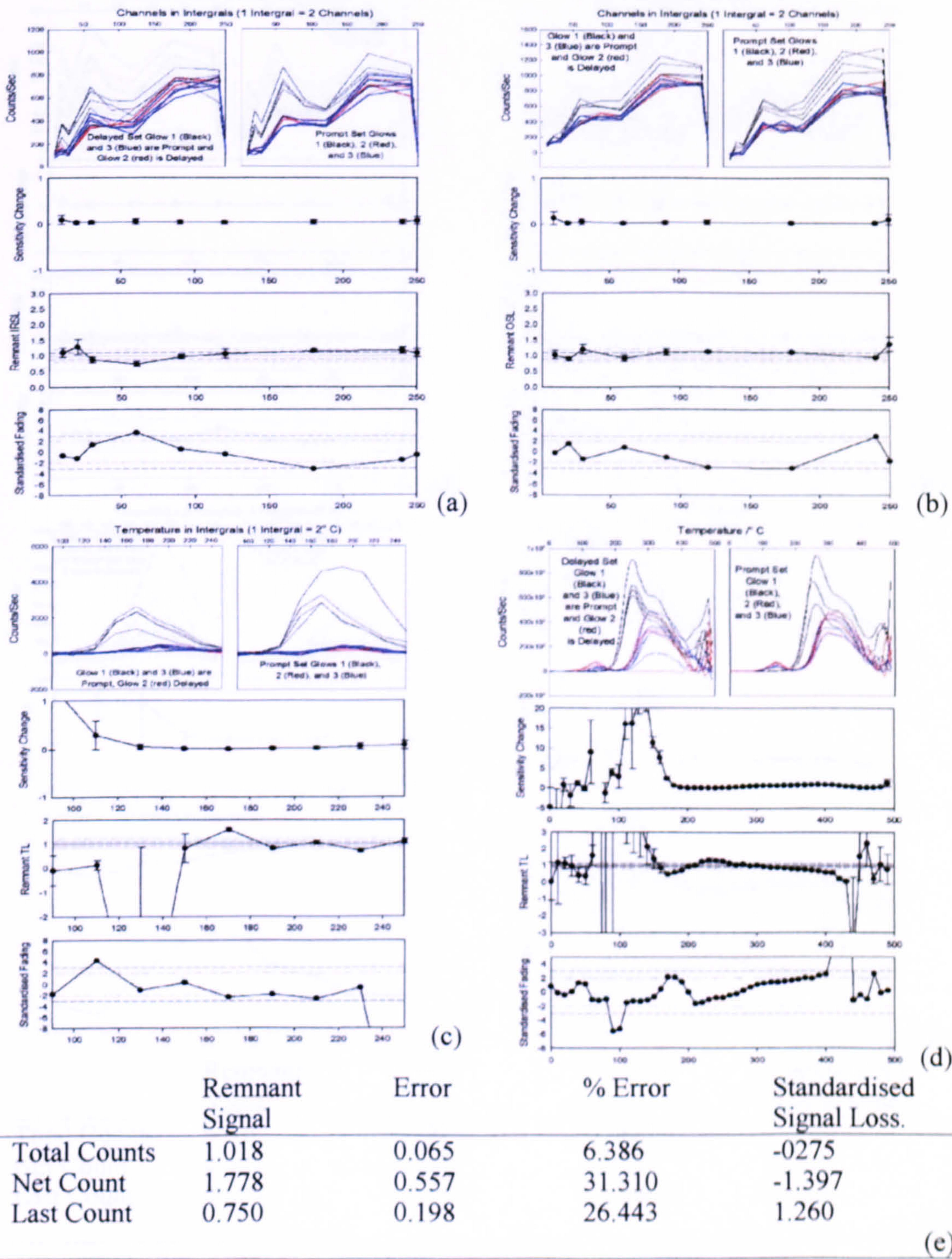


Figure B.9 Risø IRSL (a), Risø OSL (b), Risø TL (c), Manual TL (d), Manual PPSL (e) for the Peterhead granite $A_{75}P_{25}Q_0$ (2.58-2.62g/m³ SPT fraction).

B.2.7 Ross of Mull Granite.



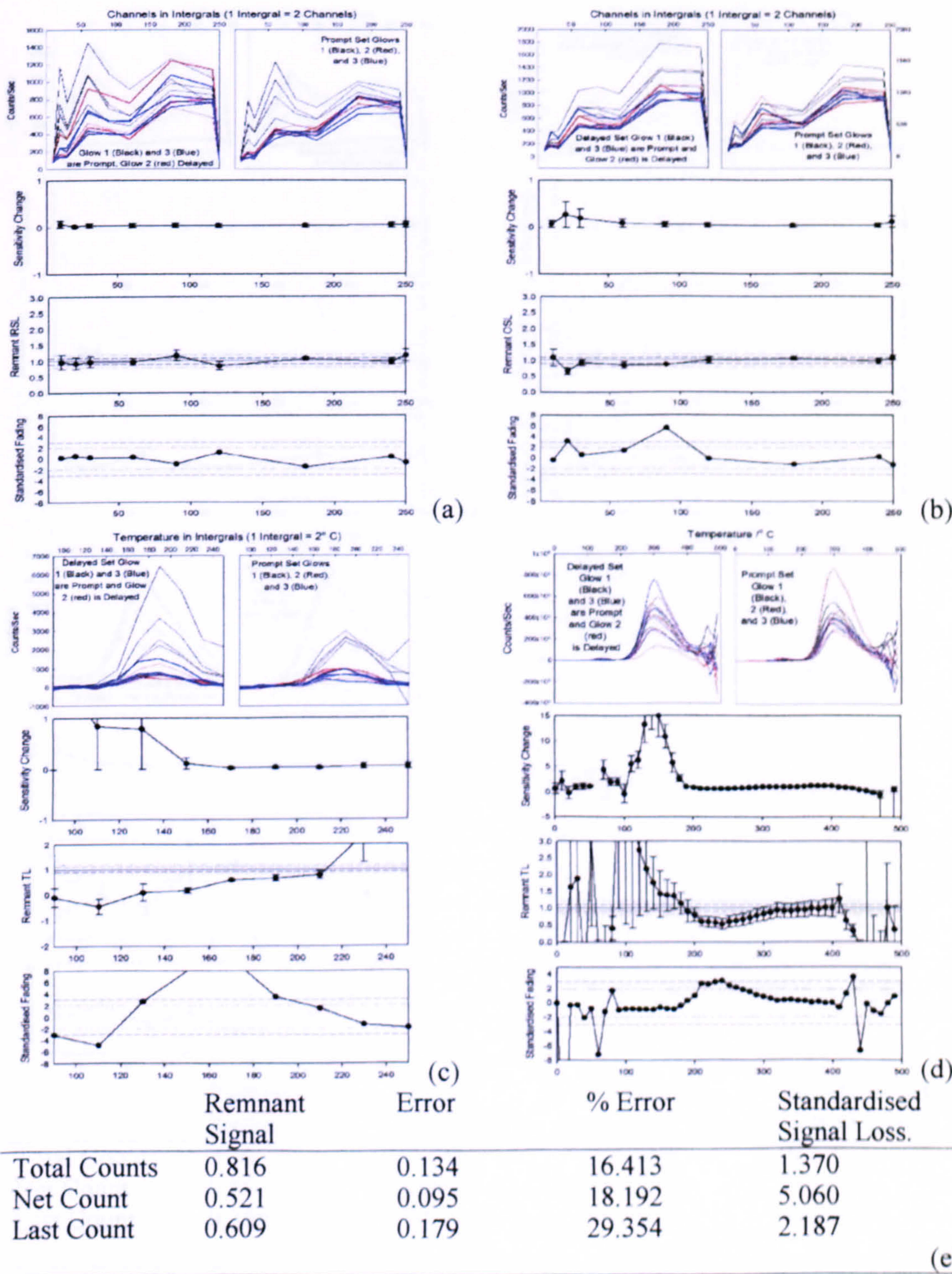
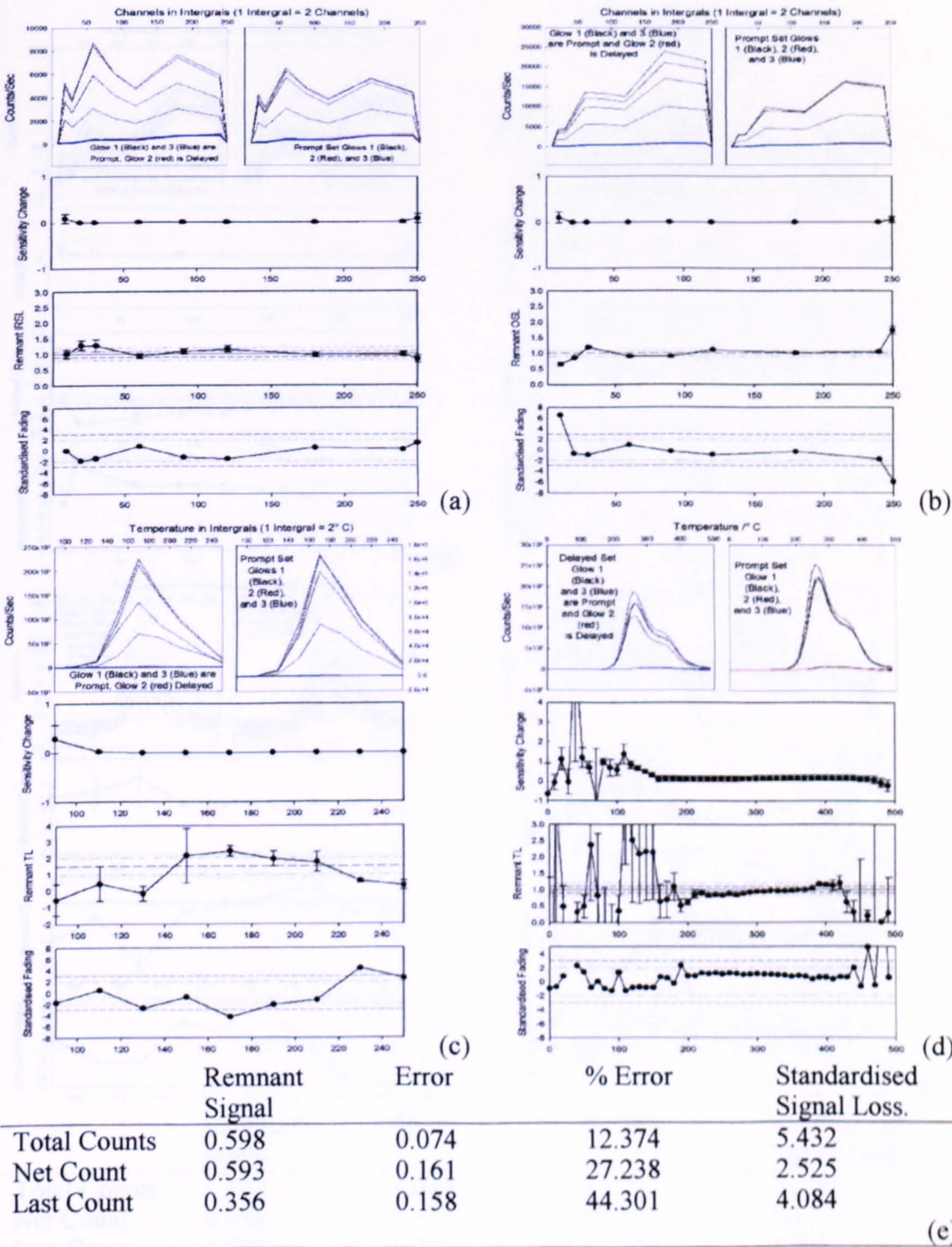


Figure B.11 Risø IRSL (a), Risø OSL (b), Risø TL (c), Manual TL (d), Manual PPSL (e) for the Ross of Mull granite (H9) $A_{40}P_{50}Q_{10}$ (2.62-2.74g/m³ SPT fraction).

B.2.8 Ross of Mull Hydroxyapatite



B.2.8 Ross of Mull Hydrothermal Syenite.

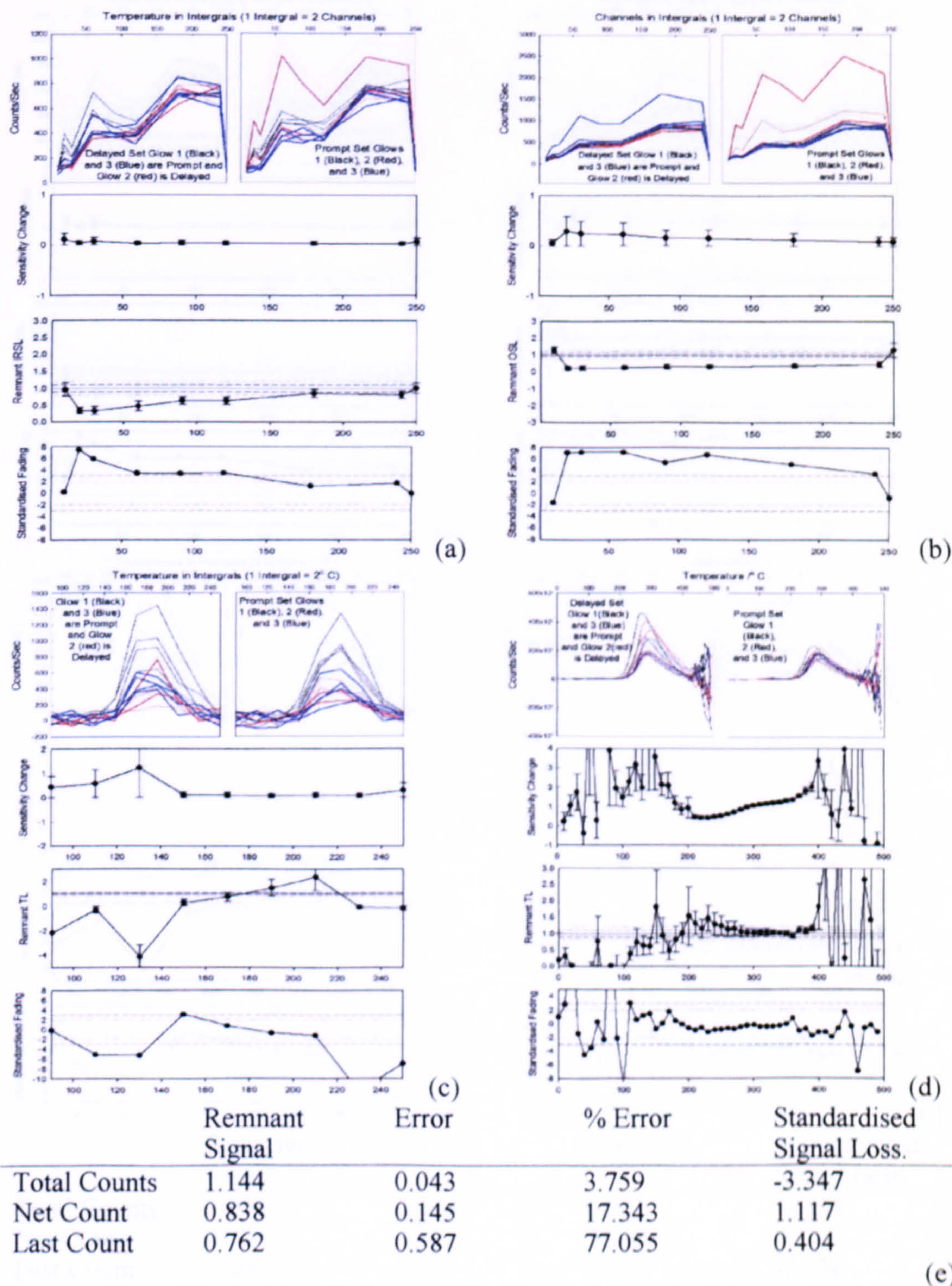


Figure B.13 Rise IRSL (a), Rise OSL (b), Rise TL (c), Manual TL (d), Manual PPSL (e) for the Ross of Mull hydrothermal syenite $A_{80}P_{20}Q_0$ (2.58-2.62g/m³ SPT fraction).

B.2.8 Ship Gravel.

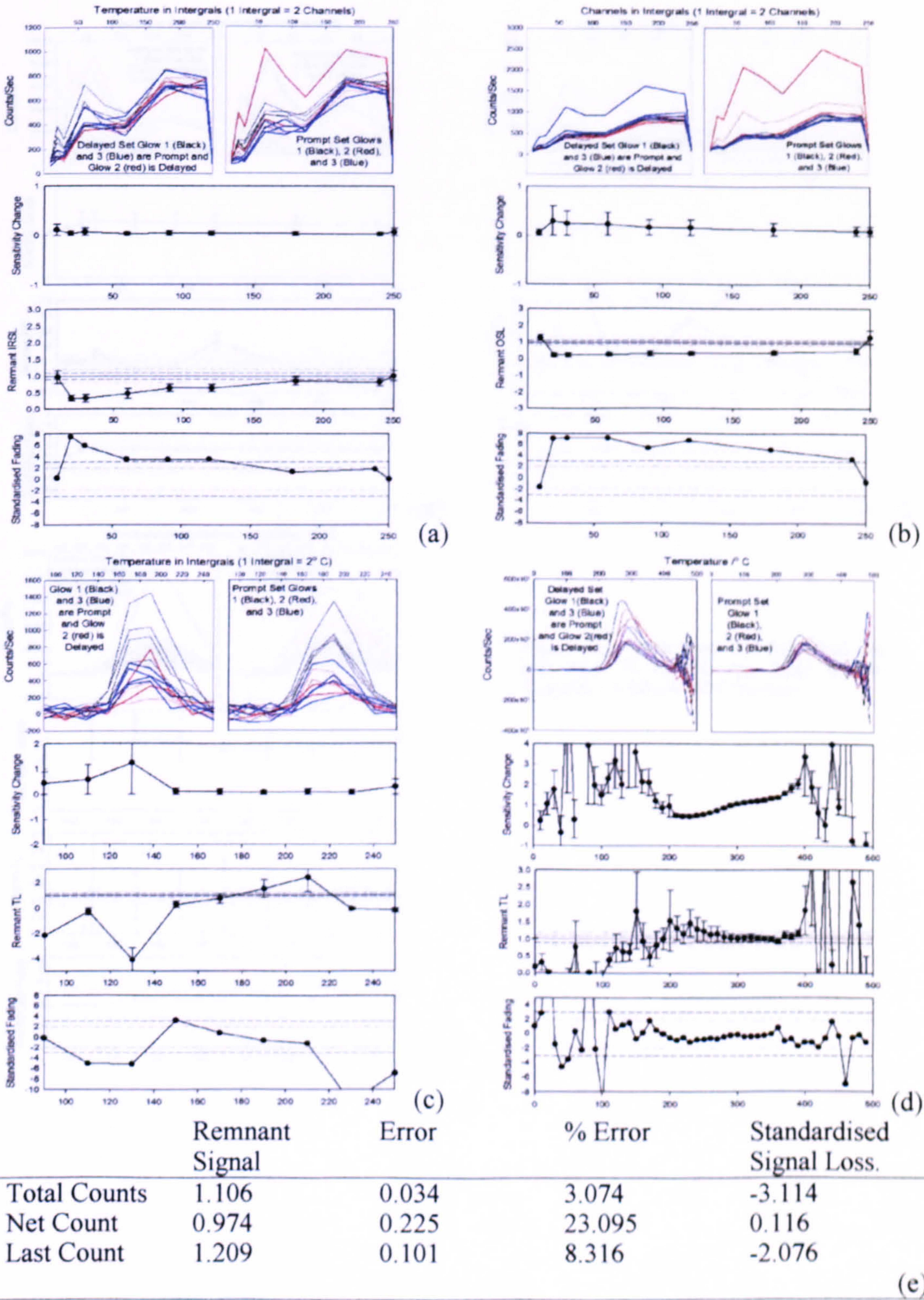


Figure B.14 Risø IRSL (a), Risø OSL (b), Risø TL (c), Manual TL (d), Manual PPSL (e) for the Ross of Mull hydrothermal syenite $A_{15}P_{85}Q_0$ (2.62-2.74g/m³ SPT fraction).

B.2.9 Shap Granite.

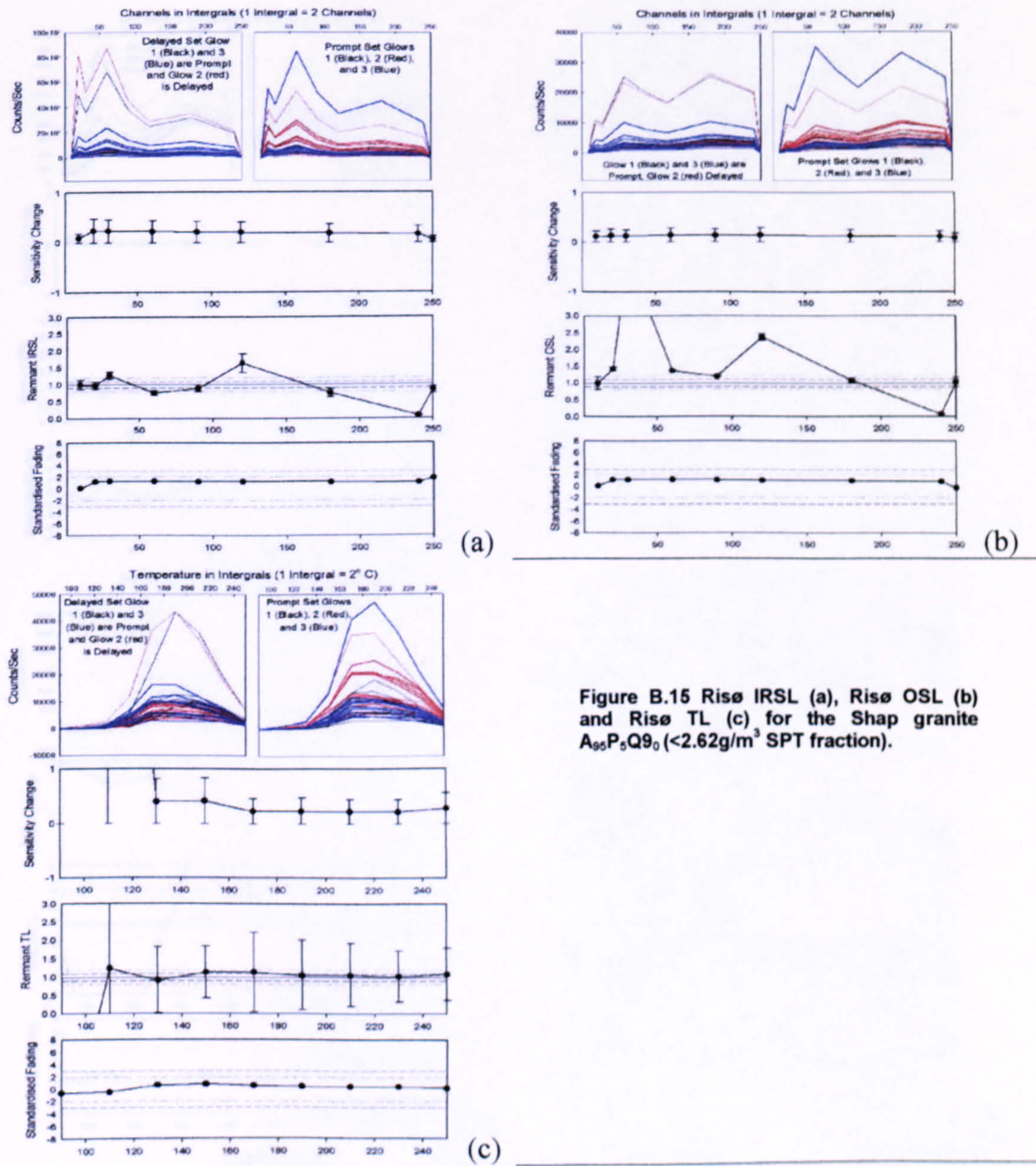
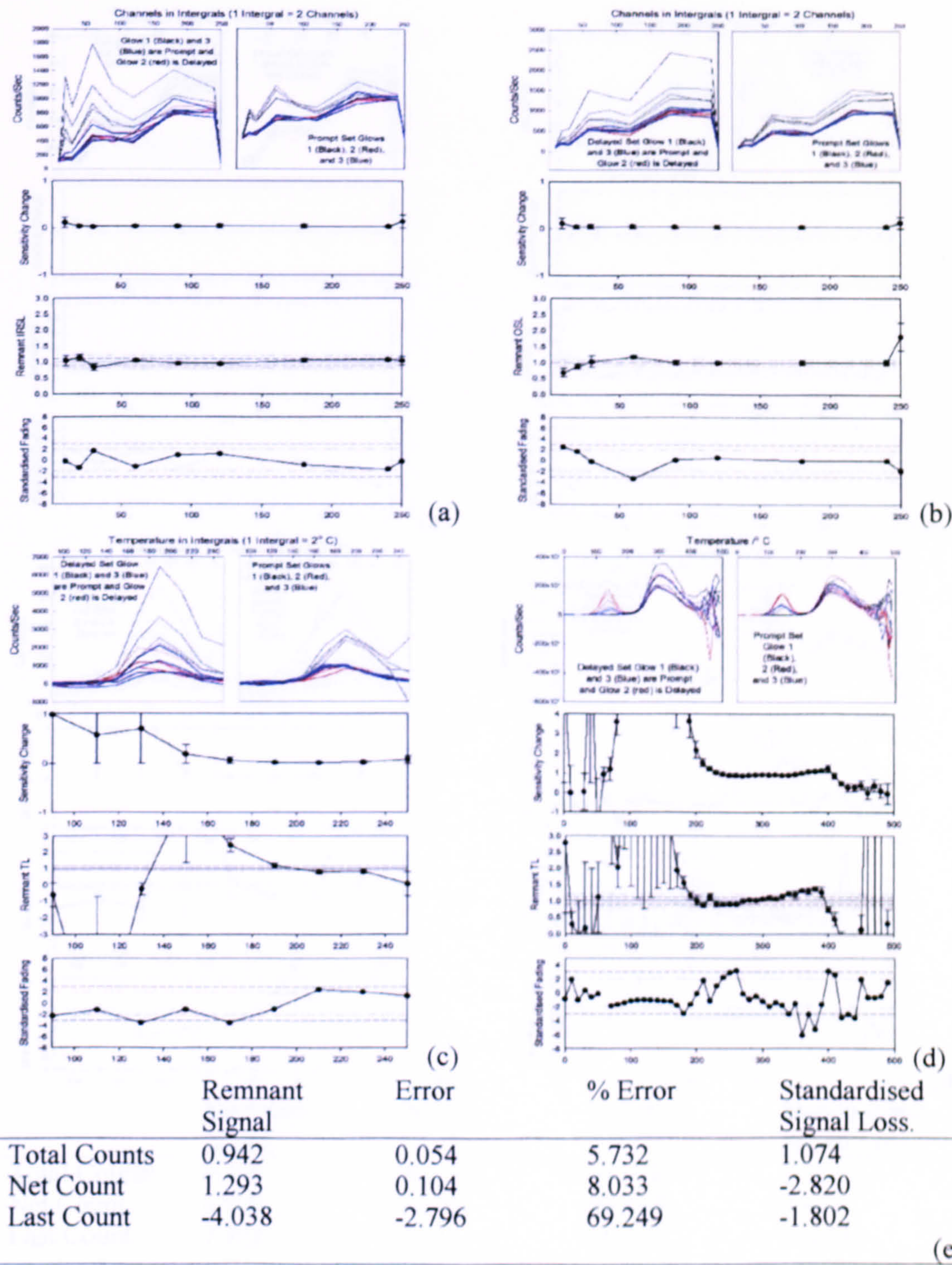


Figure B.15 Risø IRSL (a), Risø OSL (b) and Risø TL (c) for the Shap granite $A_{95}P_{5}Q_{90}$ ($<2.62\text{g/m}^3$ SPT fraction).

B.3 Silic Minor Igneous Intrusions.

B.2.10 Strontian Granodiorite.



B.3 Silicic Minor Igneous Intrusions.

B.3.1 Pitchstone Porphyry.

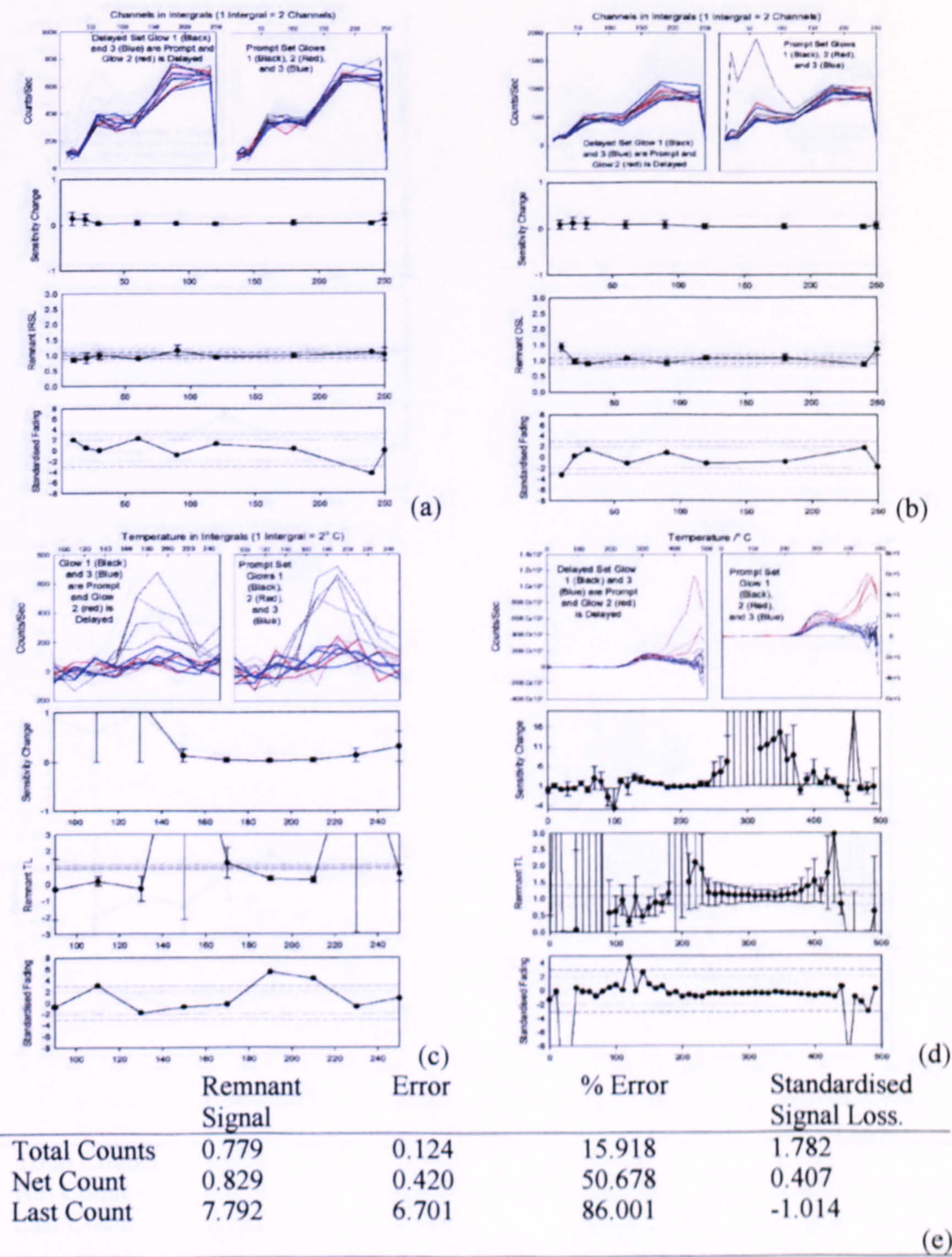


Figure B.17 Rise IRSL (a), Rise OSL (b), Rise TL (c), Manual TL (d), Manual PPSL (e) for the Bute pitchstone porphyry (H2) $A_0P_{50}Q_{50}$ (2.62-2.74g/m³ SPT fraction).

B.3.2 Bute Pitchstone Porphyry (H3).

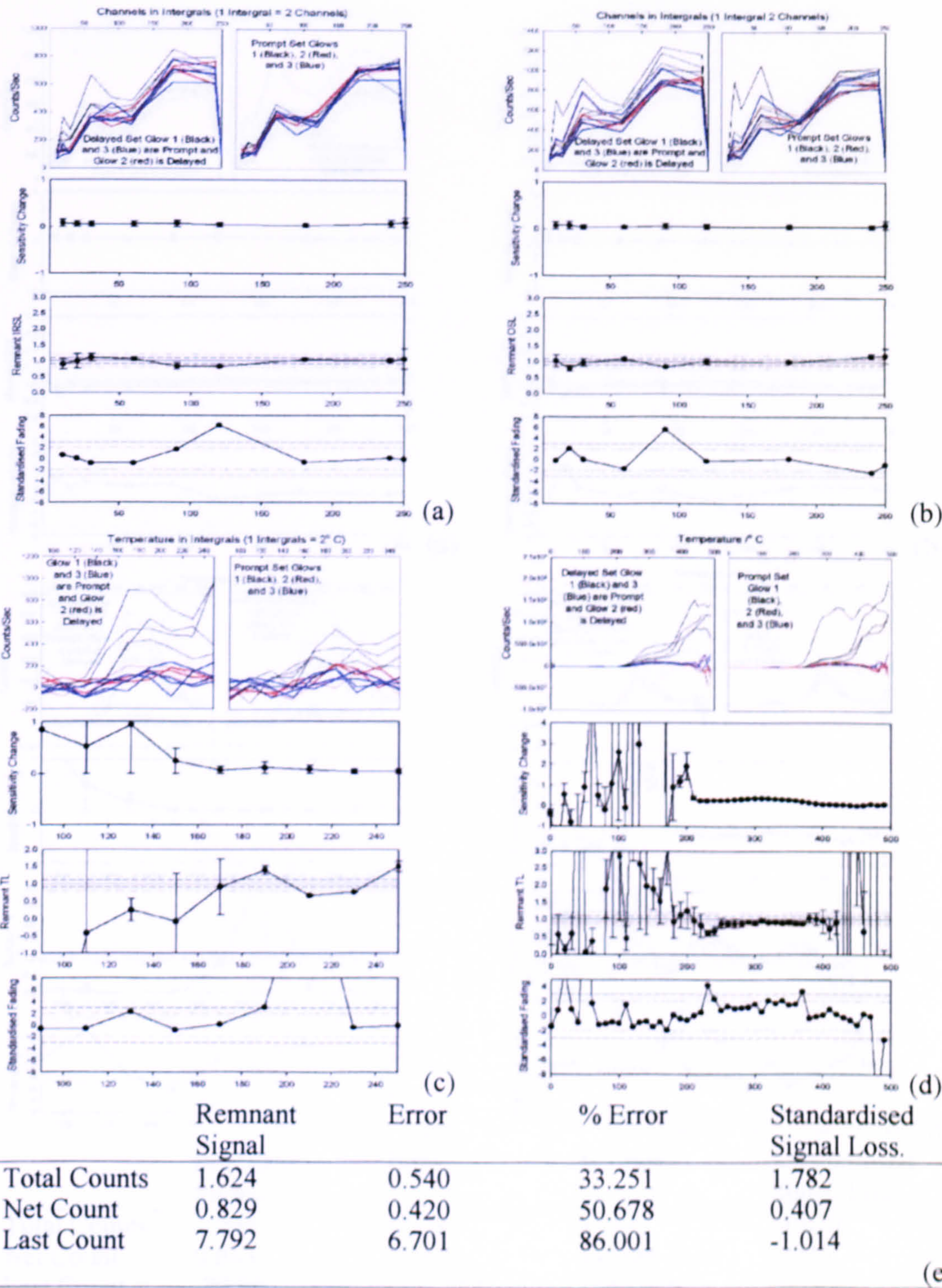


Figure B.18 Rise IRSL (a), Rise OSL (b), Rise TL (c), Manual TL (d), Manual PPSL (e) for the Bute pitchstone porphyry (H3) A₅₀P₅₀Q₀ (2.58-2.62g/m³ SPT fraction).

B.3.3 Canisp Quartz-Syenite.

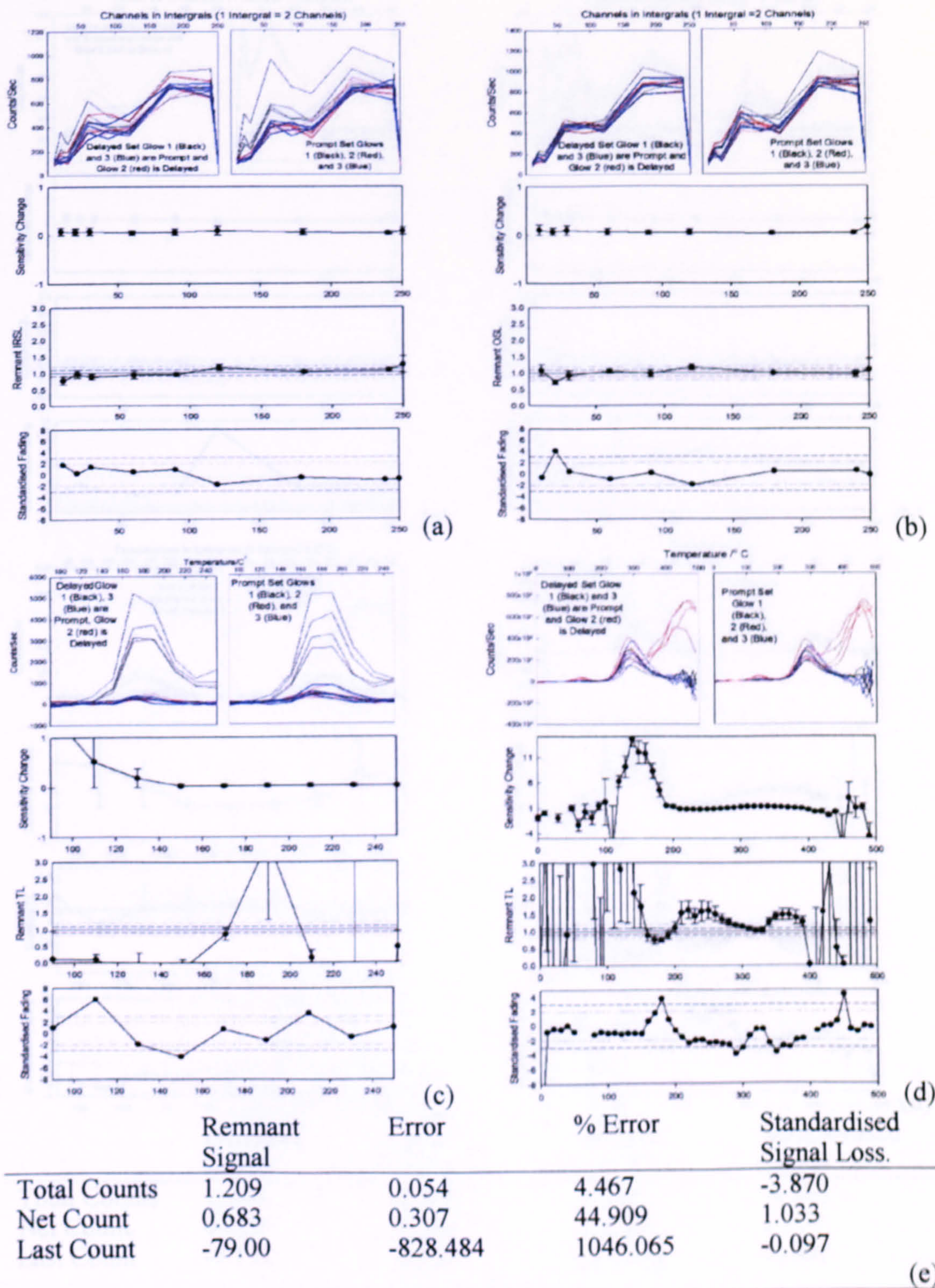
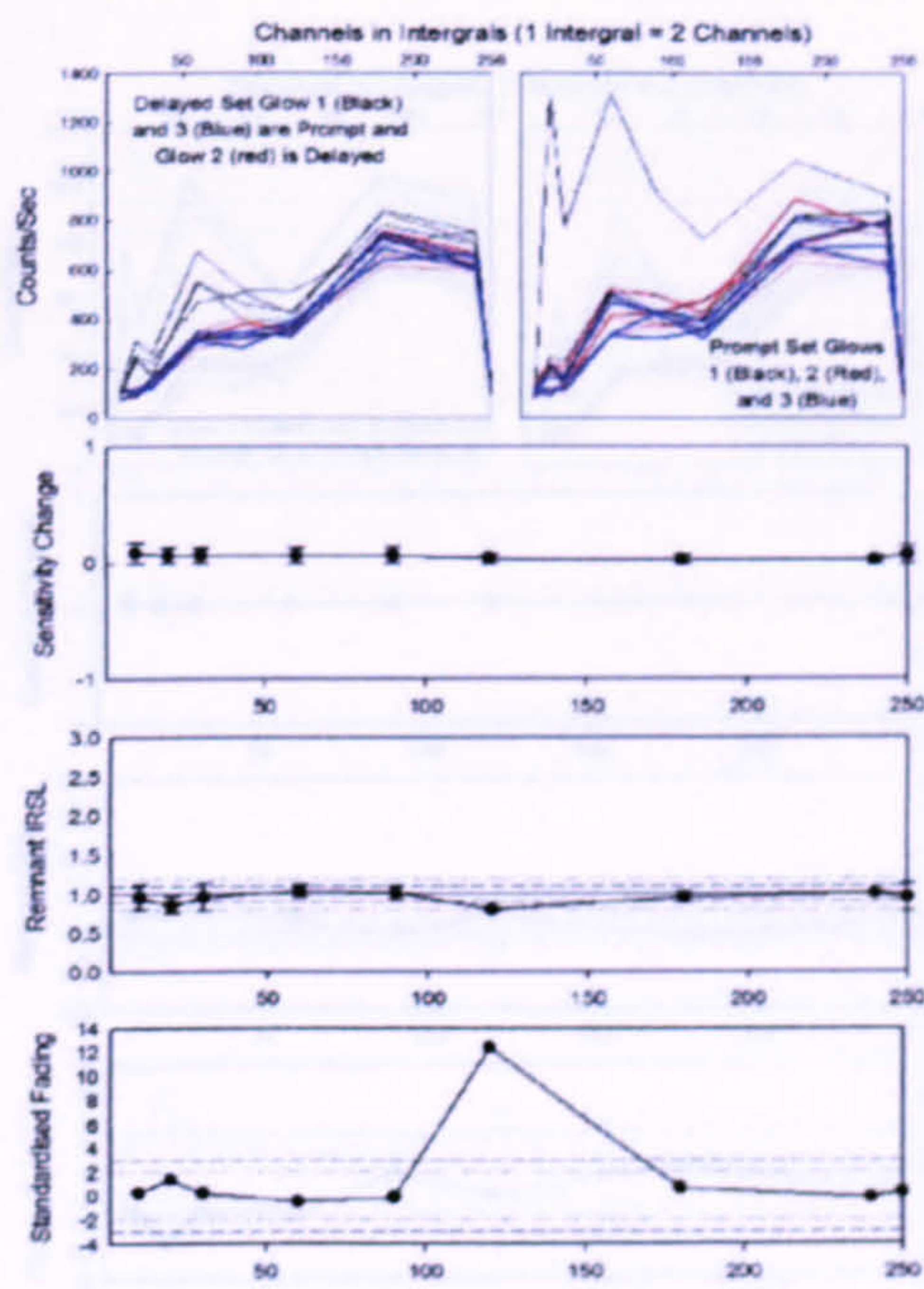
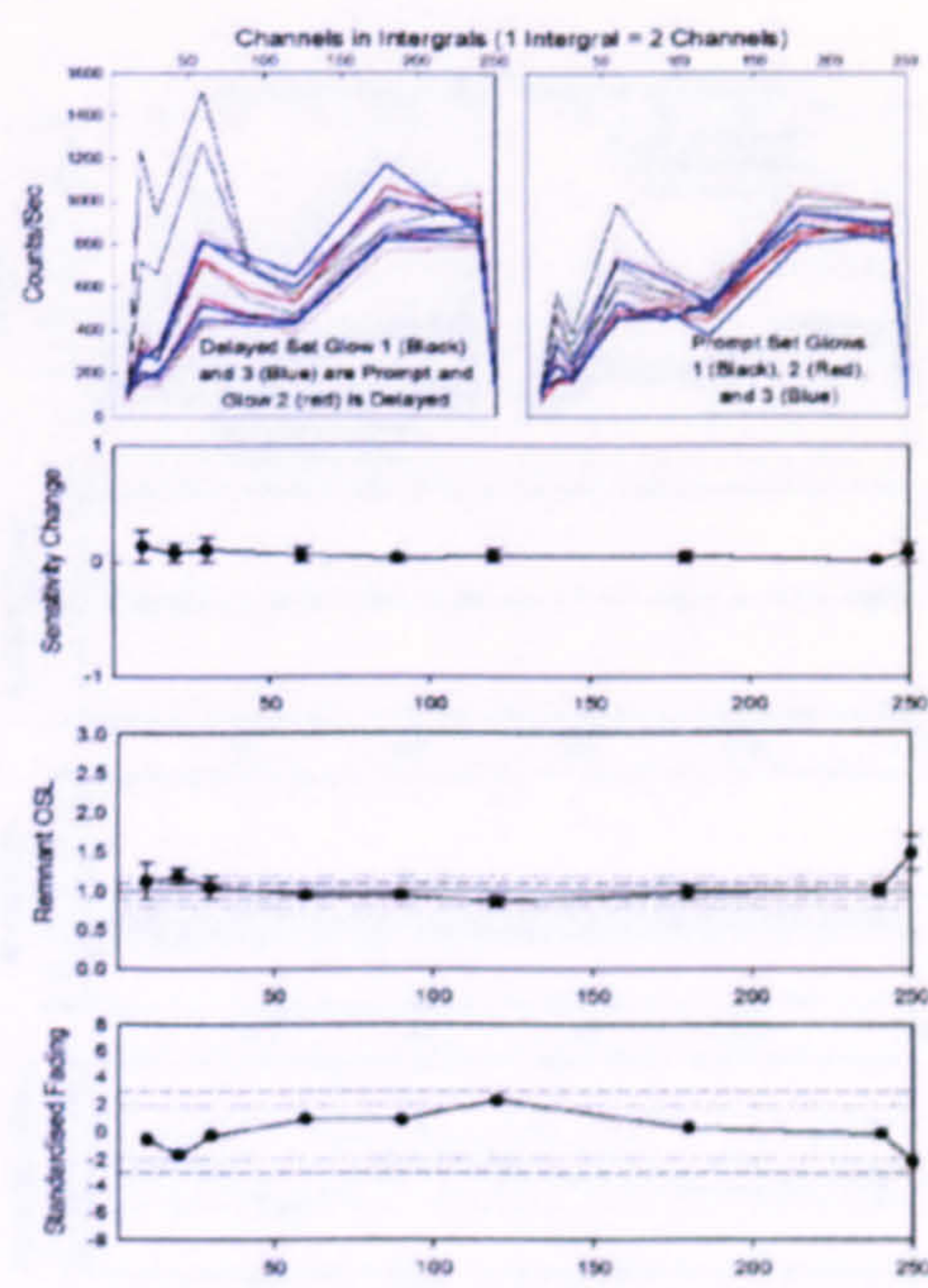


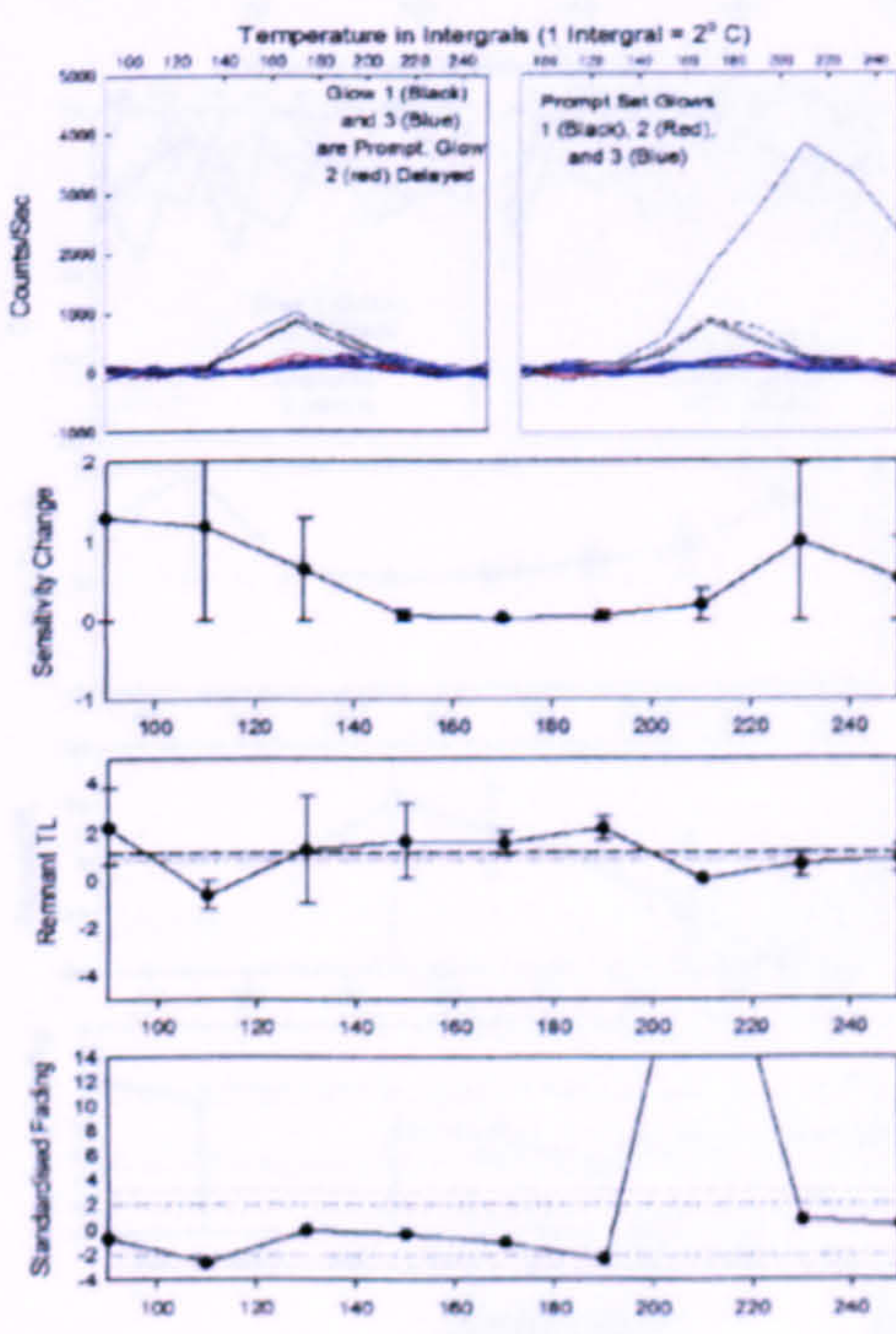
Figure B.19 Rise IRSL (a), Rise OSL (b), Rise TL (c), Manual TL (d), Manual PPSL (e) for the Canisp quartz-syenite A₅₀P₅₀Q₀ (2.58-2.62g/m³ SPT fraction).



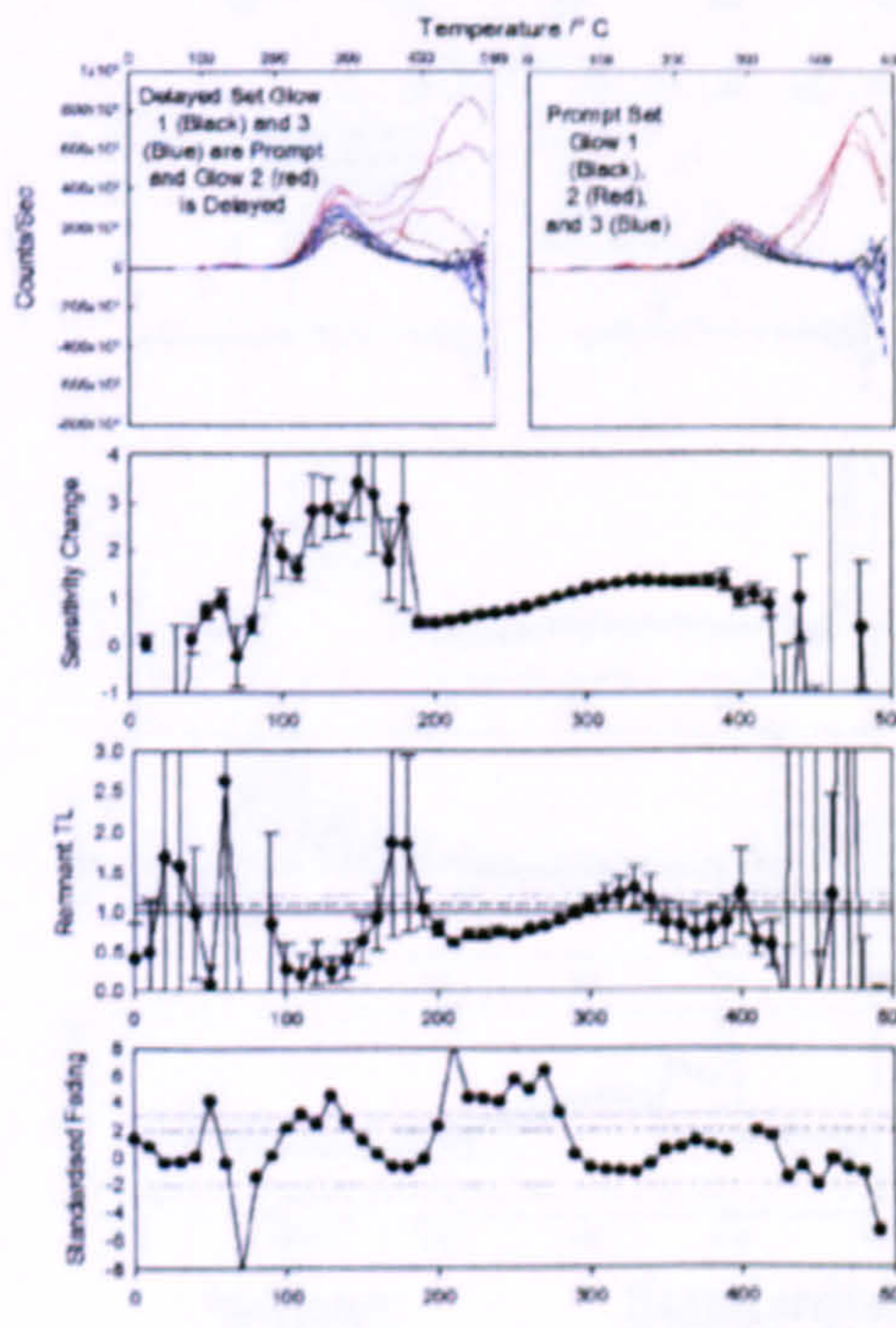
(a)



(b)



(c)



(d)

	Remnant Signal	Error	% Error	Standardised Signal Loss.
Total Counts	1.240	0.056	4.495	-4.306
Net Count	0.629	0.211	33.577	1.757
Last Count	-7.191	-26.659	370.706	-0.307

Figure B.20 Risø IRSI (a), Risø OSL (b), Risø TL (c), Manual TL (d), Manual PPSI (e) for the Canisp quartz-syenite $A_0P_{50}Q_{50}$ (2.62-2.74g/m³ SPT fraction).

B.4 Igneous Calcic Plagioclase.

B.4.1 Connemara Gabbro Pegmatite.

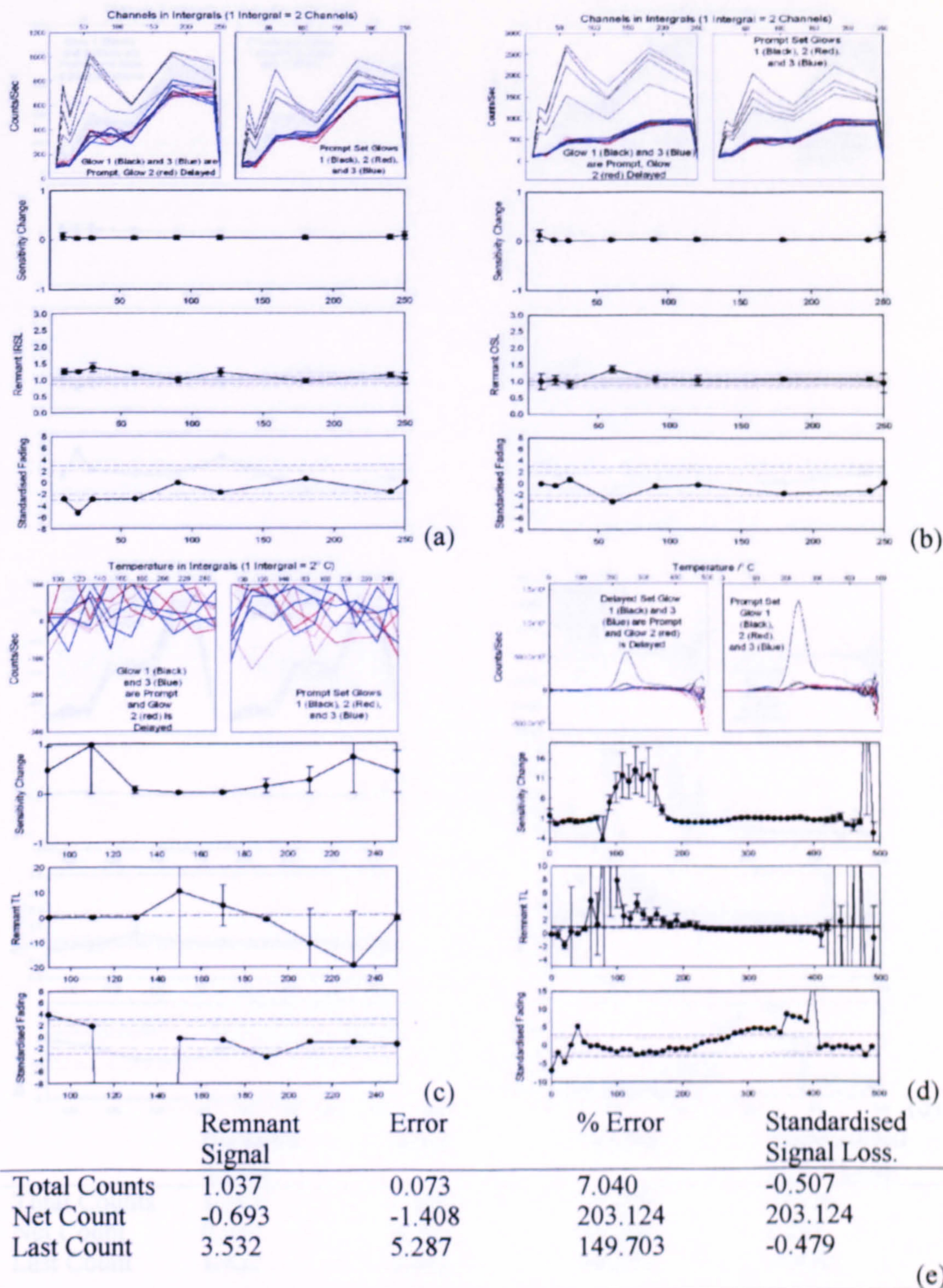


Figure B.21 Rise IRSL (a), Rise OSL (b), Rise TL (c), Manual TL (d), Manual PPSL (e) for the Connemara gabbro pegmatite $A_0P_{100}Q_0$ ($>2.74\text{g/m}^3$ SPT fraction).

B.4.2 Rum Anorthosite.

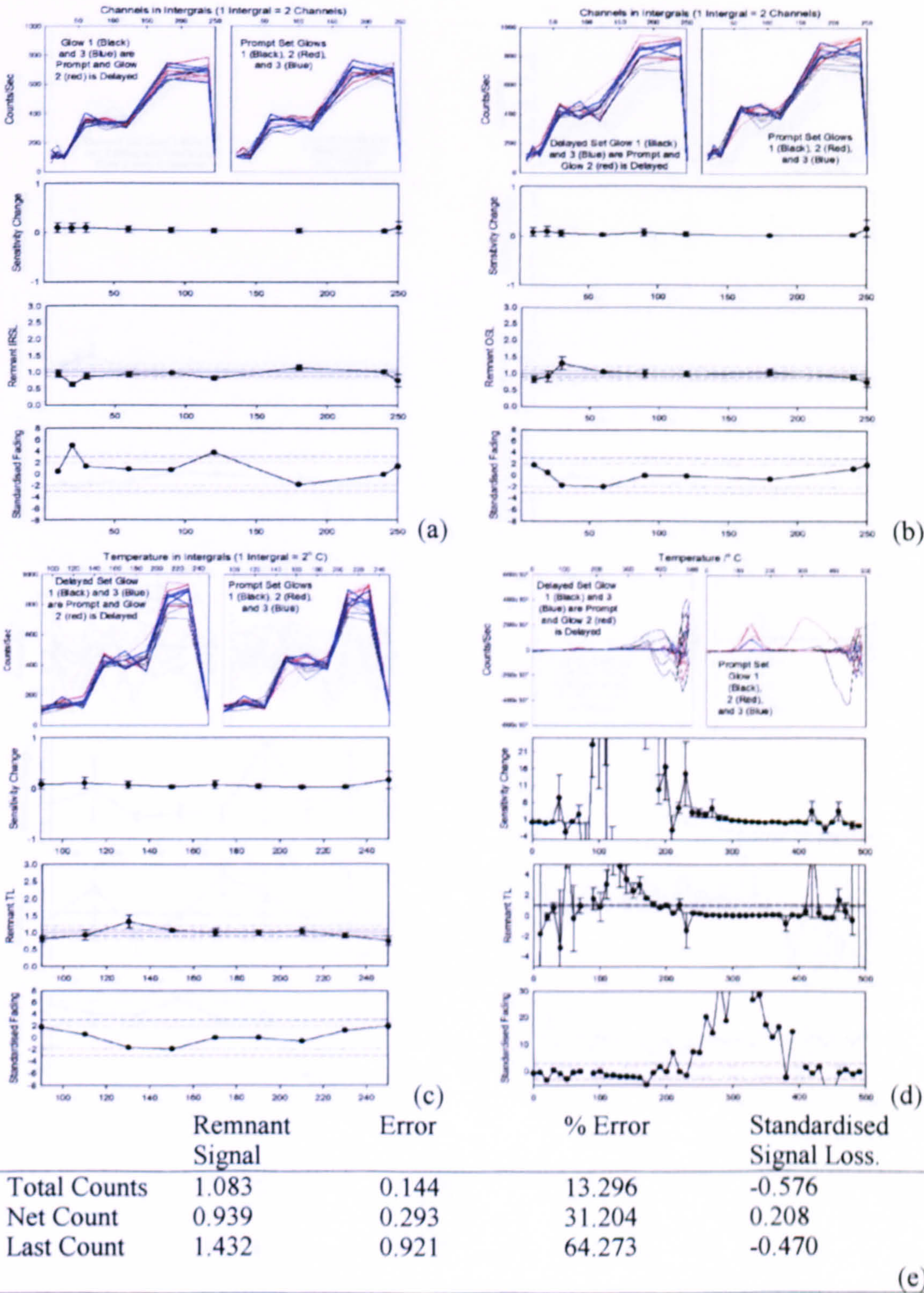
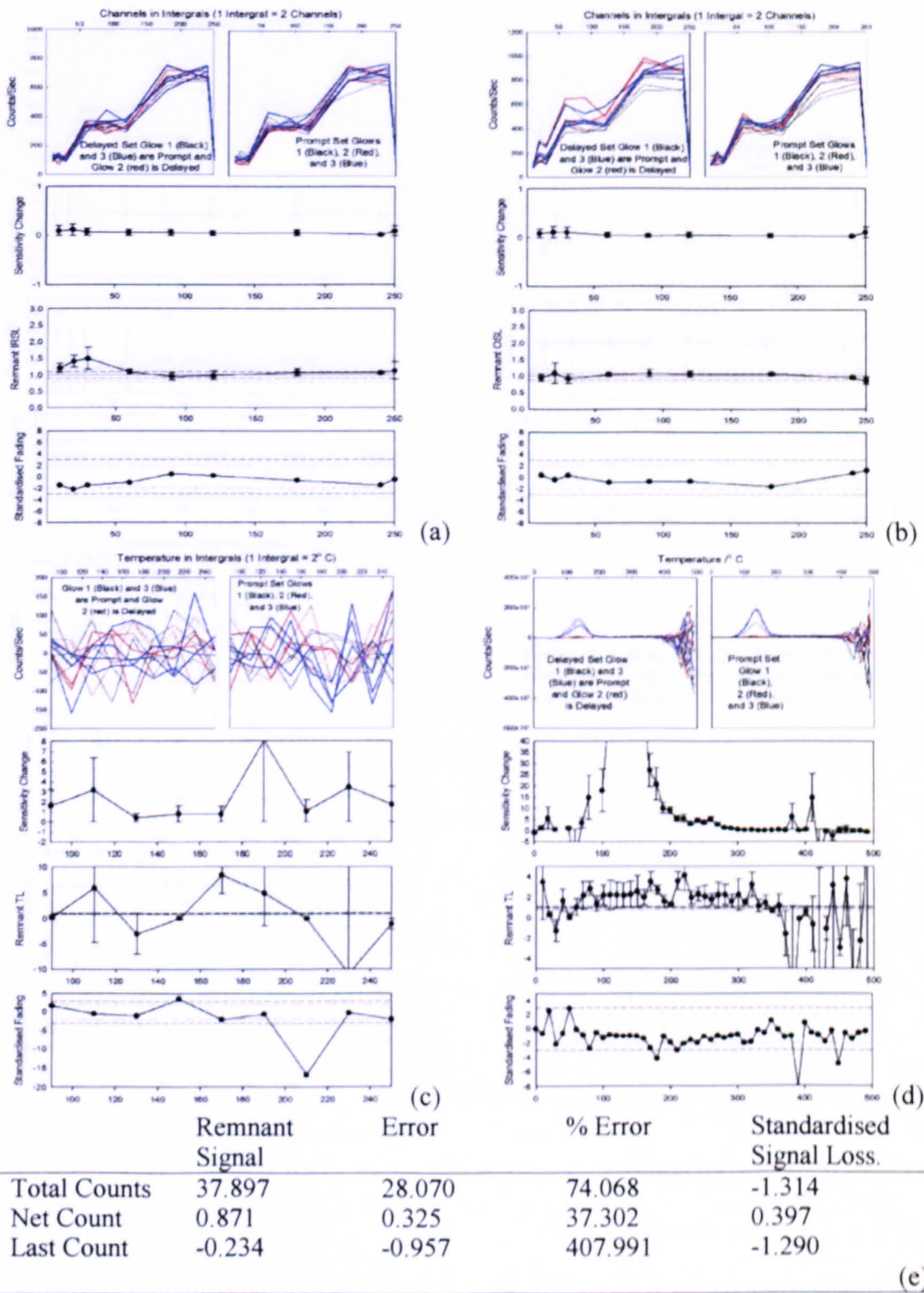


Figure B.22 Rise IRSL (a), Rise OSL (b), Rise TL (c), Manual TL (d), Manual PPSL (e) for the Rum anorthosite A₀P₁₀₀Q₀ (2.62-2.74g/m³ SPT fraction).

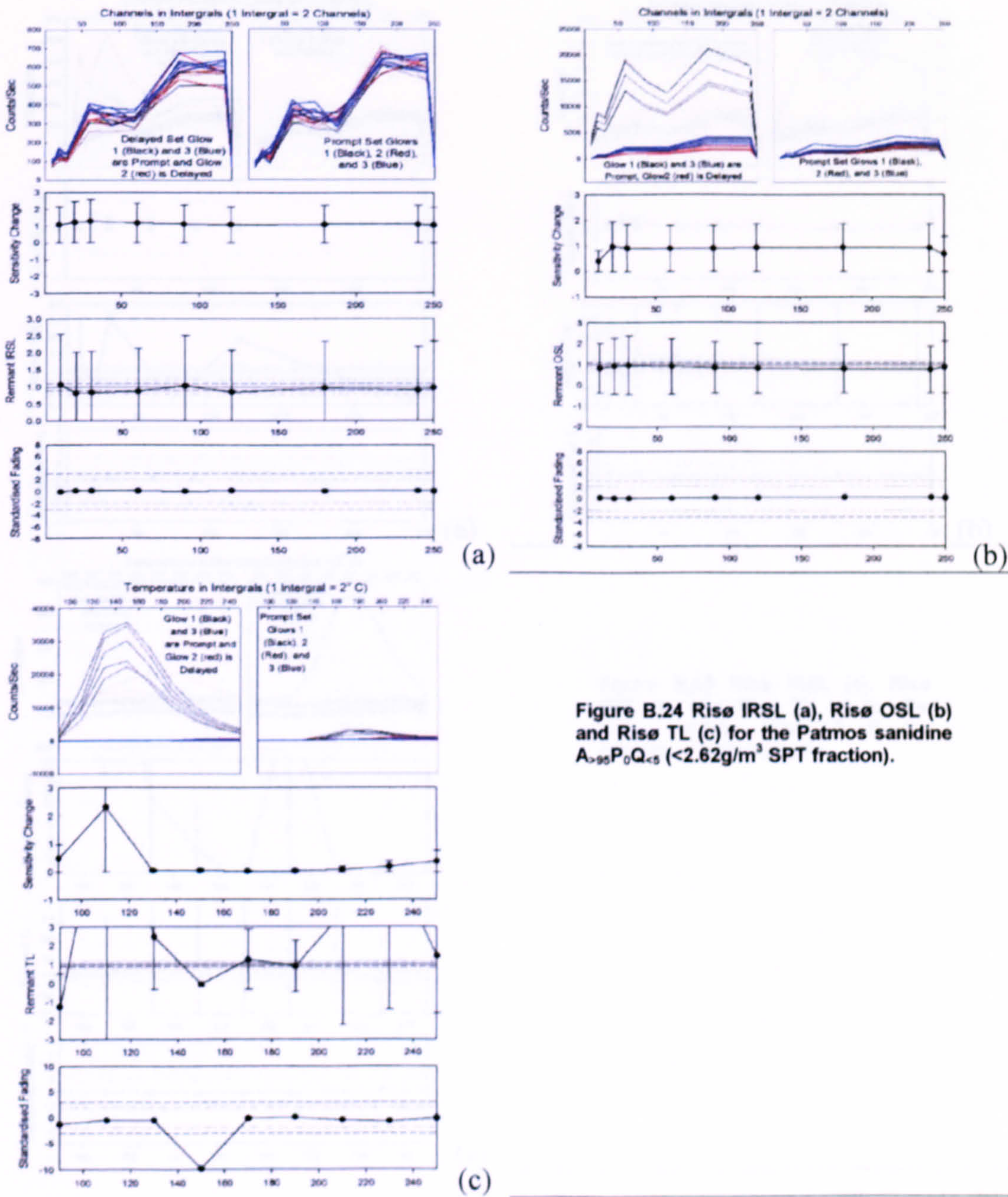
B.5 Extrusive Aggregates Rocks

B.4.3 Rum Troctolite Pegmatite.



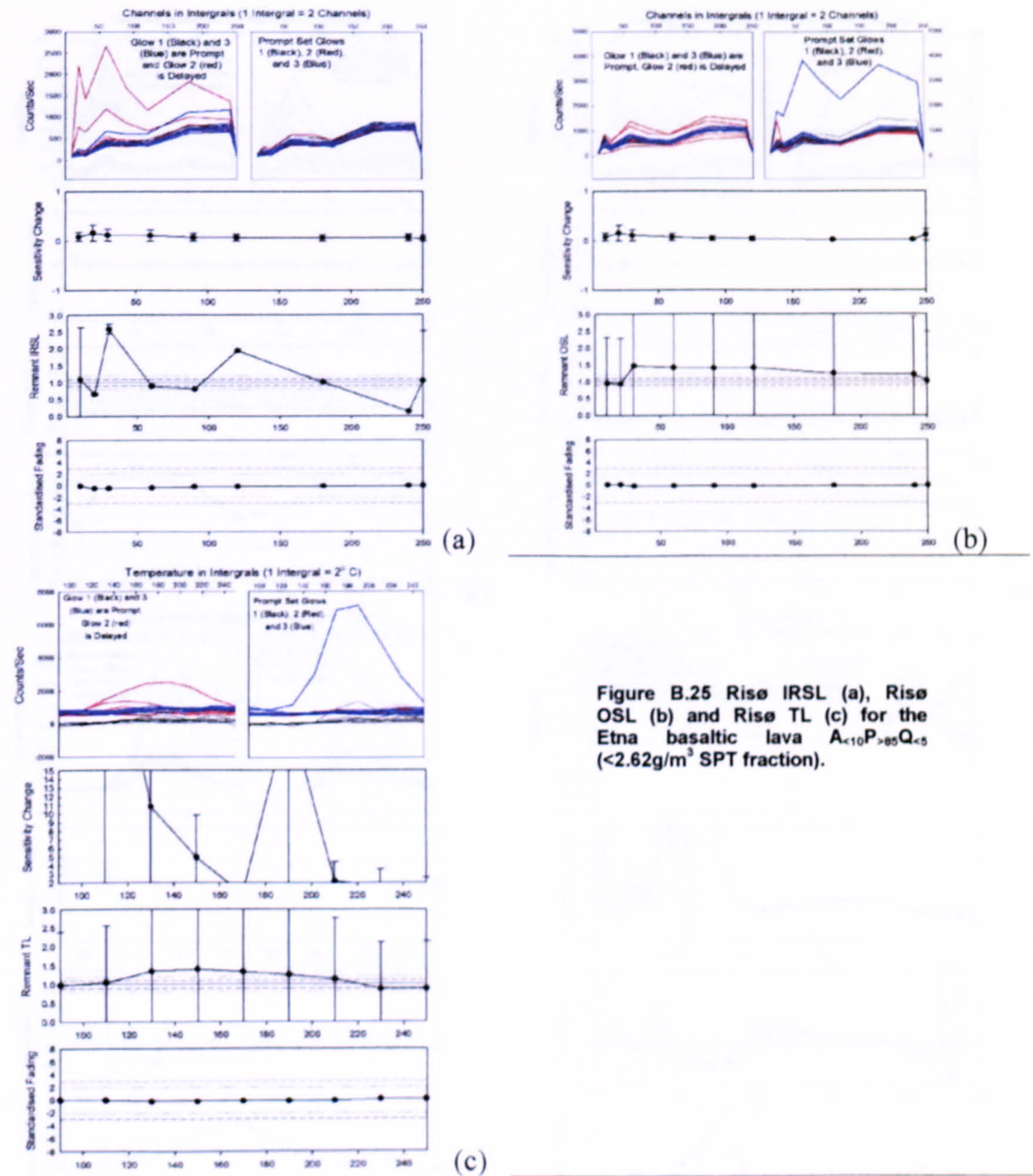
B.5 Extrusive Igneous Rocks.

B.5.1 Patmos Sanidine.



B.6 Metamorphic Rocks

B.5.2 Etna Basaltic Lava.



B.6 Metamorphic Rocks.

B.6.1 Glen Tarbert Migmatite.

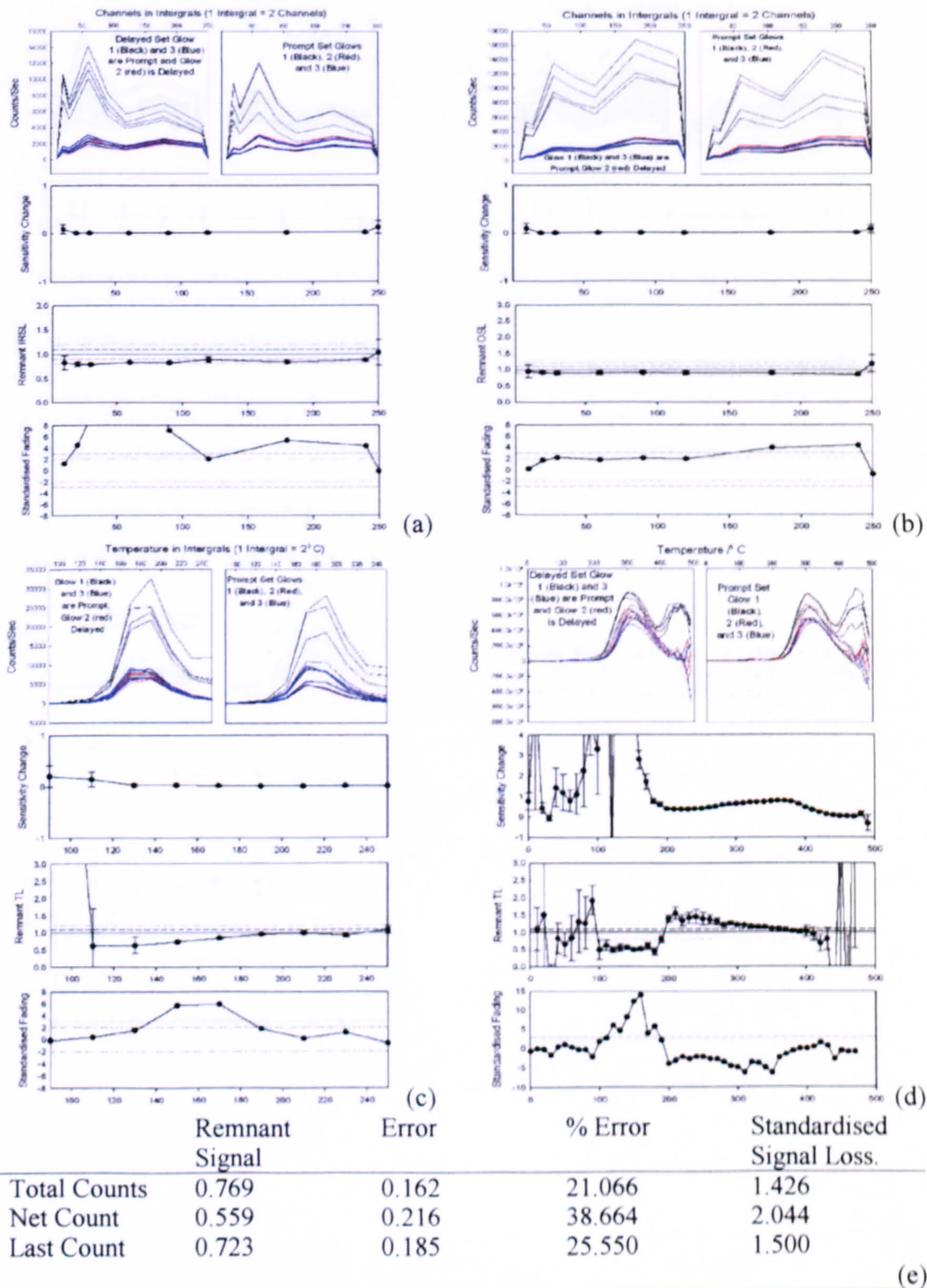


Figure B.26 Rise IRSL (a), Rise OSL (b), Rise TL (c), Manual TL (d), Manual PPSL (e) for the Glen Tarbert migmatite $A_{10}P_{30}Q_{60}$ (2.62-2.74g/m³ SPT fraction).

B.6.2 Lewisian Gneiss.

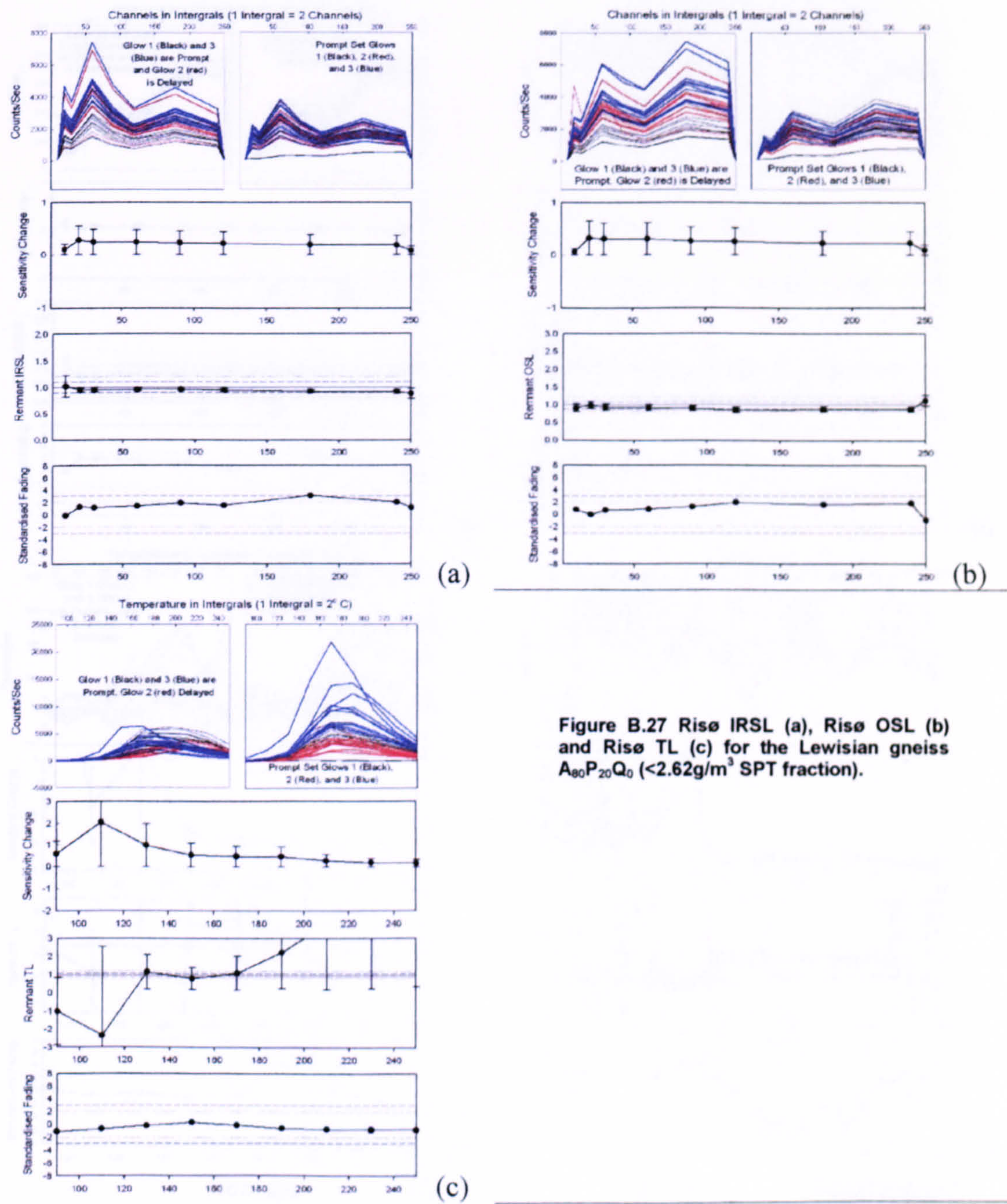
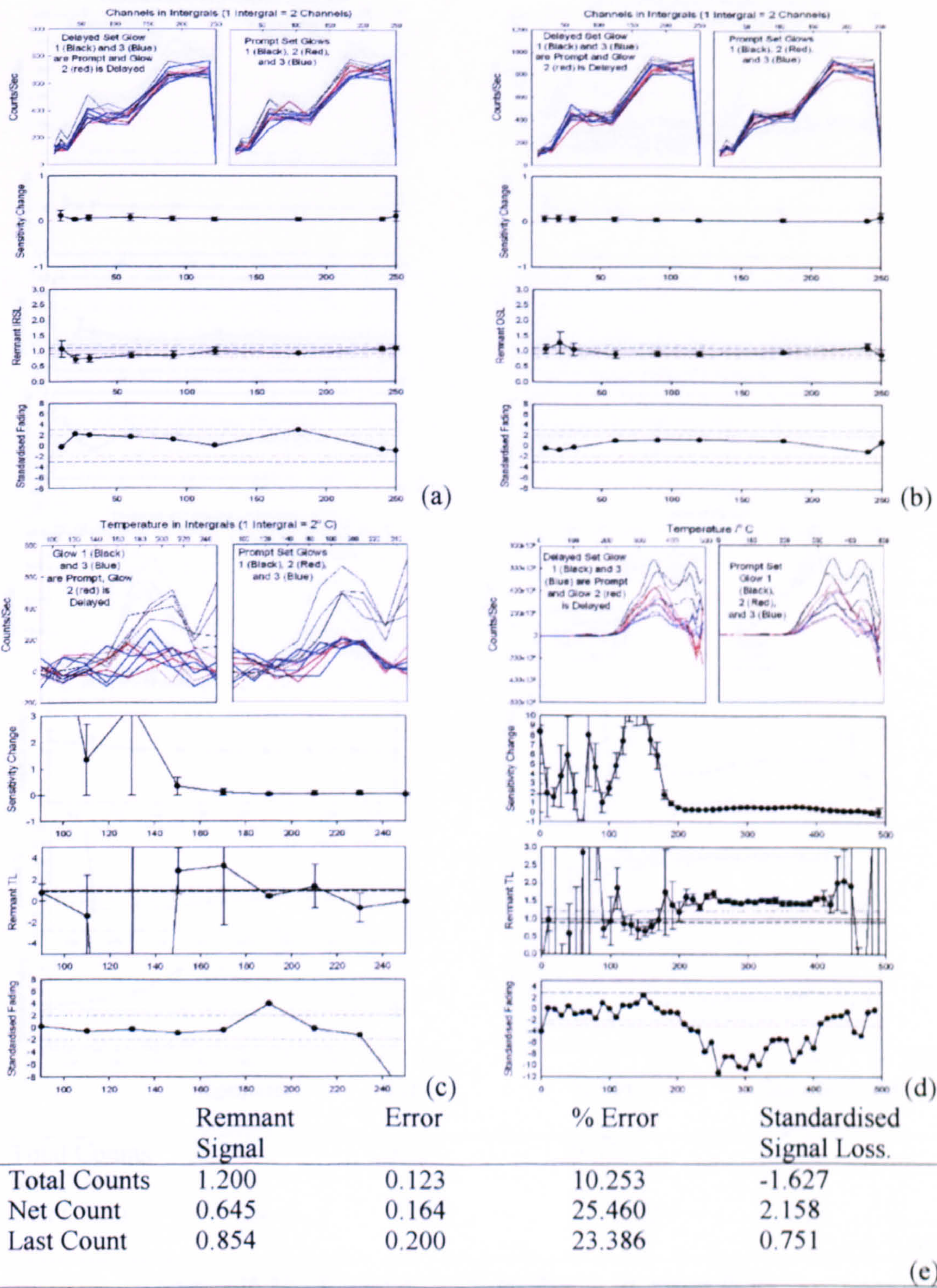


Figure B.27 Risø IRSL (a), Risø OSL (b) and Risø TL (c) for the Lewisian gneiss $A_{80}P_{20}Q_0$ ($<2.62\text{g/m}^3$ SPT fraction).

B.6.3 Torridonian Hornblende Gneiss.



B.7 Naturally Weathered and Igneous Rocks

B.7.1 Bulkier Graphs

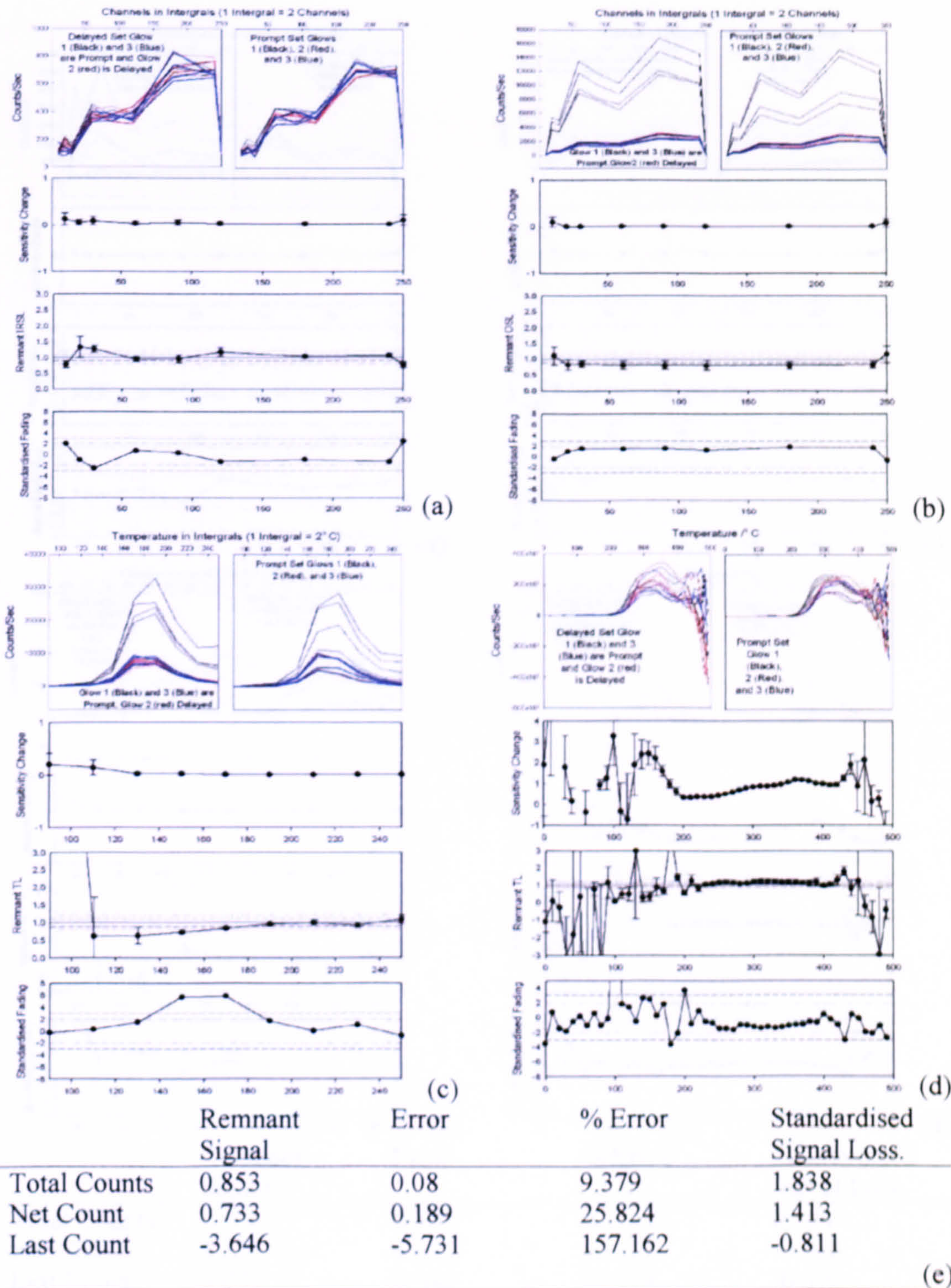


Figure B.29 Rise IRSL (a), Rise OSL (b), Rise TL (c), Manual TL (d), Manual PPSL (e) for the Torridonian hornblende gneiss A₁₀P₂₀Q₇₀ (2.62-2.74g/m³ SPT fraction).

B.7 Naturally Weathered Igneous Rocks.

B.7.1 Ballater Granite.

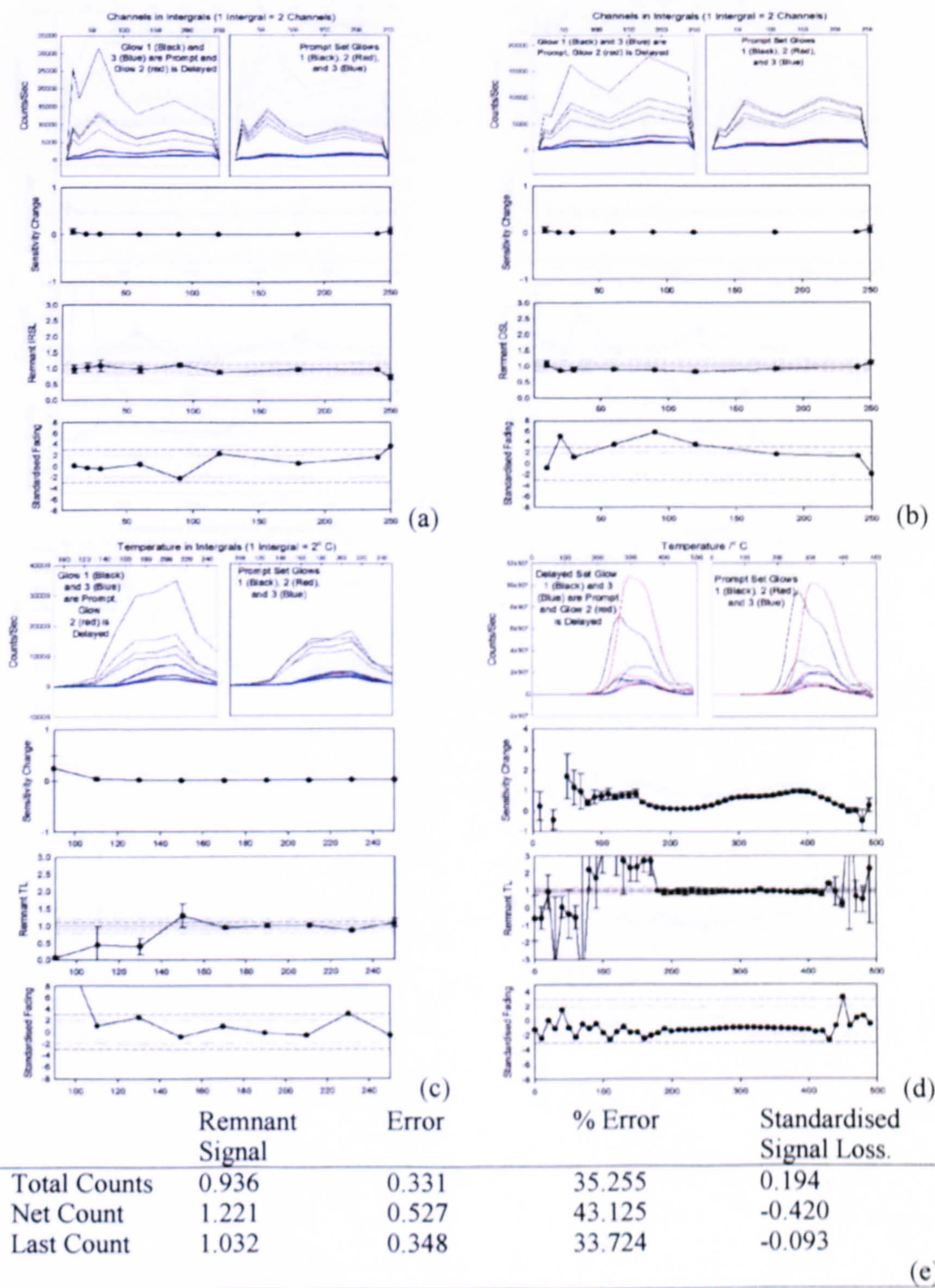


Figure B.30 Risø IRSL (a), Risø OSL (b), Risø TL (c), Manual TL (d), Manual PPSL (e) for the Ballater granite $A_{90}P_{10}Q_0$ (2.52-2.58g/m³ SPT fraction).

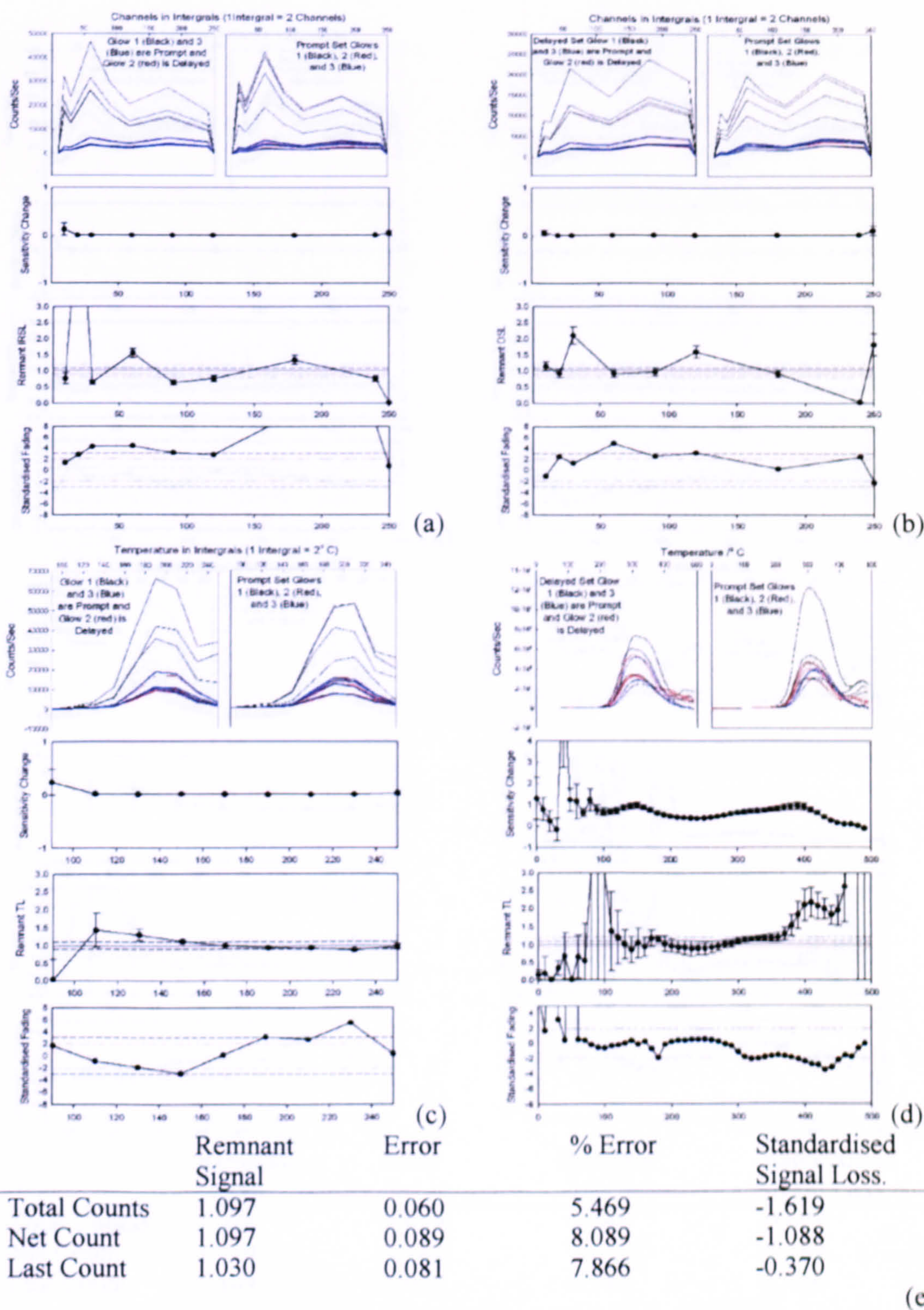


Figure B.31 Rise IRSI (a), Rise OSL (b), Rise TL (c), Manual TL (d), Manual PPSI (e) for the Ballater granite A₁₀P₈₀Q₁₀ (2.62-2.74g/m³ SPT fraction).

B.7.2 Cairngorm Granite.

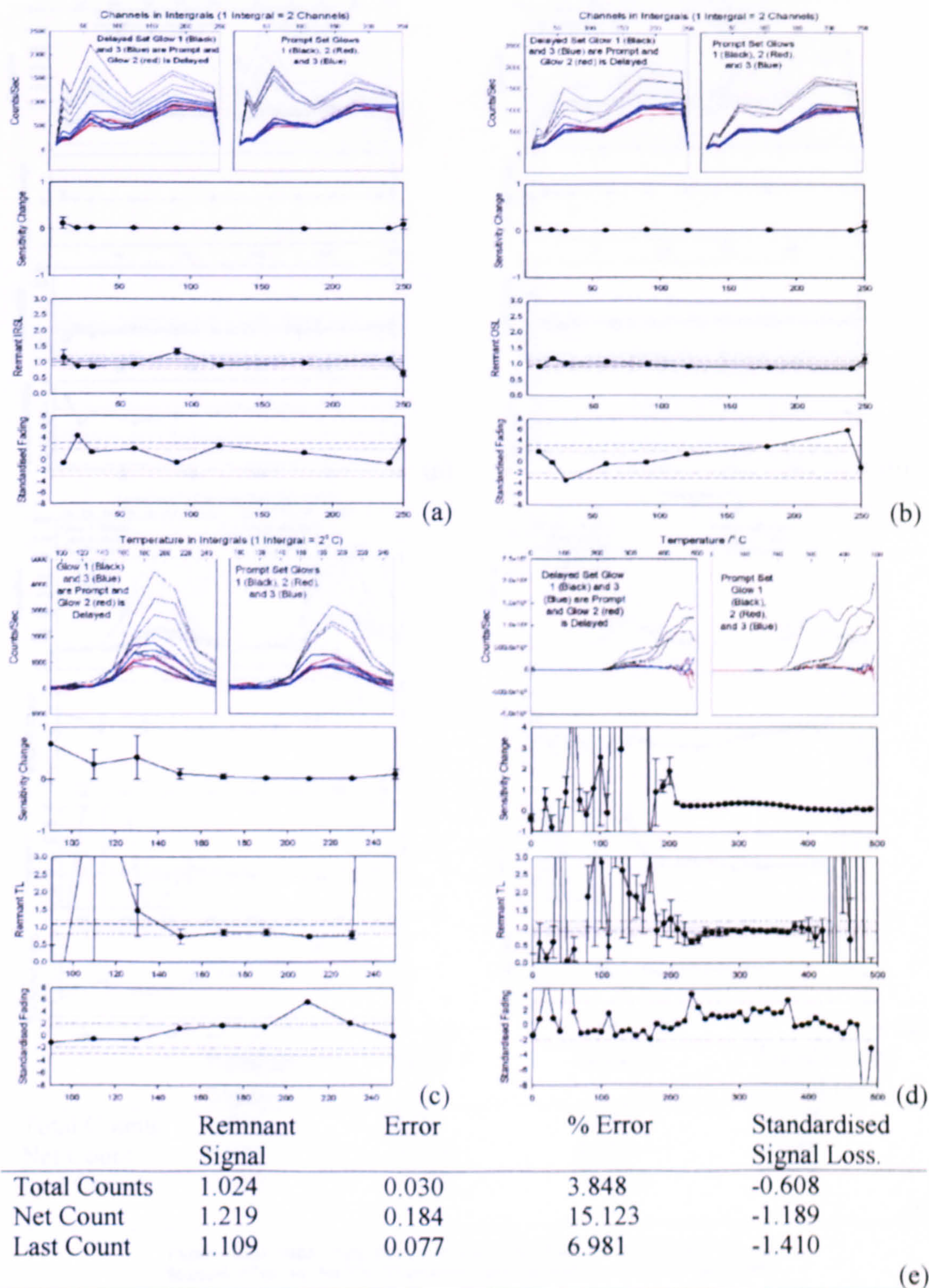


Figure B.32 Rise IRSI (a), Rise OSL (b), Rise TL (c), Manual TL (d), Manual PPSI (e) for the Cairngorm granite A₅₀P₄₅Q₅ (2.58-2.62g/m³ SPT fraction).

B.7.3 Shap Granite.

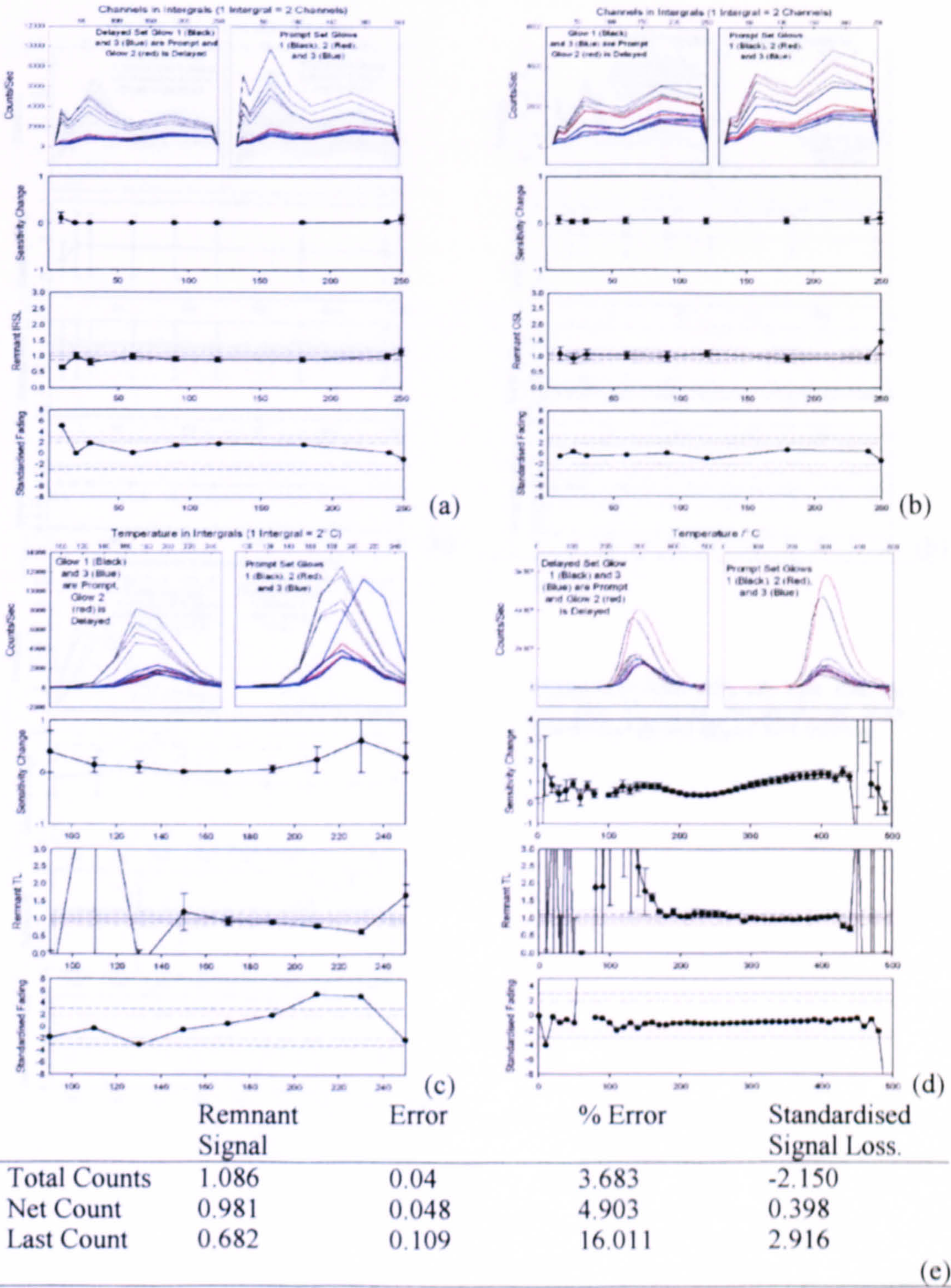
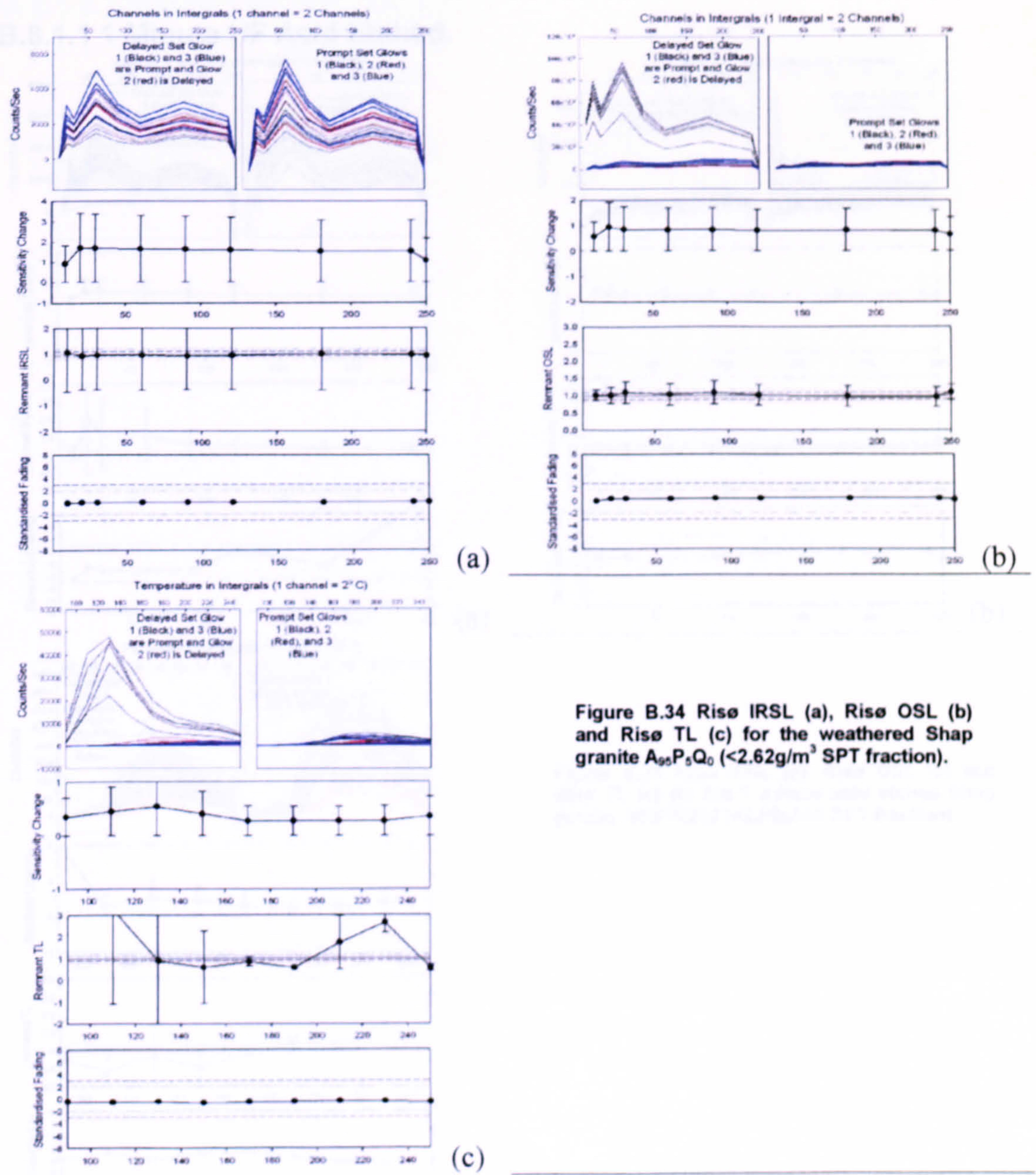


Figure B.33 Rise IRSL (a), Rise OSL (b), Rise TL (c), Manual TL (d), Manual PPSL (e) for the Cairngorm granite A₅P₅Q₉₀ (2.62-2.74g/m³ SPT fraction).

B.8 Artificially Weathered Feldspars

B.7.3 Shap Granite.



B.8 Artificially Weathered Feldspars.

B.8.1 Artificially Weathered Shap Granite.

B.8.1.1 1 Minute HF Acid Etched.

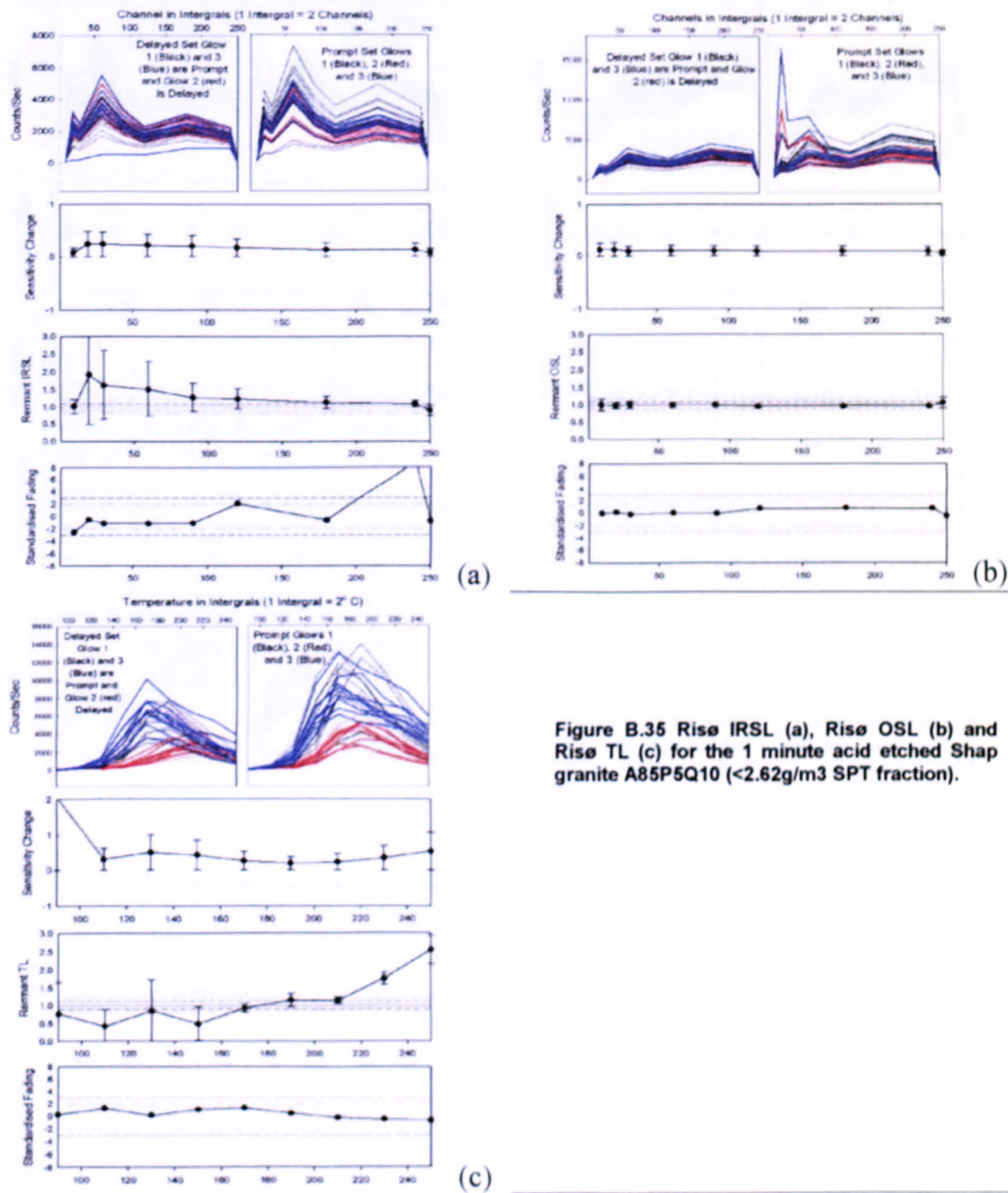


Figure B.35 Risø IRSL (a), Risø OSL (b) and Risø TL (c) for the 1 minute acid etched Shap granite A85P5Q10 (<2.62g/m3 SPT fraction).

B.8.1.2 3 Minutes HF Acid Etched.

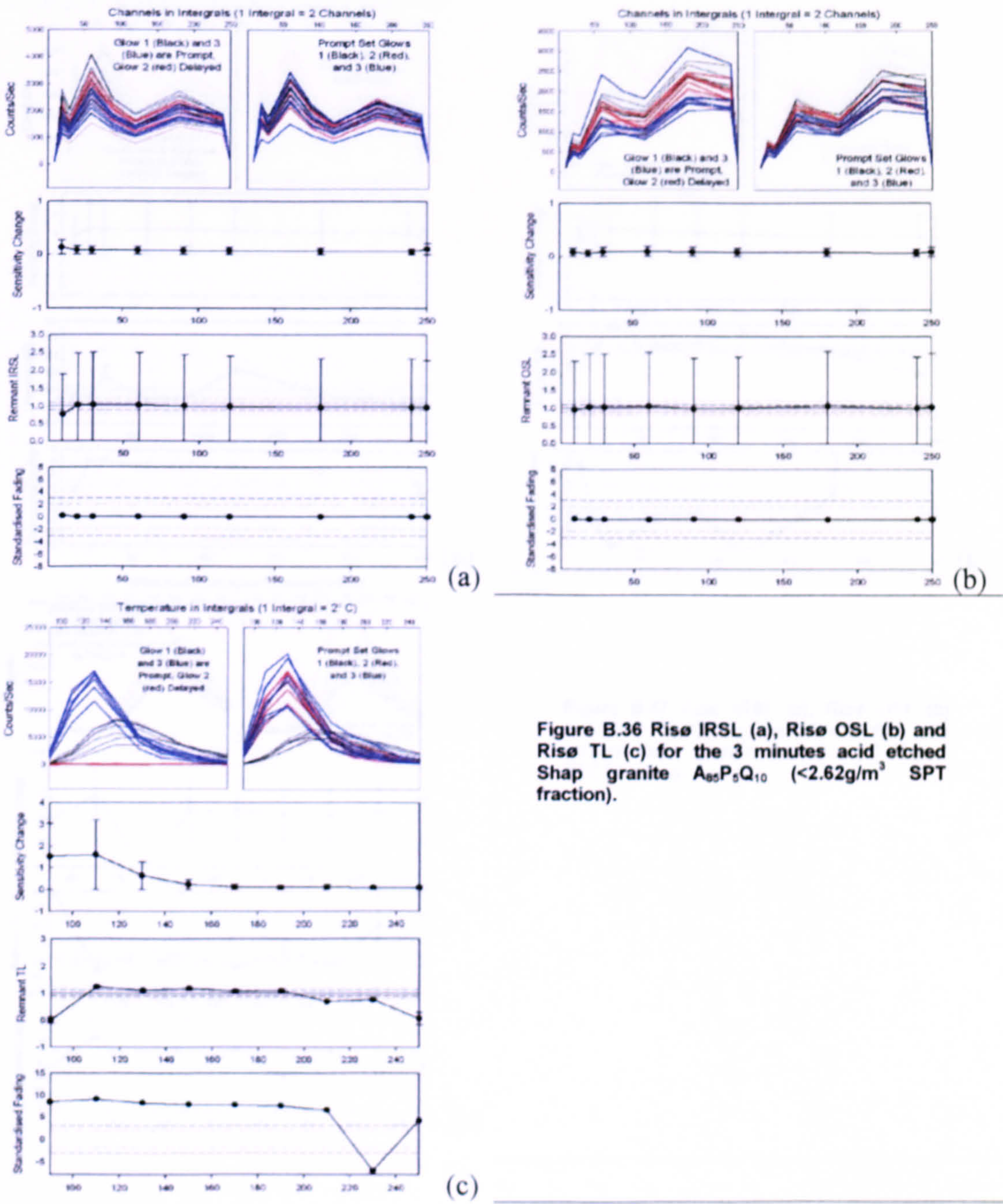
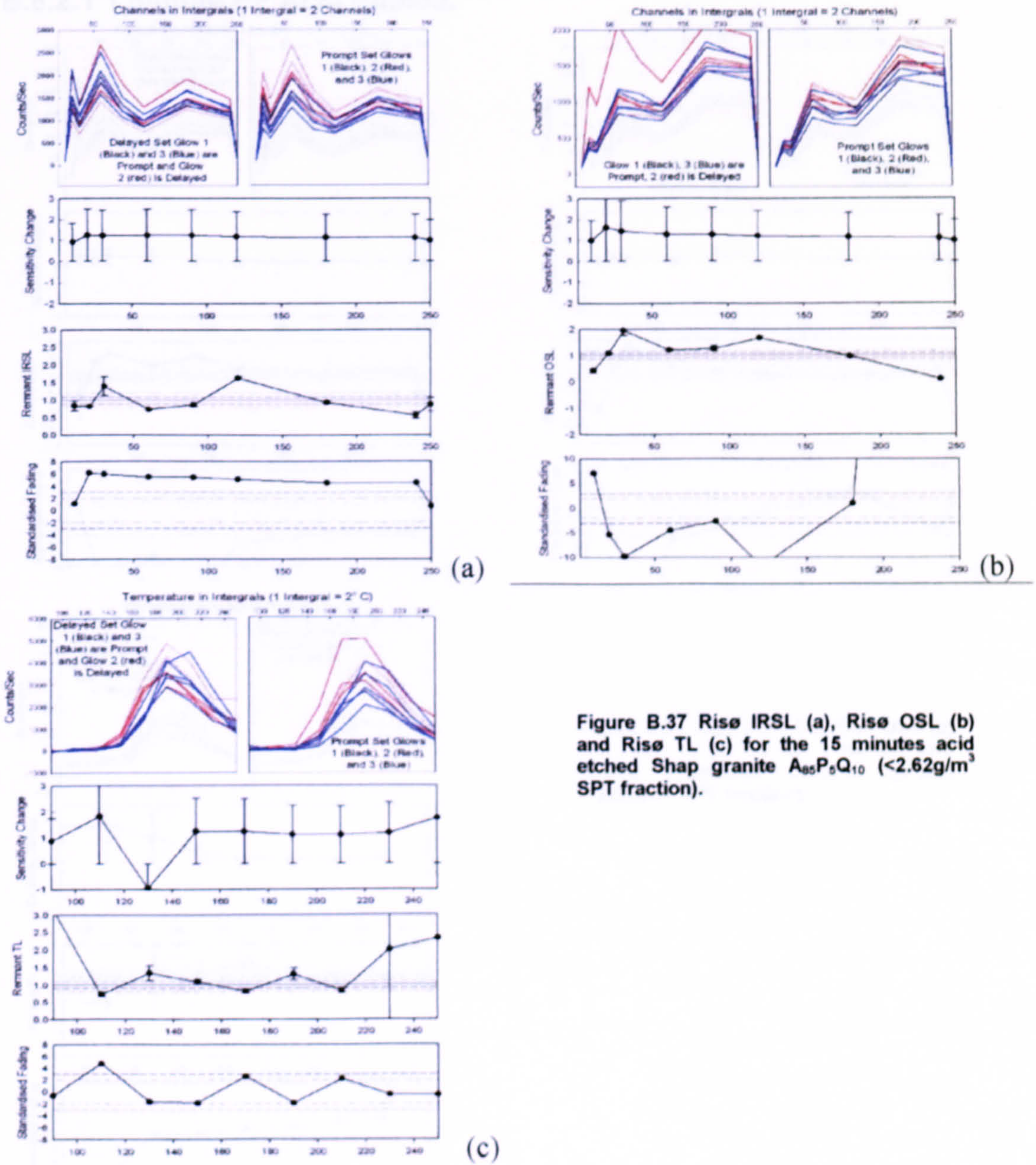


Figure B.36 Riso IRSL (a), Riso OSL (b) and Riso TL (c) for the 3 minutes acid etched Shap granite A₈₅P₅Q₁₀ (<2.62g/m³ SPT fraction).

B.8.2 Artificially Weathered Holmedale Arkose.

B.8.1.3 15 Minutes HF Acid Etched.



B.8.2 Artificially Weathered Helmsdale Arkose.

B.8.2.1 1 Minute HF Acid Etched.

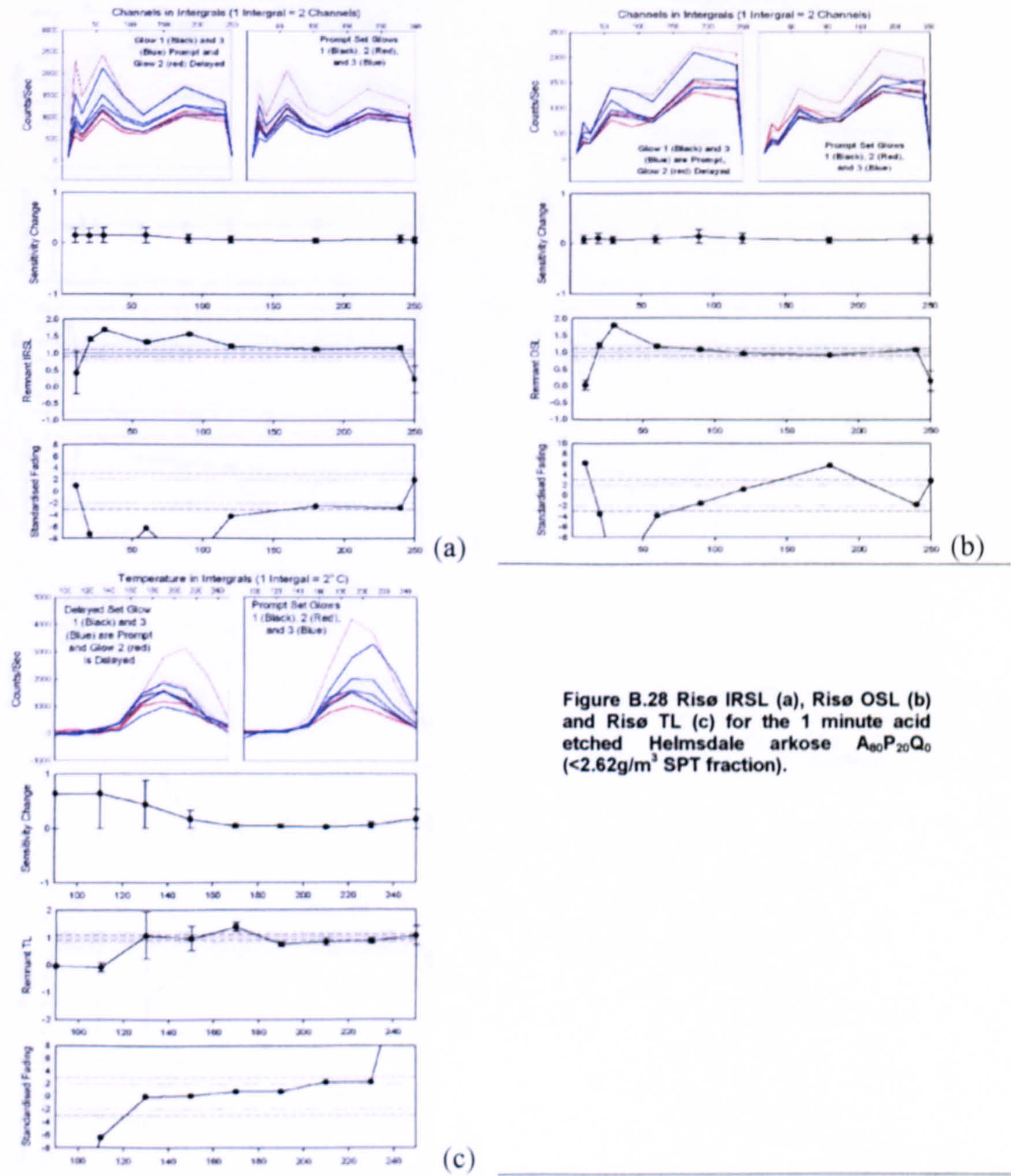


Figure B.28 Rise IRSL (a), Rise OSL (b) and Rise TL (c) for the 1 minute acid etched Helmsdale arkose $A_{80}P_{20}Q_0$ ($<2.62\text{g/m}^3$ SPT fraction).

B.8.2.2 3 Minutes HF Acid Etched.

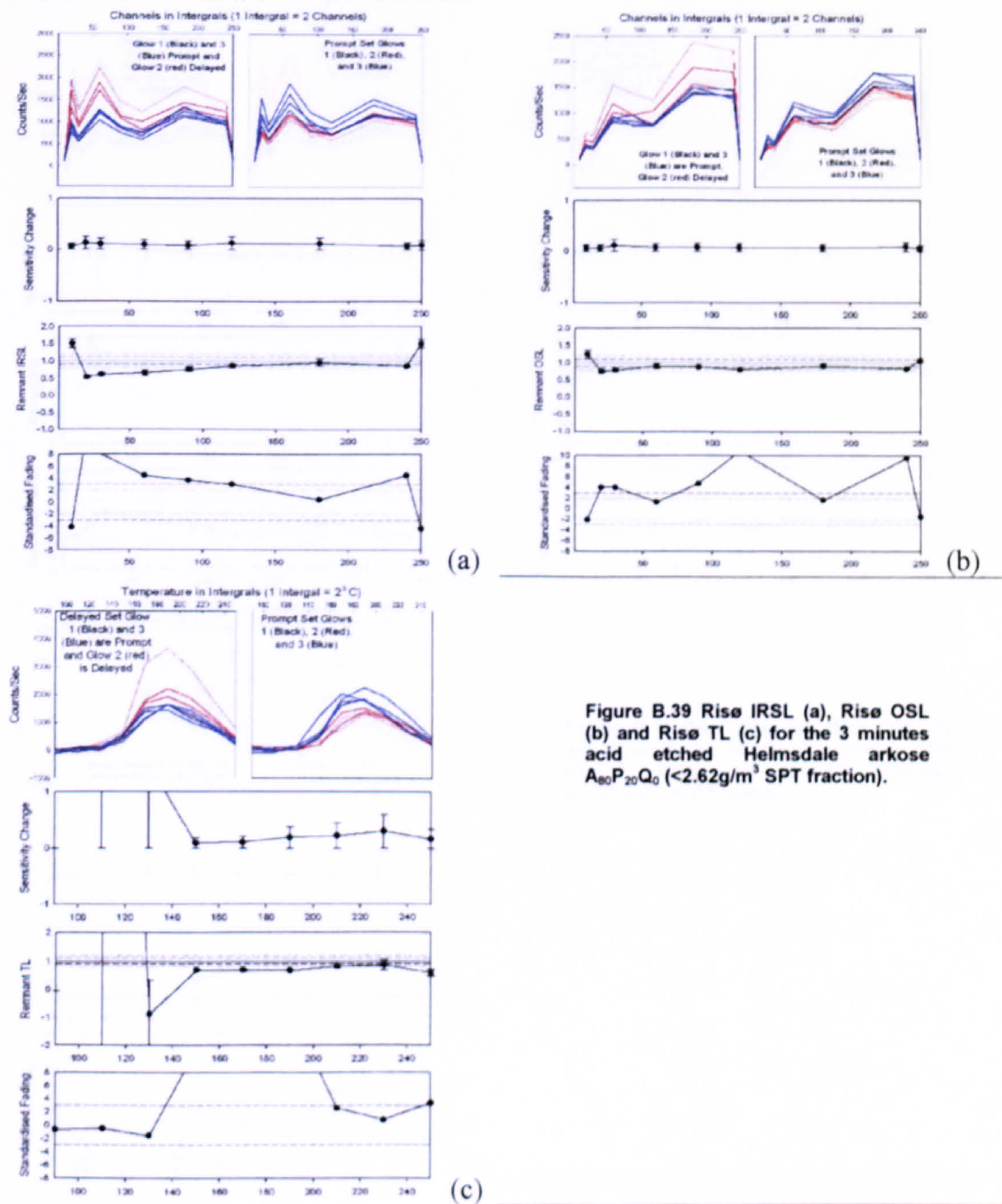


Figure B.39 Rise IRSL (a), Rise OSL (b) and Rise TL (c) for the 3 minutes acid etched Helmsdale arkose A₈₀P₂₀Q₀ (<2.62g/m³ SPT fraction).

B.8.3 Artificial Weathered Helmsdale Arkose

B.8.2.3 15 Minutes HF Acid Etched.

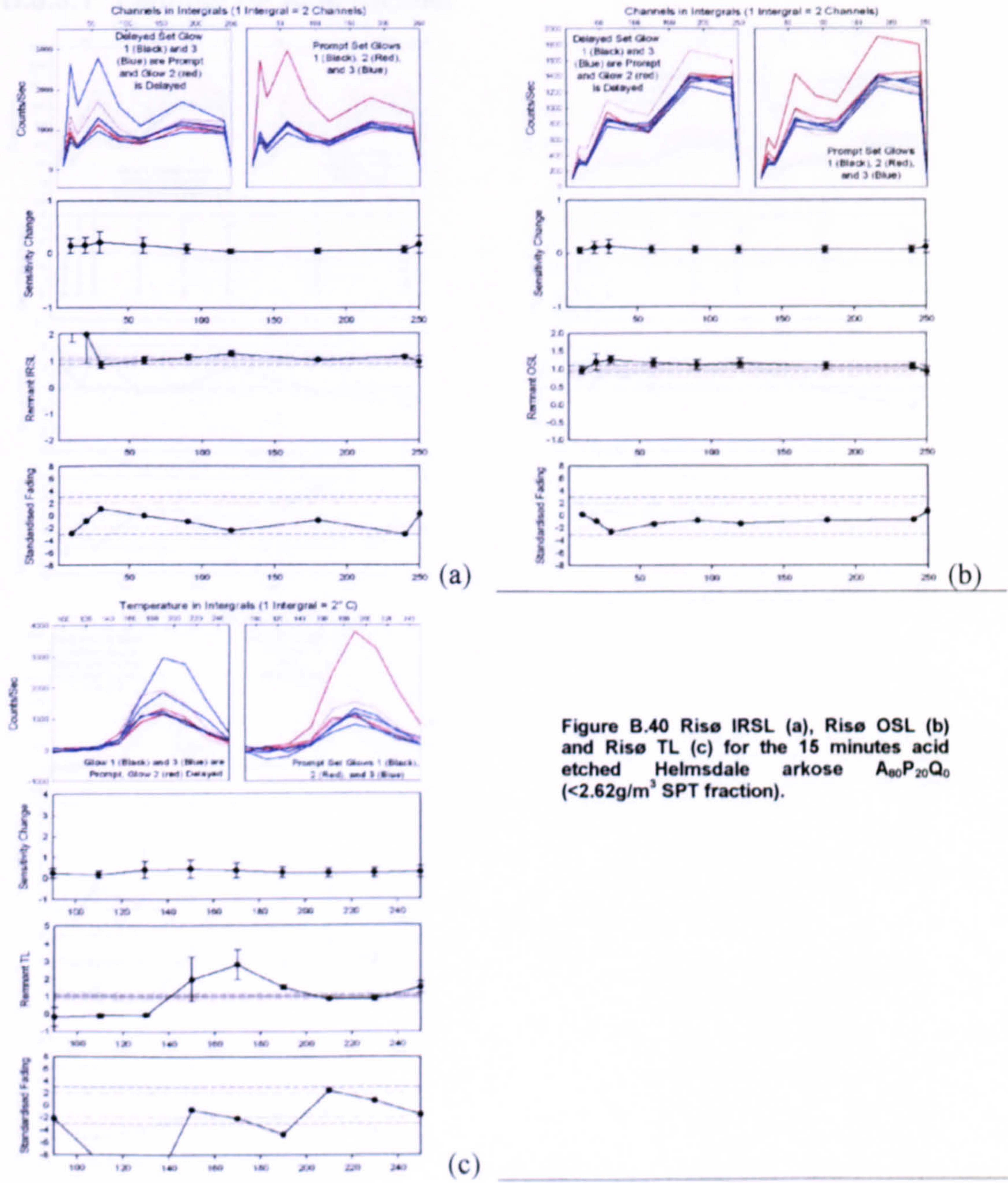


Figure B.40 Rise IRSL (a), Rise OSL (b) and Rise TL (c) for the 15 minutes acid etched Helmsdale arkose $A_{80}P_{20}Q_0$ ($<2.62\text{g/m}^3$ SPT fraction).

B.8.3 Artificially Weathered Helmsdale Granite.

B.8.3.1 1 Minute HF Acid Etched.

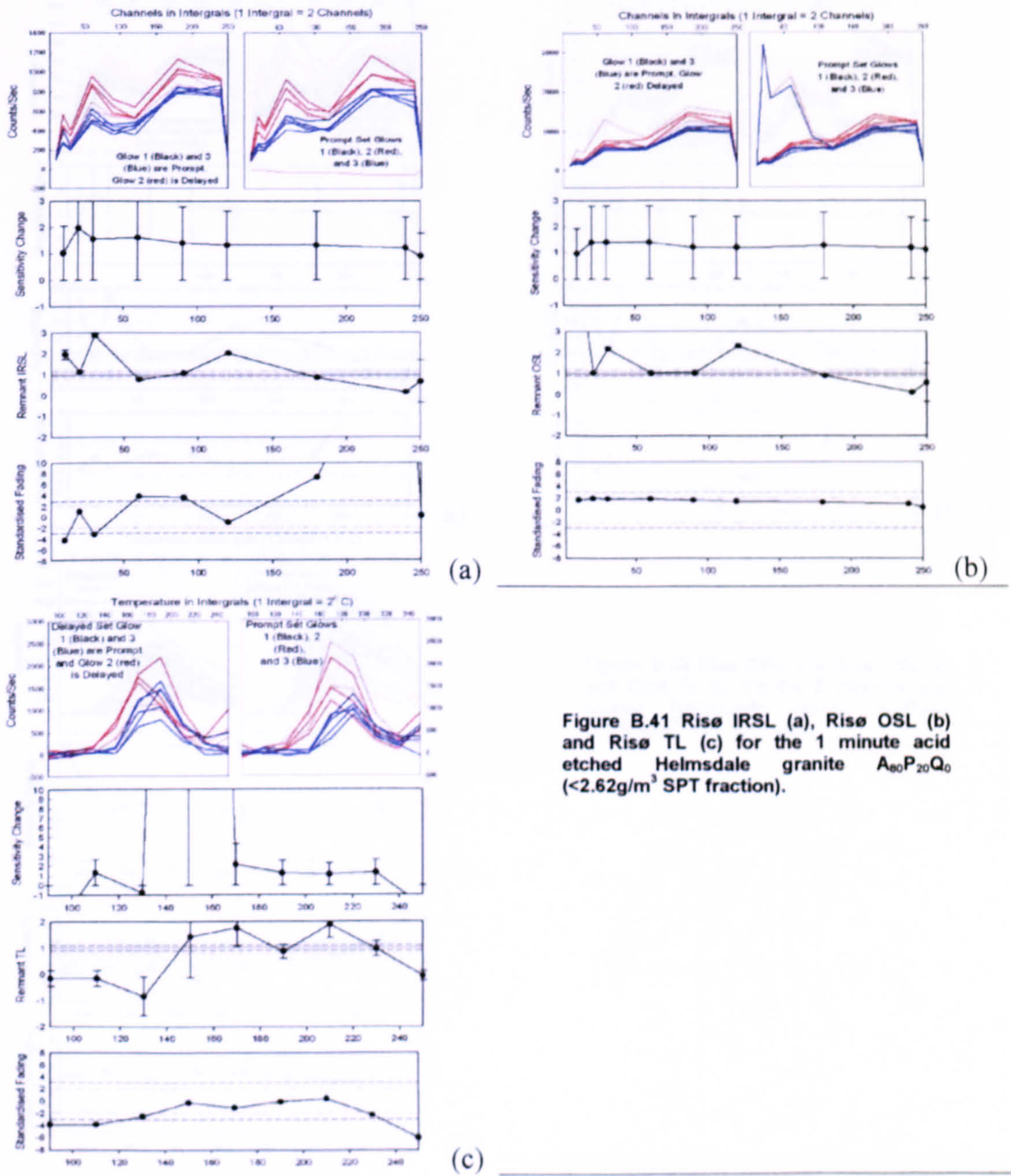


Figure B.41 Risø IRSL (a), Risø OSL (b) and Risø TL (c) for the 1 minute acid etched Helmsdale granite $A_{80}P_{20}Q_0$ ($<2.62\text{g/m}^3$ SPT fraction).

B.8.3.2 3 Minutes HF Acid Etched.

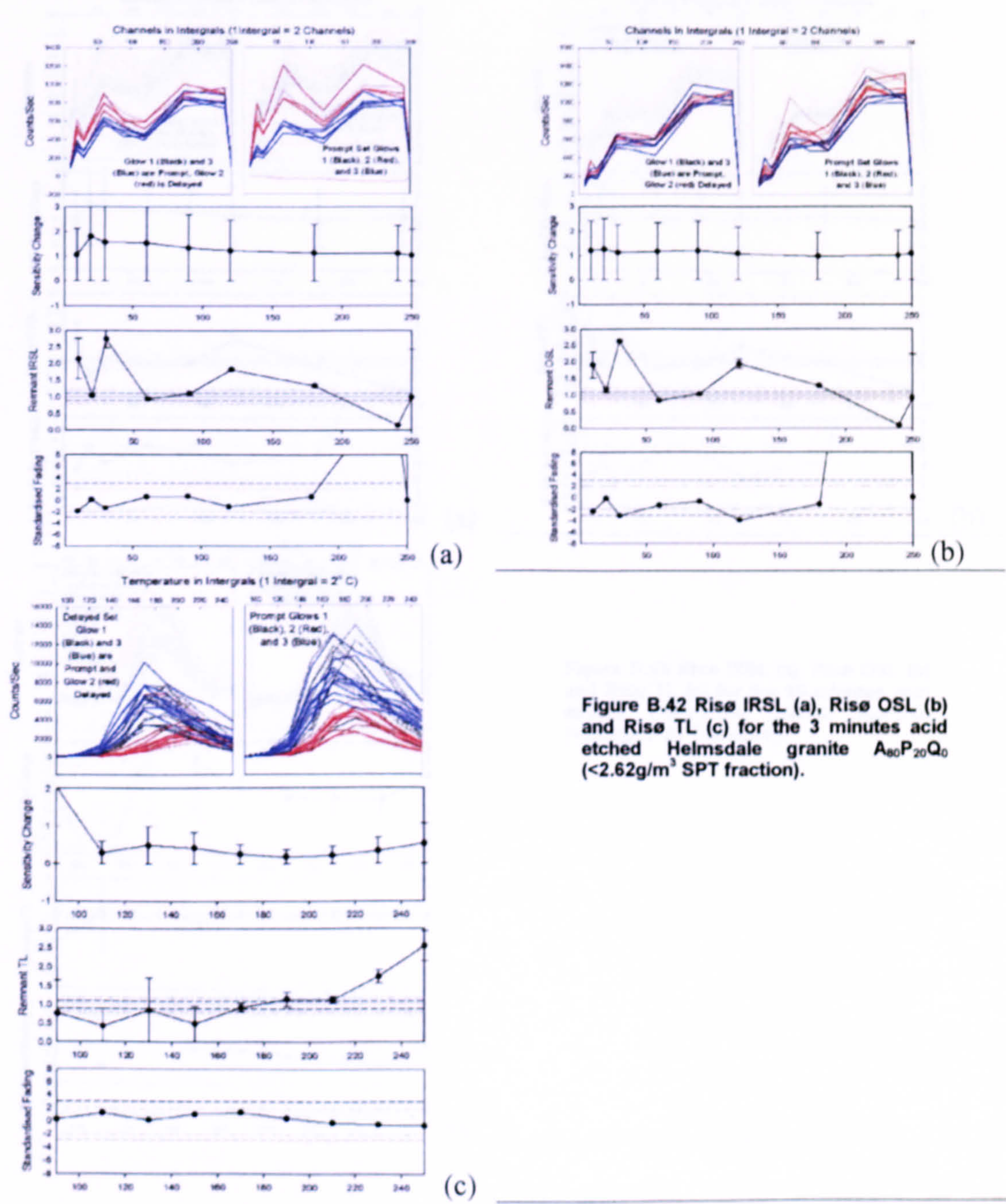


Figure B.42 Rise IRSL (a), Rise OSL (b) and Rise TL (c) for the 3 minutes acid etched Helmsdale granite $A_{80}P_{20}Q_0$ ($<2.62\text{g/m}^3$ SPT fraction).

B.9 Laboratory Standards

B.8.3.3 15 Minutes HF Acid Etched.

B.8.3.3.1

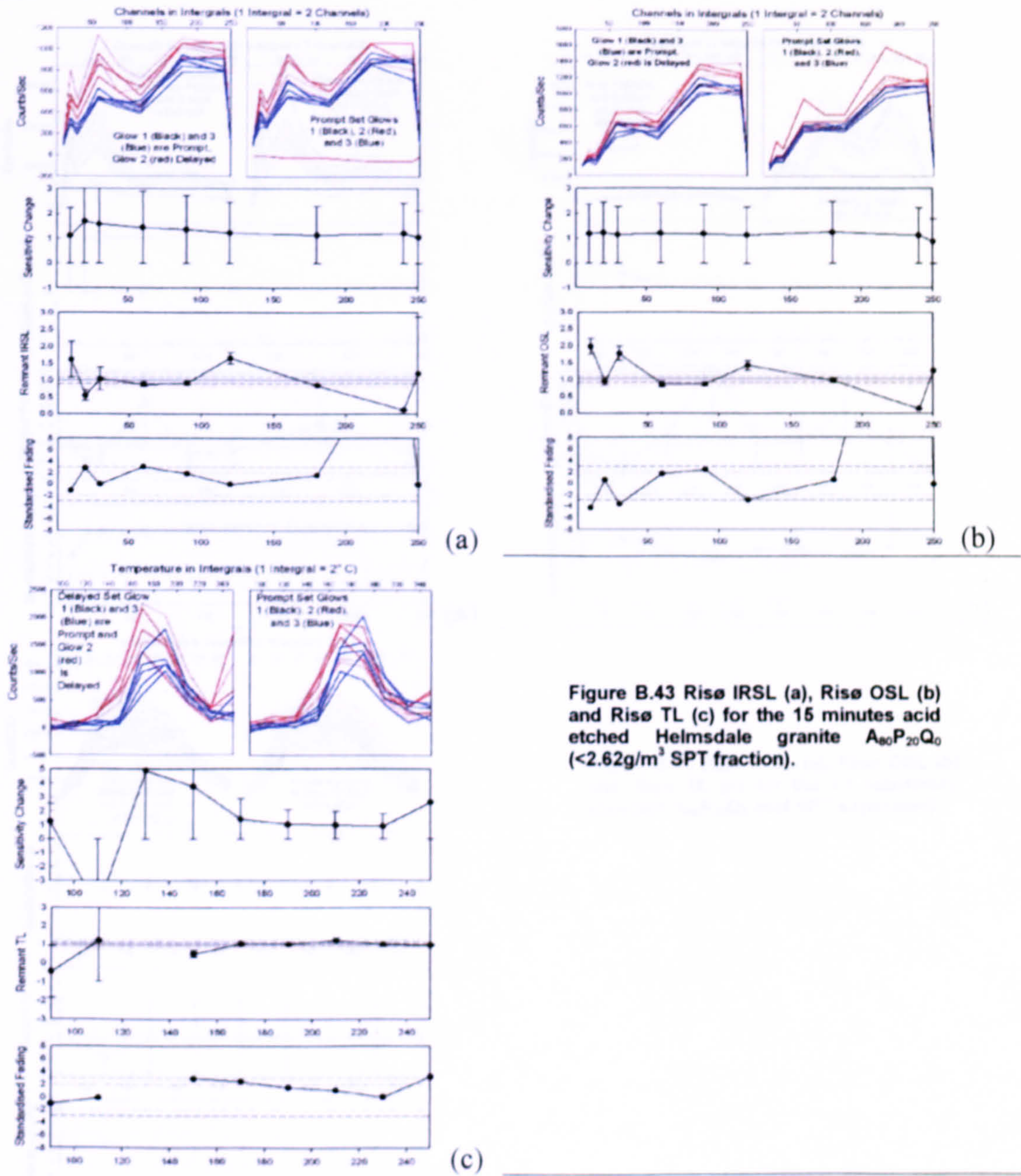


Figure B.43 Rise IRSL (a), Rise OSL (b) and Rise TL (c) for the 15 minutes acid etched Helmsdale granite A₈₀P₂₀Q₀ (<2.62g/m³ SPT fraction).

B.9 Laboratory Standard.

B.9.1 F1.

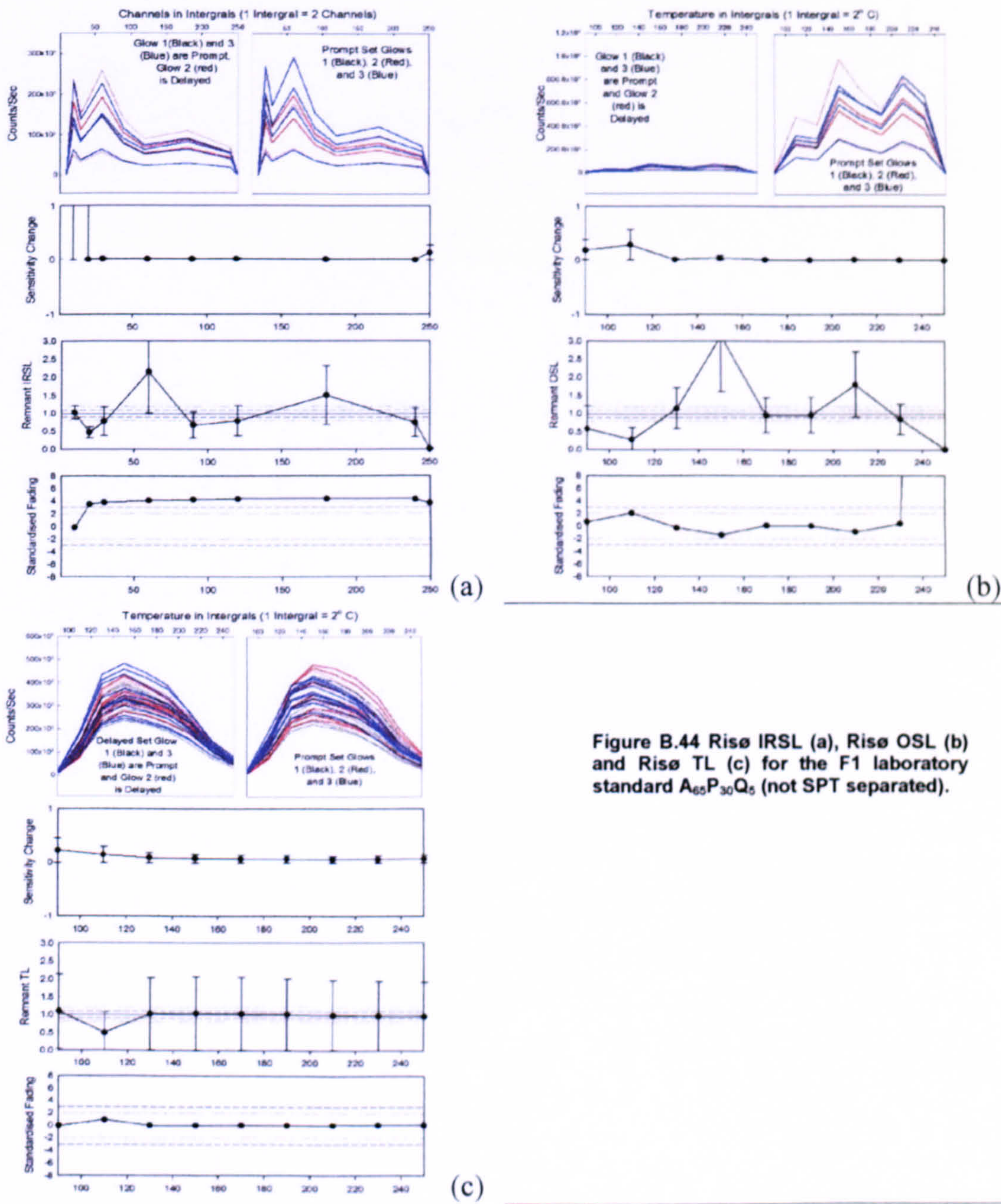


Figure B.44 Rise IRSL (a), Rise OSL (b) and Rise TL (c) for the F1 laboratory standard $A_{65}P_{30}Q_5$ (not SPT separated).



A.2.8 Ross of Mull Hydrothermal Syenite.

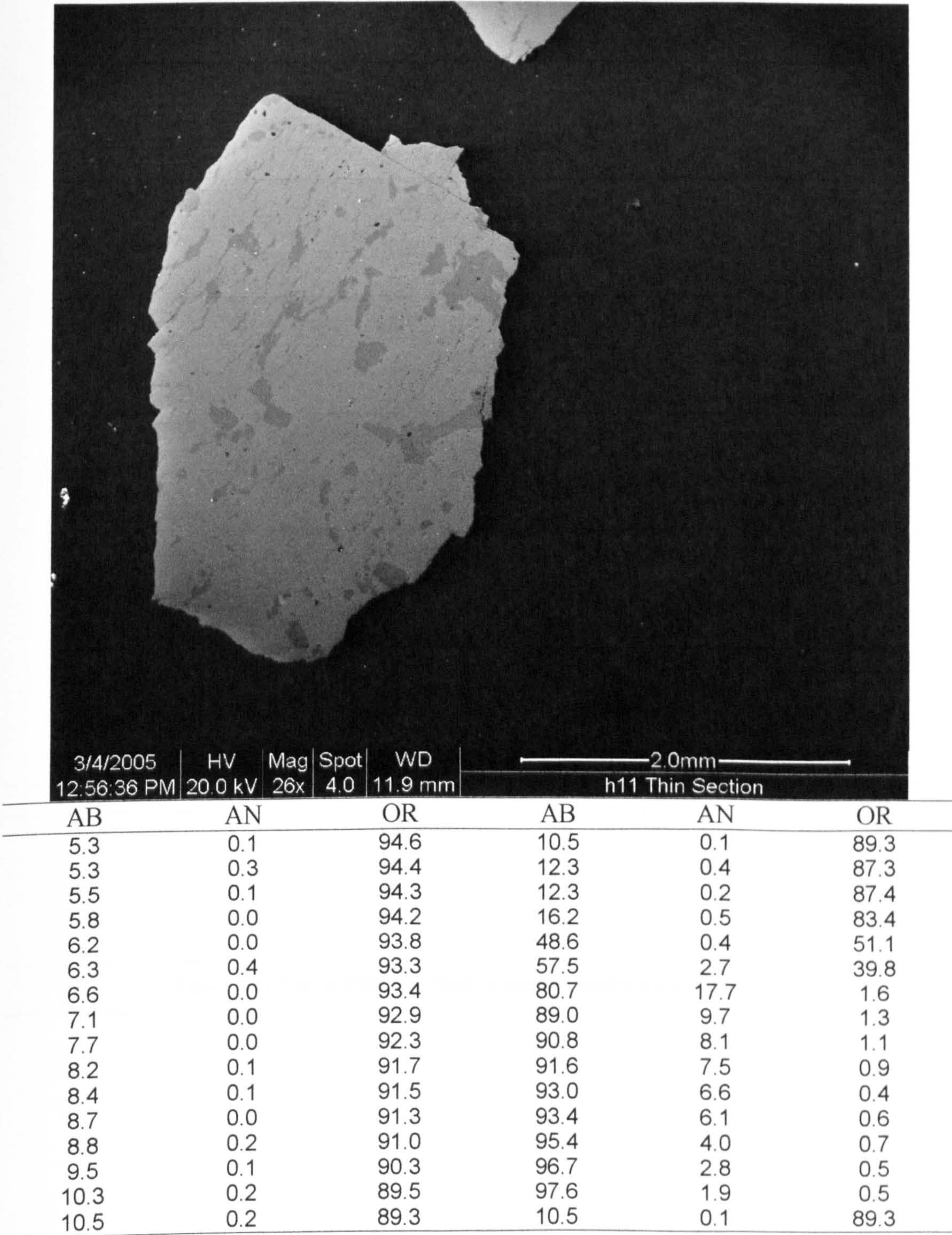


Figure A.12 Ross of Mull hydrothermal syenite – probe analysis results.